



HAL
open science

Mono-EndCapped Single-Ion Polymer Electrolytes : Synthesis & Lithium-Ion Transport Properties

Philip Overton

► **To cite this version:**

Philip Overton. Mono-EndCapped Single-Ion Polymer Electrolytes : Synthesis & Lithium-Ion Transport Properties. Polymers. Université Grenoble Alpes, 2019. English. NNT : 2019GREAV010 . tel-02191649

HAL Id: tel-02191649

<https://theses.hal.science/tel-02191649>

Submitted on 23 Jul 2019

HAL is a multi-disciplinary open access archive for the deposit and dissemination of scientific research documents, whether they are published or not. The documents may come from teaching and research institutions in France or abroad, or from public or private research centers.

L'archive ouverte pluridisciplinaire **HAL**, est destinée au dépôt et à la diffusion de documents scientifiques de niveau recherche, publiés ou non, émanant des établissements d'enseignement et de recherche français ou étrangers, des laboratoires publics ou privés.

THÈSE

Pour obtenir le grade de

DOCTEUR DE LA COMMUNAUTE UNIVERSITE GRENOBLE ALPES

Spécialité : **Sciences des Polymères**

Arrêté ministériel : 25 mai 2016

Présentée par

Philip OVERTON

Thèse dirigée par **Patrice RANNOU, Directeur de Recherche au CNRS, UMR5819-SYMMES (CNRS/CEA/UGA)**

et

encadrée par **Lionel PICARD, Ingénieur-chercheur au CEA CEA/DRT/LITEN/DEHT**

préparée au sein du **Commissariat à l'Énergie Atomique et aux Énergies Alternatives (CEA) de Grenoble, Laboratoire d'Innovation pour les Technologies des Énergies Nouvelles et des Nanomatériaux (Liten)**
dans l'**École Doctorale Chimie et Sciences du Vivant**

Electrolytes polymères monofonctionnels à conduction monocationique: Synthèse & propriétés de transport d'ions lithium

Mono-Endcapped Single-Ion Polymer Electrolytes: Synthesis & Lithium-ion Transport Properties

Thèse soutenue publiquement le 27 Mars 2019
devant le jury composé de :

M. Renaud BOUCHET

Professeur à Grenoble-INP
Laboratoire de Chimie et de Physicochimie
des Matériaux et des Interfaces (LEPMI)

Président/Examinateur

M. Bruno AMEDURI

Directeur de Recherche au CNRS
Institut Charles Gerhardt Montpellier (ICGM)

Rapporteur

M. Eric DROCKENMULLER

Professeur à l'Université Claude Bernard Lyon I
Laboratoire Ingénierie des Matériaux Polymères (IMP)

Rapporteur

M. Eric LAFONTAINE

Ingénieur au Ministère des Armées
Direction Générale de l'Armement (DGA)

Examinateur

Mme. Françoise MECHIN

Chargé de Recherche au CNRS
Laboratoire Ingénierie des Matériaux Polymères (IMP)

Examinateur



Acknowledgements

The doctoral candidate Philip Overton acknowledges the principled and focussed contributions of his experienced and insightful co-supervision team, of thesis director Dr. Patrice Rannou (CNRS/UMR5819-SyMMES Lab), and co-supervisor Dr. Lionel Picard (CEA/DRT/Liten/DEHT/STB/LM Lab).

Detailed and thoroughly considered advices were generously given by Prof. Renaud Bouchet (Grenoble-INP/UMR5279-LEPMI Lab) and Prof. Olli Ikkala (Aalto University/Dept. of Applied Physics/MolMat Lab) in the framework of the *Comité de Suivi Individuel* (CSI). I gratefully acknowledge their attention to the progress and interest in the development of this work. Their excellence in the research domains most pertinent to this thesis was evident in their constructive comments and advice during the three years of the research.

The synthetic chemistry and numerous characterisations were conducted at the Laboratoire de Matériaux (CEA/DRT/Liten/DEHT/STB/LM) at CEA-Grenoble. I thank the R&D team manager Dr. Didier Bloch and the head of the service, Dr. Sébastien Patoux.

Electrochemical impedance spectroscopy (EIS) was conducted at the laboratoire des Systèmes Moléculaires et nanoMatériaux pour l'Energie et la Santé (UMR5819-SyMMES (CNRS/CEA/UGA)) within the premises of the Institut Nanosciences & Cryogenics (INAC), at CEA-Grenoble, under guidance of Dr. Patrice Rannou and Dr. Manuel Maréchal. Their advice and expertise are gratefully acknowledged. The analysis of those data was inspired by their precise and thoughtful appraisal of the results.

This project is indebted in equal parts to financing by the *Commissariat à l'Energie Atomique et aux Energies Alternatives* (CEA) and the *Direction Générale de l'Armement* (DGA). I am grateful for the review of this work, in the forms of oral presentations and written reports, by Dr Florence Lefebvre-Joud at CEA-Grenoble/Liten and in the domain "Materiaux Chimie et Energie" (MCE) at DGA by Dr. Eric Lafontaine.

I thank in advance the jury examining this thesis, for their close inspection and evaluation of the work: Dr. Bruno Ameduri (CNRS/Institut Charles Gerhardt Montpellier (ICGM)), Prof. Renaud Bouchet (Grenoble-INP/Laboratoire de Chimie et Physicochimie des Materiaux et Interfaces (LEPMI)), Prof. Eric Drockenmuller (Université Claude Bernard Lyon I/Laboratoire Ingénierie des Matériaux Polymères (IMP)), Dr. Eric Lafontaine (Ministère des Armées/Direction Générale de l'Armement (DGA)), and Dr. Françoise Mechin (CNRS/Laboratoire Ingénierie des Matériaux Polymères (IMP)).

The help of kind colleagues at STB/LM (and beyond!) was very much appreciated. They know who they are because I have told them many times.

General Abstract in English

This thesis presents "**MonoEnd-Capped Single-Ion Polymer Electrolytes**" (**MEC-SIPes**) that are ionically conductive polymers having n repeating ethylene oxide (EO) units and an ionic functional group at one chain terminal. The library of MEC-SIPes presented are based on poly(ethylene oxide) mono methyl ether (mPEO $_n$ -OH) having EO $_n$ = 8, 10, 20, and 55. The anions of the electrolyte salt pair are covalently bound to the polymer as part of the end-group design. The mobility of the anion is thus limited by the low mobility of the polymer, relative to Li $^+$. These are "Single-Ion" conductors because the majority of ionic charge transferred by Li $^+$ cations, as demonstrated by chronoamperometry.

The end-group designs target not only ionic interactions that facilitate "Single-Ion" conduction of Li $^+$, but also other specific non-covalent interactions such as dipole-dipole, Van der Waals, and π - π stacking. End-groups having naphthalene (naph) and pyrene (pyr) **Polycyclic Aromatic Hydrocarbon (PAH)** moieties are investigated. The functional end-groups are lithiated sulfonates (-SO $_3$ Li, -PhSO $_3$ Li), a *N*-naphyl sulfonamide (-SO $_2$ N(Li)Naph), and secondary *N*-aryl amines (-N(Li)Naph, -N(Li)Pyr). Two end-groups target specific properties: **i**) a "double salt" end-group has two ionic functions at one chain end, and **ii**) a zwitterionic chain terminal that conducts Li $^+$ cations and TFSI $^-$ anions. The doubling of the number of Li $^+$ per end-group does not correlate to an expected improvement in ionic conductivity (σ). This implies that σ is limited by the physicochemical properties of the MEC-SIPE and not the Li $^+$ concentration. The zwitterionic chain terminal polymer electrolyte has a high lithium transference number (t_{Li}^+ = 0.8) that implies decreased mobility of the TFSI $^-$ counter-anion relative to Li $^+$. The best overall performance is achieved by mPEO $_n$ -N(Li)Pyr (EO $_n$ = 10, 20, 55), that has $\sigma_{AC} > 1.0 \cdot 10^{-4}$ S.cm $^{-1}$ at $T > 40$ °C, and reaches $1 \cdot 10^{-3}$ S.cm $^{-1}$ at 100 °C. It exhibits constant resistivity under galvanostatic cycling ($j = 10$ μ A.cm $^{-2}$, 10*4h periods, Li|Li cell, 40 °C) and is electrochemically stable in the 0 V-3.7 V vs. Li/Li $^+$ potential range.

In **Chapter I** the *state-of-the-art* polymer electrolytes for Li-ion batteries are reviewed. These are divided into two sub-classes: **i**) **Salt-in-Polymer (SiP)** and **ii**) "**Single-Ion**" **Polymer Electrolytes (SIPes)**. The design of polymer electrolytes towards efficient and effective ionic conductivity is emphasized. Special attention is given to concepts for the organisation of bulk morphology for the creation of ion transport pathways that efficiently percolate through the micron length scale separating electrodes of a battery. Finally, the synthetic strategy implemented is described.

The principle results of the thesis are presented and discussed in **Chapter II**. A library of MEC-SIPes are characterised in terms of their electrochemical, thermal and specific ion-transport performances. Resistive features appear at high temperature and are expected to result from the aggregation of ionic end-groups. Surprisingly, the σ_{AC} of MEC-SIPes having EO $_n$ = 55 improves by as much as half an order of magnitude with repeated cycling of temperature to above T_m of crystalline PEO (in the +40 °C to +100 °C range). The analysis of MEC-SIPes having different end-groups and PEO chains having EO $_n$ = 8, 10, 20, and 55 lead to the proposition of a tentative model for the percolation of ionic pathways through the MEC-SIPE bulk. It is hypothesized that the ionic end-groups are localised at the grain boundaries of PEO domains. Percolation of these boundaries are proposed to be improved under appropriate, mild conditions of temperature and electromagnetic force. Finally, the synthesis methods implemented in this thesis and characterizations of MEC-SIPes are described in **Chapter III**.

Résumé de la Thèse en Français

Cette thèse décrit des électrolytes polymères monofonctionnels à conduction monocationique (**MEC-SIPes**). Ces macromolécules sont constituées de n unités de répétition d'oxyde d'éthylène (OE) et d'un groupe fonctionnel ionique à une des extrémités de leur architecture macromoléculaire asymétrique. La bibliothèque des MEC-SIPes synthétisés est basée sur des poly(oxyde d'éthylène) mono méthyl éther (mPOE_n-OH) ayant 8, 10, 20 et 55 unités OE. Les anions sont liés de manière covalente au squelette polymère via une des extrémités. Leur mobilité est donc limitée par celles de ces macromolécules fonctionnelles. Les MEC-SIPes constituent des conducteurs monocationiques; la majorité des charges étant transférées par les cations Li⁺ comme démontré par chronoampérométrie.

Les extrémités de chaînes sont sélectionnées pour développer des interactions ioniques facilitant la conduction de cation Li⁺ ainsi que des interactions non-covalentes de types dipôles-dipôles, Van der Waals, et d'empilements π . Des hydrocarbures aromatiques polycycliques de type naphthalène (naph) et pyrène (pyr) sont étudiés comme extrémités de chaînes. Les groupes terminaux fonctionnels sont lithiés : sulfonates (-SO₃Li, -PhSO₃Li), *N*-naphthyl sulfonamide (-SO₂N(Li)Naph) et *N*-arylamines (-N(Li)Naph, -N(Li)Pyr). Deux types d'extrémités ciblent des propriétés spécifiques : **i**) "double-sel" possédant deux fonctions ioniques et **ii**) zwitterionique conduisant le cation Li⁺ et l'anion TFSI⁻. Le doublement du nombre de Li⁺ par groupe terminal n'autorise pas l'amélioration attendue de la conductivité ionique (σ). Ceci implique que σ est limitée par la physicochimie des chaînes polymères et non par la concentration en Li⁺. L'électrolyte polymère zwitterionique a un nombre de transport de lithium élevé ($t_{Li^+}^+ = 0,8$) qui implique une mobilité réduite de l'anion TFSI⁻ par rapport au cation Li⁺. La meilleure performance est obtenue avec le mPOE_n-N(Li)Pyr (OE_n= 10, 20, 55) : $\sigma_{AC} > 1,0 \cdot 10^{-4} \text{ S.cm}^{-1}$ à $T > 40 \text{ }^\circ\text{C}$ et $1 \cdot 10^{-3} \text{ S.cm}^{-1}$ à $100 \text{ }^\circ\text{C}$. Ce MEC-SIPE garde une résistivité constante sous cyclage galvanostatique ($j = 10 \text{ } \mu\text{A.cm}^{-2}$; 10 périodes de 4h ; pile Li|Li ; $40 \text{ }^\circ\text{C}$) et une stabilité électrochimique dans la plage de potentiel 0 V-3,7 V vs. Li/Li⁺ (pile Li|acier inoxydable; vitesse de balayage en potentiel $1,0 \text{ mV.s}^{-1}$; $40 \text{ }^\circ\text{C}$).

Le contexte de cette thèse vis à vis de l'état de l'art des électrolytes polymères pour les batteries Li-Ion est présenté dans le **chapitre I**. Deux sous-classes d'électrolytes sont discutées : **i**) les polymères dans lesquels un sel est solvaté (**SiP**) et **ii**) les polymères à conduction monocationique (**SIPes**). La conception d'électrolytes polymères efficaces à conductivité ionique améliorée est ciblée. Une attention toute particulière est accordée aux concepts d'auto-organisation hiérarchique visant à la création de chemins percolant assurant le transport d'ions sur les distances microniques séparant les électrodes d'une batterie. Enfin, la stratégie de synthèse mise en œuvre est décrite.

Les principaux résultats de cette thèse sont présentés et discutés au **chapitre II**. Une bibliothèque de MEC-SIPes est caractérisée vis-à-vis de leurs performances électrochimiques, thermiques et de leurs propriétés de transport ionique spécifiques. Des caractéristiques résistives apparaissent à haute température et sont supposées résulter de l'agrégation des groupes ioniques terminaux. Les valeurs de conductivité σ_{AC} des MEC-SIPes (55 Unités OE) s'améliorent d'un demi-ordre de grandeur lors du cyclage en température au-delà de la température de fusion des domaines cristallins de POE. La discussion se termine par la proposition d'un modèle de percolation des domaines ioniques dans les MEC-SIPes où les groupes ioniques sont localisés aux interfaces des domaines POE. La percolation des domaines ioniques devrait être améliorée dans des conditions appropriées de température et de force électromagnétique. Les méthodes de synthèse mises en œuvre dans cette thèse et les caractérisations des MEC-SIPes sont décrites au **chapitre III**.

Overview of Contents

Chapter I

I.	Polymer Electrolytes for Lithium-Ion Batteries: Context and <i>State of the Art</i>	7
1.	Lithium-Ion Batteries for Modern Electrochemical Energy Storage Technology.....	11
2.	Salt-In-Polymer Electrolytes for Lithium-Ion Batteries.....	12
3.	"Single-Ion" Polymer Electrolytes (SIPes).....	34
4.	Organisation of Soft Matter: Beyond Block Copolymers	42
5.	General Conclusions on Polymer Electrolytes for Lithium Ion Batteries	47
6.	Synthesis Strategy	49
7.	Bibliography of Chapter I.....	53

Chapter II

II.	MonoEnd-Capped Single-Ion Polymer Electrolytes (MEC-SIPes) for Lithium-Ion Transport: Results and Discussion	63
1.	Introduction.....	67
2.	Electrochemical Characterisation of MEC-SIPes	70
3.	Thermal Characterisation of MEC-SIPes.....	104
4.	Ion Transport in MEC-SIPes	123
5.	General Conclusions	160
6.	Perspectives.....	161
7.	Bibliography of Chapter II.....	163

Chapter III

III.	Experimental	165
1.	Instrumentation and Measurements	169
2.	Materials.....	171
3.	Variation of Polymer M_n According to Poly(ethylene oxide) methyl ether.....	174
4.	Synthesis of MEC-SIPes: Mono-Salts	175
5.	Synthesis of MEC-SIPes: Zwitterionic and "Double-Salt" End-Capped Polymers.....	191
6.	Conclusions on the Synthesis and Chemical Characterisation of End-Capped Single-Ion Polymer Electrolytes.....	211
7.	Bibliography of Chapter III.....	213
IV.	General Conclusion.....	215
V.	Dissemination of Results	216
VI.	List of Figures.....	217
VII.	List of Tables.....	228
VIII.	List of Abbreviations.....	231
IX.	Annex: ^1H NMR Spectra of MEC-SIPes.....	233

Chapter I

Polymer Electrolytes for Lithium-Ion Batteries: Context and *State of the Art*

Resumé

Le **chapitre I** présente le contexte de cette thèse par rapport à l'état de l'art du domaine. Les batteries lithium-ion (**LiBs**: Lithium ion Batteries) sont présentées en lien avec les applications modernes de stockage électrochimique de l'énergie. Les électrolytes polymères sont ensuite divisés en deux sous-classes : les électrolytes dans lesquels un sel est solvatoé dans une matrice polymère hôte ("**Salt-in-Polymer**" (**SiP**)) et les électrolytes polymères à conduction monocationique (**SIPEs** : Single-Ion Polymer Electrolytes)

Les électrolytes SiP sont présentés de manière générale à travers une description de leurs caractéristiques principales. Une attention particulière est ensuite accordée à la manière dont les chercheurs ont tenté d'optimiser les électrolytes SiP. Plus précisément, leurs formulations et architectures macromoléculaires sont discutées. Cet état des lieux est mis à jour en prenant en compte les efforts récents consentis pour organiser les matrices et les polymères SiP qui ont été suggérés comme des alternatives aux formulations traditionnelles à base de poly(éther)s.

Les **SIPEs** sont ensuite discutés en mettant l'accent sur les principes de leur ingénierie. Les méthodes contemporaines de synthèse des SIPEs sont décrites et discutées en termes de performances électrolytiques. Les SIPEs à extrémités de chaînes modifiées à façon par des fonctions ioniques destinées à assurer le transport des cations Li^+ présentent une combinaison d'intérêts de par **i)** leur conductivité ionique élevée, **ii)** la simplicité de leur ingénierie macromoléculaire et **iii)** l'efficacité de cette chimie pour améliorer les performances des SIPEs. Les "**MonoEnd-Capped Single-Ion Polymer Electrolytes**" (**MEC-SIPEs**) se sont inspirés du développement des SIPEs en impulsant une réflexion originale dépassant les approches traditionnelles pour optimiser les performances électrolytiques.

Les récentes avancées dans l'auto-organisation des matériaux macromoléculaires fonctionnels sont proposées en termes de piste de réflexion pour ressourcer le domaine du transport ionique dans les électrolytes polymères. Après une discussion sur les stratégies basées sur la micro-ségrégation de phase des copolymères à blocs, des alternatives sont proposées. L'ingénierie de groupements terminaux capables de diriger la structuration des chaînes polymères sont présentés comme un outil synthétique puissant permettant d'ajuster la morphologie de ces polymères de fonction. Celles-ci sont élaborées en fonction de leur potentiel de rupture scientifique pour le développement des MEC-SIPEs.

La stratégie de synthèse mise en œuvre dans cette thèse est ensuite décrite. Elle est basée sur la modification des groupes terminaux hydroxyles d'éthers monométhyliques de poly(oxyde d'éthylène) possédant des longueurs de chaîne variées. Les polymères ayant un nombre d'unités de répétition précisément choisis ($\text{EO}_n = 8-160$) sont ciblés de manière à maintenir une concentration en groupes terminaux fonctionnels (assurant le transport ionique) suffisante pour une conductivité ionique élevée. Les détails synthétiques sont décrits dans le chapitre "Experimental" (*vide infra* : **Chapitre III**). Les MEC-SIPEs présentés dans la section Stratégie de synthèse constituent la bibliothèque d'électrolytes polymères qui sont caractérisés et discutés dans le deuxième chapitre (*vide infra* : **Chapitre II**) sur les MEC-SIPEs.

Abstract

The first chapter presents the context of the thesis through review of the *state of the art*. Lithium ion Batteries (**LiBs**) are presented in terms of modern electrochemical energy storage applications. Polymer electrolytes are then divided into two sub-classes: *Salt-in-Polymer* electrolytes and "Single-Ion" Polymer Electrolytes (**SIPs**).

The *Salt-in-Polymer* (**SiP**) electrolytes are presented generally through description of their principle features. Then particular attention is paid to how researchers have attempted to optimise SiP electrolytes. Specifically, their formulations and macromolecular architectures are discussed. The review is brought up to date through discussion of recent efforts to organise SiP matrices and polymers that have been reported as alternatives to traditional formulations based on poly(ether)s.

"Single-Ion" Polymer Electrolytes (**SIPs**) are then discussed with a focus on the principles of their design. Contemporary methods of the synthesis of SIPs are outlined and discussed in terms of electrolyte performance. SIPs having modified chain terminals bearing ionic functions intended for the transport of lithium ions are of interest because of **i)** their high ionic conductivity, **ii)** simple design principle, and **iii)** effective leverage of polymer chemistry for enhancing the performance of SIPs. These "MonoEnd-Capped Single-Ion Polymer Electrolytes" (**MEC-SIPs**) are inspiration for thinking beyond traditional approaches for optimising electrolyte performance.

The recent advances in the organisation of soft matter are proposed in terms of their potential application to the domain of ion transport in polymer electrolytes. Following a discussion of strategies based on the micophase-separation of polymeric blocks, alternatives are proposed. Structure-directing point groups are presented as a powerful synthetic tool for tuning the bulk morphology of these functional polymers. These are elaborated in terms of their potential to influence the development of MEC-SIPs.

The synthesis strategy implemented in this thesis is then described. The strategy is based on modification of the hydroxyl end-groups of poly(ethylene oxide) monomethyl ethers having different polymer chain lengths. Polymers having a precisely chosen number of repeating units ($EO_n = 8-160$) are targeted to maintain a concentration of ionic end-groups that is sufficient for high ionic conductivity. The MEC-SIPs described in the Synthesis Strategy (**Section 6**) constitute the library of polymer electrolytes that are characterised and discussed in **Chapter II** (*vide infra*), on MEC-SIPs of the present work. The synthetic details of the MEC-SIPs are confined to **Chapter III** (*vide infra*).

Chapter I: Table of Contents

I.	Polymer Electrolytes for Lithium-Ion Batteries: Context and <i>State of the Art</i>	7
1.	Lithium-Ion Batteries for Modern Electrochemical Energy Storage Technology	11
2.	Salt-In-Polymer Electrolytes for Lithium-Ion Batteries	12
2.1.	Introducing Polymers as Electrolyte Materials	12
2.2.	Salt-in-Polymer (SiP) Electrolytes based on PEO	13
2.3.	Structural Organisation of Salt-In-Polymer Electrolytes	19
2.4.	Alternative Polymers for Salt-In-Polymer Electrolytes	30
2.5.	Conclusions on Salt-in-Polymer Electrolytes.....	33
3.	“Single-Ion” Polymer Electrolytes (SIPes)	34
3.1.	Introduction to Single Lithium-Ion Transport in Polymeric Electrolytes	34
3.2.	Design of SIPes	34
3.3.	Synthesis of SIPes.....	35
3.4.	MonoEnd-Capped Single-Ion Polymer Electrolytes (MEC-SIPes).....	35
3.5.	Poly(electrolyte)s	38
3.6.	Conclusions on Single-Ion Polymer Electrolytes	41
4.	Organisation of Soft Matter: Beyond Block Copolymers	42
5.	General Conclusions Polymer Electrolytes for Lithium Ion Batteries	47
6.	Synthesis Strategy	49
7.	Bibliography of Chapter I	53

1. Lithium-Ion Batteries for Modern Electrochemical Energy Storage Technology

The search for higher energy density has been the primary objective in the development of electrochemical energy storage. Lead-acid cells were surpassed by nickel-cadmium cells, then nickel-metal hydride, until the *state of the art* arrived at **Lithium-ion Batteries (LIBs)**.^[1] The rate of the discovery and development of efficient electrode and electrolyte materials, and their effective combination into powerful electrochemical cells, has limited the practical application of portable electronics, communication and transport technologies over the last 100 years.^[2]

Lithium batteries are a particularly desirable energy storage system because of their high specific energy (per unit of mass) and energy density (per unit of volume) (**Fig. I-1**).^[2,3] However rate capability, cyclability, temperature tolerance and cost are persistent criteria for the evaluation of each new generation of batteries.^[4] Furthermore, the demands of the newest technology now surpass the limitations of conventional battery design: the latest portable electronics and applications pertaining to the **Internet of Things (IoT)** require the production of lightweight, thin, flexible cells made from non-toxic materials.

The aim of creating a sustainable economy based on renewable materials and recyclable technologies requires energy storage devices that meet these same exacting standards. A concerted effort is required for the creation of the energy storage technology of the future: active electrode materials and electrolytes must be developed harmoniously. Convenient physical processing and mechanical properties make functional polymers promising candidates for integration as electrolytes in solid-state cell designs, provided that they exhibit high ionic conductivity, charge transfer efficiency and electrochemical stability over the thermal, chemical, and electrochemical operating conditions of the cell.

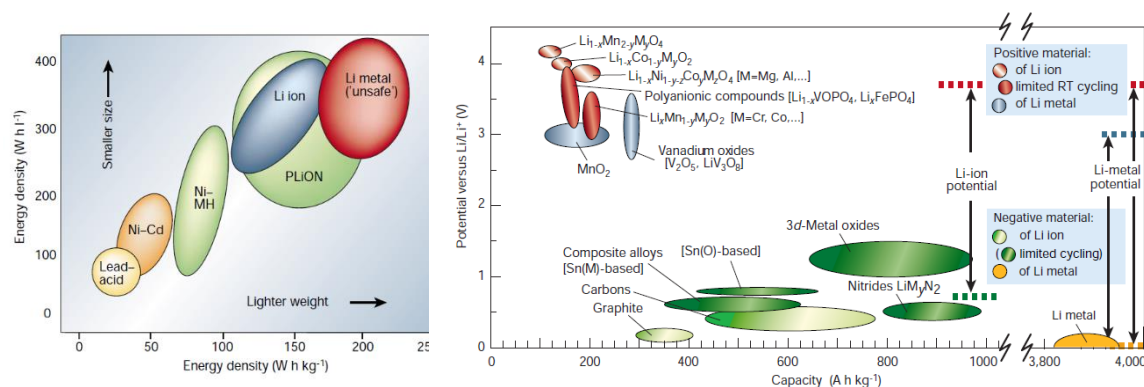


Figure I-1: (Left) A Ragone plot showing that Lithium Ion Batteries (LIBs) and Lithium Metal Batteries (LMBs) provide exceptional specific energy and energy density. (Right) The high capacity and low potential of lithium metal make this anode material attractive to the development of energy storage technology despite the hazards of its reactivity. The figures are reproduced from literature.^[3]

Much has been achieved through complex formulation chemistry of **Salt-in-Polymer (SiP)** electrolytes. These methods have been successfully adapted to electrically powered transport and portable communication technologies. However, the persistent drawbacks arising from the conduction of binary salts limit the application of SiP formulations as the long-lasting, durable electrolytes of the future. "**Single-Ion**" **Polymer Electrolytes (SIPes)** answer some of the questions raised since the conception of an all-solid-state battery, but must make a leap in ionic conductivity

at ambient temperature, rate capability, and cyclability before they become the widely accepted solution to modern battery electrolyte design.

The key-enabling properties of functional polymers can be profoundly altered by precision chemistry of their repeating units and of the polymer chain ends. Modular design of polymer end-groups can augment performance in existing, complex systems. Furthermore, a rational basis for the design of functional macromolecules exhibiting superior interfacial and hierarchical organization, high electrolyte performance and optimized ionic transport can be envisaged. A fundamental study of processes originating from and affected by end-group chemistry is therefore proposed as means to developing polymer chemistries capable of meeting the electrochemical energy storage needs of the modern world.

2. Salt-In-Polymer Electrolytes for Lithium-Ion Batteries

2.1. Introducing Polymers as Electrolyte Materials

An electrochemical cell is composed of two electrodes separated by an electrolyte, and a separator. The spontaneous discharge of the battery is dictated by the chemical potential of the electrodes. The electrodes are connected by an external electrical conductor, permitting the flow of electrons from the more negative anode to the more positive cathode. The electrolyte enables this charge transfer by permitting the transfer of ions in the opposite direction, maintaining charge balance across the cell. A secondary battery is one that can be recharged by reversing the flow of electrons and ions by application of a greater potential in the opposite direction.

The performance of a battery is generally understood with respect to its voltage, rate of charge and discharge, capacity, and power. The fundamental performance of batteries in terms of energy stored and retrieved per unit of mass or volume relies on the cell chemistry. Therefore, the best battery imaginable will have **i)** a large electrochemical potential difference between the electrodes, **ii)** a fast exchange of a small mass and volume of active species permitting fast electron transfer, and **iii)** electrochemically stable electrodes and electrolyte, enabling the efficient transfer of ions, and that are not consumed during charge and discharge of the cell.

The electrolyte is of critical importance to the performance of a battery because it enables the transfer of ions from one electrode to another during charge and discharge of the cell. Not only is excellent ionic conductivity needed, but also the electrolyte must **i)** be compatible with the (electro)chemistry of the electrodes, **ii)** form stable interfaces with both electrodes across which efficient charge transfer can occur, and **iii)** function as intended over a practical range of temperatures. The electrolytes of commercial batteries have already been well-optimised to high ionic conductivity using lithium salts dissolved in organic solvents but much improvement is required to meet the requirements of safety, reliability, energy density, and cell design for the modern world. New technologies are driving the market for better energy storage, such as research efforts for electric vehicles that demand lightweight cells having high power and energy densities.

Lithium is a highly electropositive metal (-3.04 V vs. the Standard Hydrogen Electrode) and therefore creates a high electrode potential difference across a cell based on the transfer of metal ions (**Fig. I-1**).^[5] The small ionic radius of Li furthermore permits intercalation into active electrode materials. This led researchers to pursue the lithium metal anode as the ultimate cation source,

in high energy density **Lithium Metal Batteries (LMBs)**. However high reactivity and flammability of lithium metal, and the tendency of dendrite growth on the anode prevents the development of liquid electrolytes for use in safe cell designs.^[6-8]

Solid Polymer Electrolytes (SPEs) are attractive alternatives for alleviating the design restrictions of liquid electrolytes, which may leak or combust in the event of cell failure.^[2] A solid (polymer) matrix that is inert towards a metallic lithium anode can further act as a separator and prevent dendrite growth. Such a material must be electrochemically stable over a large potential window, enabling the use of the latest high-voltage electrode materials, and facilitate high ionic conductivity. Flexible, though mechanically strong, solid electrolytes are highly sought-after, as they could be used in Li-Sulfur and Li-Air (O₂) batteries (**Fig. I-2**).^[9] However SPEs have continued to be limited by low ionic conductivity at ambient temperatures, poor cyclability, and reactivity towards the cathode. Portable electronics designed on ever-smaller scales place further pressure on cell design, demanding flexible components.

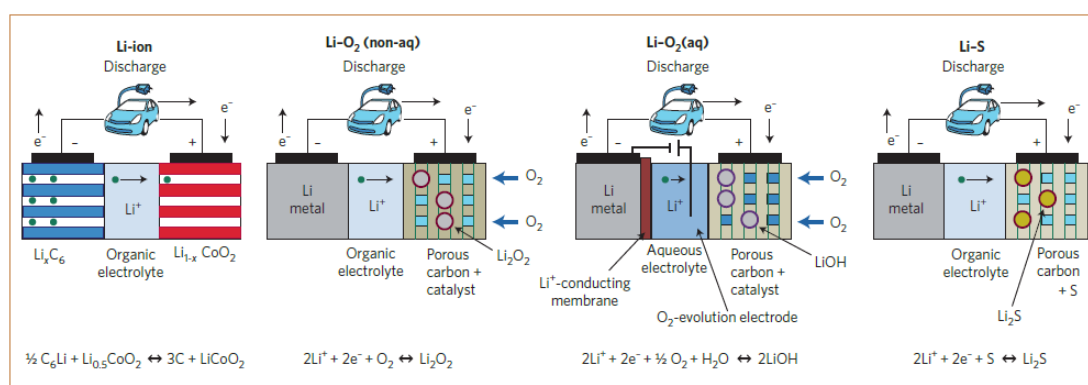


Figure I-2: (Left to Right) A schematic representation of Li-Ion, Li-O₂ (organic), Li-O₂ (aqueous), and Li-S battery chemistries. The figure is reproduced from literature.^[10]

The electrolyte must not only keep pace with advances in electrode chemistries, but also act concertedly with the active materials to enable the design and function of modern electrochemical energy storage devices. Polymers are structurally diverse, viscoelastic materials capable of meeting the demands of modern cell design. Their physico- and electrochemical properties, tuneable through modern synthetic strategies, can be tailored to achieve the necessary electrolyte performance.

2.2. Salt-in-Polymer (SiP) Electrolytes based on PEO

2.2.1. Properties of SiP Electrolytes

Decreasing the mass and volume of the electrolyte and the possibility of removing the need for a separator membrane make polymers strong candidates for creating high energy density batteries. Non-flammable polymers are the answer to safety concerns arising from the use of organic liquids to solvate lithium salts. The viscoelastic properties of polymers are also advantageous in terms of electrolyte processing and electrochemical design. These features make polymer electrolytes more attractive than all-solid-state battery chemistries that rely on inorganic ceramics,^[11] of which the large-scale production^[12] and assembly can be problematic.^[13]

Traditional polymer electrolytes are ionic conductors of binary salts. A SiP electrolyte is a formulation of a Li-salt in a polymer matrix. Poly(ethylene oxide) is a good candidate for such

systems because of its good solvation of Li-salts^[14,15] and its convenient mechanical properties, which enable easy electrolyte processing and cell construction. Since the suggestion by M. Armand and co-workers^[16,17] that PEO could be a suitable matrix for Li-ion batteries, a great variety of Li-salts has been reported and optimised for this application. It is generally accepted that mobility of ions through a polymer host is dependent on the thermally activated segmental motion of polymer chains (**Fig. I-3**).^[18] Bulky anions with low basicity and large delocalisation of their negative charge are correlated with high ionic conductivity through the electrolyte. Despite the selection of highly dissociating Li-salts, the ionic conductivities of SiP blends are greatly dependent on the formulation of the electrolyte, which may include significant mass fractions of numerous additives, and are generally less than 10^{-4} S.cm⁻¹ at ambient temperature. This is a result of the crystallisation of PEO, which **i**) traps ions in a matrix of immobile polymer segments below the melting point of the polymer, and **ii**) limits the percolation of conducting pathways through the electrolyte.

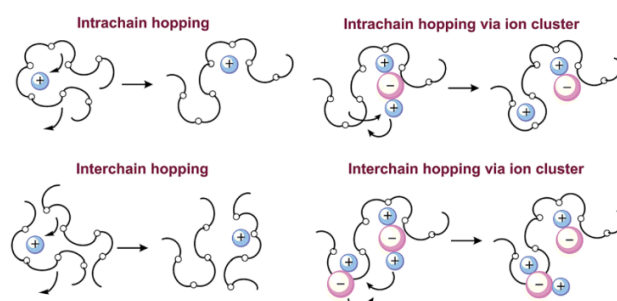


Figure I-3: An illustration of the motion of oppositely charged ions in a PEO matrix by ether-coordinated Li⁺ (left) and by ion pairs and triplet clusters (right). Top: intrachain motion of ions. Bottom: interchain motion of ions. The figure is reproduced from the literature.^[18]

Following early correlation studies that combined EIS, NMR and DSC, M. Armand and co-workers suggested that the ionic conductivity of PEO in the melted state, "*cannot a priori be described by a single [Vogel-Tamman-Fulcher] or Arrhenius law.*"^[19] They proposed that the SiP "*PEO_n/M⁺X⁻ complexes should not be classified as a function of the laws their conductivity appears to obey but as a function of the number of phases present in the system.*" With number, size and physicochemical nature of the phases not defined, it was concluded that fast ionic transport occurs in the amorphous phases of a polymer electrolyte. NMR relaxation studies yielded the conclusion that, upon crystallisation of PEO, the majority of the salt content was held in the crystalline phase and that a minority population of salt remained in the amorphous phase. Despite the mobility of this minority population, insufficient long-range percolation of the amorphous phase at $T < T_m$ makes ionic conductivity very low on the length-scale of the measurement. Grain boundaries between the amorphous and crystalline domains do not permit the movement of ions from one electrode to the other through a single phase.

The movement of oppositely charged ions through the polymer matrix further complicates optimisation of a SiP electrolyte. Taking the example of the widely studied lithium *N*-bis(trifluoromethylsulfonyl)imide [LiTFSI] salt in PEO, it has recently been computed that, for SiP blends of EO/Li= 8 and 30, Li⁺ exists in a mixed coordination environment, wherein the Li⁺ can coordinate with any of **i**) the TFSI⁻ anion, **ii**) the PEO chain, or **iii**) both the anion and the chain.^[20] The role of ion clustering was found to be greater when the concentration of salt was higher: more of the Li⁺ population was associated with ion-clusters. The aggregate size increases and the inter-

aggregate distance decreases when the salt concentration is increased. Analysis of the simulations describes a majority of asymmetric ion clusters containing an excess of TFSI⁻ at high salt concentration, which suggests that the low t_{Li}^+ observed at high salt concentrations may result from the drag effect of not only the Lewis-basic poly(ether), but also large, negatively charged aggregates in the polymer matrix.

The polarity of the polymer chain is yet another variable that must be optimized. Molecular dynamics simulations have been used to describe the formation of aggregate species in SiP blends of variable polymer chain polarity.^[21] At low polarity (low chain dipole moments), ions tend to cluster into large aggregates, ionic motions become correlated, and the long-range mobility of ions decreases. At higher polarity, the aggregate size decreases and the coordination of the cation is limited by the segmental mobility of the polymer chain. However, when the dipole moment of the polymer segment becomes sufficiently high to decrease the chain dynamics, the mobility of the ions is also decreased.

Polymer mass average molar mass (M_w) and the physicochemical nature of its end-groups affect the mechanism of ion transport. Systematic variation of the M_w of PEO having either hydroxyl or methoxy end-groups at one or both chain ends yielded a phenomenological correlation between ionic conductivity and the segmental relaxation time of the polymer.^[22] However, the ionic conductivity reaches a plateau for PEO of $M_w > 5000$ g/mol, regardless of the end-group. Below this limit, the conductivity is greatly influenced by the end-group (**Fig. I-4**). Bis-hydroxy-PEO has the lowest ionic conductivity, PEO methyl ether has higher ionic conductivity, and bis-methoxy-PEO has the highest. The three examples each follow a power-law related to the influence of viscosity on chain dynamics, as defined by the Rouse model of non-entangled chains.^[23] The limit of $M_w < 5000$ g/mol corresponds to a change in the friction coefficient of viscosity for the polymers regardless of the end-group, meaning that end-group dynamics have an effect observed at the macroscopic scale only when the degree of polymerization (DP_n , X_n) is below the entanglement limit of the chains. That is to say, the entanglement of chains has an effect on free energy that obscures the contribution of chain-end dynamics at the macroscale. It was found that polymers having hydroxyl end-groups exhibited restricted segmental mobility. In agreement with the free volume model of polymer chain dynamics, the H-bonding interactions of the hydroxyl group increase the relaxation time of the polymer chain ends. This is observed macroscopically by a decrease in ionic conductivity. By correlation of relaxation times extracted from polymer viscosity, a model for ion transport was proposed: whereas ion transport in high M_w polymers occurs mostly by high frequency movement of Li⁺ between PEO coordination sites, in low M_w polymers ion transport occurs mostly by low frequency vehicular motion of coordinated Li⁺.

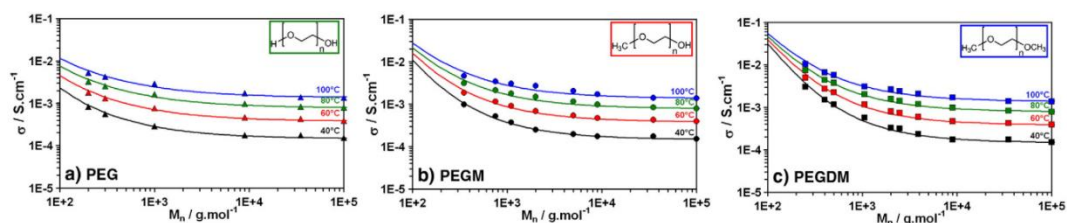


Figure I-4: The ionic conductivity of LiTFSI in PEO as a function of polymer M_w and at different temperatures. *Left to Right: (a) HO-PEO-OH, (b) H₃C-PEO-OH, and (c) H₃C-PEO-CH₃. The figure is reproduced from the literature.*^[22]

2.2.2. Formulation of SiP Electrolytes: Balancing the Properties of a Complex Blend

The thermal and mechanical properties of PEO have been sufficient to inspire work aiming to diminish the occurrence, persistence, and percolation of crystalline phases in the electrolyte. Large amorphous phases with low T_g and short persistent length (high flexibility) were targeted. The methods applied to this end can be broadly classified into two categories: **i)** the mixing of polymers with additives, which might also function as charge carriers, and **ii)** tuning of the polymer architecture. These methods are generally not exclusive and have often been applied in parallel to optimise a particular polymer-salt combination. Complex formulations have resulted in impressive performance of LIBs based on SiP blends, but the concerted effects of various blend components obscure the underlying causality of the observed properties. Deconvolution of the factors governing electrolyte performance remains a challenge today and the answer lies among a number of different mechanisms that operate in concert to yield the global output.

Adding salt to PEO tends to decrease T_m and increase T_g of the polymer.^[24] The decrease in polymer chain mobility close to T_g has been the subject of research into additional components for SiP electrolyte systems. The general aims of SiP formulation are to balance the impact of salt loading by altering the bulk mechanical and morphological properties of the electrolyte blend. The addition of organic solvents (*e.g.* ethylene carbonate, EC) to plasticize a poly(ether) matrix has been a common technique since the start of research into polymer electrolytes.^[25] Also widely reported is the formulation of low DP_n oligo(ethylene oxide)s and salt with a higher M_w polymer to produce a plasticized ionic gel.^[26] Supplementary ionic conductivity measurements in the presence of additional oligo(ether)s is common to many investigations into the performance of new salts, polymer matrices, and salt-polymer hybrids. Similarly, SiP formulations are blended with inorganic fillers (*e.g.* SiO₂, γ -LiAlO₂)^[27,28] with the aim of introducing advantageous mechanical properties to low M_w polymers, or to decrease crystallinity in high M_w polymers. Although good electrolyte performances can be achieved in this way, relative to specific physico- and electrochemical objectives, the concerted effects of several ingredients make assigning structure-property correlations and the causality of performance difficult.

Great variation in polymer architecture has been achieved on the theme of the ethylene oxide (EO) repeating unit. An early idea was to frustrate the organisation of EO units by arranging them as pendant chains of a "comb" architecture, thereby preventing regular crystalline packing observed in linear PEO. Crosslinked PEO networks were produced either by copolymerisation of ethylene oxide with a small amount of difunctional co-monomer or by post-polymerisation modification of PEO.

Numerous configurations of poly(ether)s based on the PEO repeating unit were investigated by M. Watanabe and co-workers in the 1980s. The uniform result is that crystallinity persisted in the

neat polymers at room temperature, regardless of polymer architecture, but was erased upon addition of their chosen model salt, lithium perchlorate (LiClO_4). This is distinct from linear PEO, which retains 20-50 % crystallinity, as analysed by DSC, at equivalent concentrations of salt ($\text{EO}/\text{Li}=10-100$). The T_g of the polymer blends (linear or branched/crosslinked) was uniformly around -30 °C ($\text{EO}/\text{Li}<50$). The ionic conductivities of these blends are strikingly similar, all around $1 \cdot 10^{-5} \text{ S} \cdot \text{cm}^{-1}$ at ambient temperature ($\text{EO}/\text{Li}=20$). For example, in the case of LiClO_4 -in-PEO: blending equal masses of comb-shaped poly(*p*-oligo(ethylene oxide)styrene) and linear PEO ($M_w \sim 10^6 \text{ g/mol}$),^[29] achieves much the same optimised result as urethane crosslinking of three-arm PEO ($M_n = 3 \cdot 10^3 \text{ g/mol}$, $\text{EO}_{n(\text{branch})} = 20$)^[30] in terms of T_g , percentage crystallinity, and ambient conductivity of the SiP electrolyte.

Despite the great difference in polymer architecture (comb-homopolymer in linear PEO vs. crosslinked network PEO), optimisation of salt loading to maximise ionic conductivity and minimise crystallinity yields the same electrolyte properties of conductivity, and stability. One can conclude that the loading of salt, yielding polymers having $T_g \sim -30$ °C when $\text{EO}/\text{Li} = 20$, is the dominant variable determining the performance of these electrolytes. Changes in performance by this method of blending different configurations of PEO with large doses of salt are mostly limited by the physicochemical nature of the salt. It is worth noting that the assumption of complete dissociation of LiClO_4 in the matrix is supported by SAXS measurements at room temperature, in which authors highlight the absence of patterns corresponding to the crystalline salt and no change in the crystalline pattern of PEO (if it is visible). However it is now known that ionic species aggregate at high temperature (> 80 °C) in polar polymer matrices.^[20] Knowing that the measurements of ionic conductivity were made on cooling (from *ca.* 100 °C), it is likely that the ionic species at ambient temperature are different in the impedance spectroscopy measurement to those proposed through analysis of the SAXS profile.

2.2.3. The Salt of SiP Electrolytes

Following the early reports by M. Armand and co-workers,^[16,17] an optimised salt structure has been investigated in parallel with developing a high performance polymer host. Low basicity and a large delocalisation negative charge of the anion promotes high ionic conductivity through the electrolyte. The contribution of the anion to the ionic conductivity of the electrolyte can be decreased by limiting its mobility. This can be achieved with a small molecular binary salt by increasing the size of the anion. Lewis acids (anion acceptors) can be added to the SiP formulation to decrease anion mobility by electrostatic drag effects. The largest class of Li-salts for high performance Li-ion batteries having polymer electrolytes are sulfonic species bearing electronegative fluoro- and fluoroalkyl substituents on the anion. Widely studied among these are lithium (trifluoromethanesulfonate) [**LiTf**],^[31,32] lithium bis(fluorosulfonyl)imide [**LiFSI**],^[33,34] lithium bis(trifluoromethanesulfonyl)imide [**LiTFSI**],^[24,32,34] and lithium bis(pentafluoroethanesulfonyl)imide [**LiBETI**] (Fig. I-5).^[27,35-38] These examples have low energies of dissociation, are electrochemically stable to $> 4.5 \text{ V vs. Li/Li}^+$, and are compatible with numerous electrode chemistries. They are preferred to the rival salt **LiPF₆**, which introduces the security risk of decomposition to yield HF in the presence of trace water content and reacts with carbonates to yield insulating LiF above 60 °C.^[39] Similarly, the highly soluble and conductive **LiClO₄** is unsuitable for large scale applications due to the strong oxidising nature of the Chloride (VII), and

its reactivity to carbonates at elevated temperatures and high currents.^[40] Despite the drawbacks of LiClO₄, it is often found in scientific reports because it is relatively inexpensive.



Figure I-5: The fluorinated sulfonate lithium salt (LiTf), and the sulfonylimide salts lithium salts (LiFSI, LiTFSI, and LiBETI)

The library of salts based on fluorinated sulfonic designs continues to increase. Recent examples include the C-H acid 1,1,3,3-Tetra(trifluoromethanesulfonyl)propene, which has a highly labile proton and can be converted to its lithium salt [LiTTP] by treatment with Li₂CO₃. This salt, as a 0.32 M solution in diglyme (EO/Li= 0.065), has $\sigma_{AC} = 2.3 \cdot 10^{-3} \text{ S.cm}^{-1}$ with $t_{Li}^+ \approx 0.7$ at ambient temperature (Fig. I-6).^[41] The corresponding 0.01 M solution (EO/Li= 2) has $\sigma_{AC} \approx 1.0 \cdot 10^{-4} \text{ S.cm}^{-1}$ with similar net transfer of Li⁺. The high dissociation of Li⁺ is due wide delocalisation of the anionic charge and the mobility of the anion is limited by its size.

The effective size of anions can be increased by tuning their aggregation behaviour. The formation of ionic aggregates at high temperature limits ionic conductivity by trapping of Li⁺, but this can be limited by molecular design forbidding the formation of ion pairs and triplets under conditions of aggregation. The design of such large anions has been leveraged to yield high t_{Li}^+ SiP blends of a multi-ionic polyoctahedral silsesquioxane lithium salt POSS-phenyl₇(BF₃Li)₃ in PEO (Fig. I-7).^[42] Aggregation of the decorated POSS units by exclusion of the relatively non-polar phenyl rings from the PEO matrix is proposed. The large anionic aggregates have severely reduced mobility and the majority of the charge is transferred by mobile Li⁺, affording $t_{Li^+} = 0.6$ (at 80°C). The dissociation of Li⁺ is enabled by the electron-withdrawing POSS-BF₃⁻ groups (three anions per POSS cage). The proximity of the BF₃⁻ groups and steric hindrance of the phenyl groups prevents the formation of ion pairs and triplets. These features of anionic aggregation and the dissociation of lithium concerted yield ionic conductivity around $1 \cdot 10^{-4} \text{ S.cm}^{-1}$ at 20 °C. The T_g, in the -30°C to -35 °C range, of the best performing blends (having EO/Li= 10 and 14) did not change much upon addition of LiBF₄. The authors speculate, following the evidence of the measured T_g, that the molecular dynamics of PEO did not account for the ionic conductivity of the blend. Rather, the additional Li⁺ and BF₄⁻ ions were able to form ion pairs and triplets, which were not feasible in the POSS-based blend. The ionic conductivity of the mixed salt blend fell by more than two orders of magnitude by addition of LiBF₄ to the PEO/POSS-phenyl₇(BF₃Li)₃, a three-component blend, in comparison with a two-component PEO/POSS-phenyl₇(BF₃Li)₃ blend of identical EO/Li= 10 ratio.

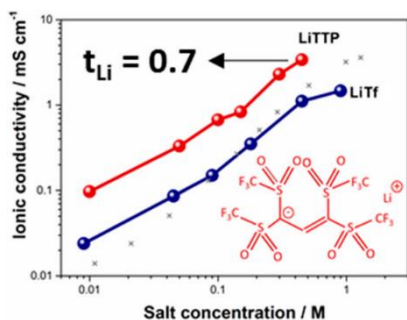


Figure I-6: The conductivity of LiTTP and LiTF in PEO at ambient temperature as a function of salt concentration (mol/g). The figure is reproduced from the literature.^[41]

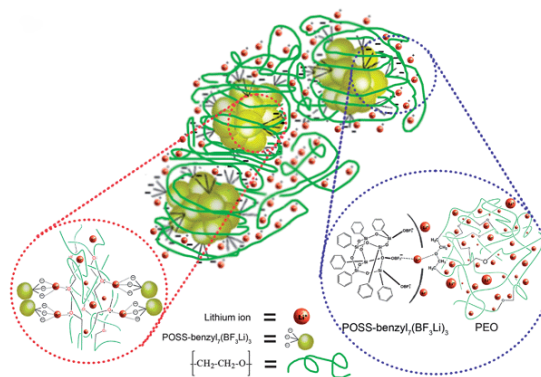
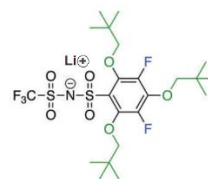


Figure I-7: Illustration of the "Janus-like" POSS-phenyl₇(BF₃Li)₃ salt and its aggregation behaviours in a PEO matrix. The figure is reproduced from the literature.^[42]

Salts based on fluorinated phenyl sulfonimides have been investigated as means towards systematic, modular variation of the anion (**Fig. I-8**).^[43] A correlation was drawn between increasing average charge of the aromatic carbons and an increase in the stability of these so-called **Fluorinated Aryl Sulfonimide Tagged ("FAST")** salts in oxidation. The wide variety of aromatic substituents available through successive S_NAr reactions yielded a library of Li-salts with generally good stability (> 4.5 V vs Li/Li⁺) but the ionic conductivity of each example was up to an order of magnitude lower than that of an equivalent blend of PEO/LiTFSI (EO/Li= 15). Neither the lithium transference number (t_{Li}^+) nor the self-diffusion coefficient of these salts has been reported.

Figure I-8: The best-performing "FAST"-salt, featuring both bulky *tert*-butylether and electron-withdrawing substituents. The figure is reproduced from the literature.^[43]



2.3. Structural Organisation of Salt-In-Polymer Electrolytes

2.3.1. Through Formulation with Structure-Directing Compounds

A "tunnel-like" structure of the polymer matrix is targeted to enable fast Li-ion transport because **i)** directed 1D ion motion could be means to greater ion transport efficiency and **ii)** chain confinement can augment desirable physicochemical properties of the polymer. The concerted movement of Li⁺ in straight channels perpendicular to the electrode plane can improve the rate of charge in discharge by confinement of Li⁺ to the shortest path between parallel plates. The organization of ionically conductive polymers and polymer blocks into such channels (between other blocks or blended additives) can have a profound effect on the mechanical, structural, and thermal properties of the conductive block. Organisation of SiP homopolymer blends is achieved using various additional components. The method was extended to SiP blends using block copolymers, and finally to Single-Ion block CoPolymer Electrolytes (*vide infra*: SIPEs to be presented in section 3).

The supramolecular self-assembly of PEO and α -cyclodextrin (α -CD) was exploited to create confined chain conformations of PEO for the conduction of Li⁺ ions (**Fig. I-9**).^[44-46] It was suggested

that confinement of PEO between lamellar phases of α -cyclodextrin can induce conformational changes in the structure of the PEO. The typical (7/2) helical structure of PEO, having a *trans-trans-gauche* orientation of sequential repeating units, was modified to an “*all-trans*” conformation. The conduction of Li^+ is improved when PEO chains are held in an *all-trans* conformation, because the interaction of Li^+ with the lone pairs of the Lewis-basic ether oxygen is inhibited by the chain conformation. This decreases the "drag effect" of the ether on the mobility of the Li^+ ion. The anion was moreover excluded from the confined channels, so the matrix favors the transport of Li^+ but not the bulky AsF_6^- . The conclusion is supported by powder WAXS and Cross-Polarization Magic Angle Spinning (CP-MAS) NMR analysis. The combined ion pair separation and directional arrangement of the PEO chains result in improved ionic conductivity of the assembled blend with respect to a comparable SiP formulation without α -CD.

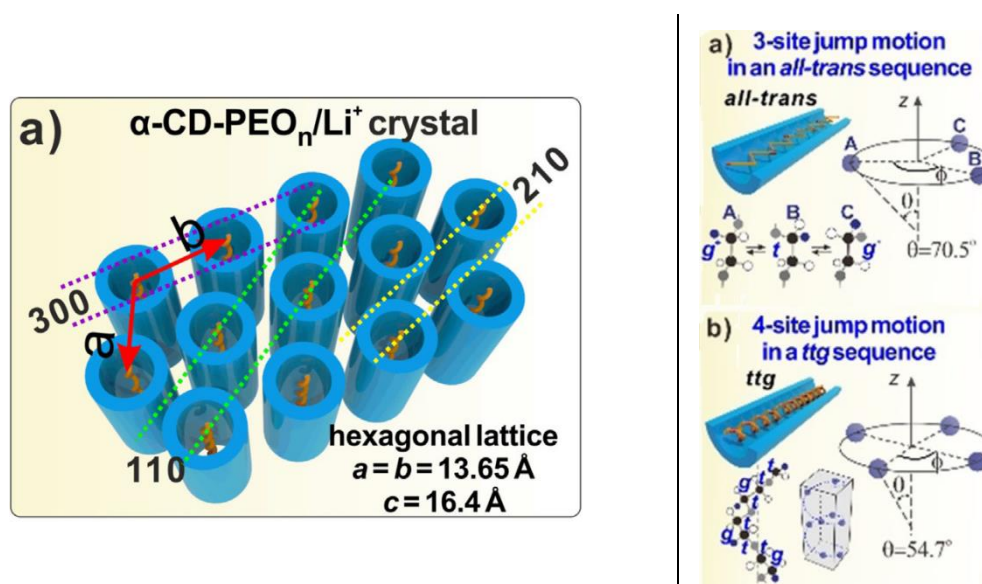


Figure I-9: (Left) An illustration of PEO/LiAsF₆ blended with α -cyclodextrin (α -CD) having a hexagonally packed morphology of PEO chains inside ordered α -CD tubes. (Right) Illustration of PEO inside the α -CD tube, in (a) an *all-trans* and (b) *trans-trans-gauche* (ttg) conformation. The figures are reproduced from the literature.^[46]

Recent developments have targeted fillers for inducing nanoscale ordering in the electrolyte. These include aligned alumina-PEO nanocomposites in which PEO/LiTFSI is blended with halloysite,^[47] an aluminosilicate $[\text{Al}_2\text{Si}_2\text{O}_5(\text{OH})_4]$ having the form of nanotubes with a negatively charged outer silica surface and a positively charged inner aluminol surface (Fig. I-10). It is proposed that supramolecular ordering in a blended electrolyte composed of halloysite nanotubes (HNT), PEO ($M_w = 4 \cdot 10^6 \text{ g/mol}$) and LiTFSI will segregate the mobile ions into quasi-1D channels.^[48] The best ionic conductivity is reported for a blend of PEO/LiTFSI (EO/Li= 15) with 10 % (w/w) HNT, where $\sigma_{AC} = 1.11 \cdot 10^{-4} \text{ S.cm}^{-1}$ (at 25 °C), $1.34 \cdot 10^{-3} \text{ S.cm}^{-1}$ (at 60 °C), and $2.14 \cdot 10^{-3} \text{ S.cm}^{-1}$ (at 100 °C). For this PEO/LiTFSI/HNT blend, good electrochemical stability in oxidation is reported in Li|stainless steel cells up to 4.78 V vs Li/Li⁺, in comparison to 4.52 V vs Li/Li⁺ for a model PEO/LiTFSI system at 100 °C (the scanning rate was 10 mV.s^{-1}).

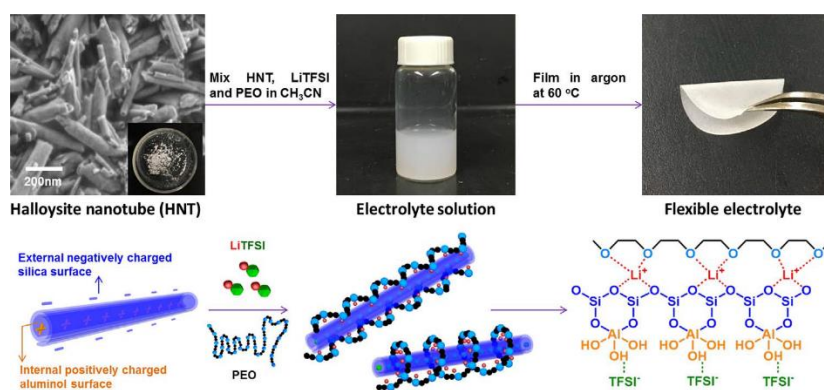


Figure I-10: An illustration of the preparation of the blended electrolyte of Halloysite Nanotubes (HNTs), LiTFSI and PEO. The components are mixed in acetonitrile and cast to form a flexible film. Top: images of the materials. Bottom: the structural formula of the components and the proposed orientation-specific ion-dipole interactions. The figures are reproduced from the literature.^[48]

2.3.2. Self-assembly of Block Copolymers

The spontaneous organization of (macro)molecules into supra(macro)molecular structures is called self-assembly.^[49] The implications of self-assembly to advanced materials design has inspired research into (macro)molecules capable of creating long-range ordered bulk morphologies. Traditional lithographic techniques have been complemented by the creation of morphologies with very small feature sizes. The common strategies for achieving synthetic self-assembly rely on **diBlock CoPolymers (diBCPs)**. The low entropy of chemically dissimilar but linked polymeric sub-blocks leads to "microphase separation" when the two blocks are above their T_g but below their **Order-Disorder Transition (ODT)** temperature (T_{ODT}). At $T > T_{ODT}$, the thermal energy of the system is superior to the enthalpy of mixing and two sub-blocks are able to mix. Therefore, segregation of the domains on a practical timescale is often achieved by pushing the system into disorder ($T > T_{ODT}$) and then allowing it to microphase-separate on cooling. Upon segregation, the two chemically different blocks typically assume coil conformations that exclude mixing and favor *like-with-like* interactions. Phase segregation minimizes the free energy of the bulk, and is determined by the free energy of the polymer chains and the entropic contribution of defects. The familiar phase diagram of the Flory-Huggins composition parameter (χN) as a function of polymer composition (f) was established^[50] for model diBCPs and then elaborated for ABC triBCPs (**Fig. I-11 & Fig. I-12**).^[51,52]

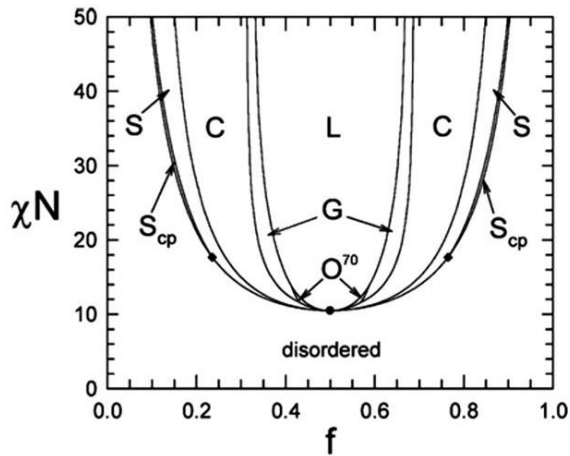


Figure I-11: A theoretical phase diagram of A-b-B diBlock CoPolymer (diBCP) morphologies as represented by the Flory-Huggins interaction parameter (χN) as a function of BCP composition (f). Indicated are regions for lamellar (L), gyroid (G), cylinder (C), spherical (S), close-packed spherical (S_{cp}), orthorhombic network (O^{70}), alternating gyroid (G^A) and disordered morphologies. The figure is reproduced from the literature.^[53]

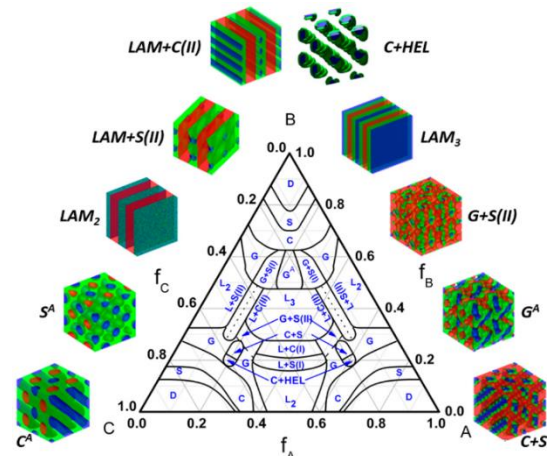


Figure I-12: A theoretical phase diagram of A-b-B-b-C tri-block copolymer (triBCP) morphologies having specific simulated parameters ($\chi_{AB}N= \chi_{BC}N= 35$ and $\chi_{AC}N= 15$). The figure is reproduced from the literature.^[52,54]

BCPs have been leveraged in the case of SiP electrolytes by designing polymers that might combine the apparently conflicting properties of ion conduction and mechanical strength. A popular approach is to design a block copolymer in which one polar block is chosen according to its ability to dissolve salt and the other, non-polar block is chosen for its convenient mechanical properties. The microphase-separation process in such BCPs is a result of the concerted effects of **i)** exclusion of the non-polar block from the electrostatic attraction between segments of the polar block and **ii)** exclusion of the non-polar block from ion-dipole interactions of the polar block with dissolved salt. Therefore, preferential dissolution of the salt into the phase of the polar block effectively increases the interaction parameter (χ) of that block and the magnitude of the increase will scale together with concentration of salt in the polar phase. However, a real polymer sample, that has a (kinetically controlled) thermal history, does not reach the ideal minimum of free energy due to the entropic contribution of defects. The annihilation of defects has been the subject of considerable research by those aiming to create more efficient pathways for ion transport between electrodes.

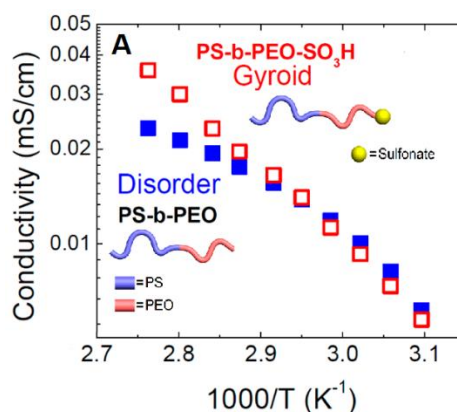
The impact of specific end-groups on the morphology of BCPs was studied by the group of professor M.J. Park and co-workers. They described the effects of (di-)hydroxyl, carboxylic acid and sulfonic acid terminals on the segregation and ionic transport properties of PS-*b*-PEO SiP electrolytes.^[55-57] The end-capped BCPs were obtained *via* chemical quenching of the anionic polymerisation of EO, to create a set of BCPs of comparable M_w , block ratios and dispersity. The identity of the end-group determined the bulk morphology of the electrolyte.

They first demonstrated how the addition -SO₃H and -SO₃Li to the PEO chain terminal induced a change in morphology of the salt-doped BCPs ($M_w= 4.6-6.6 \cdot 10^3$ g/mol; $EO_{n(PEO)} \approx 100$, $S_{n(PS)} \approx 60$; $D_w < 1.05$). The end-group concentration was 8-13 mol%. Whereas neat PS-*b*-PEO-OH is disordered, PS-*b*-PEO-SO₃H adopts a lamellar (LAM) morphology and PS-*b*-PEO-SO₃Li forms hexagonally packed cylinders (HEX) (Fig. I-13).^[55] Doping the -SO₃H and -SO₃Li end-capped BCPs with LiTFSI increases the interaction parameter of the PEO block and yields gyroid morphologies.

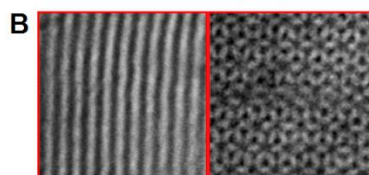
The addition of salt does not induce long-range microphase separation in the PS-*b*-PEO-OH precursor, which has a disordered morphology for all of the reported salt concentrations. The ionic conductivity of the PS-*b*-PEO-SO₃Li/LiTFSI was greater than the disordered PS-*b*-PEO-OH/LiTFSI above 60 °C (the precise values are not reported).^[55] The PS-*b*-PEO-SO₃Li/LiTFSI (LAM) had $\sigma_{AC} \approx 0.02 \cdot 10^{-3} \text{ S cm}^{-1}$ (at 60 °C; $r = 0.06$ [EO/Li = 16.7]).

Figure I-13: The End-capped BCP, PS-*b*-PEO-SO₃H. The figures (A and B) are adapted from the literature.^[55]

(A) Ionic conductivity as a function of reciprocal temperature illustrating the augmentation of conductivity of LiTFSI ($r = 0.02$; EO/Li = 50) by end-capping of PS-*b*-PEO with a sulfonic acid functional group.



(B) Transmission Electron Microscopy (TEM) images of (left) the lamellae of pristine PS-*b*-PEO-SO₃H and (right) the gyroid morphology of PS-*b*-PEO-SO₃H/LiTFSI ($r = 0.02$; EO/Li = 50).



Higher M_w PS-*b*-PEO SiP electrolytes were later presented. A precursor BCP of $M_w = 8.7\text{-}11.0$ kg/mol was used, affording a small (0.12 kg/mol) increment of end-group variation and a PEO end-group concentration around 0.4 mol%. Supramolecular ordering was correlated to the addition of an acid end-group using SAXS measurements: PS-*b*-PEO-OH had a disordered morphology while PS-*b*-PEO-SO₃H and PS-*b*-PEO-COOH formed LAM phases. All the polymers assumed LAM structures upon addition of LiTFSI, which is attributed to solvation of the salt into the PEO domain inducing phase separation of the BCP segments. However, the acid end-capped polymers had stronger Bragg peaks and narrower interfaces. The PEO domain size of the SiP blends increased in the order PS-*b*-PEO-OH < PS-*b*-PEO-SO₃H < PS-*b*-PEO-COOH. The ionic conductivity had the opposite trend, regardless of the salt loadings presented ($r = 0.03$ [EO/Li = 16.7] and $r = 0.06$ [EO/Li = 33.3]). The small end-group concentrations of around 0.4 mol% were sufficient to induce these physicochemical changes. The authors conclude that the low ionic conductivity of LiTFSI through these BCP matrices, relative to equivalent blends of PEO/LiTFSI "*may be resolved by preparing a new set of end-modified polymers with relatively bulky acidic moieties.*"

2.3.3. The Limitation of SiP Electrolytes Based on Block Copolymers

The ionic conductivity of a BCP electrolyte is inherently limited by its composition.^[58] According to the well-established phase diagram, segregation of diBCPs into lamellar morphologies occurs in a specific window of polymer composition, at around 50 % (w/w) of each sub-block (Fig. I-11).^[59] In the case of BCPs, the typical strategy is to have one sub-block providing ionic conductivity and the other providing mechanical strength. Reducing the mass fraction of the ionically conducting phase by half will have an associated decrease in ionic conductivity per mass of polymer. This upper limit, imposed by the fraction of the conducting phase, is itself impossible to reach when the free energy of the matrix is non-equilibrium due to entropic contribution of defects. Researchers have

enhanced the lamellar ordering of BCPs through macromolecular design and through application of external forces. However, a perfect lamellar BCP morphology is limited to 66 % of the conductivity achieved by the corresponding homopolymer. Decreasing the path length and directing the motion of ions into straight channels can enhance the efficiency and magnitude of ion mobility, relative to a disordered matrix, provided that the assembled paths are entirely free of defects and percolate through the entire thickness of the electrolyte. This ultimate perfection has not yet been achieved and it will not be, until we can arrange all the atoms in precisely the way we want.

Ion conductivity of a *salt-in-BCP matrix* depends not only on the mass fraction of the conductive phase and the number of percolating pathways but also on the mobility of the polar polymer segments. The organization of polymer chains is different in each phase of a microphase-separated matrix, as a result of the different χ of each sub-block. The segmental mobility of a segment close to the interface of two domains is limited by the mobility of the segments in the other phase, to which it is covalently bonded. Therefore, some fraction of the ionically conducting phase that is close to the sub-block interface is expected to have a lower ionic conductivity, relative to its ideal homopolymer. The mechanically robust PS sub-block of the widely studied PEO-*b*-PS type of BCP is proposed to limit the segmental motion of PEO segments close to the PS-PEO interface (**Fig. I-14**).^[60–63] The PEO chains close to the PS-PEO interface are effectively immobilised by the PS chains, which have a higher T_g . The PEO segments close to the interface are reasoned to have decreased thermally activated segmental motion. These do not permit the conduction of ions when $T < T_{ODT}$. When $T > T_{ODT}$, phase segregation of the BCP is lost and the polar PEO domains no longer percolate over sufficient distance to permit efficient ionic transport up to the mesoscopic/microscopic scale.

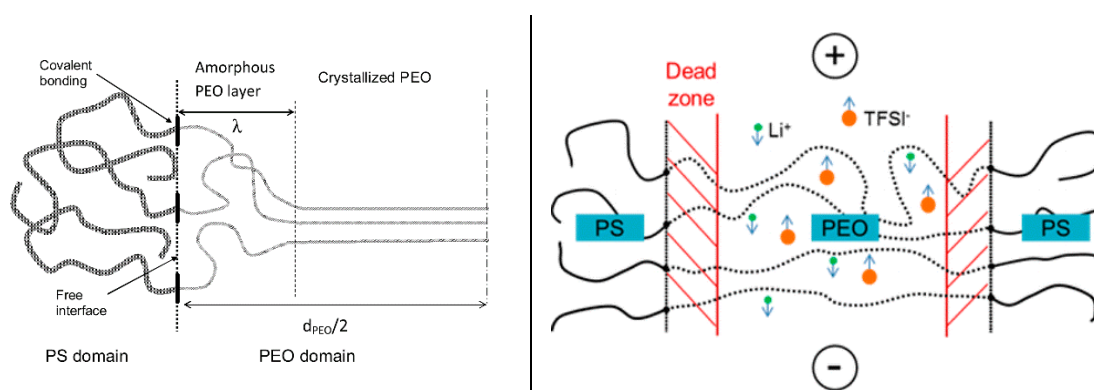


Figure I-14: Two representations of the interfacial zone proposed to limit ionic conduction in the PEO domains of PS-*b*-PEO BCPs. The PEO domain is semi-crystalline and the PS domain is amorphous. Left: close-packing of PEO close the PS-*b*-PEO interface is frustrated by the amorphous state of the PS domain.^[61] Right: the ubiquitous salt LiTFSI is mobile only in the centre of the ionically conductive PEO phase.^[63] The figures are reproduced from the literature.^[61,63]

The PEO segments close to the PS-*b*-PEO interface have low mobility and are said to decrease the ionic conductivity of the PEO phase to below its theoretical value. There are however two physical limits to the observation of this effect. Firstly, at sufficiently high DP_n of the PEO block, the relative dimension of the low-conductivity region would be sufficiently small as to be undetectable in context of the feature size of the morphology. Secondly, extension of this idea to thin films having thickness of the same order as the morphological feature length would also need to include the effects of the polymer-substrate interface and commensurate length scales on chain mobility. With these physical limits in mind, the decrease in ionic conductivity caused by segments having

reduced mobility at the sub-block interface would act concertedly with other limitations of the host morphology. Firstly, although all interfaces would have the effect of decreasing the mobility of proximal segments, not all the interfaces are at the boundary of percolating pathways. The existence of defects blocking ion transport limits the contribution of conducting grains to bulk conductivity and any measure of efficiency of conduction must account for these defects. Secondly, imperfection of the grain boundary occupies a length-scale of the same order as a polymeric segment (persistent length). The fidelity of the interface is therefore a factor in determining the size of the low ionic conduction zone. The result of these concerted effects is that the mobile ionic population is transported through the middle of conductive pathways. This is moreover expected in conductors of binary salts, in which the formation of ionic pairs and triplets, and higher aggregates at elevated temperatures, are common.

2.3.4. Orientation and Alignment of Block Copolymer Electrolytes by External Forces

The phases of a microphase-separated bulk structure can be oriented in the meso/micro-scale under mechanical forces, and by electric and magnetic fields.^[58,59] The orientation of ionically conductive phases perpendicular to the plane of the electrode is desirable for directing efficient transfer of ions from one electrode to the other. In the case of lamellar morphologies, this corresponds to a 2D arrangement of parallel channels forming the shortest path between the electrodes. Researchers have targeted the physical orientation of these channels by application of external forces.

Despite the precise synthesis of ionically conductive and mechanically robust sub-blocks, and optimisation of their relative volume fractions of BCP architectures, ionic conductivities of such designs are not yet competitive to commercially applied homopolymer and random copolymer electrolytes. One major cause of this performance deficiency is that the ionic pathways do not form a defect-free and continuous percolating system through the entire thickness of the electrolyte membrane. Non-conducting domains typically form barriers which impede the transport of ions and must be aligned through the entire bulk material if ideal conduction through a microphase-separated BCP electrolyte is to be achieved. The non-ideal morphology of BCP electrolytes over the length scale required for an electrochemical device results in ionic conductivity measurements that are at the mercy of local defects and grain boundaries.

Mechanical alignment includes methods such as mechanical shear, compression, extrusion and roll casting. Optimisation of the alignment by these methods is therefore achieved through selection of many variables. The polymer itself must be optimised in its molar mass, the volume ratio of the polymer segments, and the combination of the viscoelastic properties of the segments. Mechanical alignment techniques include programmable magnitudes of shear rate or frequency, force amplitude, and the direction of the mechanical force. The resultant morphology is thus subject to both the polymer and the alignment processing conditions.

Electric field alignment is particularly attractive because it is especially well-disposed toward aligning domains perpendicular to the plane. This *through-plane* alignment establishes channels that connect the surfaces at either side of a polymer film: the most direct route for ion transport from one electrode surface to the other during charge and discharge of a hypothetical electrochemical cell. The utilities of both direct and alternating fields have been reported, however alternating fields are particularly useful for avoiding the accumulation of mobile ions and

the creation of a counter field during alignment. Moreover, the solvation of ions has been found by theoretical modelling to lower the critical voltage required to reorient the lamellae from parallel to perpendicular configurations.^[64] The magnitude of the reduction is enhanced when the ions have higher solubility in the sub-block having lower affinity for the electrode surface. The solvation and motion of ions being rejected from the electrode interface is improved with increasing the dielectric constant of the ion-conducting sub-block. Alignment by electrical field thus informs how one might encode microphase-separation into a polymer electrolyte by chemical synthesis.

Magnetic field alignment also enables *through-plane* ordering but without the need for material contact with the polymer bulk. Large magnetic fields can be applied without risk of chemical reaction of the polymer and the process is broadly scalable.

Whereas mechanical, electrical and magnetic forces applied to the sample serve to align domains on the micronic scale (the scale of the film and the instrumentation), the efficiency of the domain connectivity through the bulk is determined on the nanoscale (the scale of the repeating units and the persistent length of a polymer chain). With this in mind, one can imagine two approaches to achieving long range ordering of ionically conductive domains: **i)** increasing the number of self-assembled units over which nanoscale self-assembly can propagate through the bulk and **ii)** increasing the dimension of the repeating unit of propagation. In the case of classic LAM organisation of BCPs, researchers are limited by the nanoscale dimension of polymer chains that microphase-separate over a small length scale relative to the required microscale dimension of a battery electrolyte.

Methods for alignment were compared by M.J. Park and N.P. Balsara for characterisation of the proton conductivity of poly(styrenesulfonate-*b*-methylbutylene) (PSS-*b*-PMB) films (**Fig. I-15**).^[65] They concluded that the proton conductivities of their 180-220 μm thick films were dominated by the persistence of grain boundaries. Electrical field, mechanical shear, and pressing alignment of solvent cast films were compared to samples prepared by solvent casting only. The PSS-*b*-PMMA had $M_w = 5 \text{ kg/mol}$, a 1:1 mass ratio of sub-blocks, and $D_w = 1.02$. The solvent cast films, without additional alignment, had an *in-plane* (parallel) to *through-plane* (perpendicular) proton conductivity ratio $\sigma_{\parallel}/\sigma_{\perp} = 1.8$. Application of electrical field ($\sigma_{\parallel}/\sigma_{\perp} = 1.3$) and mechanical shear ($\sigma_{\parallel}/\sigma_{\perp} = 1.4$) forces decreased this value. Whatever benefit to the percolation of conductive domains may have been achieved was counter-balanced by the propagation of poorly conducting grain boundaries through the material. The greatest anisotropy was observed for pressed films, which had $\sigma_{\parallel}/\sigma_{\perp} = 75$. Since LAM phases often spontaneously align parallel to the plane, it can be speculated that such anisotropy could be equally generated by long-term combined solvent casting and thermal annealing of BCP films. The question is then for how long one would be willing to wait, for the polymer electrolytes to reach thermodynamic equilibrium.

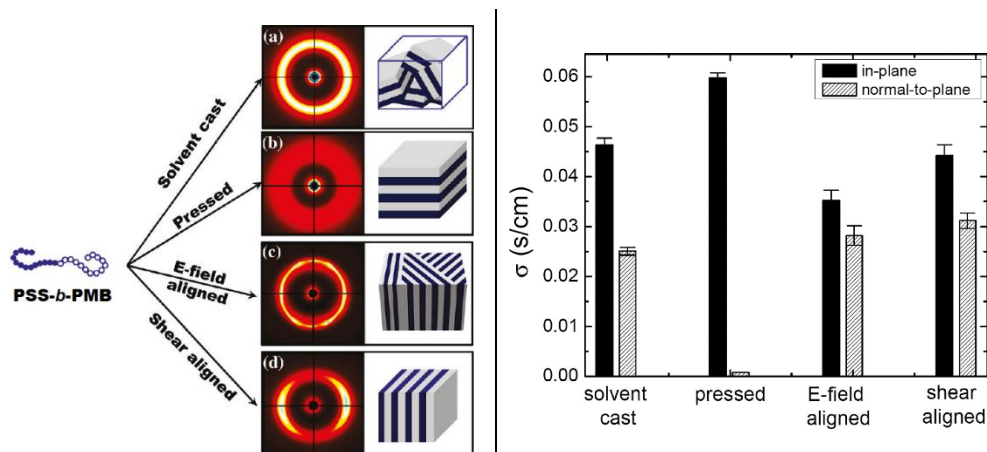


Figure I-15: (Left) SAXS images and illustrations of morphological ordering of poly(styrenesulfonate-*b*-methylbutylene) BCP films (180-220 μm thickness) made by (a) solvent casting, and aligned by (b) pressing, (c) electric field and (d) mechanical shear. (Right) Proton conductivity of the films (S/cm) at 25 $^{\circ}\text{C}$. The figure is reproduced from the literature.^[65]

Increasing the reproducibility and decreasing the timescale required for the (effective) alignment of ordered morphologies has driven researchers to develop high-energy, high-speed techniques.^[66] There exists no universal curing for all systems and multiple processes are often applied, in parallel or in series. A practical constraint (and inspiration for methodology) is the limit of industrial application of certain techniques. For example, long-term heating (annealing) is not only inefficient for mass production but can also be hazardous to organic molecules; solvent techniques are not well-adapted for use in "dry lab" industries; the economics of installing specialised equipment onto optimised assembly lines may be prohibitive. Therefore, polymers suitable for industrial techniques and instrumentation already installed to large-scale assembly lines are attractive to researchers seeking to bring the *state-of-the-art* to the doorstep of industry.

2.3.5. Molecular Architecture for Tuning Self-Assembly of Block Copolymers

Macromolecular engineering of defects into the polymer architecture has been explored as means to invoke morphological changes in the solid-state. Morphologies with smaller domains are desirable for a wide range of applications. Organisation of macromolecules on a small ($d < 10\text{ nm}$) scale requires a reduction in the size of the macromolecular architecture (*i.e.* a decrease of N). To maintain a useful morphology relative to a composition parameter χN , one would therefore seek out a "high- χ " molecular unit (sub-block). For this reason, "High χ -Low N " BCPs have attracted much attention.^[67]

A point-group can be introduced at a specific location along the backbone a polymer chain or at the chain-end. A mid-chain point defect can be thought of as a High χ -Low N sub-block. Indeed, an *A-b-B-b-C* triBCP with specific interactions invoking high- χ character in the central block can microphase-separate effectively, even when the X_n of the B sub-block is much smaller than those of the A and C sub-blocks. A widely studied BCP model system is poly(styrene)-*b*-poly(methyl methacrylate) (PS-*b*-PMMA). The easily accessible perpendicular orientation of PS-*b*-PMMA lamellae and the well-practised removal of the PMMA block by chemical etching make it particularly suitable for the fabrication of nano-patterns. However, the small difference in χ of the two sub-blocks decreases the microphase-separation efficiency of this BCP, forcing the use of high N sub-blocks, which increases the morphological feature size. This room for improvement provides a good framework for investigating how phase segregation can be chemically encoded

into a BCP. For example, the percolation of the lamellar morphology of PS-*b*-PMMA was decreased to sub 10-nm feature size by the inclusion of a 10 % (w/w) central block of poly(methacrylic acid) (**Fig. I-16**).^[68] H-bonding interactions in a small central region of the BCP enforced microphase-separation, increased the ordering range and decreased the feature size lamellar morphology. The small central block could be decreased further in size to a point-group. Line-edge roughness in PS-*b*-PMMA was decreased by introduction of specific block junctions. The H-bonding and rigidity of an asymmetric junction at the midpoint of PS-*b*-PMMA decreases interfacial width by 30 % (**Fig. I-17**).^[69]

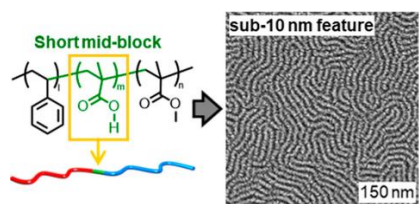


Figure I-16: Chemical structure and TEM micrograph of the PS-*b*-PMAA-*b*-PMMA copolymer. The figure is reproduced from the literature.^[68]

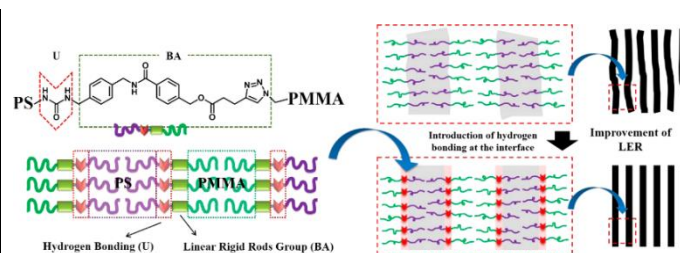


Figure I-17: Chemical structure and illustration of the lamellar arrangement of PS-*b*-PMMA having an orientation specific, H-bonding block junction. Introduction of the junction decreases line-edge roughness by 30 %. The figure is reproduced from the literature.^[69]

PEO has been demonstrated to exclude mid-chain defects based on substituted phenyl rings.^[70] The phenyl groups are expelled from the crystalline structure of PEO, causing the formation of lamellar phases. For example, phthaloyl (1,2-substituted) and isophthaloyl (1,3-substituted) rings as mid-chain defects are sufficient to induce a once-folded chain conformation, causing the formation of a spiral lamellar morphology of the "two-arm" PEO ($\text{H}_3\text{C-PEO}_{50}\text{-Ph-PEO}_{50}\text{-CH}_3$; $M_n = 2 \times 2220$ g/mol, $\text{EO}_n = 2 \times 50$). 1,4-Disubstituted 1,2,3-triazoles as mid-point defects have been demonstrated to induce a "chain flip" in two-arms PEO ($M_n = 2 \times 500$, $\text{EO}_n = 2 \times 11$).^[71] In this case, the ring is incorporated into the crystalline lamellae and causes reversal of the direction of the pitch of the PEO 7/2 helix. This interrupts organization of the polymer chains and creates semi-crystalline PEO morphology in which the triazole (\blacklozenge) is located at the grain boundary. The orientation of PEO chains within the crystalline domain follows the angle directed by the mid-chain point-group defect (**Fig. II-18**). Extension of this design invokes a miniature A-*b*-B-*b*-A triblock copolymer ($\text{H}_3\text{C-PEO}_{11}\text{-}\blacklozenge\text{-(CH}_2\text{)}_n\text{-}\blacklozenge\text{-PEO}_{11}\text{-CH}_3$; $n = 2, 3, 4$).^[72] The triazole point-groups accumulate at the crystalline-amorphous interface and cause one of the PEO₁₁ chains to be expelled from the crystalline domain. The melting temperatures were influenced by the π - π interactions of the triazole rings. Increasing the length of the alkyl spacer reduces the packing efficiency and decreases the melting temperature of the polymer (from $T_m = 29$ °C [$n = 2$], to 17 °C [$n = 4$]).

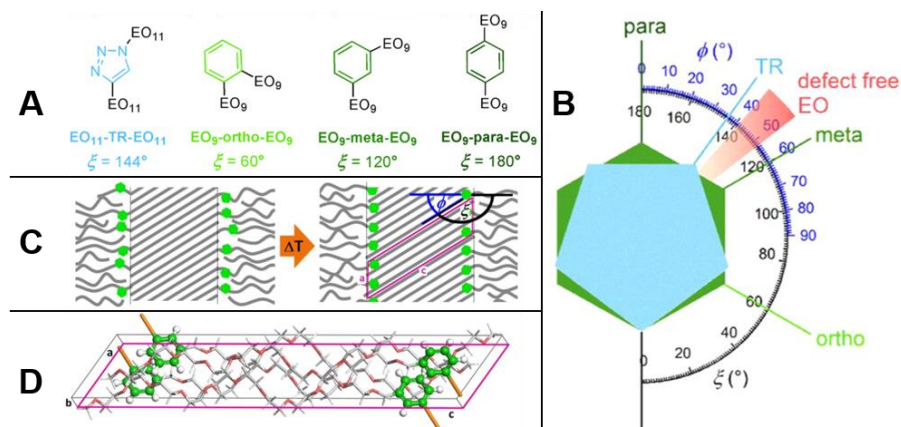


Figure I-18: (A) The point-group defects positioned mid-chain in $\text{H}_3\text{C-PEO}_{50}\text{-}\bullet\text{-PEO}_{50}\text{-CH}_3$: (L-R) 1,4-disubstituted-1,2,3-triazole; *ortho*, *meta*, and *para*-substituted phenyl rings. (B) The angle of chain tilt ($\phi = 180^\circ - \xi$) represented from the cross-section of the polymer chain (TR= triazole). (C) An illustration of how thermal annealing permits the defects through the boundary of the crystalline grain. The chain tilt angles are represented at the point-group (green dots). (D) A model illustrating the point-generated chain tilt. *The figure is adapted from the literature.*^[71]

The angle of the substitutions at the mid-chain point-defect yields different degrees of chain tilt, altering the angle of the crystal lamellae relative to the interface.^[73] All of the mid-point-defects (phenyl, triazole) are excluded from the crystalline phase at low temperature but become incorporated when the polymers are cooled from thermal annealing. WAXS analysis of the polymers revealed that the angle of chain tilt at the interface was directly correlated to the angle of the mid-point defect, and distinct from the typical chain-tilt arising from the PEO 7/2 helix (40-50°). This concept can be taken further: the triazole unit can be quaternized to yield a methyltriazolium unit at the BCP mid-point.^[74] In the case of PDMS-*b*-PEO, the ionic junction at the mid-point raises the T_{ODT} from 170 °C (triazole unit) to above 190 °C (methyltriazolium unit), higher than the decomposition temperature of the polymer. Increase of the intensity of scattering peaks in SAXS profiles of the polymers suggested long-range ordering is improved by the methyltriazolium unit. This condition of $T_{\text{ODT}} > 190$ °C of PDMS-methyltriazolium-PEO was maintained by the ionic junction even when 30 % (w/w) of additional PEO (750 g/mol; $\text{EO}_n = 17$) was added to the system. This is significant for demonstrating the segregation strength of the BCP, for when an excess of the ionically conductive PEO would not disrupt segregation of the domains.

Large aromatic junctions (at the interface of two or more sub-blocks) are capable of developing non-covalent interactions through π - π stacking. 1,4,5,8-naphthalenetetracarboxylic diimides (NTCDIs) and 3,4,9,10-perylenetetracarboxylic diimides (PTCDIs) at the block-junction of poly(styrene)-*b*-poly(L-lactide) (PS-*b*-PLLA) can support or erase the microphase separation of the BCP.⁷⁵ The microphase-separated morphologies were determined by temperature dependent forces of π - π stacking interactions and the χ_N of the two polymeric sub-blocks. The free energy minima are similar in magnitude, resulting in a self-assembly behavior that is kinetically controlled, and therefore process dependent. In general, the rate of formation of π - π stacking interactions is slower than the segregation of the polymeric sub-blocks, so combinations of solvent casting and thermal annealing were used to generate variations on lamellar and hexagonally packed morphologies. In general, fast evaporation of solvents from a film favors block segregation and yields lamellar morphologies controlled by the χ_N parameter of the polymeric sub-blocks. However, as little as 2 % (w/w) of the aromatic junctions can assemble effectively over longer timescales promoted by thermal annealing to yield hexagonally packed columns.

2.4. Alternative Polymers for Salt-In-Polymer Electrolytes

Although the field of solid polymer electrolytes (SPEs) has been dominated by variations on the theme of PEO, alternative polymer matrices could provide the properties required for enhancing the *state of the art*. There are examples of alternative SPEs that surpass the performance of PEO in terms of electrochemical and thermal stability, and lithium transference number. Indeed, the best ionic conductivity, of *ca.* 10^{-3} S.cm⁻¹, of PEO-type SiP electrolytes is only achieved above the melting temperature (T_m) of the polymer. The ionic conductivity, at $T > T_m$, of such a polymer melt cannot be reasonably classified as that of a “solid” polymer electrolyte. A good alternative to PEO would be a polymer that, for example, could be equally ionically conductive at the same temperature regime but retain the mechanical properties of a macroscopic solid. Moreover, the requirements of a battery (and its electrolyte) are different, depending on the application. It is highly unlikely that a single polymer electrolyte design would be suitable for all battery designs and applications. Higher operating temperatures now become relevant as LiBs are used in electric vehicles. Under these circumstances, polymers as safe alternatives to organic liquid electrolytes in general is a critical consideration. PEO is a good complexing agent for Li⁺. This is because of the Lewis basicity of the ether oxygens. Although the coordination strength of an ether is in fact weaker than for carbonates, esters and ketones, the multi-dentate chelation of Li⁺ by several ethers simultaneously results in a cumulative strength surpassing that of the carbonyl oxygens.^[76,77] The result is excellent solvation of Li⁺ but also slow mobility of the cation for the very same reason. Inversely, weaker complexation of Li⁺ by carbonyl oxygens can enable polymers relying on moieties of this type to permit higher net transfer of lithium, as defined by higher lithium transference numbers.

Broadening the scope of polymer electrolyte design and performance necessarily calls for systematic study of different polymer chemistries. A distinction should therefore be made between probing the fundamental properties of a particular polymer chemistry, conformation or design principle, and seeking an engineering solution to an established model. The optimisation of a material by suppression of its fundamental properties serves to obscure structure-property correlations, which are developed experimentally only through systematic study of a wide variety of examples.

For the sake of simpler classification, one can confine variations on the use of ether units under the title of poly(ether)s. For example, a poly(norbornene) homopolymer with oligo(ethylene oxide) side-chains relies on the ether for the coordination and transport of Li⁺.^[78] To look beyond poly(ether)s, and specifically PEO, it is the polar, ion-coordinating function of a polymer that is of interest. Alternatives to poly(ether)s for SiP formulations include poly(alcohol)s, poly(amine)s, poly(carbonate)s, poly(ester)s, and poly(nitrile)s, which have recently been reviewed.^[79] Performance rivalling PEO-based systems has been achieved, a variety of polymer architectures have been tested in the context of SiP electrolytes, and familiar techniques for optimisation have been applied. For example, LiClO₄ in poly(acrylonitrile) (PAN) yields $\sigma_{AC} = 6.5 \cdot 10^{-7}$ S.cm⁻¹ (AN/Li=50) at 30 °C,^[80] which is improved by blending with either Al₂O₃^[81] or silica aerogel^[82] (both have $\sigma_{AC} \approx 6 \cdot 10^{-4}$ S.cm⁻¹ at 30 °C).

Poly(carbonate)s and poly(ester)s have been proposed as electrolytes for LiBs. These polymers coordinate Li⁺ primarily *via* their carbonyl oxygens, but some coordination by the alkoxy oxygen is also possible.^[83,84] Inspiration for their use may have arisen from the application of small-

molecular carbonates as liquid solvents and plasticizers for liquid and gel electrolytes. Poly(carbonate)s have attracted interest because:

- I. The ionic conductivity of poly(carbonate)s is similar to PEO-based polymer electrolytes but with PC-based SiP electrolytes reaching $t_{\text{Li}}^+ = 0.5-0.6$, primarily due to weaker coordination of Li^+ . *This characterises greater efficiency of Li^+ transference.*
- II. For the same reason, poly(carbonate)s withstand higher concentrations of salt in SiP blends without the associated stiffening of the polymer chain. *This implies the design of high energy density batteries.*
- III. Electrochemical stability has been demonstrated beyond 4.0 V, and with some examples reaching 4.5 V vs. Li/Li^+ . *This targets high energy cathodes and therefore high-power batteries.*
- IV. Macroscale salt ionic conductivity in poly(carbonate)s persists at $T < T_m$ without the need for additional plasticizers. *This targets ionic conductivity through mechanically strong electrolyte films at ambient temperatures.*
- V. Thermal and mechanical properties can be tuned by design of their polymer architecture. For example, T_g and T_m can be tuned by changing inter-carbonyl spacing, designing comb-shaped polymers and copolymerisation with plasticizing units.

Researchers have targeted low T_g to permit comparisons to PEO, and applied these polymers as matrices for SiP electrolytes. Statistical copolymers of esters and carbonates are of particular interest because of **i**) the stability of carbonates up to 5.0 V vs Li/Li^+ and **ii**) the mechanical properties of poly(ester)s. Following investigations into how monomer design and copolymerisation could yield poly(carbonate)s and poly(ester)s of varying degrees of crystallinity,^[85] J. Mindemark and co-workers have recently applied them as SiP electrolytes. Poly(ϵ -caprolactone) (PCL) attracted some interest, as it is comparable to PEO in terms of T_m (50-60 °C) and T_g (-45°C/-60 °C). However PCL is around 30 % crystalline^[86] (depending on thermal history and processing), much lower than PEO, which can be 75-80 % crystalline^[87] at room temperature without special thermal treatment. Although PCL is stable up to 4.2 V vs. Li/Li^+ and has $\sigma_{\text{AC}} = 1.2 \cdot 10^{-6} \text{ S cm}^{-1}$ (at 30 °C) for a 10 % (w/w) loading of LiClO_4 .^[88,89] These results are comparable to poly(ether)s under similar conditions, and obtained without use of additional components in the SiP formulation.

The electrochemical stability of poly(trimethylene carbonate) (PTMC) up to 5.0 V vs. Li/Li^+ inspired researches to pursue this polymer as a candidate for high voltage cathodes such as $\text{LiMn}_{1.5}\text{Ni}_{0.5}\text{O}_4$ and LiCoPO_4 .^[90] However, when the polymer was tested in $\text{Li}|\text{PTMC-LiTFSI}|\text{LiFePO}_4$ cells, a drop in capacity upon cycling was attributed to penetration of the polymer into the porous cathode. The addition of supplementary TMC oligomers improves cycling performance.^[91] Introduction of short alkyl side-chains to PTMC affords lower T_g (-50 °C) but does not significantly improve ionic conductivity relative to the undecorated homopolymer, implying that the polarity of the matrix is the limiting feature.^[92] The low ionic conductivity of the homopolymer (*ca.* $10^{-7} \text{ S.cm}^{-1}$ at 60°C) was improved through copolymerisation with ϵ -caprolactone (ϵCL). The P(TMC-co-CL) yields membranes with decreasing T_g and increasing conductivity with increasing fractions of $\epsilon\text{-CL}$, without detrimental impact on the electrochemical stability.^[93] For example, 28 % (w/w) LiTFSI in a 60:40 (TMC: ϵCL) statistical copolymer yields $T_g = -26$ °C and $\sigma_{\text{AC}} = 1.5 \cdot 10^{-5} \text{ S.cm}^{-1}$ at 60 °C. However the ionic conductivity of the PCL homopolymer at room temperature is somewhat higher.^[89,93]

Optimisation of the P(TMC-*co*- ϵ CL) was reported for a majority CL statistical copolymer (36 wt% LiTFSI in 20:80 TMC:CL host). This blend reaches ionic conductivity that is comparable to the best poly(ether)-based SiP electrolytes. The ionic conductivity was measured as $\sigma_{AC} = 4.1 \cdot 10^{-5} \text{ S.cm}^{-1}$ at 25 °C and $1.1 \cdot 10^{-4} \text{ S.cm}^{-1}$ at 40 °C, having $t_{Li}^+ > 0.6$ at 40 °C.^[94] For comparison, the authors measure PEO₁₇/LiTFSI (EO/Li= 17; 38 % w/w LiTFSI) to have $t_{Li}^+ = 0.12$ at 40 °C. The higher t_{Li}^+ of the P(TMC-*co*- ϵ CL) blend is evidence of weaker binding of the cation to the polymer, in comparison to PEO. The authors note that achieving the ionic conductivity of their P(TMC-*co*- ϵ CL) blend at the same temperature would require significant compromise of mechanical strength in a PEO-based SiP electrolyte due to the addition of plasticizing compounds either as formulation components or as polymeric units. By contrast, neat P(TMC-*co*- ϵ CL) is demonstrated to be sufficiently conductive and at the same time robust, enabling operation as an electrolyte and separator at ambient temperature in LiBs without significant loss of capacitance (150 mA h/g), retaining close to 100 % coulombic efficiency of the cell.^[94]

The lower strength of Li⁺ coordination by poly(carbonate)s in comparison to PEO reduces the impact of salt concentration on chain stiffening. This is observed in PEO as an increase in T_g upon addition of salt. It is therefore possible load greater concentrations of salt into poly(carbonate) matrices without prohibitively decreasing mobility of the polymer chain and the associated ionic mobility. At the extreme condition, a high salt concentration yields a *polymer-in-salt* electrolyte. For example, the T_g of poly(ethylene carbonate) *decreases* upon addition of LiTFSI, yielding ionic conductivity greater than $10^{-4} \text{ S.cm}^{-1}$ at 80 mol% (EC/Li= 0.80) of LiTFSI at 80 °C.^[95] Increasing the alkyl spacer length between the carbonate groups plasticizes the polymer and correlates to an increase in ionic conductivity. For example, LiTFSI in poly(dodecamethylene carbonate) reaches $\sigma_{AC} = 4.1 \cdot 10^{-5} \text{ S cm}^{-1}$ at 80 mol% (EC/Li= 0.80) of LiTFSI at room temperature.^[96] If the $-(C_2H_2)_6-$ inter-carbonate spacer of the poly(carbonate) (PC) is exchanged for an oligo(ether) of the same number of carbons, $-(C_2H_2O)_6-$, a similar ionic conductivity is achieved in PEO-PC.^[97] However the diffusion coefficients of ⁷Li and ¹⁹F measured by NMR reveal that the diffusion of TFSI⁻ is higher than that of Li⁺ in PEO-PC at this salt concentration.^[97] The higher Li⁺ complexation strength of PEO would be accompanied by a drop in t_{Li}^+ relative to the poly(carbonate). A direct comparison including lithium transference numbers was not made by the authors. Poly(carbosilane)s having silane primary chains and pendant cyclic carbonate groups permit loading of LiTFSI as high as 400 mol% (EC/Li= 0.25) and achieve $\sigma_{AC} = 1.2 \cdot 10^{-4} \text{ S.cm}^{-1}$ at 30 °C. However, the mechanical properties have not been sufficiently reported to determine whether such a blend is macroscopically solid. Interesting behaviour has been reported for copolymers comprising cyclic ethylene carbonate pendant groups attached by a single bond to the primary chain. Despite low ionic conductivities, these polymers exhibited "super ionic" behaviour, in which the mobility of LiTFSI is decoupled from polymer segmental dynamics.^[98]

The reports of polymer electrolytes based on poly(carbonate)s by different groups collectively suggest little correlation between polymer T_g and ionic conductivity of a binary salt. Lower complexation strength of Li⁺ by carbonate relative to PEO enables more equal mobility of oppositely charged ions through the polymer host, thus achieving transference numbers around 0.5. Electrochemical stability is routinely demonstrated above 4 V vs. Li/Li⁺, enabling the combination of this electrolyte with high energy cathodes.

2.5. Conclusions on Salt-in-Polymer Electrolytes

The addition of large quantities of salt into polymer matrices has been the primary research axis into SiP electrolytes for the last 40 years. These efforts have been limited by the difference in mobility of oppositely charge ions through the polymer host. In the case of widely studied PEO-based systems, the high complexation strength of the poly(ether) reduces the mobility of Li^+ and the resultant ionic conductivity of the electrolyte is dominated by the contribution of anionic mobility. The crystallisation of PEO limits the percolation of the amorphous domains through which fast ion transport can occur. However, the plasticizing effect of salt and other components in SiP formulations effectively decrease the melting temperature of the polymer electrolyte. High conductivity at $T > T_m$ means that they operate well once the mechanical strength of the electrolyte has been lost. The apparent benefits to the safety, energy density, and battery design are therefore lost in the temperature regime in which high ionic conductivity is achieved.

Efforts to optimise the polymer by variation of the polymer architecture, for example by branching and crosslinking, show that high performance is achieved only when the segment length of the modified polymer approaches that of linear PEO. Further efforts to improve the mechanical properties of PEO-based electrolytes have targeted block copolymer architectures, wherein one of the sub-blocks affords mechanical reinforcement of the electrolyte. This approach is limited on the microscopic scale relevant to the battery application by the segregation strength of the sub-blocks and the efficiency of the percolation of ionically conductive channels. The formulation of homopolymers and block copolymers with additional components has achieved some enhancement of mechanical properties, and enabled some spontaneous, directed organisation of ions into transport channels. Moreover, the assembly of block copolymers can be directed by external alignment forces and by deposition onto patterned substrates. However, achieving structural order that is entirely free of defects, as required for maximal efficiency of transport on the mesoscopic/micronic scale, is still a great challenge.

The design of copolymers and formulations in which the mechanical properties are controlled by a non-conducting sub-block or blended species allows researchers to look beyond PEO. If mechanical strength is no longer a criterion, any ionically conductive polymer could be tried. Electrolytes based on poly(carbonate)s and poly(ester)s have already been demonstrated to have mechanical and ionically conductive properties comparable to the best offered by PEO. Alternative polymers that are electrochemically stable beyond 4 V vs. Li/Li^+ , the anodic limit of PEO, become increasingly useful in the context of the latest high-potential cathode materials. The design principles developed in SiP systems lead researchers to **i)** organise ion transport into directed pathways, **ii)** through polar polymers that coordinate weakly to Li^+ , **iii)** while maintaining mechanical integrity of the macroscopically "solid" electrolyte.

3. "Single-Ion" Polymer Electrolytes (SIPes)

3.1. Introduction to Single Lithium-Ion Transport in Polymeric Electrolytes

Despite the advantages of a polymer matrix addressed in the previous section, polymers as ionic conductors of binary salts continue to present numerous challenges to be overcome. In a dual ion conductor, both cations and anions are mobile in the host matrix. The difference in the mobility of the anion and the cation results in the formation of a concentration gradient across the electrolyte when a secondary battery is repeatedly charged and discharged. Accumulation of the anionic species at the electrode-electrolyte interface invites adverse reactions, cell polarization, dendrite growth and, ultimately, failure of the cell. Efficiency, cycle-life and charge transfer of the cell can be increased by maximising the fraction of the ionic charge transferred by the movement of lithium across the electrolyte. This increases the effective current supplied by the cell and removes the problems associated with concentration of anions at the electrode-electrolyte interface. In the case of a **Lithium ion Batteries (LiBs)** or a **Lithium Metal Batteries (LMBs)**, a "Single-Ion" conductor refers to an electrolyte in which the anion is anchored and only the lithium cation can move. This can be achieved by covalently bonding the anion onto a polymer or inorganic framework, or by effectively immobilising the anion onto an acceptor species. The fraction of charge transferred by movement of Li^+ is called the **Lithium Transference Number (LTN, t_{Li}^+)** and the performance of a SIPE can surpass that of traditional SiP blends as this value approaches unity, when all the charges are transferred by lithium cations. A single-lithium-ion conductor with $\sigma \approx 1 \cdot 10^{-4} \text{ S.cm}^{-1}$ at 60 °C is defined as the critical lower limit of ionic conductivity for practically useful SIPes in large format batteries.^[99]

3.2. Design of SIPes

The design objectives of SIPes build on those established during the development of polymer electrolytes in general. High ionic conductivity must be combined with electrochemical stability over a practical range of temperature. In order to decrease the mass of polymer electrolyte, as required for a high energy density battery, the SIPE must host a high concentration of ions and also have a high complex mechanical modulus. As for SiP electrolytes, a SIPE must act as a host for lithium ions and also conduct them. Fast and efficient ion transport can be achieved by directing the motions of ions through a high permittivity electrolyte. The ionic transport pathway should be free from prohibitive physical and energetic barriers. Injection of ions into the electrolyte and insertion of ions into the electrodes from the electrolyte should be facilitated by good wetting of the electrode surface. The electrode-electrolyte interface should not be chemically consumed during charge and discharge of the cell.

Through variation of the polymer chemistry, researchers want to know **i)** what covalently bound anions are best-suited to dissociation and transport of Li^+ through the electrolyte and **ii)** what ionically conductive matrix is best-suited to the (electro)chemistry and operating conditions of a lithium battery, *i.e.* "*What anion do I want and to what matrix should it be tethered?*" Through variation of the architecture of SIPes, researchers want also to know **i)** what is the limit of salt concentration to enable high ionic conductivity and **ii)** where on the polymer architecture should these salts be positioned to maximise their utility, *i.e.* "*How many ionic units do I need and where should they go?*"

With respect to the polymer architecture, the ionic function of a SIPE can be positioned at the chain end, at the repeating unit of the primary chain, or as a pendant group (in "comb-shaped" polymers). These design options have been widely applied to numerous primary chain chemistries, in statistical, alternating and block copolymers, and in linear, branched and network architectures.

3.3. Synthesis of SIPEs

The ionic function of a SIPE can be placed at the repeating unit and at the end-group of the polymer chain. Polymers with an ionic function at every repeating unit are poly(electrolyte)s and can be synthesized by **i**) polymerisation of ionic monomers or **ii**) post-polymerisation modification of polymers. End-groups can be defined in a polymerisation method **i**) by controlled polymerisation using a functional initiator and **ii**) by chemical quenching. End-group chemistry can enhance the physicochemical properties of a homopolymer or be implemented as means to a more elaborate synthetic strategy.^[100–103] The functional end-groups of polymers synthesized by controlled polymerisation methods can be exploited through post-polymerisation modification. Modern polymer synthesis is used to create a variety of macromolecular architectures, and the synthesis of elaborate SIPEs might require a combination of methods.

Any reactive functional group on a polymer can be exploited for post-polymerisation modification. The practical advantage of this method is that a polymer will retain its known Degree of Polymerisation (DP_n , X_n) and Dispersity in mass (D_w). Characterisation of ionic polymers can be problematic for reasons of solubility, compatibility with instrumentation and physicochemical similarity to reference standards, so it can be useful to define a precursor polymer in advance of the synthesis of a SIPE. This is of special concern for polymers with complex architectures and organic-inorganic hybrid materials. However, high conversion in post-polymerisation modification can be a challenge. Reaction kinetics may change as conversion approaches unity and proximal like-charges begin to repel each other, decreasing the repeating unit fidelity of the poly(electrolyte). Precipitation and aggregation of the poly(electrolyte) may kinetically entrap the reactive groups and effectively halt a reaction.

3.4. End-Capped Single-Ion Polymer Electrolytes (EC-SIPEs)

Some of the earliest SIPEs were poly(ether)s with anionic chain terminals. In the case of a linear polymer having an ionic function at one (MEC-SIPEs) or both (Bis-EC-SIPEs) of two chain ends, the charge carrier density is a function of the polymer DP_n . Low DP_n poly(ether)s, having a higher charge carrier (end-group) concentration, were therefore expected to exhibit higher ionic conductivity. Researchers generally correlated the conductivity of EC-SIPEs to the volume fraction of the amorphous phase of the polymer matrix by comparison of ionic conductivity measurements with DSC and WAXS/SAXS. Among polymers having the same end-group but of different DP_n , the highest ionic conductivity was observed for polymers with the lowest T_g (for poly(ether)s, these are typically in the range of $T_g \approx -20^\circ\text{C}/-60^\circ\text{C}$, see **Fig. I-19**). The optimum ionic conductivity was found in the range of $EO_n \approx 10\text{-}35$ units (for PEO, $M_w = 500\text{-}1500$ g/mol), depending on the ionic group and the whether the polymer is mono- or bis-end-capped.

After physicochemical,^[104] synthetic^[105], and electrochemical^[106,107] investigations by other groups, a systematic study was presented by H. Ohno and co-workers. They published a series of papers detailing the effect of alkali metal carboxylate ($R\text{-CO}_2M$),^[108,109] sulfonate ($R\text{-SO}_3M$)^[110] and

benzene sulfonate (R-OC(O)PhSO₃M),^[111] sulfonamide (R-SO₂N(M)R)^[112–115], and (trifluoromethylsulfonyl)imide (TFSI)^[116] end-groups on electrolyte performance.^[117–119] Oligo(ether)s bearing fluoroether-^[120] and aryl-^[121] TFSI terminals were later evaluated by the DesMarteau group.

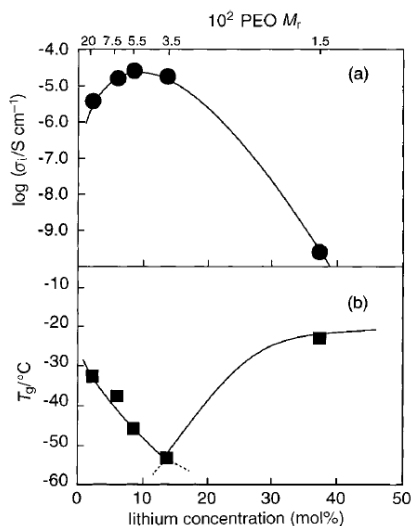


Figure I-19: (a) The ionic conductivity at 50 °C and (b) T_g of H₃C-PEO_n-SO₃Li MEC-SIPEs as a function of i) PEO M_w (*10⁻² g/mol) and ii) lithium concentration (mol%). The figure is reproduced from the literature.^[110]

Bis-end-capped polymers were usually less conductive than a comparable MEC-SIPE having the same ionic end-group. This is listed below for sulfonate end-capped polymers (Table I-1, 2A vs. 2F). Comparison of MEC-SIPEs have four times lower salt concentration than bis-EC-SIPEs of the same DP_n, but the MEC-SIPEs have ionic conductivity 2 orders of magnitude higher at 50 °C (Table I-1, 2B vs. 2E). The temperature dependent ionic conductivity of PPO₁₅-TFSILi (Table I-1, 10A) does not change much in the 60-10 °C range if the polymer DP_n is raised to X_n= 19.^[116] However, bis-end-capped PPO₂₁-(TFSILi)₂ with nearly twice the concentration of end-groups has ionic conductivity that is ca. 1-2 orders of magnitude lower. It is likely that a polymer architecture having end-groups at both chain terminals restricts chain mobility, which might be observed by an increase in the characteristic segmental relaxation time.

The ionic conductivity of PEO of the same chain length (DP_n= 23; M_w= 1000 g/mol) but with different end-groups were compared in the literature.^[112,117] Benzenesulfonate end-capped polymers were less ionically conductive than the sulfonates (Table I-1, 2→3). Sulfonamide EC-SIPEs had higher ionic conductivity than R-CO₂Li and R-SO₃Li EC-SIPEs (Table I-1, 4→6). The difference in ionic conductivity is attributed to a change in the dissociation energy of the organic salt. In the case of benzenesulfonates, this could be consequence of the inductive electron withdrawing effect of the ester increasing the electronegativity of the carbon at the *meta* (sulfonate) position. Altering the sulfonyl substituent (R) of the sulfonylimide of bis-end-capped PEO₂₃-(N(Li)SO₂R)₂ revealed a trend of ionic conductivity following the identity of R= CF₃> CH₃>Phenyl. The trend is different for mono-end-capped PPO (Table I-1, 7→9). In this case, the methyl and phenyl substituents afford similar ionic conductivities, however both are around one order of magnitude less conductive than the fluorinated derivative. However, bis-EC-SIPEs with sulfonamide and sulfonylimide end-groups have similar ionic conductivity (Table I-1, 4 and 11E).

Table I-1: Lithium ion conductivities of selected poly(ether)-based End-Capped Single-Ion Polymer Electrolytes (EC-SIPs) from the literature. References are indicated in the right-hand column (ref.). Mono- (X-●) and bis- (●-X-●) end-capped configurations are indicated. The conductivity is of the neat EC-SIPE. The polymers are organised by end-group (1-9), and by examples (A, B, C, ...) of DP_n and of measurement temperature. The M_w is of the polymer chain only.

	POLYMER End-Group	Configuration	DP _n (X _n)	M _w (g/mol)	Ionic Conductivity (S.cm ⁻¹)	T (°C)	ref.
1.		●-PEO-●	A 7	300	5.3*10 ⁻⁸	60	[108]
		●-PEO-●	B 14	600	2.6*10 ⁻⁷	60	[109]
2.		PEO-●	A 8	350	4.5*10 ⁻⁶	30	[110]
		PEO-●	B 8	350	≈2*10 ⁻⁵	50	[110]
		PEO-●	C 17	750	1.6*10 ⁻⁵	50	[110]
		PEO-●	D 45	2000	≈5*10 ⁻⁶	50	[110]
		●-PEO-●	E 9	400	≈5*10 ⁻⁷	50	[110]
		●-PEO-●	F 14	600	1.4*10 ⁻⁶	30	[110]
3.		PEO-●	A 17	750	7.0*10 ⁻⁶	50	[111]
		PEO-●	B 17	750	1.0*10 ⁻⁵	60	[109]
		PEO-●	C 45	2000	4.5*10 ⁻⁶	50	[111]
		●-PEO-●	D 14	600	1.8*10 ⁻⁶	60	[109]
		●-PEO-●	E 23	1000	2.9*10 ⁻⁶	50	[111]
		●-PEO-●	F 23	1000	5.1*10 ⁻⁶	60	[109]
4.		●-PEO-●	23	1000	2.8*10 ⁻⁵	50	[112]
5.		●-PEO-●	23	1000	1.6*10 ⁻⁵	50	[112]
6.		●-PEO-●	23	1000	3.3*10 ⁻⁶	50	[112]
7.		PPO-●	9	500	≈8*10 ⁻⁶	20	[115]
		PPO-●	9	500	≈5*10 ⁻⁵	50	[115]
8.		PPO-●	9	500	≈5*10 ⁻⁷	20	[115]
		PPO-●	9	500	≈3*10 ⁻⁶	50	[115]
9.		PPO-●	9	500	≈4 *10 ⁻⁷	20	[115]
		PPO-●	9	500	≈2*10 ⁻⁶	50	[115]
10.		PPO-●	A 15	850	3.3*10 ⁻⁶	30	[116]
		●-PPO-●	B 35	2000	1.2*10 ⁻⁶	30	[116]
11.		PEO-●	A 12	550	2.7*10 ⁻⁶	20	[121]
		PEO-●	B "	"	1.5*10 ⁻⁵	40	[121]
		PEO-●	C "	"	≈6*10 ⁻⁵	60	[121]
		PEO-●	D "	"	6.9*10 ⁻⁴	120	[121]
		●-PEO-●	E 22	1000	≈4*10 ⁻⁵	60	[121]
12.		PEO-●	A 12	550	7.1*10 ⁻⁶	25	[120]
		PEO-●	B "	"	≈1*10 ⁻⁴	60	[120]
		PEO-●	C "	"	≈1*10 ⁻³	120	[120]

3.5. Poly(electrolyte)s

A popular strategy for the synthesis of SIPEs is the polymerisation of ionic monomers. However, poly(electrolyte) homopolymers bearing only lithium salt repeating units are poor ionic conductors in the bulk-state, typically reaching ionic conductivity of $ca. 10^{-7} \text{ S.cm}^{-1}$ at 25 °C. Ionic conductivity is improved by blending the SIPE homopolymers with ionically conductive PEO. On the polymer, conductive repeating units, linkers between the salt function and the (meth)acryloyl group, and co-polymeric blocks can **i**) create ionically conductive domains proximal to the Li-ion host units and **ii**) develop plasticity throughout the bulk morphology. Anions often seen in the case of SIPEs for LiBs are lithium carboxylates (R-CO₂Li),^[122] sulfonates (R-SO₃Li)^[123,124] and sulfonylimides (R-SO₂N(Li)SO₂R').^[125,126] These anions are often used in the form of (meth)acryloyl or styrenic monomers and polymerised by radical polyaddition methods. Single-ion PEO networks comprising copolymerized sulfonate salts were reported by M. Armand *et al.* in 1995.^[127,128] These SIPEs had higher ionic conductivity than earlier examples that featured alkali metal methacrylates^[129] and phosphazene sulfonates.^[130] It was concluded that SIPEs would benefit from electron-withdrawing groups capable of delocalising the negative charge of the bound anion, following design rules developed for the anion of binary salts in high performance SiP formulations.

Many trends of SIPE performance, of homopolymers to blends, to statistical copolymers, and to BCPs, are exemplified by tracking the performance of the widely studied 4-styrenesulfonyl(trifluoromethylsulfonyl)imide) (STFSILi) repeating unit. The P(STFSILi) homopolymer can be synthesized by free-radical polymerisation of the STFSI monomer or by modification of poly(styrene sulfonate) (**Fig. I-20, A**).^[131] The resultant homopolymer was mixed with PEO into a composite solid membrane. The result was an increase in the ionic conductivity from the $ca. 10^{-6}$ to $10^{-5} \text{ S.cm}^{-1}$ at 60 °C.^[131] The performance of triblock P(STFSILi)-*b*-PEO₈₀₀-*b*-P(STFSILi) (NB: EO_n= 800), applied in a prototype battery, was reported to be superior to a conventional SiP (**Fig. I-20, B**).^[132] In this design, both the mechanical and polymerised salt functionalities are supported by the styrenic block, while PEO enables ion transport. The design yielded $\sigma \approx 1 \cdot 10^{-5} \text{ S cm}^{-1}$ at 60 °C with a polymer composition of 20 wt% STFSILi (EO/Li= 27) and exhibits single-ion conduction with $t_{\text{Li}}^+ > 0.85$. Then STFSILi was statistically arranged among ionically conductive units along the primary chain. Copolymers of STFSI with methoxy-polyethylene glycol acrylate (MPEGA) have ionic conductivities of $ca. 10^{-4} \text{ S.cm}^{-1}$ at 60 °C, superior in comparison to equivalent (EO/Li= 20.5) blends of P(STFSILi) in PEO (**Fig. I-20, C**).^[133] The P(STFSILi-*co*-MPEGA) has $t_{\text{Li}}^+ > 0.9$ and is thermally stable up to 300 °C. In the case of the *A-b-B-b-A* triBCP, changing the styrene of STFSI for propylmethacrylate yields MTFSILi, a repeating unit connecting TFSI to the poly(methacrylate) primary chain *via* a C₃ linker (**Fig. I-20, D**). Using the same length of the central PEO block (35*10³ g/mol, EO_n≈ 800), superior ionic conductivity of $ca. 10^{-4} \text{ S.cm}^{-1}$ is reached at 70 °C.^[134]

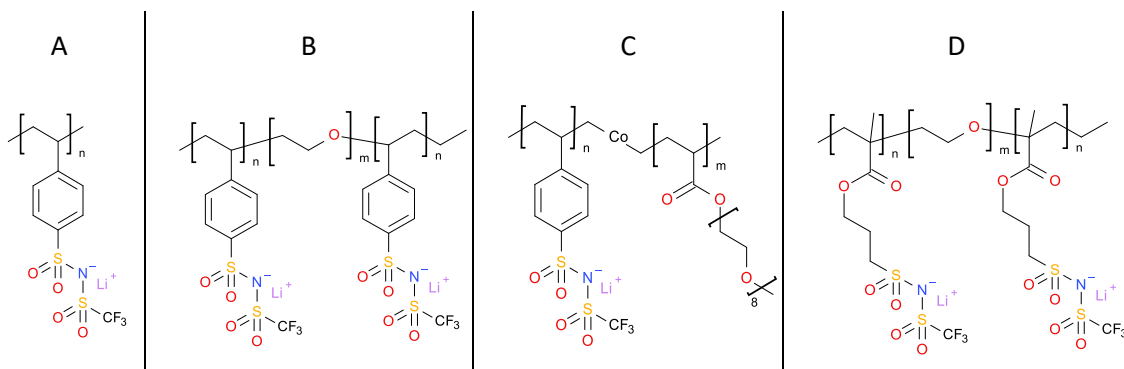


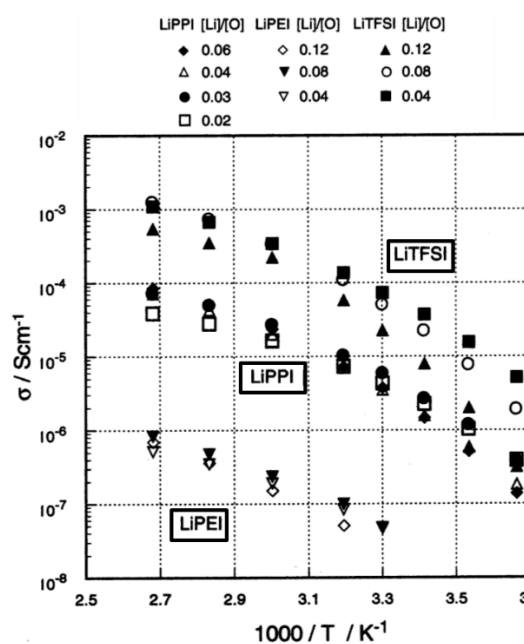
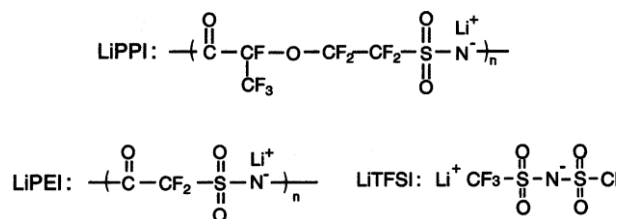
Figure I-20: The chemical structure of poly(electrolyte)s (A) P(STFSILi)^[131]; (B), the tri-BCP P(STFSILi)-b-PEO₈₀₀-b-P(STFSILi)^[132]; (C), the statistical copolymer P(STFSILi-co-MPEGA)^[133]; and (D), the tri-BCP P(MTFSILi)-b-PEO₈₀₀-b-P(MTFSILi)^[134].

The dominance of the TFSI⁻ anion in SiP formulations was inspiration to the domain of SIPEs. The research question was then posed by the Watanabe group, through a series of papers beginning in 2000, of whether a TFSI-inspired poly(anion) could push the limit of SIPE performance (**Fig. I-21**).^[135-137] Their poly(2-oxo-1-difluoroethylene sulfonylimide) (LiPEI) polycondensate homopolymer was mixed with poly(ether) precursors which were then photochemically crosslinked to form a polymer blend in which the LiPEI homopolymer was physically trapped within a poly(ether) network.^[135] A corresponding decrease of the loss tangent (δ) of tensile modulus, measured by dynamic mechanical analysis (DMA), supports the authors' claim of "good" mixing of the polymers. Increasing the mass fraction of LiPI resulted in the peak of $\tan(\delta)$ moving to higher temperature as a result of increasing number of ion-dipole interactions between the matrix and the poly(anion). The magnitude of the $\tan(\delta)$ of the native poly(ether) matrix decreased upon mixing with LiPEI, which is attributed to the decreasing fraction of non-complexed poly(ether) segments. However the intrinsic inhomogeneity of mixing two polymers prevents the formation of a homogeneous mixture.

Figure I-21: Poly(electrolyte)s based on LiTFSI. The figures are reproduced from the literature.^[136]

Below: the chemical structure of the poly(electrolyte)s LiPEI, LiPPI, and the small molecular salt LiTFSI.

Right: The ionic conductivity as a function of reciprocal temperature of LiPEI, LiPPI and LiTFSI in crosslinked network PEO.



The poly(ether)/LiPEI alloy achieved $t_{\text{Li}}^+ = 1$ and is stable in the range 0-4.0 V vs Li/Li⁺ but had ionic conductivity of *ca.* 10⁻⁶ S.cm⁻¹ at 100 °C, three orders of magnitude lower than the equivalent blend of the crosslinked poly(ether) and LiTFSI. This could be explained by **i**) low dissociation of Li⁺ from

the poly(anion) chain and **ii**) insufficient flexibility and therefore low thermally activated motion of the poly(anion). In the first case, the anionic units are covalently linked by single, configurationally symmetric $-\text{CF}_2-$ units. The result is a decrease in the delocalisation of the negative charge in comparison to the TFSI^- anion, which is symmetric across the imide by asymmetric at the sulfur. Simple comparison of the Pauling electronegativity of the TFSI^- anion draws the conclusion that the negative charge is predominantly located on the oxygen atoms; decreasing the electron-withdrawing contribution of the sulfonyl substituent decreases the contribution of electronegativity to the delocalization of the anion. The result is a uniform, high charge density along the polymer chain having high Coulombic interaction with Li^+ . The movement of Li^+ from one site to the next is a thermally activated process (regardless of the specific mechanism of ion conduction). The energy barrier of this motion is overcome when sufficient thermal energy ($k_{\text{B}}T$) is supplied to the electrolyte. The low flexibility of the LiPEI chain, as illustrated by the high temperature of peak $\tan(\delta)$, can inhibit the rate of this motion and decrease the conductivity of the poly(electrolyte).

The addition of the polar ethylene carbonate (EC) to the poly(ether)/LiPEI alloy therefore has two effects for increasing the ionic conductivity of the electrolyte formulation: **i**) plasticizing the poly(anion) and enabling greater freedom of thermally controlled motion, **ii**) shielding the Coulombic interactions of the ion pair, enabling greater dissociation of Li^+ by increasing the net dielectric constant of the matrix. Addition of 1 equivalent (w/w) of EC to the poly(ether)/LiPEI blend creates a single-ion gel electrolyte and increases of ionic conductivity of the electrolyte by two orders of magnitude across the entire range of temperatures reported. Leveraging the influence of chain flexibility and delocalisation of the anion, extension of the covalent spacing between anionic units of the poly(TFSI)-type design yielded greater ionic conductivity of the poly(electrolyte). Similarly prepared, poly(ether) blends of the 4-trifluoromethyl-pentafluoropentylene analogue LiPPI have ionic conductivities of *ca.* $10^{-5} \text{ S.cm}^{-1}$ at 30°C ($t_{\text{Li}}^+ = 0.7$), two orders of magnitude higher than the equivalent poly(ether)/LiPEI alloys.^[136]

Well-defined spacing of ionic units along the polymer primary chain has been reported. A series of alternating (AB) poly(ester)s, comprising 5-sulfoisophthalate alkali metal salts separated in the primary chain by PEO units ($X_{\text{n(PEO)}} = 9-20$), have been investigated by several groups in collaboration. The DP_n of the AB poly(ester)s was in the range of 4-8 units. The conductivity of the poly(ester) bearing lithium sulfonate (PE-Li) decreased with shortening of the length (X_n) of the PEO spacer, in the order $\sigma_{\text{AC}} = 6.3 \cdot 10^{-7} \text{ S.cm}^{-1}$ (PEO_{20}) > $2.7 \cdot 10^{-8} \text{ S.cm}^{-1}$ (PEO_{14}) > $1.7 \cdot 10^{-10} \text{ S.cm}^{-1}$ (PEO_9) at 25°C .^[138] This trend is inverse to the increase of the cation concentration and increase of polymer T_g . The temperature dependence of ionic conductivity can be normalised by correcting for the elevation of T_g when the concentration of ionic units is increased. Plotting σ_{AC} vs $T - T_g$ reveals similar, overlapping curves when the length of the PEO spacer is varied. Analysis of the frequency dependence of dielectric permittivity supports the claim that the ionic transport is coupled to and limited by the mobility of the polymer chains.^[139] The design of the polymer was then probed by independent variation of the spacer length and the number ionic units. This is achieved *via* copolymerisation of the sulfonate with non-ionic isophthalates, enabling the number of ionic units to be changed while maintaining the PEO spacer length of the condensation polymer. NMR relaxometry demonstrated that the self-diffusion of Li^+ was controlled by the mobility of the PEO chain lengths and that tuning the net EO/Li ratio has a greater influence on ionic conductivity than

the concentration of ionic units.^[140] The strong coordination of Li⁺ by ether oxygen, and not the dissociation of lithium sulfonate ion pairs, limits the mobility of the cation.

3.6. Conclusions on Single-Ion Polymer Electrolytes

"Single-Ion" transport in polymer electrolytes builds on the benefits demonstrated by the *Salt-in-Polymer* (SiP) approach. The anion is effectively immobilised through covalent bonding to entangled polymer chains. This can improve the performance of the polymer electrolyte by removing problems created by the mobile anion. However, design approaches based on PEO limit the apparent benefit of using a polymer. The percolation of crystalline phases over mesoscopic/microscopic scales continues to limit ionic conductivity at temperatures below the melting point of PEO segments. Developments beyond PEO (in the SiP domain) begin to suggest that ionic conductivity is not always limited by T_g . Strong coordination of Li⁺ by polymer chains is a benefit in terms of the dissolution of the ion but a curse in terms of hindering ionic mobility. This is certainly the case for poly(ether)s.

Researchers have begun to suggest alternative polymers to PEO and the results demonstrate that SIPEs can be well-designed using a variety of polymers having different physical properties, with specific ion transport applications in mind. In particular, poly(carbonate)s, poly(ester)s and their copolymers appear to be good candidates for further research.

The development of SIPEs has been limited by the approaches to probing the fundamental mechanisms of ion transport. The design motifs that were elaborated and optimised for SiP electrolytes have been applied to SIPEs. Although several examples are reported having impressive figures of merit, SIPEs based on traditional thinking may have reached a plateau in performance. From this point of view, the design of SIPEs having specific domains for ion conduction are highly attractive. The development of SIPEs having such domains requires further research into the particular mechanisms of "Single-Ion" transport. Inspiration for the design of SIPEs could be found in the broader context of the domain of self-assembled (functional) soft matter.

4. Organisation of Soft Matter: Beyond Block Copolymers

The organization of soft matter is a powerful paradigm for the design and synthesis of SIPEs targeting directed conduction of ions through "microphase-separated" morphologies. In the following paragraphs are outlined selected examples of high χ -low N strategies that might inspire the design and synthesis of SIPEs. A high- χ strategy can support greater asymmetry of polymer composition and represents an opportunity for increasing the volume fraction of the ionically conductive phase within a microphase-separated polymer electrolyte.^[141] As seen for engineered defects at BCP mid-points, sufficiently high χ features can be low in N. We can first imagine a BCP at 50 % (w/w) composition of each sub-block. Then we can begin decreasing the N of one block, and at the same time raise χ of that block to maintain controlled microphase-separation. At the extreme of this condition, with sufficiently high χ , N approaches unity. The small sub-block would ultimately correspond in number and in position to a polymer end-group. From this point of view, polymers end-capped with sufficiently high- χ moieties are a subset of a family of microphase-separating macromolecules that includes (low χ -high N) diBCPs and (high χ -low N) surfactants.

The consequence of this design hypothesis is that an end-group must be high χ and that asymmetric macromolecular architectures can benefit self-assembly. Macromolecular engineering of point-group defects is a means by which to encode structural order. High χ point-group design can target augmentation of free volume of the polymer. This could be achieved by designing end-groups that are **i)** expelled from crystalline packing of the polymer, or **ii)** seed the growth of crystalline domains. Intra-chain defects can perturb chain tilt and chain folding. High χ points can be designed using groups that interact with each other by Van der Waals, electrostatic, and ionic forces. Groups with rigid and complementary architectures can be physically locked into place. A combination of free volume effects and different types of physical interactions would concertedly enhance molecular organization. In the case of polymer electrolytes, such organization would need to be sympathetic to ion transport, which could furthermore enforce a particular molecular order through ionic and ion-dipole interactions. The type, length scale, time scale, and strength of interactions of these point groups would serve to enhance the properties of soft matter intended for a variety of nano to micro-scale applications.

In terms of polymer electrolyte design, this could be an effective concept when applied to a polymer chain capable of transporting ions. Two further thoughts would then be raised, for polymers organized by point-group engineering. Firstly, *how efficient would ion conduction be, through the polar polymer phase?* This could apply to SiP blends. The preferential dissolution of salt into one phase of a microphase-separated matrix has a corresponding increase in χ of that phase. This typically helps to enforce phase segregation, so directed-ion transport is envisaged through a microphase-separated matrix having a high mass fraction of the polar phase, relative to the equivalent loading of salt into a low χ high N BCP. Similarly, a single-ion conductor, in which the anionic function is tethered to the polymer chain, could benefit from organization of the bulk by specific end-group interactions. Secondly, *could the ionically or electronically conducting properties of an end-group in this design be leveraged in a battery?* In this case, would ion conduction occur as truly dissociated charged species, with movement of the cation through the polar polymer phase, or would the cations hop between ionic point-groups arranged at defects such as grain boundaries? Such polymers could be applied not only as electrolytes but also as

conductive binders that could be blended into the electrode formulation to aid the exchange of charge with the active materials.

One approach to high χ -low N macromolecules has been the development of so-called "giant molecules."^[142,143] A particular class, recently reported by Prof. Stephen Z.D. Cheng and co-workers, leverages Click chemistry protocols to create "giant surfactants"^[144] based on poly(styrene) ($X_n = 20-100$) end-capped with decorated fullerene C_{60} ^[145,146] and polyhedral oligomeric silsesquioxane (POSS).^[147-151] The high volume fraction occupied by the polyhedral units enable their reduction in N to that of a single end-group. The reported results detail the effects of having a single end-group with multiple tails and having multiple polyhedral end groups to a single polymer chain (Fig. I-22). They achieved sub-10 nm feature size and long-range ordered morphology (e.g. lamellar) while having a high (ca. 60-80 %) volume fraction of the polymer chain. This strategy enables asymmetry in volume fraction of the phases and is more amenable to the elimination of defects because of greater mobility of the unmodified chain ends. The same cannot be said for a BCP approach, for example, of PEO-*b*-PPOSS, which has been applied as a SiP electrolyte.^[152]

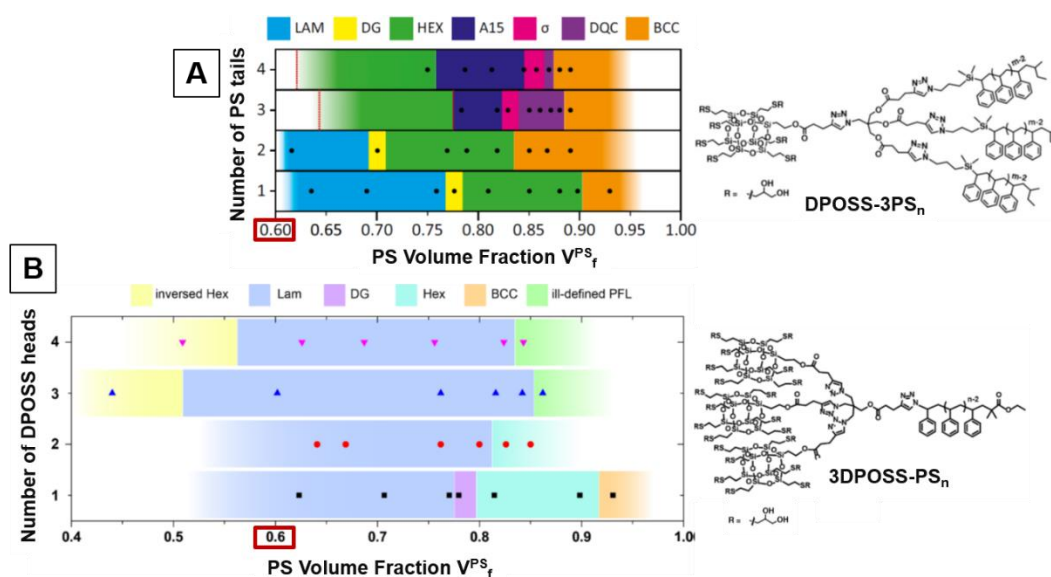


Figure I-22: Asymmetric phase segregation behaviour of POSS-based giant surfactants yields a variety of long-range morphologies. The phase diagrams are built from experimental data. The data points represent real samples. The PS volume fraction (V_{PS}^f) is displayed in the range $V_{PS}^f = 0.6-1.0$ (top) and $0.4-1.0$ (bottom). The diagrams have been scaled to aid comparison. A, top: DPOSS-PS having 1-4 PS tails. The chemical structure of the three-tailed DPOSS-3PS_n is shown as an example. B, bottom: DPOSS-PS_n having 1-4 DPOSS heads. The three-headed 3DPOSS-SP_n is shown as an example. The figure is adapted from the literature.^[147,151]

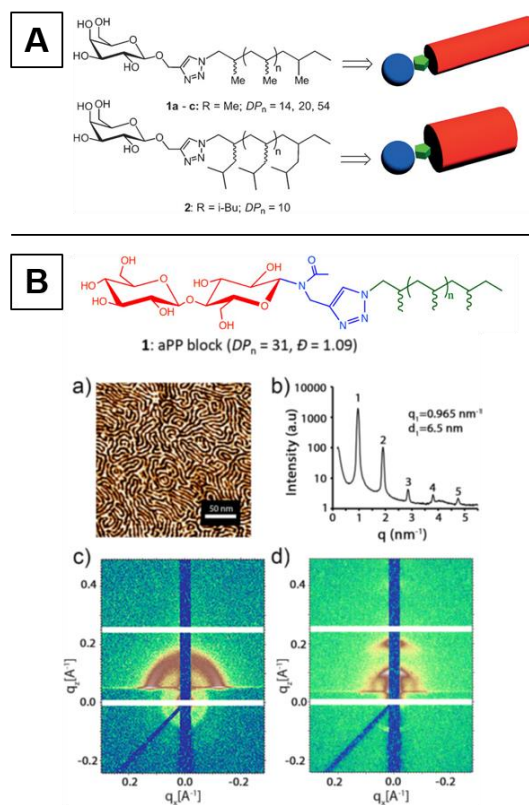
The shape of an end-group can have an impact that goes beyond the simple measure of its size. The group of Prof. L. Sita has recently reported on the organizational properties of poly(α -olefin)s end-capped with simple sugars (Fig. I-23). In terms of size, these lie between the extremes of small molecular and "giant" surfactants. They attached a β -D-galactose end-group *via* a 1,2,3-triazole linkage to one end of an atactic poly(olefin).^[153] The sugar-poly(olefin)s formed stacked bilayers, wherein the thickness of the poly(olefin) layer was tuned by the polymer DP_n ($X_n = 14$ [$D_w = 1.15$], 20 [$D_w = 1.15$], 54 [$D_w = 1.04$]). X-ray photoelectron spectroscopy (XPS) supports the films having a *head-tail-tail-head* (HTTH) stacking configuration. They demonstrated the effect of varying the spatial volume of the poly(olefin) by altering the repeating units to have either methyl or *iso*-butyl pendant groups. All the poly(olefin) phases had a sub-10 nm thickness, with the smallest obtained

by the polymer having *iso*-butyl pendants (**Fig. I-23, A**, R= *i*Bu; $X_n= 10$, $D_w= 1.04$). The impact of end-group size was developed by having two sugar units instead of one (**Fig. I-23, B**). The atactic poly(propylene) end-capped with disaccharide cellobiose had higher definition of their nanostructure, as evidenced by SAXS.^[154] The solvent cast films adopted a “fingerprint” morphology, with lamellar domains oriented perpendicular to the plane. It was then demonstrated that annealing these films at temperatures as low as 38 °C caused a change in orientation of the phases, from perpendicular to parallel to the plane. This design has sufficient segregation strength to form microphase-separated structures but also sufficient thermally controlled chain mobility to undergo phase re-orientation in the time scale of a few hours.

Figure I-23: End-capped Poly(olefins). The figures are reproduced from the literature.^[153,154]

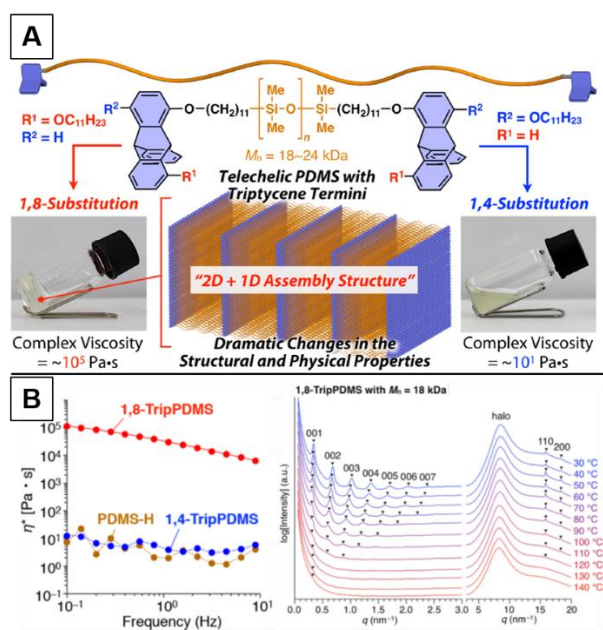
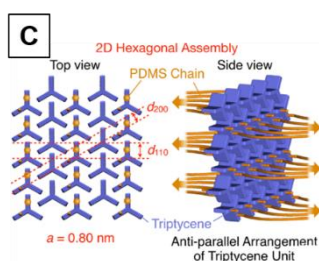
Poly(α -olefin)s end-capped with β -D-galactose via a 1,4-disubstituted 1,2,3-triazole linker. Illustrated are the “long and thin” poly(propylene) chains and the “short and fat” poly(4-methyl-1-pentene) chains (in red).

Poly(propylene) end-capped with cellobiose (red) via a triazole linker (blue). B: (a) A ps-tm AFM phase map of the solvent-cast ultrathin film ($h= 30$ nm) of polymer B on a Highly Oriented Pyrolytic Graphite (HOPG) substrate. (b) SAXS data of the unannealed sample (the lamellar spacing is $d_1= 6.5$ nm). Grazing Incidence (GI)SAXS data of the (c) solvent-cast film and (d) film after thermal annealing at 100 °C for 3 h *in vacuo*. A morphological *order-to-order* transition would explain the data, that the polymer has re-assembled its lamellae from perpendicular to parallel to the substrate.



Inspired by the remarkable long-range ordering exhibited by small-molecular derivatives of triptycene bearing short alkyl chains,^[155] F. Ishiwari and co-workers recently demonstrated how their propeller-shaped end-group is capable of directing structural order (**Fig. I-24**). The physical interlocking of the end-groups enables long range ordering with the entire length of a PDMS chain as the repeating unit.^[156] Reflection up to the 7th order (*i.e.* related to $d_{001} \rightarrow d_{007}$ distances) of the [001] primary scattering peak q^* were identified by SAXS analysis of the samples at 30°C, evidencing long-range hierarchical arrangement of polymer chains in a 2D+1D morphology that are otherwise totally amorphous in the absence of the triptycene end-group.

Figure I-24: Supramolecular assembly of triptycene end-capped PDMS ($18\text{--}24 \times 10^3$ g/mol, $X_n \approx 240\text{--}320$) via locking interactions of the propeller-shaped end-group. (A) A schematic illustration of the end-capped PDMS and its structural formula. The geometry of substitution (1,4 or 1,8) determines the long-range assembly and resultant properties of the "2D+1D" morphology. (B) Frequency dependence of shear strain (left) and 7-orders of alignment visible by SAXS measurement (right). (C) The inter-locking structure of triptycene end-groups at the "2D+1D" interface. *The figure is adapted from the literature.*^[156]



Enhancing the performance of BCP matrices might exist beyond the design of the BCP alone and include the addition of structure-defining molecules acting as supramolecular physical crosslinking units. Molecules capable of forming specific interactions with one sub-block of a BCP can change or reinforce the BCP morphology. This has already been seen with the addition of salt to BCP, which increases χ and decreases crystallinity through ion-dipole interaction with the polar sub-block. Shape- and structure-specific interactions can not only induce self-assembly but can adopt different supramolecular conformations depending on conditions of temperature, electrical, magnetic, and mechanical forces. For example, the ureido-cytosine (UrCy) Hydrogen-bonding motif has a molecular configuration enabling complementary, high association energy quadruple H-bonding interactions.^[157] This was used to establish supramolecular order at the end-group of low M_w bis-end-capped poly(propylene oxide) ($M_w = 1100$ g/mol, $PO_n = 14$).^[158] The assembled UrCy-PPO₁₄-CyUr supramolecular matrix had lamellar morphology with inter-lamellar spacing that was tunable and reversible by application of heat and shear. Addition of salt into this architecture would undoubtedly disrupt the H-bonding motif but a well-placed ionic group, perhaps in the centre of the chain or at one end-group, could add complimentary ionic conduction properties to the polymer design. Asymmetric ionic groups might provide similar structure-directing functionality.

Interactive oligomers and surfactants can influence and reinforce BCP morphologies, and also create hierarchical organisation. H-bonding interactions of oligomers has been demonstrated to increase lamellar domain sizes in poly(styrene)-*b*-poly(vinyl pyridine) (PS-*b*-P4VP) BCPs.^[159,160] The co-assembly of the BCP with H-bonding oligomers based on oligo(thiophene) having at one chain end a H-bonding phenol terminal and a short branched alkyl chain at the other affords elongation of the P4VP block.^[159] The result is a *coil-like* PS block and a comb-shaped supramolecular assembly in the P4VP phase. The large (30-50 nm) domain size of the supramolecular phase could host semiconducting nanoparticles. Low loadings (< 10 wt%) of nanoparticles resulted in a decrease in periodicity of the lamellae. The large particles caused the P4VP phase to collapse into tight channels which held the particles in parallel columns. Smaller particles ($d = 3$ nm; CdSe) however,

assembled perpendicularly across the width of the P4VP lamellae. A bis-phenol derivative is able to form bridging H-bonding interactions between P4VP blocks. The result is a comb arrangement within the P4VP phase having ordered inter-thiophene spacing of *ca.* 4.7 nm within the P4VP phase of a BCP lamellar morphology of 56 nm spacing.^[160] The result is the assembly of the H-bonding oligomer perpendicular to the direction of the P4VP lamellae. The effect is stretching of the BCP, thereby increasing the domain size of each block, and an increase in the long-range order of the BCP lamellae.

5. General Conclusions on Polymer Electrolytes for Lithium Ion Batteries

Concerted development of electrolytes and electrodes is a necessity to make functioning batteries. A sustainable energy economy demands the same accountability at every level. Therefore, it is unreasonable that a battery should be recyclable when the device it powers is not. However, the world supply and price of lithium (and materials for active cathode materials, such as nickel and cobalt) is of concern if the majority of energy is to be stored electrochemically in the future. Therefore, new cells should be of optimum performance. This requires a deeper understanding of how the cell components function. The electrolyte is crucial to battery performance because it enables the transfer of charge from one electrode to the other.

Polymers are soft materials that can be tuned to the needs of modern electrolyte chemistry, design, processing, application, and safety. The accumulated knowledge acquired through performance enhancement of polymer electrolytes must be coupled with emerging insight into macromolecular design. Alternative polymers should be explored and benchmarked appropriately to comparable examples from the best-in-class of applied electrolytes based on poly(ether)s.

The operating conditions of a battery should be taken into account. Acceptable ionic conductivity at ambient temperature remains a challenge to polymer electrolytes. To meet this requirement, researchers have worked with formulations of polymers and numerous other components such as solvents, fillers, and plasticizers. However, the advancement of performance can come at the cost of the properties of polymers that made them attractive electrolyte hosts at the outset. For example, the advantages of having a non-flammable solid polymer electrolyte are erased when it is mixed with organic solvents. A polymer having a suitable complex modulus is not expected above its melting temperature to prevent dendrite growth on Lithium metal anodes. Although impressive figures of merit have been reported, these are achieved at the cost of obscuring relations of causality that determine the performance. This is certainly the case with polymer electrolytes based on complex formulation chemistry. Decoupling the various physicochemical processes involved in ion transport becomes more difficult with each new component added to a mixture.

The search for batteries having greater energy density has lead researchers to develop high energy electrode materials demanding electrolytes that are electrochemically stable over a wide range of potentials. Cathodes that cycle at potentials greater than 4 V vs. Li/Li⁺ are now being proposed. The lithium metal anode is only accessible in context of the safety of stable, solid electrolytes that prevent dendrite growth. High performance active materials will only find successful application when there exists a stable electrolyte between the electrodes. The ionic conductivity mechanism, electrochemical stability and efficiency of ion transfer in electrolytes must be well understood to make a major leap forward in battery design.

A systematic approach seeking out specific structure-property relationships should be aimed at identifying and solving the limitations of the present *state of the art*. Single-Ion polymer electrolytes are means to achieve this because both the conductive polymer host and the ionic electrolyte are design features of a single macromolecule. The concept is especially well-suited to solve the problems originating from the transport of oppositely charged ion pairs of binary salt in a polymer host. End-capped polymers recall traditional polymer chemistry concepts and early synthetic efforts into single-ion polymer electrolytes. However, they are also means to approach the design and performance of polymer electrolytes in a generic way that is modular and adaptable to parallel developments in the electrolyte chemistry in general. Optimization of their design and structure-property relationships will improve our understanding of how solid-state electrolytes operate and therefore our methods for improving their performance.

6. Synthesis Strategy

The trends of the development of polymer electrolytes for LiBs inform the choice of synthesis strategy implemented in the present work. Several promising methods and design principles were selected and developed. In general, the synthesis strategy is inspired by previously reported work based on point-groups covalently bonded to polymer chains. This type of strategy is viewed with the aim of promoting effective and efficient ion transport. In principle, a point group can be positioned anywhere along a polymer chain. Although there is great variety in point-group polymer chemistry is possible, polymer end-groups in particular were chosen. Three practical considerations drove the approach:

- I. Polymer end-groups have long been considered in the development of new polymers and methods. Taking care of the end-groups has been an important aspect of polymer chemistry since the earliest studies into polymerization kinetics, physical transformations and bulk properties. *This provides a firm theoretical foundation on which new materials can be posed.*
- II. The end-groups are available for modification. This is achieved in practice by a variety of methods both during polymerization and modification of prefabricated polymers. A particular sample of a certain polymer can be divided into batches having the same M_w and dispersity in mass but different end-groups. *In this way, the properties of the polymer chain can be standardized and only the end-groups compared.*
- III. The availability of commercial polymers with end-groups that can be modified makes this strategy attractive from the point of view of scalability. *A defined industrial standard is a good starting point for variation of design and valorization of performance.*

The End-Capped Polymer Electrolytes (EC-SIPes) reported by H. Ohno and coworkers, and others (**Table I-1**), inspired this work. There appeared in recent years more elaborate polymer architectures based on exotic monomers and hybrid strategies, but the improvement in ionic conductivity and electrochemical stability has been incremental. Perhaps the limitations of these existing ideas are not fully understood.

The end-capped polymer electrolyte enables some key variations of physical properties that can help us to understand fundamental aspects of ion transport. The commendable performance of known EC-SIPes enables their study as neat polymer electrolytes without formulation with other compounds. However new research must keep certain figures of merit, such as ionic conductivity, the electrochemical stability window, and the lithium transference number.

Variation of the chain length of an EC-SIPE changes numerous important properties of the electrolyte. For example, the chain length is proportional to the concentration of end-groups. In the case of ionic end-groups designed for lithium ion transport, this is equivalent to variation of the concentration of binary salt. However, in EC-SIPes the anion is covalently bound to the polymer chain end, enabling "Single-Ion" transport. When the chain length is decreased to the order of a few persistent lengths (segments) of the polymer, the physical properties of the EC-SIPes will change dramatically. The correlations of chain length with physical properties such as the glass transition temperature, melting point, and mechanical modulus are very acute at the length scale of a few segments. In practice, this is less than fifty repeating units for many polymers.

Based on the trends developed by the groups summarized in Table 1, some confinement was placed on the strategy:

- I. **The polymer should be PEO.** This places EC-SIPes in context of a well-established performance of polymer electrolytes. *The impact of the end-group can be viewed in context of a known polymer.*
- II. **The EC-SIPes should have the ionic end-group at one chain end.** *The ionic conductivity of EC-SIPes having one ionic end-group is consistently reported as better than a bis-end-capped EC-SIPE having the same ionic end-group concentration.*
- III. **The polymer chain should be short.** A high concentration of ionic end-groups is required. The end-groups of a long chain polymer are too dilute to be studied effectively. Their properties are obscured by those of the chain. *It is well-reported that the best performance in ionic conductivity is often achieved using short chains having 10-20 repeating units.*

With this in mind, the following synthetic route was developed (**Fig. I-25**). Using commercial poly(ethylene oxide) monomethyl ethers (mPEO_n-OH) having different degrees of polymerization (EO_n= 8, 10, 20, 55, and 160), a library of MEC-SIPes was synthesized. It is noted that the very same batch of each mPEO_n-OH was used for the synthesis of all the different MEC-SIPes of a certain polymer chain length. This excludes variation of M_w and dispersity in mass.

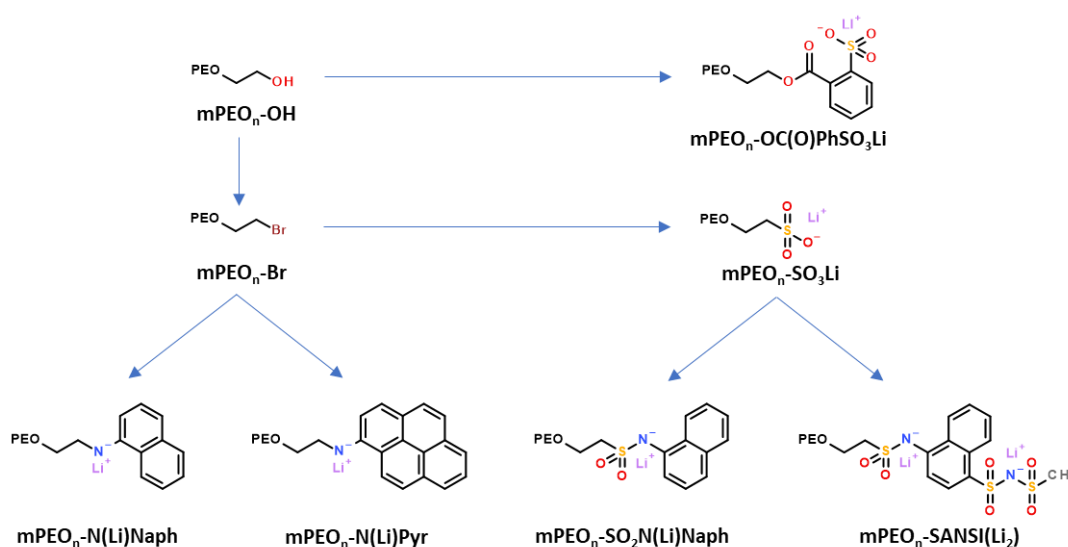


Figure I-25: An illustration of the synthesis strategy for MEC-SIPes based on mPEO_n-OH. The names of the polymers given are the ones used in the text. The details of the syntheses are described in the Experimental Chapter (*vide infra*: Chapter III).

The syntheses of the MEC-SIPes are described in the *Experimental* chapter (*vide infra*: Chapter III). In Figure 25 is illustrated how the hydroxyl end-group of mPEO_n-OH precursor was elaborated to yield comparable MEC-SIPes. The mPEO_n-SO₃Li and mPEO_n-OC(O)PhSO₃Li are compared through their having the sulfonate salt. Whereas the former has a simple ionic group at the chain end, the latter has a bent configuration at the chain end featuring phenyl ring that might enhance the interaction parameter of the end-groups relative to the PEO chain. The mPEO_n-N(Li)Naph and mPEO_n-N(Li)Pyr were synthesized for two reasons: **i)** secondary amines can be lithiated but are not widely reported for lithium ion transport, and **ii)** aryl function at the chain end. The size of the ring structure might promote the exclusion of the end-group from the organization of PEO

segments. The aromatic rings might provide additional electron density to the anion, enabling greater dissociation of Li^+ . The aromatic electrons are moreover delocalized in π bonding orbitals. **Polycyclic Aromatic Hydrocarbons (PAHs)** like naphthalene and pyrene are able to aggregate *via* interactions of instantaneous dipoles formed in aromatic electron clouds into π - π stacking arrangements. The 1-aminonaphthalene precursor of $\text{mPEO}_n\text{-N(Li)Naph}$ is furthermore utilized in the synthesis of $\text{mPEO}_n\text{-SO}_2\text{N(Li)Naph}$. N-aryl sulfonamides are not widely reported in the literature and the linkage itself might enhance the dissociation of Li^+ by the concerted effects of the electronegative heteroatoms and the donation of electron density by the aromatic rings.

The number of lithium cations coordinated to a single chain end can be doubled by modification of the end-group. The $\text{mPEO}_{55}\text{-SANSI(Li}_2)$ could have enhanced ionic conductivity resulting from the increased number of mobile Li^+ . This exceptionally large end-group is designed to maximize the interaction parameter of the chain ends. The precursor of the "double salt" end-group of $\text{mPEO}_{55}\text{-SANSI(Li}_2)$ is 1-aminonaphthalene-4-sulfonic acid (ANH). The synthetic pathway to the MEC-SIPE was developed in this work and provides means for further variation in the end-group design.

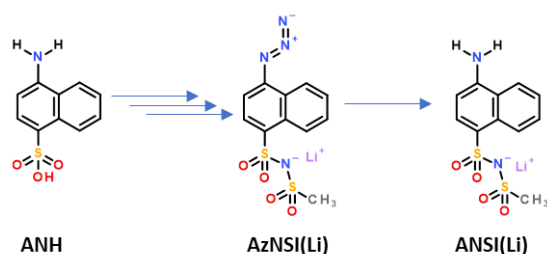


Figure I-26: The reaction scheme of the synthesis of the ANSI(Li) end-group of $\text{mPEO}_{55}\text{-SANSI(Li}_2)$. The intermediate compound AzNSI(Li) is used in the synthesis of the $\text{mPEO}_{20}\text{-}\blacklozenge\text{NSI(Li)}$ featuring a triazole linker.

The AzNSI(Li) intermediate (**Fig. I-26**) was reacted *via* copper catalysed azide-alkyne [3+2] cycloaddition to yield the $\text{mPEO}_{20}\text{-}\blacklozenge\text{NSI(Li)}$ having a 1,4-disubstituted 1,2,3-triazole linker (**Fig. I-27**). Quaternisation of this EC-SIPE yields the zwitterionic $\text{mPEO}_{20}\text{-}\blacklozenge^+\text{NSI(LiTFSI)}$. This provides an opportunity to observe the effect of having two mobile ions. Importantly, the mobility of TFSI⁻ might be decreased through ionic interactions with the positively charged triazolium. If this is the case, the $\text{mPEO}_{20}\text{-}\blacklozenge\text{NSI(LiTFSI)}$ could benefit from the plasticizing effect of TFSI⁻ with decreased anionic contribution to ionic conductivity, relative to a SiP blend of the binary salt LiTFSI in a PEO host.

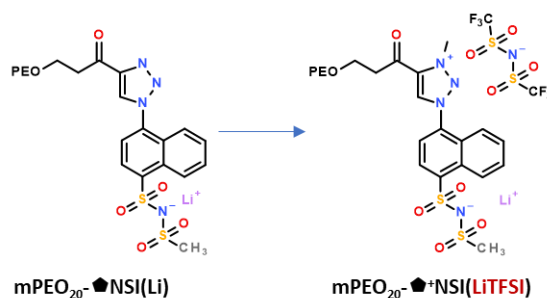


Figure I-27: The reaction scheme illustrating the $\text{mPEO}_{20}\text{-}\blacklozenge\text{NSI(Li)}$ having a triazole linker and its zwitterionic derivative $\text{mPEO}_{20}\text{-}\blacklozenge^+\text{NSI(LiTFSI)}$ having a triazolium, and two counterions (Li^+ and TFSI⁻).

The characterisation of these MEC-SIPEs and their particular ion transport properties are discussed in **Chapter II**.

7. Bibliography of Chapter I

- [1] Choi, J. W.; Aurbach, D. Promise and Reality of Post-Lithium-Ion Batteries with High Energy Densities. *Nature Reviews Materials* **2016**, *1* (4), 16013. DOI: [10.1038/natrevmats.2016.13](https://doi.org/10.1038/natrevmats.2016.13)
- [2] Armand, M.; Tarascon, J.-M. Building Better Batteries. *Nature* **2008**, *451* (7179), 652-657. DOI: [10.1038/451652a](https://doi.org/10.1038/451652a)
- [3] Tarascon, J.-M.; Armand, M. Issues and Challenges Facing Rechargeable Lithium Batteries. *Nature* **2001**, *414* (6861), 359-367. DOI: [10.1038/35104644](https://doi.org/10.1038/35104644)
- [4] Etacheri, V.; Marom, R.; Elazari, R.; Salitra, G.; Aurbach, D. Challenges in the Development of Advanced Li-Ion Batteries: A Review. *Energy & Environmental Science* **2011**, *4* (9), 3243-3262. DOI: [10.1039/C1EE01598B](https://doi.org/10.1039/C1EE01598B)
- [5] Tarascon, J.-M. Is Lithium the New Gold? *Nature Chemistry* **2010**, *2* (6), 510-510. DOI: [10.1038/nchem.680](https://doi.org/10.1038/nchem.680)
- [6] Wang, D.; Zhang, W.; Zheng, W.; Cui, X.; Rojo, T.; Zhang, Q. Towards High-Safe Lithium Metal Anodes: Suppressing Lithium Dendrites via Tuning Surface Energy. *Advanced Science* **2017**, *4* (1), 1600168. DOI: [10.1002/advs.201600168](https://doi.org/10.1002/advs.201600168)
- [7] Lin, D.; Liu, Y.; Cui, Y. Reviving the Lithium Metal Anode for High-Energy Batteries. *Nature Nanotechnology* **2017**, *12* (3), 194-206. DOI: [10.1038/nnano.2017.16](https://doi.org/10.1038/nnano.2017.16)
- [8] Cheng, X.-B.; Zhang, R.; Zhao, C.-Z.; Wei, F.; Zhang, J.-G.; Zhang, Q. A Review of Solid Electrolyte Interphases on Lithium Metal Anode. *Advanced Science* **2016**, *3* (3), 1500213. DOI: [10.1002/advs.201500213](https://doi.org/10.1002/advs.201500213)
- [9] Chen, R.; Qu, W.; Guo, X.; Li, L.; Wu, F. The Pursuit of Solid-State Electrolytes for Lithium Batteries: From Comprehensive Insight to Emerging Horizons. *Materials Horizons* **2016**, *3* (6), 487-516. DOI: [10.1039/C6MH00218H](https://doi.org/10.1039/C6MH00218H)
- [10] Bruce, P. G.; Freunberger, S. A.; Hardwick, L. J.; Tarascon, J.-M. Li-O₂ and Li-S Batteries with High Energy Storage. *Nature Materials* **2012**, *11* (1), 19-29. DOI: [10.1038/nmat3191](https://doi.org/10.1038/nmat3191)
- [11] Bachman, J. C.; Muy, S.; Grimaud, A.; Chang, H.-H.; Pour, N.; Lux, S. F.; Paschos, O.; Maglia, F.; Lupart, S.; Lamp, P.; et al. Inorganic Solid-State Electrolytes for Lithium Batteries: Mechanisms and Properties Governing Ion Conduction. *Chemical Reviews* **2016**, *116* (1), 140-162. DOI: [10.1021/acs.chemrev.5b00563](https://doi.org/10.1021/acs.chemrev.5b00563)
- [12] Schnell, J.; Günther, T.; Knoche, T.; Vieider, C.; Köhler, L.; Just, A.; Keller, M.; Passerini, S.; Reinhart, G. All-Solid-State Lithium-Ion and Lithium Metal Batteries-Paving the Way to Large-Scale Production. *Journal of Power Sources* **2018**, *382*, 160-175. DOI: [10.1016/j.jpowsour.2018.02.062](https://doi.org/10.1016/j.jpowsour.2018.02.062)
- [13] Kerman, K.; Luntz, A.; Viswanathan, V.; Chiang, Y.-M.; Chen, Z. Review-Practical Challenges Hindering the Development of Solid State Li Ion Batteries. *Journal of the Electrochemical Society* **2017**, *164* (7), A1731-A1744. DOI: [10.1149/2.1571707jes](https://doi.org/10.1149/2.1571707jes)
- [14] Fenton, D. E.; Parker, J. M.; Wright, P. V. Complexes of Alkali Metal Ions with Poly(Ethylene Oxide). *Polymer* **1973**, *14* (11), 589. DOI: [10.1016/0032-3861\(73\)90146-8](https://doi.org/10.1016/0032-3861(73)90146-8)
- [15] Wright, P. V. Electrical Conductivity in Ionic Complexes of Poly(Ethylene Oxide). *British Polymer Journal* **1975**, *7* (5), 319-327. DOI: [10.1002/pi.4980070505](https://doi.org/10.1002/pi.4980070505)
- [16] Fast Ion Transport in Solids: Electrodes and Electrolytes; Vashishta, P.; Mundy, J. N.; Shenoy, G. K. Eds. Proceedings of an International Conference, Lake Geneva, Wisconsin, USA, May 21-25, 1979. ISBN 0-444-00353-3.
- [17] Armand, M. The History of Polymer Electrolytes. *Solid State Ionics* **1994**, *69* (3), 309-319. DOI: [10.1016/0167-2738\(94\)90419-7](https://doi.org/10.1016/0167-2738(94)90419-7)
- [18] Xue, Z.; He, D.; Xie, X. Poly(Ethylene Oxide)-Based Electrolytes for Lithium-Ion Batteries. *Journal of Materials Chemistry A* **2015**, *3* (38), 19218-19253. DOI: [10.1039/C5TA03471J](https://doi.org/10.1039/C5TA03471J)
- [19] Berthier, C.; Gorecki, W.; Minier, M.; Armand, M. B.; Chabagno, J. M.; Rigaud, P. Microscopic Investigation of Ionic Conductivity in Alkali Metal Salts-Poly(Ethylene Oxide) Adducts. *Solid State Ionics* **1983**, *11* (1), 91-95. DOI: [10.1016/0167-2738\(83\)90068-1](https://doi.org/10.1016/0167-2738(83)90068-1)

- [20] Molinari, N.; Mailoa, J. P.; Kozinsky, B. Effect of Salt Concentration on Ion Clustering and Transport in Polymer Solid Electrolytes: A Molecular Dynamics Study of PEO-LiTFSI. *Chemistry of Materials* **2018**, 30(18), 6298-6306. DOI: [10.1021/acs.chemmater.8b01955](https://doi.org/10.1021/acs.chemmater.8b01955)
- [21] Wheatle, B. K.; Lynd, N. A.; Ganesan, V. Effect of Polymer Polarity on Ion Transport: A Competition between Ion Aggregation and Polymer Segmental Dynamics. *ACS Macro Letters* **2018**, 7 (10), 1149-1154. DOI: [10.1021/acsmacrolett.8b00594](https://doi.org/10.1021/acsmacrolett.8b00594)
- [22] Devaux, D.; Bouchet, R.; Glé, D.; Denoyel, R. Mechanism of Ion Transport in PEO/LiTFSI Complexes: Effect of Temperature, Molecular Weight and End Groups. *Solid State Ionics* **2012**, 227, 119-127. DOI: [10.1016/j.ssi.2012.09.020](https://doi.org/10.1016/j.ssi.2012.09.020)
- [23] Rouse, P. E. A Theory of the Linear Viscoelastic Properties of Dilute Solutions of Coiling Polymers. *The Journal of Chemical Physics* **1953**, 21 (7), 1272-1280. DOI: [10.1063/1.1699180](https://doi.org/10.1063/1.1699180)
- [24] Lascaud, S.; Perrier, M.; Vallee, A.; Besner, S.; Prud'homme, J.; Armand, M. Phase Diagrams and Conductivity Behavior of Poly(Ethylene Oxide)-Molten Salt Rubbery Electrolytes. *Macromolecules* **1994**, 27 (25), 7469-7477. DOI: [10.1021/ma00103a034](https://doi.org/10.1021/ma00103a034)
- [25] Watanabe, M.; Kanba, M.; Matsuda, H.; Tsunemi, K.; Mizoguchi, K.; Tsuchida, E.; Shinohara, I. High Lithium Ionic Conductivity of Polymeric Solid Electrolytes. *Die Makromolekulare Chemie, Rapid Communications* **1981**, 2 (12), 741-744. DOI: [10.1002/marc.1981.030021208](https://doi.org/10.1002/marc.1981.030021208)
- [26] Kitazawa, Y.; Iwata, K.; Imaizumi, S.; Ahn, H.; Kim, S. Y.; Ueno, K.; Park, M. J.; Watanabe, M. Gelation of Solvate Ionic Liquid by Self-Assembly of Block Copolymer and Characterization as Polymer Electrolyte. *Macromolecules* **2014**, 47 (17), 6009-6016. DOI: [10.1021/ma501296m](https://doi.org/10.1021/ma501296m)
- [27] Shin, J. H.; Passerini, S. PEO/LiN(SO₂CF₂CF₃)₂ Polymer Electrolytes: V. Effect of Fillers on Ionic Transport Properties. *Journal of the Electrochemical Society* **2004**, 151 (2), A238-A245. DOI: [10.1149/1.1636737](https://doi.org/10.1149/1.1636737)
- [28] Appetecchi, G. B. A New Class of Advanced Polymer Electrolytes and Their Relevance in Plastic-like, Rechargeable Lithium Batteries. *Journal of the Electrochemical Society* **1996**, 143 (1), 6-12. DOI: [10.1149/1.1836379](https://doi.org/10.1149/1.1836379)
- [29] Arbizzani, C.; Mastragostino, M.; Hamaide, T.; Guyot, A. An All Solid-State Polymer-Polymer Electrolyte-Lithium Rechargeable Battery for Room Temperature Applications. *Electrochimica Acta* **1990**, 35 (11-12), 1781-1785. DOI: [10.1016/0013-4686\(90\)87079-H](https://doi.org/10.1016/0013-4686(90)87079-H)
- [30] Watanabe, M.; Nagano, S.; Sanui, K.; Ogata, N. Ionic Conductivity of Network Polymers from Poly(Ethylene Oxide) Containing Lithium Perchlorate. *Polymer Journal* **1986**, 18 (11), 809-817. DOI: [10.1295/polymj.18.809](https://doi.org/10.1295/polymj.18.809)
- [31] Berthier, C.; Gorecki, W.; Minier, M.; Armand, M. B.; Chabagno, J. M.; Rigaud, P. Microscopic Investigation of Ionic Conductivity in Alkali Metal Salts-Poly(Ethylene Oxide) Adducts. *Solid State Ionics* **1983**, 11 (1), 91-95. DOI: [10.1016/0167-2738\(83\)90068-1](https://doi.org/10.1016/0167-2738(83)90068-1)
- [32] Vallée, A.; Besner, S.; Prud'Homme, J. Comparative Study of Poly(Ethylene Oxide) Electrolytes Made with LiN(CF₃SO₂)₂, LiCF₃SO₃ and LiClO₄: Thermal Properties and Conductivity Behaviour. *Electrochimica Acta* **1992**, 37 (9), 1579-1583. DOI: [10.1016/0013-4686\(92\)80115-3](https://doi.org/10.1016/0013-4686(92)80115-3)
- [33] Seki, S.; Takei, K.; Miyashiro, H.; Watanabe, M. Physicochemical and Electrochemical Properties of Glyme-LiN(SO₂F)₂ Complex for Safe Lithium-Ion Secondary Battery Electrolyte. *Journal of the Electrochemical Society* **2011**, 158 (6), A769-A774. DOI: [10.1149/1.3582822](https://doi.org/10.1149/1.3582822)
- [34] Zhang, H.; Liu, C.; Zheng, L.; Xu, F.; Feng, W.; Li, H.; Huang, X.; Armand, M.; Nie, J.; Zhou, Z. Lithium Bis(Fluorosulfonyl)Imide/Poly(Ethylene Oxide) Polymer Electrolyte. *Electrochimica Acta* **2014**, 133, 529-538. DOI: [10.1021/acs.jpcllett.7b00593](https://doi.org/10.1021/acs.jpcllett.7b00593)
- [35] Appetecchi, G. B.; Henderson, W.; Villano, P.; Berrettoni, M.; Passerini, S. PEO/LiN(SO₂CF₂CF₃)₂ Polymer Electrolytes: I. XRD, DSC, and Ionic Conductivity Characterization. *Journal of the Electrochemical Society* **2001**, 148 (10), A1171-A1178. DOI: [10.1149/1.1403728](https://doi.org/10.1149/1.1403728)

- [36] Appetecchi, G. B.; Passerini, S. PEO/LiN(SO₂CF₂CF₃)₂ Polymer Electrolytes: II. Characterization and Interface with Lithium. *Journal of the Electrochemical Society* **2002**, *149* (7), A891-A897. DOI: [10.1149/1.1483098](https://doi.org/10.1149/1.1483098)
- [37] Villano, P.; Carewska, M.; Appetecchi, G. B.; Passerini, S. PEO/LiN(SO₂CF₂CF₃)₂ Polymer Electrolytes: III. Test in Batteries. *Journal of the Electrochemical Society* **2002**, *149* (10), A1282-A1285. DOI: [10.1149/1.1502688](https://doi.org/10.1149/1.1502688)
- [38] Capiglia, C.; Imanishi, N.; Takeda, Y.; Henderson, W. A.; Passerini, S. PEO/LiN(SO₂CF₂CF₃)₂ Polymer Electrolytes: IV. Raman Characterization. *Journal of the Electrochemical Society* **2003**, *150* (4), A525-A531. DOI: [10.1149/1.1557963](https://doi.org/10.1149/1.1557963)
- [39] Goodenough, J. B.; Kim, Y. Challenges for Rechargeable Li Batteries. *Chemistry of Materials* **2010**, *22* (3), 587-603. DOI: [10.1021/cm901452z](https://doi.org/10.1021/cm901452z)
- [40] Xu, K. Nonaqueous Liquid Electrolytes for Lithium-Based Rechargeable Batteries. *Chemical Reviews* **2004**, *104* (10), 4303-4418. DOI: [10.1021/cr030203g](https://doi.org/10.1021/cr030203g)
- [41] Popovic, J.; Höfler, D.; Melchior, J. P.; Münchinger, A.; List, B.; Maier, J. High Lithium Transference Number Electrolytes Containing Tetratriflypropene's Lithium Salt. *The Journal of Physical Chemistry Letters* **2018**, *9* (17), 5116-5120. DOI: [10.1021/acs.jpcllett.8b01846](https://doi.org/10.1021/acs.jpcllett.8b01846)
- [42] Chinnam, P. R.; Wunder, S. L. Self-Assembled Janus-like Multi-Ionic Lithium Salts Form Nano-Structured Solid Polymer Electrolytes with High Ionic Conductivity and Li⁺ Ion Transference Number. *Journal of Materials Chemistry A* **2013**, *1* (5), 1731-1739. DOI: [10.1039/C2TA00085G](https://doi.org/10.1039/C2TA00085G)
- [43] Huang, M.; Feng, S.; Zhang, W.; Giordano, L.; Chen, M.; Amanchukwu, C. V.; Anandakathir, R.; Shao-Horn, Y.; Johnson, J. A. Fluorinated Aryl Sulfonimide Tagged (FAST) Salts: Modular Synthesis and Structure-Property Relationships for Battery Applications. *Energy & Environmental Science* **2018**, *11* (5), 1326-1334. DOI: [10.1039/C7EE03509H](https://doi.org/10.1039/C7EE03509H)
- [44] Yang, L.-Y.; Wei, D.-X.; Xu, M.; Yao, Y.-F.; Chen, Q. Transferring Lithium Ions in Nanochannels: A PEO/Li⁺ Solid Polymer Electrolyte Design. *Angewandte Chemie International Edition* **2014**, *53* (14), 3631-3635. DOI: [10.1002/anie.201307423](https://doi.org/10.1002/anie.201307423)
- [45] Yang, L.-Y.; Fu, X.-B.; Chen, T.-Q.; Pan, L.-K.; Ji, P.; Yao, Y.-F.; Chen, Q. Ionic Conductivity of β-Cyclodextrin-Polyethylene-Oxide/Alkali-Metal-Salt Complex. *Chemistry - A European Journal* **2015**, *21* (17), 6346-6349. DOI: [10.1002/chem.201406380](https://doi.org/10.1002/chem.201406380)
- [46] Fu, X.-B.; Yang, G.; Wu, J.-Z.; Wang, J.-C.; Chen, Q.; Yao, Y.-F. Fast Lithium-Ion Transportation in Crystalline Polymer Electrolytes. *ChemPhysChem* **2018**, *19* (1), 45-50. DOI: [10.1021/ja029326t](https://doi.org/10.1021/ja029326t)
- [47] Du, M.; Guo, B.; Jia, D. Newly Emerging Applications of Halloysite Nanotubes: A Review. *Polymer International* **2010**, *59* (5), 574-582. DOI: [10.1002/pi.2754](https://doi.org/10.1002/pi.2754)
- [48] Lin, Y.; Wang, X.; Liu, J.; Miller, J. D. Natural Halloysite Nano-Clay Electrolyte for Advanced All-Solid-State Lithium-Sulfur Batteries. *Nano Energy* **2017**, *31*, 478-485. DOI: [10.1016/j.nanoen.2016.11.045](https://doi.org/10.1016/j.nanoen.2016.11.045)
- [49] Khalatur, P. G.; Khokhlov, A. R. Nonconventional Scenarios of Polymer Self-Assembly. *Soft Matter* **2013**, *9* (46), 10943-10954. DOI: [10.1039/C3SM52181H](https://doi.org/10.1039/C3SM52181H)
- [50] Leibler, L. Theory of Microphase Separation in Block Copolymers. *Macromolecules* **1980**, *13* (6), 1602-1617. DOI: [10.1021/ma60078a047](https://doi.org/10.1021/ma60078a047)
- [51] Bates, F. S.; Fredrickson, G. H. Block Copolymers-Designer Soft Materials. *Physics Today* **1999**, *52* (2), 32-38. DOI: [10.1063/1.882522](https://doi.org/10.1063/1.882522)
- [52] Bates, C. M.; Bates, F. S. 50th Anniversary Perspective: Block Polymers-Pure Potential. *Macromolecules* **2017**, *50* (1), 3-22. DOI: [10.1021/acs.macromol.6b02355](https://doi.org/10.1021/acs.macromol.6b02355)
- [53] Young, W.-S.; Kuan, W.-F.; Epps, T. H. Block Copolymer Electrolytes for Rechargeable Lithium Batteries. *Journal of Polymer Science Polymer Physics* **2014**, *52* (1), 1-16. DOI: [10.1002/polb.23404](https://doi.org/10.1002/polb.23404)
- [54] Guo, Z.; Zhang, G.; Qiu, F.; Zhang, H.; Yang, Y.; Shi, A.-C. Discovering Ordered Phases of Block Copolymers: New Results from a Generic Fourier-Space Approach. *Physical Review Letters* **2008**, *101* (2), 028301. DOI: [10.1103/PhysRevLett.101.028301](https://doi.org/10.1103/PhysRevLett.101.028301)

- [55] Jo, G.; Ahn, H.; Park, M. J. Simple Route for Tuning the Morphology and Conductivity of Polymer Electrolytes: One End Functional Group Is Enough. *ACS Macro Letters* **2013**, *2* (11), 990-995. DOI: [10.1021/mz400468m](https://doi.org/10.1021/mz400468m)
- [56] Jo, G.; Kim, O.; Kim, H.; Hyeok Choi, U.; Lee, S.-B.; Jeong Park, M. End-Functionalized Block Copolymer Electrolytes: Effect of Segregation Strength on Ion Transport Efficiency. *Polymer Journal* **2016**, *48* (4), 465-472. DOI: [10.1038/pj.2015.141](https://doi.org/10.1038/pj.2015.141)
- [57] Jung, H. Y.; Mandal, P.; Jo, G.; Kim, O.; Kim, M.; Kwak, K.; Park, M. J. Modulating Ion Transport and Self-Assembly of Polymer Electrolytes via End-Group Chemistry. *Macromolecules* **2017**, *50* (8), 3224-3233. DOI: [10.1021/acs.macromol.7b00249](https://doi.org/10.1021/acs.macromol.7b00249)
- [58] Kambe, Y.; Arges, C. G.; Patel, S.; Stoykovish, M. P.; Nealey, P. F. Ion Conduction in Microphase-Separated Block Copolymer Electrolytes. *The Electrochemical Society Interface* **2017**, *26* (1), 61-67. DOI: [10.1149/2.F07171if](https://doi.org/10.1149/2.F07171if)
- [59] Arges, C. G.; Kambe, Y.; Dolejsi, M.; Wu, G.-P.; Segal-Pertz, T.; Ren, J.; Cao, C.; Craig, G. S. W.; Nealey, P. F. Interconnected Ionic Domains Enhance Conductivity in Microphase Separated Block Copolymer Electrolytes. *Journal of Materials Chemistry A* **2017**, *5* (11), 5619-5629. DOI: [10.1039/C6TA10838E](https://doi.org/10.1039/C6TA10838E)
- [60] Panday, A.; Mullin, S.; Gomez, E. D.; Wanakule, N.; Chen, V. L.; Hexemer, A.; Pople, J.; Balsara, N. P. Effect of Molecular Weight and Salt Concentration on Conductivity of Block Copolymer Electrolytes. *Macromolecules* **2009**, *42* (13), 4632-4637. DOI: [10.1021/ma900451e](https://doi.org/10.1021/ma900451e)
- [61] Gomez, E. D.; Panday, A.; Feng, E. H.; Chen, V.; Stone, G. M.; Minor, A. M.; Kisielowski, C.; Downing, K. H.; Borodin, O.; Smith, G. D.; et al. Effect of Ion Distribution on Conductivity of Block Copolymer Electrolytes. *Nano Letters* **2009**, *9* (3), 1212-1216. DOI: [10.1021/nl900091n](https://doi.org/10.1021/nl900091n)
- [62] Yuan, R.; Teran, A. A.; Gurevitch, I.; Mullin, S. A.; Wanakule, N. S.; Balsara, N. P. Ionic Conductivity of Low Molecular Weight Block Copolymer Electrolytes. *Macromolecules* **2013**, *46* (3), 914-921. DOI: [10.1021/ma3024552](https://doi.org/10.1021/ma3024552)
- [63] Bouchet, R.; Phan, T. N. T.; Beaudoin, E.; Devaux, D.; Davidson, P.; Bertin, D.; Denoyel, R. Charge Transport in Nanostructured PS-PEO-PS Triblock Copolymer Electrolytes. *Macromolecules* **2014**, *47* (8), 2659-2665. DOI: [10.1021/ma500420w](https://doi.org/10.1021/ma500420w)
- [64] Zheng, B.; Man, X.; Ou-Yang, Z.-C.; Schick, M.; Andelman, D. Orienting Thin Films of Lamellar Block Copolymer: The Combined Effect of Mobile Ions and Electric Field. *Macromolecules* **2018**, *51* (19), 7881-7892. DOI: [10.1021/acs.macromol.8b01506](https://doi.org/10.1021/acs.macromol.8b01506)
- [65] Park, M. J.; Balsara, N. P. Anisotropic Proton Conduction in Aligned Block Copolymer Electrolyte Membranes at Equilibrium with Humid Air. *Macromolecules* **2010**, *43* (1), 292-298. DOI: [10.1021/ma901980b](https://doi.org/10.1021/ma901980b)
- [66] Majewski, P. W.; Yager, K. G. Rapid Ordering of Block Copolymer Thin Films. *Journal of Physics: Condensed Matter* **2016**, *28* (40), 403002. DOI: [10.1088/0953-8984/28/40/403002](https://doi.org/10.1088/0953-8984/28/40/403002)
- [67] Sinturel, C.; Bates, F. S.; Hillmyer, M. A. High χ -Low N Block Polymers: How Far Can We Go? *ACS Macro Letters* **2015**, *4* (9), 1044-1050. DOI: [10.1021/acsmacrolett.5b00472](https://doi.org/10.1021/acsmacrolett.5b00472)
- [68] Woo, S.; Jo, S.; Ryu, D. Y.; Choi, S.-H.; Choe, Y.; Khan, A.; Huh, J.; Bang, J. Molecular Tailoring of Poly(Styrene-*b*-Methyl Methacrylate) Block Copolymer Toward Perpendicularly Oriented Nanodomains with Sub-10 Nm Features. *ACS Macro Letters* **2017**, *6* (12), 1386-1391. DOI: [10.1021/acsmacrolett.7b00856](https://doi.org/10.1021/acsmacrolett.7b00856)
- [69] Lee, K. S.; Lee, J.; Kwak, J.; Moon, H. C.; Kim, J. K. Reduction of Line Edge Roughness of Polystyrene-Block-Poly(Methyl Methacrylate) Copolymer Nanopatterns By Introducing Hydrogen Bonding at the Junction Point of Two Block Chains. *ACS Applied Materials & Interfaces* **2017**, *9* (37), 31245-31251. DOI: [10.1021/acsami.6b15885](https://doi.org/10.1021/acsami.6b15885)
- [70] Chen, E.-Q.; Xue, G.; Jin, S.; Lee, S.-W.; Mann, I.; Moon, B.-S.; Harris, F. W.; Cheng, S. Z. D. Defect Orientation on the Chain Folded Surfaces of Two-Arm Poly(Ethylene Oxide) Lamellar Crystals. *Macromolecular Rapid Communications* **1999**, *20* (8), 431-434. DOI: [10.1002/\(SICI\)1521-3927\(19990801\)20:8<431::AID-MARC431>3.0.CO;2-R](https://doi.org/10.1002/(SICI)1521-3927(19990801)20:8<431::AID-MARC431>3.0.CO;2-R)

- [71] Golitsyn, Y.; Pulst, M.; Kressler, J.; Reichert, D. Molecular Dynamics in the Crystalline Regions of Poly(Ethylene Oxide) Containing a Well-Defined Point Defect in the Middle of the Polymer Chain. *The Journal of Physical Chemistry B* **2017**, *121* (17), 4620-4630. DOI: [10.1021/acs.jpcc.7b01949](https://doi.org/10.1021/acs.jpcc.7b01949)
- [72] Samiullah, M. H.; Pulst, M.; Golitsyn, Y.; Busse, K.; Poppe, S.; Hussain, H.; Reichert, D.; Kressler, J. Solid State Phase Transitions in Poly(Ethylene Oxide) Crystals Induced by Designed Chain Defects. *Macromolecules* **2018**, *51* (11), 4407-4414. DOI: [10.1021/acs.macromol.8b00508](https://doi.org/10.1021/acs.macromol.8b00508)
- [73] Pulst, M.; Schneemann, C.; Ruda, P.; Golitsyn, Y.; Grefe, A.-K.; Stühn, B.; Busse, K.; Reichert, D.; Kressler, J. Chain Tilt and Crystallization of Ethylene Oxide Oligomers with Midchain Defects. *ACS Macro Letters* **2017**, *6* (11), 1207-1211. DOI: [10.1021/acsmacrolett.7b00757](https://doi.org/10.1021/acsmacrolett.7b00757)
- [74] Luo, Y.; Montarnal, D.; Treat, N. J.; Hustad, P. D.; Christianson, M. D.; Kramer, E. J.; Fredrickson, G. H.; Hawker, C. J. Enhanced Block Copolymer Phase Separation Using Click Chemistry and Ionic Junctions. *ACS Macro Letters* **2015**, *4* (12), 1332-1336. DOI: [10.1021/acsmacrolett.5b00767](https://doi.org/10.1021/acsmacrolett.5b00767)
- [75] Wen, T.; Lee, J.-Y.; Li, M.-C.; Tsai, J.-C.; Ho, R.-M. Competitive Interactions of π - π Junctions and Their Role on Microphase Separation of Chiral Block Copolymers. *Chemistry of Materials* **2017**, *29* (10), 4493-4501. DOI: [10.1021/acs.chemmater.7b01151](https://doi.org/10.1021/acs.chemmater.7b01151)
- [76] Fish, D.; Smid, J. Solvation of Lithium Ions in Mixtures of Tetraethylene Glycol Dimethyl Ether and Propylene Carbonate. *Electrochimica Acta* **1992**, *37* (11), 2043-2049. DOI: [10.1016/0013-4686\(92\)87120-O](https://doi.org/10.1016/0013-4686(92)87120-O)
- [77] Blint, R. J. Binding of Ether and Carbonyl Oxygens to Lithium Ion. *Journal of the Electrochemical Society* **1995**, *142* (3), 696-702. DOI: [10.1149/1.2048519](https://doi.org/10.1149/1.2048519)
- [78] Adams, M.; Richmond, V.; Smith, D.; Wang, Y.; Fan, F.; Sokolov, A. P.; Waldow, D. A. Decoupling of Ion Conductivity from Segmental Dynamics in Oligomeric Ethylene Oxide Functionalized Oxanorbornene Dicarboximide Homopolymers. *Polymer* **2017**, *116*, 218-225. DOI: [10.1016/j.polymer.2017.03.054](https://doi.org/10.1016/j.polymer.2017.03.054)
- [79] Mindemark, J.; Lacey, M. J.; Bowden, T.; Brandell, D. Beyond PEO-Alternative Host Materials for Li⁺-Conducting Solid Polymer Electrolytes. *Progress in Polymer Science* **2018**, *81*, 114-143. DOI: [10.1016/j.progpolymsci.2017.12.004](https://doi.org/10.1016/j.progpolymsci.2017.12.004)
- [80] Yang, C. R.; Perng, J. T.; Wang, Y. Y.; Wan, C. C. Conductive Behaviour of Lithium Ions in Polyacrylonitrile. *Journal of Power Sources* **1996**, *62* (1), 89-93. DOI: [10.1016/S0378-7753\(96\)02414-7](https://doi.org/10.1016/S0378-7753(96)02414-7)
- [81] Chen-Yang, Y. Polyacrylonitrile Electrolytes 1. A Novel High-Conductivity Composite Polymer Electrolyte Based on PAN, LiClO₄ and α -Al₂O₃. *Solid State Ionics* **2002**, *150* (3-4), 327-335. DOI: [10.1016/S0167-2738\(02\)00457-5](https://doi.org/10.1016/S0167-2738(02)00457-5)
- [82] Chen, Y. T.; Chuang, Y. C.; Su, J. H.; Yu, H. C.; Chen-Yang, Y. W. High Discharge Capacity Solid Composite Polymer Electrolyte Lithium Battery. *Journal of Power Sources* **2011**, *196* (5), 2802-2809. DOI: [10.1016/j.jpowsour.2010.11.058](https://doi.org/10.1016/j.jpowsour.2010.11.058)
- [83] Bogle, X.; Vazquez, R.; Greenbaum, S.; Cresce, A. von W.; Xu, K. Understanding Li⁺-Solvent Interaction in Nonaqueous Carbonate Electrolytes with ¹⁷O NMR. *The Journal of Physical Chemistry Letters* **2013**, *4* (10), 1664-1668. DOI: [10.1021/jz400661k](https://doi.org/10.1021/jz400661k)
- [84] Ong, M. T.; Verners, O.; Draeger, E. W.; van Duin, A. C. T.; Lordi, V.; Pask, J. E. Lithium Ion Solvation and Diffusion in Bulk Organic Electrolytes from First-Principles and Classical Reactive Molecular Dynamics. *The Journal of Physical Chemistry B* **2015**, *119* (4), 1535-1545. DOI: [10.1021/jp508184f](https://doi.org/10.1021/jp508184f)
- [85] Mindemark, J.; Bowden, T. Synthesis and Polymerization of Alkyl Halide-Functional Cyclic Carbonates. *Polymer* **2011**, *52* (25), 5716-5722. DOI: [10.1016/j.polymer.2011.10.027](https://doi.org/10.1016/j.polymer.2011.10.027)
- [86] Rosa, D. S.; Neto, I. C.; Calil, M. R.; Pedroso, A. G.; Fonseca, C. P.; Neves, S. Evaluation of the Thermal and Mechanical Properties of Poly(ϵ -Caprolactone), Low-Density Polyethylene, and Their Blends. *Journal of Applied Polymer Science* **2004**, *91* (6), 3909-3914. DOI: [10.1002/app.13596](https://doi.org/10.1002/app.13596)
- [87] Takahashi, Y.; Tadokoro, H. Structural Studies of Polyethers, $-(\text{CH}_2)_m\text{O}-$ _n. X. Crystal Structure of Poly(Ethylene Oxide). *Macromolecules* **1973**, *6* (5), 672-675. DOI: [10.1021/ma60035a005](https://doi.org/10.1021/ma60035a005)

- [88] Polo Fonseca, C.; Neves, S. Electrochemical Properties of a Biodegradable Polymer Electrolyte Applied to a Rechargeable Lithium Battery. *Journal of Power Sources* **2006**, *159* (1), 712-716. DOI: [10.1016/j.jpowsour.2005.10.095](https://doi.org/10.1016/j.jpowsour.2005.10.095)
- [89] Fonseca, C. P.; Rosa, D. S.; Gaboardi, F.; Neves, S. Development of a Biodegradable Polymer Electrolyte for Rechargeable Batteries. *Journal of Power Sources* **2006**, *155* (2), 381-384. DOI: [10.1016/j.jpowsour.2005.05.004](https://doi.org/10.1016/j.jpowsour.2005.05.004)
- [90] Sun, B.; Mindemark, J.; Edström, K.; Brandell, D. Polycarbonate-Based Solid Polymer Electrolytes for Li-Ion Batteries. *Solid State Ionics* **2014**, *262*, 738-742. DOI: [10.1016/j.ssi.2013.08.014](https://doi.org/10.1016/j.ssi.2013.08.014)
- [91] Sun, B.; Mindemark, J.; Edström, K.; Brandell, D. Realization of High Performance Polycarbonate-Based Li Polymer Batteries. *Electrochemistry Communications* **2015**, *52*, 71-74. DOI: [10.1016/j.elecom.2015.01.020](https://doi.org/10.1016/j.elecom.2015.01.020)
- [92] Mindemark, J.; Imholt, L.; Brandell, D. Synthesis of High Molecular Flexibility Polycarbonates for Solid Polymer Electrolytes. *Electrochimica Acta* **2015**, *175*, 247-253. DOI: [10.1016/j.electacta.2015.01.074](https://doi.org/10.1016/j.electacta.2015.01.074)
- [93] Mindemark, J.; Törmä, E.; Sun, B.; Brandell, D. Copolymers of Trimethylene Carbonate and ϵ -Caprolactone as Electrolytes for Lithium-Ion Batteries. *Polymer* **2015**, *63*, 91-98. DOI: [10.1016/j.polymer.2015.02.052](https://doi.org/10.1016/j.polymer.2015.02.052)
- [94] Mindemark, J.; Sun, B.; Törmä, E.; Brandell, D. High-Performance Solid Polymer Electrolytes for Lithium Batteries Operational at Ambient Temperature. *Journal of Power Sources* **2015**, *298*, 166-170. DOI: [10.1016/j.jpowsour.2015.08.035](https://doi.org/10.1016/j.jpowsour.2015.08.035)
- [95] Tominaga, Y.; Yamazaki, K.; Nanthana, V. Effect of Anions on Lithium Ion Conduction in Poly(Ethylene Carbonate)-Based Polymer Electrolytes. *Journal of the Electrochemical Society* **2015**, *162* (2), A3133-A3136. DOI: [10.1149/2.0211502jes](https://doi.org/10.1149/2.0211502jes)
- [96] Meabe, L.; Lago, N.; Rubatat, L.; Li, C.; Müller, A. J.; Sardon, H.; Armand, M.; Mecerreyes, D. Polycondensation as a Versatile Synthetic Route to Aliphatic Polycarbonates for Solid Polymer Electrolytes. *Electrochimica Acta* **2017**, *237*, 259-266. DOI: [10.1016/j.electacta.2017.03.217](https://doi.org/10.1016/j.electacta.2017.03.217)
- [97] Meabe, L.; Huynh, T. V.; Lago, N.; Sardon, H.; Li, C.; O'Dell, L. A.; Armand, M.; Forsyth, M.; Mecerreyes, D. Poly(Ethylene Oxide Carbonates) Solid Polymer Electrolytes for Lithium Batteries. *Electrochimica Acta* **2018**, *264*, 367-375. DOI: [10.1016/j.electacta.2018.01.101](https://doi.org/10.1016/j.electacta.2018.01.101)
- [98] Wang, Y.; Fan, F.; Agapov, A. L.; Saito, T.; Yang, J.; Yu, X.; Hong, K.; Mays, J.; Sokolov, A. P. Examination of the Fundamental Relation between Ionic Transport and Segmental Relaxation in Polymer Electrolytes. *Polymer* **2014**, *55* (16), 4067-4076. DOI: [10.1016/j.polymer.2014.06.085](https://doi.org/10.1016/j.polymer.2014.06.085)
- [99] Thomas, K. E.; Sloop, S. E.; Kerr, J. B.; Newman, J. Comparison of Lithium-Polymer Cell Performance with Unity and Nonunity Transference Numbers. *Journal of Power Sources* **2000**, *89* (2), 132-138. DOI: [10.1016/S0378-7753\(00\)00420-1](https://doi.org/10.1016/S0378-7753(00)00420-1)
- [100] Wang, C.-G.; Goto, A. Solvent-Selective Reactions of Alkyl Iodide with Sodium Azide for Radical Generation and Azide Substitution and Their Application to One-Pot Synthesis of Chain-End-Functionalized Polymers. *Journal of the American Chemical Society* **2017**, *139* (30), 10551-10560. DOI: [10.1021/jacs.7b05879](https://doi.org/10.1021/jacs.7b05879)
- [101] Willcock, H.; O'Reilly, R. K. End Group Removal and Modification of RAFT Polymers. *Polymer Chemistry* **2010**, *1* (2), 149-157. DOI: [10.1039/B9PY00340A](https://doi.org/10.1039/B9PY00340A)
- [102] Satoh, K.; Poelma, J. E.; Campos, L. M.; Stahl, B.; Hawker, C. J. A Facile Synthesis of Clickable and Acid-Cleavable PEO for Acid-Degradable Block Copolymers. *Polymer Chemistry* **2012**, *3* (7), 1890-1898. DOI: [10.1039/C1PY00484K](https://doi.org/10.1039/C1PY00484K)
- [103] Lowe, A. B. CHAPTER 2. End-group Functionalization of RAFT-prepared Polymers Using Thiol-X Chemistries. In *Polymer Chemistry Series*; Lowe, A., Bowman, C., Eds.; Royal Society of Chemistry: Cambridge, 2013; pp 28-58. DOI: [10.1039/9781849736961-00028](https://doi.org/10.1039/9781849736961-00028)
- [104] Johansson, G. Studies on Aqueous Dextran-Poly(Ethylene Glycol) Two-Phase Systems Containing Charged Poly(Ethylene Glycol) I. Partition of Albumins. *Biochimica et Biophysica Acta (BBA) - General Subjects* **1970**, *222* (2), 381-389. <https://ac.els-cdn.com/0304416570901273/1-s2.0->

[0304416570901273-main.pdf? tid=13c07783-e803-4afa-aa86-4f9c65b88c0f&acdnat=1540132702_3835f13e8d23c4665de5ca28d564f977](#)

- [105] Sépulchre, M.; Paulus, G.; Jérôme, R. Specific Functionalization of Polyoxirane by Amino, Carboxyl, Sulfo, and Halogeno End Groups. *Die Makromolekulare Chemie* **1983**, *184* (9), 1849-1859. DOI: [10.1002/macp.1983.021840910](#)
- [106] Hamaide, T.; Deore, C. L. Cationic Conductivity and Relaxation Processes in Solid Polymer Electrolytes with Lithium Perfluoroalkyl Sulfonate or Sulfonato End-Capped Poly(Ethylene Oxide). *Polymer* **1993**, *34* (5), 1038-1046. DOI: [10.1016/0032-3861\(93\)90227-2](#)
- [107] Xu, K.; Angell, C. A. Synthesis and Characterization of Lithium Sulfonates as Components of Molten Salt Electrolytes. *Electrochimica Acta* **1995**, *40* (13-14), 2401-2403. DOI: [10.1016/0013-4686\(95\)00203-Q](#)
- [108] Ohno, H.; Ito, K. Poly(Ethylene Oxide)s Having Carboxylate Groups on the Chain End. *Polymer* **1995**, *36* (4), 891-893. DOI: [10.1016/0032-3861\(95\)93124-5](#)
- [109] Ito, K.; Ohno, H. Ionic Conductivity of Poly(Ethylene Oxide) Having Charges on the Chain End. *Solid State Ionics* **1995**, *79*, 300-305. DOI: [10.1016/0167-2738\(95\)00078-K](#)
- [110] Ito, K.; Nishina, N.; Ohno, H. High Lithium Ionic Conductivity of Poly(Ethylene Oxide)s Having Sulfonate Groups on Their Chain Ends. *Journal of Materials Chemistry* **1997**, *7* (8), 1357-1362. DOI: [10.1039/A700583K](#)
- [111] Ito, K.; Tominaga, Y.; Ohno, H. Polyether/Salt Hybrid (IV). Effect of Benzenesulfonate Group(s) and PEO Molecular Weight on the Bulk Ionic Conductivity. *Electrochimica Acta* **1997**, *42* (10), 1561-1570. DOI: [10.1016/S0013-4686\(96\)00317-9](#)
- [112] Tominaga, Y.; Ito, K.; Ohno, H. Polyether/Salt Hybrid: 6. Effect of Sulfonamide Ends Having Different Alkyl Groups on the Bulk Ionic Conductivity. *Polymer* **1997**, *38* (8), 1949-1951. DOI: [10.1016/S0032-3861\(96\)00726-4](#)
- [113] Nakai, Y.; Ito, K.; Ohno, H. Ion Conduction in Molten Salts Prepared by Terminal-Charged PEO Derivatives. *Solid State Ionics* **1998**, *113-115* (1-2), 199-204. DOI: [10.1016/S0167-2738\(98\)00286-0](#)
- [114] Tominaga, Y. High Ionic Conductivity of PEO/Sulfonamide Salt Hybrids. *Solid State Ionics* **1999**, *124* (3-4), 323-329. DOI: [10.1016/S0167-2738\(99\)00224-6](#)
- [115] Tominaga, Y.; Mizumo, T.; Ohno, H. Ionic Conductivity of PPO-Sulfonamide Salt Hybrids and Their Network Polymers. *Polymers for Advanced Technologies* **2000**, *11* (8-12), 524-528. DOI: [10.1002/1099-1581\(200008/12\)11:8/12<524::AID-PAT999>3.0.CO;2-8](#)
- [116] Mizumo, T.; Ohno, H. Molten Lithium Sulfonimide Salt Having Poly(Propylene Oxide) Tail. *Polymer* **2004**, *45* (3), 861-864. DOI: [10.1016/j.polymer.2003.11.039](#)
- [117] Ito, K.; Nishina, N.; Tominaga, Y.; Ohno, H. Effect of Terminal Groups on the Ionic Conductivity of α,ω -Disubstituted Poly(Ethylene Oxide) Oligomers. *Solid State Ionics* **1996**, *86-88*, 325-328. DOI: [10.1016/0167-2738\(96\)00140-3](#)
- [118] Nakai, Y.; Ito, K.; Ohno, H. Ion Conduction in Molten Salts Prepared by Terminal-Charged PEO Derivatives. *Solid State Ionics* **1998**, *113-115* (1-2), 199-204. DOI: [10.1016/S0167-2738\(98\)00286-0](#)
- [119] Ito, K.; Ohno, H. Design of Highly Ion Conductive Polyether/Salt Hybrids. *Electrochimica Acta* **1998**, *43* (10-11), 1247-1252. DOI: [10.1016/S0013-4686\(97\)10025-1](#)
- [120] Hallac, B. B.; Geiculescu, O. E.; Rajagopal, R. V.; Creager, S. E.; DesMarteau, D. D. Lithium-Conducting Ionic Melt Electrolytes from Polyether-Functionalized Fluorosulfonimide Anions. *Electrochimica Acta* **2008**, *53* (20), 5985-5991. DOI: [10.1016/j.electacta.2008.03.061](#)
- [121] Herath, M. B.; Creager, S. E.; Rajagopal, R. V.; Geiculescu, O. E.; DesMarteau, D. D. Ionic Conduction in Polyether-Based Lithium Arylfluorosulfonimide Ionic Melt Electrolytes. *Electrochimica Acta* **2009**, *54* (24), 5877-5883. DOI: [10.1016/j.electacta.2009.05.050](#)
- [122] Tsuchida, E.; Ohno, H.; Kobayashi, N.; Ishizaka, H. Poly[(L-Carboxy)Oligo(Oxyethylene) Methacrylate] as a New Type of Polymeric Solid Electrolyte for Alkali-Metal Ion Transport. *Macromolecules* **1989**, *22* (4), 1771-1775. DOI: [10.1021/ma00194a046](#)

- [123] Zhang, S.; Deng, Z.; Wan, G. Cationic Conductivity of Blend Complexes Composed of Poly[Oligo(Oxyethylene) Methacrylate] and the Alkali Metal Salts of Poly(Sulfoalkyl Methacrylate). *Polymer Journal* **1991**, *23* (2), 73-78. DOI: [10.1295/polymj.23.73](https://doi.org/10.1295/polymj.23.73)
- [124] Park, C. H.; Sun, Y.-K.; Kim, D.-W. Blended Polymer Electrolytes Based on Poly(Lithium 4-Styrene Sulfonate) for the Rechargeable Lithium Polymer Batteries. *Electrochimica Acta* **2004**, *50* (2–3), 375-378. DOI: [10.1039/C8SM00907D](https://doi.org/10.1039/C8SM00907D)
- [125] Ma, Q.; Qi, X.; Tong, B.; Zheng, Y.; Feng, W.; Nie, J.; Hu, Y.-S.; Li, H.; Huang, X.; Chen, L.; et al. Novel Li[(CF₃SO₂)(n-C₄F₉SO₂)N]-Based Polymer Electrolytes for Solid-State Lithium Batteries with Superior Electrochemical Performance. *ACS Applied Materials & Interfaces* **2016**, *8* (43), 29705-29712. DOI: [10.1021/acsami.6b10597](https://doi.org/10.1021/acsami.6b10597)
- [126] Ma, Q.; Zhang, H.; Zhou, C.; Zheng, L.; Cheng, P.; Nie, J.; Feng, W.; Hu, Y.-S.; Li, H.; Huang, X.; et al. Single Lithium-Ion Conducting Polymer Electrolytes Based on a Super-Delocalized Polyanion. *Angewandte Chemie International Edition* **2016**, *55* (7), 2521-2525. DOI: [10.1002/anie.201509299](https://doi.org/10.1002/anie.201509299)
- [127] Benrabah, D.; Sylla, S.; Sanchez, J.-Y.; Armand, M. Cationic Conductivity in Poly(Oxyethylene Oxide) Networks. *Journal of Power Sources* **1995**, *54* (2), 456-460. DOI: [10.1016/0378-7753\(94\)02124-L](https://doi.org/10.1016/0378-7753(94)02124-L)
- [128] Benrabah, D.; Sylla, S.; Alloin, F.; Sanchez, J.-Y.; Armand, M. Perfluorosulfonate-Polyether Based Single Ion Conductors. *Electrochimica Acta* **1995**, *40* (13–14), 2259-2264. DOI: [10.1016/0013-4686\(95\)00173-C](https://doi.org/10.1016/0013-4686(95)00173-C)
- [129] Tsuchida, E.; Ohno, H.; Kobayashi, N. Single-Ion Conduction in Poly[(Oligo(Oxyethylene)Methacrylate)-Co-(Alkali-Metal Methacrylates)]. *Macromolecules* **1988**, *21* (1), 96-100. DOI: [10.1021/ma00179a020](https://doi.org/10.1021/ma00179a020)
- [130] Ganapathiappan, S.; Chen, K.; Shriver, D. F. A New Class of Cation Conductors: Polyphosphazene Sulfonates. *Macromolecules* **1988**, *21* (7), 2299-2301. DOI: [10.1021/ma00185a075](https://doi.org/10.1021/ma00185a075)
- [131] Meziane, R.; Bonnet, J.-P.; Courty, M.; Djellab, K.; Armand, M. Single-Ion Polymer Electrolytes Based on a Delocalized Polyanion for Lithium Batteries. *Electrochimica Acta* **2011**, *57*, 14-19. DOI: [10.1016/j.electacta.2011.03.074](https://doi.org/10.1016/j.electacta.2011.03.074)
- [132] Bouchet, R.; Maria, S.; Meziane, R.; Aboulaich, A.; Lienafa, L.; Bonnet, J.-P.; Phan, T. N. T.; Bertin, D.; Gignes, D.; Devaux, D.; et al. Single-Ion BAB Triblock Copolymers as Highly Efficient Electrolytes for Lithium-Metal Batteries. *Nature Materials* **2013**, *12* (5), 452-457. DOI: [10.1038/nmat3602](https://doi.org/10.1038/nmat3602)
- [133] Feng, S.; Shi, D.; Liu, F.; Zheng, L.; Nie, J.; Feng, W.; Huang, X.; Armand, M.; Zhou, Z. Single Lithium-Ion Conducting Polymer Electrolytes Based on Poly[(4-Styrenesulfonyl)(Trifluoromethanesulfonyl)Imide] Anions. *Electrochimica Acta* **2013**, *93*, 254-263. DOI: [10.1016/j.electacta.2013.01.119](https://doi.org/10.1016/j.electacta.2013.01.119)
- [134] Porcarelli, L.; Aboudzadeh, M. A.; Rubatat, L.; Nair, J. R.; Shaplov, A. S.; Gerbaldi, C.; Mecerreyes, D. Single-Ion Triblock Copolymer Electrolytes Based on Poly(Ethylene Oxide) and Methacrylic Sulfonamide Blocks for Lithium Metal Batteries. *Journal of Power Sources* **2017**, *364*, 191-199. DOI: [10.1016/j.jpowsour.2017.08.023](https://doi.org/10.1016/j.jpowsour.2017.08.023)
- [135] Watanabe, M.; Suzuki, Y.; Nishimoto, A. Single Ion Conduction in Polyether Electrolytes Alloyed with Lithium Salt of a Perfluorinated Polyimide. *Electrochimica Acta* **2000**, *45* (8–9), 1187-1192. DOI: [10.1016/S0013-4686\(99\)00380-1](https://doi.org/10.1016/S0013-4686(99)00380-1)
- [136] Watanabe, M.; Tokuda, H.; Muto, S. Anionic Effect on Ion Transport Properties in Network Polyether Electrolytes. *Electrochimica Acta* **2001**, *46* (10–11), 1487-1491. DOI: [10.1016/S0013-4686\(00\)00743-X](https://doi.org/10.1016/S0013-4686(00)00743-X)
- [137] Tokuda, H.; Muto, S.; Hoshi, N.; Minakata, T.; Ikeda, M.; Yamamoto, F.; Watanabe, M. Synthesis, Characterization, and Ion-Conductive Behavior in an Organic Solvent and in a Polyether of a Novel Lithium Salt of a Perfluorinated Polyimide Anion. *Macromolecules* **2002**, *35* (4), 1403-1411. DOI: [10.1021/ma011904n](https://doi.org/10.1021/ma011904n)

- [138] Dou, S.; Zhang, S.; Klein, R. J.; Runt, J.; Colby, R. H. Synthesis and Characterization of Poly(Ethylene Glycol)-Based Single-Ion Conductors. *Chemistry of Materials* **2006**, *18* (18), 4288-4295. DOI: [10.1021/cm0603699](https://doi.org/10.1021/cm0603699)
- [139] Fragiadakis, D.; Dou, S.; Colby, R. H.; Runt, J. Molecular Mobility and Li⁺ Conduction in Polyester Copolymer Ionomers Based on Poly(Ethylene Oxide). *The Journal of Chemical Physics* **2009**, *130* (6), 064907. DOI: [10.1063/1.3063659](https://doi.org/10.1063/1.3063659)
- [140] LaFemina, N. H.; Chen, Q.; Colby, R. H.; Mueller, K. T. The Diffusion and Conduction of Lithium in Poly(Ethylene Oxide)-Based Sulfonate Ionomers. *The Journal of Chemical Physics* **2016**, *145* (11), 114903. DOI: [10.1063/1.4962743](https://doi.org/10.1063/1.4962743)
- [141] Doerk, G. S.; Yager, K. G. Beyond Native Block Copolymer Morphologies. *Molecular Systems Design & Engineering* **2017**, *2* (5), 518-538. DOI: [10.1039/C7ME00069C](https://doi.org/10.1039/C7ME00069C)
- [142] Zhang, W.-B.; Yu, X.; Wang, C.-L.; Sun, H.-J.; Hsieh, I.-F.; Li, Y.; Dong, X.-H.; Yue, K.; Van Horn, R.; Cheng, S. Z. D. Molecular Nanoparticles Are Unique Elements for Macromolecular Science: From “Nanoatoms” to Giant Molecules. *Macromolecules* **2014**, *47* (4), 1221-1239. DOI: [10.1021/ma401724p](https://doi.org/10.1021/ma401724p)
- [143] Zhang, W.; Huang, M.; Su, H.; Zhang, S.; Yue, K.; Dong, X.-H.; Li, X.; Liu, H.; Zhang, S.; Wesdemiotis, C.; et al. Toward Controlled Hierarchical Heterogeneities in Giant Molecules with Precisely Arranged Nano Building Blocks. *ACS Central Science* **2016**, *2* (1), 48-54. DOI: [10.1021/acscentsci.5b00385](https://doi.org/10.1021/acscentsci.5b00385)
- [144] Yu, X.; Yue, K.; Hsieh, I.-F.; Li, Y.; Dong, X.-H.; Liu, C.; Xin, Y.; Wang, H.-F.; Shi, A.-C.; Newkome, G. R.; et al. Giant Surfactants Provide a Versatile Platform for Sub-10-Nm Nanostructure Engineering. *Proceedings of the National Academy of Sciences* **2013**, *110* (25), 10078-10083. DOI: [10.1073/pnas.1302606110](https://doi.org/10.1073/pnas.1302606110)
- [145] Yu, X.; Zhang, W.-B.; Yue, K.; Li, X.; Liu, H.; Xin, Y.; Wang, C.-L.; Wesdemiotis, C.; Cheng, S. Z. D. Giant Molecular Shape Amphiphiles Based on Polystyrene–Hydrophilic [60]Fullerene Conjugates: Click Synthesis, Solution Self-Assembly, and Phase Behavior. *Journal of the American Chemical Society* **2012**, *134* (18), 7780-7787. DOI: [10.1021/ja3000529](https://doi.org/10.1021/ja3000529)
- [146] Lin, Z.; Lu, P.; Hsu, C.-H.; Sun, J.; Zhou, Y.; Huang, M.; Yue, K.; Ni, B.; Dong, X.-H.; Li, X.; et al. Hydrogen-Bonding-Induced Nanophase Separation in Giant Surfactants Consisting of Hydrophilic [60]Fullerene Tethered to Block Copolymers at Different Locations. *Macromolecules* **2015**, *48* (16), 5496-5503. DOI: [10.1021/acs.macromol.5b00741](https://doi.org/10.1021/acs.macromol.5b00741)
- [147] Dong, X.-H.; Ni, B.; Huang, M.; Hsu, C.-H.; Chen, Z.; Lin, Z.; Zhang, W.-B.; Shi, A.-C.; Cheng, S. Z. D. Chain Overcrowding Induced Phase Separation and Hierarchical Structure Formation in Fluorinated Polyhedral Oligomeric Silsesquioxane (FPOSS)-Based Giant Surfactants. *Macromolecules* **2015**, *48* (19), 7172-7179. DOI: [10.1021/acs.macromol.5b01661](https://doi.org/10.1021/acs.macromol.5b01661)
- [148] Yue, K.; Huang, M.; Marson, R. L.; He, J.; Huang, J.; Zhou, Z.; Wang, J.; Liu, C.; Yan, X.; Wu, K.; et al. Geometry Induced Sequence of Nanoscale Frank–Kasper and Quasicrystal Mesophases in Giant Surfactants. *Proceedings of the National Academy of Sciences* **2016**, *113* (50), 14195-14200. DOI: [10.1073/pnas.1609422113](https://doi.org/10.1073/pnas.1609422113)
- [149] Yue, K.; Liu, C.; Huang, M.; Huang, J.; Zhou, Z.; Wu, K.; Liu, H.; Lin, Z.; Shi, A.-C.; Zhang, W.-B.; et al. Self-Assembled Structures of Giant Surfactants Exhibit a Remarkable Sensitivity on Chemical Compositions and Topologies for Tailoring Sub-10 Nm Nanostructures. *Macromolecules* **2017**, *50* (1), 303-314. DOI: [10.1021/acs.macromol.6b02446](https://doi.org/10.1021/acs.macromol.6b02446)
- [150] Li, Y.; Dong, X.-H.; Zou, Y.; Wang, Z.; Yue, K.; Huang, M.; Liu, H.; Feng, X.; Lin, Z.; Zhang, W.; et al. Polyhedral Oligomeric Silsesquioxane Meets “Click” Chemistry: Rational Design and Facile Preparation of Functional Hybrid Materials. *Polymer* **2017**, *125*, 303-329. DOI: [10.1016/j.polymer.2017.08.008](https://doi.org/10.1016/j.polymer.2017.08.008)
- [151] Huang, M.; Yue, K.; Huang, J.; Liu, C.; Zhou, Z.; Wang, J.; Wu, K.; Shan, W.; Shi, A.-C.; Cheng, S. Z. D. Highly Asymmetric Phase Behaviors of Polyhedral Oligomeric Silsesquioxane-Based Multiheaded Giant Surfactants. *ACS Nano* **2018**, *12* (2), 1868-1877. DOI: [10.1021/acsnano.7b08687](https://doi.org/10.1021/acsnano.7b08687)

- [152] Sethi, G. K.; Jiang, X.; Chakraborty, R.; Loo, W. S.; Villaluenga, I.; Balsara, N. P. Anomalous Self-Assembly and Ion Transport in Nanostructured Organic–Inorganic Solid Electrolytes. *ACS Macro Letters* **2018**, *7* (9), 1056-1061. DOI: [10.1021/acsmacrolett.8b00583](https://doi.org/10.1021/acsmacrolett.8b00583)
- [153] Thomas, T. S.; Hwang, W.; Sita, L. R. End-Group-Functionalized Poly(α -Olefinates) as Non-Polar Building Blocks: Self-Assembly of Sugar-Polyolefin Hybrid Conjugates. *Angewandte Chemie International Edition* **2016**, *55* (15), 4683-4687. DOI: [10.1002/anie.201600035](https://doi.org/10.1002/anie.201600035)
- [154] Nowak, S. R.; Hwang, W.; Sita, L. R. Dynamic Sub-10-Nm Nanostructured Ultrathin Films of Sugar–Polyolefin Conjugates Thermoresponsive at Physiological Temperatures. *Journal of the American Chemical Society* **2017**, *139* (15), 5281-5284. DOI: [10.1021/jacs.6b13285](https://doi.org/10.1021/jacs.6b13285)
- [155] Seiki, N.; Shoji, Y.; Kajitani, T.; Ishiwari, F.; Kosaka, A.; Hikima, T.; Takata, M.; Someya, T.; Fukushima, T. Rational Synthesis of Organic Thin Films with Exceptional Long-Range Structural Integrity. *Science* **2015**, *348* (6239), 1122-1126. DOI: [10.1126/science.aab1391](https://doi.org/10.1126/science.aab1391)
- [156] Ishiwari, F.; Okabe, G.; Ogiwara, H.; Kajitani, T.; Tokita, M.; Takata, M.; Fukushima, T. Terminal Functionalization with a Triptycene Motif That Dramatically Changes the Structural and Physical Properties of an Amorphous Polymer. *Journal of the American Chemical Society* **2018**, *140* (41), 13497-13502. DOI: [10.1021/jacs.8b09242](https://doi.org/10.1021/jacs.8b09242)
- [157] Lafitte, V. G. H.; Aliev, A. E.; Horton, P. N.; Hursthouse, M. B.; Bala, K.; Golding, P.; Hailes, H. C. Quadruply Hydrogen Bonded Cytosine Modules for Supramolecular Applications. *Journal of the American Chemical Society* **2006**, *128* (20), 6544-6545. DOI: [10.1021/ja0587289](https://doi.org/10.1021/ja0587289)
- [158] Cheng, C.-C.; Wang, J.-H.; Chuang, W.-T.; Liao, Z.-S.; Huang, J.-J.; Huang, S.-Y.; Fan, W.-L.; Lee, D.-J. Dynamic Supramolecular Self-Assembly: Hydrogen Bonding-Induced Contraction and Extension of Functional Polymers. *Polymer Chemistry* **2017**, *8* (21), 3294-3299. DOI: [10.1039/C7PY00684E](https://doi.org/10.1039/C7PY00684E)
- [159] Rancatore, B. J.; Kim, B.; Mauldin, C. E.; Fréchet, J. M. J.; Xu, T. Organic Semiconductor-Containing Supramolecules: Effect of Small Molecule Crystallization and Molecular Packing. *Macromolecules* **2016**, *49* (3), 833-843. DOI: [10.1021/acs.macromol.5b02449](https://doi.org/10.1021/acs.macromol.5b02449)
- [160] Lee, K. H.; Bai, P.; Rancatore, B. J.; He, B.; Liu, Y.; Xu, T. Improved Hierarchical Ordering in Supramolecules via Symmetrically Bifunctionalized Organic Semiconductor. *Macromolecules* **2016**, *49* (7), 2639-2645. DOI: [10.1021/acs.macromol.6b00317](https://doi.org/10.1021/acs.macromol.6b00317)

Chapter II

MonoEnd-Capped Single-Ion Polymer Electrolytes (MEC-SIPEs) for Lithium-Ion Transport: Results and Discussion

Résumé

Le chapitre II de cette thèse présente la caractérisation d'électrolytes polymères "MonoEnd-Capped Single-Ion Polymer Electrolytes" (MEC-SIPes). Ces polymères sont constitués de deux parties : une chaîne polymère (n *unité de répétition) et d'un seul groupe terminal ionique. La caractérisation des MEC-SIPes est présentée en termes de performances électrochimiques. Les MEC-SIPes sont placés dans le contexte du transport des cations Li^+ pour des applications de stockage électrochimique d'énergie. Ils sont comparés aux électrolytes polymères solides traditionnels composés de sel binaire mélangé à une matrice hôte polymère. Les caractérisations électrochimiques des MEC-SIPes sont présentées et discutées selon trois paramètres :

I. Conductivité Ionique

*Les MEC-SIPes ont une σ_{AC} de $1 \cdot 10^{-5}$ à $1 \cdot 10^{-3} \text{ S.cm}^{-1}$ dans la plage de $-10 \text{ }^\circ\text{C}$ à $+100 \text{ }^\circ\text{C}$. La conductivité et sa dépendance thermique varient en fonction **i)** du groupe terminal et **ii)** de la longueur de la chaîne polymère.*

II. Stabilité Electrochimique

L'application d'électrolytes aux technologies de stockage électrochimique de l'énergie nécessite la stabilité des électrolytes dans les conditions de fonctionnement d'une batterie. Les MEC-SIPes sont ainsi présentés en termes de stabilité par rapport au lithium métal. *La plupart des exemples sont stables dans la plage 0 V - $3,6 \text{ V}$ vs Li/Li^+ .*

III. Transport du Lithium

Le transfert net d'ions lithium est décrit et discuté. Il est présenté en termes de nombre de transport de lithium (LTN) des MEC-SIPes. *Les MEC-SIPes ont des LTNs compris entre $0,6$ et l'unité.*

La caractérisation des propriétés électrochimiques, thermiques et du transport ionique des MEC-SIPE permet de proposer un modèle pour le transport ionique dans cette classe d'électrolytes. Les propriétés de transport ionique peuvent être expliquées par l'organisation des différentes parties du polymère dans les phases ségréguées. Le modèle repose sur le transport du lithium à travers différentes phases des MEC-SIPes. La microségrégation de phase est provoquée par la différence de propriétés physicochimiques qui existe entre les groupes terminaux fonctionnels et la chaîne polymère. Cette classe de MEC-SIPes constitue une approche modulaire pour la conception d'électrolytes polymères à conduction monocationique. La caractérisation de la bibliothèque actuelle de MEC-SIPes ouvre la voie à de nouvelles recherches sur les MEC-SIPes possédant différentes unités de répétitions et groupes terminaux. Une approche "High χ -Low N "^[1] est suggérée comme moyen d'étude fondamentale du transport monocationique dans les électrolytes polymères.^[2]

Abstract

In the chapter II of my thesis is presented the characterisation of MonoEnd-Capped "Single-Ion" Polymer Electrolytes (MEC-SIPes). These are electrolytes composed of two parts: a polymer chain of n repeating units and a single ionic end-group. The characterisation of these MEC-SIPes is presented in terms of the electrochemical performances of the MEC-SIPE. The MEC-SIPes are placed within the context of lithium ion transport for electrochemical energy storage applications. They are compared to traditional so-called solid polymer electrolytes composed of binary salt blended into a polymer host matrix. The electrochemical characterisations of the MEC-SIPes are presented and discussed in terms of three parameters:

I. Ion Transport

The MEC-SIPes have σ_{AC} from $1 \cdot 10^{-5}$ to $1 \cdot 10^{-3} \text{ S.cm}^{-1}$ in the $-10 \text{ }^\circ\text{C}$ to $+100 \text{ }^\circ\text{C}$ range. The magnitude σ and its dependence on temperature are functions of **i)** the end-group and **ii)** the length of the polymer chain.

II. Electrochemical Stability

The application of electrolytes to energy storage technologies requires stability of the electrolytes under the operating conditions of an electrochemical cell. The MEC-SIPes are presented in terms of their stability relative to lithium metal. *Most of the examples are stable in the 0 V - 3.6 V vs Li/Li^+ range.*

III. Transport efficiency

The net transference of lithium ions is described and discussed. This is presented in terms of the Lithium Transference Number (LTN) of EC-SIPes. *The MEC-SIPes have LTNs in the 0.6 - 1.0 range.*

Characterisation of the electrochemical, thermal, and ion transport properties of MEC-SIPes permits to propose a tentative model for ion transport in this class of electrolytes. The model relies on the transport of lithium through two phases of the bulk MEC-SIPE. These phases might be the result of phase segregation of the different parts of the MEC-SIPes in the bulk state. This microphase-separation process could have its origin in the difference in the physicochemical properties of the end-groups and the polymer chain. The MEC-SIPE class is presented as a modular approach for the design of single ion polymer electrolytes. The characterisation of the present library of MEC-SIPes suggests further research on MEC-SIPes having different repeating units and end-groups. A "High χ -Low N "^[1] approach towards MEC-SIPes is promoted as means for fundamental study of "Single-Ion" transport in polymer electrolytes.^[2]

Chapter II: Table of Contents

II. MonoEnd-Capped Single-Ion Polymer Electrolytes (MEC-SIPes) for Lithium-Ion Transport: Results and Discussion	63
1. Introduction	67
1.1. Principle Objectives of the Thesis.....	67
1.2. Principle Results of the Thesis	67
2. Electrochemical Characterisation of MEC-SIPes	70
2.1. The Ionic Conductivity of MEC-SIPes	70
2.2. Electrochemical Stability of MEC-SIPes	84
2.3. Lithium Transference by MEC-SIPes	96
2.4. Conclusions on Electrochemical Characterisation of MEC-SIPes	101
3. Thermal Characterisation of MEC-SIPes	104
3.1. The Dependence of Thermal Transitions on the Polymer End-Group	104
3.2. The Dependence of Thermal Transitions on the PEO chain length	105
3.3. The Endothermic Enthalpy Change of Thermal Transitions on Heating.....	111
3.4. Conclusions on Thermal Characterisation of MEC-SIPes.....	121
4. Ion Transport in MEC-SIPes	123
4.1. The Temperature Dependence of Ionic Conductivity	123
4.2. Characteristic Frequencies of Ion Transport in MEC-SIPes	131
4.3. Improvement of Ionic Conductivity with Cycling of Temperature	149
4.4. Conclusions on Ion Transport in MEC-SIPes	157
5. General Conclusions.....	160
6. Perspectives	161
7. Bibliography of Chapter II.....	163

1. Introduction

1.1. Principle Objectives of the Thesis

The present work concerns the characterisation of MonoEnd-Capped "Single-Ion" Polymer Electrolytes (MEC-SIPes). These are electrolytes composed of two parts: a polymer chain of n repeating units and a single ionic end-group. The characterisation of the MEC-SIPes is presented in terms of how the physicochemical properties of the end-group can determine and tune the properties of the MEC-SIPE. Thermal and electrochemical characterisations of the MEC-SIPes are presented to place these electrolytes in the context of lithium ion transport for electrochemical energy storage devices.

The temperature dependence of ion conductivity is of particular interest because the thermal behaviour of MEC-SIPes is profoundly affected by the end-groups and the chain length. Thermal characterisation by Differential Scanning Calorimetry (DSC) informs analysis of Electrochemical Impedance Spectroscopy (EIS) measurements of these MEC-SIPes. EIS measurements are then extended to probe characteristic responses of the MEC-SIPes over the $-10\text{ }^{\circ}\text{C}$ to $+100\text{ }^{\circ}\text{C}$ temperature range.

1.2. Principle Results of the Thesis

1.2.1. Overview of the Presented Results

The characterisation of the MEC-SIPes is divided into the following parts: Electrochemical (Section 2), Thermal (Section 3), and Ion Transport Properties (Section 4). The properties described and discussed in each section are dependent on the end-group and the chain length of the MEC-SIPes. Electrochemical characterisation of the MEC-SIPes is presented to discuss the principle objectives of **i**) ionic conductivity, **ii**) electrochemical stability, and **iii**) the efficiency of lithium transference. Thermal characterisation of the MEC-SIPes is presented in terms of results obtained by DSC. These results inform the discussion of ion transport properties of the MEC-SIPes. Characteristic ion transport behaviours of the MEC-SIPes are then discussed in terms of thermal transitions and characteristic features observed by EIS. The ion transport properties of MEC-SIPes are the result of concerted effects determined by the physicochemical properties of the end-group and the chain.

1.2.2. Electrochemical Characterisation (Section 2)

Conductivity

Ionic conductivities of the EC-SIPes based on PEO ($\text{EO}_n = 55$) are compared to describe the effect of the functional end-group. These polymer electrolytes are based on the same monofunctional polymer precursor ($\text{mPEO}_{55}\text{-OH}$) and therefore the chemistry of the end-group is the only variable. The functional end-group effect gave ionic conductivity in the descending order $\sigma_{\text{AC}}(\text{EGrp}) = \text{-N(Li)Pyr} > \text{-N(Li)Naph} > \text{-SO}_3\text{Li} > \text{-SO}_2\text{N(Li)Naph} > \text{-OC(O)PhSO}_3\text{Li}$. The highest ionic conductivity is reported for $\text{mPEO}_n\text{-N(Li)Pyr}$, which has $\sigma_{\text{AC}} > 1 \cdot 10^{-4}\text{ S}\cdot\text{cm}^{-1}$ at $60\text{ }^{\circ}\text{C}$ and *ca.* $1 \cdot 10^{-3}\text{ S}\cdot\text{cm}^{-1}$ at $100\text{ }^{\circ}\text{C}$, depending on the PEO chain length. The σ_{AC} is calculated from EIS measurements performed on cooling from $100\text{ }^{\circ}\text{C}$. Rational design of the functional end group afforded the "double salt" MEC-SIPE, in which two anionic functions were bound to the same chain-end. However, $\text{mPEO}_{55}\text{-SANSI(Li}_2\text{)}$ had the σ_{AC} similar to $\text{mPEO}_{55}\text{-N(Li)Pyr}$ in the reported $100\text{-}40\text{ }^{\circ}\text{C}$ range. These MEC-SIPes have $\sigma_{\text{AC}} > 1 \cdot 10^{-4}\text{ S}\cdot\text{cm}^{-1}$ at $T > 60\text{ }^{\circ}\text{C}$ and compare well with a reference *Salt-in-Polymer (SiP)*

electrolyte composed of poly(ethylene oxide) dimethyl ether (mPEO₆₀m) blended with an equivalent molar quantity of the binary salt LiTFSI.

The ionic conductivity was compared for each MEC-SIPE as a function of chain length. The presented series have a maximum of σ_{AC} close to $EO_n = 20$. These are compared with mPEO₆₀m blended with LiTFSI at the same molar ratio of $EO/Li = 20$. The most conductive MEC-SIPEs have $\sigma_{AC} > 1 \cdot 10^{-4} \text{ S.cm}^{-1}$ at $T > 60 \text{ }^\circ\text{C}$.

The contribution of anionic mobility to the conductivity of MEC-SIPEs was studied. A MEC-SIPE bearing a triazole function as well as a sulfonylimide group at the end-group of PEO₂₀ was designed, synthesized, and characterised. This MEC-SIPE, mPEO₂₀-NSI(Li⁺), is compared to the quaternized polymer bearing both Li⁺ and TFSI⁻ counterions, mPEO₂₀-⁺NSI(LiTFSI). Quaternisation and doping by the TFSI⁻ anion afforded an increase of σ_{AC} by one order of magnitude. This quaternised polymer mPEO₂₀-⁺NSI(LiTFSI) had not only the highest conductivity at comparable temperatures (*ca.* 0.1-1.0 mS.cm⁻¹), but also the widest range of temperatures at which ionic conductivity could be measured (*i.e.* from -10 to 100 °C).

Electrochemical stability

The electrochemical stability of the MEC-SIPEs depends on the end-group but is intrinsically limited to potentials below +4.0 V vs. Li/Li⁺ by the PEO chain and its EO repeating units. Cyclic voltammetry of the electrolytes in asymmetric Li|MEC-SIPE|Fe coin cells revealed anodic stability in oxidation mode up to the +3.5 to +4.0 V vs. Li/Li⁺ range. Cathodic stability in reduction mode was sufficient to enable plating of steel electrodes with lithium metal for all the MEC-SIPEs except mPEO₂₀-NSI(Li), which is not stable in the reduction mode.

Stripping and plating of lithium metal electrodes is demonstrated using galvanostatic cycling with potential limitation (10 measurement periods, alternating +/-10 $\mu\text{A.cm}^{-2}$, 4 h in each direction, limiting $E < 4.5 \text{ V vs. Li/Li}^+$, at 40 °C). The charge transfer properties of the MEC-SIPEs is dependent on the polymer functional end-group. Evolution of the resistivity of the electrolytes during stripping/plating of Lithium metal in Li|MEC-SIPE|Li symmetric cells at 40 °C was observed. The MEC-SIPEs in general do not have sufficient electrochemical stability to permit application as neat electrolytes in lithium batteries using lithium metal anodes.

Transference of Lithium

The Lithium Transference Number (LTN) of the MEC-SIPEs having $EO_n = 20$ is reported in the $t_{Li}^+ = 0.7-1.0$ range (at 40 °C). The magnitude of the LTN is dependent on the polymer functional end-group. This is higher than the PEO/LiTFSI blend having equivalent Li⁺ concentration ($EO/Li = 20$) under the same measurement conditions ($t_{Li}^+ = 0.4$). The zwitterionic polymer electrolyte mPEO₂₀-⁺NSI(LiTFSI) has two mobile counter ions (Li⁺ and TFSI⁻) but also a high LTN ($t_{Li}^+ = 0.8$).

1.2.3. Thermal Characterisation (Section 3)

The thermal behaviours of the MEC-SIPEs are dependent on the functional end-group and the chain length. The MEC-SIPEs are compared to their mPEO_n-OH precursors. The addition of a single ionic end-group to the polymer chain decreases the peak temperature (T_p) of the endothermic transitions (ΔH_{endo}) observed on heating. The exothermic transitions (ΔH_{exo}) of MEC-SIPEs were decreased in both temperature and enthalpy change relative to the precursors. Erasure of crystallinity in the MEC-SIPEs is correlated to improved ionic conductivity. MEC-SIPEs having $EO_n =$

55 have measurable ionic conductivity at temperatures above 40 °C. Depression of the ΔH_{endo} transitions attributed to the melting of PEO segments is observed for MEC-SIPEs having apparently shorter chains relative to their mPEO-OH precursors. This is correlated to MEC-SIPEs of $\text{EO}_n=8, 10,$ and 20 having ionic conductivity at ambient temperature.

Variation of the rate of cooling causes the augmentation of T_p and ΔH_{endo} of certain transitions observed on heating of mPEO₂₀-N(Li)Pyr. These are compared to the mPEO₂₀-OH precursor and to the literature as basis for a tentative model of the thermal behaviour of the MEC-SIPE. The observed thermal properties the MEC-SIPE are proposed to be the result of concerted organisation of the two sub-parts of these ionically conducting macromolecules on cooling.

1.2.4. Characteristic Ion Transport Properties (Section 4)

The typical response of the bulk resistance of a polymer electrolyte is accompanied in MEC-SIPEs by the formation of other resistive features. These features in EIS are described in terms of their characteristic frequencies and the temperatures at which they appear. The frequency dependence of ionic conductivity was probed for MEC-SIPEs across the temperature ranges afforded by their design (with respect to the single functional end-group and the length of the PEO chain). The measurement window of observed frequencies is constant, with respect to the frequency range of the EIS spectrometer and experimental conditions of the measurement. However, the nature of the ionically conductive phases observed within this measurement window of frequency and temperature is determined by the physicochemical nature of the MEC-SIPE. Their properties are different to SiP electrolyte blends having comparable concentrations of lithium ions. Ion transport in MEC-SIPEs is correlated to their (macro)molecular design.

Very strikingly, repeated heating and cooling the MEC-SIPEs afforded an improvement of σ_{AC} by as much as half an order of magnitude. The best results are of the “double salt” mPEO₅₅-SANSI(Li₂) (EO/Li= 23; 0.5 wt% Li⁺; 14 wt% of functional End-Groups), and mPEO₅₅-N(Li)Pyr (EO/Li= 55; 0.3 wt% Li⁺; 9 wt% of functional End-Groups). This is a significant result for a polymer electrolyte having a low concentration of Li⁺ and a low concentration of ionic end-groups (*i.e.* lithium salts). This improvement is not observed for PEO/LiTFSI blends of equivalent salt loading. The ion transport and thermal properties of the MEC-SIPEs are examined together to propose a tentative explanation for the increase in ionic conductivity with thermal cycling.

1.2.5. Conclusions and Perspectives

Characterisation of the electrochemical, thermal and ion transport properties of MEC-SIPEs permits to propose a tentative model for ion transport in this class of electrolytes. The model relies on the transport of lithium through two phases of the bulk MEC-SIPE. These phases might be the result of phase segregation of the different parts of the MEC-SIPEs in the bulk state. This microphase-separation process might originate from the difference in the physicochemical properties of the end-groups and of the polymer chain. The MEC-SIPE class is presented as a modular approach for the design of single-ion polymer electrolytes. The characterisation of the present library of MEC-SIPEs suggests further research on EC-SIPEs having different repeating units and end-groups. A High χ -Low N approach towards EC-SIPEs is promoted as means for fundamental study of "Single-Ion" transport in polymer electrolytes.

2. Electrochemical Characterisation of MEC-SIPES

2.1. The Ionic Conductivity of MEC-SIPES

2.1.1. Overview of the Measurement Method and Analysis of the Data

The ionic conductivity of an electrolyte solution is dependent on the mobility of a solvated ion pair (**Eqn. II-1**).^[3-5]

Equation II-1: The molar ionic conductivity of an ion as a function of the ionic charge (z) and mobility (μ), where the Faraday constant $F = N_a e$. D is the diffusion coefficient, R is the ideal gas constant, and T is the temperature in kelvin.

$$\lambda_m = \mu \cdot zF = \frac{zFD}{RT} \cdot zF$$

Therefore, the ionic conductivity of the electrolyte is the sum of the conductivities of the cation and the anion (**Eqn. II-2**).

Equation II-2: The molar ionic conductivity of an electrolyte solution is the sum of the ionic conductivities (λ) of the ions, where ν is the stoichiometric quantity of the ions.

$$\Lambda_m^0 = \nu_+ \lambda_+ + \nu_- \lambda_-$$

Combining equations 1 and 2 yields the limiting ionic conductivity of the electrolyte (Λ_m), defined in the Nernst-Einstein equation (**Eqn. II-3**). This molar value limits the conductivity of the electrochemical cell relative to the molar quantity of ions in the electrolyte (*i.e.* the concentration of salt between the electrodes).

Equation II-3: The limiting molar ionic conductivity of an electrolyte solution.

$$\Lambda_m = (\nu_+ z_+^2 D_+ + \nu_- z_-^2 D_-) \cdot \frac{F^2}{RT}$$

The ionic conductivity of the electrolyte is a function of the mobility of the ion pair, as expressed by the Nernst-Einstein equation (**Eqn. II-3**). In the case of a MEC-SIPE, the anion is covalently bound to the polymer chain. The mobility of the anion is thus limited by the mobility of the polymer chain. When the polymer chain is sufficiently long to permit entanglement of chain segments, the mobility of the chain (and therefore the anions) is effectively minimised. In the practical timescale of experimental analysis and battery usage, the mobility of the anions is close to zero. Therefore MEC-SIPES are expected to have decreased ionic conductivity as a consequence of decreased anionic mobility. However, the efficiency of charge transfer by Li^+ is expected to increase as the fraction of charge transferred by Li^+ approaches unity.

The ionic conductivity is calculated from **Electrochemical Impedance Spectroscopy (EIS)**. The electrolyte is placed between parallel plates of blocking (non-injecting) electrodes and a sinusoidal voltage (V) is applied at varying angular frequency (ω) and constant amplitude (V_0).

Equation II-4: The applied sinusoidal voltage having angular frequency (ω) at a constant amplitude (V_0) in electrochemical impedance spectroscopy (EIS).

$$V = V_0 [\cos(\omega t) + i \sin(\omega t)]$$

The current (I) is then recorded as a function of the applied potential. The impedance (Z) is a complex function defined as the sum of its real (Z') and imaginary parts (Z''):

Equation II-5: The definition of electrochemical complex impedance (Z).

$$\frac{V}{I} = Z = Z' + iZ''$$

With the real (Z') and imaginary (Z'') parts having the following identities:

Equation II-6: the identities of the real (Z') part of the complex impedance (Z).

$$Z' = \frac{R_b}{\left[1 + (\omega C_g R_b)^2\right]}$$

Equation II-7: the Identity of the imaginary part (Z'') of the complex impedance (Z)

$$Z'' = \frac{\left[1 + (\omega C_g R_b)^2\right] \left(1 + \frac{C_{dl}}{C_g}\right)}{\omega C_{dl} \left[1 + (\omega C_g R_b)^2\right]}$$

Where ω is the angular frequency ($\text{rad}\cdot\text{s}^{-1}$), C_g is the capacitance of the cell geometry, C_{dl} is the capacitance of the electrical double layer at the electrode-electrolyte interface, and R_b is the bulk resistance. Rearrangement of the equations of Z' and Z'' yields the equation defining the semi-circular plot observed when the imaginary impedance (Z'') is plotted as a function of the real impedance (Z') in the complex plan. The resultant complex representation is the Nyquist plot.

Equation II-8: Rearrangement of Z' (Eqn. 6) and Z'' (Eqn. 7) affords the semi-circular, complex relation of the Nyquist plot.

$$\left(\frac{R_b}{2}\right)^2 = \left(Z' - \frac{R_b}{2}\right)^2 + (Z'')^2$$

This enables plotting of the imaginary part (Z'') as a function of (Z') in the complex plane, to obtain a semi-circular relationship with a centre at $Z' = (R_b/2)$, $Z'' = 0$, on the real (Z') axis. The intercept of this semi-circle (at $Z' = R_b$, $Z'' = 0$) is determined by the bulk resistance of the electrolyte. The value of this feature on the real axis is used to calculate the ionic conductivity ($\text{S}\cdot\text{cm}^{-1}$) of the electrolyte using R_b in the following equation:

Equation II-9: The ionic conductivity ($\sigma / \text{S}\cdot\text{cm}^{-1}$) is the product of bulk resistance (R_b / Ω) and the cell constant, where l is the electrolyte thickness (cm) and A is the electrode surface area (cm^2)

$$\sigma = \frac{1}{R_b} \cdot \frac{l}{A}$$

R_b can be identified either by direct inspection of the Nyquist plot or, in the case of deviation from the ideal shape, by fitting the experimental data to an appropriate equivalent circuit model.

2.1.2. The effect of End-Group design

The physicochemical character of the ionic function of a SIPE has a large effect on the bulk ionic conductivity of the electrolyte. The SIPEs are compared at constant PEO chain length ($\text{EO}_n = 55$) for temperatures in the 40-100 °C range. The EC-SIPEs having $\text{EO}_n = 55$ and a single ionic end-group thus have a ratio of $\text{EO}/\text{Li} = 55$, and the bulk concentration of lithium salt is one salt (end-group) per chain. Poly(ethylene oxide) dimethyl ether ($\text{H}_3\text{C}-\text{PEO}_{60}-\text{CH}_3$) having non-interacting methyl chain ends is used as a comparison to the synthesized MEC-SIPEs. This polymer abbreviated hereafter as $\text{mPEO}_{60\text{m}}$ is blended with one molar equivalent of the ubiquitous salt LiTFSI . The resultant SiP ($\text{mPEO}_{60\text{m}}/\text{LiTFSI}$) blend has a concentration of one salt per polymer chain and a ratio of $\text{EO}/\text{Li} = 60$.

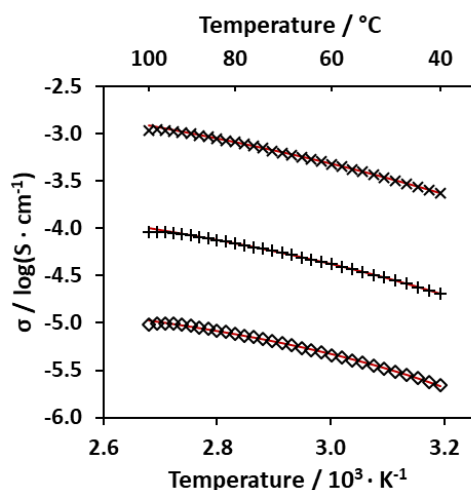


Figure II-1: The conductivity ($\sigma / \text{S} \cdot \text{cm}^{-1}$) as a function of Temperature ($T / 10^3 \cdot \text{K}^{-1}$) for mPEO₆₀m/LiTFSI (EO/Li= 60) SiP blend (x), mPEO₅₅-SO₃Li (+), mPEO₅₅-OC(O)PhSO₃Li (◇). The VTF fit of each set are represented (red lines, -). The measurements were conducted on cooling (100 → 40 °C).

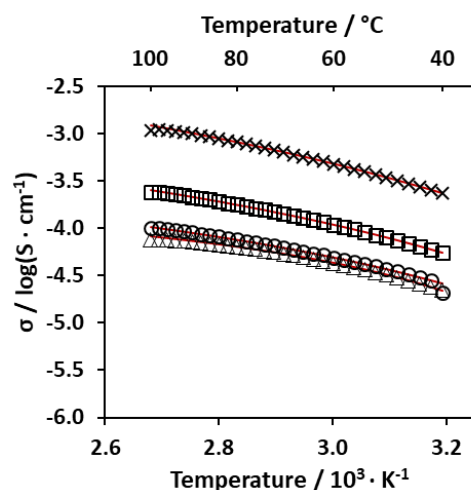


Figure II-2: The conductivity ($\sigma / \text{S} \cdot \text{cm}^{-1}$) as a function of Temperature ($T / 10^3 \cdot \text{K}^{-1}$) for mPEO₆₀m/LiTFSI (EO/Li= 60) SiP blend (x), mPEO₅₅-N(Li)Pyr (□), mPEO₅₅-N(Li)Naph (○), and mPEO₅₅-SO₂N(Li)Naph (△). The VTF fit of each set are represented (red lines, -). The measurements were conducted on cooling (100 → 40 °C).

The polymer electrolytes studied at constant PEO chain length (**Fig. II-1** & **Fig. II-2**) are measured according to the same protocol: heating from ambient temperature (of *ca.* 20 °C) to 100 °C, and recording of the electrochemical impedance spectrum (EIS) on cooling down to 40 °C. The lines drawn are generated by least-squares fitting of the experimental data to the Vogel-Tamman-Fulcher (VTF) relation.^[6,7] The agreement of σ with the VTF model will be discussed in a broader context, in **Section 4**.

The ionic conductivity (σ) of the SiP mPEO₆₀m/LiTFSI (EO/Li= 60) follows the expected trend: reaching $1 \cdot 10^{-3} \text{ S} \cdot \text{cm}^{-1}$ at 100 °C, and then decreasing with temperature upon cooling. A similar shape of σ as a function of reciprocal temperature is observed for the MEC-SIPEs. The polymer mPEO₅₅-SO₃Li represents the simplest MEC-SIPE in terms of functional end-group design and has an ionic conductivity σ of *ca.* 1 order of magnitude lower than the comparable SiP blend (**Fig. II-1**). The incorporation of a phenyl ring into the end-group of the polymer mPEO₅₅-OC(O)PhSO₃Li results in a further drop of σ to an order of magnitude lower than mPEO₅₅-SO₃Li. The *N*-naphthyl sulfonamide end-capped mPEO₅₅-SO₂N(Li)Naph (**Fig. II-2**) has a similar dependence of ionic conductivity on reciprocal temperature to the sulfonate (**Fig. II-1**). The sulfonamide and the corresponding secondary amine mPEO₅₅-N(Li)Naph have almost identical performance (**Fig. II-2**). However, increasing the size of the aryl substituent improves the ionic conductivity. The pyrene-functionalised mPEO₅₅-N(Li)Pyr has an ionic conductivity of *ca.* half an order of magnitude higher than the naphthyl-functionalised MEC-SIPE (**Fig. II-2**).

All of the MEC-SIPE polymers having EO_n= 55 crystallised below 40 °C. The growth of crystalline domains decreased the percolation of the amorphous ionically conductive domains through the microscopic dimension of the measurement (*through plane* measurements in between blocking (gold) electrodes separated by *ca.* 50-100 μm). The corresponding perturbation of the complex impedance resulted in non-ideal fitting of the Nyquist plot and a large drop in apparent ionic conductivity of the electrolytes. The same drop in σ was observed for the SiP mPEO₆₀m/LiTFSI blend.

The effect of lithium concentration was probed for an MEC-SIPE of the same PEO chain length. The lithium ion concentration at the functional chain end was increased by elaboration of the end-group design. By modifying the functional end group to have two anionic functions, the EC-SIPE mPEO₅₅-SANSI(Li₂) is created. This MEC-SIPE has two lithium ions associated with the end group by ionic interactions. The bulk lithium concentration of this MEC-SIPE is therefore double that of an EC-SIPE having a single anionic function at the end-group.

The temperature dependence of the ionic conductivity of mPEO₅₅-SANSI(Li₂) (EO/Li= 23) is compared to mPEO₅₅-SO₂N(Li)Naph (EO/Li= 55) and to the SiP mPEO₆₀m/LiTFSI (EO/Li= 60) blend (**Fig. II-3**). Although the concentration of Li⁺ is doubled, the polymer mPEO₅₅-SANSI(Li₂) has ionic conductivity only slightly higher than the mono-salt mPEO₅₅-SO₂N(Li)Naph, at T > 60 °C. If salt concentration was the major limitation of σ , one would expect an increase in σ proportional to the increase in lithium concentration. However, the two salt functions of mPEO₅₅-SANSI(Li₂) (*i.e.* the -SO₂N(Li)Naph- and the -SO₂N(Li)SO₂CH₃) are unlikely to have the same energy of dissociation. The salt having the lower energy of ion dissociation would have the higher contribution to the conduction of Li⁺ ions. The small increase in ionic conductivity of mPEO₅₅-SANSI(Li₂) compared to mPEO₅₅-SO₂N(Li)Naph implies that the bulk concentration of Li⁺ is not the only limiting condition of this performance.

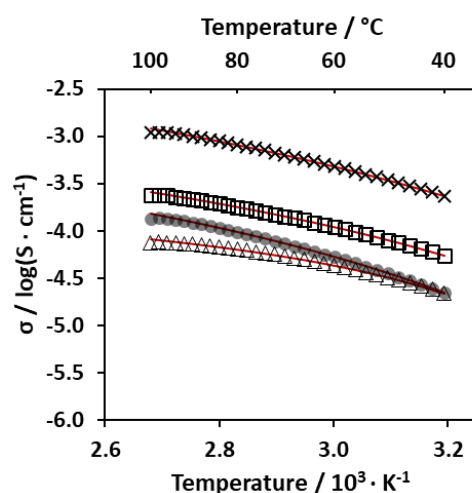


Figure II-3: The conductivity ($\sigma / S \cdot \text{cm}^{-1}$) as a function of Temperature ($10^3 \cdot \text{K}^{-1}$) for mPEO₅₅-SANSI(Li₂) (filled circles, ●), mPEO₆₀m/LiTFSI (EO/Li= 60) SiP blend (x), mPEO₅₅-N(Li)Pyr (□) and mPEO₅₅-SO₂N(Li)Naph (△). The VTF fit of each set are represented (red lines, -). The measurements were conducted on cooling (100 → 40 °C).

It is significant that the mono-salt mPEO₅₅-N(Li)Pyr has the highest ionic conductivity of all the MEC-SIPEs having EO_n= 55. The high performance of the pyrene-functional EC-SIPE might result from any or all of the following:

- I. Improved dissociation of Li⁺. Donation of aromatic electron density from the pyrene might increase delocalisation of the anionic charge and thus decrease the interaction energy of the ion pair. A decrease in the interaction energy of the ion pair would enable faster transfer of Li⁺ between coordination sites. This would increase the mobility of Li⁺ and afford increased ionic conductivity. However, the dissociation energy alone is not sufficient to explain the superior performance of mPEO₅₅-N(Li)Pyr. A highly dissociated salt pair does not afford ionic conductivity unless the Li⁺ is able to percolate effectively

through the (microscopic: *vide supra*) length scale of the measurement. A delocalised Li⁺ does not contribute to ionic conductivity unless it is able to travel from one electrode to the other.

- II. Improved number and type of specific interactions of the ionic end-groups might improve the percolation of conductive pathways through the bulk electrolyte. The -N(Li)Pyr end-groups might associate in the bulk electrolyte through ionic and π - π stacking interactions. Improved π - π stacking of -N(Li)Pyr might improve the ionic conductivity of mPEO₅₅-N(Li)Pyr relative to mPEO₅₅-N(Li)Naph (**Fig. II-3**).
- III. Mixed contributions of ionic and electronic conduction. The pyrene group might be considered as a molecular analogue of electronically conductive graphene. The multi-ring aromatic might contribute electronic conductivity to the bulk MEC-SIPE if the end-groups are closely associated through specific intermolecular forces.

These possible phenomena (i-iii) could explain the high conductivity performance observed of mPEO₅₅-N(Li)Pyr in EIS. The specific interactions of end-groups, the percolation of ionically conductive pathways, and a possible mixed contribution of ionic and electronic conductivity would moreover act concertedly to yield the high performance observed. However, EIS analysis of the present set of MEC-SIPEs alone does not provide definitive evidence of these possible structure-property correlations.

2.1.3. The effect of PEO chain length

The ionic conductivity of MEC-SIPEs is dependent on the Degree of Polymerisation (DP_n) of PEO. The concentration of ionic end groups varies inversely with the PEO chain length. Increasing the length of the PEO chain decreases the bulk concentration of functional end-groups. The molar quantity of ion pairs for a given cell dimension determines the ionic conductivity of the electrolyte.

The concentration of salt is quantified for purposes of comparison by calculating the mass fraction of salt in the polymer electrolyte. In the case of a SiP electrolyte, the calculation is the mass of salt divided by the sum of the mass of salt and the mass of the polymer (**Eqn. II-10**).

Equation II-10: The mass fraction of salt (ϕ_{salt}) in a Salt-in-Polymer (SiP) blend

$$\phi_{m(salt)} = \frac{m_{salt}}{(m_{salt} + m_{polymer})}$$

In the case of a MEC-SIPE, the salt is the functional end group of the polymer. To account for the variation of the mass of the functional end group (ion pair), the above equation is applied. The identity of the salt is the functional end group and the mass of the polymer is that of the polymer (PEO) chain only.

Equation II-11: The mass fraction of salt (ϕ_{salt}) in a MonoEnd-Capped Single-Ion Polymer Electrolyte (MEC-SIPE) having an ionic (*i.e.* lithium salt) function at the polymer chain end. The mass of the end-group (m_{EGrp}) is, for a MEC-SIPE, equivalent to the mass of a given binary salt ion pair. The mass of the polymer corresponds to the chain of repeating units only (*i.e.* the PEO chain).

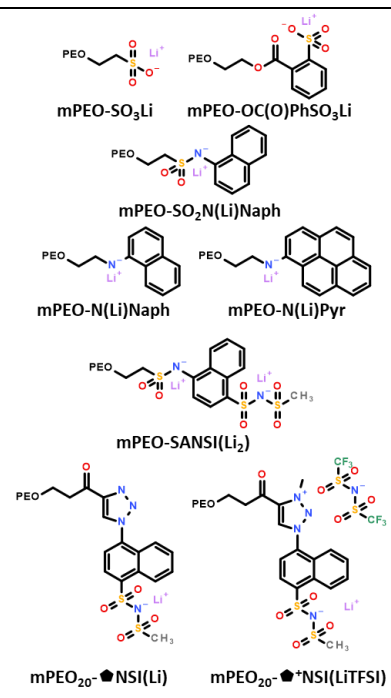
$$\phi_{m(EGrp)} = \frac{m_{EGrp}}{(m_{EGrp} + m_{chain})}$$

The different end-groups presented have different molecular masses. Changing the end-group of the MEC-SIPE results in a change in the concentration of lithium per unit mass of MEC-SIPE at

constant EO/Li ratio. The concentrations and mass fractions of ionic end-groups, and the lithium concentrations of the different EC-SIPEs in this work are summarised (**Table II-1**).

Table II-1: The Degree of Polymerisation (DP_n / EO_n), Number Average Molecular Mass ($M_n / \text{g.mol}^{-1}$), the mass fraction of the end-group ($\phi_{m(\text{EGrp})}$) and the mass fraction of lithium ($\phi_{m(\text{Li})}$) of the presented MEC-SIPEs having different functional End-Group Identities.

MEC-SIPE					
End-Group Identity	(g.mol^{-1})	DP_n (EO_n)	$M_n(\text{MEC-SIPE})$ (g.mol^{-1})	$\phi_{m(\text{EGrp})}$	$\phi_{m(\text{Li})}$
-SO ₃ Li	87	8	470	0.18	0.015
		10	530	0.16	0.013
		20	990	0.09	0.007
		55	2480	0.04	0.003
-OC(O)PhSO ₃ Li	207	8	590	0.35	0.012
		10	650	0.32	0.011
		20	1110	0.19	0.006
		55	2600	0.08	0.003
-SO ₂ N(Li)Naph	213	8	600	0.36	0.012
		10	655	0.33	0.011
		20	1115	0.19	0.006
		55	2610	0.08	0.003
-N(Li)Naph	148	8	540	0.28	0.013
		10	590	0.25	0.012
		20	1050	0.14	0.007
		55	2550	0.06	0.003
-N(Li)Pyr	223	8	610	0.37	0.011
		10	670	0.34	0.011
		20	1130	0.20	0.006
		55	2620	0.09	0.003
-SANSI(Li ₂)	377	55	2770	0.136	0.005
-●NSI(Li)	401	20	1300	0.308	0.005
-● ⁺ NSI(LiTFSI)	696	20	1600	0.436	0.004



The conductivities of the MEC-SIPEs were compared as a function of chain length ($EO_n = 8, 10, 20, 55$) for each functional end group. The maximum ionic conductivity for each polymer is observed for PEO $DP_n = 20$. The maximum of the ionic conductivity, with respect to temperature, is dependent on the functional end-group of the MEC-SIPE.

The ionic conductivity of the MEC-SIPEs is compared to SiP blends of $mPEO_{60}m/LiTFSI$. In the case of the SiP, the quantity of salt (LiTFSI) is varied according to the ratio of ethylene oxide units per lithium cation (EO/Li). Three SiP blends are presented in terms of their ionic conductivity as a function of temperature (**Fig. II-4**), corresponding to EO/Li loadings of 10, 20, and 60. The conductivity of the SiP electrolyte increases with salt concentration (**Fig. II-6**). The SiP blends all exceed $1 \cdot 10^{-4} \text{ S.cm}^{-1}$ above $40 \text{ }^\circ\text{C}$ and exceed $1 \cdot 10^{-3} \text{ S.cm}^{-1}$ at $100 \text{ }^\circ\text{C}$ (**Fig. II-4**). However, the addition of salt enables the effective conduction of ions at temperatures below $40 \text{ }^\circ\text{C}$ in the case of $mPEO_{60}m/LiTFSI$ having EO/Li = 20 and EO/Li = 10. This will be discussed with respect to MEC-SIPE polymers of equivalent EO/Li ratios.

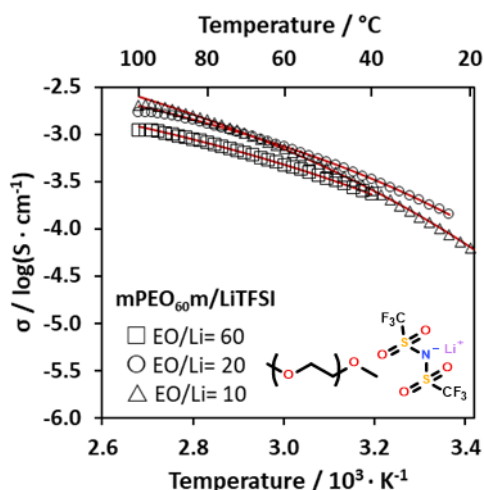


Figure II-4: The conductivity ($\sigma / \text{S} \cdot \text{cm}^{-1}$) as a function of Temperature ($T / 10^3 \cdot \text{K}^{-1}$) for the SiP mPEO₆₀m/LiTFSI blend having different EO/Li ratios. The experimental data of the blends EO/Li= 60 (\square), EO/Li= 20 (\circ) and EO/Li= 10 (\triangle) were recorded on cooling from 100 °C. The data are fitted to the VTF model (red lines, -).

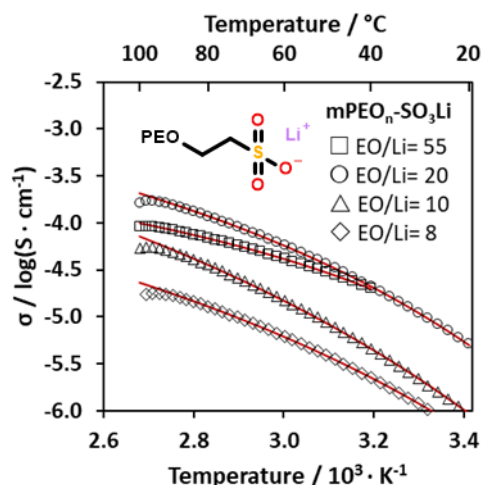


Figure II-5: The conductivity ($\sigma / \text{S} \cdot \text{cm}^{-1}$) as a function of Temperature ($T / 10^3 \cdot \text{K}^{-1}$) for the MEC-SIPE mPEO_nSO₃Li having different EO/Li ratios. The EO/Li ratio is fixed according to the polymer DP_n (EO_n). The experimental data of EO/Li= 55 (\square), EO/Li= 20 (\circ) and EO/Li= 10 (\triangle) and EO/Li=8 (\diamond) were recorded on cooling from 100 °C. The data are fitted to the VTF model (red lines, -).

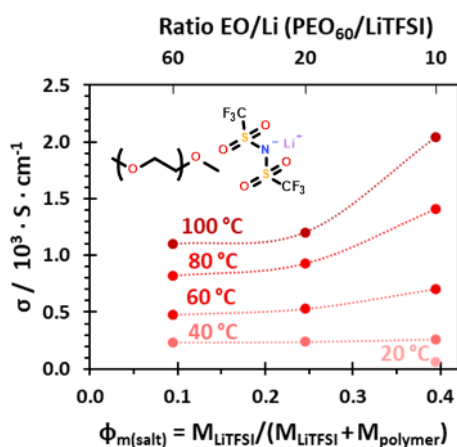


Figure II-6: The conductivity ($\sigma / \text{S} \cdot \text{cm}^{-1}$) of mPEO₆₀m/LiTFSI as a function of the mass fraction (ϕ_m) of salt (LiTFSI). The corresponding ratio of EO/Li is also displayed. The lines (\cdots) are drawn as a guide for the eye only. The experimental data correspond to those displayed in Figure II-4.

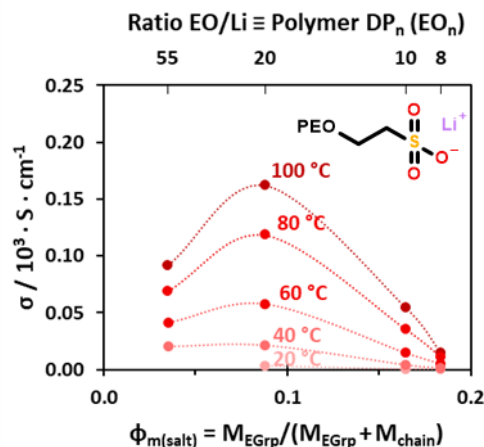


Figure II-7: The conductivity ($\sigma / \text{S} \cdot \text{cm}^{-1}$) of mPEO_n-SO₃Li as a function of the mass fraction (ϕ_m) of salt (the polymer end-group). The corresponding ratio of EO/Li is also displayed. Here the ratio EO/Li for the MEC-SIPE is determined by the polymer DP_n (EO_n). The lines (\cdots) are drawn as a guide for the eye only. The experimental data correspond to those displayed in Figure II-5.

The SiP blends can be compared to the ionic conductivities of MEC-SIPEs having different PEO chain lengths. The ionic conductivity of the MEC-SIPE mPEO_n-SO₃Li having EO_n= 8, 10, 20, and 55 (Fig. II-5) is lower than the comparable SiP electrolyte (Fig. II-4). A difference in σ of more than one order of magnitude is realised when the PEO chain length of mPEO_n-SO₃Li is varied in the range EO_n= 8-55. This is evidence of a high dependence of σ on the functional end-group concentration. The highest ionic conductivity is achieved by mPEO₂₀-SO₃Li (EO/Li= 20) across the entire measurement range presented (Fig. II-5). It is notable that the ionic conductivities of mPEO_n-SO₃Li having EO/Li= 55 and EO/Li= 20 are the same at 40 °C despite the large difference in the concentration of ionic end-groups.

Whereas the concentration of Li^+ in the SiP electrolyte is dependent on the loading of the small molecular salt (**Fig. II-4**), the concentration of Li^+ of the MEC-SIPE is dependent on the chain length (DP_n) of the polymer electrolyte. The dependence of the ionic conductivity on the concentration of Li^+ for the two different electrolytes is presented. Whereas σ of the SiP electrolyte increases at higher salt concentration (**Fig. II-6**), the optimum in σ of $\text{mPEO}_n\text{-SO}_3\text{Li}$ (**Fig. II-7**) is reached at an intermediate concentration of ionic end-groups ($\text{EO/Li} = 20$). The conductivity is represented in the linear scale to emphasize this fact (**Fig. II-6 & Fig. II-7**). The difference in σ , of *ca.* one order of magnitude, is evident for Li^+ concentrations of $\text{EO/Li} = 55$ and $\text{EO/Li} = 20$. However, the difference is much greater for higher concentrations of salt. It is also notable that the same EO/Li ratio is achieved at lower ionic content for the MEC-SIPE, in comparison to the SiP electrolyte. This is because the molecular mass of the lithium sulfonate end-group (SO_3^-Li^+) has a lower molecular mass ($88.0 \text{ g}\cdot\text{mol}^{-1}$) than LiTFSI ($287 \text{ g}\cdot\text{mol}^{-1}$). The result is that the MEC-SIPE has a higher density of Li^+ per mole of ionic species (*i.e.* salt).

The ionic conductivity of the MEC-SIPEs having different end-groups is presented for the same PEO chain lengths as for the model polymer $\text{mPEO}_n\text{-SO}_3\text{Li}$ ($\text{EO/Li} = 8, 10, 20$, and 55). The lower conductivity of $\text{mPEO}_{55}\text{OC(O)PhSO}_3\text{Li}$ ($\text{EO/Li} = 55$) in comparison to $\text{mPEO}_{55}\text{-SO}_3\text{Li}$ (**Fig. II-1**) is representative of the general performance of this EC-SIPE having different PEO chain lengths (**Fig. II-8**). The $\text{mPEO}_n\text{OC(O)PhSO}_3\text{Li}$ design has maximal σ of $2.2 \cdot 10^{-5} \text{ S}\cdot\text{cm}^{-1}$ at $100 \text{ }^\circ\text{C}$ ($\text{EO/Li} = 8$).

The ionic conductivity of $\text{mPEO}_n\text{-SO}_2\text{N(Li)Naph}$ is generally greater than that measured of $\text{mPEO}_n\text{-OC(O)PhSO}_3\text{Li}$, reaching *ca.* $1 \cdot 10^{-4} \text{ S}\cdot\text{cm}^{-1}$ at $100 \text{ }^\circ\text{C}$ for each of the MEC-SIPEs having $\text{EO/Li} = 8, 10$, and 20 (**Fig. II-9**). These two MEC-SIPEs, despite having very different functional end-groups, have similar mass fractions of end-groups. Their end-groups occupy maximally $\phi_{\text{m(salt)}} = 0.35$ for the shortest polymer chains presented ($\text{EO}_n = 8$). Although there is *ca.* one order of magnitude difference in the σ of these two MEC-SIPEs, the trend of σ as a function of $\phi_{\text{m(salt)}}$ follows a similar trend for both MEC-SIPEs (**Fig. II-10 & Fig. II-11**). Both polymers have maximal σ for $\text{EO/Li} = 20$, and higher σ for $\text{EO/Li} = 8$ than for $\text{EO/Li} = 10$.

The large difference between the ionic conductivities of the sulfonates of the MEC-SIPEs might be a result of the electron-withdrawing effect of the phenyl substituent of $\text{mPEO}_n\text{-OC(O)PhSO}_3\text{Li}$. The phenyl ester is an electron-withdrawing group (EWG) due to both resonance and inductive effects. The decrease in electron density at the lithium sulfonate of $\text{mPEO}_n\text{-OC(O)PhSO}_3\text{Li}$ arising from the EWG *ortho* to the lithium salt can decrease the dissociation of Li^+ from the end-group. This would increase the activation energy of the dissociation of the ion pair and impact the temperature dependent conductivity of the $\text{mPEO}_n\text{-OC(O)PhSO}_3\text{Li}$ end-group.

The $\text{mPEO}_n\text{-SO}_2\text{N(Li)Naph}$ is generally less conductive than the simple sulfonate end-capped $\text{mPEO}_n\text{-SO}_3\text{Li}$ and more conductive than the $\text{mPEO}_n\text{-OC(O)PhSO}_3\text{Li}$. The great difference in the functional end-group does not allow direct comparison of these three MEC-SIPEs. It is nevertheless demonstrated that $\text{mPEO}_n\text{-SO}_2\text{N(Li)Naph}$ has ionic conductivity (**Fig. II-11**) comparable to the model $\text{mPEO}_n\text{-SO}_3\text{Li}$ (**Fig. II-9**).

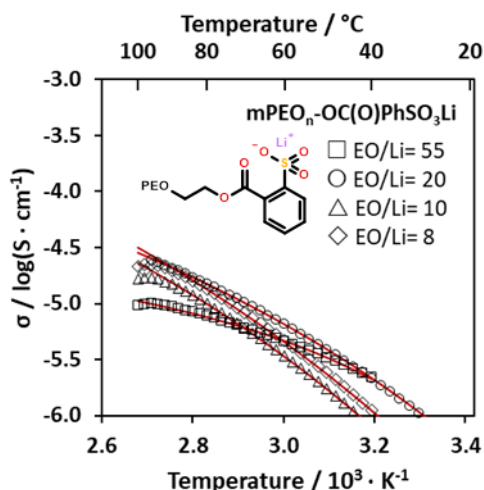


Figure II-8: The conductivity ($\sigma / \text{S} \cdot \text{cm}^{-1}$) as a function of Temperature ($T / 10^3 \cdot \text{K}^{-1}$) for $m\text{PEO}_n\text{OC(O)PhSO}_3\text{Li}$ having different EO/Li ratios. The EO/Li ratio is fixed according to the polymer DP_n (EO_n). The experimental data of EO/Li= 55 (\square), EO/Li= 20 (\circ) and EO/Li= 10 (\triangle) and EO/Li=8 (\diamond) were recorded on cooling from 100 °C. The data are fitted to the VTF model (red lines, -).

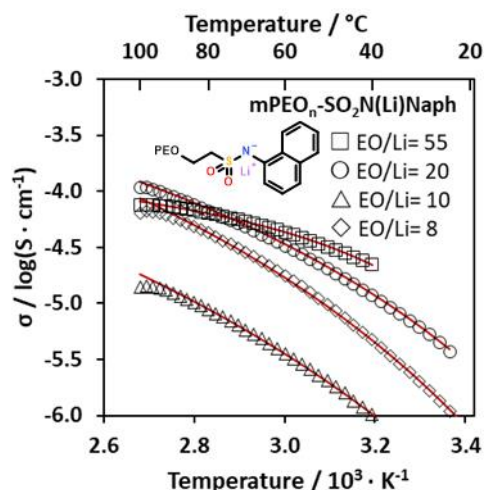


Figure II-9: The conductivity ($\sigma / \text{S} \cdot \text{cm}^{-1}$) as a function of Temperature ($T / 10^3 \cdot \text{K}^{-1}$) for $m\text{PEO}_n\text{-SO}_2\text{N(Li)Naph}$ having different EO/Li ratios. The EO/Li ratio is fixed according to the polymer DP_n (EO_n). The experimental data of EO/Li= 55 (\square), EO/Li= 20 (\circ) and EO/Li= 10 (\triangle) and EO/Li=8 (\diamond) were recorded on cooling from 100 °C. The data are fitted to the VTF model (red lines, -).

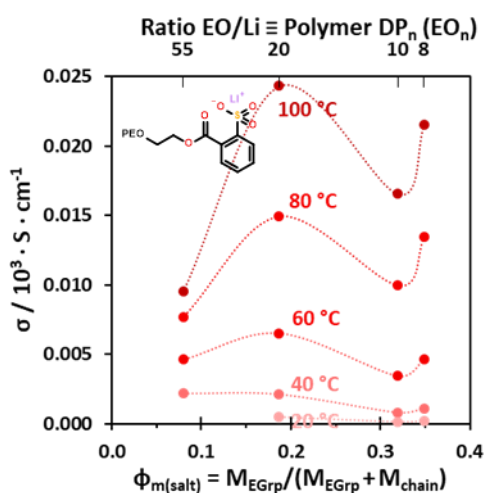


Figure II-10: σ ($\text{S} \cdot \text{cm}^{-1}$) of $m\text{PEO}_n\text{-OC(O)PhSO}_3\text{Li}$ as a function of the mass fraction (ϕ_m) of the polymer end-group. The corresponding ratio of EO/Li is also displayed. The lines (\cdots) are drawn as a guide for the eye only. The experimental data correspond to those displayed in Figure II-8.

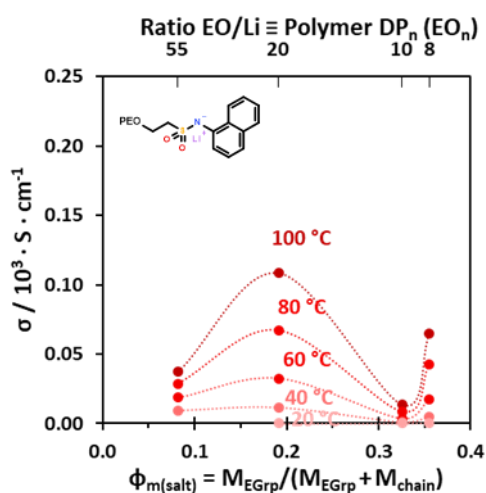


Figure II-11: σ ($\text{S} \cdot \text{cm}^{-1}$) of $m\text{PEO}_n\text{-SO}_2\text{N(Li)Naph}$ as a function of the mass fraction (ϕ_m) of the polymer end-group. The corresponding ratio of EO/Li is also displayed. The lines (\cdots) are drawn as a guide for the eye only. The experimental data correspond to those displayed in Figure II-9.

The MEC-SIPEs having lithiated secondary amines have higher ionic conductivity than the sulfonates and the sulfonamide. The mPEO_n-N(Li)Naph EC-SIPEs with EO/Li= 55, 20, and 8 all reach $1 \cdot 10^{-4} \text{ S.cm}^{-1}$ at 100 °C (**Fig. II-12**). The mPEO₁₀-N(Li)Naph (EO/Li= 10) has σ one order of magnitude higher than the polymers having the same end-group but different EO_n. Whereas mPEO₈-N(Li)Naph has $\sigma = 8.5 \cdot 10^{-5} \text{ S.cm}^{-1}$ at 100°C, mPEO₁₀-N(Li)Naph has $\sigma = 8.7 \cdot 10^{-4} \text{ S.cm}^{-1}$ at 100°C (**Fig. II-12**). This large difference is unexpected. We are left to tentatively propose that it might be the result of specific end-group interactions facilitated by the thermal behaviour of a PEO₁₀ chain. The specific dependence of σ on PEO chain length of mPEO_n-N(Li)Naph highlights that the relationship between chain dynamics and the functional end-group chemistry is neither straightforward nor trivial. In this case, high ionic conductivity is increased or decreased by one order of magnitude in correlation with a difference of a small number of EO units.

Replacing the naphthalene ring with a pyrene one dramatically changes the temperature dependence of ionic conductivity of the MEC-SIPEs bearing aryl amine end-groups. All of the mPEO_n-N(Li)Pyr EC-SIPEs exceed $1 \cdot 10^{-4} \text{ S.cm}^{-1}$ above 60 °C (**Fig. II-13**). The larger aryl ring function of mPEO_n-N(Li)Pyr is illustrated by the shift in the $\phi_{m(\text{salt})}$ (**Fig. II-15**) in comparison to mPEO_n-N(Li)Naph (**Fig. II-14**). The dependence of σ on $\phi_{m(\text{salt})}$ for mPEO_n-N(Li)Pyr (**Fig. II-15**) follows the same trend as for the sulfonates and the sulfonamide, having maximal σ for EO/Li= 20 and higher σ for EO/Li= 8 than for EO/Li= 10.

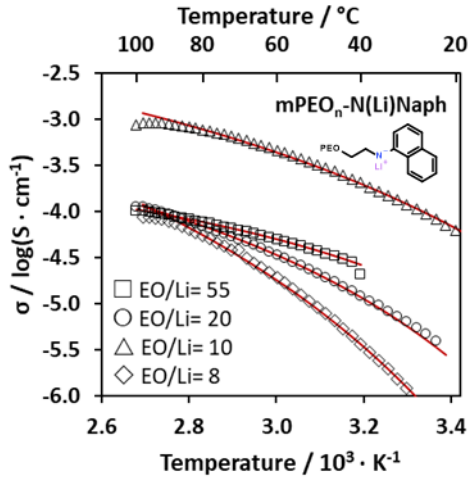


Figure II-12: The conductivity ($\sigma / S \cdot \text{cm}^{-1}$) as a function of Temperature ($T / 10^3 \cdot \text{K}^{-1}$) for $m\text{PEO}_n\text{N}(\text{Li})\text{Naph}$ having different EO/Li ratios. The EO/Li ratio is fixed according to the polymer DP_n (EO_n). The experimental data of EO/Li= 55 (\square), EO/Li= 20 (\circ) and EO/Li= 10 (\triangle) and EO/Li=8 (\diamond) were recorded on cooling from 100 °C. The data are fitted to the VTF model (red lines, -).

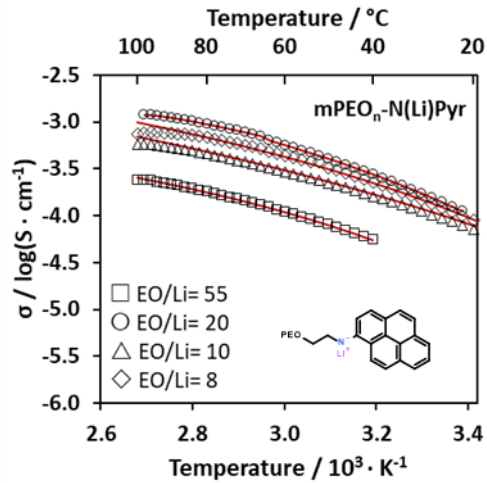


Figure II-13: The conductivity ($\sigma / S \cdot \text{cm}^{-1}$) as a function of Temperature ($T / 10^3 \cdot \text{K}^{-1}$) for $m\text{PEO}_n\text{N}(\text{Li})\text{Pyr}$ having different EO/Li ratios. The EO/Li ratio is fixed according to the polymer DP_n (EO_n). The experimental data of EO/Li= 55 (\square), EO/Li= 20 (\circ) and EO/Li= 10 (\triangle) and EO/Li=8 (\diamond) were recorded on cooling from 100 °C. The data are fitted to the VTF model (red lines, -).

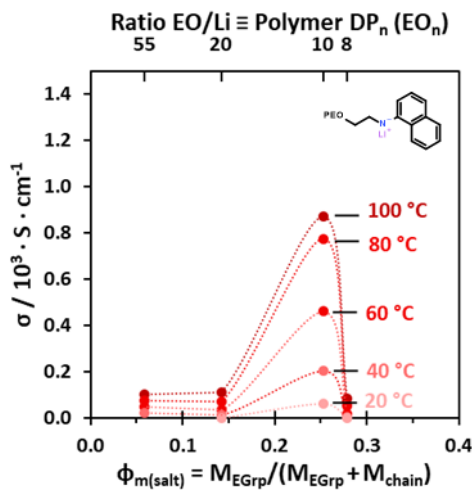


Figure II-14: σ ($S \cdot \text{cm}^{-1}$) of $m\text{PEO}_n\text{N}(\text{Li})\text{Naph}$ as a function of the mass fraction (ϕ_m) of the polymer end-group. The corresponding ratio of EO/Li is also displayed. The lines (\cdots) are drawn as a guide for the eye only. The experimental data correspond to those displayed in Figure II-12.

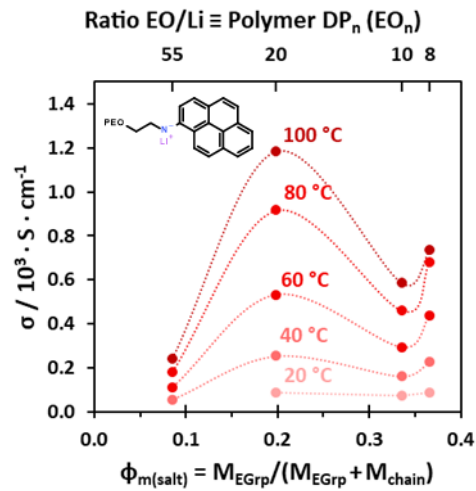


Figure II-15: σ ($S \cdot \text{cm}^{-1}$) of $m\text{PEO}_n\text{N}(\text{Li})\text{Pyr}$ as a function of the mass fraction (ϕ_m) of the polymer end-group. The corresponding ratio of EO/Li is also displayed. The lines (\cdots) are drawn as a guide for the eye only. The experimental data correspond to those displayed in Figure II-13.

The MEC-SIPes $m\text{PEO}_n\text{-SO}_2\text{N}(\text{Li})\text{Naph}$ and $m\text{PEO}_n\text{-N}(\text{Li})\text{Naph}$ have a weaker dependence of σ on the polymer chain length (EO_n) compared to the model polymer $m\text{PEO}_n\text{-SO}_3\text{Li}$. The $m\text{PEO}_n\text{-SO}_2\text{N}(\text{Li})\text{Naph}$ (Fig. II-9) and $m\text{PEO}_n\text{-N}(\text{Li})\text{Naph}$ (Fig. II-12) have conductivity close to $1 \cdot 10^{-4} S \cdot \text{cm}^{-1}$ at 100 °C, regardless of the EO/Li ratio. However, there is a larger variation of maximum σ for $m\text{PEO}_n\text{-SO}_3\text{Li}$ (Fig. II-5). This might be related to the association of polymer end-groups, which persists in the case of the MEC-SIPes having naphthalene groups, even when the end groups are effectively diluted by elongation of the polymer chains.

The naphthalene structural motif is elaborated in the form of the "double salt" $m\text{PEO}_{55}\text{-SANSI}(\text{Li}_2)$, however the resultant ionic conduction (at EO/Li= 27, $\phi_{m(\text{Li})} = 0.005$) of this polymer (Fig. II-3) did not greatly exceed that of $m\text{PEO}_{55}\text{-SO}_2\text{N}(\text{Li})\text{Naph}$ (at EO/Li =55, $\phi_{m(\text{Li})} = 0.003$) despite having a

higher apparent concentration of Li^+ and lower EO/Li ratio (**Table II-1**). This suggests that ionic conductivities of these EC-SIPEs are first limited by the PEO chain length and molecular dynamics rather than the concentration of lithium.

With variation of the PEO chain length, the best results in terms of ionic conductivity are generally reached for EC-SIPEs having EO/Li= 20. Outliers are the high σ of mPEO₁₀-N(Li)Naph (EO/Li= 10) and the uniformly superior σ of mPEO_n-N(Li)Pyr. The naphthalene synthon was further elaborated to enable systematic comparison of the polymers featuring naphthalene rings. The polymer mPEO₅₅-SANSI(Li₂) (EO/Li= 23) is comparable to the class based on PEO₂₀ (EO/Li= 20) if one considers the difference in Li^+ concentration to be small (**Fig. II-16**).

The attempt was made with mPEO₅₅-SANSI(Li₂) to increase σ by increasing the concentration of Li^+ at the end-group. The design of the end-group uses two different anionic functions: **i**) the sulfonamide [$-\text{SO}_2\text{N}^-(\text{Li}^+)-$] and **ii**) the bis-sulfonylimide [$-\text{SO}_2\text{N}^-(\text{Li}^+)\text{SO}_2-$]. The MEC-SIPE mPEO₂₀- \blacklozenge NSI(Li) was created using part of the protocol developed for the SANSI end-group. The naphthalene ring is connected to the PEO chain by a 1,2,3-triazole ring. The anionic function is the bis-sulfonylimide. The 1,2,3-triazole is electronically neutral and is not directly lithiated during the synthesis of the EC-SIPE. Subsequent quaternisation of the EC-SIPE to yields the zwitterionic mPEO₂₀- \blacklozenge^+ NSI(LiTFSI).

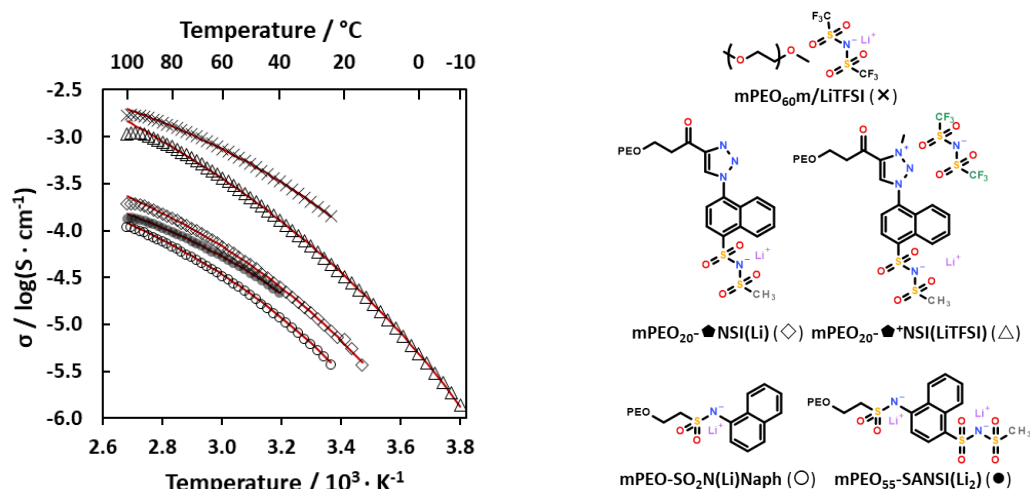


Figure II-16: The conductivities ($\sigma / \text{S} \cdot \text{cm}^{-1}$) of mPEO₂₀-SO₂N(Li)Naph (O), mPEO₅₅-SANSI(Li₂) (●), mPEO₂₀- \blacklozenge NSI(Li) (◇), mPEO₂₀- \blacklozenge^+ NSI(LiTFSI) (△) and the SiP electrolyte mPEO_{60m}/LiTFSI (EO/Li= 20) (X) as functions of reciprocal temperature ($T / 10^3 \cdot \text{K}^{-1}$). The data are fitted to the VTF model (red lines, -).

The ionic conductivity of mPEO₂₀- \blacklozenge NSI(Li) has a dependence on reciprocal temperature that has a similar shape to mPEO₂₀-SO₂N(Li)Naph but at higher values (**Fig. 16**). The σ of the double salt mPEO₅₅-SANSI(Li₂) (EO/Li= 23) lies between the σ of these mono-salts (EO/Li= 20). The mPEO₂₀- \blacklozenge NSI(Li) remains ionically conductive with good wetting of the electrode surface at 18 $^{\circ}\text{C}$, the lowest temperature accessible by these MEC-SIPEs having EO_n \geq 20 and only Li^+ counterions. Quaternisation of mPEO₂₀- \blacklozenge NSI(Li) yields mPEO₂₀- \blacklozenge^+ NSI(LiTFSI). The quaternized MEC-SIPE has two mobile counterions: Li^+ and TFSI⁻. This MEC-SIPE has the highest σ of the MEC-SIPEs based on sulfonamide and sulfonylimide anionic functions. It has σ comparable to the best performing mono-salt MEC-SIPEs: the mPEO_n-N(Li)Pyr group (EO_n= 8, 10, and 20), and the exceptional mPEO₁₀-N(Li)Naph (EO/Li= 10). The increase in conductivity of the zwitterionic MEC-SIPE is correlated to the addition of a second mobile species. The TFSI⁻ anion contributes to the transfer of charge

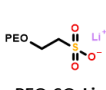
between the electrodes. Whereas the mPEO₂₀- \blacklozenge NSI(Li) mono-salt MEC-SIPE is ionically conductive down to 18 °C, the zwitterionic mPEO₂₀- \blacklozenge^* NSI(LiTFSI) maintains measurable ionic conductivity down to -10 °C (**Fig. 16**). Direct comparison of these two MEC-SIPEs allows the conclusion that low temperature conductivity is afforded by the plasticizing effect of the TFSI⁻ anion. This is the lowest temperature accessed by any of the MEC-SIPEs having EO_n= 20. The MEC-SIPEs having shorter PEO chains (PEO₈ and PEO₁₀) also have ionic conductivity at sub-ambient temperatures. Low temperature ionic conductivity will be discussed in **Section 4**.

2.1.4. Conclusions on Ionic Conductivity of MEC-SIPes

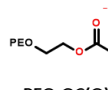
The ionic conductivities (σ) of MEC-SIPes are compared according to the identity of the end-group and the length of the PEO chain. These values are compared to SiP blends of mPEO₆₀m/LiTFSI having EO/Li ratios of 10, 20, and 60. Whereas σ increases with salt concentration for the model SiP electrolytes, it is optimised at intermediate EO/Li ratios in MEC-SIPes. The optimum for MEC-SIPes based on PEO chains appears to be close to EO_n= 20. The σ of selected MEC-SIPes are summarised below (**Table II-2**).

Table II-2: Table of summarised ionic conductivity ($\sigma / \text{S.cm}^{-1}$) and corresponding lithium transference number (LTN) of selected MEC-SIPes (for transference of Lithium, see Section 2.3). The LTN was calculated using the Bruce-Vincent method. The σ_{AC} was measured using blocking (gold) electrodes. These data are illustrated above (Section 2.1.3). The two LTNs are the chronoamperometric (t_{Li}^*) and corrected (t_{Li}^*) values. The data of the SiP electrolyte mPEO₆₀m/LiTFSI (EO/Li= 20) are listed for comparison.

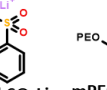
Polymer Electrolyte MEC-SIPE			$\sigma_{AC} (\text{S.cm}^{-1})$					LTN	
#	Polymer	End-Group	20 °C	40 °C	60 °C	80 °C	100 °C	t_{Li}^*	t_{Li}^*
1	mPEO ₂₀ -	SO ₃ Li	5.1*10 ⁻⁶	2.1*10 ⁻⁵	5.8*10 ⁻⁵	1.2*10 ⁻⁴	1.6*10 ⁻⁴	0.65	0.76
2		OC(O)PhSO ₃ Li	4.5*10 ⁻⁷	2.1*10 ⁻⁶	6.5*10 ⁻⁶	1.5*10 ⁻⁵	2.4*10 ⁻⁵	1.10	1.03
3		SO ₂ N(Li)Naph	2.4*10 ⁻⁸	1.2*10 ⁻⁵	3.2*10 ⁻⁵	6.7*10 ⁻⁵	1.1*10 ⁻⁴	0.73	0.91
4		N(Li)Naph	2.5*10 ⁻⁸	1.2*10 ⁻⁵	3.4*10 ⁻⁵	7.0*10 ⁻⁵	1.1*10 ⁻⁴	0.82	0.85
5		N(Li)Pyr	8.9*10⁻⁵	2.5*10⁻⁴	5.3*10⁻⁴	9.1*10⁻⁴	1.2*10⁻³	0.70	0.83
6		●NSI(Li)	6.9*10 ⁻⁶	2.5*10 ⁻⁵	6.8*10 ⁻⁵	1.4*10 ⁻⁴	1.9*10 ⁻⁴	-	-
7		● ⁺ NSI(LiTFSI)	3.2*10⁻⁵	1.3*10⁻⁴	3.7*10⁻⁴	7.8*10⁻⁴	1.1*10⁻³	0.82	1.00
8	mPEO ₅₅ -	SANSI(Li ₂)		2.2*10 ⁻⁵	5.3*10 ⁻⁵	9.7*10 ⁻⁵	1.3*10 ⁻⁴	0.98	0.95
<i>Salt-in-Polymer (SiP) Blend</i>									
9	mPEO ₆₀ m/LiTFSI	(EO/Li= 20)		3.3*10⁻⁴	7.4*10⁻⁴	1.3*10⁻³	1.7*10⁻³	0.25	-



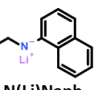
mPEO-SO₃Li



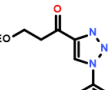
mPEO-OC(O)PhSO₃Li



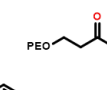
mPEO-N(Li)Naph




mPEO-SO₂N(Li)Naph




mPEO-N(Li)Pyr



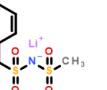
mPEO₂₀-●NSI(Li)



mPEO₂₀-●⁺NSI(LiTFSI)



mPEO₅₅-SANSI(Li₂)



mPEO₆₀m/LiTFSI

The conductivities of mPEO_n-SO₃Li and mPEO_n-OC(O)PhSO₃Li agree well with those reported by H. Ohno and co-workers, from whose work the synthesis protocol was adapted.^[8,9] The mPEO_n-SO₃Li has σ of *ca.* one order of magnitude lower than the model SiP electrolyte. The mPEO_n-SO₂N(Li)Naph has similar performance. This is encouraging in terms of end-group design because the end-group has very different chemistry. The mPEO_n-N(Li)Naph also has similar performance but the mPEO_n-N(Li)Pyr design has the highest σ for all chain lengths of PEO relative to MEC-SIPes having only Li⁺ as the counterion. The "double-salt" mPEO₅₅-SANSI(Li₂) has similar performance to mPEO₅₅-N(Li)Pyr. These MEC-SIPes having EO_n= 55 have σ similar to EC-SIPes having EO_n= 20, which illustrates the scope for end-group design to determine σ relative to end-group concentration.

MEC-SIPes having EO_n= 20 generally had the highest ionic conductivities. These MEC-SIPes tend to flow at room temperature, allowing easy manipulation of small quantities for the fabrication of coin cells. These properties together enable the characterisation of the electrochemical stability

(Section 2.2) and lithium transference (Section 2.3) of MEC-SIPs having different functional end-groups at constant PEO chain length while keeping the ratio EO/Li= 20.

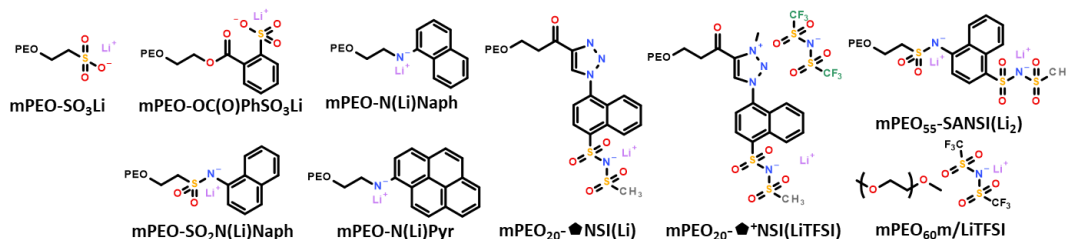
2.2. Electrochemical Stability of MEC-SIPs

2.2.1. Water Content of MEC-SIPs

The MEC-SIPs were dried in a vacuum oven (< 10 mbar, 70 °C, > 24 h) prior to assembly of coin cells. The water content of the EC-SIPs was calculated using the Karl Fischer titration method.^[10] The results are summarised below (**Table II-3**). The MEC-SIPs have *ca.* one to two molecules of water for every ten ionic end-groups. This corresponds to a range of 160-2900 ppm. There is no clear correlation between the mass fraction of the end-group and the water content of the MEC-SIP. The *N*-aryl amines (**Table II-3**; 4 and 5) have lower water content than mPEO₂₀-SO₂N(Li)Naph, suggesting that the secondary amines are more effectively dried under the applied conditions. The zwitterionic mPEO₂₀- \blacklozenge^+ NSI(LiTFSI) (**7**) has lower water content than its precursor (**6**). This might be related to the displacement of water at the triazole by TFSI⁻ at the triazolium. Of the EC-SIPs, the mPEO₂₀-N(Li)Pyr (**5**), mPEO₂₀- \blacklozenge^+ NSI(LiTFSI) (**7**), and mPEO₅₅-SANSI(Li₂) (**8**) have the lowest water content and also the highest ionic conductivity. Only mPEO₂₀- \blacklozenge^+ NSI(LiTFSI) (**7**) has water content close to that of the model SiP blend (**9**).

Table II-3: Table of the water concentration [H₂O] of MEC-SIPs having different end-groups and EO_n= 20 (except **8**, EO_n= 55). The [H₂O] is listed as (i) number of moles of water per mole of ionic end-groups (mol/mol), and (ii) parts per million (ppm; μg/g). The σ_{AC} (S.cm⁻¹) and lithium transference number (LTN, see Section 2.3) is listed for reference. The two LTNs are the chronoamperometric (t_{Li}^+) and corrected (t_{Li}^{+*}) values. The data of the SiP electrolyte mPEO₆₀m/LiTFSI (EO/Li= 20) are listed for comparison.

Polymer Electrolyte MEC-SIPE		σ_{AC} (S.cm ⁻¹)	LTN		[H ₂ O]		End-Group	
#	Polymer	40 °C	t_{Li}^+	t_{Li}^{+*}	mol/mol	ppm	g.mol ⁻¹	$\phi_{m(EGrp)}$
1	mPEO ₂₀ -SO ₃ Li	2.1*10 ⁻⁵	0.65	0.76	0.11	2075	87	0.09
2	OC(O)PhSO ₃ Li	2.1*10 ⁻⁶	1.10	1.03	0.11	1748	207	0.19
3	SO ₂ N(Li)Naph	1.2*10 ⁻⁵	0.73	0.91	0.18	2898	213	0.19
4	N(Li)Naph	1.2*10 ⁻⁵	0.82	0.85	0.14	2380	148	0.14
5	N(Li)Pyr	2.5*10⁻⁴	0.70	0.83	0.08	1230	223	0.20
6	\blacklozenge^+ NSI(Li)	2.5*10 ⁻⁵	-	-	0.14	1900	401	0.31
7	\blacklozenge^+ NSI(LiTFSI)	1.3*10⁻⁴	0.82	1.00	0.01	160	696	0.44
8	mPEO ₅₅ -SANSI(Li ₂)	2.2*10 ⁻⁵	0.98	0.95	0.05	715	377	0.14
<i>Salt-in-Polymer (SiP) Blend</i>							LiTFSI	
9	mPEO₆₀m/LiTFSI (EO/Li= 20)	3.3*10⁻⁴	0.25	-	0.03	130	g.mol ⁻¹ 287	$\phi_{m(salt)}$ 0.25



These MEC-SIPs were dried under the same protocol but vary in water content. The adventitious water will react on contact with lithium metal. The formed lithium hydroxide passivates the lithium electrode surface and decreases the charge transferred across the electrode-electrolyte interface during electrochemical methods. LiOH is highly corrosive and can degrade most of the

battery components on contact. Moreover, water is able to have dipole interactions with ionic centres. This improves the dissociation of Li^+ from the covalently bound anions of the MEC-SIPes. The increased dissociation of Li^+ would increase the ionic conductivity of the MEC-SIPE.

2.2.2. Cyclic Voltammetry

The electrochemical stability of the MEC-SIPes based on PEO are inherently limited by the electrochemical stability of the PEO chain, which is stable up to *ca.* $E \approx +4.0$ V vs. Li/Li^+ against active electrodes but can reach $+5.0$ V vs. Li/Li^+ in asymmetric $\text{Li}|\text{stainless steel}$ cells. The **Electrochemical Stability Window (ESW)** can be further dependent on the polymer functional end-groups.

Cyclic voltammetry (CV) was conducted using lithium metal anodes and stainless-steel cathodes, in coin cells of an asymmetric $\text{Li}|\text{MEC-SIPE}|\text{Stainless Steel}$ configuration. The temperature was set to 40 °C for the MEC-SIPes having $\text{EO}_n = 20$ and to 60 °C for the $\text{mPEO}_{55}\text{-SANSI}(\text{Li}_2)$ "double salt" having $\text{EO}_n = 55$. The potential sweep rate was $1.0 \text{ mV}\cdot\text{s}^{-1}$ with measurement of the current at 1 s intervals. Separate cells were used to probe cathodic (reduction) and anodic (oxidation) stability of the MEC-SIPes. All the coin cells were equilibrated for 4 h at 40 °C prior to launching the measurement. These results were benchmarked against $\text{mPEO}_{60}\text{m}/\text{LiTFSI}$ having a molar ratio of $\text{EO}/\text{Li} = 20$. The results are presented below, in voltammograms displaying the current density j ($\mu\text{A}\cdot\text{cm}^{-2}$) as a function of potential (V vs Li/Li^+). The electrolytes were cycled from the open circuit to a maximum potential difference. The potential limit was increased by incremental steps of 0.2 V. The last potential sweep measured in each of oxidation and reduction is displayed for the electrolytes to illustrate the limit of electrochemical stability (the ESW). The potential is measured directly from the coin cell, without an external (calibrated) reference electrode. The cell potential is quoted relative to the Li/Li^+ redox couple of the anode (-3.04 V vs. **Standard Hydrogen Electrode [SHE]**). The potential relative to the SHE is calculated and displayed as a secondary horizontal axis for reference only.

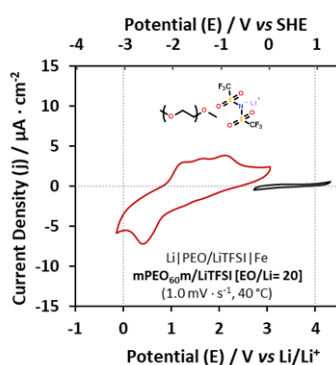


Figure II-17: CV of $\text{mPEO}_{60}\text{m}/\text{LiTFSI}$ ($\text{EO}/\text{Li} = 20$)

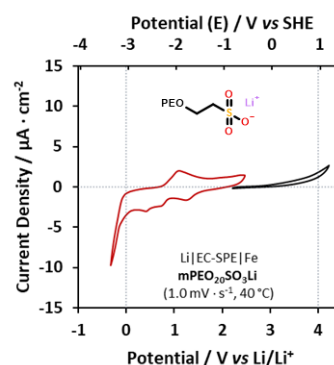


Figure II-18: CV of $\text{mPEO}_{20}\text{-SO}_3\text{Li}$

The electrochemical stability of the presented MEC-SIPes is benchmarked against that of the model SiP electrolyte $\text{mPEO}_{60}\text{m}/\text{LiTFSI}$ ($\text{EO}/\text{Li} = 20$). The SiP electrolyte is stable beyond 4.0 V vs Li/Li^+ in oxidation and reaches 0 V vs. Li/Li^+ in reduction mode (**Fig. II-17**). Some electrochemical processes are visible in reduction mode but these do not prevent cycling of the electrolyte down to 0 V vs. Li/Li^+ . Sweeping the potential down to 0 V vs. Li/Li^+ suggested that the electrolyte was sufficiently stable to permit stripping and plating of lithium metal. The $\text{mPEO}_{20}\text{-SO}_3\text{Li}$ was similarly stable in the potential range of $0.0 - 4.0$ V vs. Li/Li^+ . Redox processes are also visible for $\text{mPEO}_{20}\text{-SO}_3\text{Li}$ in reduction mode.

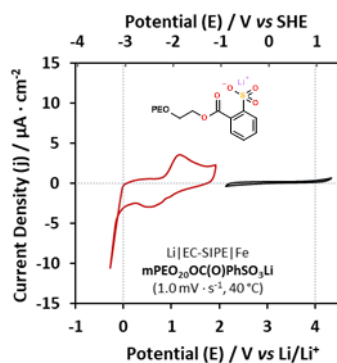


Figure II-19: CV of mPEO₂₀-OC(O)PhSO₃Li

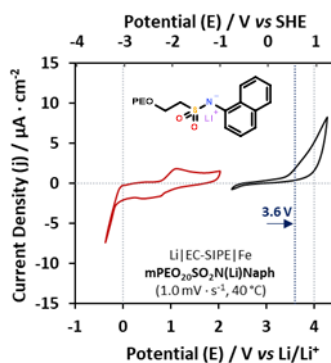


Figure II-20: CV of mPEO₂₀-SO₂N(Li)Naph

The MEC-SIPE mPEO₂₀-OC(O)PhSO₃Li (**Fig. II-19**) has the same ESW as mPEO₂₀-SO₃Li (**Fig. II-18**). However, mPEO₂₀-SO₂N(Li)Naph has an irreversible process on oxidation (**Fig. II-20**). CV of mPEO₂₀-SO₂N(Li)Naph suggests that the limiting potential in oxidation is of ca. 3.6 V vs. Li/Li⁺. However, this MEC-SIPE remains sufficiently electrochemically inert to enable the plating of the stainless-steel electrode surface in reduction mode at potentials lower than 0 V vs. Li/Li⁺. The sulfonate (**Fig. II-19**) and the sulfonamide (**Fig. II-20**) exhibit similar redox peak potentials in reduction mode.

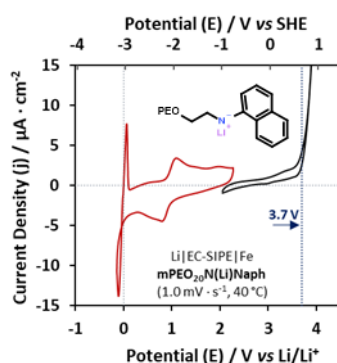


Figure II-21: CV of mPEO₂₀-N(Li)Naph

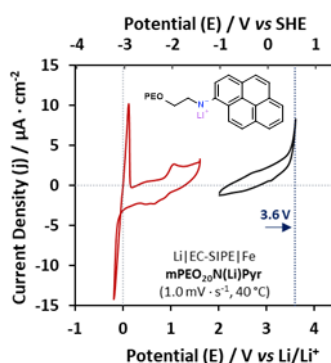


Figure II-22: CV of mPEO₂₀-N(Li)Pyr

The MEC-SIPEs having aromatic amines exhibit similar electrochemical behaviour in CV. The plating and stripping of lithium metal is observed in the CV of both mPEO₂₀-N(Li)Naph (**Fig. II-21**) and mPEO₂₀-N(Li)Pyr (**Fig. II-22**) in reduction mode. These MEC-SIPEs moreover have peak potentials for redox processes in reduction mode that are similar to those observed for mPEO₂₀-OC(O)PhSO₃Li (**Fig. II-19**) and mPEO₂₀-SO₂N(Li)Naph (**Fig. II-20**). These MEC-SIPEs have different anionic end-groups and yet exhibit the same redox behaviours observed as a local minimum and a local maximum in reduction mode. This suggests that the observed current has an origin that is common to all of the polymer electrolytes. The electrolytes all contain adventitious water that was not removed by drying and trapped during the fabrication of the coin cells. The electrochemical potential of the hydrolysis of water ($E^0 = -1.23$ V vs. SHE $\equiv 1.81$ V vs Li/Li⁺) is higher than the redox couple observed during CV of the polymer electrolytes.^[5] However this standard potential (E^0) would decrease at elevated temperature and depend on the concentration of the reacting species, following the Nernst equation (**Eqn. II-12**).^[3] The reaction is moreover under kinetic control defined by the potential sweep rate, the solubility of water in the electrolyte, and the concentration of water.

Equation II-12: The Nernst equation for electrochemical potential, where R is the ideal gas constant ($8.314 \text{ V.C.K}^{-1} \cdot \text{mol}^{-1}$), n is the number of stoichiometric electrons in the balanced redox equation, F is Faraday's constant ($96485 \text{ C.mol}^{-1} \cdot e^{-1}$) and Q is the reaction quotient.

$$E = E^0 - \frac{RT}{nF} \cdot \ln(Q)$$

One possible explanation for the additional peaks observed in reduction mode (Fig. II-17 – II-22) is the redox processes of oxides at the surface of the stainless-steel cathode. This hypothesis could be tested by repeating the CV protocols using a copper cathode. Disappearance of the peaks in $\text{Li}|\text{MEC-SIPE}|\text{Cu}$ cells would confirm this claim.

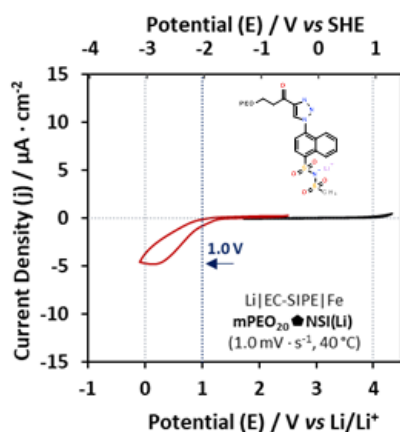


Figure II-23: CV of $\text{mPEO}_{20}\text{-NSI(Li)}$

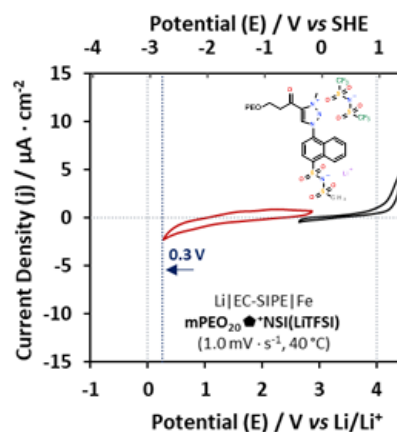


Figure II-24: CV of $\text{mPEO}_{20}\text{-NSI(LiTFSI)}$

Although $\text{mPEO}_{20}\text{-NSI(Li)}$ is stable up to 4.0 V vs. Li/Li^+ , it is not stable in reduction to potentials below 1.0 V vs. Li/Li^+ (Fig. II-23). Quaternisation of this MEC-SIPE yielded the zwitterionic polymer electrolyte $\text{mPEO}_{20}\text{-NSI(LiTFSI)}$, which has an ESW of 0.3-4.0 V vs. Li/Li^+ (Fig. 24). The improved stability on reduction is a direct result of the chemical modification of the end-group. Potential sweeps to below 0.3 V vs. Li/Li^+ were not performed on this MEC-SIPE. The $\text{mPEO}_{55}\text{-SANSI(Li}_2\text{)}$ has a longer PEO chain ($\text{EO}_n = 55$) but a similar mass fraction of end-groups ($\phi_{\text{m(EGrp)}} = 0.14$). It appears to have and ESW of 0-3.8 V vs. Li/Li^+ (Fig. II-25).

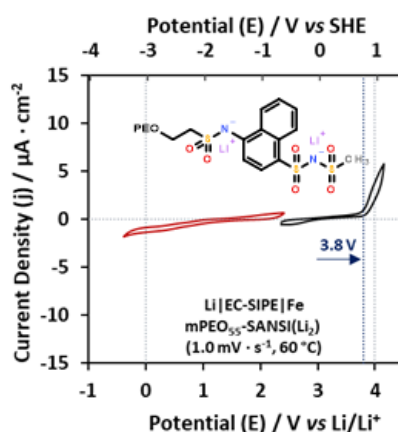


Figure II-25: CV of $\text{mPEO}_{55}\text{-SANSI(Li}_2\text{)}$

2.2.3. Galvanostatic Cycling

Stripping and plating of lithium by the *N*-Aryl functional EC-SIPes mPEO₂₀-N(Li)Naph and mPEO₂₀-N(Li)Pyr was demonstrated by CV (**Fig. II-21** & **Fig. II-22**). However, the other MEC-SIPes did not strip and plate lithium metal under the same conditions. The transfer of lithium metal was tested further by galvanostatic cycling with potential limitation (GCPL) at 40 °C. The limit of potential was set to 4.5 V vs. Li/Li⁺ in symmetric Li|MEC-SIPE|Li coin cells. The current was fixed to 10 μA.cm⁻² and applied for 4 h in each direction. The polymer electrolytes were cycled by alternating the polarity a symmetrical Li|MEC-SIPE|Li cell. The first charge is named "forward" and the next charge in the opposite cell polarity is "reverse", and so on. A sequence of one forward and one reverse charge constitutes one cycle. Five cycles were measured of each MEC-SIPE. A cycle constitutes a forward and a reverse flow of Li⁺ over a total of 8 h. The applied current of 10 μA.cm⁻² is an order of magnitude lower than commonly used during charge and discharge of commercial batteries. These experiments do not represent real-world operating parameters of batteries but do probe the electrochemical stability of the MEC-SIPes.

The amount of lithium transferred was calculated from the integral of the current over one period of four hours (one period having one direction of current flow). All of the cells had an electrode surface area of 1.131 cm² (radius= 0.3 cm). A constant current of 11.31 μA (10 μA.cm⁻²) was applied for 4 h and constituted a total charge transfer of Q= 0.16 C (A.s). Division by Faraday's constant (96,485 C.mol⁻¹) yields the number of transferred electrons $n_e = 1.68 \cdot 10^{-3}$ mol. Assuming that 1 e⁻ corresponds to one redox couple equal to the transfer of one lithium ion [Li⁺ + e⁻ \rightleftharpoons Li⁰], n_e is equal to the moles of lithium transferred in 4 h. The density of the lithium metal electrode is 0.534 g.cm⁻³, so the charge transferred corresponds to a hypothetical disc of 1.68*10⁻³ moles of lithium, a diameter of 1.6 mm (the standard for a coin cell) and a thickness of 108 nm. Accordingly, for the radius of the electrodes used in this report (d= 0.6 cm), a theoretical disc of lithium metal having a thickness of 774 nm was transferred. This is equal to around 0.9-1.5 % of the thickness of the electrolyte (50-80 μm).

The resistivity of the electrolytes was calculated according to the relation $U=R \cdot I$ and the electrode surface area, then plotted as a function of the transferred charge. The only difference among the MEC-SIPes being the end-group chemistry, classification of the polymer electrolytes according to the evolution of their resistivity can be considered as a first approximation of the electrochemical stability of the functional end-groups.

The MEC-SIPEs are divided into the following five categories (A-E):

A. MEC-SIPEs have constant resistivity as a function of transferred charge.

End-group: -OC(O)PhSO₃Li (Fig. II-25), -N(Li)Naph (Fig. II-26), -N(Li)Pyr (Fig. II-27).

The plot is in the form of a horizontal line for each galvanostatic period (4 h). Some deviation from the maximum theoretical charge ($Q = 0.16$ C) is a result of the short time of a few seconds required for inversion of cell polarity. This is observed as a difference in the maximum Q of the forward and reverse charge periods.

Fig. II-26→II-28: (Top) The resistivity ($\rho / 10^{-3} \cdot \Omega \cdot m$) as a function of charge (Q) during galvanostatic cycling of the MEC-SIPEs mPEO₂₀-OC(O)PhSO₃Li (Fig. II-26), mPEO₂₀-N(Li)Naph (Fig. II-27), and mPEO₂₀-N(Li)Pyr (Fig. II-28). The first five cycles are shown. The arrows (\rightarrow) indicate the evolution of ρ upon cycling. (Bottom) The GEIS spectra of the same samples measured before (\circ) and after (\diamond) GCPL. The data are fitted to an equivalent circuit (black lines, -).

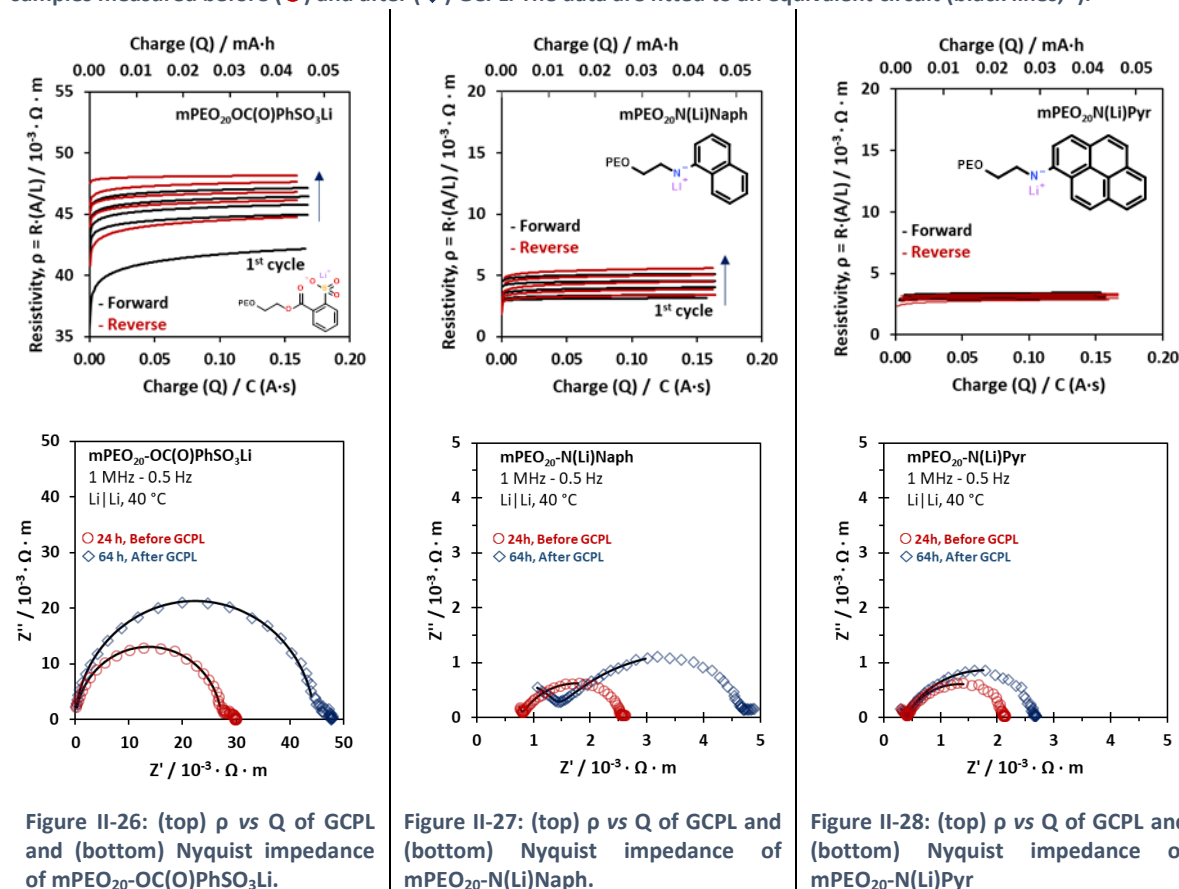


Figure II-26: (top) ρ vs Q of GCPL and (bottom) Nyquist impedance of mPEO₂₀-OC(O)PhSO₃Li.

Figure II-27: (top) ρ vs Q of GCPL and (bottom) Nyquist impedance of mPEO₂₀-N(Li)Naph.

Figure II-28: (top) ρ vs Q of GCPL and (bottom) Nyquist impedance of mPEO₂₀-N(Li)Pyr

Galvanostatic Electrochemical Impedance Spectroscopy (GEIS) of these same samples, measured before and after GCPL, reveal different behaviours of the EC-SIPEs. These data together yield the following observations of resistivity under GCPL:

- I. The mPEO₂₀-OC(O)PhSO₃Li has slightly lower resistivity (ρ) on the first cycle (Fig. II-26). Successive cycling of mPEO₂₀-OC(O)PhSO₃Li reveals constant resistivity for each charge period, with evolution of the resistivity upon cycling. The resistivity of the bulk mPEO₂₀-OC(O)PhSO₃Li electrolyte is high and increases by 60 % as a result of GCPL (Fig. II-26). The evolution of ρ reveals that this EC-SIPE is not stable during GCPL.
- II. The mPEO₂₀-N(Li)Naph has higher ionic conductivity (Fig. II-12) and so its lower resistivity is expected (Fig. II-27). The evolution of ρ upon cycling is less than that observed for

mPEO₂₀-OC(O)PhSO₃Li. However, the cell resistivity increases by 100 % of the value measured by GEIS before the first cycle. The GEIS of mPEO₂₀-N(Li)Naph reveals evolution of the resistivities both the electrolyte and the electrode-electrolyte interface. This implies **i)** that this MEC-SIPE is unstable on contact with Lithium metal, and **ii)** that adverse reactions occur within the bulk of the EC-SIPE.

- III.** The mPEO₂₀-N(Li)Pyr has the lowest ρ , which increases by 25 % after cycling (**Fig. II-28**). The bulk resistivity of this MEC-SIPE remains the same before and after GCPL. The evolution in cell resistivity is attributed to instability of the electrode-electrolyte interface.

The order of decreasing gross evolution of ρ follows the order of decreasing water content (mol/mol) of the EC-SIPEs:

$$mPEO_{20}\text{-OC(O)PhSO}_3\text{Li (0.14)} > mPEO_{20}\text{-N(Li)Naph (0.11)} > mPEO_{20}\text{-N(Li)Pyr (0.08)}.$$

Reaction of water with the lithium metal electrode might be the cause of the increase in resistivity. One possible cause of the increase in the resistivity of the electrode-electrolyte interface is the reaction of water with the lithium metal. The produced LiOH is highly corrosive and could then further increase interfacial resistance through passivation of the electrode surface and reaction with the electrolyte. However, the increase in ρ as a percentage of the cell resistivity measured by GEIS before and after GCPL has the following trend:

$$mPEO_{20}\text{-N(Li)Naph (+100 \%)} > mPEO_{20}\text{-OC(O)PhSO}_3\text{Li (+60 \%)} > mPEO_{20}\text{-N(Li)Pyr (+25 \%)}.$$

This change in the order of the trend corresponds to the increase in the bulk resistance of mPEO₂₀-N(Li)Naph. The change in the bulk of that electrolyte might be the result of corrosion by LiOH. There is lower evolution of the bulk resistivity of mPEO₂₀-N(Li)Pyr, which has the lowest water content.

In conclusion, these MEC-SIPEs have constant resistivity as a function of transferred charge. However, evolution of the resistivity is observed during GCPL. The trend in the evolution of ρ follows the trend of increasing water content. Evolution of the bulk resistivities of both mPEO₂₀-OC(O)PhSO₃Li and mPEO₂₀-N(Li)Naph are observed. These MEC-SIPEs are not stable on contact with lithium metal. The mPEO₂₀-N(Li)Pyr has the lowest water content and also the lowest evolution of ρ . The bulk resistivity of this MEC-SIPE does not change as a result of GCPL. The 25 % increase in the interface resistance of mPEO₂₀-N(Li)Pyr might be correlated to the water content of this MEC-SIPE. The mPEO₂₀-N(Li)Pyr is the most stable of these three examples.

B. MEC-SIPEs have increasing resistivity as a function of transferred charge.

End-group: -SO₃Li (Fig. II-29), -SO₂N(Li)Naph (Fig. II-30).

The plot is in the form of a slope of increasing resistivity. After the first cycle of one forward and one reverse galvanostatic period, the behaviour is close to constant upon cycling, with close to the same maximum in resistivity reached per unit charge. The mPEO₂₀-SO₂N(Li)Naph (**Fig. II-30**) has slightly higher ρ than mPEO₂₀-SO₃Li (**Fig. II-29**) as a function of transferred charge. The sulfonamide also has greater curvature and evolution of resistivity upon cycling.

Fig. II-29 and Fig. II-30: (Top) The resistivity ($\rho / 10^{-3} \cdot \Omega \cdot m$) as a function of charge (Q) during galvanostatic cycling of the MEC-SIPEs mPEO₂₀-SO₃Li (Fig. II-29), mPEO₂₀-SO₂N(Li)Naph (Fig. II-30). The first five cycles are shown. The arrows (\rightarrow) indicate the evolution of ρ upon cycling. (Bottom) The GEIS spectra of the same samples measured before (\circ) and after (\diamond) GCPL. The experimental data are fitted to an equivalent circuit black lines (-).

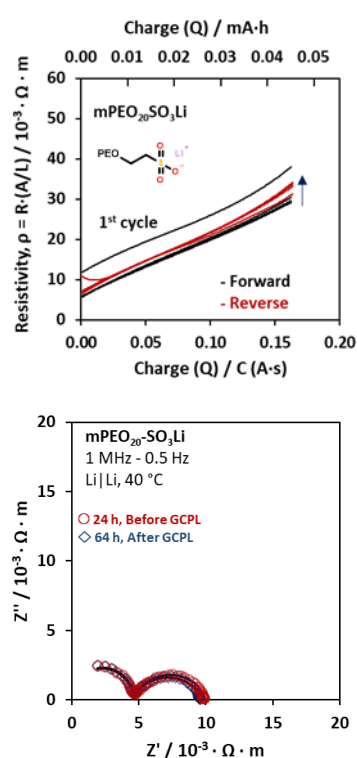


Figure II-29: (top) ρ vs Q of GCPL and (bottom) Nyquist impedance of mPEO₂₀-SO₃Li

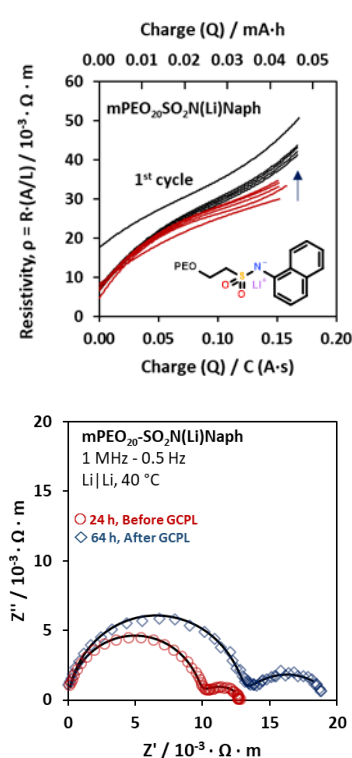


Figure II-30: (top) ρ vs Q of GCPL and (bottom) Nyquist impedance of mPEO₂₀-SO₂N(Li)Naph

Although the mPEO₂₀-SO₃Li (Fig. II-29) has a lithium sulfonate salt like mPEO₂₀-OC(O)PhSO₃Li (Fig. II-26), its behaviours observed by GCPL and GEIS are very different. These MEC-SIPEs have similar water content, corresponding to 11 mol% of the MEC-SIPE (Table II-3). However, there is no evolution of the cell resistivity of mPEO₂₀-SO₃Li, as measured by GEIS before and after GCPL. This MEC-SIPE appears to be quite stable under the applied conditions. However, the ρ of mPEO₂₀-SO₃Li increases per unit Q during each GCPL period. This resembles the behaviour of a capacitor, rather than the response expected of a conductor. The same trend with greater curvature is observed for mPEO₂₀-SO₂N(Li)Naph.

The mPEO₂₀-SO₂N(Li)Naph has a higher resistivity than mPEO₂₀-SO₃Li. The GEIS of these MEC-SIPEs reveals two resistive features, attributed to the bulk MEC-SIPE (at high frequency) and to the electrode-electrolyte interface (at low frequency). It is estimated, using an equivalent circuit model, that the interfacial ρ of mPEO₂₀-SO₃Li (5300 $\Omega \cdot m$) and mPEO₂₀-SO₂N(Li)Naph (6900 $\Omega \cdot m$) after GCPL are higher than the same features of the EC-SIPEs in group A (see above). This higher interfacial resistance might be the cause of the curvature of the plot of ρ vs Q. The curvature is greater for mPEO₂₀-SO₂N(Li)Naph, which not only has greater interfacial ρ , but also a higher water content (18 mol%). These two observations can be related: reaction of water at the electrode-electrolyte interface generates degradation products that cause passivation of the interface.

In conclusion, the observed trend of ρ vs Q in group **B** is consistent with passivation of the electrode surface and high electrode-electrolyte interfacial resistivity. The increase in interfacial resistivity results in the buildup of charge at the electrode-electrolyte interface during GCPL and evolution of ρ vs Q resembling a parallel plate capacitor.

C. MEC-SIPE has evolving resistivity as a function of transferred charge upon cycling.

End-group: - $\text{NSI}(\text{LiTFSI})$

The zwitterionic $\text{mPEO}_{20}\text{-NSI}(\text{LiTFSI})$ has constant resistivity as a function of transferred charge for the first cycle (**Fig. II-31, A**). The resistivity of the second cycle increases with transferred charge. The slope of resistivity is increasing with galvanostatic cycling. The GEIS spectra measured of the same sample (**Fig. II-31, B**) reveal similar behaviour to the resistivities observed of $\text{mPEO}_{20}\text{-N}(\text{Li})\text{Naph}$ (**Fig. II-27**), however the resistivity of the cell is much higher. The bulk of $\text{mPEO}_{20}\text{-NSI}(\text{LiTFSI})$ has low resistivity (370 $\Omega\cdot\text{m}$) but the electrode-electrolyte interface has high resistivity (12700 $\Omega\cdot\text{m}$). Both of these resistivities increase after GCPL. The bulk resistivity increases to 770 $\Omega\cdot\text{m}$ (+110 %). This might be caused by insufficient connectivity of conductive domains in the electrolyte. The interfacial resistivity increases to 15400 $\Omega\cdot\text{m}$ (+20 %). This is evidence of an unstable electrode-electrolyte interface. The result of these combined effects is an evolution of $\rho(Q)$ during charge transfer. The $\text{mPEO}_{20}\text{-NSI}(\text{LiTFSI})$ has 1 mol% water content, the lowest of the present library of MEC-SIPEs (**Table II-3**), so the electrochemical stability of the electrolyte not likely to be controlled by the humidity in this case. The adverse reactivity that causes the increase in cell resistivity originates from the chemical structure of the MEC-SIPE. Given the known high performance of the TFSI⁻ anion and the bisulfonil imide, instability of the carbonyl-triazolium linker might be the cause of the observed behaviours.

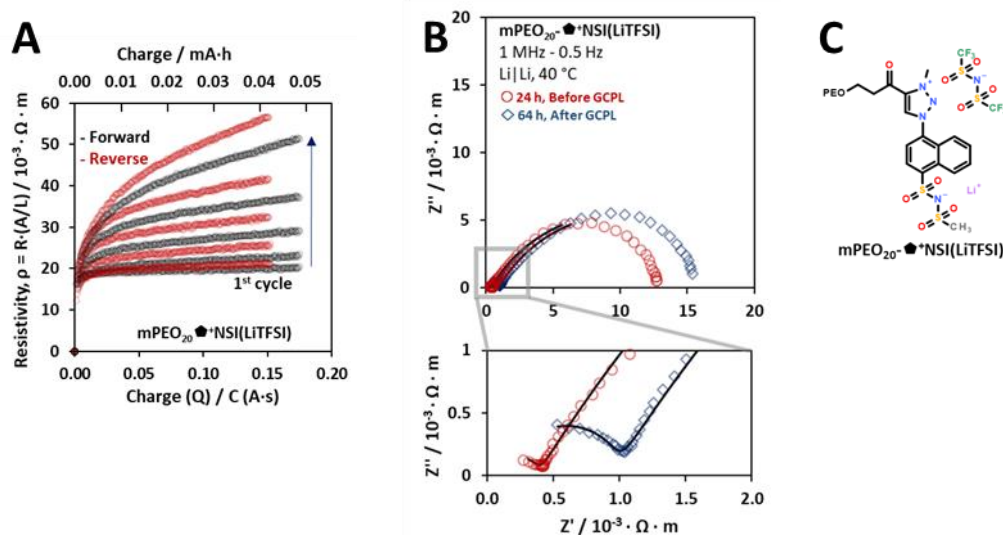


Figure II-31: (A) The resistivity ($\rho / 10^{-3} \cdot \Omega \cdot \text{m}$) as a function of charge (Q) during galvanostatic cycling of $\text{mPEO}_{20}\text{-NSI}(\text{LiTFSI})$. The first five cycles are shown. The arrows (\rightarrow) indicate the evolution of ρ upon cycling ρ vs Q of GCPL. (B) Nyquist plots of GEIS spectra measured before (\circ) and after (\diamond) GCPL. (C) the chemical structure of $\text{mPEO}_{20}\text{-NSI}(\text{LiTFSI})$.

D. The Salt-in-Polymer electrolyte

A SiP electrolyte having the same EO/Li= 20 ratio was formulated for comparison to the EC-SiPEs having EO_n= 20. During the 24 h equilibration period prior to launch of GCPL, the cell resistivity of the SiP evolved by one order of magnitude. This is observed by GEIS spectra measured at one-hour intervals (examples are shown in Fig. II-32, A and B).

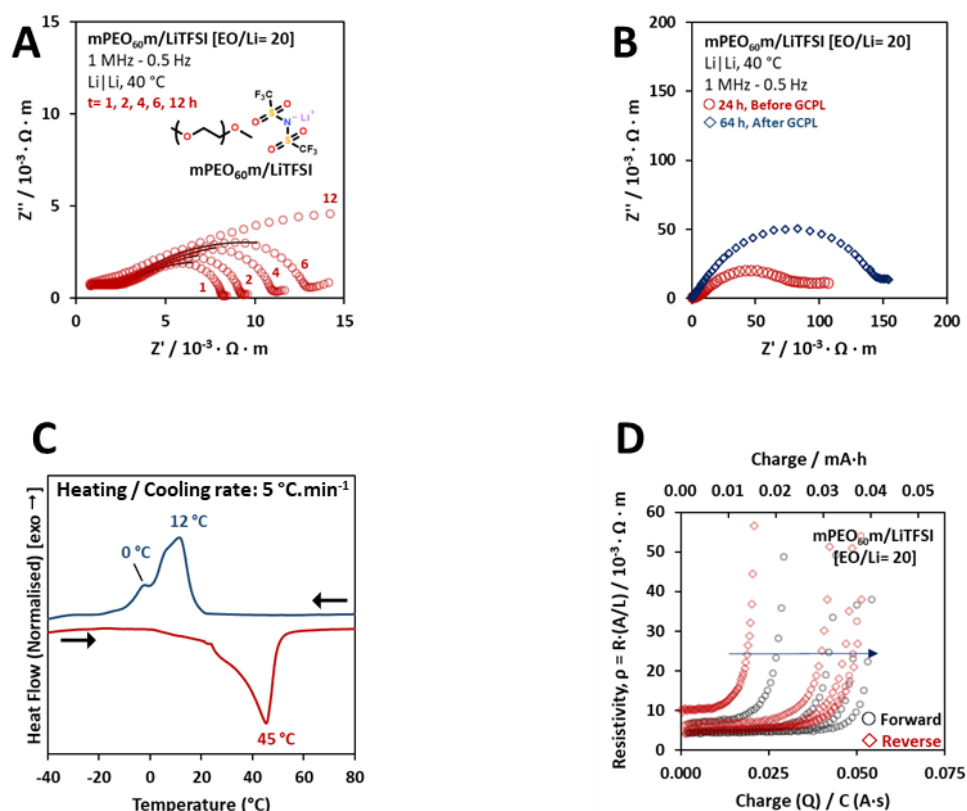


Figure II-32: Analysis of mPEO₆₀m/LiTFSI (EO/Li= 20) (A) Nyquist plots of GEIS spectra showing evolution of the cell resistivity during equilibration at 40 °C before GCPL. (B) Nyquist plots of |GEIS spectra measured before (○) and after (◇) GCPL. (C) DSC traces of the polymer electrolyte. Arrows (→) indicated the direction of heating and cooling at a rate of 5 °C.min⁻¹. (D) The resistivity ($\rho / 10^{-3} \cdot \Omega \cdot m$) as a function of charge (Q) during galvanostatic cycling of mPEO₆₀m/LiTFSI (EO/Li= 20). The first five cycles are shown. The arrow (→) indicates the evolution of ρ upon cycling.

Differential Scanning Calorimetry (DSC) analysis of the electrolyte reveals an exothermic transition having a peak temperature (T_p) at 12 °C on cooling, and an endothermic transition having a peak temperature $T_p = 45$ °C on heating (Fig. II-32, C). The coin cell was prepared using the melted SiP but it was permitted to cool to ambient temperature before the launch of GCPL. The GCPL was conducted at 40 °C. This temperature might be insufficient to fully melt the electrolyte. Crystallinity of the mPEO₆₀m at 40 °C might limit the ionic conductivity of the electrolyte. The measurements of σ in Section 2.1 were conducted on cooling and the temperature of 40 °C was not maintained for the long period applied during GCPL. The ripening of the crystalline domains of the SiP during the 64 h of the combined GEIS and GCPL measurements might be the cause of the high resistivity and low charge transfer of the SiP (Fig. II-32, D). However the limit of Q increases upon cycling, from 0.01 A.s (2nd cycle) to 0.05 A.s (5th cycle). The mobility of the few ions in the amorphous phase of the SiP might plasticize the SiP and cause the slight increase in Q. However, in general the SiP is unstable under the applied conditions.

E. Instability upon galvanostatic cycling.

End-group: - \blacklozenge NSI(Li), -SANSI(Li₂) [at 60 °C]

The mPEO₂₀- \blacklozenge NSI(Li) is not electrochemically stable on contact with lithium metal. This is revealed by the large evolution of cell resistivities at 40 °C before launch of GCPL (Fig. II-33). Both the bulk and interfacial resistivities of the MEC-SIPE increase during the equilibration period. The last three GEIS spectra gave the same result. Instability of this MEC-SIPE during galvanostatic cycling is expected because of the high resistivity of the cell. For simplicity of the representation, only the forward charge transfers are shown in the plot of ρ vs Q. The resistivity of the electrolyte caused by adverse reactions with lithium metal prohibits charge transfer during the galvanostatic periods.

Fig. II-33 and Fig. II-34: (Top) The resistivity ($\rho / 10^{-3} \cdot \Omega \cdot m$) as a function of charge (Q) during galvanostatic cycling of mPEO₂₀- \blacklozenge NSI(Li) (Fig. II-33) and mPEO₅₅-SANSI(Li₂) (Fig. II-34). For simplicity of presentation, only the forward polarisation periods of the first 5 cycles are shown in plots of ρ vs Q. (Bottom) Nyquist plots of representative GEIS spectra of the same samples measured before GCPL are shown below each plot of ρ vs Q. The experimental data are represented by red lines (-).

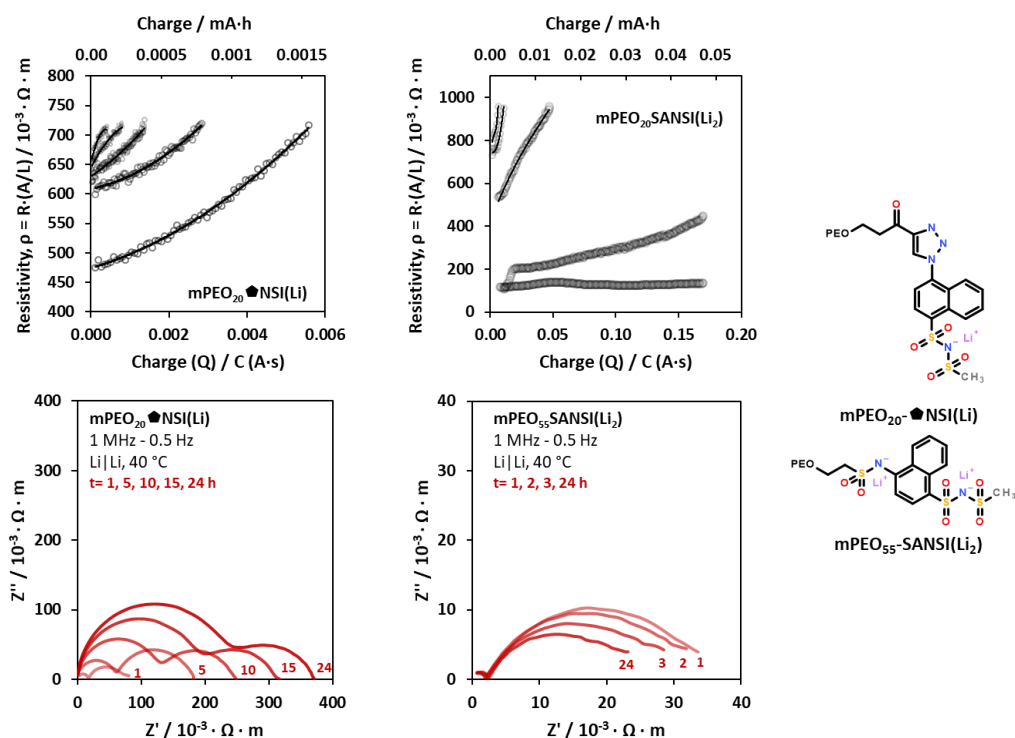


Figure II-33: (top) ρ vs Q of GCPL and (bottom) examples of GEIS of mPEO₂₀- \blacklozenge NSI(Li) Figure II-34: (top) ρ vs Q of GCPL and (bottom) examples of mPEO₅₅-SANSI(Li₂)

Whereas the other polymers were tested at 40 °C, the "double salt" mPEO₅₅-SANSI(Li₂) was tested at 60 °C to promote good wetting of the electrode surface by the electrolyte having $EO_n = 55$ ($M_{n(EC-SIPE)} \approx 2770 \text{ g} \cdot \text{mol}^{-1}$). The bulk resistivity remained constant (2300 $\Omega \cdot m$) but the interfacial resistivity decreases to an equilibrium value (20600 $\Omega \cdot m$) before GCPL was launched. Rapid evolution of resistivity is evidence that mPEO₅₅-SANSI(Li₂) is not stable under GCPL at 60 °C. The GEIS spectra of mPEO₂₀- \blacklozenge NSI(Li) and mPEO₅₅-SANSI(Li₂) measured after GCPL do not permit reliable modelling by an equivalent circuit.

2.2.4. Conclusions on Electrochemical Stability of MEC-SIPes

The MEC-SIPes prepared under the reported procedure have persistent water content. The drying protocol should be extended and intensified if EC-SIPes are to be applied in lithium-ion batteries. The water content of the presented SIPes (in the 170-3000 ppm range) would be prohibitive to the functioning of traditional *salt-in-polymer* (SiP) electrolytes. The assembled coin cells containing the present SIPes, using Li metal electrodes, were tested under conditions of cyclic voltammetry, galvanostatic cycling, and chronoamperometry without cell failure. This implies that the water does not affect the functioning of these electrolytes in the same way as it would in SiP formulations.

The ESW of the presented MEC-SIPes is limited by the functional end-group chemistry. Most of the EC-SIPes do not reach ~ 4 V vs. Li/Li⁺, the practical limit for PEO-based polymer electrolytes. Therefore, their application is limited to electrode chemistries that have cathodes of lower potential vs. Li/Li⁺, such as those of Li-S batteries. However, this projection is based on CV using a steel cathode. The CV in oxidation mode therefore does not represent the true (electro)chemical stability of these SIPes on contact with active materials, which might change, especially at high charge and discharge capacities. The electrochemical stabilities of the SIPE end-groups could be analysed and decoupled from that of the polymer chain through study of model compounds. For example, a small-molecular analogue of a proposed end-group could be dissolved in a suitable solvent of known ESW. Such a formulation could be analysed by CV within the potential range permitted by the solvent. Further, a copper cathode might enable more accurate analysis of MEC-SIPE stability in reduction mode, if the additional peaks observed in the 0.8-1.2 V range are caused by redox processes of oxides at the surface of stainless steel.

Stability in terms of stripping and plating of lithium metal is characterised by galvanostatic cycling with potential limitation (GCPL). The EC-SIPes having secondary N-aryl amine end-groups have high σ , are stable up to ~ 3.6 V vs. Li/Li⁺ (CV) and have reversible transfer charge at $j = 10 \mu\text{A}\cdot\text{cm}^{-2}$ with the lowest evolution of resistivity. CV and GCPL together demonstrate that the mPEO₂₀- \blacklozenge NSI(Li) is unstable in contact with lithium metal. Despite its high conductivity, the electrolyte cannot transfer charge under the applied conditions. However, the quaternized mPEO₂₀- \blacklozenge^+ NSI(LiTFSI) has **i)** high ionic conductivity, and **ii)** low water content. GCPL demonstrates that this MEC-SIPE can transfer charge at $j = 10 \mu\text{A}\cdot\text{cm}^{-2}$. Further investigation of the evolution of the electrode-electrolyte interface is required to valorise the electrochemical stability of this MEC-SIPE.

2.3. Lithium Transference by MEC-SIPEs

2.3.1. Method

The results of ionic conductivity of the MEC-SIPEs presented in Section 2.1 inform the discussion of lithium transference by the EC-SIPEs. The MEC-SIPEs based on PEO₂₀ were studied. This is because **i)** these polymers typically had the highest ionic conductivity for MEC-SIPEs bearing a certain functional end-group, and **ii)** their convenient viscoelastic properties enable easy and reproducible preparation of samples and assembly of coin cells in a glovebox. Selecting the polymer electrolytes having the same chain length directs the comparison of the EC-SIPEs relative to the concentration of lithium expressed by the EO/Li ratio. In terms of the mass fraction of end-groups of the bulk MEC-SIPE ($\phi_{m(\text{EGrp})}$), this ratio EO/Li = 20 corresponds to $\phi_{m(\text{EGrp})}$ in the 0.1-0.5 range (**Table II-4**). The mass fraction of lithium is small for all of the electrolytes (0.4-0.7 wt%). The ionic conductivity of the MEC-SIPEs based on PEO₂₀ was sufficiently high to enable electrochemical testing of the neat (solvent-free) polymers at 40 °C. The efficiency of Lithium ion transfer was measured using lithium metal electrodes in coin cells with a Li|MEC-SIPE|Li symmetric configuration. Chronoamperometry (CA) at constant potential, according to the method proposed by Bruce and Vincent,^[11,12] was applied to calculate the Lithium Transference Number (LTN).

Table II-4: The Degree of Polymerisation (DP_n / EO_n), Number Average Molar Mass (M_n / g.mol⁻¹), the mass fraction of the end-group ($\phi_{m(\text{EGrp})}$) and the mass fraction of lithium ($\phi_{m(\text{Li})}$) of the presented MEC-SIPEs having different End-Group Identities. The SiP electrolyte mPEO₆₀m/LiTFSI (EO/Li = 20) is listed for reference.

MEC-SIPE					
End-Group		DP _n	M _{n(EC-SIPE)}	$\phi_{m(\text{EGrp})}$	$\phi_{m(\text{Li})}$
Identity	(g.mol ⁻¹)	(EO _n)	(g.mol ⁻¹)		
-SO ₃ Li	87	20	989	0.09	0.007
-OC(O)PhSO ₃ Li	207	20	1109	0.19	0.006
-SO ₂ N(Li)Naph	213	20	1115	0.19	0.006
-N(Li)Naph	148	20	1051	0.14	0.007
-N(Li)Pyr	223	20	1125	0.20	0.006
-SANSI(Li ₂)	377	55	2773	0.14	0.005
-◆NSI(Li)	401	20	1303	0.31	0.005
-◆ ⁺ NSI(LiTFSI)	696	20	1598	0.44	0.004

SiP mPEO _n m/LiTFSI [EO/Li = 20]					
Salt		DP _n	M _{n(mPEOm)}	$\phi_{m(\text{Salt})}$	$\phi_{m(\text{Li})}$
Identity	(g.mol ⁻¹)	(EO _n)	(g.mol ⁻¹)		
LiTFSI	287	60	2732	0.25	0.006

EIS to low alternating frequency of applied potential was attempted (Galvanostatic Electrochemical Impedance Spectroscopy, GEIS). However, the low frequencies (down to 50 mHz) applied to the EC-SIPEs resulted in an alternating current having a long time periods of current flow in a single direction. For example, an oscillation of 50 mHz effectively applies a direct current in each direction for 10 hours. This single data point in GEIS requires 20 hours of measurement.

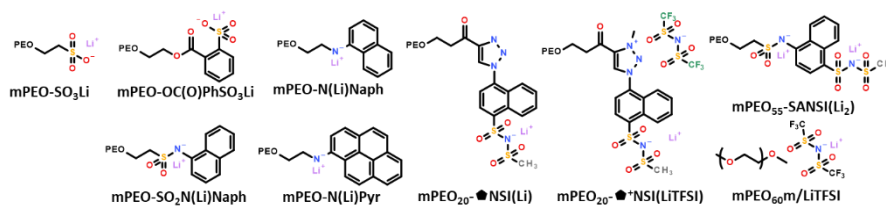
The applied current density required for sufficient electromagnetic force to measure a precise EIS spectrum of the MEC-SIPEs is $20 \mu\text{A}\cdot\text{cm}^{-2}$, double that applied in GCPL (Section 2.2.3). With the responses under GCPL in mind, it is not surprising that the MEC-SIPEs are not stable at under GEIS at these conditions. The large evolution of cell resistance during the low frequency GEIS period augments the complex impedance. The obtained experimental data do not permit accurate evaluation of bulk resistivity of the electrolyte relative to the diffusion of ions. The electrode-electrolyte interface often occupies a large frequency range and perturbs the impedance of the bulk and diffusion processes. This is seen in the GEIS spectra measured before and after CA (**Fig. II-34**). By contrast, the Bruce-Vincent method was completed in the 22 to 26 hours range, including equilibration of the cell before launching the CA.

2.3.2. Results

The Lithium Transference Number (LTN) of each MEC-SIPE was determined by chronoamperometry. The results are summarised in **Table II-5**. The values defined for the MEC-SIPEs are in the range $t_{\text{Li}}^+ \approx 0.7\text{-}1.0$, and are higher than the mPEO₆₀m/LiTFSI blend having the same EO/Li = 20 ratio ($t_{\text{Li}}^+ = 0.25$).

Table II-5: Table of summarised ionic conductivity ($\sigma / \text{S}\cdot\text{cm}^{-1}$) and corresponding lithium transference number (LTN) of selected MEC-SIPEs. The LTN was calculated from chronoamperometry using the Bruce-Vincent method. The σ_{AC} was measured by EIS using either (blocking) gold electrodes (Au|Au) or lithium metal (Li|Li) electrodes at 40 °C (except 8; 60 °C). The σ_{AC} [Li|Li] is that measured immediately i) before and i) after chronoamperometry (CA). The two LTNs listed are the chronoamperometric (t_{Li}^+) and corrected (t_{Li}^{+*}) values. The data of the SiP electrolyte mPEO₆₀m/LiTFSI (EO/Li= 20) are listed for comparison. [12]

#	Polymer Electrolyte <i>MEC-SIPE</i>		$\sigma_{\text{AC}} (10^6 * \text{S}\cdot\text{cm}^{-1})$ at 40 °C			LTN	
			Au Au	Li Li ⁽¹⁾	Li Li ⁽²⁾	t_{Li}^+	t_{Li}^{+*}
	Polymer	End-Group	Before CA	After CA			
1	mPEO ₂₀ -	SO ₃ Li	21	1.3	1.1	0.65	0.76
2		OC(O)PhSO ₃ Li	2.1	1.1	1.1	1.10	1.03
3		SO ₂ N(Li)Naph	12	2.1	2.1	0.73	0.91
4		N(Li)Naph	12	6.8	5.5	0.82	0.85
5		N(Li)Pyr	250	6.6	4.7	0.70	0.83
6		◆NSI(Li)	25	-	-	-	-
7		◆ ⁺ NSI(LiTFSI)	130	5.5	6.9	0.82	1.00
8	mPEO ₅₅ -	SANSI(Li ₂)	5.3 ^(60°C)	0.9 ^(60°C)	1.1 ^(60°C)	0.98	0.95
9	<i>Salt-in-Polymer (SiP) Blend</i> mPEO ₆₀ m/LiTFSI (EO/Li= 20)		330			0.25	-



Two values of LTN are listed above (**Table II-5**). The first (t_{Li}^+) is found by simple comparison of the current at the beginning and at the end of the CA period. The density of data points enabled an average of the initial ($t_0 = 0.1 \text{ s} \rightarrow t_i = 1.0 \text{ s}$) and the steady state current ($t_{ss} = 11 \text{ h} \rightarrow t_{ss} = 12 \text{ h}$) to be considered. The first value of the LTN is defined by the ratio $t_{Li}^+ = I_0/I_{ss}$. The evolution of the electrode-electrolyte interface was corrected according to the cell resistance calculated from GEIS measurements made immediately before and after the CA period (**Eqn. II-13**). The Nyquist representations these GEIS measurements are presented and discussed below (**Fig. II-34**).

Equation II-13: Correction of the transference number (t^*) through multiplication by the evolution in cell resistance. I_0 is the initial current and I_{ss} is the steady state current measured by CA. ΔV is the applied potential. R is the resistance. The terms R_0 and R_{ss} are calculated from EIS measurements made immediately before (R_0) and after (R_{ss}) the CA period.

$$t_{Li}^+ = \frac{I_{ss}(\Delta V - I_0 R_0)}{I_0(\Delta V - I_{ss} R_{ss})}$$

The σ_{AC} (Au|Au) of certain MEC-SIPEs approaches that of the model SiP electrolyte mPEO₆₀m/LiTFSI having the same ratio of EO/Li= 20 (**Table II-5**; # 5, 7, 9). The mPEO₂₀-N(Li)Pyr has σ_{AC} of the same order of magnitude as the SiP electrolyte but the LTN of the MEC-SIPE is ca. three times higher. This is significant because the MEC-SIPE has similar conductivity and the majority of the current is derived from the transfer of lithium ions ($t_{Li}^+ \approx 0.8$). The MEC-SIPEs in **Table II-5** having -SO₃Li (**1**), -SO₂N(Li)Naph (**3**) and -N(Li)Naph (**4**) end-groups all have σ_{AC} of ca. $10^{-5} \text{ S.cm}^{-1}$ at 40 °C and an LTN of $t_{Li}^+ \approx 0.7$ or higher. This σ is around the typical magnitude reported for "single ion" polymer electrolytes in recent years.^[12] The moderate LTN is fair in context of low DP_n MEC-SIPEs, that do not have entangled polymer chains, and the evolution of the interface under the conditions of measurement. The mPEO₂₀-OC(O)PhSO₃Li has a high LTN but $\sigma_{AC} = 2.1 \cdot 10^{-6} \text{ S.cm}^{-1}$ at 40 °C. This σ is good in context of an LTN approaching unity. The "double salt" mPEO₅₅-SANSI(Li₂) has a longer PEO chain (EO_n) but a similar lithium concentration (EO/Li= 23). Its σ_{AC} is lower than all of the MEC-SIPEs having EO_n= 20 except mPEO₂₀-OC(O)PhSO₃Li.

The mPEO₂₀- \blacklozenge NSI(Li) is not electrochemically stable in contact with lithium metal (see Section 2.2). The great improvement of the ESW upon quaternisation permits the transfer of Li⁺ by the zwitterionic mPEO₂₀- \blacklozenge ⁺NSI(LiTFSI). The high LTN of mPEO₂₀- \blacklozenge ⁺NSI(LiTFSI) is remarkable because this polymer electrolyte has two mobile ions: Li⁺ and TFSI⁻. A LTN of close to 0.5 is expected in the case of equal mobility of the cation and the anion. However, mPEO₂₀- \blacklozenge ⁺NSI(LiTFSI) has $t_{Li}^+ \approx 0.8$, which is corrected to unity by accounting for evolution of the electrode-electrolyte interface. The value of LTN approaching unity requires that the TFSI⁻ has lower mobility relative to Li⁺. The combined results of ionic conductivity, ESW, and LTN describe the mPEO₂₀- \blacklozenge ⁺NSI(LiTFSI) to be **i)** of the same order of ionic conductivity, and **ii)** of equivalent electrochemical stability to a representative PEO/LiTFSI SiP blend of the same EO/Li= 20 ratio. The MEC-SIPE and the SiP electrolyte moreover have very similar water content (160 and 130 ppm respectively, **Table II-3**). However, mPEO₂₀- \blacklozenge ⁺NSI(LiTFSI) has a LTN around three times higher than the SiP electrolyte. This is evidence that the TFSI⁻ has decreased mobility in mPEO₂₀- \blacklozenge ⁺NSI(LiTFSI) compared to the SiP. The difference in chemistry is that of the functional end-group. The positive charge of the triazolium might be the cause of the decreased anionic mobility through ionic interactions in the bulk. The high σ is evidence that the Li⁺ is highly mobile. However, GCPL reveals the limited electrochemical stability of the mPEO₂₀- \blacklozenge ⁺NSI(LiTFSI).

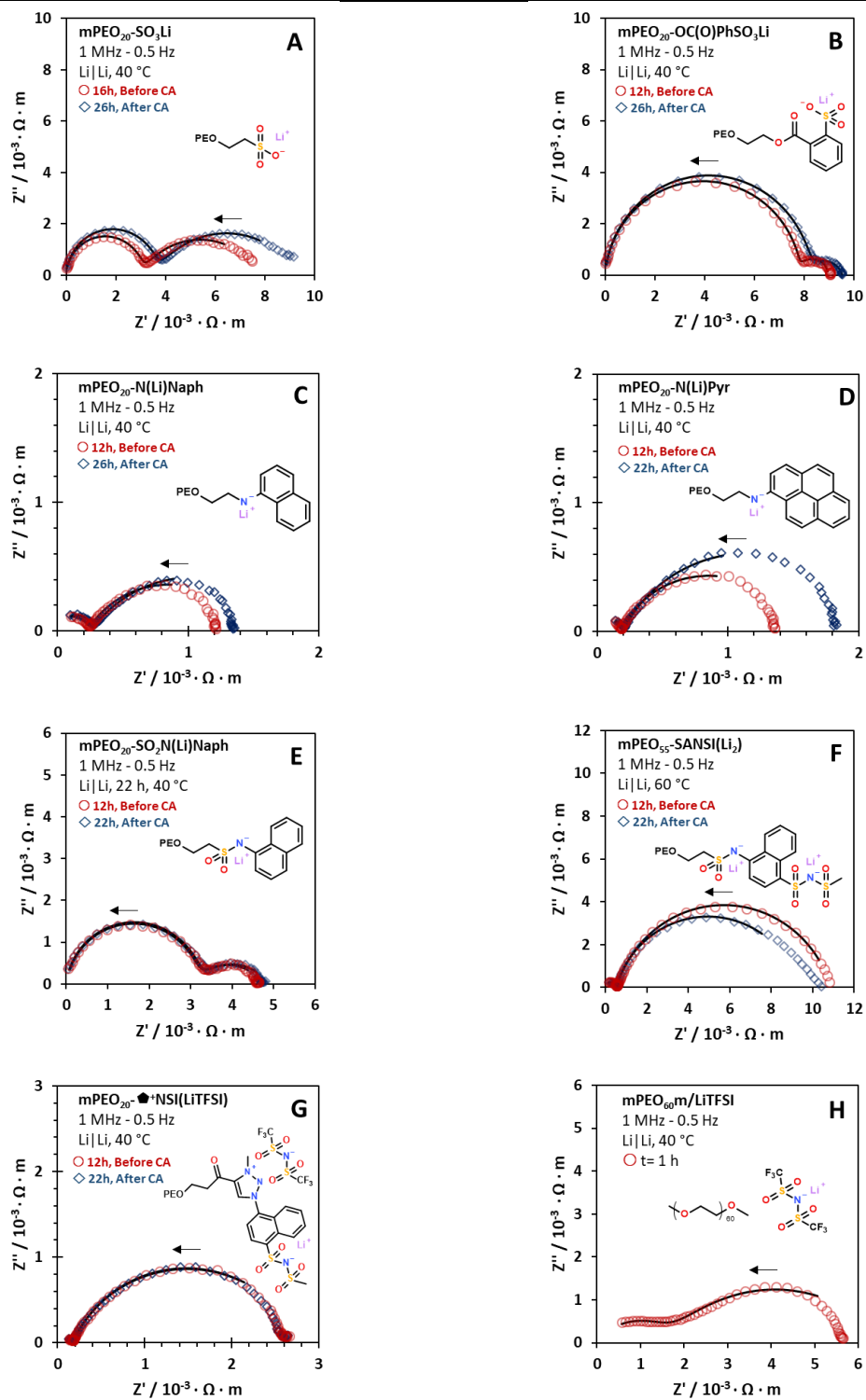


Figure II-35: Nyquist plots of EIS spectra (1.0 MHz \rightarrow 0.5 Hz) measured of polymer electrolytes in Li|Li coin cells before (○) and after (◇) chronoamperometry (CA). These spectra were used to correct for the change in cell potential resulting from the CA method. EIS was conducted at 40 °C (A-E, G-H) and at 60 °C (F). The MEC-SIPES having $EO_n = 20$ and different functional end-groups are shown: $-SO_3Li$ (A), $-OC(O)PhSO_3Li$ (B), $-N(Li)Naph$ (C), $-N(Li)Pyr$ (D), $-SO_2N(Li)Naph$ (E), $-NSI(LiTFSI)$ (G). The long-chain "double salt" EC-SIPE mPEO₅₅-SANSI(Li₂) (F) is shown. The SiP electrolyte mPEO_{60m}/LiTFSI (H) is shown for comparison. The experimental data are fitted to an equivalent circuit model (black lines, -). Arrows (\leftarrow) indicate the direction of increasing frequency.

The GEIS of the MEC-SIPEs, performed before and after CA, are presented in **Fig. II-35**. The electrode-electrolyte interface is visible in the Nyquist representation as the second semi-circle, observed at lower frequencies than the bulk resistivity. Comparing the shapes of these spectra suggests a correlation between end-group chemistry and resistivity of the interface. Consider first the MEC-SIPEs having aryl functions at the extremity of the chain (*i.e.* MEC-SIPEs of the configuration mPEO-A-Li⁺-aryl). The MEC-SIPEs having -N(Li)Naph (**Fig. II-35, C**), -N(Li)Pyr (**D**) and -SO₂N(Li)Naph (**E**) have electrode-electrolyte interfacial resistivities in the 1-2 kΩ.m range. However, mPEO₂₀-SO₃Li (**A**), having the sulfonate at the extreme end of the chain, has interfacial resistivities in the 5-6 kΩ.m range. The bent geometry of the mPEO₂₀-OC(O)PhSO₃Li (**B**) is correlated this resistivity being decreased to the 1-2 kΩ.m range, similar to the other aryl MEC-SIPEs. The aryl groups placed at the extremity of the chain might decrease the resistivity of the solid electrolyte interface (SEI).

The 50 °C melting temperature of the PEO segments of mPEO₅₅-SANSI(Li₂) requires high temperature to ensure good wetting of the electrode surface. The CA and GEIS analyses were therefore performed at 60 °C. The effect of temperature is significant. The mPEO₂₀-SO₂N(Li)Naph (**Fig. II-35, E**) has interfacial resistivity $\rho_{SEI} < 2$ kΩ.m and mPEO₂₀- \blacklozenge^+ NSI(LiTFSI) has $\rho_{SEI} < 3$ kΩ.m (**G**). However, the mPEO₅₅-SANSI(Li₂) has $\rho_{SEI} \approx 10$ kΩ.m (**Fig. II-35, F**). The sulfonamide and the sulfonylimide are present in the other MEC-SIPEs (E, G), so the increase in ρ_{SEI} in mPEO₅₅-SANSI(Li₂) could be the result of either or both of **i**) PEO chain length and **ii**) temperature. The longer chain of mPEO₅₅-SANSI(Li₂) decreases the *number* of end-groups per mass of PEO. Although the ratio EO/Li= 23, the ratio EO/SANSI= 55. This results in fewer functional end-groups in contact with the electrode surface, which would increase the resistance of transferring charge between the electrode and the electrolyte. The temperature of 60 °C was applied to melt the PEO chains and sufficient wetting of the electrode surface is assumed. However, the elevated temperature might result in adverse reactivity of the MEC-SIPE with lithium metal. Although mPEO₅₅-SANSI(Li₂) is apparently stable, according to cyclic voltammetry (**Fig. II-25**), the stability of the MEC-SIPE under charge transfer conditions is limited, according to galvanostatic cycling (**Fig. II-34**). The mPEO₅₅-SANSI(Li₂) insufficiently stable at 60 °C to be considered for high temperature applications. The decrease in ionic conductivity does not permit at ambient temperature applications. The elevated temperature of the measurements prevents direct comparison of the LTN of mPEO₅₅-SANSI(Li₂) with those of the EC-SIPEs having (EO_n= 20), which were measured at 40 °C.

2.3.3. Conclusions on the Efficiency of Lithium Transfer by MEC-SIPEs

The presented MEC-SIPEs exhibit *moderate to high* transference of lithium ions. This is quantified by LTN values in the 0.7-1.0 range at 40 °C. The evolution of the SEI is lower for MEC-SIPEs having aryl functions at the extremity of the chain end, relative to mPEO₂₀-SO₃Li. The evolution of the SEI effectively increases the cell resistivity relative to the same electrolytes between blocking (gold) electrodes. Elevation of the temperature might decrease the resistivity of the SEI. However, the GEIS of mPEO₅₅-SANSI(Li₂) at 60 °C shows large interfacial resistance. The high LTN of mPEO₂₀- \blacklozenge^+ NSI(LiTFSI) ($t_{Li}^+ > 0.8$) implies decreased mobility of the TFSI⁻ anion relative to a blend of LiTFSI in PEO bis-terminated by non-interacting, methoxy end-groups ($t_{Li}^+ = 0.25$). The MEC-SIPEs having EO_n= 20 have sufficient ionic conductivity at 40 °C to enable CA and GEIS measurements. However, the SiP does not have an ideal form of its complex impedance at 40 °C. Evolution of the SiP resistivity at 40 °C (**Fig. II-32**) suggests that the SiP is not fully amorphous at this temperature.

2.4. Conclusions on Electrochemical Characterisation of MEC-SIPEs

Polymer electrolytes based on PEO are presented. The ionic conductivity is dependent on the end-group chemistry (Section 2.1.2). The length of the PEO chain determines the mass fraction of ionic end-groups in the bulk MEC-SIPE (Section 2.1.3). This is expected to be optimal at PEO chain lengths close to $EO_n \approx 20$. The MEC-SIPEs are capable of conducting lithium ions at low end-group concentrations ($EO_n = 55$, $\phi_{m(EGrp)} < 10$ wt%). The highest ionic conductivity is observed for MEC-SIPEs having the -N(Li)Pyr end group. The mPEO₅₅-N(Li)Pyr (EO/Li= 55) has $\sigma > 10^{-4}$ S.cm⁻¹ at $T > 40$ °C, which is less than one order of magnitude lower than a blend of mPEO₆₀m/LiTFSI (EO/Li= 60). The mPEO₂₀-N(Li)Pyr (EO/Li= 20) has σ similar to the SiP mPEO₆₀m/LiTFSI having the same EO/Li ratio. Ambient temperature ionic conductivity is accessible with EC-SIPEs based on PEO having $EO_n \leq 20$. The water content of the EC-SIPEs under the reported conditions of sample preparation is around 1-2 molecules per ten functional end-groups (Section 2.2.1). No clear and unambiguous correlation found between the water content and the ionic conductivities of the MEC-SIPEs.

The MEC-SIPEs are limited in electrochemical stability by the functional end-group. Although PEO is reported to be stable up to *ca.* 4 V vs. Li/Li⁺, the MEC-SIPEs are limited to 3.6-3.8 V vs. Li/Li⁺ (Section 2.2.2). This limit in oxidation makes the MEC-SIPEs unsuitable for use in cell chemistries that rely on high potential cathodes. However, the present library of functional end-groups might be applied in emerging Li-S and Li-O₂ batteries that cycle at < 3.5 V vs. Li/Li⁺.^[13]

In particular, the secondary arylamines mPEO_n-N(Li)Naph and mPEO_n-N(Li)Pyr have high ionic conductivity, are stable in the range of 0 ↔ 3.6 V vs. Li/Li⁺ (CV) and under applied current of 10 μ A.cm⁻² (GCPL). Evolution of the electrode-electrolyte interface at 40 °C implies that electrode passivation is unavoidable when the reported MEC-SIPEs are placed in contact with lithium metal (Section 2.3.2). The resistivity of is lower for MEC-SIPEs having aryl groups at the extremity of the chain in comparison to the mPEO₂₀-SO₃Li. Placing the ionic function at the chain side of the end-group might decrease the occurrence of undesirable reactions between the functional end-group and lithium metal.

The Lithium Transference Number (LTN) of the MEC-SIPEs is in the $t_{Li}^+ \approx 0.7-1.0$ range at 40 °C (Section 2.3.2). The majority of charge is transferred by mobile Li⁺ ions. This is three to four times higher than a comparable mPEO₆₀m/LiTFSI blend SiP electrolyte. An LTN of less than unity might be the result of vehicular motion of EC-SIPEs having non-entangled PEO segments ($EO_n = 20$). The high LTN of the zwitterionic mPEO₂₀- \blacklozenge^+ NSI(LiTFSI) ($t_{Li}^+ > 0.8$) implies decreased mobility of the TFSI⁻ anion. This might be the result of ionic interactions with the positive charge of the triazolium.

A polymer electrolyte having a single ionic function as an end-group can achieve $\sigma > 10^{-4}$ S.cm⁻¹ at ambient temperature. The mass of ionic functions can be as low as 10 wt% of the bulk polymer electrolyte. This is achieved without need of formulation with additional compounds such as plasticizers. Further research is envisioned with respect to the PEO chain and the identity of the functional end-group. Decoupling the contributions of, for example, **i**) the dissociation of ions from the end-groups, **ii**) the ion-solvating power of the polymer, and **iii**) the thermal motions of the polymer segments and of the end-groups is a great challenge. This requires a library of MEC-SIPEs based on rational design principles targeting specific electrochemical, thermal, physical, and structural properties.

The electrochemical characterisation of the MEC-SIPes suggests the following perspectives for the development of polymer electrolytes for lithium ion transport:

- I. Ionic conductivity appears to be limited by the dynamics of the polymer chain and the end-group rather than simply the concentration of the end-group (*i.e.* salt), which in MEC-SIPes is a function of the polymer chain length. Therefore, the thermodynamics and kinetics of MEC-SIPes should be investigated for targeting improved performance in ionic conductivity. The MEC-SIPE concept could be exploited for other polyether-based polymers, and beyond.^[14] Ionic end-groups should be investigated for polymer electrolytes based on other repeating unit chemistries such as poly(carbonate)s, poly(ester)s, and their copolymers. The correlation of ionic conductivity and the repeating unit of homopolymers should be exposed along two research axes: **i)** the physical and **ii)** the thermal properties of the polymer segments. This requires systematic variation polymer segments having a variety of physical and thermal properties. For example, a combination of electrochemical and rheological analyses should be applied to determine structure-property correlations along axes such as ionic conductivity and the complex mechanical modulus. This should be executed at first with two libraries of MEC-SIPes: **A)** constant end-group with variation of repeating unit of the chain, and **B)** a chain composed of a selected repeating unit with end-groups having different physical properties. Both axis A and B require variation of the polymer chain length at intervals of the order of a few multiples of the persistent length (*e.g.* 1–6* persistent length). Polymer segments having low activation energy of thermal motion should be targeted for low temperature applications. Polymer segments with high thermal stability should be targeted for high temperature applications. The interaction strength of polymer chains should be varied according to two axes: **i)** the strength of the coordination of Li⁺ ions, and **ii)** inter-segmental interactions. This is required, to decouple these processes having a concerted impact on σ .
- II. The water content has been measured for MEC-SIPes having EO_n= 20. If the water is physically associated with the polymer end-groups, the water content might vary with the end-group concentration. The water content of the MEC-SIPes having different chain lengths must be measured. These values should be compared with the ionic conductivity of the MEC-SIPes. This might help to explain the non-uniform relationships of σ vs. the mass fraction of end-groups (ϕ_m), since water has a much higher dielectric permittivity ($\epsilon \approx 80$) than PEO ($\epsilon \approx 10$).^[25]
- III. The rational design of end-groups should take inspiration from the results of Section 2.1 (for example, the high σ of secondary *N*-aryl amines). The ionic conductivity is improved by decreasing the activation energy of the dissociation of the ion pair. This might be achieved through greater delocalisation of the anionic charge at the end-group. In the case of *N*-aryl amines, electron-donating groups at the *para* and *ortho* positions of the aryl ring relative to the anionic linker would contribute electron density through inductive and resonance effects. This might improve σ through increased dissociation of Li⁺. Systematic variation of aromatic groups having different electron-donating and electron withdrawing groups would expose structure-property relations with crucial implications to ionic conductivity (**Illustration 1**).



Illustration 1 – Hypothetical end-group designs based on an *N*-aryl secondary amine. The aryl ring is modified with Electron Withdrawing Groups (EWGs), and Electron Donating Groups (EDGs). A phenyl ring is illustrated for simplicity.

- IV.** The electrochemical stability of the ionic functions remains a challenge for high voltage applications. The present library might be well-suited to low voltage applications but will not function as intended in contact with Lithium metal anodes and high voltage cathodes that reversibly insert lithium ions at $E > 3.7$ V *vs.* Li/Li⁺. In particular, the secondary aryl amines could have sufficiently fast and stable response to charge transfer at $E \leq 3.6$ V *vs.* Li/Li⁺. The anodic stability of mPEO₂₀-**◆**⁺NSI(Li) precludes further investigation of MEC-SIPEs having conjugated 1,2,3-triazole functions. However, quaternisation resulted afforded the zwitterionic mPEO₂₀-NSI(LiTFSI), which had improved stability in reduction mode. Based on the results of mPEO₂₀-**◆**⁺NSI(LiTFSI), zwitterionic functions are promising in terms of both σ and ESW. The zwitterionic end-group can selectively transport Li⁺ while at the same time benefit from the physicochemical properties of the counter anion. Numerous combinations of bound zwitterionic groups and counterions are imaginable. The bound sulfonimide-triazolium group with the LiTFSI salt is a promising start. The same MEC-SIPE without the conjugated ester (**Illustration 2**) could be compared to the present example, to test the implications of the ester on the performance of the end-group, especially in terms of electrochemical stability.

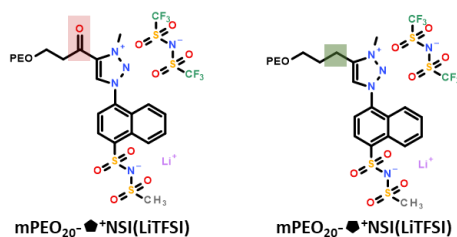


Illustration 2 – The MEC-SIPE mPEO₂₀-**◆**⁺NSI(LiTFSI) and an analogous MEC-SIPE that does not have an ester bond.

- V.** The majority of charge is transferred by Lithium ions. Non-unity Li⁺ transference numbers might be correlated to vehicular motion of non-entangled chains. Investigation of chain length and the chemistry of the repeating unit would clarify the relationship.
- VI.** The evolution of the resistivity of the electrode-electrolyte interface is a persistent limitation for MEC-SIPEs in contact with lithium metal. In particular, the effect of temperature should be studied to determine the limits of EC-SIPEs in applied technologies. GEIS measured in Li|Li coin cells suggests decreased evolution of the electrode-electrolyte interface of MEC-SIPEs having aryl end-groups, in comparison to the sulfonate end-capped mPEO₂₀-SO₃Li. A design based on the "polymer-anion-aryl function" template might be effective in the pursuit of MEC-SIPEs having high electrochemical stability.

3. Thermal Characterisation of MEC-SIPes

3.1. The Dependence of Thermal Transitions on the Polymer End-Group

Poly(ethylene oxide) is a semi-crystalline polymer that has well-defined temperatures of melting (T_m) and crystallisation (T_c). The transition temperatures are defined in this report by temperature (T_p) at which the peak enthalpy change is measured during the heating or cooling scans. These do not vary above the entanglement limit of PEO. The thermal transitions of the model PEO, having non-interacting methoxy end-groups (mPEO_{60m}), and its SiP blends, containing different concentrations of LiTFSI, are compared by Differential Scanning Calorimetry (DSC) analysis (Fig. 36). The salt LiTFSI plasticizes PEO. The decrease in the degree of crystallinity is observed as a depression of the T_p of both the exothermic enthalpy change (ΔH_{exo}) of crystallisation and endothermic enthalpy change (ΔH_{endo}) of melting.

Fig. II-36 and Fig. II-37: DSC thermograms of mPEO_{60m} and SiP blends of mPEO_{60m}/LiTFSI (Fig. 36), and MEC-SIPes based on mPEO₅₅-OH (Fig. 37). The direction of heating (red) and cooling (blue) are indicated. The DSC traces are individually normalised in heatflow (W.g⁻¹) according to the sample mass. The heating and cooling rates are 5°C.min⁻¹. The second cycle of heating and cooling is displayed for each sample.

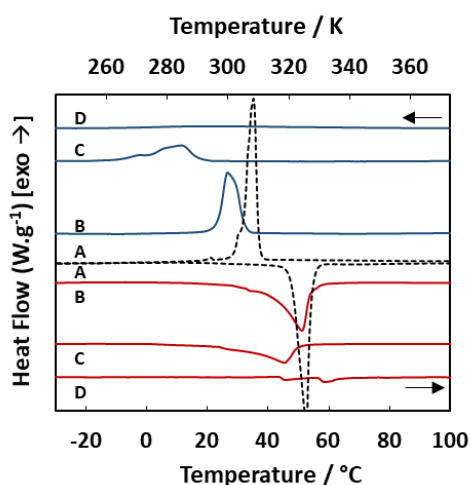


Figure II-36: DSC thermograms of mPEO_{60m} (A) and mPEO_{60m}/LiTFSI having different EO/Li ratios: (B) EO/Li= 60, (C) EO/Li= 20, and (D) EO/Li= 10.

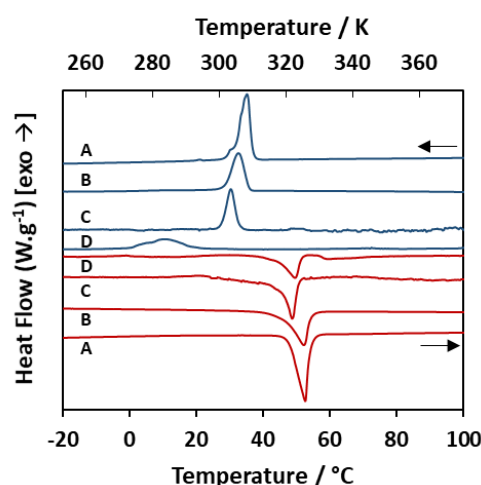


Figure II-37: DSC thermograms of mPEO₅₅-OH (A) and MEC-SIPes based on mPEO₅₅- having different end-groups: (B) -SO₃Li, (C) -SO₂N(Li)Naph, and (D) -SANSI(Li₂).

The neat polymer (dashed line ---) is plotted to the same scale as the polymer blends (*i.e.* it is normalised according to the sample mass). Increasing the concentration of LiTFSI results in a depression of T_m and ΔH_{exo} . The peak areas of the SiP are much smaller, illustrating the depression of ΔH . The observed ΔH_{exo} and ΔH_{endo} of the samples presented are tabulated in Table II-6. The endothermic processes on heating are observed at lower temperatures for the SiP having EO/Li= 60 and EO/Li= 20. The SiP having EO/Li= 10 exhibits two thermal transitions on heating. The first transition on heating might be the breaking of the few polymer-polymer interactions permitted at this high concentration of salt. The second might be the breakup of ion clusters formed through ionic aggregation above T_m during the first heating cycle. No ΔH_{exo} is observed on cooling at 5°C/min the SiP having the highest loading of LiTFSI (EO/Li= 10).

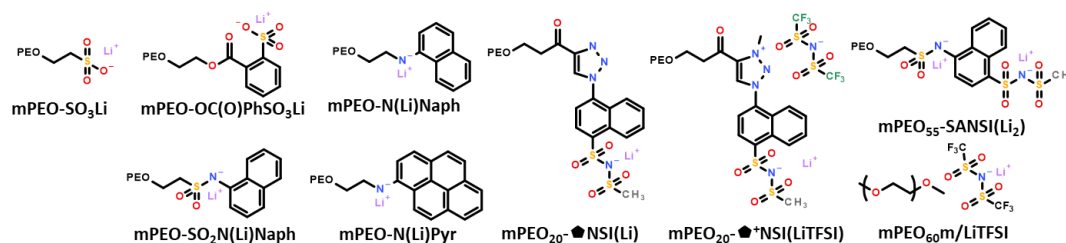
Table II-6: The mass fraction of salt ($\phi_{m(\text{salt})}$), the endothermic enthalpy change (ΔH_{endo}) and peak temperature (T_p) of the enthalpy change on heating at $5^\circ\text{C}\cdot\text{min}^{-1}$ from -40°C . The mPEO₆₀m/LiTFSI having different concentrations of salt are compared. The salt concentration is listed in terms of the ratio of ethylene oxide repeating units to lithium ions (EO/Li).

EO/Li	$\phi_{m(\text{salt})}$	ΔH_{endo} (J.g ⁻¹)	T_p (°C)
-	0.00	165	52
60	0.10	101	51
20	0.25	66	45
10	0.39	19	46, 59

The melting and crystallisation behaviours of MEC-SIPEs having EO_n= 55 are compared to those of the precursor polymer, mPEO₅₅-OH (**Fig. II-37**). The effect of functional end-groups on the thermal transitions of MEC-SIPEs having EO_n= 55 on heating is a small change of T_p but a decrease of ΔH_{endo} by 25-45 % (**Table II-7**). The largest difference is observed for the mPEO₅₅-SANSI(Li₂), which has the highest ionic concentration (EO/Li= 23) and the largest functional end-group mass fraction ($M_{\text{EGrp}} = 377 \text{ g}\cdot\text{mol}^{-1}$, $\phi_{\text{EGrp}} = 0.14$).

Table II-7: The T_p and ΔH_{endo} of phase transitions observed on heating at $5^\circ\text{C}\cdot\text{min}^{-1}$. The MEC-SIPEs having EO_n= 55 are compared to the precursor, mPEO₅₅-OH.

MEC-SIPE (EO _n = 55)			Heating		Cooling	
End-Group	M_n (g.mol ⁻¹)	$\phi_{m(\text{EGrp})}$	ΔH_{endo} (J.g ⁻¹)	T_p (°C)	$-\Delta H_{\text{exo}}$ (J.g ⁻¹)	T_p (°C)
mPEO ₅₅ -OH	2412	0.007	168	53	167	35
-SO ₃ Li	2482	0.035	124	52	112	32
-OC(O)PhSO ₃ Li	2603	0.080	121	52	116	23
-N(Li)Naph	2543	0.059	128	56	130	37
-N(Li)Pyr	2619	0.085	129	51	88	18
-SO ₂ N(Li)Naph	2626	0.082	94	49	75	30
-SANSI(Li ₂)	2772	0.136	89	50, 60	68	11



The variation of T_p and ΔH_{exo} is large on cooling of MEC-SIPEs in comparison to the precursor, mPEO₅₅-OH (see **Table II-7**). The degree of crystallisation is decreased by functional end-group, as demonstrated by the decrease in ΔH_{exo} . The rate of the crystallisation affects the temperature at which the peak enthalpy change occurs. Slower crystallisation processes will have lower T_p of the corresponding ΔH_{exo} process. No definitive trend is apparent with respect the mass fraction of functional end-groups. Not only does the functional end-group affect the degree of crystallinity in the MEC-SIPE, but also the kinetics of the crystallisation.

3.2. The Dependence of Thermal Transitions on the PEO chain length

3.2.1. The Precursor mPEO_n-OH

The thermal transitions of PEO and of MEC-SIPEs based on PEO are profoundly affected by the length of the PEO chain. The thermal behaviours of the MEC-SIPEs are reported relative to the mPEO_n-OH precursors to better understand the effect of the functional end-group. As will be

described in this section (*vide supra*), a number of thermal transitions are observed during a heating or cooling DSC scans applied to certain polymer samples. This is true for the relatively simple mPEO_n-OH precursors as well as for the MEC-SIPEs, which have interacting ionic end-groups. A first order endothermic process on heating of a high M_w semi-crystalline polymer might be designated the enthalpy of melting (ΔH_m) of crystalline phases. This is the case for the mPEO_n-OH precursors having longer chains (EO_n= 55 and 160). However, the polymers having shorter chains (EO_n= 8, 10, and 20) exhibit several transitions on heating and cooling in the -40 °C to +100 °C range. A single type of polymer organisation cannot "melt" more than once. Therefore, there must be more than one type of bulk organisation of polymers that exhibit multiple endothermic processes on heating.

The particular nature of the observed transitions cannot be defined by DSC analysis alone. Characterisation of the polymers by DSC at different scanning rates, together with X-ray diffraction analysis and/or polarised optical microscopy (POM) together might reveal what types of macromolecular (dis)order are present. However, one can reasonably assume that, in the -40 °C to +100 °C range, the total transformation is from **i**) a solid polymer having some degree of organisation at low temperature to **ii**) a polymer melt at high temperature. The different transitions are therefore identified purely as exothermic (ΔH_{exo}) and endothermic (ΔH_{endo}) and not as specific enthalpy changes of crystallisation or melting. The characteristic temperature these transitions is quoted as that of the maximum enthalpy change. Each energy transition is thus reported according to an energy change (ΔH) and its associated peak temperature (T_p).

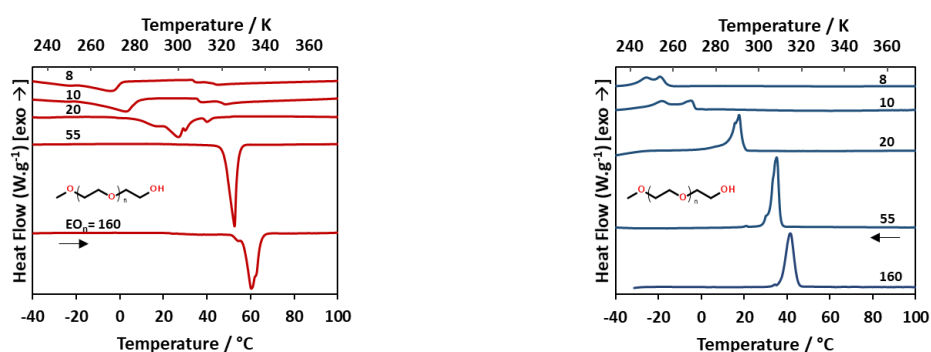


Figure II-38: DSC thermograms on heating (left) and cooling (right) of mPEO_n-OH having different PEO chain lengths. The number of repeating units (EO_n= 8, 10, 20, 55, and 160) are labelled for each trace. The arrows indicated the directions of heating (→) and cooling (←). The traces are individually normalised according to the sample mass (W.g⁻¹). The heating/cooling rate is 5°C.min⁻¹. The second heating and cooling DSC scans for each sample are displayed.

The thermal transitions of the mPEO_n-OH precursors are presented in DSC traces displayed in **Fig. II-38**. On heating, the peak temperature (T_p) of the ΔH_{endo} process decreases from PEO₁₆₀-OH (T_p = 60 °C) to PEO₅₅ (T_p = 53 °C). However, four transitions of mPEO₂₀-OH, and two transitions are observed for each of mPEO₁₀-OH and PEO₈-OH (**Fig. II-36**). On cooling, the temperature of crystallisation decreases as the PEO chain length decreases, from PEO₁₆₀-OH (T_p = 42 °C) to PEO₅₅-OH (T_p = 35 °C). The mPEO₂₀-OH has an asymmetric endothermic trace (T_p = 18 °C) with a skew towards low temperature. Two exothermic transitions are observed on cooling of each of PEO₁₀ (T_p = -5 °C, -18 °C) and PEO₈ (T_p = -19 °C, -26 °C) (**Fig. II-37**). The ΔH_{endo} on heating and the ΔH_{exo} on cooling decrease as the chain length decreases from mPEO₅₅-OH to mPEO₈-OH. However, the enthalpy changes of mPEO₁₆₀-OH are lower than those of mPEO₅₅-OH. This might be related to the dispersity in mass (\mathcal{D}_m) of the samples: the mPEO₁₆₀-OH might have a higher \mathcal{D}_m than mPEO₅₅-OH.

If this is true, the plasticising effect of low M_w chains could reduce the enthalpy of the thermal transitions. The temperatures of the transitions remain higher than those of mPEO₅₅-OH due to positive skew originating from the entanglement of higher M_w chains.

Table II-8: The peak temperature (T_p / °C) of thermal transitions observed by DSC of mPEO_n-OH having different PEO chain lengths (DP_n / $EO_n= 8, 10, 20, 55,$ and 160). The T_p is defined as the temperature of the maximum recorded change in enthalpy (ΔH / $J.g^{-1}$). The T_p values are listed intuitively, increasing from left to right. Overlapping peaks are grouped by parentheses [T_p]. The data correspond to the DSC thermograms of heating (Fig. 36) and cooling (Fig. 37) shown above (traces A-D).

EO_n		<i>Heating: T_p (°C) / ΔH_{endo} ($J.g^{-1}$)</i>		<i>Cooling: T_p (°C) / ΔH_{exo} ($J.g^{-1}$)</i>	
8	T_p (°C)	[-24 -4]	[35 45]	[-26 -19]	
	ΔH ($J.g^{-1}$)	91	34	-73	
10	T_p (°C)	3	[37 49]	[-18 -5]	
	ΔH ($J.g^{-1}$)	113	52	-103	
20	T_p (°C)	[16 27 30 40]		18	
	ΔH ($J.g^{-1}$)	143		-117	
55	T_p (°C)		53		35
	ΔH ($J.g^{-1}$)		168		-167
160	T_p (°C)		60		42
	ΔH ($J.g^{-1}$)		159		-161

The ΔH and the temperatures of the peak enthalpy change are summarised in **Table 8**. The numerous peaks observed on and cooling of mPEO_n-OH having shorter chains ($EO_n= 8, 10,$ and 20) are overlapped and often more than one peak must be integrated at once. Thus, the enthalpy changes of the individual peaks often cannot be deconvoluted with the present data set. A heating and cooling rate of $5^\circ C.min^{-1}$ was the best compromise in terms of peak and baseline fidelity, however variation of the heating and cooling rate in DSC could help to deconvolute the complex transitions observed.

3.2.2. MEC-SIPes based on mPEO_n-OH

Complex thermal transitions are observed for the MEC-SIPes. As presented above for the mPEO_n-OH precursors, the small peaks of transitions on heating often overlap and cannot be deconvoluted at constant heating rate. Specific enthalpy changes cannot be assigned to these thermal transitions. The exothermic transitions on cooling of MEC-SIPes having short chains ($EO_n= 8, 10, 20$) are often not visible at the selected cooling rate of $5^\circ C.min^{-1}$. The specific natures of all the numerous transitions observed of the reported library of MEC-SIPes in this work, having a range of PEO chain lengths and different types of end-groups, cannot be deconvoluted from the presently available data. What can be quantified is the total enthalpy change on heating of the EC-SIPes (discussed in Section 3.3).

Presented below is a brief overview of the observed DSC traces. The following general trends are observed:

1. The addition of an ionic group to the chain-end shifts the T_p of thermal transitions.
2. The MEC-SIPes have smaller enthalpy changes than the corresponding mPEO_n-OH precursor.
3. The numerous ΔH_{endo} transitions on heating of MEC-SIPes having $EO_n= 20$ shift in T_p relative to the mPEO₂₀-OH precursor. The change in T_p is **i)** related to the functional end-group and **ii)** different for different transitions at constant heating rate.
4. Exothermic transitions are observed on *heating* of some MEC-SIPes having $EO_n= 20$ (mPEO_n-SO₃Li, -OC(O)PhSO₃Li, and -SO₂N(Li)Naph). These are melting processes that were kinetically trapped during cooling.

5. Stretching of transitions on heating and cooling towards low temperature (negative skew) is often observed relative to the mPEO_n-OH precursor. This might be the result of the rate of temperature change acting to **i)** blend multiple processes to appear as a single first order transition, and/or **ii)** shift the peak temperature of a slow thermal transition.

The above points (1→5) are exemplified by the thermal transitions of mPEO_n-SO₃Li (**Fig. II-39**).

I. On heating:

(1, 2) The T_p and ΔH_{endo} of thermal transitions observed on cooling mPEO_n-SO₃Li are smaller than those of the mPEO_n-OH precursors having the same chain length. The ΔH_{endo} of the short chain polymers are very much decreased relative to mPEO_n-OH. The effect of the ionic end-groups on the bulk thermal properties of the MEC-SIPE might increase non-linearly relative to a decrease in EO_n. For example, the transition temperatures on heating of mPEO₈-SO₃Li are higher than those of mPEO₁₀-SO₃Li. One might expect the MEC-SIPE having the shorter chain to melt first, however the higher concentration of ionic end-groups in the MEC-SIPE having EO_n= 8 appears to reverse this trend. **(3)** The ΔH_{endo} and T_p of mPEO₂₀-SO₃Li have lower values compared to mPEO₂₀-OH. **(4)** Unlike the precursor, a ΔH_{exo} peak is observed *on heating* of mPEO₂₀-SO₃Li. This is evidence of the crystallisation of structures that had become kinetically trapped during the previous cooling ramp. These are subsequently destroyed by heating in the 20-60 °C temperature range. **(5)** Although the T_p of transitions of the mPEO_n-SO₃Li having longer chains (EO_n= 55 and 160) are similar to those of the precursors, the magnitude of ΔH_{endo} is decreased and there is considerable stretching of these transitions towards lower temperatures.

II. On cooling:

(1, 2) The ΔH_{exo} of thermal transitions of mPEO_n-SO₃Li are smaller than those of the mPEO_n-OH precursors having the same EO chain length, and the corresponding peak temperatures are shifted. The ΔH_{exo} of mPEO_n-SO₃Li having longer chains (EO_n= 55 and 160) have lower enthalpy change and occur at lower temperatures. Two small ΔH_{exo} transitions are observed on cooling of mPEO₈-SO₃Li ($T_p = 5\text{ °C}, -11\text{ °C}$); none are observed on cooling of mPEO₁₀-SO₃Li.

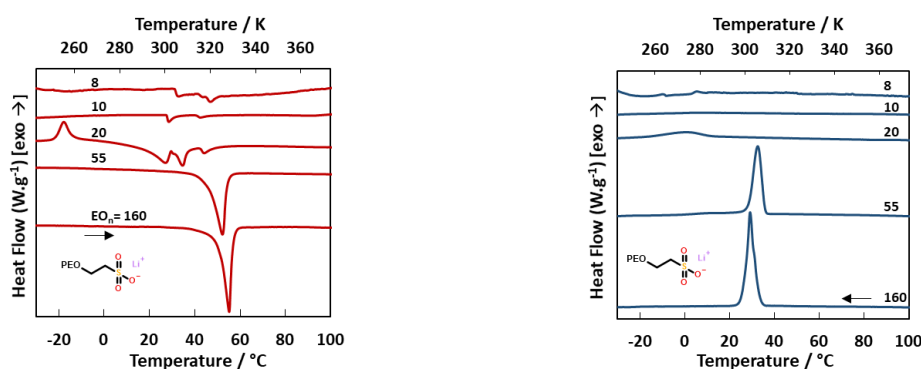


Figure II-39: DSC thermograms on heating (left) and cooling (right) of mPEO_n-SO₃Li having different PEO chain lengths. The direction of heating (→) and cooling (←) are indicated. The traces are individually normalised according to the sample mass (W.g⁻¹). The heating/cooling rate is 5°C.min⁻¹. The second heating and cooling DSC scans are displayed for each sample.

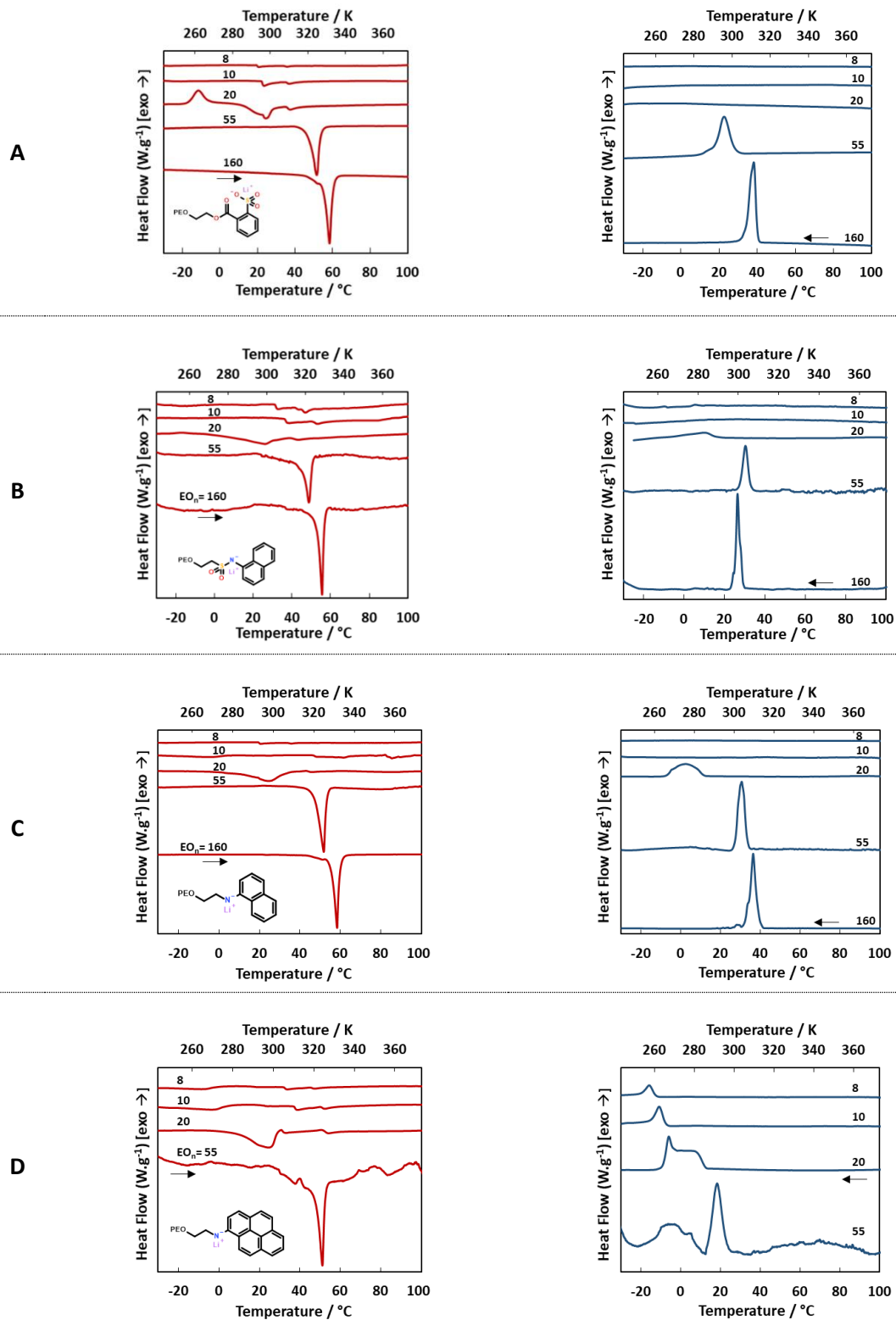


Figure II-40: DSC thermograms on heating (left) and cooling (right) of MEC-SIPes having different functional end-groups: -OC(O)PhSO₃Li (A), -SO₂N(Li)Naph (B), -N(Li)Naph (C), and -N(Li)Pyr (D). The traces are labelled with the number of EO repeating units of the EC-SIPE (EO_n= 8, 10, 20, 55, and 160). The arrows indicate the direction of heating (→) and cooling (←). The traces are individually normalised according to the sample mass (W.g⁻¹). The heating/cooling rate is 5°C.min⁻¹. The second heating and cooling DSC scans for each sample are displayed.

Similar trends are observed of the MEC-SIPEs having other functional end-groups (**Fig. II-40, A-D**).

I. On Cooling:

Of the MEC-SIPEs having the shortest chains ($EO_n = 8$ and 10), only $mPEO_n-SO_2N(Li)Naph$ (**B**) and $mPEO_n-N(Li)Pyr$ (**D**) exhibit ΔH_{exo} transitions on cooling. No ΔH_{exo} processes are observed on cooling of the $mPEO_n-OC(O)PhSO_3Li$ having $EO_n = 8, 10,$ and 20 (**A**).

The $mPEO_{20}-N(Li)Naph$ has a broad, low-temperature ΔH_{exo} on cooling (**B**; $T_p = 2$ °C) that is lower than the corresponding transition of $mPEO_{20}-SO_2N(Li)Naph$ (**C**; $T_p = 11$ °C). Note that these MEC-SIPEs differ in only the inclusion or absence of the $-SO_2-$ unit of the end-group, yet this is enough to yield this change in their thermal behaviours. The decrease in the apparent ΔH_{exo} on cooling and the appearance of the ΔH_{exo} on heating of $mPEO_{20}-SO_2N(Li)Naph$ might be related to the interaction kinetics of the $-SO_2N(Li)Naph$ end-group. The higher T_p of the $mPEO_{20}-SO_2N(Li)Naph$ might be a consequence of the interaction energy of the end-group. The difference in interaction energy might result from dipole interactions and steric restrictions originating from the $-SO_2-$ unit of the aryl sulfonamide. For example, thermal rotation around the sulfonamide linkage might be slower than rotation about the secondary amine. This could be the cause of the higher T_p and lower ΔH_{exo} on cooling of $mPEO_{20}-N(Li)Naph$, and the appearance of the ΔH_{exo} on heating.

II. On heating:

The ΔH_{exo} transitions having T_p close to $0^\circ C$ of the short chain ($EO_n = 8$ and 10) $mPEO_n-OH$ precursors are shifted to lower temperatures in the MEC-SIPEs. As with $mPEO_{20}-SO_3Li$ (**Fig. II-39**), a ΔH_{exo} process is observed on heating of $mPEO_{20}-OC(O)PhSO_3Li$ (**Fig. II-40, A**), and $mPEO_{20}-SO_2N(Li)Naph$ (**Fig. II-40, B**). The multiple ΔH_{exo} transitions of $mPEO_{20}-OH$ in the $20-40^\circ C$ range are very much blended in the EC-SIPEs having $EO_n = 20$ and different functional end-groups: $-OC(O)PhSO_3Li$ (**A**), $-SO_2N(Li)Naph$ (**B**), and $-N(Li)Naph$ (**C**). Three distinct ΔH_{exo} transitions are observed on heating of $mPEO_{20}-N(Li)Pyr$ (**D**). Stretching of the ΔH_{exo} transition to lower temperature is observed of every EC-SIPE having $EO_n = 55$.

Of particular interest is the $mPEO_{20}-N(Li)Pyr$, which has one large and two small ΔH_{exo} transitions on heating (**D**). The asymmetrical shape of the first large transition ($T_p = 25^\circ C$) implies that this trace comprises more than one process. Indeed, an asymmetric trace is observed on cooling of this MEC-SIPE. The $mPEO_n-N(Li)Pyr$ having short chains ($EO_n = 8, 10$) exhibit thermal processes that have similar T_p to their $mPEO_n-OH$ precursors but with ΔH_{endo} and ΔH_{exo} that are lower. The $mPEO_n-N(Li)Pyr$ has the most complex behaviour on heating and on cooling, exhibiting broad transitions in both directions.

3.3. The Endothermic Enthalpy Change of Thermal Transitions on Heating

3.3.1. Evolution of Enthalpy Relative to End-Group Design and PEO Chain Length

The magnitude of the enthalpy change of thermal transitions is lower for MEC-SIPEs having shorter PEO chains. Furthermore, the MEC-SIPEs have lower ΔH_{exo} and ΔH_{endo} in comparison to their $m\text{PEO}_n\text{-OH}$ precursors. At constant chain length, $\phi_{m(\text{EGrp})}$ increases proportionally to the mass of the functional end-group. The ionic end-groups are large in comparison to the hydroxyl end-group of the precursor and so have higher ϕ_{EGrp} . The endothermic enthalpy change (ΔH_{endo}) is presented as the total energy transferred during all the thermal transitions that occur when the polymers are heated from low temperature (-40°C) to the melt state at $+100^\circ\text{C}$. In the case of $m\text{PEO}_{55}\text{-OH}$ and $m\text{PEO}_{160}\text{-OH}$, this corresponds to an endothermic process with a single minimum in energy. The ΔH_{endo} of the polymers having lower EO_n is the sum of all the process observed upon heating of the sample. Thus, ΔH_{endo} represents the order-to-disorder enthalpy change of the presented polymers. The total ΔH_{endo} defined in this way, across the measured temperature range (from -40°C to 100°C), is plotted as a function of ϕ_{EGrp} . The value of ΔH_{endo} tends to decrease with decreasing EO_n and increasing ϕ_{EGrp} for a set of polymers having the same functional end-group.

The total ΔH_{endo} of the thermal transitions observed on heating are plotted as a function of the mass fraction of the end-group (ϕ_{EGrp}) in **Figs. II-41→44**). In the case of the $m\text{PEO}_n\text{-OH}$ precursors, the end-group is the hydroxyl (R-OH) group and is relatively small compared to the polymer chain (**Fig. II-41**). The decrease in the magnitude of ΔH_{endo} is therefore very steep as a function of ϕ_{EGrp} . The addition of the salt LiTFSI to PEO plasticizes the polymer and decreases ΔH_{endo} . The value of ΔH_{endo} of the $m\text{PEO}_{60}\text{m/LiTFSI SiP}$ blend decreases with increasing mass fraction of salt (**Fig. II-41**; $\phi_{m(a)}$; $a = \text{LiTFSI}$). The enthalpy change of heating these polymers is compared to the enthalpy change of melting fully crystalline PEO having $M_w = 4000 \text{ g}\cdot\text{mol}^{-1}$ ($\Delta H_m = 215.6 \text{ J}\cdot\text{g}^{-1}$).^[15] The observed enthalpy change on heating the polymers in this work can be expressed as a fraction of this maximum value, yielding an estimate of the degree of crystallinity of the polymers. By this estimate, the neat polymers having $\text{EO}_n = 55$ ($2400 \text{ g}\cdot\text{mol}^{-1}$) and $\text{EO}_n = 160$ ($7050 \text{ g}\cdot\text{mol}^{-1}$) are 70-80 % crystalline under the applied thermal history of cooling from the melted state (at $+100^\circ\text{C}$) at a rate of $5^\circ\text{C}\cdot\text{min}^{-1}$ to -40°C . The addition of LiTFSI to $m\text{PEO}_{60}\text{m}$ decreases the crystallinity of the polymer from around 50 % (EO/Li= 60) to around 10 % (EO/Li= 10) (**Fig. II-41**).

Figures II-41→II-44: The endothermic enthalpy change ($-\Delta H_{\text{endo}}$) on heating of polymers from -40°C to $+100^{\circ}\text{C}$ ($+5^{\circ}\text{C}\cdot\text{min}^{-1}$) at a function of the mass fraction of ionic, polymer end-groups ($\phi_{m(\text{EGrp})}$). The percentage crystallinity of the sample is calculated as a fraction of ΔH_m of fully crystalline PEO having $M_w = 4000 \text{ g}\cdot\text{mol}^{-1}$ ($215.6 \text{ J}\cdot\text{g}^{-1}$). The $-\Delta H_{\text{endo}}$ of MEC-SIPEs is compared to i) the $m\text{PEO}_n\text{-OH}$ precursors having different DP_n ($\text{EO}_n = 160, 55, 20, 10,$ and 8) and ii) $m\text{PEO}_{60}\text{m/LiTFSI}$ of different EO/Li ratios (EO/Li = 60, 20, and 10) (Fig. II-41). The EO_n values for polymers are quoted next to the data points. The MEC-SIPEs are listed below each figure. The lines are drawn as a guide for the eye only.

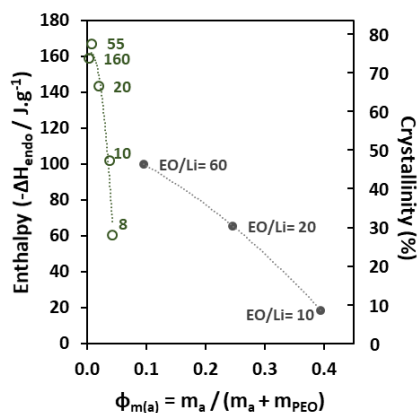


Figure II-41: $-\Delta H_{\text{endo}}$ vs. $\phi_{m(\text{EGrp})}$ of MEC-SIPEs i) $m\text{PEO}_n\text{-OH}$ (\circ) and $m\text{PEO}_{60}\text{m/LiTFSI}$ of different EO/Li ratios (\bullet). $\phi_{m(a)}$: for $m\text{PEO}_n\text{-OH}$, $a = \text{OH}$; for the SiP, $a = \text{LiTFSI}$.

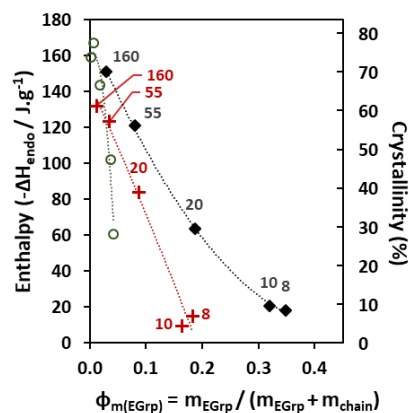


Figure II-42: $-\Delta H_{\text{endo}}$ vs. $\phi_{m(\text{EGrp})}$ of MEC-SIPEs ii) $m\text{PEO}_n\text{-OH}$ (\circ), $m\text{PEO}_n\text{-SO}_3\text{Li}$ ($+$), and $m\text{PEO}_n\text{OC(O)PhSO}_3\text{Li}$ (\blacklozenge).

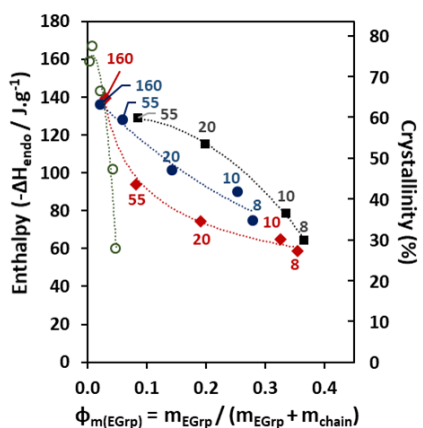


Figure II-43: $-\Delta H_{\text{endo}}$ vs. $\phi_{m(\text{EGrp})}$ of EC-SIPEs iii) $m\text{PEO}_n\text{-OH}$ (\circ), $m\text{PEO}_n\text{-SO}_2\text{N(Li)Naph}$ (\blacklozenge), $m\text{PEO}_n\text{-N(Li)Naph}$ (\bullet), and $m\text{PEO}_n\text{-N(Li)Pyr}$ (\blacksquare)

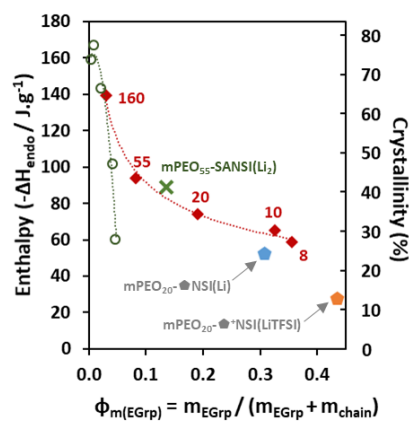


Figure II-44: $-\Delta H_{\text{endo}}$ vs. $\phi_{m(\text{EGrp})}$ of EC-SIPEs iv) $m\text{PEO}_n\text{-OH}$ (\circ), $m\text{PEO}_n\text{-SO}_2\text{N(Li)Naph}$ (\blacklozenge), $m\text{PEO}_{55}\text{-SANSI(Li}_2\text{)}$ (\times), $m\text{PEO}_{20}\text{-NSI(Li)}$ (\bullet), and $m\text{PEO}_{20}\text{-NSI(LiTFSI)}$ (\blacklozenge)

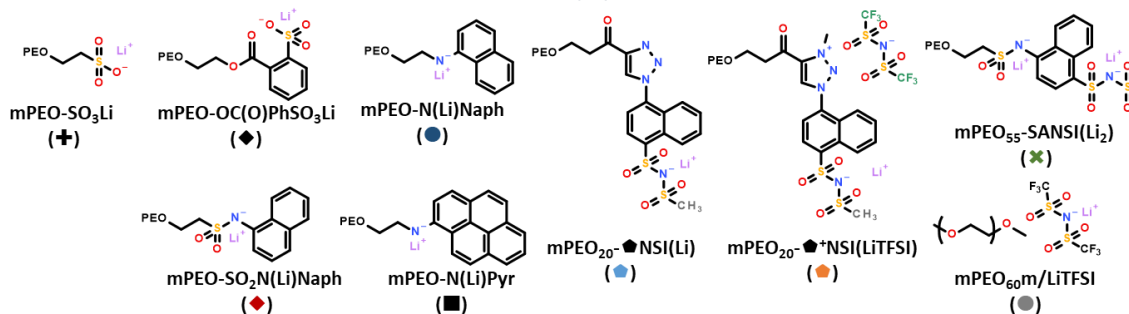


Fig. II-45 and Fig. II-46: The conductivity ($\sigma / \text{S}\cdot\text{cm}^{-1}$) as a function of Temperature ($T / 10^3\cdot\text{K}^{-1}$) for the MEC-SIPE $\text{mPEO}_n\text{-SO}_3\text{Li}$ (Fig. II-52) and $\text{mPEO}_n\text{-OC(O)PhSO}_3\text{Li}$ (Fig. II-53) having different EO/Li ratios. The EO/Li ratio is fixed according to the polymer DP_n (EO_n). The experimental data of EO/Li= 55 (\square), EO/Li= 20 (\circ) and EO/Li= 10 (\triangle) and EO/Li=8 (\diamond) were recorded on cooling from 100 °C. The data are fitted to the VTF model (red lines, -).

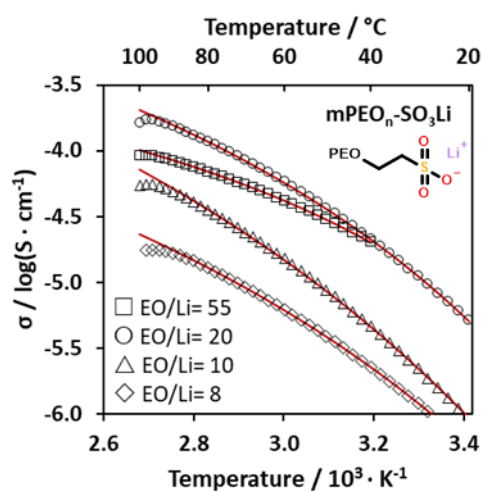


Figure II-45: The conductivity ($\sigma / \text{S}\cdot\text{cm}^{-1}$) of $\text{mPEO}_n\text{-SO}_3\text{Li}$ as a function of Temperature ($T / 10^3\cdot\text{K}^{-1}$). The data is reproduced from Figure II-5.

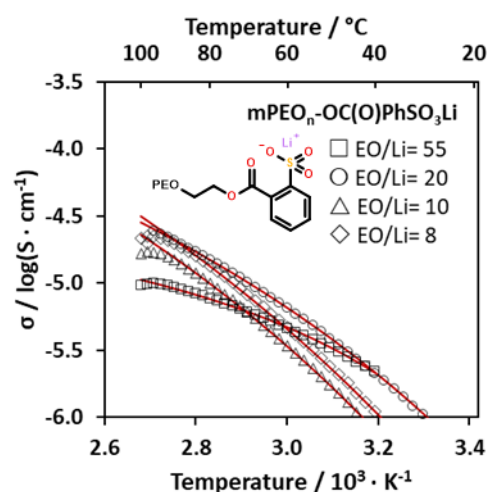


Figure II-46: The conductivity ($\sigma / \text{S}\cdot\text{cm}^{-1}$) of $\text{mPEO}_n\text{-OC(O)PhSO}_3\text{Li}$ as a function of Temperature ($T / 10^3\cdot\text{K}^{-1}$). The data is reproduced from Figure II-8.

Decreasing the PEO chain length and increasing $\phi_{\text{m(EGrp)}}$ tends to diminish the degree of crystallinity. The ΔH_{endo} of $\text{mPEO}_n\text{-SO}_3\text{Li}$ is lower than the corresponding $\text{mPEO}_n\text{-OH}$ having the same DP_n (Fig. II-42). There is also a positive shift in $\phi_{\text{m(EGrp)}}$ due to the larger mass of the functional end-group. The decrease in ΔH_{endo} of $\text{mPEO}_n\text{-OC(O)PhSO}_3\text{Li}$ is similar to that of $\text{mPEO}_n\text{-SO}_3\text{Li}$ (Fig. II-42). However, the phenylsulfonate end-group has higher mass than the sulfonate and so there is a larger shift towards higher values of $\phi_{\text{m(EGrp)}}$. Despite the similar values of ΔH_{endo} for these EC-SIPEs, the σ of $\text{mPEO}_n\text{-SO}_3\text{Li}$ is higher than that of $\text{mPEO}_n\text{-OC(O)PhSO}_3\text{Li}$. There is one order of magnitude difference in σ (Fig. II-45 & Fig. II-46) of the two MEC-SIPEs having $\text{EO}_n=55$ and almost identical *order-to-disorder* enthalpy change (Fig. II-42). For the MEC-SIPEs having different PEO chain lengths, the σ of $\text{mPEO}_n\text{-SO}_3\text{Li}$ (Fig. II-54) is higher than the corresponding $\text{mPEO}_n\text{-OC(O)PhSO}_3\text{Li}$ (Fig. II-55) for all chain lengths except $\text{EO}_n=8$. The effect of the stereochemistry and electron-withdrawing ability of the aryl ring of $\text{mPEO}_n\text{-OC(O)PhSO}_3\text{Li}$ to decrease ionic conductivity relative to $\text{mPEO}_n\text{-SO}_3\text{Li}$ is minimised by decreasing the EO/Li ratio.

The minimum values of ΔH_{endo} of the MEC-SIPEs having $-\text{SO}_2\text{N(Li)Naph}$, $-\text{N(Li)Naph}$, and $-\text{N(Li)Pyr}$ end-groups do not fall below the lowest ΔH_{endo} of the $\text{mPEO}_n\text{-OH}$ precursor ($\text{EO}_n=8$) (Fig. II-43). These MEC-SIPEs having **i**) functional end-groups bearing multi-ring aromatic rings and **ii**) the same polymer-anion-aryl configuration have a correlation of higher ΔH_{endo} with higher ionic conductivity. For example, $\text{mPEO}_{55}\text{-SO}_2\text{N(Li)Naph}$ has the lowest ΔH_{endo} of the $\text{EO}_n=55$ MEC-SIPEs (Fig. II-43), and also the lowest ionic conductivity (Fig. II-2). The $\text{mPEO}_n\text{-N(Li)Pyr}$ has the highest ΔH_{endo} (Fig. II-43) and also the highest σ (Fig. II-13) for every PEO chain length tested ($\text{EO}_n=8, 20$, and 55), except for the MEC-SIPE having $\text{EO}_n=10$. The $\text{mPEO}_{10}\text{-N(Li)Naph}$ has the highest ΔH_{endo} (Fig. II-50) and also the highest σ (Fig. II-12) of the MEC-SIPEs having $\text{EO}_n=10$.

The highest ionic conductivity of all the MEC-SIPEs presented was achieved with $\text{mPEO}_{20}\text{-N(Li)Pyr}$ (Fig II-13). This $\text{mPEO}_{20}\text{-N(Li)Pyr}$ has the highest ΔH_{endo} ($115 \text{ J}\cdot\text{g}^{-1}$) of any of the presented MEC-SIPEs based on $\text{mPEO}_{20}\text{-OH}$. This value of ΔH_{endo} is close to those measured for some MEC-SIPEs having $\text{EO}_n=55$ and ΔH_{endo} in the $120\text{-}130 \text{ J}\cdot\text{g}^{-1}$ range (Fig II-42-43). This relation of higher ΔH_{endo}

with higher σ is contrary to the expectation that a greater fraction of amorphous phases (and therefore lower ΔH_{endo}) yields higher ionic conductivity. This might be because the ΔH_{endo} of the MEC-SIPEs, and in particular mPEO_n-N(Li)Pyr, is a consequence of the organisations of the PEO chain and of the MEC-SIPE functional end-groups. In this case, the total ΔH_{endo} transformation (from the ordered state at low temperature to a disordered state at high temperature) represents the destruction of **i**) interactions between PEO segments, **ii**) interactions between functional end-groups. The end-groups might moreover be either incorporated into or expelled from the structural organisation of PEO segments. Strongly-interacting end-groups could furthermore exclude PEO segments from the organisation of MEC-SIPE chain-ends by preferential ion-ion and ion-dipole interactions. If such competing processes are present in MEC-SIPEs, they would act concertedly to organise the MEC-SIPEs in the bulk state.

The "double-salt" mPEO₅₅-SANSI(Li₂) has higher σ (**Fig. II-3**) and lower ΔH_{endo} (**Fig. II-44**) than mPEO₅₅-SO₂N(Li)Naph having the same PEO chain length (EO_n= 55). The mPEO₂₀-**◆**NSI(Li), which has a very bulky end-group, has the lowest ΔH_{endo} (51.2 J.g⁻¹) of all the MEC-SIPEs based on mPEO₂₀-OH (**Fig. II-44**). Quaternisation of this MEC-SIPE yields the zwitterionic mPEO₂₀-**◆**⁺NSI(LiTFSI), which has lower ΔH_{endo} (26.6 J.g⁻¹) (**Fig. II-44**). This reduction in ΔH_{endo} is directly correlated with two effects of the quaternisation: **i**) the addition of the TFSI⁻ anion and **ii**) the change of the stereochemistry of the linker. The triazole of mPEO₂₀-**◆**NSI(Li) has a bent conformation due to the lone pair of the 1-nitrogen. Quaternisation of this function changes the hybridisation of this nitrogen atom from Sp₃ to Sp₂. Incorporation of the planar triazolium into the end-group architecture results in a planar geometry extending from the ester to the naphthalene rings. Changing from the bent geometry of the triazole link to the planar of the triazolium link will influence the packing of the MEC-SIPE end-group in the bulk state. These two effects of quaternisation act concertedly to decrease the ΔH_{endo} of the transition from the ordered to the disordered state of mPEO₂₀-**◆**⁺NSI(LiTFSI).

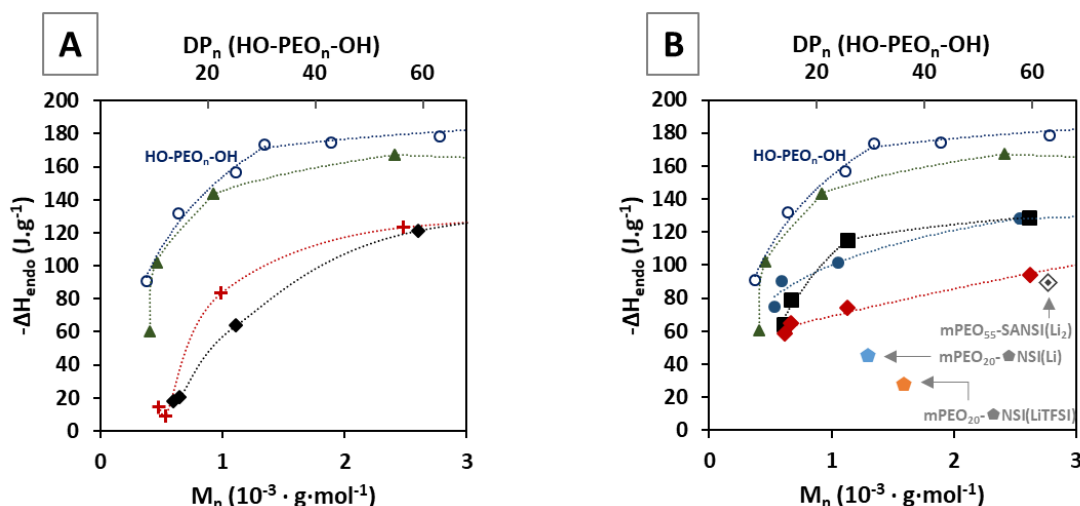
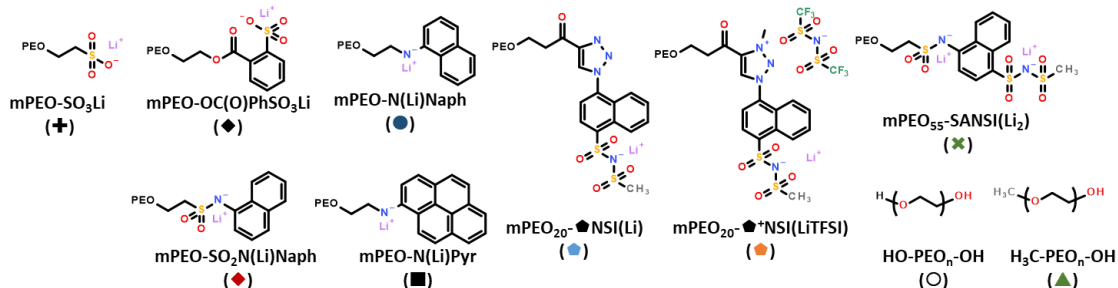


Figure II-47: The ΔH_{endo} of selected EC-SIPES as a function of M_n ($\text{g}\cdot\text{mol}^{-1}$) are compared with $m\text{PEO}_n\text{-OH}$ precursors (\blacktriangle), and values for $\text{HO-PEO}_n\text{-OH}$ (O) reported in the literature.^[16] (Left, A): MEC-SIPES having $-\text{SO}_3\text{Li}$ ($\color{red}+$), $-\text{OC}(\text{O})\text{PhSO}_3\text{Li}$ (\blacklozenge) end-groups. (Right, B): $-\text{SO}_2\text{N}(\text{Li})\text{Naph}$ ($\color{red}\blacklozenge$), $-\text{N}(\text{Li})\text{Pyr}$ (\blacksquare), $-\text{N}(\text{Li})\text{Naph}$ (\bullet), $-\text{SANSI}(\text{Li}_2)$ (\blacklozenge), $-\text{NSI}(\text{Li})$ (\bullet) and $-\text{NSI}(\text{LiTFSI})$ ($\color{orange}\bullet$) end-groups. The lines are drawn as a guide for the eye only.



The ΔH_{endo} of selected MEC-SIPES are compared to the ΔH_m of $\text{HO-PEO}_n\text{-OH}$ reported in the literature (Fig. II-54).^[16] The DP_n axis of the figure applies only to the polymers of the literature and to the $m\text{PEO}_n\text{-OH}$ precursors; the polymers in this work are plotted according to M_n only. The series of $m\text{PEO}_n\text{-OH}$ precursors have good agreement with the bis-hydroxy terminated polymers of the literature at low M_n but have lower ΔH_{endo} than expected for the higher DP_n polymers ($\text{EO}_n=55, 160$). The literature values come from PEO samples that were crystallised over very long time periods. However, in the present report a fixed thermal history of cooling at $5^\circ\text{C}\cdot\text{min}^{-1}$ is applied. This time scale is too short (cooling too fast) to obtain fully crystalline (defect-free) samples of PEO. This is the most likely explanation for the divergence in the ΔH_{endo} of high DP_n $m\text{PEO}_n\text{-OH}$ precursors from their expected values.

However, the MEC-SIPES have significantly lower ΔH_{endo} . Whereas in Figs. II-42→II-44 this is presented as a function of the concentration of ionic end-groups, here the total ΔH_{endo} is a function of polymer M_n . Again, the trend for MEC-SIPES is those having higher ΔH_{endo} have higher σ . For example, The $m\text{PEO}_{20}\text{-SO}_3\text{Li}$ has higher σ than $m\text{PEO}_{20}\text{-OC}(\text{O})\text{PhSO}_3\text{Li}$ (Fig II-47, A). Similarly, the $m\text{PEO}_n\text{-N}(\text{Li})\text{Naph}$ and $m\text{PEO}_n\text{-N}(\text{Li})\text{Pyr}$ have higher σ than $m\text{PEO}_n\text{-SO}_2\text{N}(\text{Li})\text{Naph}$ (Fig. II-47, B). The $m\text{PEO}_{55}\text{-SANSI}(\text{Li}_2)$ and the triazole/triazolium MEC-SIPES are special cases without variation in PEO chain length. Furthermore, the plasticising effect of the TFSI⁻ anion prevents comparison of $m\text{PEO}_{20}\text{-NSI}(\text{LiTFSI})$ with the other MEC-SIPES having $\text{EO}_n=20$.

3.3.2. Evolution of Thermal Transitions by Variation Thermal History

The mPEO₂₀-N(Li)Pyr has the highest ionic conductivity of all MEC-SIPEs, and the highest crystallinity of MEC-SIPEs based on mPEO₂₀-OH. The high σ might be a consequence of a favourable structural ordering process of the MEC-SIPE. The structural organisation of the MEC-SIPE is destroyed on heating and large values of ΔH_{endo} are required to break this organisation. Three transitions are observed when mPEO₂₀-N(Li)Pyr was heated at 5°C.min⁻¹ from -40°C to +100°C. This implies that three types of structures are destroyed. Cycling of heating and cooling ramps in DSC measurements reveals that these structures are reversibly created at low temperatures and destroyed at high temperatures. Comparison of mPEO₂₀-N(Li)Pyr and its mPEO₂₀-OH precursor will reveal the effect of the end-group on the thermal transitions of the polymer.

Different types of structural organisation are formed through thermodynamically and kinetically controlled processes. Below a certain temperature, the thermal energy of the (macro)molecules in the bulk state is lower than the interaction energy of the molecules (or parts of a macromolecule). The distance (length scale) over which supramolecular organisation occurs is dependent on **i)** the concentration of the interacting species and **ii)** the time permitted for their diffusion and interaction in the bulk state. Thus, variation of the cooling rate will determine the extent to which interacting species can become organised. Observation of slow processes on cooling is difficult in practice because the ΔH_{exo} of the thermal transitions on forming organised structures will be spread over a wide temperature range when the sample is cooled. The measurement of ΔH_{exo} is highly dependent on the measurement conditions and experimental setup. For example, a cooling a sample from +100°C to -40°C at a rate of 0.10°C.min⁻¹ requires more than 23 hours. A measurement over this time period is susceptible to instrumental errors such as the stabilities of the baseline, the flow of inert gas, and stability of the thermostat.

However (macro)molecular organisation is often more easily destroyed than it is created. The ΔH_{endo} on heating provides indirect evidence of the structures that were created in the sample during the previous cooling scan. The thermal transitions of this champion MEC-SIPE were thus investigated by changing the rate of the cooling ramp in DSC and measuring ΔH_{endo} on heating at a constant rate (5°C.min⁻¹). The results are compared to the identical experiment performed on the mPEO₂₀-OH precursor. The first cooling ramp is 5.00°C.min⁻¹. This rate was decreased for successive cooling cycles, to the lowest rate of 0.10°C.min⁻¹. There is considerable evolution of thermal transitions of both the mPEO₂₀-OH precursor (**Fig. II-48**) and the mPEO₂₀-N(Li)Pyr (**Fig. II-49**) under these conditions.

The thermal transition observed close to ambient temperature on heating of mPEO₂₀-OH (**Fig. II-48**) has constant T_p and increasing ΔH_{endo} (66→102 J.g⁻¹) when the cooling rate is decreased from 5.00 to 0.10°C.min⁻¹ (**Table II-9**). The measured T_p of ca. 20-30°C is consistent with the temperature and the endothermic enthalpy change of melting extended chain crystals of low DP_n PEO,^[16] which have short chains (relative to the persistent length of PEO) that do not form folded-chain crystals.^[17] The crystalline phases formed by short-chain PEO (DP_n< ~40) are formed exclusively of extended chains. The increase in ΔH_{endo} (J.g⁻¹) on heating is proportional to an increase in the mass fraction of this type of molecular organisation. Therefore, decreasing the rate of cooling permits the organisation of a greater mass fraction of PEO segments into extended-chain crystalline phases.

Table II-9: The peak temperature (T_p / °C) and endothermic enthalpy change ($-\Delta H_{\text{endo}}$) of thermal transitions observed when heating mPEO₂₀-OH at 5°C.min⁻¹ after cooling ramps of decreasing rates (5.00, 2.50, 1.00, 0.50, 0.25, and 0.10°Cmin⁻¹). The $-\Delta H_{\text{endo}}$ marked (*) cannot be calculated due to the poorly defined baseline.

Cooling rate (°C.min ⁻¹)		T_p (°C)		
		$-\Delta H_{\text{endo}}$ (J.g ⁻¹)		
0.10	T_p	[20.0 25.7]	[43.7 ^a 65.5 ^b 76.0 ^c]	*
	ΔH	102.9		
0.25	T_p	[19.3 25.0]	37.5	69.6
	ΔH	85.0	32.5	2.4
0.50	T_p	[19.9 24.3 29.7]		60.3
	ΔH	77.4		2.7
1.00	T_p	[19.6 28.6]		54.6
	ΔH	76.0		3.2
2.50	T_p	[18.9 28.3]		50.1
	ΔH	75.0		2.6
5.00	T_p	28.6		48.8
	ΔH	66.0		9.2

Table II-10: The peak temperature (T_p / °C) and endothermic enthalpy change ($-\Delta H_{\text{endo}}$) of thermal transitions observed when heating mPEO₂₀-N(Li)Pyr at 5°C.min⁻¹ after DSC cooling scans of decreasing rates (5.00, 2.50, 1.00, 0.50, 0.25, and 0.10°Cmin⁻¹).

Cooling rate (°C.min ⁻¹)		T_p (°C)		
		$-\Delta H_{\text{endo}}$ (J.g ⁻¹)		
0.10	T_p	22.5	[38.9 49.0]	[72.6 ^a 78.0 ^b]
	ΔH	99.4	45.1	18.2
0.25	T_p	23.1	[39.0 45.6]	71.6
	ΔH	96.2	44.8	16.0
0.50	T_p	23.2	38.4	64.4
	ΔH	91.6	38.8	7.5
1.00	T_p	23.4	30.9	52.4
	ΔH	89.5	10.8	6.0
2.50	T_p	22.4	30.9	52.4
	ΔH	85.7	10.6	5.8
5.00	T_p	22.8	32.7	51.4
	ΔH	80.2	9.6	5.7

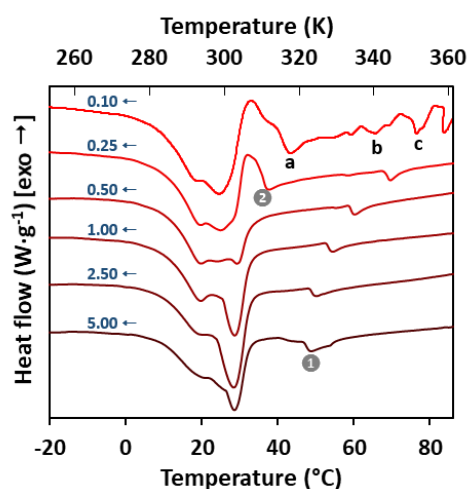


Figure II-48: The DSC thermograms of mPEO₂₀-OH measured *on heating* after cooling DSC scans of decreasing cooling rate (see Table II-9 for details). The rates of cooling of the precedent DSC scans are indicated. The traces are normalised according to the sample mass and displaced vertically by an arbitrary value. The labelled peaks (a, b, c) refer to values listed in Table II-9.

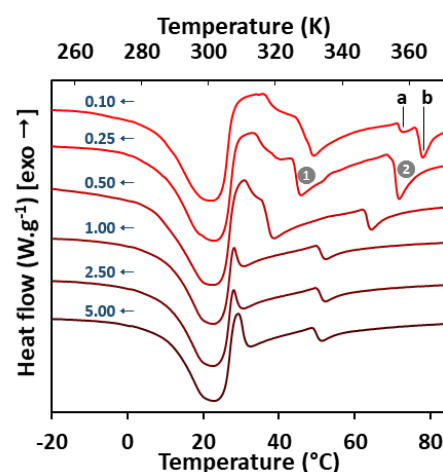


Figure II-49: The DSC thermograms of mPEO₂₀N(Li)Pyr measured *on heating* after DSC cooling scans of decreasing cooling rate (see Table II-10 for details). The rates of cooling of the precedent DSC scans are indicated. The traces are normalised according to the sample mass and displaced vertically by an arbitrary value. The labelled peaks (a, b) refer to values in Table II-10.

Two transitions having higher T_p appear when mPEO₂₀-OH is cycled with decreasing rate of the cooling scan: (1) a small ΔH_{endo} (**Fig. II-48**; 1), and (2) a larger ΔH_{endo} having $T_p \approx 38^\circ\text{C}$, that appears after the sample has been cooled at $0.25^\circ\text{C}\cdot\text{min}^{-1}$ (**Fig. II-48**; 2). The high temperature peak (1) evolves from $T_p \approx 50^\circ\text{C}$, after cooling at $5.00^\circ\text{C}\cdot\text{min}^{-1}$, to $T_p \approx 70^\circ\text{C}$ after cooling at $0.25^\circ\text{C}\cdot\text{min}^{-1}$ (**Table II-9**). This is higher than the T_p associated with crystallisation of PEO segments. However, the ΔH_{endo} of this peak (1) does not evolve significantly. The ΔH_{endo} , which is nearly constant, implies that the mass fraction of species involved in this type of organisation does not change when the rate of cooling is decreased. The magnitude of the ΔH_{endo} of the high T_p transition is small relative to the ΔH_{endo} of melting of the crystalline PEO chain segments. This small peak (1) might be the enthalpic contribution of the destruction of end-group interactions, which are a small mass fraction of the bulk (for mPEO₂₀-OH, $\phi_{\text{m(OH)}} \approx 0.02$). However, the type of the organisation might change. Then the difference in T_p is related to the strength of the association energy of the intermolecular interactions.

Under the cooling conditions used in this work, the ΔH_{endo} of mPEO₂₀-OH observed at $T \approx 20\text{-}30^\circ\text{C}$ is around 70 % crystalline by mass, by comparison to the trend of chain extended crystalline PEO reported in the literature (**Table II-9**; cooling rate = $0.10^\circ\text{C}\cdot\text{min}^{-1}$).^[16] The remaining 30 % of the sample mass is occupied either by organised molecules (or parts of molecules) or by amorphous domains. The existence of different types of organisation are evinced by the ΔH_{endo} observed in the $30\text{-}80^\circ\text{C}$ range.

The mPEO₂₀-OH has DP_n below a reasonable estimate of the upper limit for the DP_n of PEO that forms a majority of extended chain crystals ($EO_n < \sim 40$).^[16] The formation of these crystalline phases is enhanced by slower cooling rates because longer time scales minimise the kinetic entrapment of defects. The slower cooling rates permits extended ripening of the crystalline domains. This is observed as an increase in ΔH_{endo} when a larger mass fraction of these phases are melted in the next heating scan. Hydroxyl groups can allow for H-bonding interactions and are rejected by crystalline ordering of PEO segments. The hydroxyl groups are therefore assumed to be localized at the surface of crystalline phases, at the grain boundary of crystalline and amorphous phases. The interaction strength of H-bonding might be enhanced by ripening of the crystalline grains into larger domains having higher organisation at their grain boundaries. This leads to an increase in T_p of the small ΔH_{endo} process associated with the breaking of H-bonds. The ΔH_{endo} of this peak remains small because of the small mass fraction of hydroxyl end-groups and the short distances over which the H-bonding phases percolate.

The thermal transition of mPEO₂₀-N(Li)Pyr having $T_p = 22\text{-}23^\circ\text{C}$ (**Fig. II-49**) is identified to be the melting of PEO segments, by comparison to the behaviour of the mPEO₂₀-OH precursor (**Fig. II-48**). The ΔH_{endo} of this transition is higher when the rate of cooling lower, from $\Delta H_{\text{endo}} \approx 80 \text{ J}\cdot\text{g}^{-1}$ (cooling at $5.00^\circ\text{C}\cdot\text{min}^{-1}$) to $\Delta H_{\text{endo}} \approx 100 \text{ J}\cdot\text{g}^{-1}$ (cooling at $0.10^\circ\text{C}\cdot\text{min}^{-1}$) (**Table II-10**). Both the maximum value and the increase in ΔH_{endo} of the PEO segments of mPEO₂₀-N(Li)Pyr ($80.2 \rightarrow 99.4 \text{ J}\cdot\text{g}^{-1} = +24\%$) is less than that observed for the similar peak of mPEO₂₀-OH ($66.0 \rightarrow 102.9 \text{ J}\cdot\text{g}^{-1} = +55\%$).

The end-group mass fraction of mPEO₂₀-N(Li)Pyr ($\phi_{\text{m(EGrp)}} = 0.20$) is ten times larger than that of mPEO₂₀-OH ($\phi_{\text{m(EGrp)}} = 0.02$). The ΔH_{endo} of the high T_p transitions observed on heating of mPEO₂₀-N(Li)Pyr (**Fig. II-49**; 1 and 2) are larger than those of the precursor. The ΔH_{endo} and T_p of these transitions are independent of cooling rate when $dT/dt \geq 1.00^\circ\text{C}\cdot\text{min}^{-1}$ (**Table II-10**). However, both

ΔH_{endo} and T_p are higher when $dT/dt \leq 0.50^\circ\text{C}\cdot\text{min}^{-1}$. For example, $\Delta H \textcircled{1}$ ($44.8 \text{ J}\cdot\text{g}^{-1}$) and $\Delta H \textcircled{2}$ ($16.0 \text{ J}\cdot\text{g}^{-1}$) together represent 39 % of the total endothermic heat transfer on heating after cooling at $0.25^\circ\text{C}\cdot\text{min}^{-1}$, which is an increase from 16 % after cooling at $5.00^\circ\text{C}\cdot\text{min}^{-1}$ (**Table II-10**). After cooling at $0.10^\circ\text{C}\cdot\text{min}^{-1}$, four overlapping processes are observed above the melting temperature of the PEO segments ($T_p = 39, 49, 73,$ and 78°C) and represent 39 % of the total ΔH_{endo} observed on heating mPEO₂₀-N(Li)Pyr after a cooling ramp of $0.10^\circ\text{C}\cdot\text{min}^{-1}$. The change in ΔH_{endo} and T_p of processes above the melting of PEO in mPEO₂₀-N(Li)Pyr is dramatic when the cooling rate $dT/dt \leq 0.50^\circ\text{C}\cdot\text{min}^{-1}$, which means that these enthalpy changes correspond to organisation that occurs slowly on cooling.

The melting temperatures of the PEO segments in mPEO₂₀-N(Li)Pyr (**Table II-10**, $T_p = 23^\circ\text{C}$) and in mPEO₂₀-OH (**Table II-9**; when $dT/dt = 0.10^\circ\text{C}$, $T_p \approx 23^\circ\text{C}$) are lower than expected, by comparison to T_m reported for fully crystalline PEO previously reported by other authors.^[16] Comparing the melting of PEO segments in mPEO₂₀-N(Li)Pyr ($T_p = 23^\circ\text{C}$) with the literature is means to estimate the number of EO units per chain. The T_m reported in the literature is plotted as a function of polymer M_n (**Fig. II-50**). The data is fitted by an exponential curve over the appropriate range of PEO DP_n ($\text{EO}_n = 9\text{-}31$), corresponding to PEO that forms exclusively chain-extended crystals on cooling. Using the fitted formula, the observed T_p (23°C) corresponds to PEO having $\text{EO}_n \approx 14$ units. The equation used to estimate the number of EO units (**Eqn. II-14**) and examples of calculated values (**Table II-11**) are shown below. This number fits well with the 7/2 helical conformation of PEO segments in the bulk state, in which 7 repeating EO units constitute two turns of the helical pitch and have a periodicity of 19.2\AA .^[18]

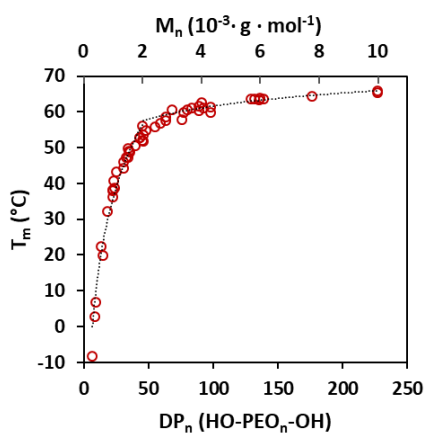


Figure II-50: The T_m ($^\circ\text{C}$) reported as values of peak enthalpy change of melting (ΔH_m) as a function of the DP_n of HO-PEO_n-OH. The data are taken from the literature.^[16,17,19] The lines are logarithmic fits of the data. The equation used: $\text{EO}_n = 9\text{-}46$, $T_m = 29.6 \cdot \ln(M_n) - 168.5$; $T_m = 29.6 \cdot \ln(\text{EO}_n) - 56.5$ [$R^2 = 0.97$].

Equation II-14: T_m ($^\circ\text{C}$) as a function of the Number Average Molar Mass ($M_n / \text{g}\cdot\text{mol}^{-1}$) of HO-PEO_n-OH, as determined by fitting the data displayed in Figure 57 ($\text{EO}_n = 9\text{-}46$, $R^2 = 0.97$).

$$T_m = 29.602 \cdot \ln(M_n) - 168.49$$

Table II-11: Example values obtained from Eqn. II-14.

T_m ($^\circ\text{C}$)	M_n ($\text{g}\cdot\text{mol}^{-1}$)	DP _n (EO_n)
22	623	13.8
23	645	14.2
24	667	14.7

This leads us to a revision of the oversimplified situation where one considers that a MEC-SIPE is composed of two chemically distinct parts: the PEO chain and the functional end-group. Indeed, the thermal properties of the polymer are not segregated precisely across the C-N bond (**Fig. II-51**). With the experimental data obtained from this work and the literature values of T_p , one can tentatively propose the EC-SIPE mPEO₂₀-N(Li)Pyr is assuming a segregated structure of phases determined by **i)** by the organisation of ethylene oxide units and **ii)** by the organisation of the functional end-groups (**Fig. II-58**). However, the PEO chain does not organise into crystalline phases having the ΔH_{endo} and T_p expected for PEO of 20 repeating units. The PEO chain is

apparently of lower DP_n . The EO units that behave in the manner of lower DP_n PEO could be located at the opposite end of the chain to the chemically distinct, functional end-group. These units can have thermal behaviour independent of the end-group and behave like "native" PEO. However, the EO units closer to the end-group are affected by its thermal transitions. These perturbed EO* units organise relative to the functional end-group at higher temperatures than the native PEO.

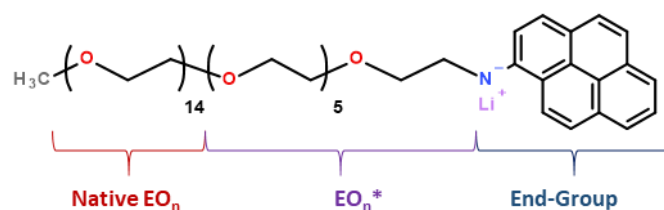


Figure II-51: An illustration of a hypothetical model of the MEC-SIPE mPEO₂₀-N(Li)Pyr. The poly(ethylene oxide) monomethyl ether chain is composed of two parts: i) "Native" EO_n units that crystallise and melt as expected of those in extended chain conformation, and ii) EO_n* units that are perturbed by the physicochemical character of the proximal functional End-Group.

The mass fractions of the phases are represented by the ΔH_{endo} observed on heating and are dependent on the cooling rate that determines the thermal history of the sample. The sample is disorganised at high temperature and then allowed to organise on cooling. When the cooling rate is lower, a higher mass fraction of the bulk is organised. The T_p of endothermic process related to the melting of native PEO chain segments ($T_p \approx 23^\circ\text{C}$) is lower than those of the functional end-group segments (having several transitions in the $T_p = 30\text{-}80^\circ\text{C}$ range). Therefore, one can expect the native PEO to become organised (crystalline) at lower temperatures, while the functional end-group segments can begin to become organised at higher temperatures. The driving forces of the organisation of these phases is not clear because several processes are likely to act concertedly in the bulk EC-SIPE. For example: whereas ionic end-groups might have electrostatic attraction at $T > T_m(\text{PEO})$, the thermal vibration of PEO chains might exclude bulky species such as the pyrene, thus promoting the aggregation of the end-groups. Pyrene itself might furthermore contribute to the organisation of end-groups through π - π stacking interactions. Each of these processes is dependent on temperature and cooling rate. The large difference in the ΔH_{endo} of the high T_p processes might be related to the interaction energy of the functional end-groups. The low ΔH_{endo} of hydroxyl groups of mPEO₂₀-OH might be explained by their short-range interactions and limited percolation through the bulk. The higher ΔH_{endo} of the end-groups of the MEC-SIPE might be explained by stronger end-group interactions that percolate over greater distances in the bulk.

The thermodynamic and kinetic situation is further complicated by the motion of Li⁺ cations when an electric field is applied across the sample. Electrochemical Impedance Spectroscopy (EIS) measurements made on the MEC-SIPEs in the present work last several hours while cooling the sample down from 100 °C (details are given in **Section 4**, and in the **Experimental** Chapter). The range of cooling rates used in DSC analysis provides insight into the timescale over which the organisation of phases in the bulk MEC-SIPE might occur. Indeed, these macromolecules become organised over a timescale of several hours. The slowest cooling ramp in DSC requires over 16.6 h to cool the sample from 100°C to 0°C (0.10°C.min⁻¹). An EIS protocol, in which the spectrum is measured at intervals of 2°C on cooling from 100°C, requires a similar amount of time to complete (accounting for an equilibration time of 10 min between measurements). The time spent at high

temperature and the electromagnetic force applied to the ionically conductive EC-SIPE might be enough to promote organisation of the electrolyte.

3.4. Conclusions on Thermal Characterisation of MEC-SIPEs

The MEC-SIPEs have lower total ΔH_{endo} of transitions on heating than the $m\text{PEO}_n\text{-OH}$ precursors having the same chain length. The MEC-SIPEs that have higher ionic conductivity also have higher total ΔH_{endo} of transitions on heating (**Fig. II-47**). The $m\text{PEO}_{20}\text{-}^{\ominus}\text{NSI}(\text{LiTFSI})$ is an exception to this trend. This is likely to be the result of the plasticising effect of the TFSI⁻ anion. Variation of the cooling rate is examined with the $m\text{PEO}_{20}\text{-N(Li)Pyr}$ having both high ionic conductivity and high ΔH_{endo} on heating. Comparison of this MEC-SIPE with its $m\text{PEO}_{20}\text{-OH}$ precursor reveals a trend with decreasing cooling rate. The MEC-SIPE is permitted to organise more effectively when the cooling rate is slow. This implies that the organisation of the MEC-SIPE occurs *via* slow processes. The MEC-SIPE is proposed to benefit from strong interaction of its end-groups. This is observed indirectly by increase in both ΔH_{endo} and T_p of thermal transitions on heating at a constant rate after cooling at decreasing rates. The observations made lead to the hypothesis that the MEC-SIPE is segregated in the bulk state into phases having thermal properties dominated by either the interactions of the functional end-group or by interactions of the PEO chain.

In review of the results of thermal characterisation, and in particular the implications of Section 3.3.2 on the segregation of an end-capped homopolymer, the following perspectives might be considered for the design, synthesis and characterisation of MEC-SIPes:

- I. Geometry of the end-group might have either a constructive or a destructive impact on the formation of well-defined, segregated, percolating phases. Simple variations in geometry might be accessed through variation of an aromatic ring motif. For example, easily accessible variations could be based on aminoanthracenes (**Illustration 3**). These changes in configuration at constant end-group composition will profoundly inform the design of MEC-SIPes from the point of view of the thermodynamics, kinetics, and high χ interactions of the end-group.

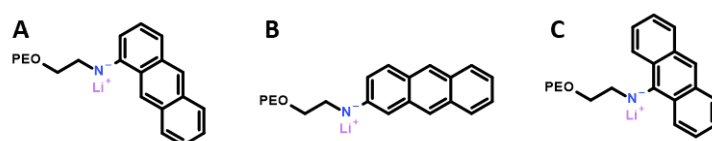


Illustration 3: Variations of end-group design based on aminoanthracenes having their amines in the A) 1-C, B) 2-C, and C) the 10-C positions.

- II. Segregation of the (*e.g.* PEO) homopolymer chain should be investigated not only as a function of the physicochemical properties of the chain + end-group combination but also in terms macromolecular architecture. Frustration of homopolymer chain dynamics might enhance phase segregation. This can be achieved by numerous methods. For example, an accessible research axis for comparison to the present library of MEC-SIPes might be the variation of the number of polymer chain "tails" and end-group "heads" to obtain a comparable set of multi-head and multi-tail MEC-SIPes. (**Illustration 4**).

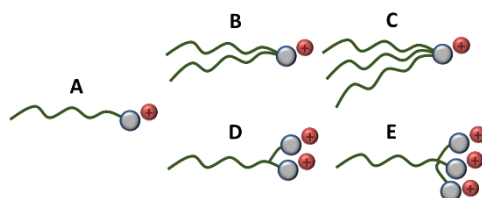


Illustration 4: Variations of polymer architecture based on a "simple" MEC-SIPE (A). The multi-tail (B & C) and multi-head (D & E) polymers are expected to have enhanced physical and thermal properties as a consequence of their architectures.

4. Ion Transport in MEC-SIPeS

4.1. The Temperature Dependence of Ionic Conductivity

The ionic conductivity of the presented MEC-SIPeS is dependent on temperature. A phenomenological model, originally proposed by Vogel, Tamman, and Fulcher,^[6,7] is widely used for the characterisation of ionic conduction behaviours of polymer electrolytes. A simplified version of this model is applied in the present work (**Eqn. II-15**).

Equation II-15: The simplified Vogel-Tamman-Fulcher (VTF) model, as applied to ionic conductivity (σ), where σ_0 is a pre-exponential factor, B is a term related to the thermal activation energy (E_a) and Boltzmann constant (k_B), T is the temperature in kelvin and T_0 is the equilibrium glass transition temperature.

$$\sigma = \sigma_0 \cdot e^{\left(\frac{B}{T-T_0}\right)}$$

This exponential relation was originally applied as means to model the temperature dependant viscosity of glass-forming materials.^[6,7,20] Ionic transport in polymers is characterised by the VTF model assuming that the motion of ions is controlled by the thermally dependent motion of polymer segments. One therefore relies on the following statements to be true:

- I. The polymer is divided into segments of a single persistent length having a uniform dependence of mobility on temperature.
- II. The mobile ions are fully dissolved in the solvent polymer. *i.e.* binary salts are completely dissociated and the mobile ions move independently of each other.
- III. The ions move concertedly with the polymer segments.

The accuracy of the fit obtained by the VTF model is furthermore dependent on the difference $T - T_0$, with the validity of the fit diminishing rapidly at temperatures far from the glass transition. It is taken for granted that the cell constant does not change. In practice this is not always the case. For example, the cell constant might change according to **i)** the volume of the electrolyte, and **ii)** the electrode-electrolyte contact (sometimes called "wetting" of the electrode surface). Changes in volume might arise as a result of thermally induced phase transitions in the bulk material. Changes in the electrode-electrolyte contact might occur as a result of **i)** thermally-induced phase transitions, and **ii)** chemical reaction of the electrolyte with the electrode material. Undesirable (electro)chemical reaction of the electrolyte with the electrode can produce insulating products that effectively decrease the electrode-electrolyte contact area.

The VTF model was fitted to the measured ionic conductivity in the present work (Section 2.1). The values of the pre-exponential factor (σ_0), the term related to the activation energy ($B \sim E_a/k_B$) and the equilibrium glass transition temperature (T_0) obtained cannot be easily compared across different MEC-SIPeS having different end-groups and PEO chain lengths. This is expected because **i)** the measurement temperatures are relatively far from the expected T_g of the polymers, likely to be in the -30 to -50°C range, and **ii)** the measurement temperatures cover a range over which thermal transitions occur, as evinced by DSC (**Section 3**). A single VTF fit according to one set of parameters is therefore not expected to be representative of the ionic conductivity behaviour of the MEC-SIPeS across the entire measurement range.

The VTF equation (**Eqn. II-15**) can be rearranged into a linear form (**Eqn. II-16**). The derivative of this equation $\delta \ln(\sigma)/\delta T$ yields a plot having a slope equal to B, the term related to the activation

energy. In this case, the activation energy refers to the energy cost of the transport of ions through the electrolyte. In a manner familiar to the study of intensive properties such as viscosity, the derivative is multiplied by the temperature (T) to define the reduced activation energy $W(T) = T \cdot [\delta \ln(\sigma) / \delta T]$ within a useful range of temperature. Plotting $W(T)$ as a function of temperature thus affords a comparison of the activation energy of ionic conductivity of the polymer electrolytes under the reported conditions of temperature.

Equation II-16: The natural logarithm of the VTF formula (Eqn. II-15).

$$\ln(\sigma) = B \cdot \frac{1}{(T - T_0)} + \ln(\sigma_0)$$

Equation II-17: The derivative of Eqn. II-16 multiplied by T yields the reduced activation energy, $W(T)$.

$$W(T) \equiv T \cdot \frac{\delta \ln(\sigma)}{\delta T} = T \cdot \frac{-B}{(T - T_0)^2}$$

In the case of a single ionic transport mechanism, one expects a straight line of $W(T)$. A single regime over the entire measurement range could be appropriately modelled by one set of VTF parameters. However, there is a change in the slope of the reduced derivative as a function of temperature. The plot of $W(T)$ is presented with temperature values in reverse order to make easier comparisons to the familiar plot of $\log(\sigma)$ vs. $T(K^{-1})$.

The dependence of ionic conductivity of MEC-SIPEs as a function of temperature is compared to SiP electrolyte blends of mPEO₆₀m/LiTFSI. The ionic conductivity data must have small intervals of temperature to provide certainty of the trends observed. The measurements must be conducted over a wide range of temperatures to provide a good indication of changes in the thermal dependence of conductivity. The MEC-SIPEs having longer PEO chains and the SiP mPEO₆₀m/LiTFSI having a high ratio of EO/Li do not permit ionic conductivity measurements at temperatures much lower than $T \approx 40$ °C. However, MEC-SIPEs having shorter chains and the SiP blends having EO/Li= 10 exhibit sufficient ionic conductivity at lower temperatures to enable measurements on cooling across the +100°C to 0°C range. The σ of the SiPs having EO/Li= 10 are shown below (**Fig. II-52**). The corresponding plot of $W(T)$ is given for the SiPs having EO/Li= 60, 20, and 10 (mPEO₆₀m/LiTFSI), and for mPEO₁₀m/LiTFSI, EO/Li= 10 (**Fig. II-53**). The curvature of $W(T)$ at the extremes of the temperature range are not considered when posing linear fits to the data. At high temperature, the curvature results from the change in the direction of the heating/cooling scans. At low temperature, the imperfect percolation of crystalline phases decreases ionic conductivity. Therefore, the effective temperature range for fitting the data is fixed for all data sets from 90°C to the last data point permitting good fit of the complex impedance on cooling.

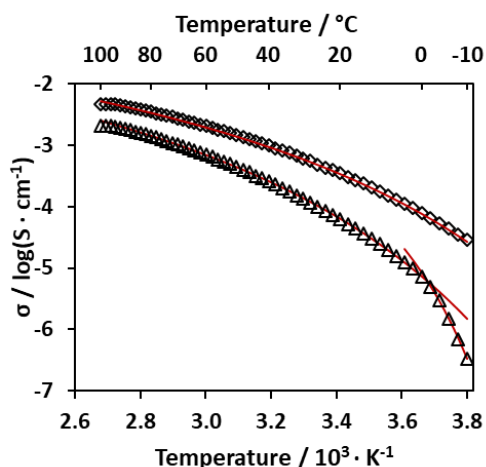


Figure II-52: The σ ($S \cdot cm^{-1}$) of mPEO_{60m}/LiTFSI (EO/Li= 10) (○) and mPEO_{10m}/LiTFSI (EO/Li= 10) (△) as a function of T (K⁻¹). The red lines are VTF fits of the data.

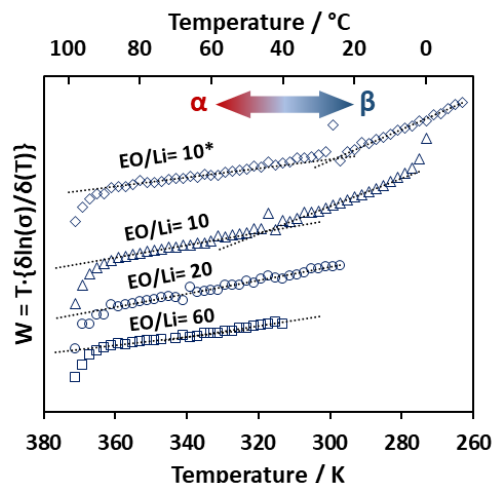


Figure II-53: $W(T)$ plots of the SiP electrolyte mPEO_{60m}/LiTFSI having different EO/Li= 60 (□), 20 (○), and 10 (△); and mPEO_{10m}/LiTFSI (marked*) having EO/Li= 10 (◇). Dotted lines (···) are linear fits of the data. The data series are plotted as a function of T(K) and displaced vertically by an arbitrary value.

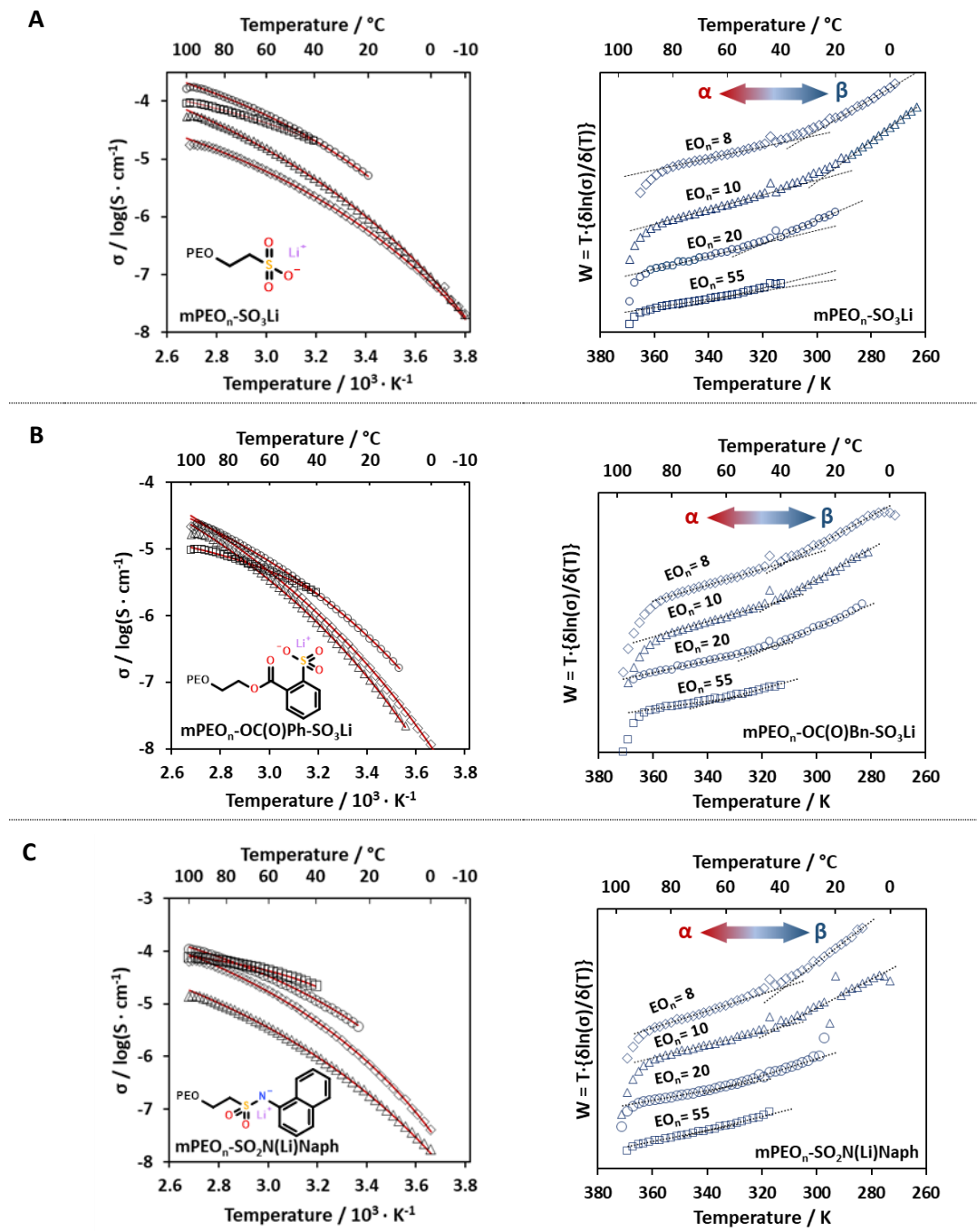
The SiP having EO/Li= 60 and 20 have a single slope of activation energy across their respective temperature ranges (**Fig. 53**). However, the data of SiPs having EO/Li= 10 exhibit a transition from a process having a lower activation energy at high temperature (α) to a higher activation energy at low temperature (β). The change in the slope of $W(T)$ is evidence of a change in the activation energy of ionic conduction. The temperatures accessible for ionic conductivity measurements is moreover far from the T_g of PEO. These two facts prevent reasonable evaluation of the data across the +100 to -10°C range by the VTF model. Presented below are the fitting parameters of the VTF equation for the conductivity data of the SiP electrolytes (**Table II-12**).

Table II-12: VTF fitting parameters determined by least squares method for the ionic conductivity data of SiP blends of mPEO_{60m}/LiTFSI and mPEO_{10m}/LiTFSI. The symbols correspond to those used in Figures 52 and 53.

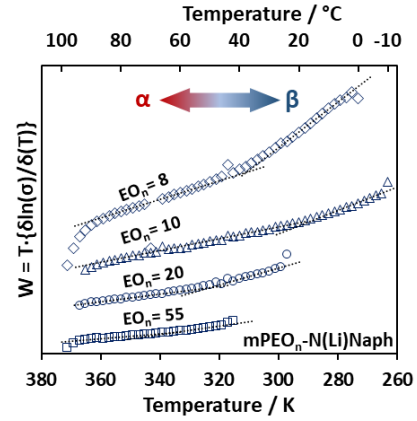
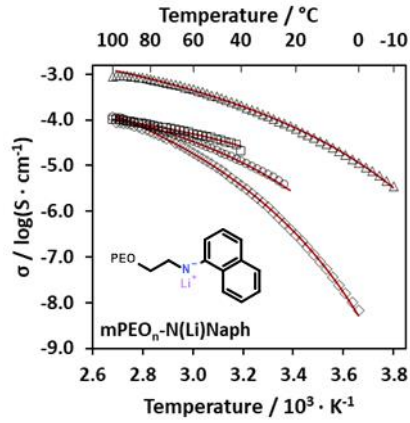
		DP _n (EO _n)	EO/Li	T (°C)	$\sigma_0 \times 10^2$	-B	T ₀ (K)
1	◇	10	10	100→-10	18.3	655	189
2	△	60	10	100→0 0→-10	18.1 15.5	745 395	200 233
3	○	60	20	100→40	4.27	505	209
4	□	60	60	100→22	2.66	531	201

As we have come to expect for MEC-SiPEs, $W(T)$ is dependent on both the functional end-group and the length of the PEO chain. The σ of MEC-SiPEs having EO_n= 8, 10, 20, and 55 was calculated from EIS measurements using blocking (gold) electrodes from +100°C down to the lowest temperature permitting a good fit of the complex impedance spectrum. The derivatives of these same data were calculated to characterise the MEC-SiPEs. The ionic conductivities of the MEC-SiPEs are presented next to the corresponding plots of $W(T)$ (**Fig. 54**).

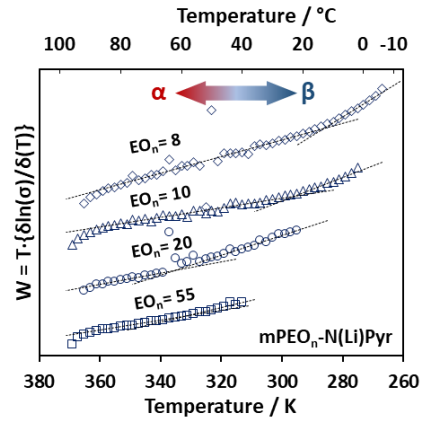
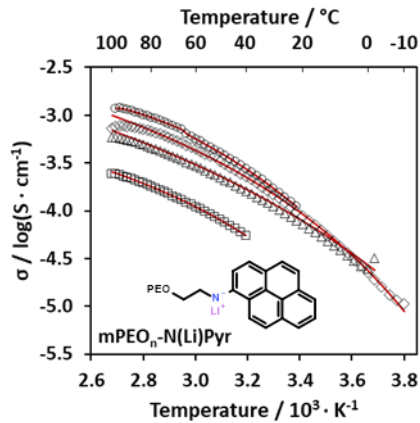
Figure II-54: (Left) The ionic conductivity [$\log(S \cdot \text{cm}^{-1})$] and (Right) $W(T) = T \cdot \{\delta \ln(\sigma) / \delta(T)\}$ of MEC-SIPes having different functional end-groups: $-\text{SO}_3\text{Li}$ (A), $-\text{OC(O)PhSO}_3\text{Li}$ (B), $-\text{SO}_2\text{N(Li)Naph}$ (C), $-\text{N(Li)Naph}$ (D), $-\text{N(Li)Pyr}$ (E), $-\text{NSI(Li)}$ and $-\text{NSI(LiTFSI)}$ (F), and $-\text{SANSI(Li}_2)$ (G). The MEC-SIPes having different EO_n are presented: $\text{EO}_n = 8$ (\diamond), 10 (\triangle), 20 (\circ), and 55 (\square). The same symbols are used both for the σ and $W(T)$ plots. The MEC-SIPE is indicated within the chart area of each plot. The red lines (-) are VTF fits of the experimental ionic conductivity data (symbols). The dotted lines (\cdots) are linear fits of the $W(T)$ function (symbols). The $W(T)$ data series are plotted as a function of temperature and displaced vertically by an arbitrary value.



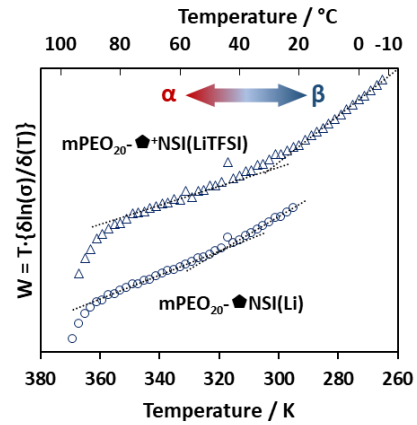
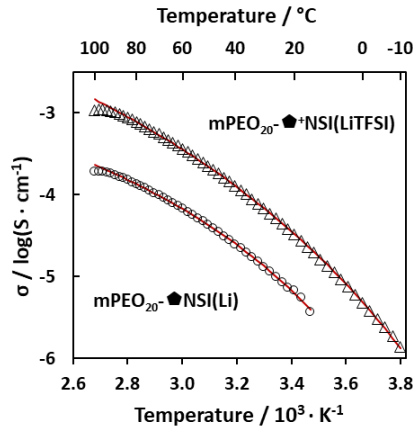
D



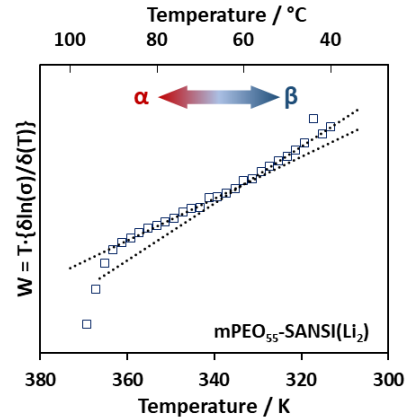
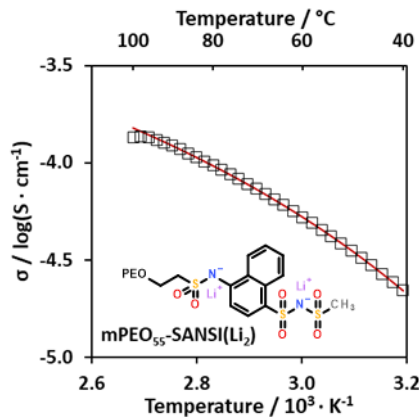
E



F



G



The slope of $W(T)$ is related to the activation energy of ion transport through the electrolyte. The MEC-SIPEs exhibit a transition in $W(T)$ with a high temperature ion transport regime (α) and a low temperature transport regime (β). The slope of $W(T)$ at high temperature is compared to the slope at low temperature. To make the presentation more intuitive, the slope of $W(T)$ is plotted in its negative sign, such that a higher value represents a higher activation energy. This is visualised with $W(T)$ plotted with temperatures in reverse order: a higher (negative) gradient represents a higher activation energy (Fig. II-54, A-G).

All of the polymer electrolytes have lower activation energy at higher temperature and higher activation energy at lower temperature. The SiP blends having $EO/Li > 10$ do not have sufficient ionic conductivity to permit EIS measurements at $T < \sim 40$ °C. However, their high temperature conductivity is measured and the slope of $W(T)$ estimated using a linear fit (Fig. II-53). The SiP blends having $EO/Li = 10$ have both a high temperature (α) and a low temperature (β) ionic conductivity (σ). The activation energy ($-B$) for $\sigma(\alpha)$ is lower than for $\sigma(\beta)$. The MEC-SIPEs $mPEO_n-SO_3Li$ and $mPEO_n-OC(O)PhSO_3Li$ have $-B(\alpha)$ that are similar to the SiPs (Fig. II-55, A), regardless of the PEO chain length. As illustrated by the labelled EO_n values in the figure, EO_n is inversely proportional to $\phi_{m(EGrp)}$. The magnitude of $-B$ tends to increase with $\phi_{m(EGrp)}$ by a relatively small amount for high temperature conductivity, $\sigma(\alpha)$. The magnitude of $-B$ increases with $\phi_{m(EGrp)}$ by a larger amount for low temperature conductivity, $\sigma(\beta)$. The trends of $-B$ (Fig. II-55, A) resemble the trend of σ of $mPEO_n-SO_3Li$ (Fig. II-7) and $mPEO_n-OC(O)PhSO_3Li$ (Fig. II-10) as a function of $\phi_{m(EGrp)}$. The two data together (σ vs. ϕ_m , and $-B$ vs. ϕ_m) support the observation of an optimum conductivity at an intermediate EO/Li ratio: there is a trade-off between the concentration of functional end-groups (*i.e.* Li^+), the activation energy of σ (represented by $-B$) that determines ion mobility, and the percolation of conductive phases through the semi-crystalline polymer matrix (Fig. II-55, A).

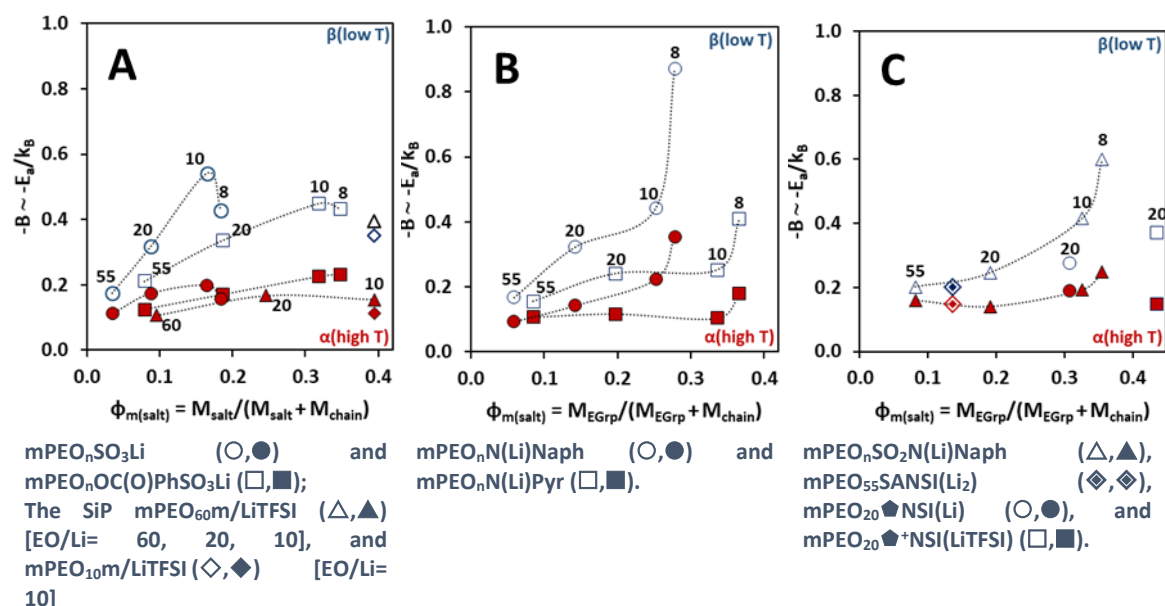


Figure II-55: The slope $-B$ of $W(T)$ is presented as a function of $\phi_{m(salt)}$ of MEC-SIPEs (listed below the plots, A-C). The slope of $W(T)$ at high T (α , red, filled symbols) and at low T (β , blue, open symbols) are shown. The linear fits of $W(T)$ used to obtain the slope $-B$ are shown in Figure II-54 (A-G). In the case of MEC-SIPEs, $\phi_{m(salt)}$ is the mass fraction of the ionic end-group; for the SiP electrolytes, $\phi_{m(salt)}$ is the mass fraction of LiTFSI. For the EC-SIPEs, the polymers having $EO_n = 55, 20, 10$, and 8 are shown and some EO_n values are labelled for reference.

The reduced activation energy ($-B$) of the aryl-functional $m\text{PEO}_n\text{-N(Li)Naph}$ and $m\text{PEO}_n\text{-N(Li)Pyr}$ increases when the chain length (EO_n) is decreased for both high temperature (α) and low temperature (β) ion transport (**Fig. II-55, B**). The increase in $-B$ is larger for $\sigma(\beta)$ than for $\sigma(\alpha)$. The increase is largest for the MEC-SIPes having the shortest PEO chains ($\text{EO}_n = 8$, and 10). There is a similar trend of increasing $-B$ for $m\text{PEO}_n\text{-SO}_2\text{N(Li)Naph}$ (**Fig. II-55, C**). Although its $-B(\alpha)$ is similar to those of the other MEC-SIPes, the σ of $m\text{PEO}_n\text{-SO}_2\text{N(Li)Naph}$ is lower than of $m\text{PEO}_n\text{-N(Li)Pyr}$, which has lower reduced activation energy in both the α and β temperature ranges. The change in $-B$ of $m\text{PEO}_{55}\text{-SANSI(Li}_2)$ is small (**Fig. II-55, C**) over the +100 to +40°C temperature range of measured σ (**Fig. II-54, G**). The calculated $-B(\alpha)$ and $-B(\beta)$ of this MEC-SIPE are low and similar to the values calculated for the other $\text{EO}_n = 55$ polymers. However, this polymer has $\text{EO/Li} = 23$.

Quaternisation of the $m\text{PEO}_{20}\text{-}\blacklozenge\text{NSI(Li)}$ yields the zwitterionic $m\text{PEO}_{20}\text{-}\blacklozenge^+\text{NSI(LiTFSI)}$, which has a lower $-B(\alpha)$ and a higher $-B(\beta)$ (**Fig. II-55, C**). As illustrated above, the zwitterion also has higher σ over a wider temperature range than the $m\text{PEO}_{20}\text{-}\blacklozenge\text{NSI(Li)}$ (**Fig. II-54, F**). The high σ is achieved with respect to a high LTN of the $m\text{PEO}_{20}\text{-}\blacklozenge^+\text{NSI(LiTFSI)}$, $t_{Li}^+ \approx 0.8$. The σ of $m\text{PEO}_{20}\text{-}\blacklozenge^+\text{NSI(LiTFSI)}$ at low temperature might be a result of the plasticizing effect of the TFSI⁻ anion. This hypothesis is supported indirectly by the low ΔH_{endo} observed on heating of this polymer in DSC (**Fig. II-44**), which suggests a very low mass fraction of organised phases in the bulk.

The dependence of $-B$ and σ on the functional end-group concentration ($\phi_{\text{m(EGrp)}}$) is complex and would benefit from analysis of a finer gradation of PEO chain lengths (*i.e.* having more samples in the range $\text{EO}_n = 10\text{-}50$). From the data presently available, σ is optimised at an intermediate chain length ($\text{EO/Li} \approx 20$ for most functional end-groups). The magnitude of B has a small variation as a function of $\phi_{\text{m(EGrp)}}$ at high temperature (α). However, a noticeable increase in $B(\alpha)$ is observed for the aryl end-groups having $\text{EO/Li} = 8$. The increase of $-B$ with $\phi_{\text{m(EGrp)}}$ is greater at low temperature (β) than at high temperature (α). For each MEC-SIPE, the trend of $-B(\beta)$ vs. $\phi_{\text{m(EGrp)}}$ has the same shape as the corresponding trend of $-B(\alpha)$ vs. $\phi_{\text{m(EGrp)}}$.

Two linear fits were made to estimate $-B(\alpha)$ and $-B(\beta)$ of the MEC-SIPes. The temperature at the intercept of these lines, at $W(\alpha) = W(\beta)$ is calculated and plotted as a function of $\phi_{\text{m(EGrp)}}$. $T[W(\alpha) = W(\beta)]$ is furthermore compared to the T_p of ΔH_{endo} transitions observed on heating in DSC (**Fig. II-62**). The comparison with ΔH_{endo} transitions is not made directly because the EIS measurement (by which $W(T)$ is obtained) and the DSC measurement (by which ΔH_{endo} is observed) are made under very different kinetic conditions. The EIS data are gathered on cooling; the T_p correspond to the peak ΔH_{endo} of thermal transitions on heating. The EIS measurements are moreover made over a longer timescale: the impedance spectra are gathered at intervals of 2°C on cooling from 100°C with cooling rate of 1°C.min⁻¹ and an equilibration time of 10 minutes at each measurement temperature. The DSC heating scans on heating were measured from -40°C, at a rate of 5°C.min⁻¹. The T_p are thus expected to be overestimates due to thermal lag of the of ΔH_{endo} transitions on heating. However, it is useful to represent these data together, to put the intercept of $W(\alpha) = W(\beta)$ into context of MEC-SIPes having complex thermal behaviours.

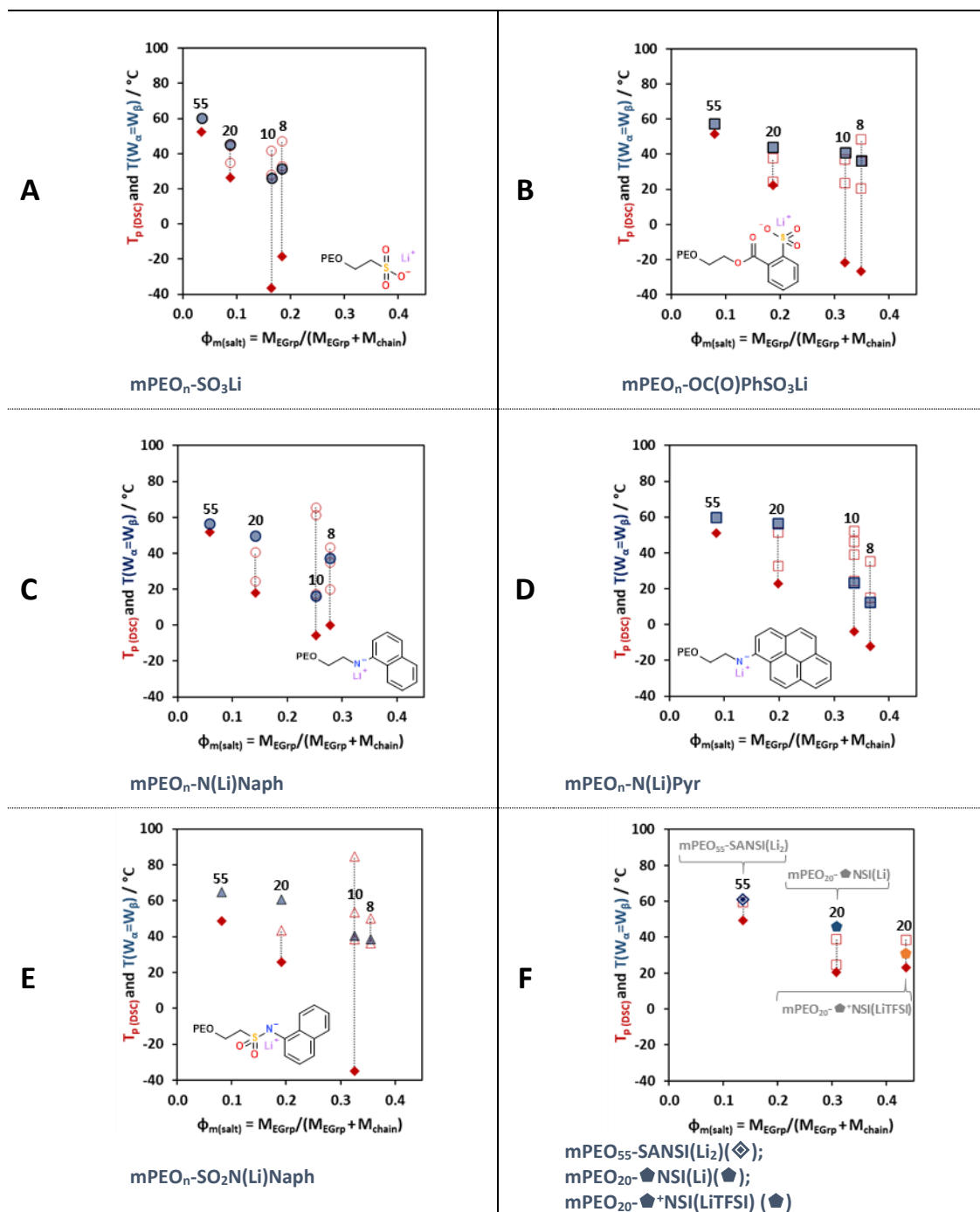


Figure II-56: The $W(T)$ transition temperature $T[W(\alpha)=W(\beta)]$ (blue, filled symbols; ●, ■, ▲) on cooling (EIS) and the T_p (red, open symbols, ○, □, △) of ΔH_{endo} transitions on heating (DSC) of MEC-SIPES having different end-groups: -SO₃Li (A; ●, ○), -OC(O)PhSO₃Li (B; ■, □), -N(Li)Naph (C; ●, ○), -N(Li)Pyr (D; ■, □), -SO₂N(Li)Naph (E; ▲, △). The polymers mPEO₅₅-SANSI(Li₂) (◇), mPEO₂₀-NSI(Li) (◆), and mPEO₂₀-NSI(LiTFSI) (♣) are shown (F). The red diamonds (◆) indicate the T_p of the first ΔH_{endo} transition on heating of each MEC-SIPE (DSC). Dotted lines (⋯) are drawn to link data sets of MEC-SIPES of the same DP_n (labelled: EO_n= 55, 20, 10, and 8).

The transition of $W(T)$ at $T[W(\alpha)=W(\beta)]$ is close to the T_p of the single ΔH_{endo} transition of MEC-SIPEs that have $EO_n = 55$ (**Fig. II-62**). This heat transfer, being close to the T_m of the $mPEO_{55}$ -OH precursor, is defined by the melting of PEO chains. DSC reveals that the MEC-SIPEs based on shorter PEO chains exhibit a number of transitions. The ΔH_{endo} having the lowest T_p on heating compares well to the melting of PEO chain segments (**Fig. 50**). The trend of these first transitions on heating follow the same trend as the $T[W(\alpha)=W(\beta)]$ intercepts as a function of $\phi_{m(\text{salt})}$ (**Fig. II-62, A-E**). Emphasis is not placed the exact values of T_p because of the difference in the kinetic conditions of the measurements. The T_p attributed to the melting of PEO segments and $T[W(\alpha)=W(\beta)]$ can be different by as much as 20-30 °C. However, the similarity of the trends is well-pronounced.

The crystallisation of PEO at low $\phi_{m(\text{salt})}$ ($EO_n = 55$) limits percolation of conductive phases in the MEC-SIPEs. All of the MEC-SIPEs of $EO_n = 20$ have T_p of all transitions on heating at temperatures lower than $T[W(\alpha)=W(\beta)]$. This implies that high temperature conductivity, $\sigma(\alpha)$, of the MEC-SIPEs is the range of temperatures at which MEC-SIPE bulk is fully melted. On cooling, the MEC-SIPEs having $EO_n = 20$ pass $T[W(\alpha)=W(\beta)]$ and enter a temperature range having a higher activation energy. This regime of $\sigma(\beta)$ continues until the growth of crystalline grains limits percolation of the conductive phases, and ionic conductivity falls rapidly.

MEC-SIPEs of the shortest chain lengths ($EO_n = 10$, and 8) have high temperature transitions close to their $T[W(\alpha)=W(\beta)]$ intercept temperatures. The high temperature behaviour of these MEC-SIPEs is complicated by the high concentration (approaching $\phi_{m(\text{salt})} = 0.4$) of interacting end-groups. However, the high temperature transitions (observed on heating in DSC) do correspond to organisation of the MEC-SIPEs that occurs on cooling. They are reversible and dependent on the rate of cooling. The effect of the end-groups is represented by the large variation in the magnitude of $-B(\beta)$ at high $\phi_{m(\text{salt})}$ (low EO_n). The activation energy of ion transport appears to be affected by the interaction of ionic species (end-groups) of the MEC-SIPEs on cooling, and this phenomenon is magnified by concentration.

4.2. Characteristic Frequencies of Ion Transport in MEC-SIPEs

4.2.1. Resistive Features at Low Temperatures: Case Study of $mPEO_8$ -N(Li)Pyr.

The greatest changes in the activation energy of ion transport are observed for high functional end-group concentrations (high $\phi_{m(\text{salt})}$). In the present work, this corresponds to MEC-SIPEs having short PEO chains ($EO_n = 8, 10$). The $mPEO_{20}$ -N(Li)Pyr is presented having several thermal transitions observed on heating in DSC (**Fig. II-49**). The $mPEO_8$ -N(Li)Pyr has higher activation energy (represented by $-B$, **Fig. II-55, B**) of ion transport in both its high temperature $W(\alpha)$ and its low temperature $W(\beta)$ range (**Fig II-54, E**). Ion transport at low temperatures provides an opportunity to thermally trap organised structures of a polymer electrolyte. Electrochemical Impedance Spectroscopy (EIS) reveals the evolution of interfaces in the MEC-SIPE. The EIS spectra were first collected on cooling from +100 to -10°C (the conductivity and $W(T)$ data are presented above, in **Fig II-54, E**). Examples of sub-ambient temperature EIS data are shown below as Nyquist plots (**Fig. II-63**). The MEC-SIPE is then immediately heated from the lowest temperature (-10°C) and the interfaces that evolve at low temperature are observed in the EIS spectrum on heating. The Nyquist plots of the data collected on heating (**Fig. II-64**) illustrate the destruction of the interfaces

that develop at low temperature. This analysis is possible because the MEC-SIPE retains microscale ion transport at low temperature.

Fig. II-57 and Fig. II-58: Nyquist plots of EIS data collected on cooling (Fig. II-57) and heating (Fig. II-58) of mPEO₈N(Li)Pyr. The experimental data (circles, ○) are fitted by an equivalent circuit model (red lines, -). The equivalent circuit is shown below (Eqn II-18). Arrows (←) indicate the direction of increasing frequency (1 MHz ← 1 Hz). The plots at the bottom (B) are expanded representations of the plots at the top (A).

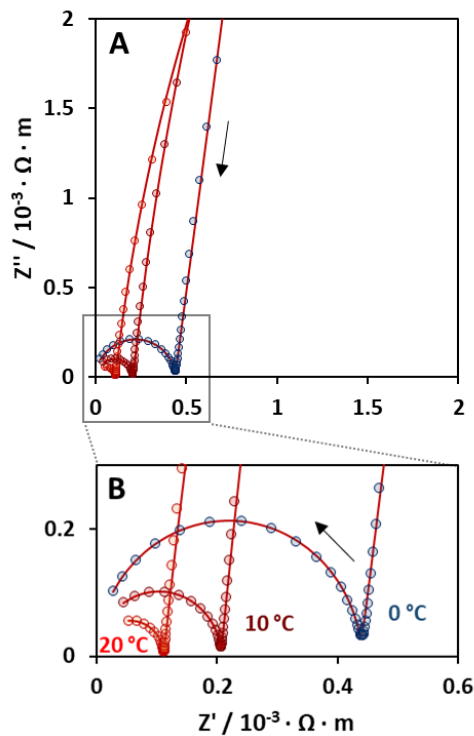


Figure II-57: Nyquist plots of EIS data measured on cooling of mPEO_n-N(Li)Pyr.

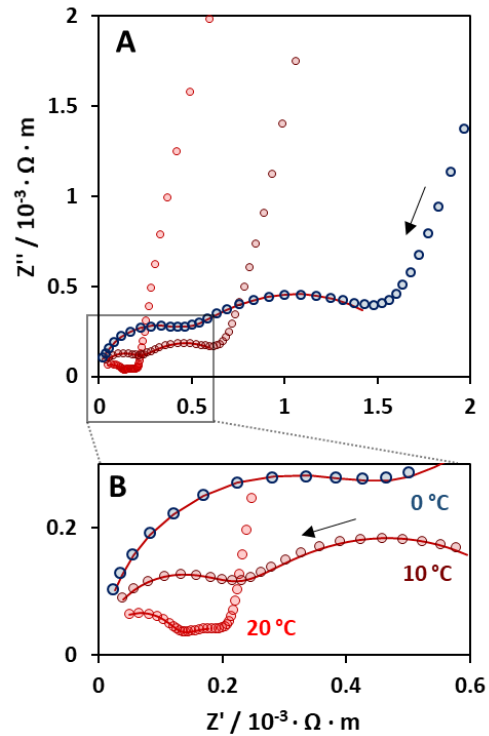
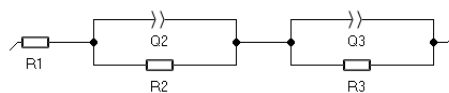


Figure II-58: Nyquist plots of EIS data measured on heating of mPEO₈-N(Li)Pyr.

The spectra were fitted using the equivalent circuit model below (Eqn. II-18). The circuit was chosen according to the elements used. The resistors represent the instrumental setup (R_1), the bulk electrolyte (R_2), and the second feature that develops at sub-ambient temperatures (R_3). Constant phase elements (Q_2 , Q_3) were connected in parallel to the resistors, to account for non-ideal evolution of the double layer capacitance.

Equation II-18: The equivalent circuit model used to fit the EIS spectra of mPEO₈-N(Li)Pyr measured at low temperature. The complex impedance $Z(\nu)$ is represented in terms of frequency (ν), resistance (R), capacitance of constant phase elements (Q), and a form factor (α); $j^2 = -1$ ($j \neq \pm 1$).



$$Z(\nu) = R_1 + \frac{R_2}{R_2 Q_2 (j2\pi\nu)^{\alpha_2} + 1} + \frac{R_3}{R_3 Q_3 (j2\pi\nu)^{\alpha_3} + 1}$$

The evolution of the resistive features observed in the EIS of mPEO₈-N(Li)Pyr on heating (examples shown in Fig. II-58) were modelled using an equivalent circuit (Eqn. II-18). These features are named in this report after the elements of the equivalent circuit (Fig. II-59). The higher frequency feature (R_2/Q_2) and the lower frequency feature (R_3/Q_3) are analysed as functions of temperature (Fig. II-60).

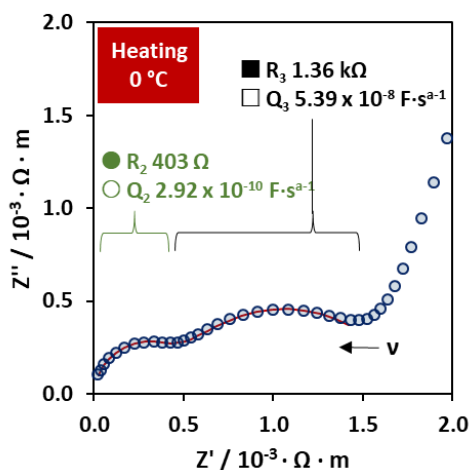


Figure II-59: An example Nyquist plot illustrating the high frequency Q_2/R_2 and the lower frequency Q_3/R_3 features observed on heating from -10°C . The arrow (\leftarrow) indicates the direction of increasing frequency.

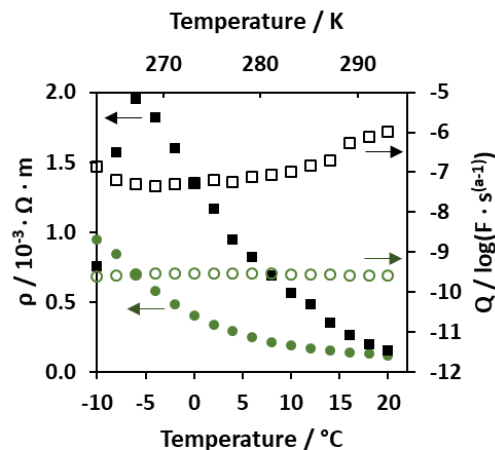


Figure II-60: The resistivity (ρ) and the corresponding capacitance (Q , open symbols) at a function of temperature on heating of $m\text{PEO}_8\text{-N(Li)Pyr}$ from -10°C to $+20^\circ\text{C}$. The higher frequency feature Q_2/R_2 (circles; \circ, \bullet) and the lower frequency feature Q_3/R_3 (squares; \square, \blacksquare) are displayed.

The resistances R_2 and R_3 (Fig. II-59) both decrease when the temperature is increased (Fig. II-60). The formation of the resistive feature R_3/Q_3 at low temperature ($T = 0 \rightarrow -10^\circ\text{C}$) is consistent with thermal transition assigned to the melting of PEO segments (observed in DSC on heating, at $T_p = -12^\circ\text{C}$). This T_p is lower than the $W(T)$ transition temperature defined by the intercept, $T[W(\alpha) = W(\beta)] = +13^\circ\text{C}$ (Fig. II-62, D). The quality of the fit to the equivalent circuit decreases when the R_3/Q_3 feature becomes small, on heating from $T = -10^\circ\text{C}$ to $T > +24^\circ\text{C}$. The R_3/Q_3 feature disappears at $T > +36^\circ\text{C}$.

Whereas the capacitance Q_2 remains constant ($Q_2 \approx 3 \cdot 10^{-10} \text{ F.s}^{(\alpha-1)}$), the capacitance of Q_3 increases with temperature, from $Q_3 = 5.0 \cdot 10^{-8}$ (at $T = -6.0^\circ\text{C}$) to $Q_3 = 1.0 \cdot 10^{-6} \text{ F.s}^{(\alpha-1)}$ (at $T = +20^\circ\text{C}$) (Fig. II-60). The difference between these trends of capacitance is more than two orders of magnitude. These resistive features could therefore originate from two different phenomena related to the MEC-SIPE. Whereas the low frequency R_3/Q_3 feature disappears at $T > +36^\circ\text{C}$, the semi-circle of the high frequency feature R_2/Q_2 remains until high temperatures. The R_2/Q_2 becomes too small to fit the equivalent circuit elements at $T > +80^\circ\text{C}$ on heating, and reforms in the Nyquist representation on cooling through the $+70 \rightarrow +60^\circ\text{C}$ range.

In the Nyquist representation, local minimum of the imaginary part of the impedance (Z'') is read from the axis of the real part (Z') to evaluate the resistance of the bulk electrolyte. This value of resistance is found equally as the plateau of the real part (Z') as a function of frequency (ν) (Fig. II-61). This type of analysis can be achieved using the maximum of the derivative $[(\delta Z'/\delta \nu) \rightarrow 0]$ to identify the plateau of the real part of the impedance (Fig. II-62). It is noted that the frequencies of the measurement are represented in the complex plane of the Nyquist plot to be increasing toward the origin (e.g. Fig. II-59). However, the treatment of Z' vs $\log(\nu)$ presents the frequencies increasing away from the origin, from left to right (Fig. II-61).

Fig. II-61 and Fig. II-62: The EIS data collected of mPEO₈-N(Li)Pyr on heating from 10°C → 20°C (+2°C increments). The data of EIS at 30°C (orange line, -) and 40°C (red circles, ○; red line, -) are also shown. Arrows (→) illustrate the direction of heating. The data are collected as discrete frequencies but displayed as lines for visualisation of the trends. The data points of the real part of the impedance (Z') collected at 40°C (red circles, ○) are shown as an example (Fig. II-61). The derivative of these same data are plotted as a function of frequency (ν, log(Hz)) (Fig. II-62).

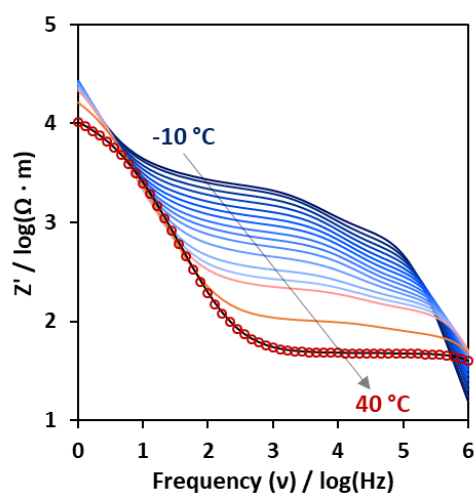


Figure II-61: A double logarithmic plot of the real part of the impedance (Z') as a function of frequency (ν).

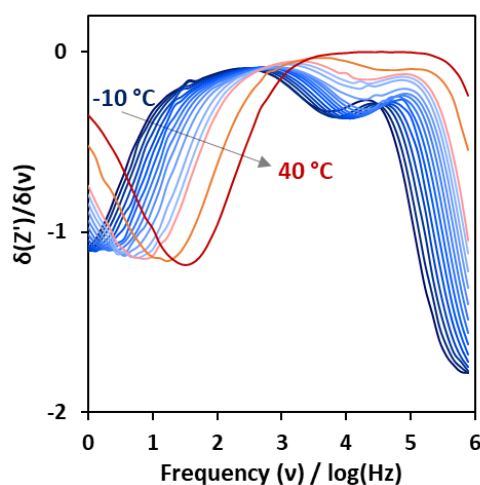


Figure II-62: The derivative $\delta(Z')/\delta(\nu)$ of real part of the impedance (Z') as a function of logarithmic frequency (ν).

The two features of resistance (R_2 and R_3) observed in the Nyquist representation (Fig. II-59) are observed as plateaus in the plot of the real part of the impedance (Z') as a function of logarithmic frequency (ν, log(Hz)) (Fig. II-61). The resistivity and characteristic frequency of these features are extracted by correlating the experimental data to the maxima of the derivative $\delta(Z')/\delta(\nu)$ (Fig. II-62). The two features are visible at the lowest temperature (-10°C). The R_3 feature is erased by temperature and the derivative has a single maximum at 40°C. The resistance of the real part (Z') at the frequency of the maximum of $\delta(Z')/\delta(\nu)$, at 40°C, corresponds to R_2 , the bulk resistance of the MEC-SIPE (48 Ω.m; $2.1 \cdot 10^{-4}$ S.cm⁻¹).

The Nyquist plot highlights the major contributions to resistivity by presentation of the impedance of the electrolyte in the complex plane. The extraction of the resistivity and conductivity of the electrolyte from Z' as a function of frequency enables the characterisation of the electrolyte without reliance on the fitting of the experimental data to an equivalent circuit. The application of an equivalent circuit relies on the assumption that all the impedance phenomena of the equivalent circuit correspond in theory to the mode(s) of ion transport in an electrolyte. Assumptions might be made for well-described electrolyte formulations of fully dissolved and dissociated binary salts in low viscosity solvents. These same assumptions might not necessarily apply to binary salts in viscoelastic, semi-crystalline polymers over a wide range of temperatures. "Single Ion" conductors moreover present a theoretical challenge in that the anion is assumed to be immobilised through covalent bonding to the stationary polymer chain. Analyses performed by DSC and the trends of reduced activation energy $W(T)$ demonstrate that the ion transport properties of these MEC-SIPEs are not simple. However, the high LTN of the EC-SIPEs demonstrates that, with respect to the stability of the interface in contact with lithium metal electrodes, the great majority of charge is carried by Li⁺. The logic and range of a relatively simple design motif of polymer chain with a modified end-group affords a basis of comparison among the

MEC-SIPes, the electrochemical characterisation of which can be further probed by treatment of EIS spectra.

4.2.2. Characteristic Frequencies of Ion Transport in MEC-SIPes

The complex impedance Z is made up of a real (Z') and an imaginary (Z'') part. Analysis of the impedance spectrum in the Nyquist plot serves to highlight the most resistive parts of the electrolyte. The resistivity (ρ) and capacitance (Q) of the bulk electrolyte are extracted from the Nyquist representation and correspond respectively to a local minimum and a local maximum of Z'' (Fig. II-63). The Z' and Z'' components can be equally plotted as a function of frequency in a double logarithmic plot (Fig. II-64). The plateau of Z' corresponds to the resistivity (ρ) of the electrolyte at the same frequency (f_p) as a local minimum of Z'' . The capacitance (Q) corresponds to a local maximum of Z'' (Fig. II-64). The position of Q can be approximately checked in this case by counting the data points down from the highest frequency and comparing the position of Q in the plot of Z'' vs. f (Fig. II-64) with the Nyquist plot (Fig. II-63). The frequency is plotted as $\log(v/2\pi)$ to exaggerate the shape of the data. The resistance obtained from the plateau of Z' at f_p can be used to calculate the conductivity of the electrolyte in the usual way, $\sigma = (1/\Omega) \cdot (\text{Length}/\text{surface Area})$.

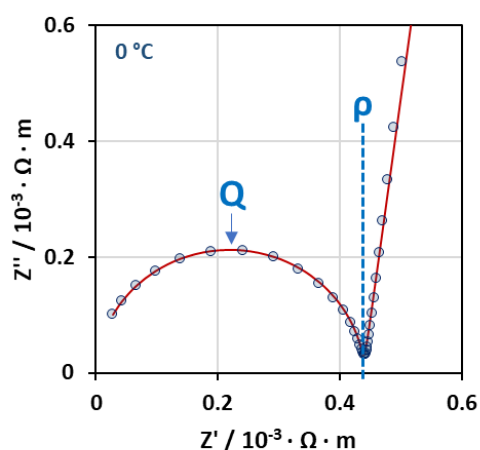


Figure II-63: A Nyquist plot of the EIS spectrum of mPEO₈N(Li)Pyr. The experimental data (○) was collected at 0°C, on cooling from 100°C. The bulk electrolyte resistivity ($\rho = 441 \Omega \cdot \text{m}$) and capacitance ($Q = 0.308 \cdot 10^{-9} \text{ F} \cdot \text{s}^{(a-1)}$; $a = 0.979$). The fit of the equivalent circuit (Eqn. 17) is displayed (red line, -).

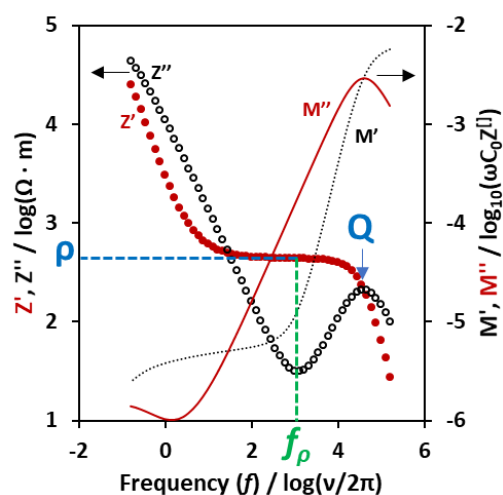


Figure II-64: A double logarithmic plot of Z' (●) and Z'' (○) as functions of frequency ($f = \nu/2\pi$) of mPEO₈N(Li)Pyr at 0°C on cooling from 100°C. The corresponding moduli M' (red line, -) and M'' (dotted line, ...) are shown.

It can be useful to process the data using the modulus (M) of the impedance (Z). The crossing points of the moduli are sometimes clearer to see than those of Z' and Z'' . The complex modulus is composed of real and imaginary parts, and is calculated from Z' and Z'' by multiplication by the angular frequency ($\omega = \nu \cdot 2\pi$), the vacuum permittivity (ϵ_0), and a cell constant (Eqn. II-19).

Equation II-19: The complex modulus (M) of the complex impedance (Z), where $\omega = \nu \cdot 2\pi$; $C_0 = \epsilon_0 \cdot (A/L)$; A is the electrode surface area and L is the thickness of the electrolyte.

$$Z = Z' + jZ''$$

$$M = jM'' - M'$$

$$M' = -\omega C_0 Z''$$

$$M'' = \omega C_0 Z'$$

Whereas the impedance emphasizes the resistive parts of the EIS (for example, the local minimum of Z''), the moduli emphasize the ion transport parts of the EIS (for example, the local minimum of M''). The conductivity is obtained by calculation using the resistance of the plateau of Z' corresponding a local minimum in Z'' . The conductivity is thus obtained at a certain frequency, f_ρ (Fig. II-64). This characteristic frequency increases with increasing temperature. The $mPEO_n-N(Li)Pyr$ have the highest ionic conductivity and largest mass fraction of functional end-groups ($\phi_{m(salt)}$) of the presented MEC-SIPes having different PEO chain lengths. These were chosen to investigate a possible trend in characteristic frequency (Fig. II-66).

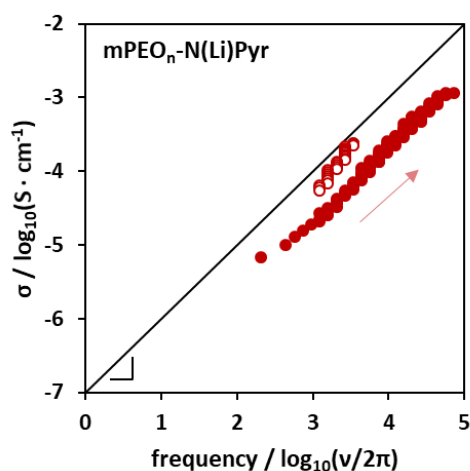


Figure II-65: A double logarithmic plot of the frequency dependence of σ of $mPEO_nN(Li)Pyr$. MEC-SIPes having short chains ($EO_n=8, 10$, and 20 ; ●) are overlapping and the longest chain $EO_n=55$ (○) is shifted in coordinates. The arrow (→) indicates the direction of increasing temperature. The reference line (-) has a slope of 1.

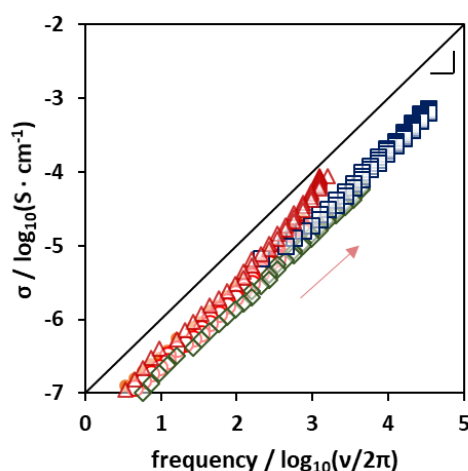


Figure II-66: Conductivity vs. Frequency of MEC-SIPes having $EO_n=8$ and different functional end-groups: -N(Li)Pyr (□), -N(Li)Naph (△), -SO₂N(Li)Naph (◇), -SO₃Li (○) and -OC(O)PhSO₃Li (●). The arrow (→) indicates the direction of increasing temperature. The reference line (-) has a slope of 1.

The trends of increasing ionic conductivity with increasing characteristic frequency appear to be similar. The EIS spectra of $mPEO_nN(Li)Pyr$ ($EO_n=8, 10, 20$, and 55) were computed to yield linear dependence with a slope close to unity (± 0.02) in the double log plot of conductivity ($\sigma / \log(S \cdot cm^{-1})$) as a function of frequency ($f / \log(\nu/2\pi)$). The frequency dependence of the ionic conductivity showed a uniform trend, independent of the polymer chain length (*i.e.* the concentration of ionic end-groups) when the PEO chains are short ($EO_n=8, 10$, and 20). However, the $mPEO_{55}N(Li)Pyr$ is slightly shifted towards lower frequencies (Fig. II-65).

Changing the functional end-group does not significantly alter the trend of σ vs f . This was tested using the EIS data of MEC-SIPes having the highest functional end-group concentrations ($EO/Li=8$). A small variation is observed in the coordinates of the trends, however the slope and tendency of increasing ionic conductivity and frequency with temperature remain the same (Fig. II-66).

MEC-SIPes having higher ionic conductivity also have higher characteristic frequency of their conductivity, over the measured range of temperature.

The trend of σ vs. f is checked against the SiP electrolyte mPEO₆₀m/LiTFSI having different concentrations of salt (EO/Li= 10, 20, and 60). The SiP formulations follow the same trend as the MEC-SIPes. Higher ionic conductivity invariably corresponds to higher frequency. The SiP blends have overlapping plots independent of salt concentration. The SiP data overlaps with those of MEC-SIPes having EO_n= 8.

In conclusion, the characteristic frequency of the ionic conductivity of the bulk electrolyte does not change with salt concentration in the model SiP electrolyte or functional end-group concentration of the presented MEC-SIPes. The ionic conductivity increases proportionally with characteristic frequency. Changing the functional end-group does not have a large effect on the coordinates of this trend. MEC-SIPes having the same functional end-group and different PEO chain lengths have the same coordinates on the double logarithmic plot of σ vs. f when the PEO chain is short (EO_n= 8, 10, and 20). However, there is a shift towards lower frequencies for the MEC-SIPes having longer chains (EO_n= 55). The end-groups with the highest ionic conductivity have the highest characteristic frequency with respect to temperature.

4.2.3. Characteristic Frequencies of mPEO₈-N(Li)Pyr: Dependence on Temperature

The resistive features of mPEO₈-N(Li)Pyr observed on heating (Section 4.2.1) are observed in the Nyquist plot as local minima in the complex plane, and as plateaus in the plot of Z' as a function of frequency. The characteristic frequency of a resistive feature corresponds to a local minimum in Z'' as a function of frequency (**Fig. II-64**). The intercept of Z' and Z'' where at which Z'' increases above Z' with increasing frequency corresponds to the characteristic frequency of the capacitance (Q) of the feature. Q is equally found at the local maximum of the semi-circular form in the complex plane of the Nyquist representation (**Fig. II-63**). The measurement window by the instrumental limits of the 1 Hz → 1 MHz frequency range. However, the characteristic frequency of the resistive features changes with temperature. A different form of the EIS spectrum is observed in the measurement window (frequency range) when the temperature changes (*e.g.* **Fig. II-67** → **Fig. II-68**). The electrolytes can be characterised by the frequency dependence of all the different features observed within the measured frequency range, with respect to measurement temperature. Decreasing the chain length of PEO increases the functional end-group concentration and increases the temperature range of ion transport. A MEC-SIPE with a short PEO chain and a large mass fraction of functional end-groups thus provides the best possibility of observing a change in the temperature dependence of ion transport.

Fig. II-67 and Fig. II-68: Examples of EIS spectra of mPEO₈-N(Li)Pyr measured at 80°C (Fig. II-67) and 0°C (Fig. II-68) on cooling from cooling from 100°C. The real (Z' , ●) and imaginary (Z'' , ○) impedances, and their real (M'' , red lines -) and imaginary (M' , dashed lines ---) moduli are presented in a double logarithmic plot as functions of frequency ($f / \log(v/2\pi)$). The positions of the resistivity (ρ) the associated characteristic frequency (f_ρ), and the capacitance (Q) are indicated. The identities of ρ , f_ρ , and Q are numbered (2, 3) relative to the equivalent circuit model (Eqn. II-18).

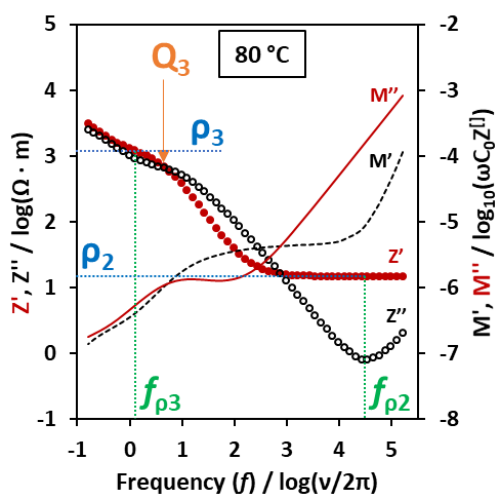


Figure II-67: The EIS spectrum of mPEO₈-N(Li)Pyr measured at 80°C.

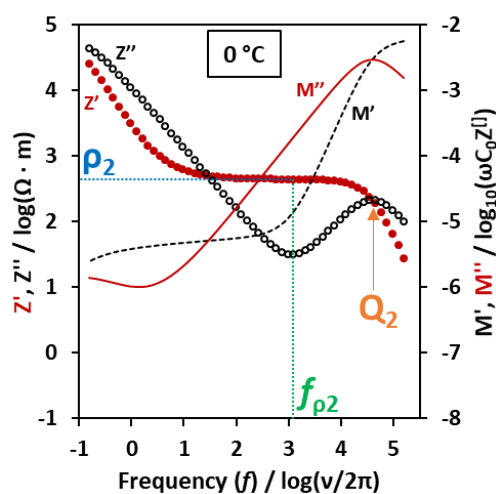


Figure II-68: The EIS spectrum of mPEO₈-N(Li)Pyr measured at 0°C.

The features observed in the fixed frequency range from 1 Hz ($\log(f) = -0.8$) to 1 MHz ($\log(f) = 5.2$) change on cooling. This is illustrated by examples of EIS spectra measured of mPEO₈-N(Li)Pyr on cooling from 100°C. These are compared to the trend of the temperature dependence of ion transport as illustrated by the reduced activation energy, $W(T)$. The transition temperature of $W(T)$ mPEO₈-N(Li)Pyr is calculated by intercept of linear fits of the high temperature $W(\alpha)$ and low temperature $W(\beta)$ trends, yielding $T[W(\alpha) = W(\beta)] = 13^\circ\text{C}$ (Fig. 54, E). Two representative data sets of the MEC-SIPE are shown (Fig. II-67, Fig. II-68): one EIS spectrum at $T > T[W(\alpha) = W(\beta)]$ (at 80°C) and one at $T < T[W(\alpha) = W(\beta)]$ (at 0°C). It is noted that 80°C is far above the temperature range at which the MEC-SIPE undergoes ΔH_{endo} transitions on heating. The ΔH_{endo} transitions of mPEO₈-N(Li)Pyr have $T_p = -12, 15, \text{ and } 35^\circ\text{C}$ on heating. The transition having $T_p = -12^\circ\text{C}$ is hypothesized to be the melting of the native PEO segment by comparison to the literature (Fig. II-50). The MEC-SIPE is therefore expected to be fully melted at 80°C.

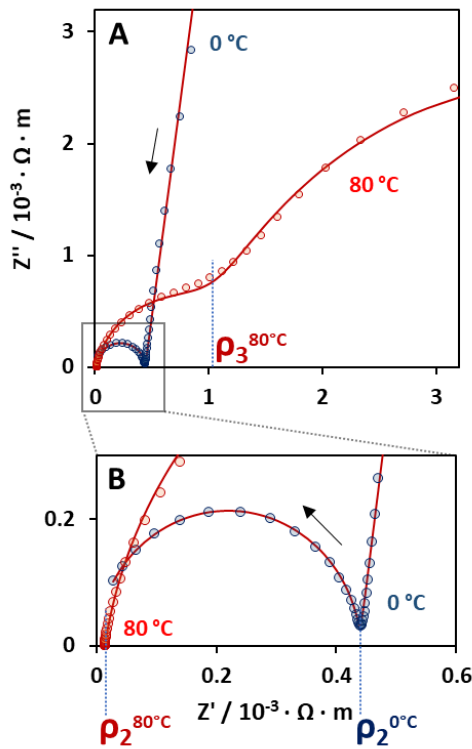


Figure II-69: Nyquist plots of the EIS spectra of mPEO₈-N(Li)Pyr measured at 80°C (red, ○) and 0°C (blue, ○) on cooling from 100°C. The experimental data are the same as those shown above (Fig. II-67 and Fig. II-68). Red lines (-) represent the equivalent circuit model (Eqn. II-18). Arrows (←) indicate the direction of increasing frequency.

The bulk resistivity (ρ_2) is observed at low frequency in both cases. The lower resistivity (higher conductivity) of mPEO₈-N(Li)Pyr at 80°C corresponds to a higher value of f_{ρ_2} than the same feature measured at 0°C. However, a low frequency feature (ρ_3) is observed at high temperature (**Fig. II-69**). This feature (ρ_3) has an associated characteristic frequency (f_3) and capacitance (Q_3). The magnitude of Q_3 could not be reliably calculated by fitting this feature in the Nyquist representation to an equivalent circuit because few data points are available in this range of frequencies. However, the ionic conductivity (σ) and characteristic frequency (f_ρ) of all the features could be computed from the EIS spectra obtained on cooling, using the plot of the spectrum as a function of frequency. It is clear from the Nyquist plot (**Fig. II-69**) that the ρ_3 feature does not meet the real axis. The calculation of the ionic conductivity using the obtained value of ρ_3 is therefore a large underestimate of the true resistivity of the feature. However, the crossing of Z' with Z'' (and M'' with M'), where the imaginary part becomes greater than the real part with increasing frequency (**Fig. II-67**), remains a robust value. This corresponds to the Q_3 of the low frequency resistive feature and can be tracked with respect to its characteristic frequency (f_α) and the measurement temperature.

The evolution of the crossing points of Z' and Z'' corresponding to Q_2 and Q_3 is presented as a function of their characteristic frequencies. The value of ionic conductivities of the crossing points are calculated from Z' . The evolution of each Q is therefore presented as conductivity value (σ_α) and a characteristic frequency (f_α) relative to the measurement temperature. Most of the features are observed in the EIS spectrum measured at 18°C (**Fig. II-70**). The crossing point where the charge transfer (Z' and its modulus M'') exceeds charge storage (Z'' and its modulus, M') is

identified at the characteristic frequency f_x (\circ) and assigned a resistivity ρ_x from Z' (it is not shown in **Fig. II-70**; ρ_x is close in magnitude to ρ_2). The combined results, calculated from EIS spectra measured on cooling of mPEO₈-N(Li)Pyr from 100°C to -10°C, are shown below (**Fig. II-71**).

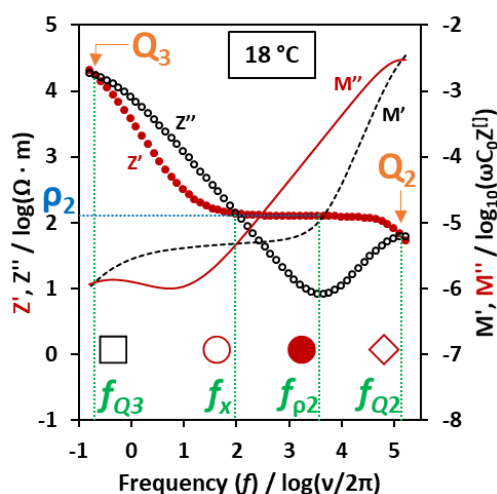


Figure II-70: The EIS spectrum of mPEO₈-N(Li)Pyr measured at 18°C on cooling from 100°C. The features Q₂ and Q₃ are both visible. The characteristic frequencies f_{Q3} (\square), f_x (\circ), f_{ρ_2} (\bullet), and f_{Q2} (\diamond) are shown. The same symbols are used in Figure II-71.

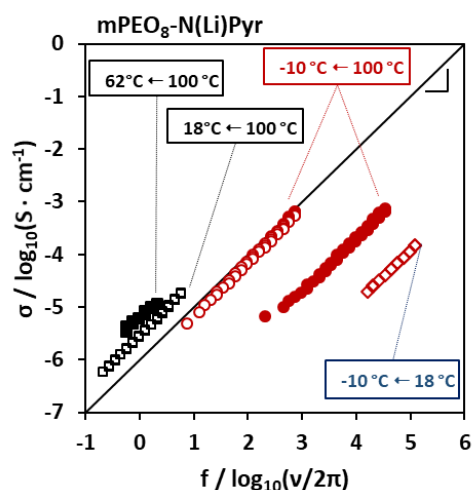


Figure II-71: The characteristic frequencies of features observed in EIS spectra of mPEO₈-N(Li)Pyr on cooling from 100°C. The double logarithmic plot of σ vs f is calculated from the resistance of Z' . The features (left to right) ρ_3 (\blacksquare), Q_3 (\square), ρ_x (\circ), ρ_2 (\bullet), and Q_2 (\diamond) are shown. Each feature is labelled with the temperature range over which it is observed, within the instrumental limits. The line (-) is a reference of $y=x$.

The different features found in the EIS spectra of mPEO₈-N(Li)Pyr appear over different ranges of temperature on cooling (**Fig. II-71**). The low frequency crossover Q₃ is observed in the high temperature range, from 100°C down to 18°C. The local minimum of Z'' ρ_3 (**Fig. II-67**) is observed above 62°C (**Fig. II-71**). The bulk resistance at ρ_2 is observed over the entire measurement range. The crossing point at f_x , where the charge transfer part (Z' , M') exceeds the charge storage part (Z'' , M''), is also observed from 100°C down to -10°C. However, Q₂, the maximum in the charge storage character at high frequency, is observed only at $T \leq 18^\circ\text{C}$. These features of the EIS spectrum can be plotted as functions of the bulk ionic conductivity and placed in context of the dependence of the bulk conductivity on reciprocal temperature (**Fig. II-72**). In this case, the bulk ionic conductivity (σ) is calculated from the Nyquist plot, at the intercept with the real axis obtained by fitting the complex impedance to a model circuit. In this representation, the bulk ionic conductivity is plotted as a function of reciprocal temperature (the temperature in degrees Celsius is given in the secondary vertical axis for reference). The features described above are plotted as functions of their characteristic frequencies and displaced vertically according to the bulk ionic conductivity.

How to read Figure II-72: The familiar plot of ionic conductivity (σ) as a function of reciprocal temperature ($10^3 \cdot K^{-1}$) is shown (blue line, -). The points of the secondary vertical axis of T ($^{\circ}C$) are fixed relative to the calculated σ . The features of the EIS spectrum (Fig. II-67 & II-68) are plotted at their characteristic frequencies (f) and displaced vertically according to the bulk ionic conductivity. The value of ρ_2 (\bullet) is the feature having σ close to the bulk value, except that it is not extrapolated to the real axis in the complex plane ($Z''=0$). For example, one can ask the question: which features of the EIS spectrum are observed at $40^{\circ}C$? Answer: Q_3 (\square), ρ_x (\circ), and ρ_2 (\bullet). The temperature ranges of the features are labelled in Figure 85.

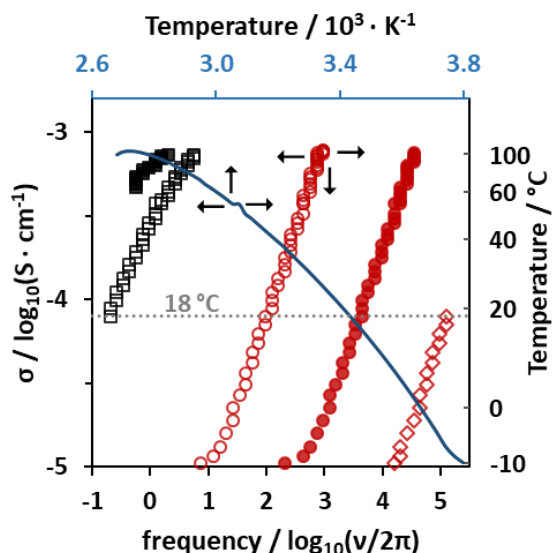


Figure II-72: The bulk ionic conductivity (σ) of mPEO₈-N(Li)Pyr (blue line, -) as a function of T ($10^3 \cdot K^{-1}$). The features of the EIS spectra at their characteristic frequencies (f) are plotted relative to σ and T ($^{\circ}C$). These are (left to right) ρ_3 (\blacksquare), Q_3 (\square), ρ_x (\circ), ρ_2 (\bullet), and Q_2 (\diamond). The temperature at which four features are observed ($18^{\circ}C$) is indicated (\cdots).

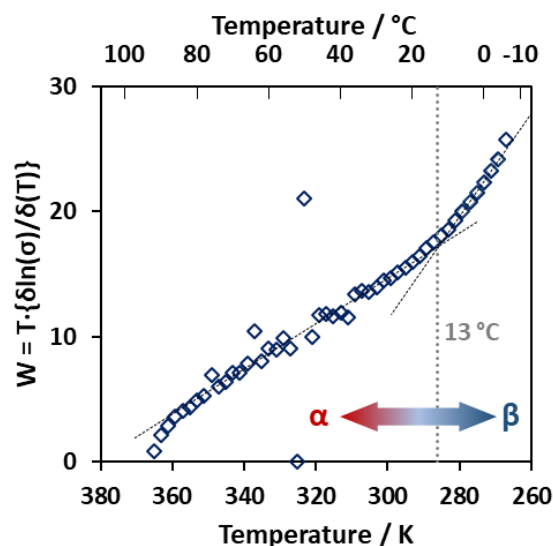


Figure II-73: The reduced activation energy $W(T)$ of mPEO₈-N(Li)Pyr (\diamond) as a function of temperature. The dashed lines ($---$) are linear fits of the high (α) and low (β) temperature trends. The intercept of these lines ($13^{\circ}C$) is indicated (\cdots).

The resistive features have decreasing characteristic frequencies when the temperature decreases on cooling (Fig. II-72). In the case of mPEO₈-N(Li)Pyr, three features shift across the limits of the frequency range. The ρ_3 (\blacksquare) and Q_3 (\square) features move to lower frequencies and out of the instrumental range on cooling. The Q_2 (\diamond) feature appears at the high frequencies at low temperature. Which features are observed depends on the temperature. The EIS spectrum measured at $100^{\circ}C$ comprises a different set of features to the EIS spectrum measured at $0^{\circ}C$.

The low frequency feature Q_3 (\square) disappears and the high frequency feature Q_2 (\diamond) appears at the same temperature ($18^{\circ}C$). The Q_3 and Q_2 features correspond to charge storage phenomena that exist within the electrolyte but are visible within the EIS spectrum frequency range only within a certain range of temperatures. Increasing temperature increases the characteristic frequency of the features of the EIS spectrum. Below $18^{\circ}C$, Q_3 has a characteristic frequency lower than the lower limit of the spectrum. The relaxation time of Q_3 is too long to be observed at low temperature. Above $18^{\circ}C$, Q_2 has a characteristic frequency higher than the upper limit of the spectrum. The relaxation time of Q_2 is too short to be observed at high temperature.

The reduced activation energy $W(T)$ of mPEO₈-N(Li)Pyr has a complex form (Fig. II-73). The curvature close to the start of the EIS measurements conducted on cooling is related to changing the direction of temperature change from heating to cooling, and is observed for all samples. $W(T)$ then follows a straight line in the 95 - $70^{\circ}C$ range. $W(T)$ is very sensitive to variation in temperature dependence, such that a variation of 1-2 % in the rate of decrease of σ on cooling can cause $W(T)$

to fluctuate by around 10 units. Fluctuation in $W(T)$ is observed on cooling in the 60-30°C, the same range over which ΔH_{endo} transitions are observed on heating in DSC. The intercept of linear fits estimates the $T[W(\alpha)=W(\beta)]$ transition at 13°C, above the lowest ΔH_{endo} observed on heating that corresponds to the melting of PEO chains (-12°C). The transition temperature $T[W(\alpha)=W(\beta)]$ at 13°C (**Fig. II-73**) is close to the crossover temperature of the features in the EIS spectrum (**Fig. II-72**). The two different treatments of the same data arrive at the same observation: *the polymer electrolyte behaves differently above and below a certain temperature within the limits of frequency of the EIS spectrum.*

A phenomenon can continue to exist outside a particular frame of reference. Even if the low frequency resistive part described by ρ_3 and Q_3 moves beyond the lower limit of the frequency range of the measurement, it continues to be a feature of the ionic transport properties of the electrolyte. Therefore, no definitive transition temperature can be inferred directly from the evidence presented in **Fig. II-72** and **Fig. II-73**. However, the different features of the EIS spectrum occupy mass within the electrolyte and will affect the bulk ionic transport, regardless of how the conductivity value is calculated.

The conductivity measured by fitting of the data to an equivalent circuit model (**Fig. II-54, E**) and the corresponding $W(T)$ are necessarily functions of the type, number and volume of ionic transport phases in the electrolyte. The MEC-SIPE mPEO₈-N(Li)Pyr is a single macromolecule composed of two chemically distinct parts: **i**) a Lewis basic oligo(ether) and **ii**) an ionic end-group equipped with a large aromatic ring system. Two distinct resistive features are observed in the EIS spectrum at high temperature (**Fig. II-67**). Since the two parts of the MEC-SIPE are covalently linked, these features are part of the same macromolecule. The EIS spectrum reveals the relaxation of ionic species in response to electromagnetic force. The lithium transference number of the EC-SIPE demonstrates that the majority of charge is carried by Li⁺ (measured of mPEO₂₀-N(Li)Pyr, $t_{\text{Li}}^+ = 0.7$ at 40°C). The low frequency ρ_3/Q_3 feature forms at high temperature and has a longer relaxation time in response to the applied electromagnetic force. It could be a consequence of ionic aggregate species that form at high temperature. In this case, the relaxation time of charges might be slower due to cumulative proximity effects of closely associated ionic species.

4.2.4. Characteristic Frequencies of mPEO_n-N(Li)Pyr: Dependence on PEO Chain Length

Variation of the PEO chain length changes which features are observed in EIS at a given temperature when all other variables are kept constant. The temperature dependencies of characteristic frequencies of mPEO_n-N(Li)Pyr having different PEO chain lengths ($EO_n = 8, 10, 20,$ and 55) are presented (**Fig. II-74, A-D**). The data of mPEO₈-N(Li)Pyr shown in **Fig. II-74 (A)** are identical to those in **Fig. II-72**. The ionic conductivity calculated from ρ_2 at frequency f_2 is omitted. The ionic conductivity value calculated by extrapolation of the complex impedance to the real axis of the Nyquist plot is given for each plot (the blue line, corresponding to σ on the vertical axis).

Low frequency features are observed at high temperatures in the MEC-SIPEs having $EO_n = 8$ and 20 (**Fig. II-74, A and C**). These low frequency features are not observed for MEC-SIPEs having $EO_n = 20$ and 55 (**Fig. II-74, B and D**). The high frequency feature Q_2 , corresponding to the double layer polarisation of the bulk electrolyte, is observed for mPEO₂₀-N(Li)Pyr at 18°C but is omitted from the figure because perturbation of the complex impedance prevented good fitting of the data to the equivalent circuit model. This is a consequence of crystallisation of the native PEO segments,

which decreases ion transport at this temperature (the ΔH_{endo} peak of the native PEO segment observed on heating in DSC has $T_p = 23^\circ\text{C}$). Thus, EIS analysis of mPEO₂₀-N(Li)Pyr measured on cooling is limited to the 100°C to 20°C range.

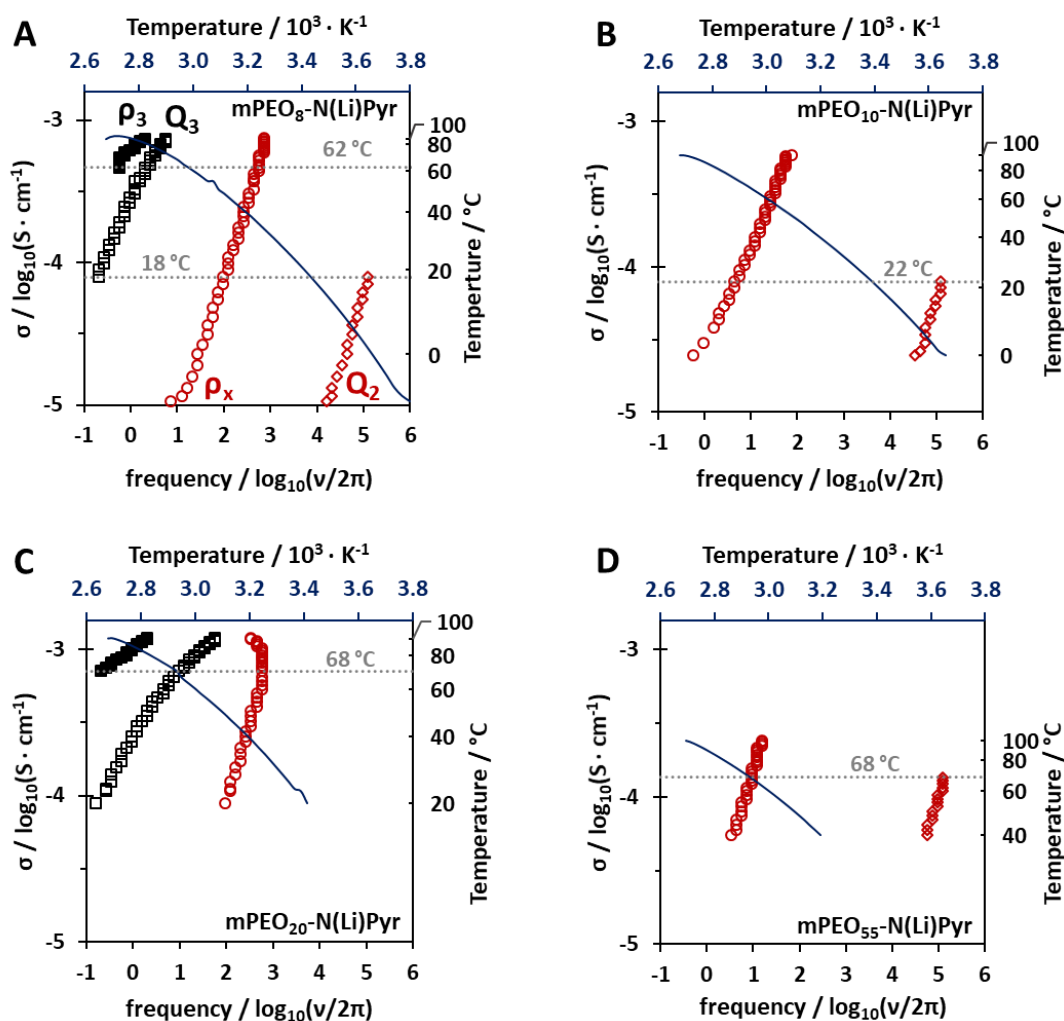


Figure II-74: The bulk ionic conductivity (σ) of mPEO_n-N(Li)Pyr (blue line, -) as a function of T ($10^3 \cdot \text{K}^{-1}$). The MEC-SIPE having $\text{EO}_n = 8$ (A), 10 (B), 20 (C), and 55 (D) are shown. The features of the EIS spectra (e.g. Fig II-67 and Fig. II-68) at their characteristic frequencies (f) are plotted and displaced vertically according to the bulk ionic conductivity (σ). These are labelled in A: ρ_3 (■), Q_3 (□), ρ_x (○), and Q_2 (◇). The temperatures ($^\circ\text{C}$) at which certain features enter or exit the frequency window are indicated and labelled (grey dotted lines, ...).

A possible explanation for the appearance and disappearance of the low frequency features relative to PEO chain length of mPEO_n-N(Li)Pyr could be the following:

$\text{EO}_n = 8$

A large mass fraction of functional end-groups ($\phi_{\text{m(EGrp)}} = 0.37$) are able to aggregate at high temperature. Charges have different relaxation times according to the particular conductive phase. One phase could be the low frequency (long relaxation time) population. The MEC-SIPEs mPEO₈-SO₂N(Li)Naph and mPEO₈-SO₃Li also have low frequency (Q_3) features (*vide infra*: Fig. II-77, B and E).

EO_n= 10

Increasing the length of the PEO chain decreases the mobility of the short, non-entangled MEC-SIPE in the chain-extended conformation. The low frequency population has decreased mobility and longer relaxation times. The low frequency feature is shifted to below the lower limit of the EIS spectrum range. None of the EC-SIPEs having EO_n= 10 have Q₃ features, except mPEO₁₀-SO₃Li at T > 90°C (*vide infra*: **Fig. II-77, B**).

EO_n= 20

Increasing the length of the PEO chain enables sufficient separation of the chain-ends to permit two populations of PEO units: **i**) "Native EO_n" segments and **ii**) EO_n* segments perturbed by the thermal behaviour of the functional end-group. In this case, the native EO_n= 14 (2 helices comprising 7 EO repeating units each) and the perturbed EO_n*= 6 (**Fig. II-75**). The effective MEC-SIPE (EO_n* + End-Group) is short and aggregates have short relaxation times. The low frequency feature has a characteristic frequency above the lower limit of the EIS spectrum range.

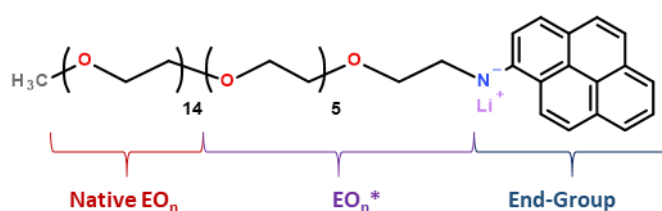


Figure II-75: An illustration of a hypothetical model of the MEC-SIPE mPEO₂₀-N(Li)Pyr. The mPEO chain is composed of two parts: **i**) "Native" EO_n units, and **ii**) EO_n* units that are perturbed by the proximal functional End-Group.

EO_n= 55

The mass fraction of functional end-groups is small ($\phi_{m(\text{EGrp})} = 0.09$). A fraction of those has a long relaxation time. The small, low frequency population makes a small contribution to the complex impedance. The Q₃ feature is not observed. The Nyquist representation implies the existence of a resistive population in the MEC-SIPE at high temperature (**Fig. II-76**). In the Nyquist plot, a second resistive feature (R₃/Q₃) might cause the perturbation of the meeting point of the first semi-circle and the spur attributed to ion diffusion processes (Z'' > Z'). In this case, no Q₃ crossing point is visible in the corresponding plot of Z' and Z'' as functions of frequency. This perturbation is observed in the Nyquist representation in the entire 100°C to 40°C range. An illustration of this hypothesis is given below (**Fig. II-76**). At 60°C, on cooling from 100°C, all the native PEO segments of the MEC-SIPE are expected to be in the melted state. Indeed, no crossing point of Q₃ is observed (**Fig. II-74, D**) because it is obscured by the low frequency diffusion process.

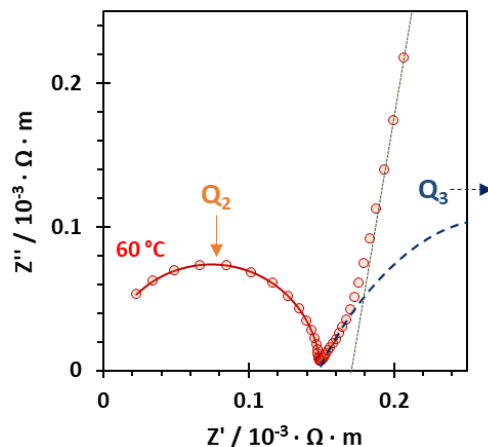
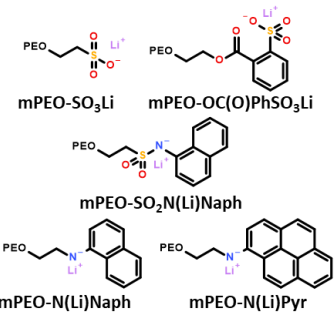


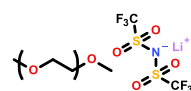
Figure II-76: A Nyquist representation of the EIS spectrum (○) measured of mPEO₅₅-N(Li)Pyr at 60°C on cooling from 100°C. The data is fitted with an equivalent circuit (Eqn. II-18; red line, -). The diffusion spur (green dotted line, ···) and a hypothetical R₃/Q₃ feature (blue dashed line, - -) are indicated. The position of Q₃ is obscured by the diffusion spur.

4.2.5. Characteristic Frequencies of Short-Chain MEC-SIPes: Dependence on the End-Group

The high concentration of functional end-group in short chain MEC-SIPes ($\phi_{m(\text{EGrp})}$, **Table II-13**) permits observation of multiple features in EIS over a large range of temperature. Moreover, EIS spectra of EC-SIPes having EO_n= 8 have different frequency dependent features (**Fig. II-77, A-E**). The appearance of the low frequency feature Q₃ above the lower limit of frequency is dependent on the polymer functional end-group (**Fig. II-77; A, B, E**). This might be related to aggregation of the functional end-groups. The aggregation of functional end-groups might be a consequence of **i)** exclusion from the native PEO domain, and **ii)** specific interactions of the end-groups. It is argued above that the PEO chain requires a certain number of units to develop a "native" PEO segmental character (**Fig. II-75**). To be consistent, the MEC-SIPes having EO_n= 8 must be exempt from this type of driving force. The PEO₈ chain is short and cannot entangle with PEO segments of other MEC-SIPes. These oligomers are therefore considered to be rigid oligomers with a large mass fraction of interacting functional end-groups. In the case of MEC-SIPes having EO_n= 8, the aggregation of the functional end-groups is limited to the direct interaction of the end-groups. This might be a consequence of several types of interactions that could act concertedly. These include ionic, dipole-dipole, Van der Waals, and π - π stacking interactions.

Table II-13: The Degree of Polymerisation (DP_n / EO_n), Number Average Molar Mass ($M_n / g.mol^{-1}$), the mass fraction of the functional end-group ($\phi_{m(EGrp)}$) and the mass fraction of lithium ($\phi_{m(Li)}$) of the presented MEC-SIPEs having different End-Group Identities.

MEC-SIPE						
	End-Group Identity	DP_n (EO_n)	$M_n(EG-SIPE)$ ($g.mol^{-1}$)	$\phi_{m(EGrp)}$	$\phi_{m(Li)}$	
	($g.mol^{-1}$)					
	-SO ₃ Li	87	8	474	0.18	0.015
	-OC(O)PhSO ₃ Li	207	8	594	0.35	0.012
	-SO ₂ N(Li)Naph	213	8	600	0.36	0.012
	-N(Li)Naph	148	8	536	0.28	0.013
	-N(Li)Pyr	223	8	610	0.37	0.011

SiP mPEO _n m/LiTFSI						
	Salt Identity	DP_n (EO_n)	$M_n(mPEOm)$ ($g.mol^{-1}$)	$\phi_{m(Salt)}$	$\phi_{m(Li)}$	
	($g.mol^{-1}$)					
	LiTFSI	287	10	476	0.38	0.09

The EIS data illustrated in **Fig. II-77 (A-F)** could be explained by comparing the functional end-groups. The Q_3 feature is observed at high temperature in the EIS of mPEO₈-N(Li)Pyr (**Fig. II-77, A**), mPEO₈-SO₃Li (**B**), and mPEO₈-SO₂N(Li)Naph (**E**). These functional end-groups are very different: we have an amine (**A**), a sulfonate (**B**), and a sulfonamide (**E**) salt. The large pyrene ring structure of mPEO₈-N(Li)Pyr might promote aggregation of the functional end-groups *via* π - π interactions. The mPEO₈-N(Li)Naph (**C**) has a smaller, naphthalene group in the place of the pyrene and Q_3 is not observed. Decreasing the interaction strength of the aryl function erases the Q_3 feature from the EIS window. The large ring structure of the pyrene increases the interaction parameter of the functional end-group relative to the smaller naphthalene. The Q_3 feature appears at high temperature in the EIS of mPEO₈-SO₂N(Li)Naph (**E**). The specific geometry of the sulfonamide and the dipole forces at the ionic linker augment the interaction parameter of the functional end-group relative to the naphthylamine.

The mPEO₈-SO₃Li has a Q_3 feature at high temperature (**Fig. II-77, B**). The ionic interactions of the sulfonate can promote the association of the end-groups. However, the mPEO₈-OC(O)PhSO₃Li does not have a Q_3 feature (**Fig. II-77, D**). The electron density at the sulfonate is decreased when it is *ortho* to an ester group due to inductive and resonance effects transmitted through the phenyl ring. The geometry of the mPEO₈-OC(O)PhSO₃Li end group points the sulfonate back towards the PEO chain. The geometry and electrostatic effect might concertedly decrease the interaction parameter of the functional end-group. The low frequency Q_3 feature is not observed.

The MEC-SIPEs (**Fig. II-77, A-E**) are compared to the SiP blend of mPEO₁₀m/LiTFSI ($EO/Li=10$) (**F**). The SiP has a slightly longer chain ($EO_n=10$) but an equimolar ratio of salt to polymer chains ($EO/Li=10$). The blend has the highest mass fraction of salt (compared to the mass of functional end-groups in MEC-SIPEs) and the lowest mass fraction of lithium (**Table. II-13**). Like the MEC-SIPEs, the SiP exhibits a low frequency feature at high temperature. Aggregation of ions at high temperature is well-reported in blends of binary salts in a polymer host matrix. However, in the SiP case, the anion is not covalently bound to the polymer. The low frequency feature might be the result of the aggregation of ionic species at high temperature.^[21,22] The resulting proximity effects of charges might reduce the mobility of the charged species. These species would have a

longer relaxation time in response to electromagnetic force and therefore a lower characteristic frequency. However, if aggregation of ionic species occurs in MEC-SIPes, it would necessarily be related to organisation of the PEO chain, since the anion is covalently bound to the polymer chain end.

Variation of the length of the PEO chain (Section 4.2.4) and variation of the functional end-group (4.2.5) profoundly change the form of the EIS spectrum observed at high temperature and at low temperature. The appearance of a low frequency (R_3/Q_3) feature might be the result of aggregation of ionic species. That is not to say specifically that R_3/Q_3 (or R_2/Q_2) is some particular type of aggregate. Rather, the aggregation of ionic species is possible in MEC-SIPes relative to the interaction parameter of the ionic end-groups. Short-chain MEC-SIPes might be arranged according to the interaction of functional end-groups. The functional end-group and the proximal repeating units (proposed here to be perturbed by the functional end-group and known as EO_n^*) might be segregated from the native PEO in MEC-SIPes having $EO_n \geq 20$. The segregation and organisation of MEC-SIPes, and the ionic end-groups in particular, might create different phases through which ionic transport is possible. One of these is fast (observed at high frequency) and another is slow (observed at lower frequency).

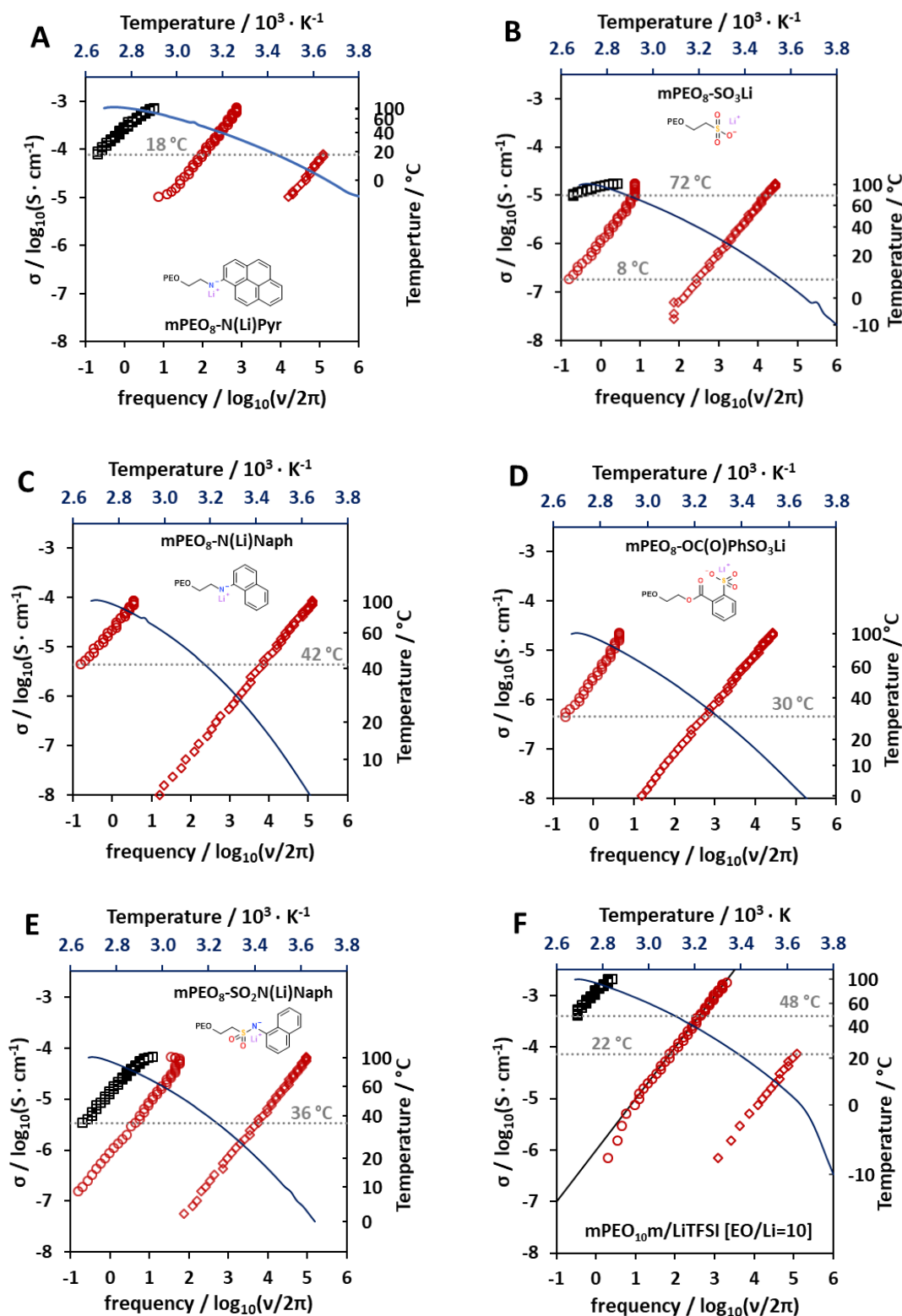


Figure II-77 (A-F): The bulk ionic conductivity (σ) as a function of T ($10^3 \cdot K^{-1}$) of MEC-SIPes having $EO_n=8$ and different functional end-groups: -N(Li)Pyr (A), -SO₃Li (B), -N(Li)Naph (C), -OC(O)PhSO₃Li (D), and -SO₂N(Li)Naph (E). The SiP blend mPEO₁₀m/LiTFSI (EO/Li= 10) is shown for reference (F). The features of the EIS spectra (see Fig. II-67 and Fig. II-68) at their characteristic frequencies (f) are plotted and displaced vertically according to the bulk ionic conductivity (σ). These are Q_3 (\square), ρ_x (\circ), and Q_2 (\diamond). The temperatures ($^{\circ}C$) at which certain features enter or exit the frequency window are indicated and labelled (grey dotted lines, ...).

4.3. Improvement of Ionic Conductivity with Cycling of Temperature

The ionic conductivity of the MEC-SIPes was measured as a function of temperature using blocking (gold) electrodes. The measurements were conducted over a range of temperatures and fitted to the VTF model on cooling. EIS spectra were taken at intervals of 2°C on heating and on cooling with 10 minutes of equilibration time at each temperature. The MEC-SIPes were cycled at least two times between the maximum and minimum temperature to verify that the measurement is reproducible. The MEC-SIPes having shorter chains ($EO_n=8, 10, \text{ and } 20$) produce overlapping plots of σ as a function of temperature and exhibit no change on cycling of the temperature ramps. The same is true for the SiP electrolytes based on blends of mPEO₆₀m/LiTFSI ($EO/Li= 10, 20, \text{ and } 60$) and mPEO₁₀m/LiTFSI ($EO/Li= 10$).

However, the MEC-SIPes having $EO_n= 55$ exhibit an increase in σ on cycling. For these MEC-SIPes in particular, the measurement ramps are programmed as follows:

1. Ambient temperature $\rightarrow 100^\circ\text{C}$
2. $100^\circ\text{C} \rightarrow 40^\circ\text{C}$
3. $40^\circ\text{C} \rightarrow 100^\circ\text{C}$
4. Repeat steps 2 \rightarrow 3.

These MEC-SIPes were cycled up to four times and exhibited a net increase in σ of *ca.* half of an order of magnitude (**Fig. II-78, A-E**). The data presented of MEC-SIPes having $EO_n= 55$ in earlier sections of this thesis are obtained from the last cycle of each of these examples. The ionic conductivity was calculated from Nyquist plots using an equivalent circuit model and the temperature dependence of σ on cooling from 100°C was fitted to the VTF equation. These results are compared and the implications discussed in context of the ion transport behaviours of the MEC-SIPes (Section 4.2).

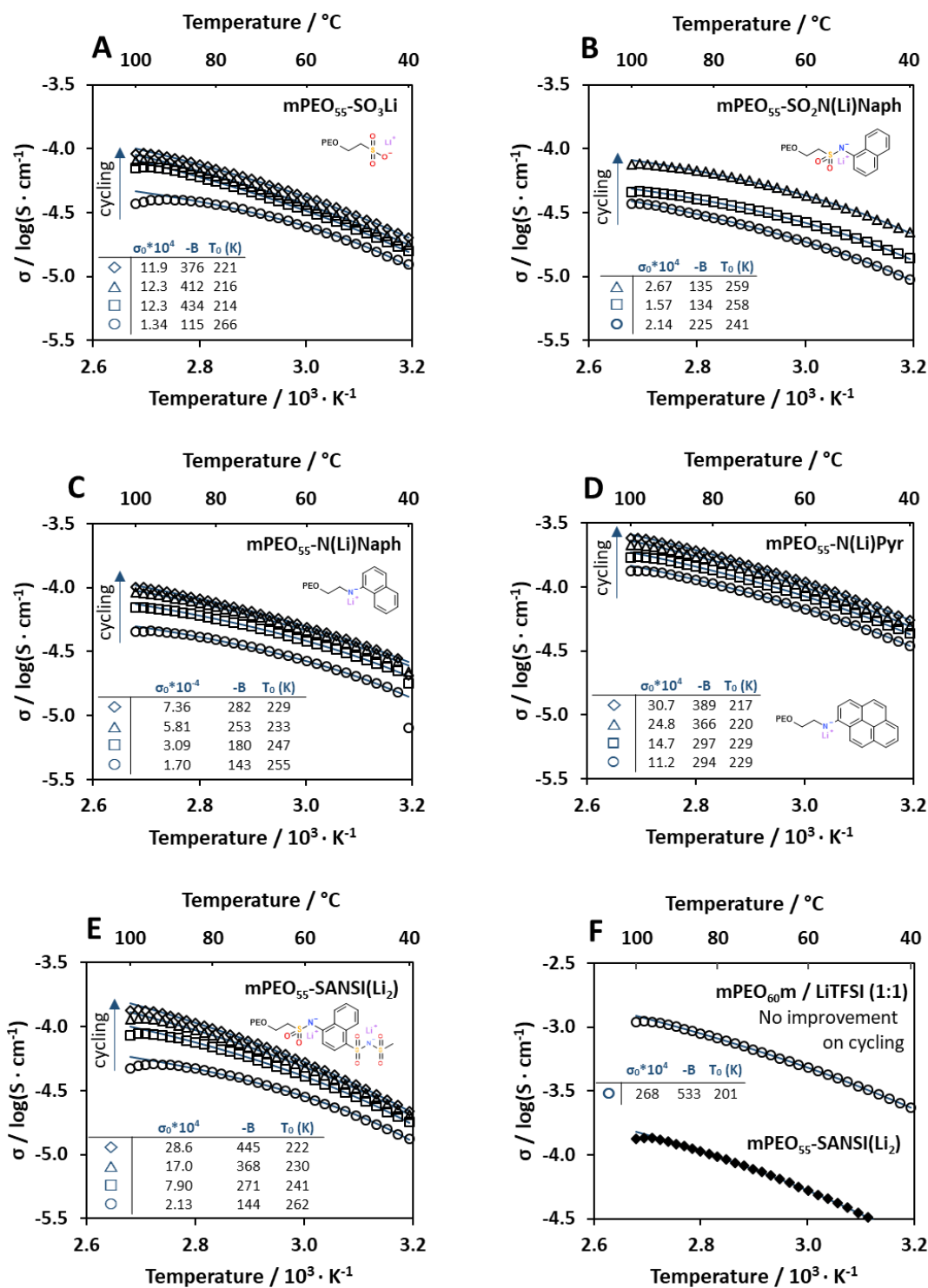


Figure II-78 (A-F): Conductivity (σ) as a function of T ($10^3 \cdot K^{-1}$) is shown for MEC-SIPes having $EO_n = 55$ and different functional end-groups: -SO₃Li (A), -SO₂N(Li)Naph (B), -N(Li)Naph (C), -N(Li)Pyr (D), and -SANSI(Li₂) (E). A SIP electrolyte mPEO_{60m}/LiTFSI ($EO/Li = 60$) is shown for reference (F) relative to the 4th cycle (\diamond) of mPEO₅₅-SANSI(Li₂). An insufficient amount of data was obtained for mPEO₅₅-OC(O)PhSO₃Li to enable comparison here. The impedance measurements were conducted every 2°C in the temperature range i) 60 → 100°C, ii) 100 → 40°C, and iii) 40 → 100°C, then repeating ramps ii) and iii). The displayed data were collecting during successive cooling (100 → 40°C) cycles: 1st (○), 2nd (□), 3rd (△), and 4th (◇) for all polymers except B (three ramps only). The VTF fits (blue lines, -) were calculated from the 90 → 40°C range. The VTF fitting parameters are tabulated in each plot.

As previously described, the VTF model cannot truly apply to these MEC-SIPes. However, the model is shown and the values are tabulated above (**Fig. II-78**). The pre-factor (σ_0) and in the term related to activation energy ($-B$) generally increase upon cycling. The equilibrium glass transition temperature (T_0) varies by as much as ± 15 K after the first cycle. These results together imply that the temperature dependence as well as the magnitude of σ is changing over successive temperature ramps.

A change in σ could be the result of three phenomena:

I. Reaction with the electrode surface.

The MEC-SIPes having short chains have identical chemistry to those having long chains. EC-SIPes having a certain functional end-group were synthesized and purified by the same methods. However, the short-chain MEC-SIPes did not exhibit a change in σ on cycling. The long chain MEC-SIPes ($EO_n = 55$) are not expected to react differently to short chain MEC-SIPes.

II. A change in the cell constant during the measurement.

The EIS measurements were conducted using a cell having spring to maintain constant pressure on the electrolyte. This prevents volume expansion of the electrolyte augmenting the inter-electrode distance. The distance between the electrolytes is fixed by a low-density poly(ethylene) spacer of known thickness measured prior to sample loading. The thickness of the spacers used varied in the range 50-100 μm , which gives a small variation in cell constant. The constant inter-electrode distance is determined by the measurement setup. Volume retraction of the electrolyte would result in a decrease in the electrode-electrolyte contact surface area and a *decrease* in σ .

III. Wetting of the electrode surface at high temperature.

The MEC-SIPes having $EO_n = 55$ exhibit melting in the 40-60°C range. Heating of the electrolyte melts the MEC-SIPE and wets the surface of the electrode. This increases the electrode-electrolyte contact surface area and improves ionic conductivity. The loading of samples into the cell is performed at elevated temperature for this practical reason. Indeed, σ during the first heating ramp is inferior to equivalent temperature at the first cooling ramp. However, the low sample mass of the MEC-SIPes is combined with long measurement times. If wetting were the cause of the improvement in σ , it is not expected to result in consistent improvement of σ over as many as 4 cycles of heating and cooling. Assuming that measurement of the EIS spectrum takes 2 minutes, knowing that the heating and cooling rate is $1^\circ\text{C}\cdot\text{min}^{-1}$, and using a fixed equilibration time of 10 minutes at each measurement temperature, 4 cycles represents more than 37 hours at $T > 60^\circ\text{C}$. The MEC-SIPes of μg sample mass are expected to melt during the first heating ($60 \rightarrow 100^\circ\text{C}$, 4.7 h) of the first cycle (9.3 h at $T > 60^\circ\text{C}$).

The three phenomena discussed above are therefore excluded and cannot account for the improvement in σ of MEC-SIPes having $EO_n = 55$. The perturbation of the complex impedance illustrated in Figure II-76 is a common feature of the long chain MEC-SIPes in the 40°C to 100°C range. The feature is visible but often small. This can prevent reliable modelling of the complex impedance using an equivalent circuit comprising two parallel R/Q couples in series (**Eqn. II-18**).

The best opportunity to investigate the low frequency phenomenon is in the EIS spectra of mPEO₅₅-SANSI(Li₂) (**Fig. II-79**). This polymer has the highest mass fraction of functional end-groups ($\phi_{m(\text{salt})} = 0.136$) of the MEC-SIPEs having EO_n = 55. However, the mass fraction of lithium remains small ($\phi_{m(\text{Li})} = 0.005$). The low frequency feature of this EC-SIPE is most accessible for modelling.

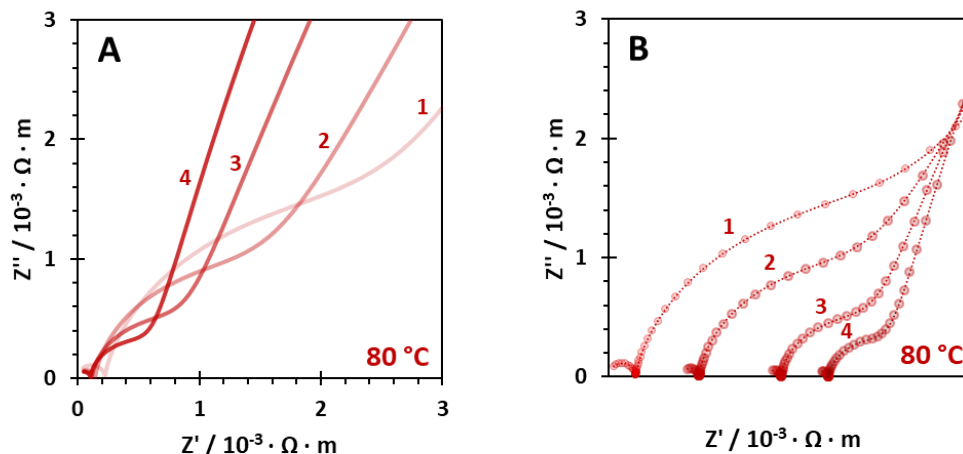


Figure II-79: Selected Nyquist plots of EIS spectra measured of mPEO₅₅-SANSI(Li₂) at 80°C during four successive cycles (labelled 1-4) on cooling from 100°C. The panels are (A) overlapping data represented by red lines; and (B) the experimental data (red circles, O) are plotted in the complex plane and displaced along the real (Z') axis by an arbitrary value. The dotted lines (...) are a guide for the eye only.

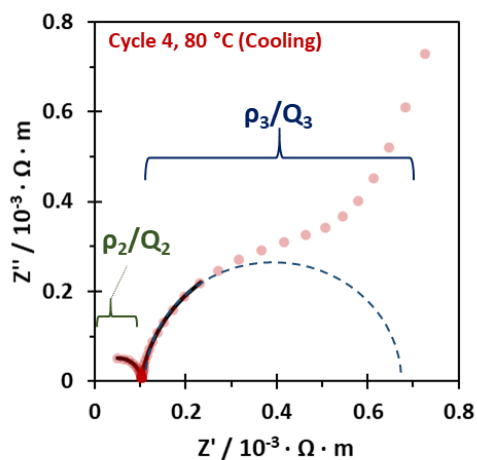


Figure II-80: Nyquist plot of EIS spectrum of mPEO₅₅-SANSI(Li₂) measured at 80°C on cooling during cycle 4 (circles, ●) fitted by the equivalent circuit (Eqn. II-18; black line, -). The features at high frequency (ρ_2/Q_2) and low frequency (ρ_3/Q_3) are labelled. The shape of ρ_3/Q_3 is illustrated (dashed line, - -).

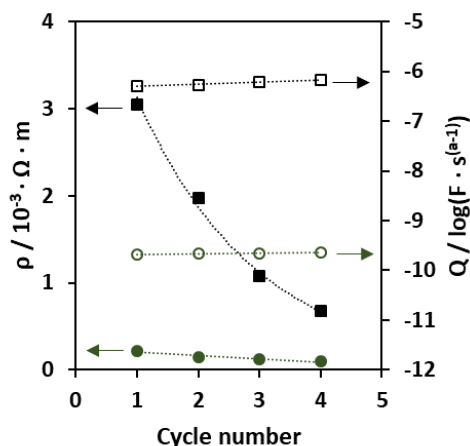


Figure II-81: The resistivity (ρ , filled symbols) and the corresponding capacitance (Q , open symbols) of two features in EIS spectra of mPEO₅₅-SANSI at 80°C on cooling from 100°C. Cycle numbers refer to the spectra illustrated in Figure 86. The higher frequency feature ρ_2/Q_2 (circles; ○, ●) and the lower frequency feature ρ_3/Q_3 (squares; □, ■) are displayed. Lines are drawn as a guide for the eye only.

The modelling of the two features of mPEO₅₅-SANSI(Li₂) is illustrated in **Fig. II-80**. The two features are modelled together using one equivalent circuit (**Eqn. II-18**). The resistivity and capacitance of the two features are calculated from EIS measured at 80°C on cooling during four successive cycles and the evolution plotted as a function of cycle number (**Fig. II-81**). The capacitances of the two features are almost constant. The resistivity of the low frequency feature decreases by a much greater amount than the resistivity of the high frequency feature.

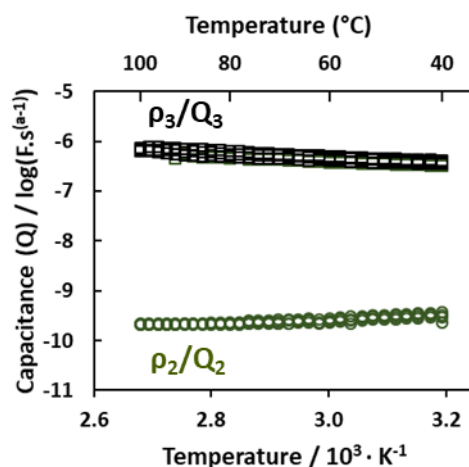


Figure II-82: The capacitance ($F.s^{(a-1)}$) of the ρ/Q features of $mPEO_{55}$ -SANSI(Li_2) as functions of T ($10^3.K^{-1}$). The data are calculated by fitted to a single equivalent circuit (Eqn. II-18). The overlapping values of four successive cooling ramps are shown for ρ_2/Q_2 (open green circles, \circ) and ρ_3/Q_3 (open black squares, \square).

The capacitance of the two features does not change significantly either as a function of temperature or as a result of thermal cycling (Fig. II-82). Therefore, there is no change in the electrochemistry of either feature during cycling. However, the ionic conductivity of each is improved by thermal cycling. The two features are modelled together using one equivalent circuit (Eqn. II-18). The ionic conductivity of the ρ_2/Q_2 feature (Fig. II-83) agrees very well with the values calculated using an equivalent circuit comprising a single parallel R/Q couple on the data of that feature alone (Fig. II-54, E). The ρ_3/Q_3 feature (Fig. II-84) has a larger increase in ionic conductivity (of *ca.* 1 order of magnitude) than the ρ_2/Q_2 feature (of *ca.* half an order of magnitude) as a result of thermal cycling. The augmentation of σ per cycle of the ρ_3/Q_3 feature does not appear to decrease with successive cooling scans.

Fig. II-83 & Fig. II-84: The ionic conductance (Ω^{-1}) as a function of temperature ($10^3.K^{-1}$) of two features of $mPEO_{55}$ -SANSI(Li_2). The high frequency ρ_2/Q_2 (Fig. II-83) and the low frequency ρ_3/Q_3 (Fig. II-84) features are fitted to the same equivalent circuit (Eqn. II-18) but plotted separately. The conductance calculated of the 1st (\circ), 2nd (\square), 3rd (\triangle), and 4th (\diamond) successive cooling ramps are shown. The VTF fits (blue lines, -) were calculated from the 90 \rightarrow 40°C range.

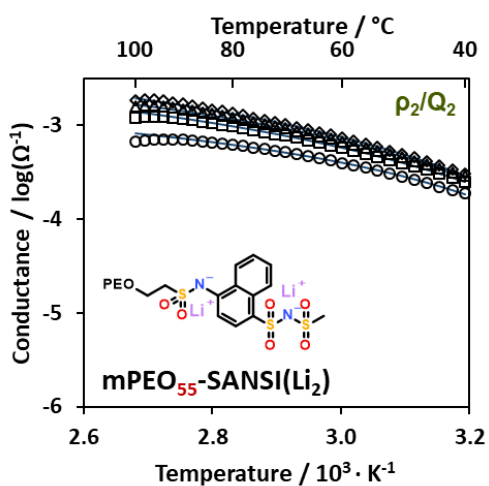


Figure II-83: The high frequency ρ_2/Q_2 feature.

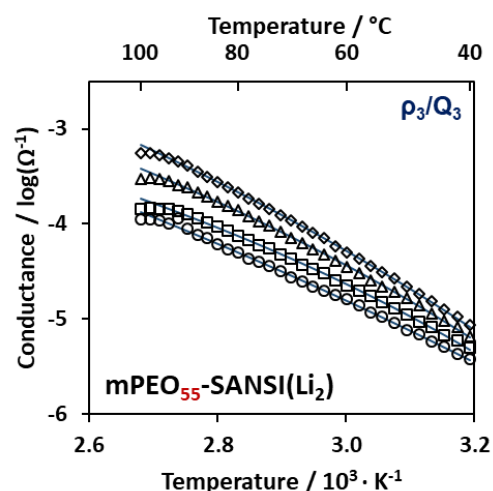


Figure II-84: The low frequency ρ_3/Q_3 feature.

The temperature dependence of σ was fitted to the VTF equation. The fitting parameters are listed below (**Table II-14**). The VTF parameters evolve consistently for the ρ_2/Q_2 feature. Whereas both σ_0 and $-B$ increase in magnitude with cycling, T_0 decreases. The VTF fitting parameters of the ρ_3/Q_3 feature are anomalous: the parameters of ramp 4 does not agree with the trend of ramps 1→3. The σ of ρ_3/Q_3 appears to have a linear dependence to temperature descending from the usual curvature close to 100 °C (which might be related to the reversal of the direction of temperature change). The data of ρ_3/Q_3 is fitted to the Arrhenius equation and the fitting parameters follow a consistent trend (**Table II-14**). Both σ_0 and $-E_a$ increase in magnitude with thermal cycling.

The $W(T)$ functions of both ρ_2/Q_2 and ρ_3/Q_3 were calculated from the same data. The $W(T)$ of ρ_2/Q_2 (**Fig. II-85**) has the same change in slope as was calculated by fitting these same data by a single parallel R/Q couple (**Fig. II-54, G**). $W(T)$ is very sensitive to fluctuations in σ . The $W(T)$ calculated for ρ_3/Q_3 is too disperse to permit a confident linear fit (**Fig. II-86**). The forms of $W(T)$ for ρ_2/Q_2 and ρ_3/Q_3 decrease confidence in the fitting parameters obtained using the VTF and Arrhenius models. However, the dependence of the σ of ρ_3/Q_3 on reciprocal temperature is remarkably linear. The tendency of $-B$ (VTF) and $-E_a$ (Arrhenius) to increase in magnitude (**Table II-14**) is important for describing the effect of thermal cycling on this MEC-SIPE, even if the values are not accurate, as they imply an increase in the activation energy of ionic conduction with thermal cycling.

Table II-14: Fitting parameters of the ρ_2/Q_2 and ρ_3/Q_3 features calculated by fitting of the σ of mPEO₅₅-SANSI(Li₂) on cooling from 100°C to 40°C. The fits were made over the 90 °C→ 40 °C range. Both features were fitted to the VTF equation. The ρ_3/Q_3 feature is additionally fitted to the Arrhenius equation. The numbers (#) in the sequence of the cooling ramps are listed. In the Arrhenius equation E_a is the activation energy (J.mol⁻¹) and R is the ideal gas constant (8.314 J.K⁻¹.mol⁻¹).

VTF: ρ_2/Q_2				VTF: ρ_3/Q_3				Arrhenius: ρ_3/Q_3		
#	$\sigma_0 \cdot 10^3$	-B	T_0 (K)	#	σ_0	-B	T_0 (K)	#	$\sigma_0 \cdot 10^{-3}$	$-E_a$ (kJ.mol ⁻¹)
4	33.8	407	227	4	321	3095	136	4	10855	72.3
3	23.4	365	230	3	16.4	2280	158	3	1229	67.3
2	9.98	252	245	2	14.6	2681	133	2	70	60.6
1	3.14	150	260	1	13.7	2929	119	1	18	57.8

$$\sigma = \sigma_0 \cdot e^{\left(\frac{-B}{|T-T_0|}\right)}$$

$$\sigma = \sigma_0 \cdot e^{\left(\frac{-E_a}{RT}\right)}$$

These features are visible in the presentation of the impedance spectrum as a function of frequency (**Fig. II-87**). The characteristic frequencies of ρ_3 , Q_3 , ρ_x , and Q_2 are plotted and displaced vertically according to the ionic conductivity of the ρ_2/Q_2 feature (**Fig. II-88**).

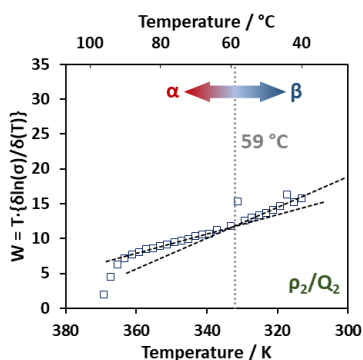


Figure II-85: $W(T)$ of the ρ_2/Q_2 feature of mPEO₅₅-SANSI(Li₂) calculated from the 4th cooling ramp of EIS measurements with thermal cycling. Linear fits of the high T (α) and low T (β) regimes are shown (dotted lines, ...). The intercept transition temperature is labelled, $T[W(\alpha)=W(\beta)]=59^\circ\text{C}$.

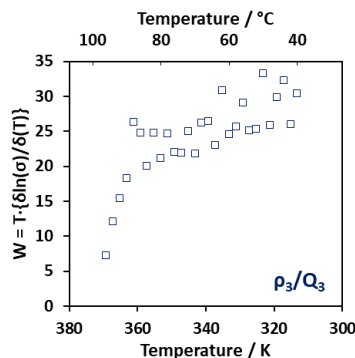


Figure II-86: $W(T)$ of the ρ_3/Q_3 feature of mPEO₅₅-SANSI(Li₂) calculated from the 4th cooling ramp of EIS measurements with thermal cycling.

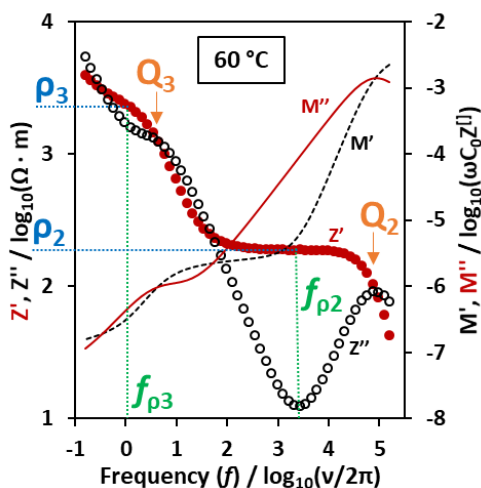


Figure II-87: Representative EIS spectrum of mPEO₅₅-SANSI(Li₂) measured at 60°C on cooling from 100°C (4th cycle). The Q_2 and Q_3 features are labelled.

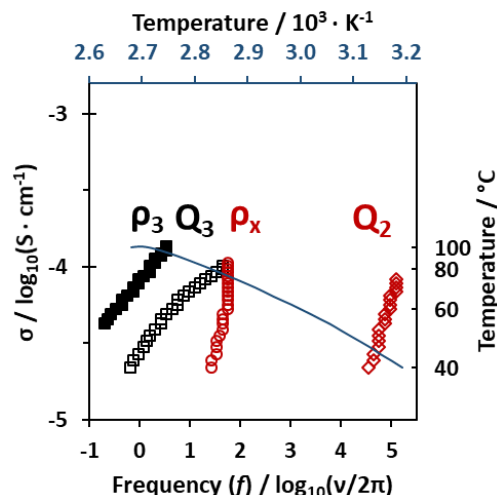


Figure II-88: The σ of the ρ_2/Q_2 couple of mPEO₅₅-SANSI(Li₂) as a function of T ($10^3 \cdot \text{K}^{-1}$). The characteristic frequencies of ρ_2 (■), Q_3 (□), ρ_x (○), and Q_2 (◇) are plotted on the x-axis and displaced vertically according to σ of the ρ_2/Q_2 couple.

It is proposed that the second (ρ_3/Q_3) feature is a consequence of ionic end-groups, which occurs relative to the thermally controlled motions of PEO segments. When the MEC-SIPE chain length is long ($\text{EO}_n=55$), the functional end-groups constitute a small mass fraction of the bulk. If their aggregation persists even at low concentration, it is the result of high interaction strength (high χ). It is reasonable to suggest that such behaviour would be visible only in the MEC-SIPEs having the largest, most physicochemically distinct functional end-groups with respect to the PEO chain.

In the case of the present library of MEC-SIPEs, the large, chemically distinct end-group is exemplified by mPEO₅₅-SANSI(Li₂). It is important to note that even MEC-SIPEs having $\text{EO}_n=55$ are still too short ($M_{n(\text{PEO})}=2400 \text{ g}\cdot\text{mol}^{-1}$) to form folded chain crystalline PEO phases and that chain entanglement is not expected. The shortest PEO chains to form folded crystals have $\text{EO}_n=70-90$ ($M_n=3000-4000 \text{ g}\cdot\text{mol}^{-1}$).^[17] If the aggregation of functional end-groups causes the creation of a second ion transport phase (Section 4.2), then the evolution of these phases under conditions of

temperature is related to **i)** the efficiency of ion transport within these phases, **ii)** the mass fraction of the bulk that they occupy, and **iii)** the percolation of these phases over the microscale length of the EIS measurement.

It is shown above that both the ρ_2/Q_2 (**Fig. II-83**) and the ρ_3/Q_3 (**Fig. II-84**) features increase in ionic conductance upon thermal cycling. Their capacitances are constant with temperature and with thermal cycling (**Fig. II-82**). Their constant capacitance excludes a change in the (electro)chemical properties of these features. Given that the functional end-groups are expected to be expelled from PEO domains at temperatures close to the fusion of PEO segments, one imagines the ionic end-groups at the boundary of PEO grains. The increase in ionic conductivity with thermal cycling is in this way associated with the ripening of grains and the percolation of grain boundaries through the bulk polymer electrolyte. This is provocative because grain boundaries are traditionally portrayed as highly resistive features that decrease microscale ionic conductivity. In the above examples (**Fig. II-78, A-E**) 4 cycles is not enough to reach optimisation of this effect, where σ would be limited by the concentration of functional end-groups, for all of the presented end-capped polymer electrolytes.

4.4. Conclusions on Ion Transport in MEC-SIPEs

The trends of the ionic conductivities of MEC-SIPEs (Section 2.1) are discussed in context of their high transference of lithium (Section 2.3), and their complex thermal behaviours (Section 3). Close inspection of the temperature dependence of ionic conductivity (Section 4.1) and the characteristic features observed at different temperatures (Section 4.2) leads us to propose a tentative model for describing ionic transport processes in MEC-SIPEs.

It is useful at this point to summarise briefly the observations and conclusion of the previous sections of this manuscript. Until this point, it is reported:

1. The magnitude of ionic conductivity is determined by the functional end-group at constant PEO chain length.
2. The magnitude of ionic conductivity is dependent on the concentration of ionic end-groups. For MEC-SIPEs, the mass fraction of functional ionic functions is proportional the length of the PEO chain.
3. The PEO chain of mPEO₂₀-N(Li)Pyr has thermal behaviour implying a segregated polymer architecture comprising "native" PEO segments and a perturbed EO_n* segment proximal to the functional end-group.
4. Multiple thermal transitions observed on heating of MEC-SIPEs having short PEO chains (EO_n= 8, 10, 20) are evidence of more than one type of structural organisation in the bulk MEC-SIPEs. Multiple ways of organising a single entity implies segregation of the parts of the entity.
5. The reduced activation energy $W(T)$ has a change from a low temperature dependence at high temperature to a high dependence at low temperature. This is evidence of a change in the activation energy of the ionic transport as a function of temperature. The transition temperature is above the melting point of native PEO segments of short chain MEC-SIPEs (EO_n= 8, 10, 20). The native PEO is therefore expected to be disordered when approaching and crossing the transition temperature on cooling. Ionic species are expected to aggregate at high temperature, when PEO segments are melted.
6. Characteristic features are observed in EIS. These are dependent on the functional end-group. In particular, MEC-SIPEs having functional end-groups expected to have higher interaction parameters exhibit two features: one at high frequency and one at low frequency. The two resistive features are identified by characteristic frequencies at Q₂ (high frequency f_{Q2}) and Q₃ (low frequency f_{Q3}). The existence of two features might correspond to two resistive phases. The existence of these features might be related to aggregation of ionic species and, in the case of MEC-SIPEs, these are the polymer functional end-groups.
7. The low frequency characteristic feature Q₃ is directly observed for MEC-SIPEs having EO_n= 55 if the functional end-group is large enough. The mPEO₅₅-SANSI(Li₂) provides an opportunity to study this phenomenon.

Thermal cycling of the MEC-SIPEs provides us with indirect evidence of the percolation of conductive phases through the bulk state. In the case of functional end-groups at the boundary of PEO domains, it is the grain boundary that is the more highly conductive, least resistive, high frequency ρ_2/Q_2 feature. Inspection of **Fig. II-84** affords a comparison with σ of the magnitude expected of "single-ion" polymer electrolytes without significant structural organisation at the microscopic scale. The best estimate of the activation energy of ρ_3/Q_3 phase (**Table. II-14**) implies that a higher activation energy is required for ionic transport than in the higher frequency ρ_2/Q_2 phase.

This is consistent with a model of high conductivity (low activation energy) transport in phases of closely interacting ionic end-groups and low conductivity (high activation energy) transport in phases of low concentration of ionic end-groups. The percolation of the conductive phases is enabled by the thermally activated motion of the end-groups. Their association is enabled by interactions such as ionic, dipole-dipole, Van der Waals, and π - π stacking. The result is a polymer electrolyte having percolating, conductive phases at the boundary of PEO grains (**Fig. II-89**). This is inverse to the grain boundary hypothesis of solid-state electrolytes made of inorganic materials (ceramics). In those systems, ionic transport occurs *via* successive, discrete motions of ions from their occupied lattice positions to available vacancies. In that scenario, a grain boundary is a defect in the lattice structure that imposes a high activation energy barrier to ionic transport. In the case of MEC-SIPEs, the association of functional end-groups is expected to occur at the boundary of PEO domains, if the PEO chain is long enough to become segregated into "native" and "EO_n* + end-group" phases. The exclusion of hydroxyl end-groups from extended-chain PEO crystalline phases is widely accepted. Here, extended-chain PEO phases are expected to exclude ionic end-groups. The high χ ionic end-groups are moreover able to interact via strong forces. *In this scenario, a grain boundary is a conductive phase through which ion transport occurs via the thermally activated motions of closely associated ionic functions.* These boundaries are composed of soft matter that organises under mild processing conditions (compared to ceramics). Ionic groups that are not incorporated into the high conductivity (boundary) phase are kinetically trapped defects. The size of this population is decreased by slow cooling and repeated thermal cycling above the melting temperature of the grains. As more of the ionic end-groups are incorporated into percolating conductive phases, the bulk resistivity of the electrolyte decreases at constant capacitance. The result is a polymer electrolyte that increases in ionic conductivity with thermal processing under conditions of a small, oscillating electromagnetic force.

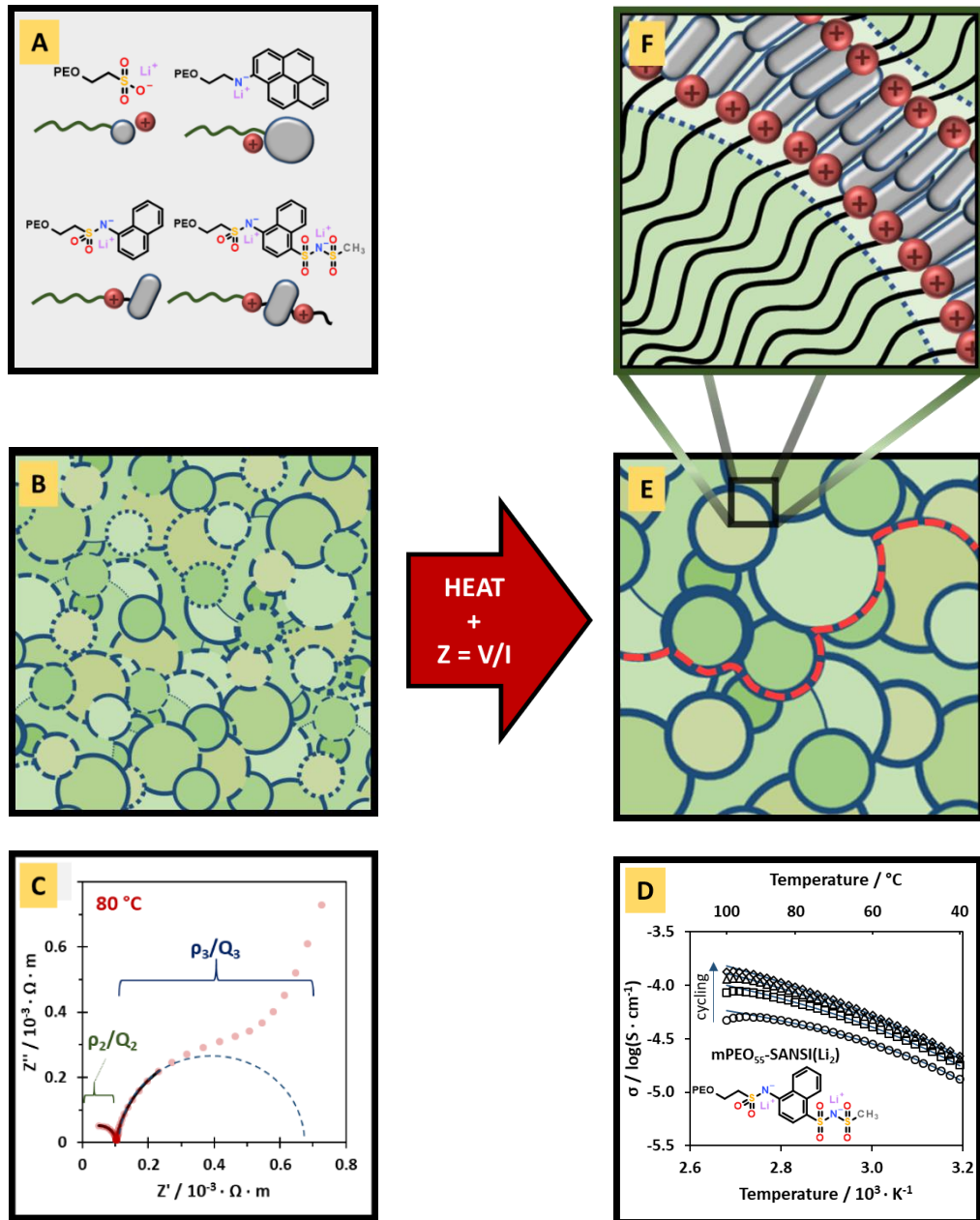


Figure II-89: A graphical abstract illustrating the tentative model of how MEC-SIPes afford efficient conduction of ions in the bulk state. The MEC-SIPes (examples shown in panel A) are segregated in the bulk state (B) due to the low N-high χ macromolecular design based on functional ionic end-groups. Low frequency resistive features (C) are evidence of imperfection in ion transport. The ionic conductivity increases with cycling (D) under mild conditions of temperature and electromagnetic force. This might be the result of improved the percolation of ionically conductive pathways (E) composed of functional ionic end-groups localised at the boundary of PEO grains (F). In the panels B and C, the grain boundaries are represented by blue lines (sometimes incomplete). Panel E is an attempt to illustrate a percolating pathway (red dashed line, - - -) as a continuum of grain boundaries. In panel B the percolation of grain boundaries is incomplete, so a good path is hard to find.

5. General Conclusions

The End-Capped "Single-Ion" Polymer Electrolyte is a versatile, modular design. Considerable variation of the functional end-group is possible and can be applied to the terminal of a polymer chain. The identity of the polymer chain in this thesis is the widely studied poly(ethylene oxide). However, any polymer chain that is attractive for the application should reasonably be considered. The MEC-SIPE model provides an opportunity to study ion transport in a neat polymer electrolyte. Without the use of additional ingredients and formulation chemistry, these MEC-SIPEs achieve performance that is in line with contemporary standards in terms of ionic conductivity, stability and transference of lithium ions. Electrochemical stability against lithium metal should be improved if such polymers are to be applied as electrolytes in high voltage cells.

There appears in a library of sufficient synthetic variation an opportunity to study the fundamental ion transport properties of "single-ion" polymer electrolytes. Varying the chain length of a MEC-SIPE is the synthetic equivalent of a magnifying glass on the segmental and end-group dynamics of a polymer chain. The dependence of ion transport performance on chain length (and therefore the concentration of ionic end-groups) is expected to depend very much on the physicochemical properties of the polymer chain. Therefore, the parameters of chain length and end-group identity should be thought of in terms of the repeating persistent length of the polymer. In the case of PEO, this is well-defined in the bulk state as a $7/2$ helical structure having two turns of the helical pitch comprising 7 ethylene oxide repeating units. This should be considered when varying the polymer chain.

Thermal characterisation reveals complex yet very interesting behaviours of the MEC-SIPEs. These occur over time scales that permit practical thermal processing. This is a considerable advantage over block copolymer electrolytes that require intensive optimisation of polymer composition and processing techniques. The optimisation of a relatively simple MEC-SIPE provides insight into the interplay of the polymer chain and the ionic function in determining the performance of the electrolyte.

The ionic transport in MEC-SIPEs might occur in segregated phases that are optimised under appropriate processing conditions. Here, temperature and a small electromagnetic force applied by an electromagnetic impedance spectrometer is enough to improve ionic conductivity by around half an order of magnitude. Cycling of the MEC-SIPEs implies that the measured ionic conductivity might be optimised further. These soft materials might transport ions in an unexpected way: *along the "boundaries" of polymer "grains"*.

6. Perspectives

Valorisation of the proposed model of conductive grain boundaries requires further investigation. For example, the evolution and percolation of grain boundaries could be studied by polarised optical microscopy (POM), and wide-angle vs. small angle X-ray scattering (WAXS vs. SAXS). POM might visualise the evolution of phases under certain conditions of temperature informed by DSC. Scattering techniques would define number and the length scale of different organised phases at appropriate temperatures. In particular, **Grazing Incidence WAXS / SAXS (GI-WAXS/SAXS)** could be used to probe what organisation of MEC-SIPEs might occur at the interface with a solid surface. These types of structural characterisations are essential for defining the merit of ionic transport properties of MEC-SIPEs in terms of the structural organisation of the polymer electrolyte in the bulk state. Analysis of these data in context of EIS spectroscopy could define key structure-property correlations that would enable the design and synthesis of MEC-SIPEs capable of hierarchical self-organization organisation over up to a few microns (*i.e.* the typical distance separating electrodes in battery) required for optimisation of ionic transport in electrochemical storage devices.

Correlations between grain size and persistent length of polymer chains might be probed by applying the same functional end-group to different polymers. For example, by variation of the degree of polymerisation in increments of commensurate persistent lengths relative to the polymer chain chemistry, a relationship between the interaction strength of the functional end-group, the grain size of polymer domains, and the flexibility of the polymer chain could be established. It is expected that a high- χ functional end-group is required for the design of a MEC-SIPE that will spontaneously form segregated phases in the bulk. With MEC-SIPEs having PEO chains already presented, one might reasonably approach ionically conductive poly(carbonate) and poly(ester) chain chemistries for the synthesis of a comparable library of MEC-SIPEs. Indeed, if fast ion transport occurs by association of functional end-group at the boundary of polymer grains, the physical and thermal properties of the polymer chain could be considered in preference over the ability to conduct ions. Thus, highly flexible poly(siloxane)s could be considered. The electrochemical stability of MEC-SIPEs will remain a concern as they must be developed in context of applied active electrode materials. Fluorinated poly(ether)s and poly(olefin)s could be the answer to the question of electrochemical stability.

The variation of the polymer repeating unit and chain length would permit investigation of the effect of chain segment mobility on the ion transport properties of MEC-SIPEs. In particular, the glass transition (T_g) could be measured. The Ohno group reported T_g in the -20 to -60 °C range for mPEO_n-SO₃Li (EO_n= 5-45) and correlated these values as having an inverse relationship to ionic conductivity.^[23] Measurement of such low T_g values by DSC requires specially adapted instrumentation and protocols involving rapid heating from low temperatures. Dynamic Mechanical Analysis (DMA) is excluded for short-chain polymers (such as those presented in this work) which do not entangle and cannot be cast into films. An alternative might be to determine T_g using rheology.^[24] A rheometer fitted with specialised cooling apparatus might be used to measure the T_g of short-chain MEC-SIPEs using oscillating, frequency sweeps to define the mechanical storage (G') and loss (G'') moduli. The T_g should then be defined as the temperature at which G' decreases and G'' approaches a local maximum, in the region approaching a local maximum in their loss coefficient ($\tan \delta = G''/G'$). Time-temperature superposition of frequency

dependent viscosity is applicable only if one assumes that the polymers are amorphous, homogeneous, and isotropic. This is unlikely to be appropriate for High χ -Low N macromolecules such as MEC-SIPes, and particularly those presented here, which have semi-crystalline PEO chains.

MEC-SIPes might be considered as a family in a larger class of point-group modified polymers. In the case of MEC-SIPes, the point group is at the chain terminal and is intended to function as a host for ion transport. The position of this point group along the polymer chain could be varied to probe specific structure-property relationships targeting supramolecular organisation. The position of the ionic point group could be commensurate or incommensurate with the persistent length, to selectively promote order and disorder in the bulk electrolyte.

The MonoEnd-Capped Single-Ion Polymer Electrolyte is an elegantly simple and generic approach to design and synthesize polymer electrolytes. It should be exploited toward the next generation of electrolytes for high performance electrochemical energy storage devices.

7. Bibliography of Chapter II

- [1] Sinturel, C.; Bates, F. S.; Hillmyer, M. A. High χ -Low N Block Polymers: How Far Can We Go? *ACS Macro Letters* **2015**, 4 (9), 1044-1050. DOI: [10.1021/acsmacrolett.5b00472](https://doi.org/10.1021/acsmacrolett.5b00472)
- [2] Zhang, H.; Li, C.; Piszcz, M.; Coya, E.; Rojo, T.; Rodriguez-Martinez, L. M.; Armand, M.; Zhou, Z. Single Lithium-Ion Conducting Solid Polymer Electrolytes: Advances and Perspectives. *Chemical Society Reviews* **2017**, 46 (3), 797-815. DOI: [10.1039/C6CS00491A](https://doi.org/10.1039/C6CS00491A).
- [3] Atkins, P. W.; De Paula, J.; Keeler, J. Atkins. Physical Chemistry, 11th edition; Oxford University Press: Oxford New York, 2018.
- [4] Springer Handbook of Electrochemical Energy; Breitkopf, C., Swider-Lyons, K., Eds.; Springer: Berlin Heidelberg, 2017.
- [5] Electroanalytical Methods: Guide to Experiments and Applications, 2., rev. and extended ed.; Scholz, F., Bond, A. M., Eds.; Springer: Berlin, 2010.
- [6] Fulcher, G. S. Analysis of Recent Measurements of the Viscosity of Glasses. *Journal of the American Ceramic Society* **1925**, 8 (6), 339-355. DOI: <https://doi.org/10.1111/j.1151-2916.1925.tb16731.x>.
- [7] Tammann, G.; Hesse, W. Die Abhängigkeit Der Viscosität von Der Temperatur Bie Unterkühlten Flüssigkeiten. *Zeitschrift für anorganische und allgemeine Chemie* **1926**, 156 (1), 245-257. DOI: <https://doi.org/10.1002/zaac.19261560121>.
- [8] Ito, K.; Nishina, N.; Ohno, H. High Lithium Ionic Conductivity of Poly(Ethylene Oxide)s Having Sulfonate Groups on Their Chain Ends. *Journal of Materials Chemistry* **1997**, 7 (8), 1357-1362. DOI: [10.1039/a700583k](https://doi.org/10.1039/a700583k).
- [9] Ito, K.; Tominaga, Y.; Ohno, H. Polyether/Salt Hybrid (IV). Effect of Benzenesulfonate Group(s) and PEO Molecular Weight on the Bulk Ionic Conductivity. *Electrochimica Acta* **1997**, 42 (10), 1561-1570. DOI: [10.1016/S0013-4686\(96\)00317-9](https://doi.org/10.1016/S0013-4686(96)00317-9).
- [10] Wheatle, B. K.; Lynd, N. A.; Ganesan, V. Effect of Polymer Polarity on Ion Transport: A Competition between Ion Aggregation and Polymer Segmental Dynamics. *ACS Macro Letters* **2018**, 7 (10), 1149-1154. DOI: [10.1021/acsmacrolett.8b00594](https://doi.org/10.1021/acsmacrolett.8b00594).
- [11] Bruce, P. G.; Vincent, C. A. Steady State Current Flow in Solid Binary Electrolyte Cells. *Journal of Electroanalytical Chemistry and Interfacial Electrochemistry* **1987**, 225 (1-2), 1-17. DOI: [10.1016/0022-0728\(87\)80001-3](https://doi.org/10.1016/0022-0728(87)80001-3).
- [12] Bruce, P. G.; Vincent, C. A. Polymer Electrolytes. *Journal of the Chemical Society, Faraday Transactions* **1993**, 89 (17), 3187-3203. DOI: [10.1039/ft9938903187](https://doi.org/10.1039/ft9938903187).
- [13] Bruce, P. G.; Freunberger, S. A.; Hardwick, L. J.; Tarascon, J.-M. Li-O₂ and Li-S Batteries with High Energy Storage. *Nature Materials* **2012**, 11 (1), 19-29. DOI: [10.1038/nmat3191](https://doi.org/10.1038/nmat3191).
- [14] J. Mindemark, J.; Lacey, M. J.; Bowden, T.; Brandell, D. Beyond PEO—Alternative host materials for Li⁺-conducting solid polymer electrolytes. *Progress in Polymer Science* **2018**, 281, 114-143. DOI: [10.1016/j.progpolymsci.2017.12.004](https://doi.org/10.1016/j.progpolymsci.2017.12.004)
- [15] Beaumont, R. H.; Clegg, B.; Gee, G.; Herbert, J. B. M.; Marks, D. J.; Roberts, R. C.; Sims, D. Heat Capacities of Propylene Oxide and of Some Polymers of Ethylene and Propylene Oxides. *Polymer* **1966**, 7 (8), 401-417. DOI: [10.1016/0032-3861\(66\)90055-3](https://doi.org/10.1016/0032-3861(66)90055-3).
- [16] Buckley, C. P.; Kovacs, A. J. Melting Behaviour of Low Molecular Weight Poly (Ethylene-Oxide) Fractions. In *Polymere Aspekte*; Steinkopff: Darmstadt, 1975; Vol. 58, pp 44-52. DOI: [10.1007/BFb0117122](https://doi.org/10.1007/BFb0117122).
- [17] Buckley, C. P.; Kovacs, A. J. Melting Behaviour of Low Molecular Weight Poly (Ethylene-Oxide) Fractions: 2. Folded Chain Crystals. *Colloid and Polymer Science* **1976**, 254 (8), 695-715. DOI: [10.1007/BF01643767](https://doi.org/10.1007/BF01643767).
- [18] Tadokoro, H.; Chatani, Y.; Yoshihara, T.; Tahara, S.; Murahashi, S. Structural Studies on Polyethers, [- (CH₂)_m-O-]_n. II. Molecular Structure of Polyethylene Oxide. *Die Makromolekulare Chemie* **1964**, 73 (1), 109-127. DOI: [10.1002/macp.1964.020730109](https://doi.org/10.1002/macp.1964.020730109).

- [19] Romankevich, O. V.; Frenkel, S. Y. Equilibrium Melting Point of Polyethylene Oxide. *Polymer Science U.S.S.R.* **1980**, 22 (11), 2647-2654. DOI: [https://doi.org/10.1016/0032-3950\(80\)90109-4](https://doi.org/10.1016/0032-3950(80)90109-4).
- [20] Cyrot, M. A Possible Origin for the Vogel-Fulcher Law. *Physics Letters A* **1981**, 83 (6), 275-278. DOI: [https://doi.org/10.1016/0375-9601\(81\)90982-8](https://doi.org/10.1016/0375-9601(81)90982-8).
- [21] Wang, W.; Tudryn, G. J.; Colby, R. H.; Winey, K. I. Thermally Driven Ionic Aggregation in Poly(Ethylene Oxide)-Based Sulfonate Ionomers. *Journal of the American Chemical Society* **2011**, 133 (28), 10826-10831. DOI: <https://doi.org/10.1021/ja201405v>.
- [22] Wheatle, B. K.; Lynd, N. A.; Ganesan, V. Effect of Polymer Polarity on Ion Transport: A Competition between Ion Aggregation and Polymer Segmental Dynamics. *ACS Macro Letters* **2018**, 7(10), 1149-1154. DOI: [10.1021/acsmacrolett.8b00594](https://doi.org/10.1021/acsmacrolett.8b00594).
- [23] Ito, K.; Nishina, N.; Ohno, H. High Lithium Ionic Conductivity of Poly(Ethylene Oxide)s Having Sulfonate Groups on Their Chain Ends. *Journal of Materials Chemistry* **1997**, 7 (8), 1357-1362. DOI: [10.1039/A700583K](https://doi.org/10.1039/A700583K)
- [24] Sperling, L. H. *Introduction to Physical Polymer Science*, 4th ed.; Wiley: Hoboken, N.J, 2006.
- [25] Arnold, K.; Herrmann, A.; Pratsch, L.; Gawrisch, K. The Dielectric Properties of Aqueous Solutions of Poly(Ethylene Glycol) and Their Influence on Membrane Structure. *Biochimica et Biophysica Acta (BBA) - Biomembranes* **1985**, 815 (3), 515–518. DOI: [10.1016/0005-2736\(85\)90381-5](https://doi.org/10.1016/0005-2736(85)90381-5)

Chapter III

Experimental

Resumé

Le **chapitre III** de cette thèse présente les méthodes de caractérisation et les protocoles de synthèse d'électrolytes polymères monofonctionnels à conduction monocationique (MEC-SIPEs). Les méthodes de caractérisation sont divisées en fonction de leurs types (**Section 1**): les méthodes de caractérisation chimique (**1.1**), électrochimique (**1.2**), physique (**1.3**) et thermique (**1.4**) sont décrites.

Les matériaux utilisés dans les synthèses sont répertoriés (**Section 2**). Le calcul de la masse molaire moyenne en nombre (M_n) des précurseurs d'éthers monométhyliques de poly(oxyde d'éthylène) ($mPEO_n-OH$) ayant n *unités de répétitions sont décrits (**Section 3**).

Les protocoles de synthèse sont divisés en deux parties selon la stratégie de synthèse décrite au chapitre I: la synthèse des MEC-SIPE "mono-sel" (**Section 4**) et des MEC-SIPE zwitterioniques et "double sel" (section 5). Les mono-sels sont les MEC-SIPEs à base de $mPEO_n-OH$ ayant les groupes terminaux suivants : sulfonates, $-SO_3Li$ et $-OC(O)PhSO_3Li$, sulfonamide $-SO_2N(Li)Naph$, et les *N*-arylamines secondaires $-N(Li)Naph$ et $-N(Li)Pyr$. Les complexes MEC-SIPEs de la **Section 5** sont précédés par les synthèses de leurs groupes terminaux multifonctionnels. Ensuite, les synthèses de $mPEO_{20}-\blacklozenge NSI(Li)$, du MEC-SIPE zwitterionique $mPEO_{20}-\blacklozenge^+ NSI(LiTFSI)$ et du MEC-SIPE "double sel" $mPEO_{55}-SANSI$ sont décrites. Tous les MEC-SIPEs de ce travail ayant un degré de polymérisation particulier (DP_n) sont synthétisés à partir du même lot de précurseur de $mPEO_n-OH$. Par conséquent, les MEC-SIPEs ayant le même nombre de n unités répétitives ont les mêmes M_n , DP_n et la même dispersité en masse. Les détails des caractérisations chimiques des MEC-SIPEs sont énumérés après chaque protocole de synthèse. Les spectres RMN et FTIR représentatifs mesurés sur les échantillons sont produits et illustrés.





Abstract

In Chapter III of this thesis are presented characterisation methods and synthesis protocols of MonoEnd-Capped "Single-Ion" Polymer Electrolytes (MEC-SIPes). The characterisation methods are divided according to the type of characterisation (**Section 1**): the Chemical (**1.1**), Electrochemical (**1.2**), Physical (**1.3**), and Thermal (**1.4**) characterisation methods are described.

The materials used in the syntheses are listed (**Section 2**). The calculation and variation of the number average molar mass (M_n) of the poly(ethylene oxide) monomethyl ether (mPEO_n-OH) precursors having n repeating units are described (**Section 3**).

The synthesis protocols are divided into two parts according to the synthesis strategy outlined in **Chapter I**: the synthesis of the "mono salt" MEC-SIPes (**Section 4**), and of the zwitterionic and "double salt" MEC-SIPes (**Section 5**). The mono salts are the MEC-SIPes based on mPEO_n-OH having the following end-groups: the sulfonates **-SO₃Li** and **-OC(O)PhSO₃Li**, the sulfonamide **-SO₂N(Li)Naph**, and the *N*-aryl secondary amines **-N(Li)Naph** and **-N(Li)Pyr**. The complex MEC-SIPes in Section 5 are preceded by the synthesis of their multifunctional end-groups. Then the syntheses of mPEO₂₀-**NSI(Li)**, the zwitterionic mPEO₂₀-**NSI(LiTFSI)**, and the "double salt" mPEO₅₅-**SANSI(Li₂)** are described. All of the MEC-SIPes in this work having a particular degree of polymerisation (DP_n) are synthesized from the same batch of mPEO_n-OH precursor. Therefore MEC-SIPes having the same number of n repeating units have the same M_n , DP_n , and dispersity in mass. The details of the chemical characterisations of the MEC-SIPes are listed after each of the synthesis protocols. Representative NMR and FTIR spectra measured of the samples are presented and illustrated.

Chapter III: Table of Contents

III. Experimental	165
1. Instrumentation and Measurements	169
1.1. Chemical Characterisation	169
1.2. Electrochemical Characterisation	169
1.3. Physical Characterisation by High Performance Liquid Chromatography–Time-of-Flight Mass Spectroscopy (HPLC-TOF MS)	171
1.4. Thermal Characterisation by Differential Scanning Calorimetry (DSC)	171
2. Materials	171
3. Variation of Polymer M_n According to Poly(ethylene oxide) monomethyl ether	174
4. Synthesis of MEC-SIPes: Mono-Salts	175
4.1. Synthesis of bromo-end-capped poly(ethylene oxide) monomethyl ether, mPEO _n -Br.....	175
4.2. Synthesis of aminonaphthalene–end-capped poly(ethylene oxide) monomethyl ether, mPEO _n -N(Li)Naph	176
4.3. Synthesis of aminopyrene–end-capped poly(ethylene oxide) monomethyl ether, mPEO _n -N(Li)Pyr	177
4.4. Chemical Characterisation of mPEO _n -Br, mPEO _n -N(Li)Naph and mPEO _n -N(Li)Pyr	179
4.5. Synthesis of Sulfonate-end-capped poly(ethylene oxide) monomethyl ether, mPEO _n -SO ₃ Li	182
4.6. Synthesis of N-(naphthyl)sulfonamide–end-capped poly(ethylene oxide) monomethyl ether, mPEO _n -SO ₂ N(Li)Naph.....	184
4.7. Chemical Characterisation of mPEO _n -SO ₃ Li and mPEO _n -SO ₂ N(Li)Naph	186
4.8. Synthesis of Benzene Sulfonate-End-Capped poly(ethylene oxide) monomethyl ether, mPEO _n -OC(O)PhSO ₃ Li.....	188
4.9. Chemical Characterisation of mPEO _n -OC(O)PhSO ₃ Li	190
5. Synthesis of MEC-SIPes: Zwitterionic and "Double-Salt" End-Capped Polymers	191
5.1. Synthesis of 4-azidonaphthalene-1-sulfonic acid sodium salt (AzNSO ₃ Na)	191
5.2. Synthesis of 4-azidonaphthalene-1-sulfonyl(methylsulfonyl)imide potassium salt [AzNSI(K)] ..	192
5.3. Synthesis of 4-aminonaphthalene-1-sulfonyl(methylsulfonyl)imide potassium salt [ANSI(K)] ..	193
5.4. Chemical Characterisation of ANSO ₃ Li and its derivatives AzNSO ₃ Na, AzNSO ₂ Cl, AzNSI(K), and ANSI(K).....	194
5.5. Synthesis of naphthalene-1-sulfonyl(methylsulfonyl)imide lithium salt end-capped poly(ethylene oxide) monomethyl ether [mPEO-  NSI(Li)].	201
5.6. Chemical Characterisation of mPEO ₂₀ -C(O)C≡CH and mPEO ₂₀ -  NSI(Li)	203
5.7. Synthesis of the Zwitterionic polymer mPEO ₂₀ -  ⁺ NSI(LiTFSI).....	206
5.8. Chemical Characterisation of the Zwitterionic polymer mPEO ₂₀ -  ⁺ NSI(LiTFSI).....	206
5.9. Synthesis of the "Double-Salt" 4-sulfonylaminonaphthalene-1-sulfonyl(methylsulfonyl)imide–end-capped poly(ethylene oxide) monomethyl ether, mPEO ₅₅ -SANSI(Li ₂)	208
5.10. Chemical Characterisation of the mPEO ₅₅ -SANSI(Li ₂) "Double Salt"	209
6. Bibliography of Chapter III	211

1. Instrumentation and Measurements

1.1. Chemical Characterisation

1.1.1. Fourier Transform Infrared (FTIR) Spectroscopy

FTIR spectroscopy was performed using a Thermo Scientific Nicolet™ 6700 spectrometer equipped with a DTGS KBr detector and adapted for Attenuated Total Reflection (ATR) measurements using a Thermo Scientific "Diamond HATR" module. The background and sample measurements relied on 64 scans across the $\tilde{\nu} = 4000\text{-}400\text{ cm}^{-1}$ range with a resolution of 2 cm^{-1} .

1.1.2. Karl Fischer Titration

Karl Fischer titration^[1] was performed on a GRS Scientific™ Cuo-Lo Aquamax KF Moisture Meter, in a glovebox under argon atmosphere ($< 10\text{ ppm O}_2$) at 25°C . The analytes were dried in a vacuum oven ($< 10\text{ mbar}$, 70°C , $> 24\text{ h}$) prior to sample preparation. The samples were (10 g/L) solutions in anhydrous DMSO of i) MonoEnd-Capped Single-Ion Polymer Electrolytes and ii) salt-polymer blends of $\text{H}_3\text{C-PEO}_{60}\text{-CH}_3/\text{LiTFSI}$. The sample volume was $200\ \mu\text{L}$. The results presented are an average of 3 titrations. The water content of the polymer samples (in ppm) was determined relative to that of the solvent DMSO, which was determined as an average of 5 titrations. The commercial Karl-Fischer solution Hydranal® Coulomat E, containing sulfur dioxide, imidazolium halides and alcohol, was purchased from Honeywell (Fluka).

1.1.3. Nuclear Magnetic Resonance (NMR) Spectroscopy

NMR was performed using a Bruker Avance™ III 400 MHz spectrometer connected to a Bruker Ultrashield™ 400 Plus magnet bearing a multinuclear, tuneable PA BBO (5 mm) probe, operating at 400.132 MHz (^1H), 100.624 MHz (^{13}C), 155.506 MHz (^7Li), and 376.498 MHz (^{19}F). All spectra were recorded at 298 K . The Free Induction Decay (FID) was collected over 128 (^1H), 2048 (^{13}C), 16 (^7Li), and 64 (^{19}F) scans. The sample volume was 0.5 mL ; the sample concentration was either 10 g/L (samples of relative molecular mass M [or M_n] $< 400\text{ g/mol}$) or 30 g/L (polymers, $M_n > 400\text{ g/mol}$) in either DMSO-d_6 or CDCl_3 .

1.2. Electrochemical Characterisation

1.2.1. Fabrication and Testing of Electrochemical Cells

Methods including Chronoamperometry (CA), Cyclic Voltammetry (CV), Galvanostatic Electrochemical Impedance Spectroscopy (GEIS), and Galvanostatic Cycling with Potential Limitation (GCPL) were performed using Biologic™ VMP-2 and VMP-3 potentiometers. The electrolytes were loaded into coin-cells of either symmetric $\text{Li}|\text{Li}$ or asymmetric $\text{Li}|\text{Fe}$ (stainless-steel) configuration. The cell constant was determined by the distance between the electrodes ($50\ \mu\text{m} < L < 100\ \mu\text{m}$) and the electrode surface area ($A = 1.131\text{ cm}^2$), as maintained by a low-density poly(ethylene) (LDPE) spacer. The polymers were dried under reduced pressure ($< 10\text{ mbar}$, 70°C , $> 24\text{ h}$) prior to loading. The cells were constructed in a glovebox under argon atmosphere ($\text{H}_2\text{O} \approx 4\text{-}6\text{ ppm}$). The temperature was controlled using a Weissttechnik® LabEvent benchtop temperature test chamber. Electrochemical testing was begun ($t = 0$) within 1 h of cell assembly. Specific equilibration times for each measurement are stated individually. Potentiostatic Electrochemical Impedance Spectroscopy (PEIS) was conducted using symmetric $\text{Au}|\text{Au}$ blocking electrodes (see section 1.2.6).

1.2.2. Chronoamperometry (CA)

CA was performed using symmetric Li|Li cells. The cells were equilibrated for 12 h at 40°C, with monitoring of the evolution of their complex impedance by GEIS at 1 h intervals. Potentiostatic polarisation at 40°C was triggered by an applied potential of 10 mV. The current was monitored at intervals of 0.1 s ($t_0 \rightarrow t = 30$ s) and then intervals of 5 s ($t = 30$ s $\rightarrow t = 10$ h). The steady-state Li^+ transference number was determined by the ratio of the steady-state and the initial current (I_{ss}/I_0). The potential drop resulting from evolution of the cell resistance was corrected by the potential determined by GEIS measurements before and after the CA experiment (see **Eqn. III-1**).

Equation III-1: Determination of the (Li^+) steady-state transference number by combined PEIS and CA measurements, where I_0 = the maximum current after cell polarisation; I_{ss} = the steady-state current ($t_{\text{max}}= 10$ h); ΔV_{CA} = the applied potential; ΔV_{α} = the cell potential determined by GEIS before CA; ΔV_{ω} = the cell potential determined by GEIS after CA.

$$t_{\text{Li}^+} = \frac{I_{ss}(\Delta V_{CA} - \Delta V_{\alpha})}{I_0(\Delta V_{CA} - \Delta V_{\omega})}$$

1.2.3. Cyclic Voltammetry (CV)

CV was performed using symmetric Li|Fe (Stainless-Steel) cells at a cycling rate of 1.0 mV/s. Separate cells were prepared for cycling in oxidation and in reduction mode. The initial potential was set to the open circuit voltage (OCV). The cells were equilibrated to the experimental temperature for 1 h prior to the first cycle. The temperature was 40°C unless otherwise stated. Cycles were measured in increments of 0.20 V vs. OCV.

1.2.4. Galvanostatic Electrochemical Impedance Spectroscopy (GEIS)

GEIS was performed using symmetric Li|Li cells and relied on an ac amplitude of 20 $\mu\text{A}/\text{cm}^2$. The frequency range was 1.0 MHz-0.5 Hz, unless otherwise stated. The frequency range was covered by 10 measurement points per decade in a logarithmic progression. The impedance at each frequency was measured three times. The waiting period between frequencies was 0.5 s. The temperature was 40°C unless otherwise stated. Equilibration time(s) and measurement sequences are quoted in the discussion of results.

1.2.5. Galvanostatic Cycling with Potential Limitation (GCPL)

GCPL was performed using symmetric Li|Li cells. The cells were equilibrated for 24 h at 40 °C, measuring GEIS (1.0 MHz-0.5 Hz) every 1 h to monitor the evolution of the complex impedance of the cell. The applied current was 10 $\mu\text{A}/\text{cm}^2$, alternating the polarisation of the cell every 4 h for a total of 40 h at 40°C. A final GEIS measurement at 40°C was repeated after GCPL to review the evolution of the complex resistance of the cell after GCPL.

1.2.6. Potentiostatic Electrochemical Impedance Spectroscopy (PEIS)

PEIS measurements using gold blocking electrodes were conducted on a Materials Mates™ 7260 Impedance Analyser. The samples were placed inside a Controlled Environment Sample Holder (CESH) cell comprising symmetric gold, blocking electrodes in a parallel configuration (Au|Au). The temperature was controlled using a Biologic™ Intermediate Temperature System (ITS) thermostat. All samples were dried under reduced pressure prior to loading (< 10 mbar, 100°C, 24 h). Sample handling and preparation, and assembly of the cell was performed in a glovebox under argon atmosphere (< 8.0 ppm O_2). A low-density poly(ethylene) spacer of known thickness was used to calculate the cell constant. All samples were equilibrated for 10 min at each temperature before measurement of the impedance was begun. The measurement relied on an ac amplitude

of 10 mV, and was carried out over the frequency range 1.0 MHz-1.0 Hz, measuring 10 points per decade in a logarithmic progression. When changing temperature, the heating and cooling rate was 1°C/min ($\pm 0.02^\circ\text{C}/\text{min}$). During equilibration and the measurement, the temperature error was $\pm 0.02^\circ\text{C}$. The resistance of the bulk electrolyte was calculated from complex Nyquist ($\text{Im}(Z'')$ vs $\text{Re}(Z')$) plots obtained from the impedance measurements. The conductivity was calculated according to Equation 2.

Equation III-2: Conductivity ($\sigma / \text{S}\cdot\text{cm}^{-1}$) calculated according to the reciprocal resistance multiplied by the cell constant (L/A)

$$\sigma (\text{S} \cdot \text{cm}^{-1}) = \frac{1}{R(\Omega)} \times \frac{L(\text{cm})}{A(\text{cm}^2)}$$

The conductivity was modelled using the Vogel-Tamman-Fulcher (VTF) relation originally proposed to describe the temperature dependence of the viscosity of glasses.^[2-4] The relation was solved by a non-linear least-squares trial-and-error method using the "Solver" utility in the Microsoft Office (2016) Excel™ software. Empirical evidence suggests that the ionic conductivity of polymer electrolytes could be well fitted by using the approximate relation of $T_0 \approx T_g - 50 \text{ K}$.^[5] Using this as a guide, an initial condition of $T_0 = 200 \text{ K}$ was proposed with respect to the T_g of PEO-based electrolytes, that are often reported to be in the range 220-250 K.^[6]

Equation III-3: The dependence of conductivity on temperature according to the Vogel-Tamman-Fulcher (VTF) relation, in which σ_0 is a pre-exponential factor, B is a constant related to the activation energy (E_a), and T_0 is the equilibrium glass transition temperature.

$$\sigma = \sigma_0 \cdot \exp(-B/[T - T_0])$$

1.3. Physical Characterisation by High Performance Liquid Chromatography–Time-of-Flight Mass Spectroscopy (HPLC-TOF MS)

HPLC-MS-TOF was performed on an Agilent Technologies™ 6230 TOF LC/MS equipped with a 1260 Infinity Sampler. Samples were prepared as 1 g/L solutions in methanol. The injection volume was 1.00 μL into an eluent flow of 0.400 mL/min in methanol at 40°C. A UV detection fixed at $\lambda = 250 \text{ nm}$ verified sample injection. The TOF unit operates at 4 GHz using a pressure of 1.92 Torr. The source gas flow was 8.000 L/min at 325°C, vaporising the sample at 25 psig through a 0.061 μA capillary to a 5.07 μA measurement chamber in negative polarity mode. Measurements are reported as an average of 5*1 μL samples. Equilibration of 2.0 s was followed by TOF acquisition at a rate of 1 spectrum/s, measuring 9887 transients of mass-to-charge ratios over the range 25-3200 m/z calibrated according to 10 analytical standards.

1.4. Thermal Characterisation by Differential Scanning Calorimetry (DSC)

DSC was performed using a Setram™ Instrumentation (KEP Technologies) DSC 131 Evo. Samples were dried in a vacuum oven (< 10 mbar, 70°C, > 24 h) prior to the measurement. The sample of mass 5.0-20.0 mg was placed in a 30 μL aluminium pan. Samples were heated from ambient temperature to 120°C and then cooled to -50°C before the measurement was begun. All heating and cooling ramps of samples were conducted under argon gas flow of 0.20 L/min. The heating/cooling rates were set to 5.0°C/min; the data analysed and presented is of the second heating and cooling runs unless otherwise stated.

2. Materials

Reagents and solvents were purchased from commercial suppliers and used as received, unless otherwise stated.

Reagent	Description
(+)-Sodium L-Ascorbate	Na-Asc, CAS 134-03-2, crystalline, > 98 %, Sigma
1-aminonaphthalene	1-naphthylamine, CAS 134-32-7, > 99 %, Aldrich
1-aminopyrene	1-pyrenamine, CAS 1606-67-3, 97 % Aldrich
2-sulfobenzoic acid cyclic anhydride	2,1-benzoxathiol-3-one-1,1-dioxide, CAS 81-08-3, 90 %, technical grade, Sigma-Aldrich
4-aminonaphthalene-1-sulfonic acid	ANSO ₃ H, CAS 84-86-6, 97 %, Aldrich
Alumina	Al ₂ O ₃ , CAS 1344-28-1, "approximately 150 mesh," super (200 m ² /g), for column chromatography, Sigma-Aldrich
Amberlite® IR120 hydrogen form	The Dow Chemical Company, CAS 39389-20-3, Sigma-Aldrich
Benzoic Acid	CAS 65-85-0, > 99.5 %, ACS reagent, Sigma-Aldrich
Copper(II) Sulfate pentahydrate	CuSO ₄ ·5H ₂ O, CAS 7758-99-7, > 98.0 %, ACS reagent, Sigma-Aldrich
Hydrochloric Acid	HCl, CAS 7647-01-0, 37 %, ACS reagent, EMD Millipore
Hydranal® Coulomat E	Ethanol-based solution for Karl Fischer titration, Honeywell (Fluka)
Lithium Carbonate	Li ₂ CO ₃ , CAS 554-13-2, > 99.0 %, ACS reagent, Sigma-Aldrich
Lithium Hydride	LiH, CAS 7580-67-8, powder, 30 mesh, 95 %, Aldrich
Lithium Hydroxide monohydrate	LiOH·H ₂ O, CAS 1310-66-3, 98.0 %, ACS reagent, Sigma-Aldrich
Magnesium Chloride	MgCl ₂ , CAS 7786-30-3, anhydrous, > 98 %, Sigma
Magnesium Sulfate	MgSO ₄ , CAS 7487-88-9, anhydrous, > 99.5 %, reagent grade, EMD Millipore
Poly(ethylene oxide) methyl ether	Poly(ethylene oxide) monomethyl ether, mPEO-OH, CH ₃ (OCH ₂ CH ₂) _n OH, CAS 9004-74-4, Aldrich; "Average Mn" = 350, 500, 750, 2000, and 5000 g/mol.
<i>N,N</i> -Dimethylformamide	DMF, CAS 68-12-2, [i] anhydrous, 99.8 %, Sigma-Aldrich; and [ii] HPLC Grade, > 99 %, EMD Millipore
Potassium Carbonate	K ₂ CO ₃ , CAS 584-08-7, > 99.0 %, ACS reagent, Sigma-Aldrich
Propargyl Bromide	CAS 106-96-7, purum, 80 % (w/w) in toluene, Sigma-Aldrich
Propiolic Acid	CAS 471-25-0, 95 %, Aldrich
Silica Gel	High-purity grade, pore size 60 Å, 220-440 mesh (40-63 µm particle size), for flash chromatography, Sigma-Aldrich
Sodium Azide	NaN ₃ , CAS 26628-22-8, > 99.5 %, ReagentPlus, Sigma-Aldrich
Sodium Bicarbonate	NaHCO ₃ , CAS 144-55-8, > 99.7 %, ACS reagent, Sigma-Aldrich
Sodium Hydride	NaH, CAS 7646-69-7, dry, 90 %, Aldrich
Sodium Nitrite	NaNO ₂ , CAS 7632-00-0, > 97.0 %, ACS reagent, Sigma-Aldrich
Sulfuric acid	H ₂ SO ₄ , CAS 7664-93-9, 95.0-98.0 %, ACS reagent, EMD Millipore
Thionyl Chloride	SOCl ₂ , CAS 7719-09-7, 97 %, reagent grade, Sigma-Aldrich
Triethylamine	TEA, CAS 121-44-8, > 99.5 %, Sigma-Aldrich
Triphenylphosphine	PPh ₃ , CAS 603-35-0, 99 %, ReagentPlus, Sigma-Aldrich

Solvent	Description
Acetonitrile	CH ₃ CN, CAS 75-05-8, anhydrous, 99.8 %, Sigma-Aldrich
Chloroform	CHCl ₃ , CAS 67-66-3, > 99.5 %, contains amylenes, Sigma-Aldrich
Chloroform-d	CDCl ₃ , CAS 865-49-6, 99.8 atom % D, Aldrich

Solvent	Description
Dichloromethane	CH ₂ Cl ₂ , DCM, CAS 75-09-2, [i] anhydrous, > 99.8 %, contains 40-150 ppm amylenes, Sigma-Aldrich; and [ii] HPLC grade, contains amylenes, EMD Millipore
Diethyl ether	CAS 60-29-7, [i] anhydrous, > 99.7 %, contains 1 ppm butylated hydroxytoluene BHT, Sigma-Aldrich; and [ii] HPLC-grade, > 99 %, inhibitor-free, Sigma-Aldrich
Dimethyl Sulfoxide-d ₆	DMSO-d ₆ , CAS 2206-27-1, [i] 99.96 atom % D, Aldrich; and [ii] Magnisolv™, 99.8 atom % D with TMS 0.03 %, EMD Millipore
Ethanol	EtOH, CAS 64-17-5, [i] absolute, Sigma-Aldrich; and [ii] 96 %, HPLC grade, EMD Millipore
Ethyl Acetate	EtOAc, CAS 141-78-6, 99.7 %, HPLC grade, EMD Millipore
Methanol	MeOH, CAS 67-56-1, [i] anhydrous, 99.8 % Sigma-Aldrich; and [ii] HPLC grade, > 99 % EMD Millipore
<i>N,N</i> -Dimethylformamide	DMF, CAS 68-12-2, [i] anhydrous, 99.8 %, Sigma-Aldrich; and [ii] HPLC Grade, > 99 % EMD Millipore
Toluene	CAS 108-88-3, [i] anhydrous, 99.8 %, Sigma-Aldrich; and [ii] > 99.5 %, ACS reagent, Sigma-Aldrich

3. Variation of Polymer M_n According to Poly(ethylene oxide) monomethyl ether

End-capped polymer electrolytes bearing lithium salt end-groups at one terminal were synthesized from commercial poly(ethylene oxide) monomethyl ether (mPEO_n-OH) of different degrees of polymerisation (DP_n). The polymers having commercially designated molar mass were analysed by ¹H NMR spectroscopy to determine their number-average molar mass (M_n , g/mol). Since there is one methyl ether unit per polymer chain, the number average degree of polymerisation (EO_n) is equal to the weighted (¹H) ratio of the integrals obtained from the ¹H NMR spectrum (**Eqn. III-4**).

Equation III-4: Calculation of EO_n from the integral of ¹H NMR signals

$$EO_n = \frac{(\int 4H_{C_2H_4O})/4}{(\int 3H_{OCH_3})/3}$$

The number average molar mass of ethylene oxide units in the polymer chain ($M_{n(EO)}$) is calculated as the mass of an ethylene oxide repeating unit multiplied by EO_n (**Eqn. III-5**)

Equation III-5: Calculation of the number average molar mass of the polymer chain

$$M_{EO_n} = M_{C_2H_4O} \times EO_n$$

Addition of the molecular mass of the end-groups yields the number average molar mass of the polymer (Eqn. 6).

Equation III-6: Calculation of polymer $M_{n(NMR)}$ (g/mol) by summation of the molecular mass of the end-groups with that of the sum of ethylene oxide repeating units.

$$M_n [H_3C-(C_2H_4O)_n-OH] = M_{CH_3} + M_{EO_n} + M_{OH}$$

The $M_{n(NMR)}$ was used to calculate the yields of the reactions, where the mass of the hydroxyl of the mPEO_n-OH precursor is exchanged for another functional end-group. The polymers are referred according to the EO_n determined in this work (**Table III-1**). The exact same batch of polymers were used for each of the syntheses, to exclude the possibility of variation in either EO_n or Dispersity in mass ($\overline{Dw} = M_w/M_n$).

Table III-1: Commercial poly(ethylene oxide) monomethyl ether used in the synthesis of SIPes, quoting the M_n (NMR) and DP_n (EO_n) determined in this work

M_w (comm) (g/mol)	M_n (NMR) (g/mol)	DP _n EO _n
350	404	8
500	459	10
750	919	20
2000	2412	55
5000	7047	160

The mPEO_n-OH precursors were used to synthesize bromo-end-capped poly(ethylene oxide) monomethyl ether (mPEO_n-Br) of PEO EO_n= 8, 10, 20, 55, and 160. The same samples of mPEO_n-Br were used as precursors to all the other MonoEnd-Capped Single-Ion Polymer Electrolytes (MEC-SIPes) presented in the following sections.

4. Synthesis of MEC-SIPes: Mono-Salts

4.1. Synthesis of bromo-end-capped poly(ethylene oxide) monomethyl ether, mPEO_n-Br

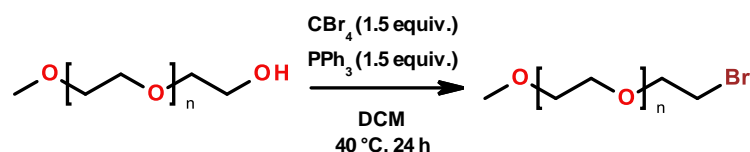


Figure III-1: Synthesis of bromo-end-capped poly(ethylene oxide) monomethyl ether via the Appel reaction with carbon tetrabromide and triphenylphosphine in dichloromethane (DCM).

The reaction of triphenylphosphine and tetrabromomethane with alcohol, known as the Appel reaction,^[7] was used to prepare bromo-end-capped poly(ethylene oxide) monomethyl ethers (mPEO_n-Br) of EO_n= 8-160. The method applied here was adapted from the literature.^[8] Poly(ethylene oxide) monomethyl ether (mPEO_n-OH) was dried in a vacuum oven (100°C, < 10 mbar, 72 h) prior to use. A dry flask was charged with mPEO_n-OH (**Table. III-2**) as a 20 % (w/w) solution in anhydrous DCM and placed under argon atmosphere. To the stirring solution was added solid CBr₄ (1.5 molar equiv.) and the flask was cooled to 0°C. To the cooled solution was added PPh₃ (1.5 molar equiv.), with stirring at 0°C over 20 min. The reaction proceeded with gentle heating (40°C, 24 h) under argon. The solution turned from clear colourless to clear orange (M_w(PEO)= 350 g/mol [EO_n= 8], 500 g/mol [EO_n= 10]) or yellow ochre (M_w(PEO)= 750 g/mol [EO_n= 20], 2000 g/mol [EO_n= 55], 5000 g/mol [EO_n= 160]). The reaction mixture was stored in the cold (-20°C) overnight.

Table III-2: The masses and moles of mPEO_n-OH, CBr₄ and PPh₃ used in the synthesis of polymers of different DP_n (EO_n).

mPEO _n -OH			CBr ₄		PPh ₃	
M _w (comm) (g/mol)	mass (g)	mol x 10 ³	mass (g)	mol x 10 ³	mass (g)	mol x 10 ³
350	5.25	15.0	7.46	22.48	5.90	22.48
500	5.00	10.0	4.98	15.01	3.94	15.01
750	15.00	20.0	9.95	30.00	7.87	30.00
2000	20.00	10.0	4.97	15.00	3.93	15.00
5000	25.62	5.1	2.55	7.69	2.02	7.69

The white solid precipitate mixture of triphenyl phosphine oxide and excess triphenyl phosphine was filtered from the solution. The precipitate mixture was washed with DCM (3 x 20 mL). The DCM solutions were combined, dried over MgSO₄ and concentrated under reduced pressure. The concentrated solutions were stored cold (-20°C, > 4 h), filtered again, then evaporated to dryness. The higher polymers (PEO_n= 55, 160) were additionally dropped through cold diethyl ether (3 x 200 mL).

The residue was taken up in anhydrous toluene. To the suspension of white solid in yellow solution was added MgCl₂ (1.5 molar equiv.), which is known to form an insoluble complex with triphenyl phosphine oxide.^[9] The mixture was stirred (30°C, 16 h), then stored in the cold (-20°C, > 4 h). The suspension was filtered cold, and the cake was washed with toluene (3 x 20 mL). The solvent was removed under reduced pressure (60°C, < 10 mbar, 24 h). The higher polymers (PEO_n = 55, 160) were additionally dropped through cold diethyl ether (3 x 200 mL). The residue was taken up in CHCl₃ and stored cool (2-8°C, > 4 h). The polymer in chloroform solution was filtered cold three times and the solvent was evaporated under reduced pressure to obtain the polymer bearing

bromo end-groups (mPEO_n-Br) as a low viscous melt (PEO_n = 8, 10), a waxy solid (PEO_n = 20) or as a solid (PEO_n = 55, 160) at room temperature, having a decreasing intensity of yellow colouration with increasing polymer DP_n. Yields greater than quantitative are the result of residual triphenyl phosphine oxide (O=PPh₃). The polymers were used without further purification, taking into account the mass of residual O=PPh₃ observed by ¹H NMR spectroscopy of the crude product. For FTIR and NMR spectroscopy, and representative examples of spectra, please see section 5.4.

The masses of the reagents and the polymer yields are summarised in **Table III-3**.

Table III-3: The synthesis of mPEO_n-Br from mPEO_n-OH via the Appel reaction. The commercial mass average molar masses (M_{w(comm)}) of mPEO_n-OHs were used to calculate the masses of reagents required. The number-average molar mass (M_{n(NMR)}), as determined in this work using NMR spectroscopy, is quoted and the yield is calculated using these values. For ease of reading, the polymers are referred to by their commercially designated M_w and calculated number-average degree of polymerisation (DP_n, EO_n), as determined by NMR spectroscopy.

mPEO _n -OH					mPEO _n -Br			
M _{w(comm)} (g/mol)	M _{n(NMR)} (g/mol)	DP _n (X _n)	mass (g)	mol x 10 ³	M _{n(NMR)} (g/mol)	mass (g)	mol x 10 ³	yield (%)
350	404	8	5.25	12.99	467	7.89	16.89	130
500	459	10	5.00	10.9	522	6.72	12.9	118
750	919	20	15.00	16.3	982	19.03	19.4	119
2000	2412	55	20.00	8.3	2475	23.00	9.3	112
5000	7047	160	25.62	3.6	7110	24.87	3.5	96

4.2. Synthesis of aminonaphthalene-end-capped poly(ethylene oxide) monomethyl ether, mPEO_n-N(Li)Naph

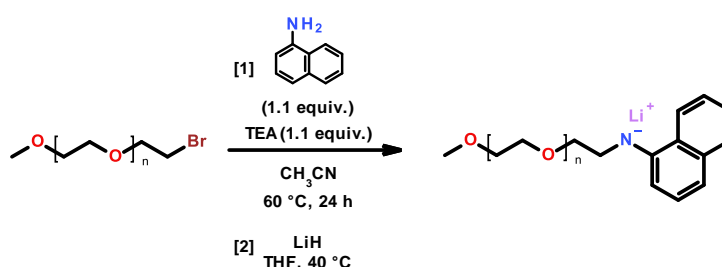


Figure III-2: Synthesis of aminonaphthalene-end-capped poly(ethylene oxide) monomethyl ether via reaction of the bromo-end-capped derivative with 1-aminonaphthalene.

An oven-dried flask was charged with dry mPEO_n-Br (see section 5.1). To the polymer was added triethylamine (1.1 equiv.) and 1-aminonaphthalene (1.1 equiv.) in anhydrous acetonitrile (**Table III-4**). The total volume of acetonitrile was fixed to yield a 20 % (w/w) polymer solution. The flask was sealed and the solution was heated (60 °C, 24 h). The reaction mixture was acidified with 1 M HCl (1.1 equiv.) and heated (60 °C, 4 h). The volatiles were then removed under high vacuum (60 °C, < 10 mbar). The residue was taken up in ethyl acetate, stored cold (-20 °C, > 4 h) and filtered three times. The filtered ethyl acetate solution was dried over K₂CO₃, then evaporated under reduced pressure (60 °C, < 10 mbar).

Table III-4: Masses and moles of mPEO_n-Br, 1-aminonaphthalene and triethylamine used in the synthesis of aminonaphthalene-end-capped poly(ethylene oxide) monomethyl ether, mPEO_n-N(Li)Naph, of different PEO DP_n (EO_n).

mPEO _n -OH DP _n (EO _n)	mPEO _n -Br			1-aminonaphthalene		triethylamine	
	M _n (NMR) (g/mol)	mass (g)	mol x 10 ³	mass (g)	mol x 10 ³	mass (g)	mol x 10 ³
8	467	1.044	2.24	0.367	2.46	0.249	2.46
10	522	0.851	1.63	0.268	1.79	0.182	1.79
21	982	1.000	1.02	0.167	1.12	0.113	1.12
55	2475	1.101	0.44	0.073	0.49	0.050	0.49
160	7110	1.119	0.16	0.026	0.17	0.018	0.17

The polymer bearing 1-aminonaphthalene end-groups was dissolved (50 % w/w) in anhydrous THF and degassed by three freeze-pump-thaw cycles using liquid nitrogen to freeze the solution. The solution was treated with LiH (6.0 equiv.) and heated with stirring (40°C, 1 h) under argon atmosphere. The flask was exposed to air and methanol was added dropwise until no more gas evolved from the solution. The solvent was evaporated under reduced pressure (60°C, < 10 mbar) and the residue was taken up in DCM stored cold (-20°C, > 4 h) and filtered three times. The solvent was evaporated under vacuum to obtain the product mPEO_n-N(Li)Naph as a low viscous melt (PEO_n= 8, 10, and 20) or as a solid at room temperature (PEO_n= 55, 160). Lithiation of the polymers was confirmed by ⁷Li NMR. For FTIR and NMR spectroscopy, and representative examples of spectra, please see section 5.4. The yields are listed in **Table III-5**.

Table III-5: Masses and yields of aminonaphthalene-end-capped poly(ethylene oxide) monomethyl ether of different PEO DP_n (EO_n). Molar quantities and yields are calculated according to the M_n(NMR).

mPEO _n -OH DP _n (EO _n)	mPEO _n -Br			mPEO _n -N(Li)Naph			
	M _n (NMR) (g/mol)	mass (g)	mol x 10 ³	M _n (NMR) (g/mol)	mass (g)	mol x 10 ³	Yield (%)
8	467	1.044	2.24	535	0.982	1.84	82
10	522	0.851	1.63	590	0.847	1.44	88
21	982	1.000	1.02	1050	0.982	0.94	92
55	2475	1.101	0.44	2543	0.939	0.37	83
160	7110	1.119	0.16	7178	0.822	0.11	73

4.3. Synthesis of aminopyrene-end-capped poly(ethylene oxide) monomethyl ether, mPEO_n-N(Li)Pyr

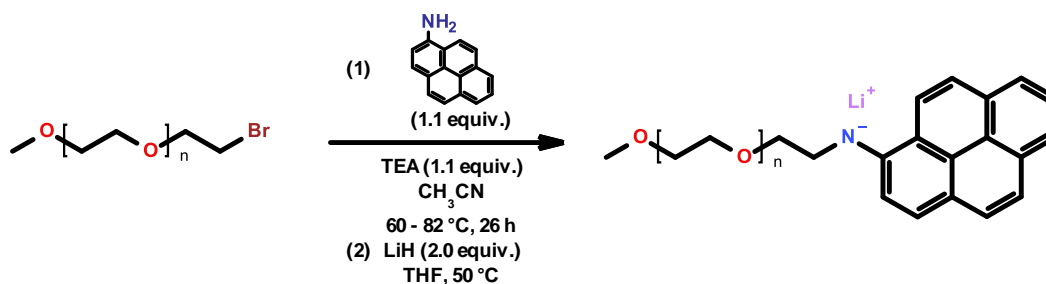


Figure III-3: Synthesis of aminopyrene-end-capped poly(ethylene oxide) monomethyl ether via reaction of the bromo-end-capped derivative with 1-aminopyrene under reflux.

An oven-dried flask was charged with a solution of dry mPEO_n-Br (see section 5.1) in anhydrous CH₃CN (**Table III-6**). To this was added sequentially triethylamine (1.1 equiv.) and 1-aminopyrene

(1.1 equiv.) in anhydrous CH₃CN. The total volume of CH₃CN yielded a 20 % (w/w) polymer solution. The solution was heated (60°C, 24 h), then under reflux (82°C, 2 h). The reaction mixture was cooled to room temperature and acidified with a slight excess of 1 M HCl and heated (60°C, 4 h). The volatiles were evaporated under reduced pressure at 60°C. The residue was taken up in EtOAc, stored cold (-20°C, > 4h) and filtered cold three times. The solution was dried over K₂CO₃ and the solvent removed under reduced pressure (< 10 mbar, 60°C, 24 h) to obtain the target polymer bearing a secondary amine, mPEO_n-NHPyr.

Table III-6: Masses and moles of mPEO_n-Br, 1-aminopyrene and triethylamine used in the synthesis of aminopyrene-end-capped poly(ethylene oxide) monomethyl ether, mPEO_n-N(Li)Pyr, of different PEO DP_n (EO_n).

mPEO _n -OH	mPEO _n -Br			1-aminopyrene		triethylamine	
DP _n (EO _n)	M _{n(NMR)} (g/mol)	mass (g)	mol x 10 ³	mass (g)	mol x 10 ³	mass (g)	mol x 10 ³
8	467	0.505	1.08	0.258	1.19	0.136	1.19
10	522	0.473	0.91	0.217	1.00	0.094	1.00
20	982	0.988	1.01	0.240	1.11	0.135	1.11
55	2475	1.03	0.42	0.099	0.46	0.056	0.46
160	7110	0.977	0.14	0.033	0.15	0.021	0.15

The polymer bearing 1-aminopyrene end-groups was dissolved 50 % (w/w) in anhydrous THF and degassed by three freeze-pump-thaw cycles using liquid nitrogen to freeze the solution. To this solution was added LiH (2.0 equiv.). The mixture was stirred with gentle heating (50 °C, 18 h). The reaction was quenched with methanol, and the volatiles were evaporated under reduced pressure (60°C, < 10 mbar). The residue was taken up in CHCl₃, stored cold (-20°C, > 4 h) and filtered cold three times. The solvent was evaporated under vacuum to obtain the product mPEO_n-N(Li)Pyr as a low viscous melt (PEO_n= 8, 10), as a waxy solid (PEO_n= 20) or as a solid at room temperature (PEO_n= 55, 160). Lithiation of the polymers was confirmed by ⁷Li NMR. For FTIR and NMR spectroscopy, and representative examples of spectra, please see section 4.4. The yields are listed in **Table III-7**.

Table III-7: Masses and yields of aminopyrene-end-capped poly(ethylene oxide) monomethyl ether of different PEO DP_n (EO_n). Molar quantities and yields are calculated according to the M_{n(NMR)}.

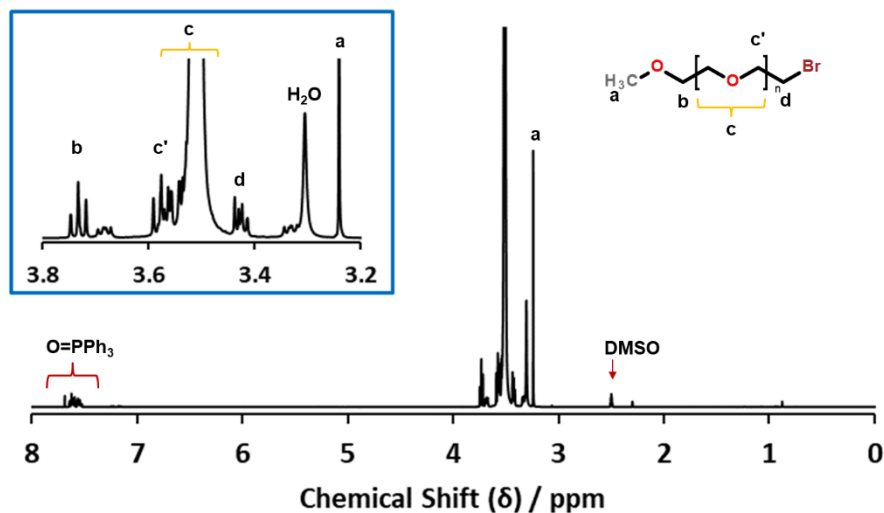
mPEO _n -OH	mPEO _n -Br			mPEO _n -N(Li)Pyr			
DP _n (EO _n)	M _{n(NMR)} (g/mol)	mass (g)	mol x 10 ³	M _{n(NMR)} (g/mol)	mass (g)	mol x 10 ³	Yield (%)
8	467	0.505	1.08	609	0.354	0.58	54
10	522	0.473	0.91	664	0.374	0.56	62
20	982	0.988	1.01	1124	0.814	0.72	72
55	2475	1.03	0.42	2617	0.454	0.17	42
160	7110	0.977	0.14	7252	0.822	0.11	83

4.4. Chemical Characterisation of mPEO_n-Br, mPEO_n-N(Li)Naph and mPEO_n-N(Li)Pyr

4.4.1. NMR Spectroscopy

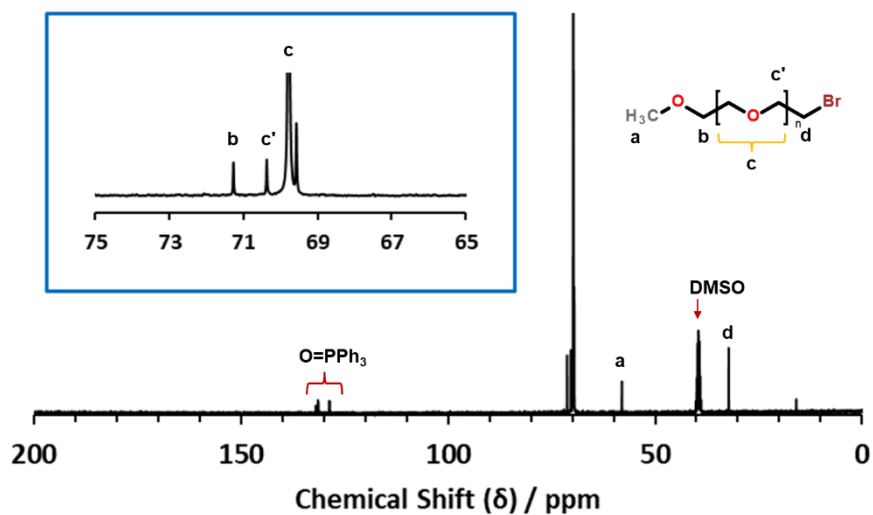
mPEO₂₀-Br

¹H NMR Spectroscopy



¹H NMR (DMSO-d₆, 298 K) chemical shift (δ / ppm): 3.24 (s, 3H, CH₃^a), 3.43 (m, 2H, CH₂^b), 3.51 (br, CH₂^c), 3.57 (t, *J* = 5.00 Hz, 2H, CH₂^{c'}), 3.73 (t, *J* = 5.12 Hz, 2H, CH₂^d).

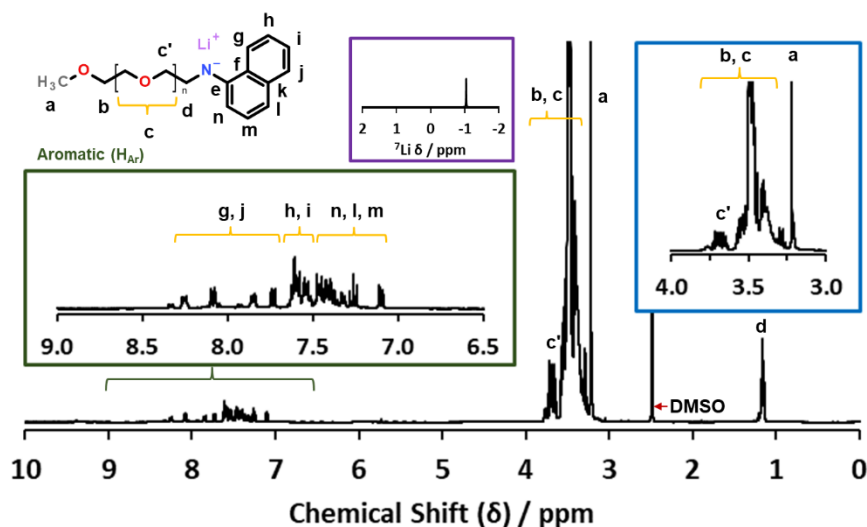
¹³C NMR Spectroscopy



¹³C NMR (CDCl₃, 298 K) chemical shift (δ / ppm): 32.22 (CH₃^d), 58.03 (CH₂^a), 69.80 (CH₂^c), 70.40 (CH₂^{c'}), 71.29 (CH₂^b).

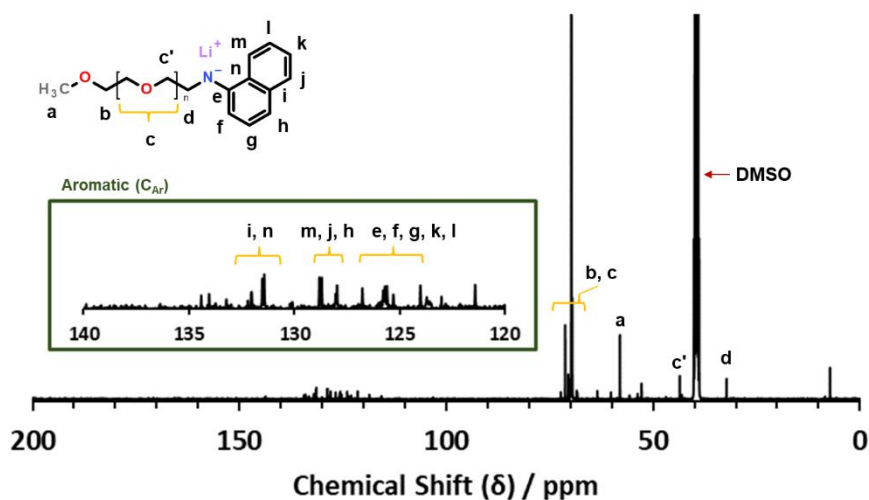
*m*PEO₂₀-N(Li)Naph

¹H and ⁷Li NMR Spectroscopy



¹H NMR (DMSO-d₆, 298 K) chemical shift (δ / ppm): 1.16 (br, 2H, CH₂^d), 3.21 (s, 3H, CH₂^a), 3.40, 3.48, 3.58 (br, CH₂^{b, c}), 3.65 (br, 2H, CH₂^{c'}); 7.09, 7.26, 7.33-7.45 (H_{Ar}^{l, m, n}); 7.58, 7.61 (H_{Ar}^{h, i}); 7.75, 7.86, 8.08, 8.25 (H_{Ar}^{g, j}). \int [CH₃^a]= 3H; \int [H_{Ar}^{g-j, l-n}]= 7H. INSET (green) magnified region of the ¹H spectrum, 6.5-9.0 ppm. INSET (purple): ⁷Li NMR (CDCl₃, 298 K) chemical shift (δ)= -1.13 ppm.

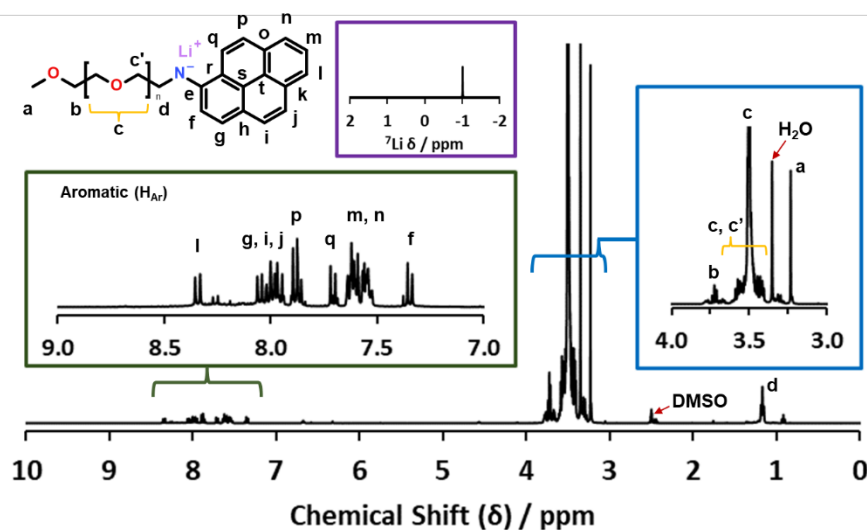
¹³C NMR Spectroscopy



¹³C NMR (DMSO-d₆, 298 K) chemical shift (δ / ppm): 32.26 (CH₂^d), 43.56 (CH₂^{c'}), 58.04 (CH₂^a), 68.49, 69.77, 70.53 (CH₂^c), 72.33 (CH₂^b); 123.01, 123.71, 124.01, 125.70, 126.76 (C_{Ar}^{e, f, g, k, l}); 127.97, 128.69, 128.81 (C_{Ar}^{h, j, m}); 131.42 132.02 (C_{Ar}^{i, n}).

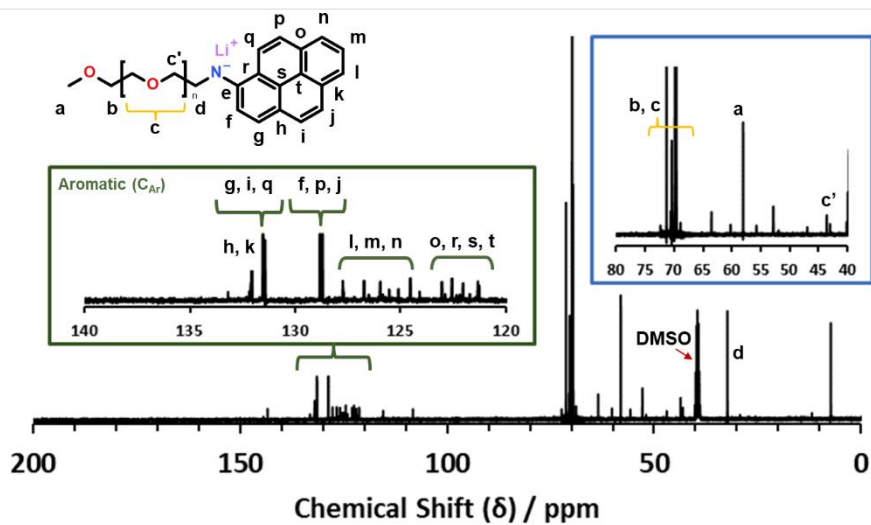
*m*PEO₂₀-N(Li)Pyr

¹H and ⁷Li NMR Spectroscopy



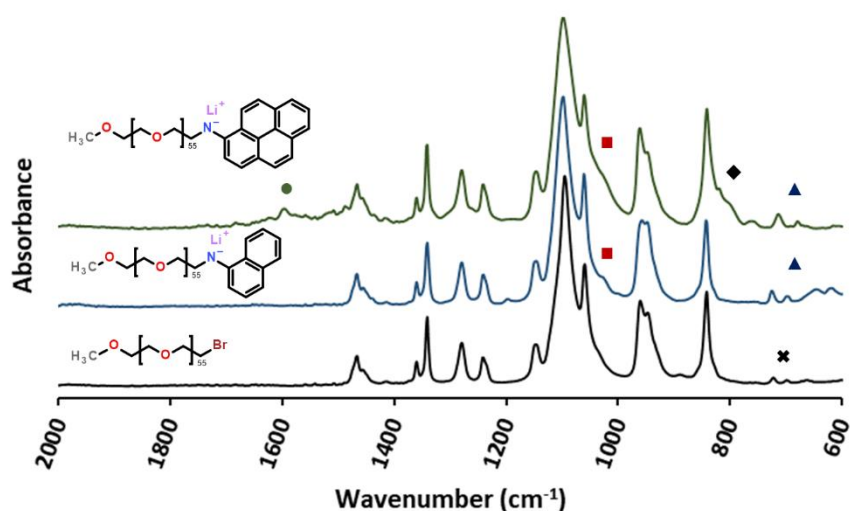
¹H NMR (DMSO-d₆, 298 K) chemical shift (δ / ppm): 1.17 (br, 2H, CH₂^d), 3.24 (s, CH₂^a), 3.50 (br, m, CH₂^{c, c'}), 3.72 (br, 2H, CH₂^b); 7.35 (H_{Ar}^f); 7.57, 7.69 (H_{Ar}^{m, n}); 7.74 (H_{Ar}^q); 7.86 (H_{Ar}^p); 7.94, 8.07 (H_{Ar}^{g, i, j}); 8.35 (H_{Ar}^l). INSET (purple): ⁷Li NMR (CDCl₃, 298 K) chemical shift (δ) = -1.01 ppm.

¹³C NMR Spectroscopy



¹³C NMR (DMSO-d₆, 298 K) chemical shift (δ / ppm): 32.3 (CH₂^d), 43.6 (CH₂^a), 58.1 (CH₂^a), 69.6, 69.8, 70.4 (CH₂^c), 71.3 (CH₂^b); 121.3, 121.7, 122.0, 123.0 (C_{Ar}^{o, r, s, t}); 124.5, 125.1, 125.5, 126.0, 126.7, 127.7 (C_{Ar}^{l, m, n}); 128.7 (C_{Ar}^{f, p, j}); 131.4 (C_{Ar}^{g, i, q}); 133.2 (C_{Ar}^{h, k}).

4.4.2. FTIR Spectroscopy



FTIR Spectroscopy frequencies of characteristic peak absorbances (wavenumbers, $\tilde{\nu}$ / cm^{-1}). The spectra are normalised to the difference in magnitude of the maximum and minimum absorbance in the 4000-600 cm^{-1} range and displaced by an arbitrary value. **mPEO₅₅-N(Li)Pyr**: 2885 ($-\text{CH}_2-$, ether; not shown); 1098 (■, $-\text{CH}_2\text{O}-$, ether); 724, 697, 645, 617 (▲, aryl). **mPEO₅₅-N(Li)Naph**: 2885 ($-\text{CH}_2-$, ether; not shown); 1098 (■, $-\text{CH}_2\text{O}-$, ether); 724, 697, 645, 617 (▲, aryl). **mPEO₅₅-Br**: 2865 ($-\text{CH}_2-$, ether; not shown); 1465, 1346, 1325, 1281, 1243, 1198, 1096 (■, $-\text{CH}_2\text{O}-$, ether), 1039, 996, 948, 844; 722, 698, 662 (✱, C-Br). The FTIR spectrum of mPEO₅₅-Br is equivalent to that of (anhydrous) mPEO₅₅-OH, except for the appearance of the C-Br absorbance (✱). The FTIR spectrum of mPEO₅₅-OH is shown in section 5.9.2.

4.5. Synthesis of Sulfonate-end-capped poly(ethylene oxide) monomethyl ether, mPEO_n-SO₃Li

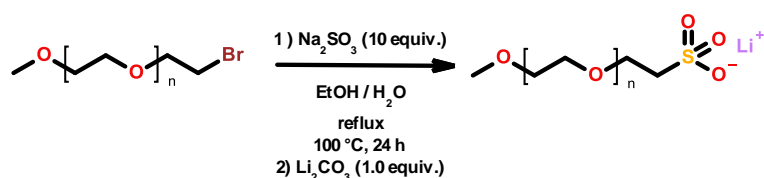


Figure III-4: Synthesis of sulfonate-end-capped poly(ethylene oxide) monomethyl ether via reaction of the bromo-end-capped derivative with sodium sulphite under reflux.

Sulfonate-end-capped poly(ethylene oxide) monomethyl ethers (mPEO_n-SO₃Li) were prepared by methods adapted from the literature.^[10-12] A flask was charged with mPEO_n-Br (see section 5.1) as a 50 % (g/mL) solution in ethanol (**Table III-8**). To this was added Na₂SO₃ (10.0 molar equiv.) in distilled water such that the final solvent mixture was 1:10 (v/v) EtOH/H₂O. The reaction mixture was heated under reflux (100°C, 24 h), after which time EtOH was added to make the solvent mixture 1:1 (v/v) EtOH/H₂O.

Table III-8: Masses and moles of bromo-end-capped poly(ethylene oxide) monomethyl ether, mPEO_n-Br, and sodium sulfite used in the synthesis of mPEO_n-SO₃Li of different DP_n (EO_n). The M_w of the mPEO_n-Br is calculated arithmetically from the commercial M_w of the corresponding mPEO_n-OH precursor (see synthesis of mPEO_n-Br for reference).

mPEO _n -OH DP _n (EO _n)	mPEO _n -Br			Na ₂ SO ₄	
	M _{w(comm)} (g/mol)	mass (g)	mol x 10 ³	mass (g)	mol x 10 ³
8	413	4.87	11.8	14.86	117.9
10	563	4.87	8.6	10.89	86.4
20	813	8.80	10.8	13.64	108.2
55	2063	15.06	7.3	9.20	73.0
160	5063	18.08	3.6	4.50	35.7

The white precipitate was filtered from solution and the solvents were evaporated under reduced pressure at 60°C. The residue was acidified as a solution in 2M HCl (10.0 equiv.). The water and excess HCl were removed under reduced pressure (~1 mbar, 60°C, 16 h). The residue was taken up in CHCl₃, stored cold (-20°C, > 4 h), filtered, and evaporated three times. The residue was taken up in distilled water and treated with Li₂CO₃ (1.0 equiv.). After stirring (30°C, 1 h), the water was evaporated under reduced pressure (< 10 mbar, 60°C). The residue was taken up in CHCl₃, stored cold (-20°C, > 4 h), filtered, and evaporated three times. The higher DP_n polymers (PEO_n = 55, 160) were additionally dropped through cold diethyl ether (3 x 200 mL). The products were dried under reduced pressure (< 10 mbar, 60°C, 72 h). The polymers bearing lithium sulfonate end-groups (mPEO_x-SO₃Li) were obtained as low viscosity melts (PEO_n = 8, 10), a waxy solid (PEO_n = 20) or as solids (PEO_n = 55, 160) at room temperature. Lithiation of the polymers was confirmed by ⁷Li NMR. For FTIR and NMR spectroscopy, and representative examples of spectra, please see section 5.7. The yields are summarised in **Table III-9**.

Table III-9: Yields of lithium sulfonate-end-capped poly(ethylene oxide) monomethyl ether obtained by reaction of mPEO-Br with sodium sulphite. Molar quantities and yields are calculated according to the M_{n(NMR)}.

mPEO _n -OH DP _n (EO _n)	mPEO-Br			mPEO-SO ₃ Li			
	M _{n(NMR)} (g/mol)	mass (g)	mol x 10 ³	M _{n(NMR)} (g/mol)	mass (g)	mol x 10 ³	yield (%)
8	467	4.87	13.91	474	3.44	9.64	69
10	522	4.87	9.33	529	4.10	7.75	83
20	982	8.80	8.96	989	8.86	8.95	Quantitative
55	2475	15.06	6.08	2482	15.33	6.17	Quantitative
160	7110	18.08	2.54	7117	18.43	2.59	Quantitative

4.6. Synthesis of N-(naphthyl)sulphonamide-end-capped poly(ethylene oxide) monomethyl ether, mPEO_n-SO₂N(Li)Naph

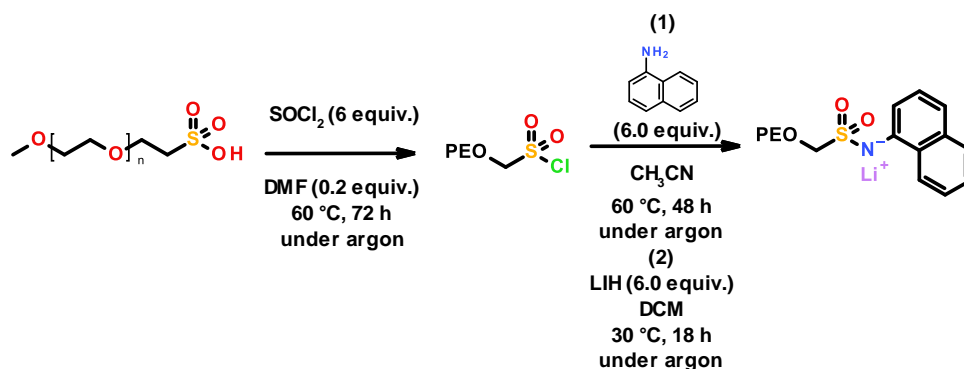


Figure III-5: Synthesis of N-(naphthyl)sulphonamide-end-capped poly(ethylene oxide) monomethyl ether.

The synthesis of sulfonamides was adapted from methods reported in the literature.^[13,14] A dry flask was charged with dry mPEO_n-SO₃H (see section 5.5) and anhydrous DMF (0.2 equiv.). The mixture was stirred under argon flow (60 °C, 1 h). To the hot mixture was added SOCl₂ (6.0 equiv.) dropwise under a blanket of argon (**Table III-10**). The mixture was purged with gentle argon flow (1 h) and the reaction proceeded with stirring under argon atmosphere (60 °C, 72 h). The excess SOCl₂ and the HCl by-product were vaporized by stirring and heating under reduced pressure until constant mass (200-1 mbar, 40 °C; except for PEO EO_n= 55 and 160, T= 60 °C). The polymers, bearing sulfonyl chloride end-groups (mPEO_n-SO₂Cl) and containing residual DMF solvent, were stored in the cold (-20 °C) and used without further purification within 24 h of preparation.

Table III-10: The masses and moles of mPEO-SO₃H, SOCl₂ (126.04 g/mol, d= 1.64 g/cm³ at 25 °C) and DMF (73.10 g/mol, d= 0.95 g/cm³ at 25 °C) used in the synthesis of mPEO-SO₂Cl of different DP_n (EO_n).

mPEO-SO ₃ H				SOCl ₂			DMF		
DP _n (EO _n)	M _{w(comm)} (g/mol)	mass (g)	mol x 10 ³	mass (g)	mol x 10 ³	vol (cm ³)	mass (g)	mol x 10 ³	vol (cm ³)
9	414	2.394	5.78	4.373	34.70	2.67	0.085	1.16	0.089
10	564	3.058	5.42	4.100	32.53	2.50	0.079	1.08	0.084
20	983	7.347	7.47	5.651	44.84	3.45	0.109	1.49	0.115
55	2064	12.240	5.93	4.485	35.58	2.73	0.087	1.19	0.091
160	5064	14.976	2.96	2.236	17.74	1.36	0.043	0.59	0.046

A 1 mol/L solution of 1-aminonaphthalene (2.0 equiv.) in anhydrous CH₃CN was degassed by three freeze-pump-thaw cycles, using liquid nitrogen to freeze the solution. This solution was added dropwise to mPEO_n-SO₂Cl under argon flow at room temperature (**Table III-11**). Heating of the higher DP_n polymers (EO_n= 55, 160) under argon atmosphere was required to aid mixing of the reagents (60 °C, 10 min). The flask was sealed and the reaction proceeded with heating under argon atmosphere (40 °C, 48 h). The reaction was quenched with K₂CO₃ (6.0 equiv., 10 % w/w in deionised water), diluted with CH₃CN (40 mL), then filtered.

Table III-11: Masses and moles of mPEO-SO₂Cl and 1-aminonaphthalene (143.19 g/mol) used in the synthesis of N-(naphthyl)sulphonamide-end-capped poly(ethylene oxide) monomethyl ether. The M_w of the polymers was calculated according to the commercial designation.

mPEO _n -SO ₂ Cl				1-aminonaphthalene	
DP _n (EO _n)	M _{w(comm)} (g/mol)	mass (g)	mol x 10 ³	mass (g)	mol x 10 ³
8	433	0.600	1.39	0.397	2.77
10	583	0.750	1.29	0.368	2.57
20	833	1.750	2.10	0.602	4.20
55	2083	3.000	1.44	0.412	2.88
160	5083	3.500	0.69	0.197	1.38

The polymers were purified by the method (A or B) according to the DP_n (EO_n) of PEO.

- A. The lower DP_n polymers (EO_n= 8, 10, 20) were evaporated to dryness under reduced pressure at 60 °C. The residue was taken up in CHCl₃ and extracted with 0.5 M HCl (3 x 20 mL) and washed with brine (1 x 10 mL). The organic solution was evaporated to dryness. The residue was taken up in DCM, dried over K₂CO₃, then filtered and evaporated again.
- B. The higher DP_n polymers (EO_n= 55, 160) were concentrated in CH₃CN and dropped through cold diethyl ether (3 x 300 mL).

The polymers bearing sulfonamide end-groups were dried under reduced pressure (< 10 mbar, 60°C, 24 h). The residue was dissolved in anhydrous DCM (5 mL) and placed under argon atmosphere. To the stirring solution at room temperature was added LiH (6.0 equiv.) under a blanket of argon. The mixture was stirred (30°C, 16 h). Lithiation was quenched by exposing the mixture to air and adding methanol dropwise until the evolution of hydrogen gas stopped. The solution was diluted with DCM (40 mL), washed with deionised water (3 x 10 mL) and brine (10 mL). The aqueous phases were back-extracted with DCM. The combined organics were dried over K₂CO₃, filtered, and evaporated. The product polymers (mPEO_n-SO₂N(Li)Naph) were dried under reduced pressure (< 10 mbar, 60°C, 72 h). The higher DP_n polymers (EO_n= 55, 160) were additionally freeze-dried from their solutions in deionised water. Lithiation of the polymer was confirmed by ⁷Li NMR. For FTIR and NMR spectroscopy, and representative examples of spectra, please see section 4.7. The yields are summarised in **Table III-12**.

Table III-12: The moles and yield of N-(naphthyl)sulphonamide-end-capped poly(ethylene oxide) monomethyl ether from the corresponding sulfonyl chloride. The number-average molar mass (M_{n(nmr)}) and DP_n (EO_n) were determined by NMR spectroscopy. The yield is calculated using these values.

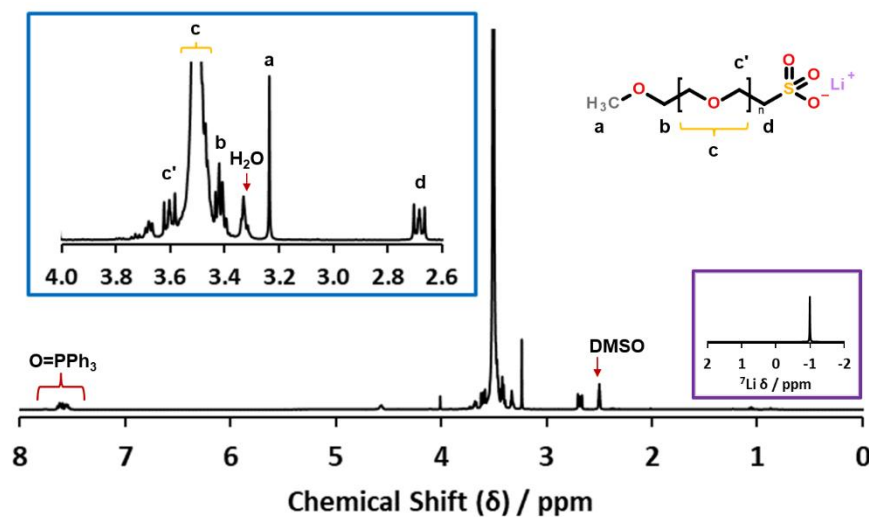
mPEO _n -SO ₂ Cl				mPEO _n -SO ₂ N(Li)-Naph			
DP _n (EO _n)	M _{n(NMR)} (g/mol)	mass (g)	mol x 10 ³	M _{n(NMR)} (g/mol)	mass (g)	mol x 10 ³	yield (%)
8	487	0.600	1.23	593	0.747	1.26	Quantitative
10	541	0.750	1.39	648	0.846	1.31	94
20	1002	1.750	1.75	1108	1.873	1.69	97
55	2495	3.000	1.20	2601	3.250	1.25	Quantitative
160	7130	3.500	0.49	7236	3.570	0.49	Quantitative

4.7. Chemical Characterisation of mPEO_n-SO₃Li and mPEO_n-SO₂N(Li)Naph

4.7.1. NMR Spectroscopy

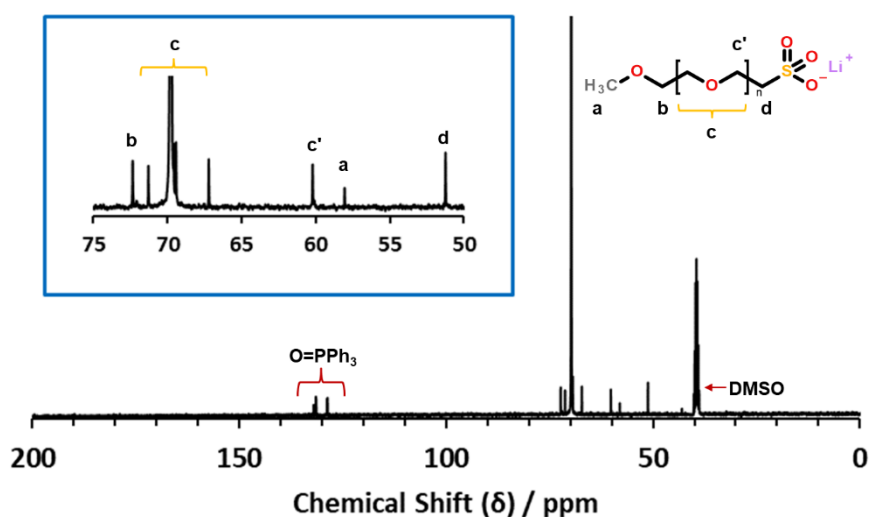
mPEO₂₀-SO₃Li

¹H and ⁷Li NMR Spectroscopy



¹H NMR (DMSO-d₆, 298 K) chemical shift (δ / ppm): 2.69 (br, 2H, CH₂^d), 3.24 (s, 3H, CH₃^a), 3.50 (br, CH₂^c), 3.59 (br, 2H, CH₂^{c'}). INSET (blue) magnified region of the ¹H spectrum, 2.6-4.0 ppm. INSET (purple): ⁷Li NMR (DMSO_{d6}, 298 K) chemical shift (δ) = -1.00 ppm.

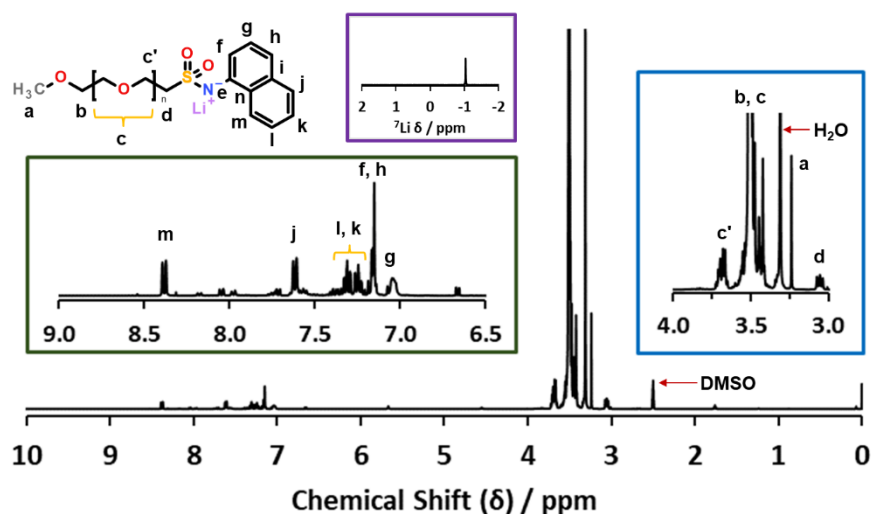
¹³C NMR Spectroscopy



¹³C NMR (DMSO-d₆, 298 K) chemical shift (δ / ppm): 51.2 (CH₂^d), 58.0 (CH₃^a), 60.2 (CH₂^c), 67.20, 69.4, 69.8, 71.3 (CH₂^c), 72.3 (CH₂^b).

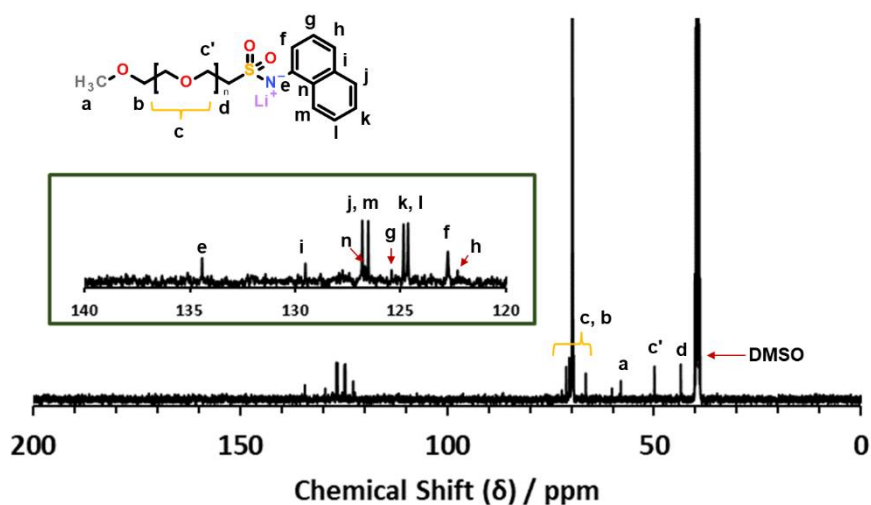
*m*PEO₂₀-SO₂N(Li)Naph

¹H and ⁷Li NMR Spectroscopy



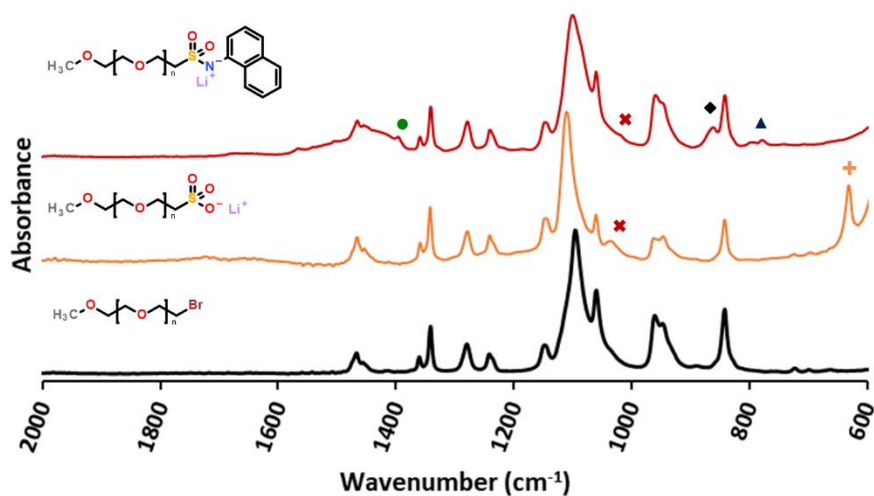
¹H NMR (DMSO-d₆, 298 K) chemical shift (δ / ppm): 2.69 (br, 2H, CH₂^d), 3.24 (s, 3H, CH₃^a), 3.51 (CH₂^{b,c}), 3.61 (br, 2H, CH₂^{c'}), 7.04 (br, 1H, H_{Ar}^g), 7.15 (br, 1H, H_{Ar}^{f,h}), 7.24 (br, 1H, H_{Ar}^k), 7.31 (br, 1H, H_{Ar}^l), 7.61 (br, 1H, H_{Ar}^j), 8.37 (br, 1H, H_{Ar}^m). INSET: ⁷Li NMR (DMSO-d₆, 298 K) chemical shift (δ / ppm): -1.04.

¹³C NMR Spectroscopy



¹³C NMR (DMSO-d₆, 298 K) chemical shift (δ / ppm): 43.6 (CH₃^d), 49.9 (CH₃^{c'}), 58.03 (CH₂^a); 66.5, 69.8, 70.5, 71.3 (CH₂^{b,c}); 122.8 (C_{Ar}^f); 124.6, 124.9 (C_{Ar}^{k,l}); 126.5, 126.8 (C_{Ar}^{j,m}); 126.7 (C_{Ar}ⁿ); 129.5 (C_{Ar}ⁱ); 134.4 (C_{Ar}^e).

4.7.2. FTIR Spectroscopy



FTIR Spectroscopy frequencies of characteristic peak absorbances (wavenumbers, $\tilde{\nu}$ / cm^{-1}). The spectra are normalised to the difference in magnitude of the maximum and minimum absorbance in the 4000-600 cm^{-1} range and displaced by an arbitrary value. **mPEO₅₅-SO₂N(Li)Naph**: 2885 (–CH₂–, ether; not shown); 1392 (●, N-aryl sulfonamide), 1279, 1241, 1146 (◆, –SO₂–, asymmetric stretching); 1147, 1101, 1061 (■, –CH₂O–, ether); 1027 (*, –SO₂–, symmetric stretching); 862 (◆, naphthalene); 779 (◆, C_{Ar}–H). **mPEO₅₅-SO₃Li**: 1036 (*); 632 (+)

4.8. Synthesis of Benzene Sulfonate-End-Capped poly(ethylene oxide) monomethyl ether, mPEO_n-OC(O)PhSO₃Li

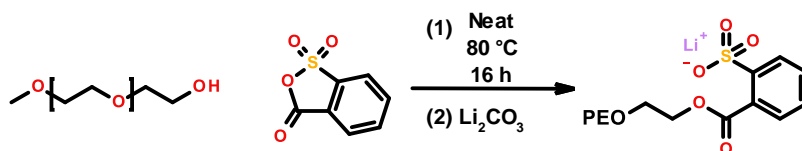


Figure III-6: Synthesis of benzene-sulfonate end-capped mPEO-OC(O)PhSO₃Li

Poly(ethylene oxide) monomethyl ether was end-capped with benzenesulfonate lithium salt (mPEO_n-OC(O)PhSO₃Li) *via* ring-opening reaction with 2-sulfolobenzoic acid cyclic anhydride (SBACA). The synthesis protocol was adapted from the literature.^[15] The SBACA (ALDRICH, technical grade, 90 %) was recrystallised from chloroform.

An oven-dried flask was charged with dry mPEO_n-OH and heated with stirring under argon flow (100°C, 1 h). The temperature was reduced to 60°C and to the stirring, molten mPEO_n-OH was added SBACA (1.20 equiv.) slowly in batches. The reaction mixture was heated with stirring under argon atmosphere (80°C, 16 h). During the course of the reaction, the clear colourless PEO and the white powder SBACA became a clear, burnt amber colour. The masses of reagents are summarised in **Table III-13**.

Table III-13: The masses and moles of mPEO and SBACA used in the synthesis of polymers of different DP_n (EO_n).

mPEO _n -OH			SBACA		
M _{w(comm)} (g/mol)	mass (g)	mol x 10 ³	mass (g)	mol x 10 ³	
350	3.50	10.00	2.21	12.00	
500	3.10	6.20	1.37	7.44	
750	10.18	13.57	3.00	16.29	
2000	20.00	10.00	2.21	12.00	
5000	50.00	10.00	2.21	12.00	

The reaction mixture was purified by the method (A or B) according to the DP_n of the polymer.

A. PEO EO_n= 8, 10

Diethyl ether (10 x 50 mL) was layered over the reaction mixture at room temperature and the immiscible layers were stirred slowly in a sealed flask (10 min). The diethyl ether was decanted and the reaction mixture was evaporated to dryness under reduced pressure (60 °C, < 10 mbar, 24 h).

B. PEO EO_n= 20, 55, 160

The reaction mixture was diluted with CHCl₃ (5 mL) and dropped through cold diethyl ether (3 x 200 mL). The residue was taken up in CHCl₃ and evaporated to dryness under reduced pressure (80 °C, < 10 mbar, 24 h).

The products collect from purification (A or B) were then neutralised. The polymer, bearing a sulfonic acid end-group, was dissolved in water, then treated with Li₂CO₃ (1.0 equiv.). When no more gas evolved from the solution, the polymer was dried first by rotary evaporation, then further in a vacuum oven (80°C, < 10 mbar, 72 h). The product was taken up in anhydrous CHCl₃, stored cold (-20°C, > 4 h) and then filtered cold, three times. The solvent was removed under reduced pressure to obtain the target polymer product. For FTIR and NMR spectroscopy, and representative examples of spectra, please see section 5.9.

The masses of the reagents and the polymer yields are summarised in **Table III-14**.

Table III-14: The synthesis of mPEO_n-OC(O)Ph-SO₃Li via ring-opening of SBACA by reaction with mPEO-OH. The commercial mass average molar masses (M_{w(comm)}) of mPEO_n-OHs were used to calculate the masses of reagents required. The number-average molar mass (M_n), calculated in this work using NMR spectroscopy, is quoted. The yield is calculated using M_{n(NMR)}. For ease of reading, the polymers are referred to by their DP_n, as calculated from M_{n(NMR)}.

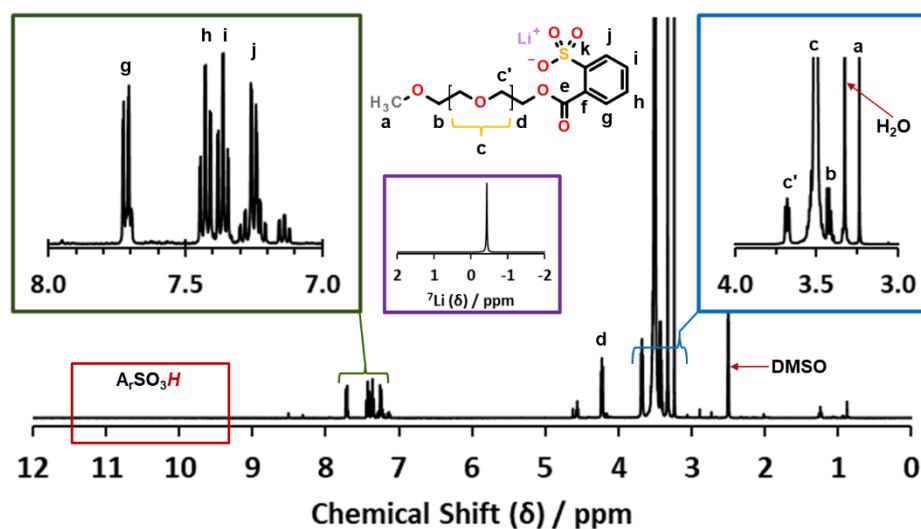
mPEO _m -OH					SBACA			mPEO _m -OC(O)Ph-SO ₃ Li			
M _{w(comm)} (g/mol)	M _{n(NMR)} (g/mol)	DP _n (EO _n)	mass (g)	mol x 10 ³	mass (g)	mol x 10 ³	molar eq.	M _{n(NMR)} (g/mol)	mass (g)	mol x 10 ³	yield (%)
350	404	8	3.50	12.20	2.21	12.00	0.98	454	4.11	9.04	74
500	459	10	3.10	6.76	1.37	7.44	1.10	649	2.12	3.27	48
750	919	20	10.18	11.08	3.00	16.29	1.47	1109	11.92	10.75	97
2000	2412	55	20.00	8.29	2.21	12.00	1.45	2603	20.67	7.94	96
5000	7047	160	50.00	7.10	2.21	12.00	1.69	7237	46.55	6.43	91

4.9. Chemical Characterisation of mPEO_n-OC(O)PhSO₃Li

4.9.1. NMR Spectroscopy

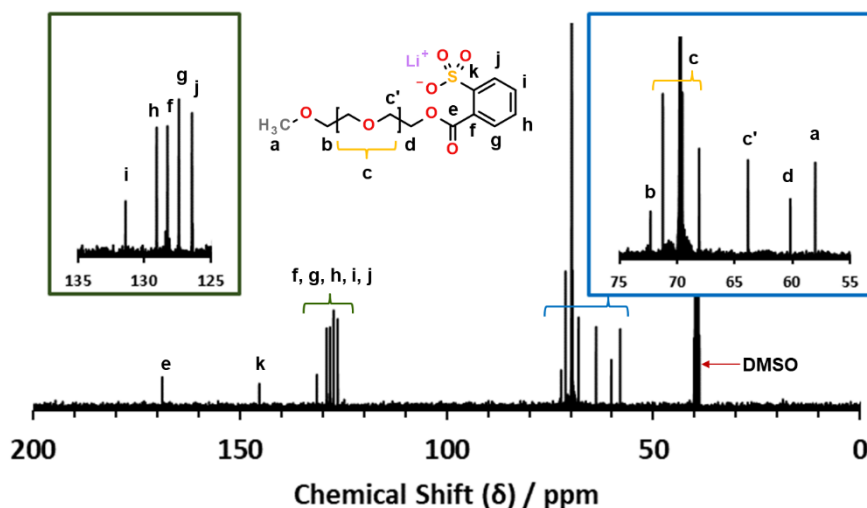
mPEO₂₀-OC(O)PhSO₃Li

¹H and ⁷Li NMR Spectroscopy



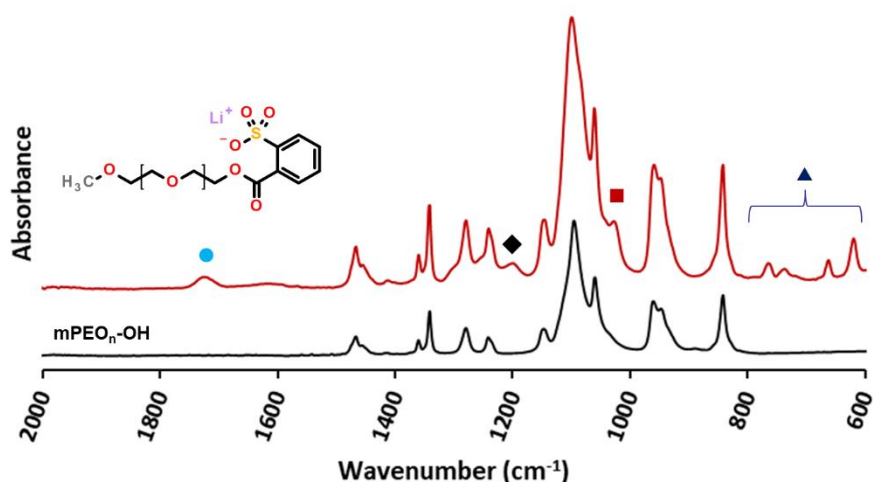
¹H NMR (DMSO-d₆, 298 K) chemical shift (δ / ppm): 3.24 (s, 3H, CH₃^a), 3.44 (m, 2H, CH₂^b), 3.51 (br, CH₂^c), 3.68 (t, J = 5.00 Hz, 2H, CH₂^{c'}), 4.23 (t, J = 5.12 Hz, 2H, CH₂^d), 7.25 (m, 1H, H_{Ar}^j), 7.37 (t, J = 7.49 Hz, 1H, H_{Ar}ⁱ), 7.45 (t, J = 7.49 Hz, 1H, H_{Ar}^h), 7.72 (d, J = 7.48 Hz, 1H, H_{Ar}^g).

¹³C NMR Spectroscopy



¹³C NMR (DMSO-d₆, 298 K) chemical shift (δ / ppm): 58.0 (CH₃^a), 60.2 (CH₂^d), 63.9 (CH₂^{c'}), 68.1, 69.9, 71.3 (CH₂^c), 72.3 (CH₂^b), 126.4 (C_{Ar}^j), 127.4 (C_{Ar}^g), 128.3 (C_{Ar}^f), 129.1 (C_{Ar}^h), 131.4 (C_{Ar}ⁱ), 145.4 (C_{Ar}^k), 168.9 (OC^e=O).

4.9.2. FTIR Spectroscopy



FTIR Spectroscopy frequencies of characteristic peak absorbances (wavenumbers, $\tilde{\nu}$ / cm^{-1}). The spectra are normalised to the difference in magnitude of the maximum and minimum absorbance in the 4000-400 cm^{-1} range and displaced vertically by an arbitrary value. The mPEO₅₅-OH is shown as a reference at 50 % relative absorbance intensity. **mPEO₅₅-OC(O)PhSO₃Li**: 2881 (–CH₂–, ether; not shown); 1724 (●, C=O stretching, ester), 1199 (◆, –SO₂–, asymmetric stretching); 1145, 1098, 1060 (–CH₂O–, ether); 1027 (■, –SO₂–, symmetric stretching); 764, 737, 662, 619 (▲, C_{Ar}-H, benzene)

5. Synthesis of MEC-SIPes: Zwitterionic and "Double-Salt" End-Capped Polymers

5.1. Synthesis of 4-azidonaphthalene-1-sulfonic acid sodium salt (AzNSO₃Na)

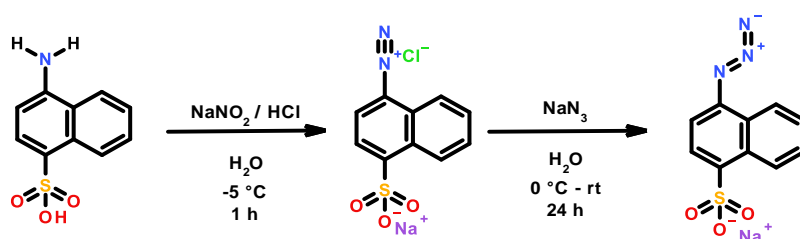


Figure III-7: Synthesis of 4-azidonaphthalene-1-sulfonic acid sodium salt (AzNSO₃Na) via nucleophilic aromatic substitution.

The synthesis of the azide functional group *via* the diazonium salt was adapted from the literature.^[16–18] Solid 4-aminonaphthalene-1-sulfonic acid (ANSO₃H, 40.00 g, 179 mmol) was mixed with deionized water (190 mL) in a two-neck reaction flask equipped with a dropping funnel and a thermometer. The resultant paste was cooled to 0°C and to this was added concentrated HCl (33.00 mL, 1.075 mol, 6 equiv.) dropwise. The magenta solution was stirred for 20 min with cooling to –5°C. A solution of NaNO₂ (18.54 g, 268 mmol, 1.5 equiv.) in water (135 mL) was added dropwise to the reaction mixture at –5°C – 0°C, over 45 min. After a further 15 min at 0°C, NaN₃ (46.59 g, 716 mmol, 4 equiv.) in water (675 mL) was added dropwise over 2 h at 0°C. The reaction suspension turns from pale magenta to bright orange. More water (500 mL) was added and the

temperature to rise slowly from 0°C to room temperature. Stirring was continued (24 h total, from the addition of NaN₃).

The reaction mixture was filtered and the precipitate washed with cold water (400 mL total). The precipitate was recrystallized from EtOH/H₂O mixtures and air dried at room temperature to obtain the product 4-azidonaphthalene-1-sulfonic acid sodium salt (AzNSO₃Na) as orange crystals (271 g/mol, 39.9 g, 147 mmol, 82.1 % yield). ¹H NMR analysis did not indicate any remaining aromatic amine protons. FTIR analysis of the product did not indicate the presence of the aromatic amine, absorbance characteristic of the azo group was observed; there was no change in the N₃ absorbance before and after recrystallisation from EtOH/H₂O. ¹H NMR (DMSO-d₆, 298 K) chemical shift (δ / ppm): 7.37 (d, *J* = 7.80 Hz, 1H, H_{Ar}^b), 7.55 (m, 2H, H_{Ar}^{g,h}), 7.98 (d, *J* = 7.76 Hz, 1H, H_{Ar}^c), 8.02 (d, *J* = 7.84 Hz, 1H, H_{Ar}ⁱ), 8.84 (d, *J* = 8.04 Hz, 1H, H_{Ar}^f). ¹³C NMR (DMSO-d₆, 298 K) chemical shift (δ / ppm): 112.95 (C_{Ar}^b), 121.65 (C_{Ar}ⁱ), 124.70 (C_{Ar}^h), 125.94 (C_{Ar}^j), 125.79 (C_{Ar}^f), 126.53 (C_{Ar}^c), 127.87 (C_{Ar}^g), 129.96 (C_{Ar}^e), 136.44 (C_{Ar}^a), 141.16 (C_{Ar}^d). MS-TOF (*m/z*) : AzNSO₃⁻ = 248.01 (predicted: AzNSO₃Na = 271.23, AzNSO₃⁻ = 248.24). For FTIR and NMR spectroscopy, and representative examples of spectra, please see section 6.4.

5.2. Synthesis of 4-azidonaphthalene-1-sulfonyl(methylsulfonyl)imide potassium salt [AzNSI(K)]

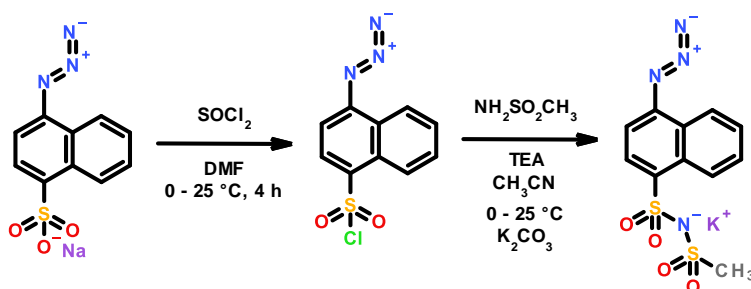


Figure III-8: Synthesis of 4-azidonaphthalene-1-sulfonyl(methylsulfonyl)imide

An oven-dried 3-neck flask was charged with 4-azidonaphthalene-1-sulfonic acid sodium salt (AzNSO₃Na 1.75H₂O, 30.00 g, 98.77 mmol) was in dry DMF (500 mL). 50 mL of the solvent was distilled out under reduced pressure (39-40 mbar, solvent obtained at 67-68°C). The flask was cooled to 0°C under argon flow, then SOCl₂ (15 mL, 24.6 g, 206 mmol, 2.09 equiv.) was added dropwise at 0°C under argon over 15 min. The reaction mixture was allowed to warm to 20°C with stirring (4 h). The reaction mixture was poured into an equivalent volume of brine and filtered. The precipitate was washed with deionised water (4 x 50 mL), then taken up in EtOAc. The solution was dried over K₂CO₃ and filtered. The product was recrystallised from EtOAc to obtain needle-like orange crystals (22.1 g, 82.4 mmol, 83.4 % yield). The product 4-azonaphthalene-1-sulfonyl chloride (AzNSO₂Cl) was stored under argon at -20°C and used within 24 h of the synthesis. ¹H NMR (DMSO-d₆, 298 K) chemical shift (δ / ppm): 7.37 (d, *J* = 7.80 Hz, 1H, H_{Ar}^b), 7.54 (ddd, *J* = 1.36, 6.71, 8.24 Hz, 1H, H_{Ar}^h), 7.59 (ddd, *J* = 1.53, 6.80, 8.24 Hz, 1H, H_{Ar}^g), 7.98 (d, *J* = 7.84 Hz, 1H, H_{Ar}^c), 8.02 (d, = 8.00 Hz, 1H, H_{Ar}ⁱ), 8.83 (d, *J* = 8.20 Hz, 1H, H_{Ar}^f). ¹³C NMR (DMSO-d₆, 298 K) chemical shift (δ / ppm): 113.04 (C_{Ar}^b), 121.81 (C_{Ar}ⁱ), 124.88 (C_{Ar}^h), 125.88 (C_{Ar}^j), 126.10 (C_{Ar}^f), 126.74 (C_{Ar}^c), 127.79 (C_{Ar}^g), 129.97 (C_{Ar}^e), 136.74 (C_{Ar}^a), 140.85 (C_{Ar}^d).

An oven-dried flask was charged with 1-azidonaphthalene-4-sulfonyl chloride (21.75 g, 81.3 mmol) in dry CH₃CN (300 mL). The solution was cooled to 0°C and purged with argon gas flow (30 min).

Freshly distilled TEA (16.40 g, 162.5 mmol, 2.0 equiv.) was added to the stirring reaction mixture under argon. Methanesulfonamide (15.45 g, 162.5 mmol, 2.0 equiv.) in dry CH₃CN (100 mL) was added dropwise to the reaction solution under argon flow at 0°C. The reaction was stirred under gentle heating (30°C, 48 h). The reaction was monitored by silica gel Thin Layer Chromatography (TLC), ¹H NMR and IR spectroscopy. When the starting material was no longer visible in the TLC (1:1 MeOH / CHCl₃ solution phase) trace, FTIR analysis confirmed the presence of sulfonamide functions in the reaction mixture. FTIR did not indicate any absorbance corresponding to SO₂Cl (1358 cm⁻¹). The reaction mixture was concentrated, then partitioned with EtOAc (500 mL). The precipitated salt was removed by filtration and the filtrate was washed with 1M HCl (3 x 50 mL) and deionised water (3 x 50 mL). The combined organic phases were dried over K₂CO₃. The solvent was removed under reduced pressure. The product 4-azidonaphthalene-1-sulfonyl(methylsulfonyl)imide potassium salt [AzNSI(K)] was recrystallised from EtOAc/MeOH mixtures to yield fine orange crystals (364.44 g/mol, 12.54 g, 34.4 mmol, 42.3 % yield. Total yield AzNSO₃Na → AzNSI(K) = 35.3 %; total yield ANSO₃H → AzNSI(K) = 29.0 %). ¹H NMR (DMSO-d₆, 298 K) chemical shift (δ / ppm): 2.74 (s, 3H, CH₃), 7.44 (d, *J* = 7.96 Hz, 1H, H_{Ar}^b), 7.59 (ddd, 1H, *J* = 1.32, 6.72, 8.63 Hz, H_{Ar}^h), 7.65 (ddd, *J* = 1.49, 6.88, 8.63 Hz, 1H, H_{Ar}^g), 8.06 (d, *J* = 7.92 Hz, 1H, H_{Ar}^c), 8.07 (d, *J* = 8.04 Hz, 1H, H_{Ar}ⁱ), 8.79 (d, *J* = 8.48 Hz, 1H, H_{Ar}^f). ¹³C NMR (DMSO-d₆, 298 K) chemical shift (δ / ppm): 42.72 (CH₃), 112.81 (C_{Ar}^b), 121.99 (C_{Ar}ⁱ), 125.83 (C_{Ar}^j), 126.25 (C_{Ar}^h), 126.93 & 126.98 (C_{Ar}^{c,f}), 127.25 (C_{Ar}^g), 129.35 (C_{Ar}^e), 138.34 (C_{Ar}^a), 138.70 (C_{Ar}^d). MS-TOF (*m/z*): 325.01 (predicted: AzNSI(K) = 364.44, AzNSI⁻ = 325.34). For FTIR and NMR spectroscopy, and representative examples of spectra, please see section 6.4.

5.3. Synthesis of 4-aminonaphthalene-1-sulfonyl(methylsulfonyl)imide potassium salt [ANSI(K)]

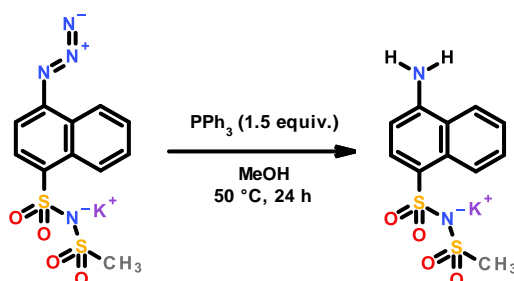


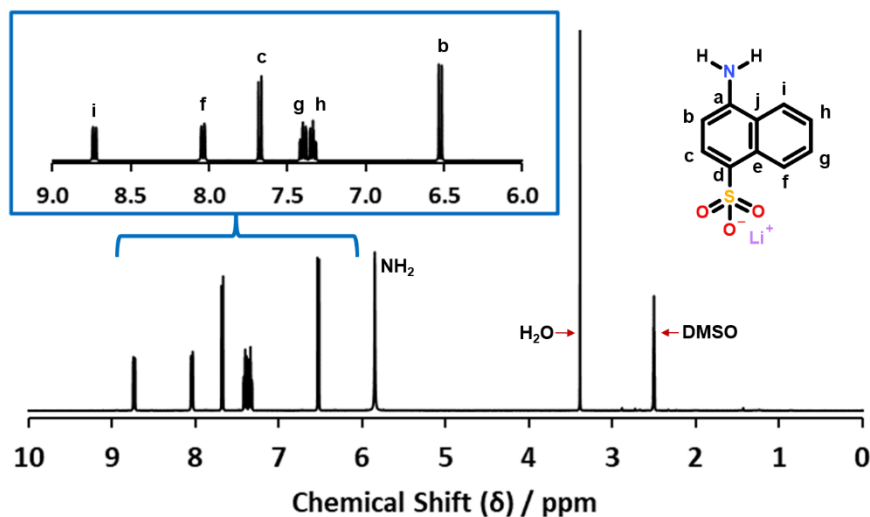
Figure III-9: Synthesis of 4-aminonaphthalene-1-sulfonyl(methylsulfonyl)imide potassium salt [ANSI(K)]

In a dry flask were mixed 4-azidonaphthalene-1-sulfonyl(methylsulfonyl)imide potassium salt (AzNSIK, 2.000 g, 6.13 mmol) and triphenylphosphine (2.246 g, 9.19 mmol, 1.5 equiv.) in methanol (200 mL). The reaction flask was covered with aluminium foil and heated with stirring (50°C, 6 h). The methanol was distilled from the reaction mixture under reduced pressure and the product was isolated by silica column chromatography (MeOH:CHCl₃ gradient = 9:1 → 3:2). The product 4-aminonaphthalene-1-sulfonyl(methylsulfonyl)imide potassium salt [ANSI(K)] was obtained as the second fraction and the solvents were removed under reduced pressure (< 10 mbar, 40°C) to obtain the product as an orange solid (1.624 g, 5.41 mmol, AzNSI(K) → ANSI(K) 88.2 % yield; ANSO₃H → ANSI(K) 31.1 %). The product could not be recrystallized from any of CHCl₃, EtOAc, EtOH, MeOH or alcohol-water mixtures. The product was insufficiently soluble in polar organic solvents to enable measurement of *m/z* by MS-TOF. For FTIR and NMR spectroscopy, and representative examples of spectra, please see section 6.4.

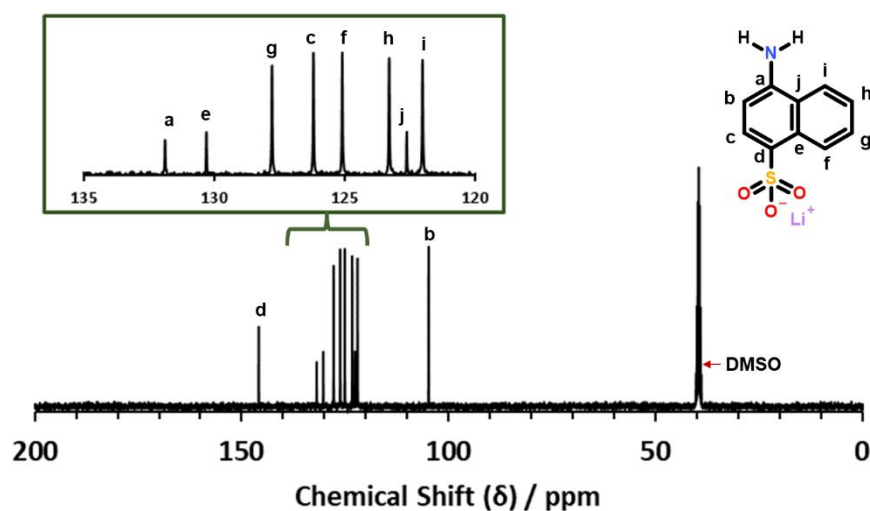
5.4. Chemical Characterisation of ANSO₃Li and its derivatives AzNSO₃Na, AzNSO₂Cl, AzNSI(K), and ANSI(K).

5.4.1. NMR Spectroscopy

¹H and ¹³C spectroscopy of ANSO₃Li

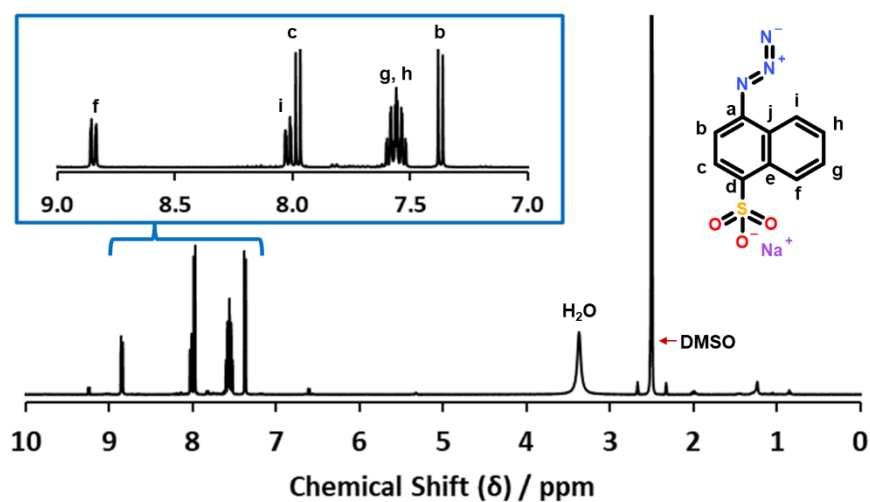


¹H NMR (DMSO-d₆, 298 K) chemical shift (δ / ppm): 5.84 (s, 2H, NH₂), 6.52 (d, *J* = 7.76 Hz, 1H, H_{Ar}^b), 7.33 (ddd, 1H, *J* = 1.46, 6.68, 8.63 Hz, H_{Ar}^h), 7.39 (ddd, *J* = 1.32, 6.68, 8.63 Hz, 1H, H_{Ar}^g), 7.67 (d, *J* = 7.88 Hz, 1H, H_{Ar}^c), 8.04 (d, *J* = 8.60 Hz, 1H, H_{Ar}ⁱ), 8.73 (d, *J* = 8.44 Hz, 1H, H_{Ar}^f).

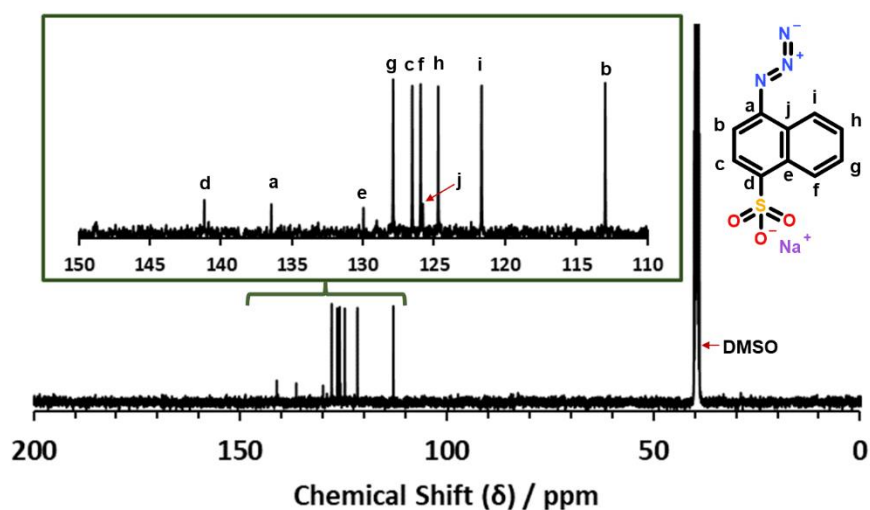


¹³C NMR (DMSO-d₆, 298 K) chemical shift (δ / ppm): 104.82 (C_{Ar}^b), 122.61 (C_{Ar}ⁱ), 122.00 (C_{Ar}^j), 123.28 (C_{Ar}^h), 125.08 (C_{Ar}^f), 126.19 (C_{Ar}^c), 127.77 (C_{Ar}^g), 130.29 (C_{Ar}^e), 131.88 (C_{Ar}^a), 145.88 (C_{Ar}^d).

^1H and ^{13}C spectroscopy of AzNSO_3Na

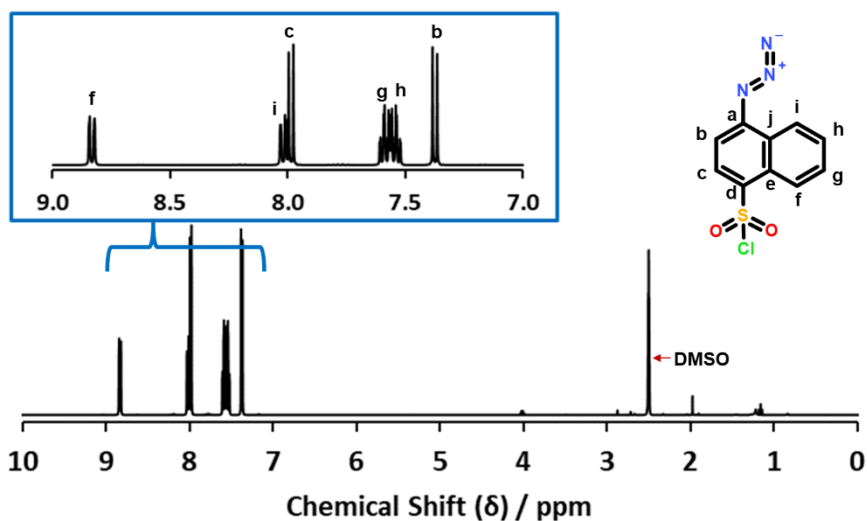


^1H NMR (DMSO- d_6 , 298 K) chemical shift (δ / ppm): 7.37 (d, J = 7.80 Hz, 1H, $\text{H}_{\text{Ar}}^{\text{b}}$), 7.55 (m, 2H, $\text{H}_{\text{Ar}}^{\text{g,h}}$), 7.98 (d, J = 7.76 Hz, 1H, $\text{H}_{\text{Ar}}^{\text{c}}$), 8.02 (d, J = 7.84 Hz, 1H, $\text{H}_{\text{Ar}}^{\text{i}}$), 8.84 (d, J = 8.04 Hz, 1H, $\text{H}_{\text{Ar}}^{\text{f}}$).

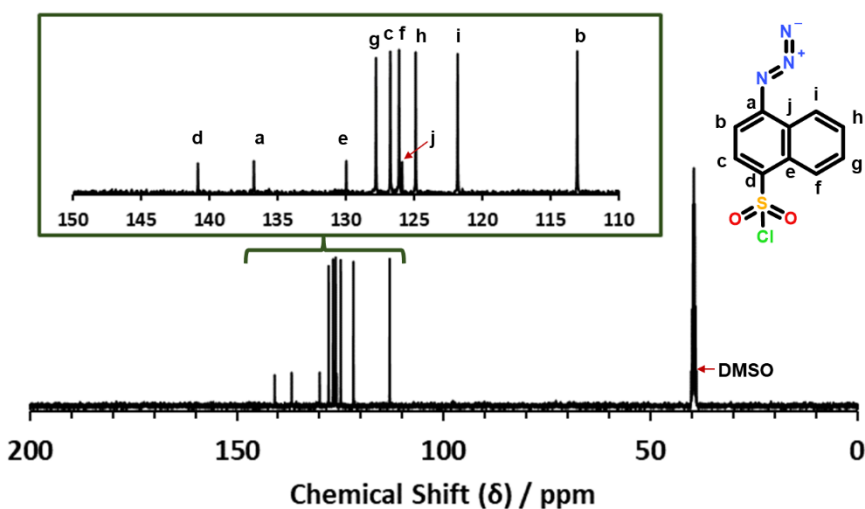


^{13}C NMR (DMSO- d_6 , 298 K) chemical shift (δ / ppm): 112.95 ($\text{C}_{\text{Ar}}^{\text{b}}$), 121.65 ($\text{C}_{\text{Ar}}^{\text{i}}$), 124.70 ($\text{C}_{\text{Ar}}^{\text{h}}$), 125.94 ($\text{C}_{\text{Ar}}^{\text{j}}$), 125.79 ($\text{C}_{\text{Ar}}^{\text{f}}$), 126.53 ($\text{C}_{\text{Ar}}^{\text{c}}$), 127.87 ($\text{C}_{\text{Ar}}^{\text{g}}$), 129.96 ($\text{C}_{\text{Ar}}^{\text{e}}$), 136.44 ($\text{C}_{\text{Ar}}^{\text{a}}$), 141.16 ($\text{C}_{\text{Ar}}^{\text{d}}$).

^1H and ^{13}C spectroscopy of AzNSO_2Cl



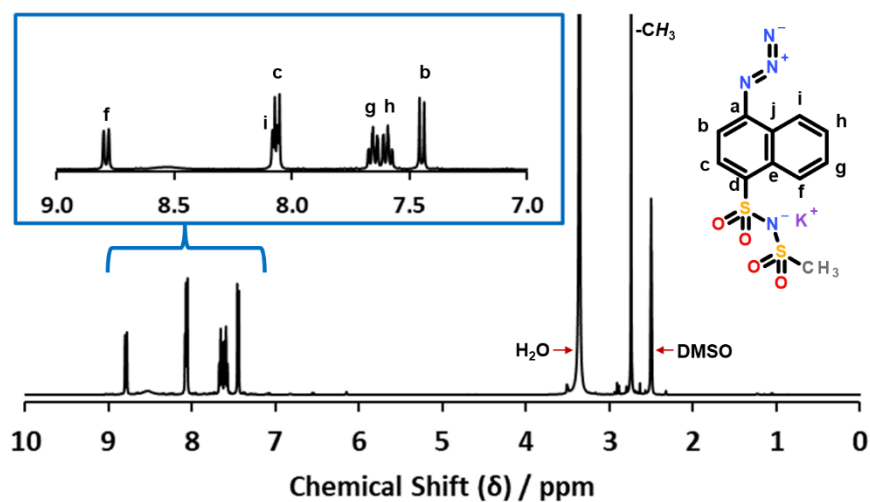
^1H NMR (DMSO- d_6 , 298 K) chemical shift (δ / ppm): 7.37 (d, J = 7.80 Hz, 1H, $\text{H}_{\text{Ar}}^{\text{b}}$), 7.54 (ddd, J = 1.36, 6.71, 8.24 Hz, 1H, $\text{H}_{\text{Ar}}^{\text{h}}$), 7.59 (ddd, J = 1.53, 6.80, 8.24 Hz, 1H, $\text{H}_{\text{Ar}}^{\text{g}}$), 7.98 (d, J = 7.84 Hz, 1H, $\text{H}_{\text{Ar}}^{\text{c}}$), 8.02 (d, J = 8.00 Hz, 1H, $\text{H}_{\text{Ar}}^{\text{i}}$), 8.83 (d, J = 8.20 Hz, 1H, $\text{H}_{\text{Ar}}^{\text{f}}$).



^{13}C NMR (DMSO- d_6 , 298 K) chemical shift (δ / ppm): 113.04 ($\text{C}_{\text{Ar}}^{\text{b}}$), 121.81 ($\text{C}_{\text{Ar}}^{\text{i}}$), 124.88 ($\text{C}_{\text{Ar}}^{\text{h}}$), 125.88 ($\text{C}_{\text{Ar}}^{\text{j}}$), 126.10 ($\text{C}_{\text{Ar}}^{\text{f}}$), 126.74 ($\text{C}_{\text{Ar}}^{\text{c}}$), 127.79 ($\text{C}_{\text{Ar}}^{\text{g}}$), 129.97 ($\text{C}_{\text{Ar}}^{\text{e}}$), 136.74 ($\text{C}_{\text{Ar}}^{\text{a}}$), 140.85 ($\text{C}_{\text{Ar}}^{\text{d}}$).

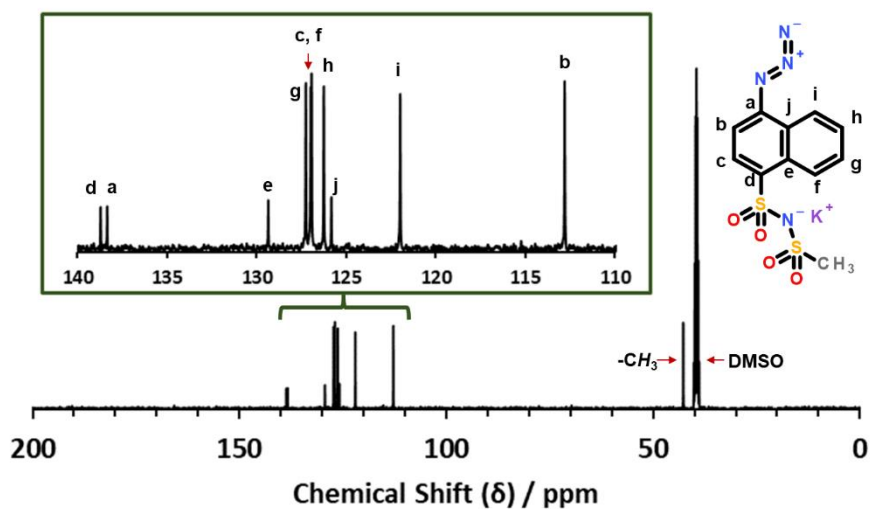
^1H and ^{13}C , HSQC and HMBC spectroscopy of AzNSI(K)

^1H NMR Spectroscopy



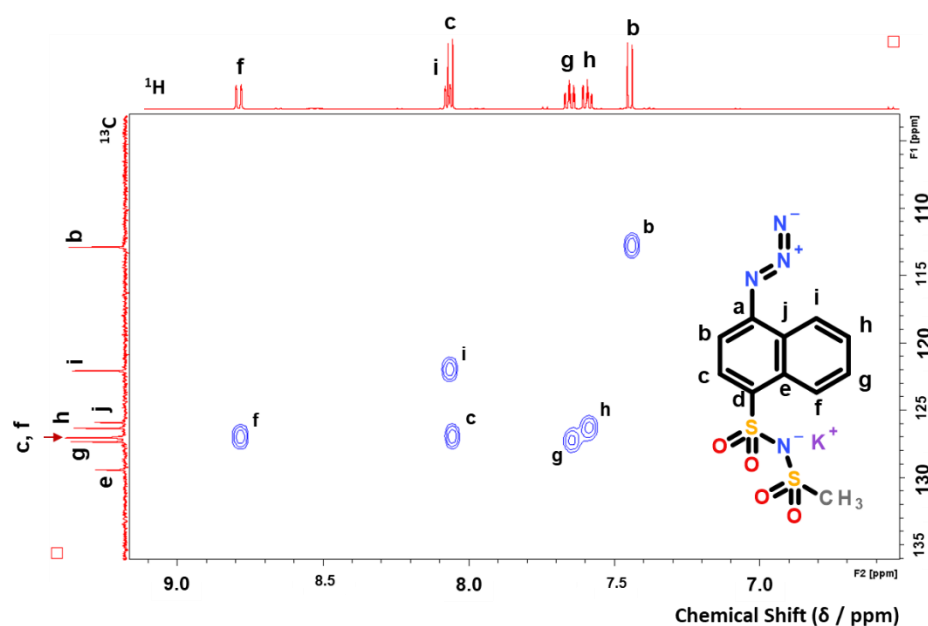
^1H NMR (DMSO- d_6 , 298 K) chemical shift (δ / ppm): 2.74 (s, 3H, CH₃), 7.44 (d, J = 7.96 Hz, 1H, H_{Ar}^b), 7.59 (ddd, 1H, J = 1.32, 6.72, 8.63 Hz, H_{Ar}^h), 7.65 (ddd, J = 1.49, 6.88, 8.63 Hz, 1H, H_{Ar}^g), 8.06 (d, J = 7.92 Hz, 1H, H_{Ar}^c), 8.07 (d, J = 8.04 Hz, 1H, H_{Ar}ⁱ), 8.79 (d, J = 8.48 Hz, 1H, H_{Ar}^f).

^{13}C NMR Spectroscopy

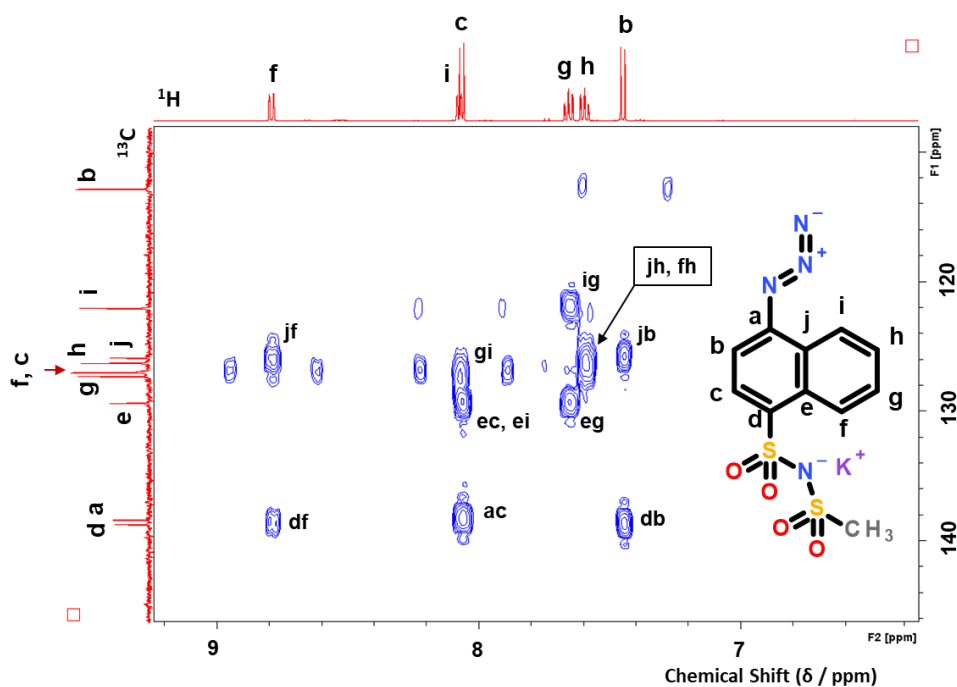


^{13}C NMR (DMSO- d_6 , 298 K) chemical shift (δ / ppm): 42.72 (CH₃), 112.81 (C_{Ar}^b), 121.99 (C_{Ar}ⁱ), 125.83 (C_{Ar}^j), 126.25 (C_{Ar}^h), 126.93, 126.98 (C_{Ar}^{c,f}), 127.25 (C_{Ar}^g), 129.35 (C_{Ar}^e), 138.34 (C_{Ar}^a), 138.70 (C_{Ar}^d).

Heteronuclear Single Quantum Coherence (HSQC) Spectroscopy



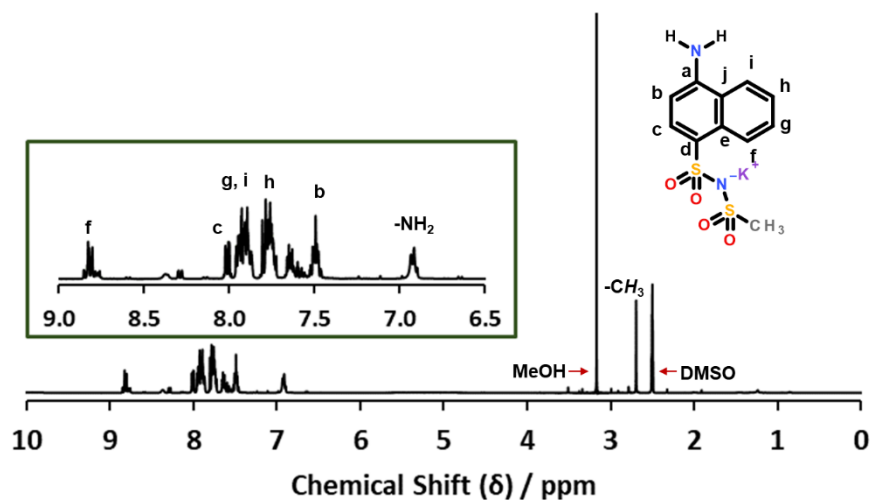
Heteronuclear Single Quantum Coherence (HSQC) NMR used to attribute C-H coupling of aromatic nuclei of AzNSI(K) (DMSO- d_6 , 298 K). The identities of the nuclei are elucidated with respect to the (red) exterior projections of the ^{13}C (left; 100 MHz, 98-136 ppm) and ^1H (top; 400 MHz, 6.5-9.1 ppm) 1D spectra.



Heteronuclear Multiple Bond Correlation (HMBC) NMR of AzNSI(K) (DMSO- d_6 , 298 K, 400 MHz): The identities of the nuclei are elucidated with respect to the (red) exterior projections of the ^{13}C (left) and ^1H (top) 1D spectra. The HMBC NMR identities are indicated according to the ^{13}C and ^1H nuclei, using the identifiers displayed in structural formula of AzNSI(K). The identifiers are in the form such that $\text{C}^i\text{H}^f \equiv \text{jf}$. Unlabelled blue signals are phase artifacts of the HMBC spectrum.

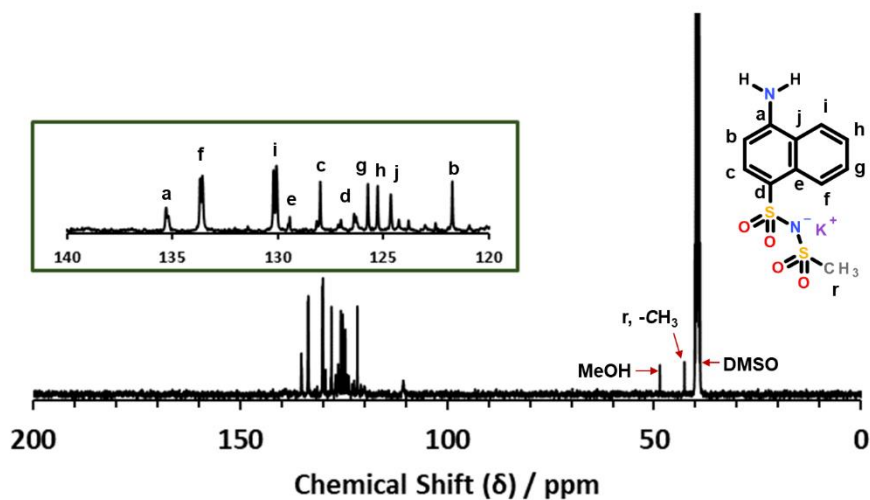
^1H and ^{13}C spectroscopy of ANSI(K)

^1H NMR Spectroscopy



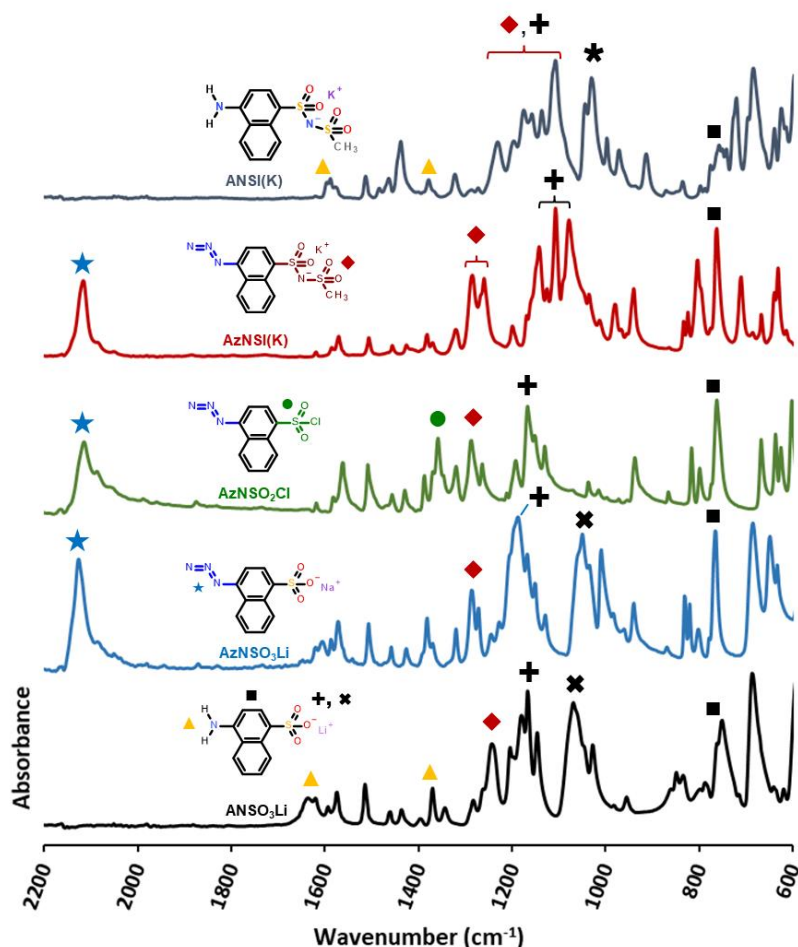
^1H NMR (DMSO- d_6 , 298 K) chemical shift (δ / ppm): 2.69 (s, 3H, CH_3), 3.16 (s, residual MeOH), 6.92 (br, 2H, NH_2), 7.48 (br, $\text{H}_{\text{Ar}}^{\text{b}}$), 7.64 (m, $\text{H}_{\text{Ar}}^{\text{h}}$), 7.92 (m, $\text{H}_{\text{Ar}}^{\text{g,i}}$), 8.01 (br, $\text{H}_{\text{Ar}}^{\text{c}}$), 8.82 (d, $J = 8.48$ Hz, 1H, $\text{H}_{\text{Ar}}^{\text{f}}$); $\int[\text{CH}_3] = 3\text{H}$; $\int[\text{b,c,g,h,i}] = 5\text{H}$.

^{13}C NMR Spectroscopy



^{13}C NMR (DMSO- d_6 , 298 K) chemical shift (δ / ppm): 42.67 ($r, -\text{CH}_3$), 48.61 (residual MeOH), 121.74 ($\text{C}_{\text{Ar}}^{\text{b}}$), 124.65 ($\text{C}_{\text{Ar}}^{\text{j}}$), 125.28 ($\text{C}_{\text{Ar}}^{\text{h}}$), 125.74 ($\text{C}_{\text{Ar}}^{\text{g}}$), 126.23, 127.01 ($\text{C}_{\text{Ar}}^{\text{d, d'}}$), 128.00 ($\text{C}_{\text{Ar}}^{\text{c}}$), 130.10 ($\text{C}_{\text{Ar}}^{\text{i}}$), 133.60 ($\text{C}_{\text{Ar}}^{\text{f}}$), 135.26 ($\text{C}_{\text{Ar}}^{\text{a}}$).

5.4.2. FTIR Spectroscopy



FTIR Spectroscopy frequencies of characteristic peak absorbances (wavenumbers, $\tilde{\nu}$ / cm⁻¹). The spectra are normalised to the difference in magnitude of the maximum and minimum absorbance in the 4000-525 cm⁻¹ range and displaced vertically by an arbitrary value. Sample preparation of ANSO₃Li was carried out as follows: the acid ANSO₃H was mixed with water and neutralised with LiOH. The solution of the Li-salt was filtered of remaining insoluble acid and dried under reduced pressure (< 10 mbar, 100°C, 72 h) to obtain the target compound at quantitative yield. AzNSO₃Li, AzNSO₂Cl and AzNSIK were recrystallised prior to the measurement. **ANSO₃Li**: 3400 (N-H stretching, -NH₂, not displayed); 1636 (▲, N-H bending, -NH₂); 1370 (▲, C-N stretch, C-NH₂); 1242 (◆, -SO₂- asymmetric stretching); 1166 (+, -SO₂- symmetric stretching); 1068 (✕, -SO₂O⁻); 750 (■, Aryl C-H out-of-plane [oop] bending). **AzNSO₃Na**: 2126 (★, R-N=N=N stretch); 1285 (◆, -SO₂- asymmetric stretch); 1187 (+, -SO₂- symmetric stretching); 1049 (✕, -SO₂O⁻); 764 (■, Aryl C-H_{oop}). **AzNSO₂Cl**: 2115 (★, R-N=N=N stretch); 1358 (●, -SO₂Cl); 1287 (◆, -SO₂- asymmetric stretching); 1166 (+, -SO₂- symmetric stretching); 762 (■, Aryl C-H_{oop}). **AzNSI(K)**: 2117 (★, R-N=N=N stretch); 1295, 1284 (◆, -SO₂- asymmetric stretching); 1144, 1106, 1077 (+, -SO₂- symmetric stretching); 762 (■, Aryl C-H_{oop}). **ANSI(K)**: 3450 (N-H stretching, -NH₂, not displayed); 3059 (CH, aromatic, not displayed); 1587 (▲, N-H bending, -NH₂); 1437 (S=O stretching); 1377 (▲, C-N stretching, aromatic amine); 1230, 1195, 1156, 1136, 1106 (◆, -SO₂- asymmetric stretching; +, -SO₂- symmetric stretching); 1043 (✕, S=O stretching); 756 (■, Aryl C-H out-of-plane [oop] bending).

5.5. Synthesis of naphthalene-1-sulfonyl(methylsulfonyl)imide lithium salt end-capped poly(ethylene oxide) monomethyl ether [mPEO- \blacklozenge NSI(Li)].

5.5.1. Synthesis of mPEO₂₀-AzNSI(Li)

Synthesis of the alkyl-functional precursor mPEO₂₀C(O)C \equiv CH

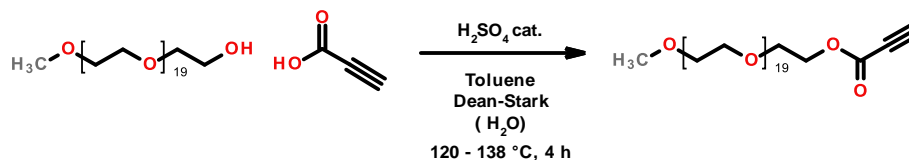


Figure III-10: Synthesis of alkyl-functional mPEO₂₀C(O)C \equiv CH ($M_{n(\text{NMR})} = 971$ g/mol) via acid-catalysed esterification under Dean-Stark conditions.

Synthesis of alkyne-terminated PEO was adapted from the literature.^[21] An oven-dried flask was charged with dry mPEO₂₀-OH ($M_{n(\text{NMR})} = 919$ g/mol, 10.0 g, 10.8 mmol) in dry toluene (100 mL). The flask was heated to 125°C and 15 mL of the solvent was distilled away. The solution was allowed to cool to < 100°C. To the stirring solution was added propiolic acid (1.87 g, 26.7 mmol, 2.45 equiv., ~1.64 mL) using an oven-dried glass syringe and needle under argon flow. Catalytic concentrated sulfuric acid (4 drops) was added and the solution was heated under reflux (125°C, 1 h), then under Dean-Stark conditions (120-138°C, 4 h). The clear yellow solution was then concentrated under reduced pressure to obtain a yellow oil. The residue was taken up in DCM (60 mL), washed with saturated NaHCO₃ (3 x 10 mL), then brine (1 x 20 mL). The combined aqueous phases were back-extracted with DCM (10 mL). The combined organics were dried over MgSO₄ and the solvent removed under reduced pressure. The oily residue was taken up in EtOH (30 mL) and treated with activated carbon (0.1 g, 40°C, 1 h). The suspension was filtered and the solvent removed under reduced pressure. The residue was taken up in DCM and passed over a short plug of silica gel (0.5 g). The solvent was evaporate to obtain product polymer as a clear oil ($M_{n(\text{NMR})} = 971$ g/mol, 8.440 g, 8.65 mmol, 80 % yield). For FTIR and NMR spectroscopy, and representative examples of spectra, please see section 6.6.

Synthesis of mPEO₂₀- \blacklozenge NSI(Li) via Copper-Catalysed Azide-Alkyne Cycloaddition (CuAAC)

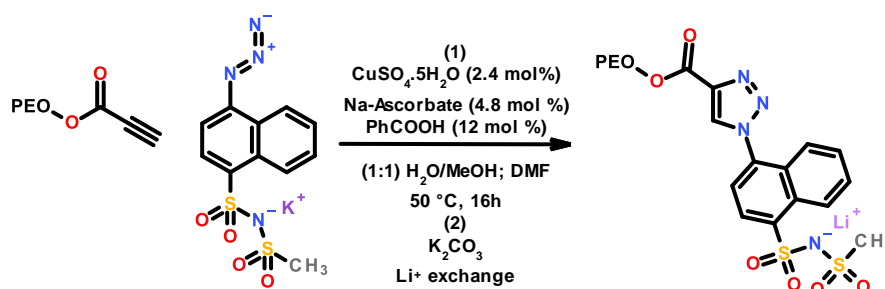


Figure III-11: Synthesis of 4-(1,2,3-triazo)-naphthalene-1-sulfonyl(methylsulfonyl)imide lithium salt end-capped poly(ethylene oxide) monomethyl ether via CuAAC

The method for Copper Catalysed Azide-Alkyne Cycloaddition (CuAAC) was adapted from the literature.^[21] The particular use of benzoic acid was inspired by the literature in an attempt to promote a higher yield.^[22] To a solution of CuSO₄.5H₂O (9.3 mg, 3.74 x 10⁻⁵ mol, 0.024 equiv.) in deionised water (6 mL) was added first sodium ascorbate (14.8 mg, 7.48 x 10⁻⁵ mol, 0.048 equiv.) then benzoic acid (22.8 mg, 1.87 x 10⁻⁴ mol, 0.12 equiv.), with stirring. An orange suspension formed in the clear blue Cu(II) solution upon addition of sodium ascorbate. Alkyl-functional

mPEO₂₀C(O)C≡CH (971 g/mol, 1.50 g, 1.54 × 10⁻³ mol) in deionised water (4 mL) was added to the flask and the reaction mixture was stirred (30°C, 1 h). The 4-azidonaphthalene-1-sulfonyl(methylsulfonyl)imide potassium salt (AzNSIK, 364.02 g/mol; 671.4 mg, 1.84 × 10⁻³ mol, 1.2 equiv.; for synthesis, see section 5.2) in 1:6 water/methanol (14 mL) was added and the reaction mixture was heated (50°C, 4 h). Due to poor solubility of the reagents and no change in the FTIR characteristic peak absorbance of the azide (2117 cm⁻¹), the solvent was distilled under reduced pressure (50°C) and replaced with DMF (20 mL). The resultant clear, dark red solution was stirred under gentle heat (50°C, 16 h).

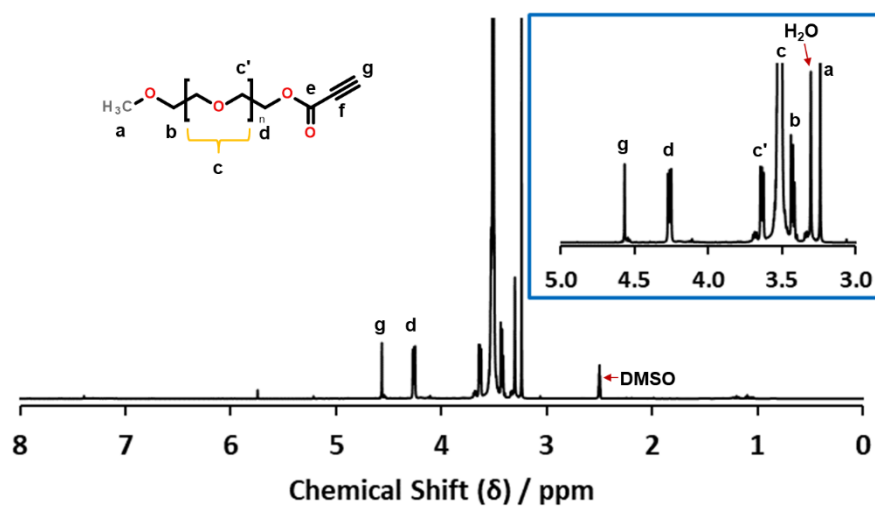
The solvent was distilled from the reaction mixture under reduced pressure (50°C, < 1 mbar) and the residue was taken up in CHCl₃. The product solution in CHCl₃ was stored in the cold (-20°C, > 2 h) and filtered three times. The solution in CHCl₃ (10 mL) was then washed with 0.1 M KOH (3 × 2 mL), deionised water (3 × 2 mL) and brine (3 × 2 mL). The aqueous phases were each back-extracted with CHCl₃ (1 × 2 mL). The combined organic phases were dried over K₂CO₃ and the solvent was removed to obtain the end-capped polymer bearing a sulfonimide end-group as its potassium salt (1.08 × 10⁻³ mol; 70 % crude yield if the polymer bearing the potassium salt has M_n = 1335 g/mol). The crude polymer in THF was passed over a short plug of silica gel (0.5 g). The polymer solution in THF was concentrated to ~50 % w/w and then passed through a Li⁺ ion-exchange column (Amberlite® crosslinked poly(styrenesulfonate) lithium salt) using THF as the eluent. The solvent was removed under reduced pressure to obtain the product as a viscous polymer melt (M_{n(NMR)} = 1303 g/mol; PEO_n = 20) at ambient temperature (0.987 g, 7.57 × 10⁻⁴ mol, 49 % with respect to the polymer). For FTIR and NMR spectroscopy, and representative examples of spectra, please see section 6.6.

5.6. Chemical Characterisation of mPEO₂₀-C(O)C≡CH and mPEO₂₀-NSI(Li)

5.6.1. NMR Spectroscopy

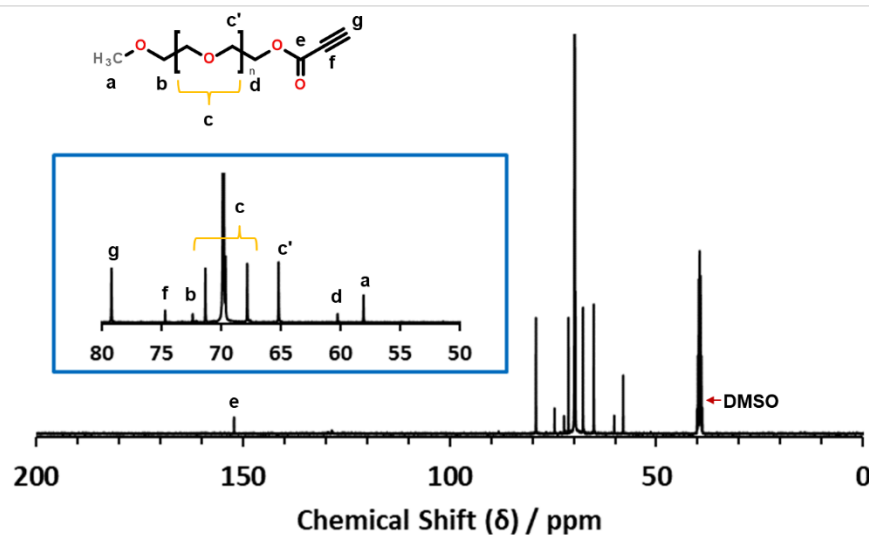
mPEO₂₀-OC(O)C≡CH

¹H NMR Spectroscopy



¹H NMR (DMSO-d₆, 298 K) chemical shift (δ / ppm): 3.24 (s, 3H, CH₃^a), 3.43 (br t, *J* = 4.86 Hz, CH₂^{c'}), 3.50 (br, CH₂^c), 3.63 (t, *J* = 4.60 Hz, 2H, CH₂^b), 4.26 (t, *J* = 4.62 Hz, 2H, CH₂^d), 4.57 (s, 1H, C≡CH^g). INSET (blue): ¹H NMR spectrum (3.0-5.0 ppm).

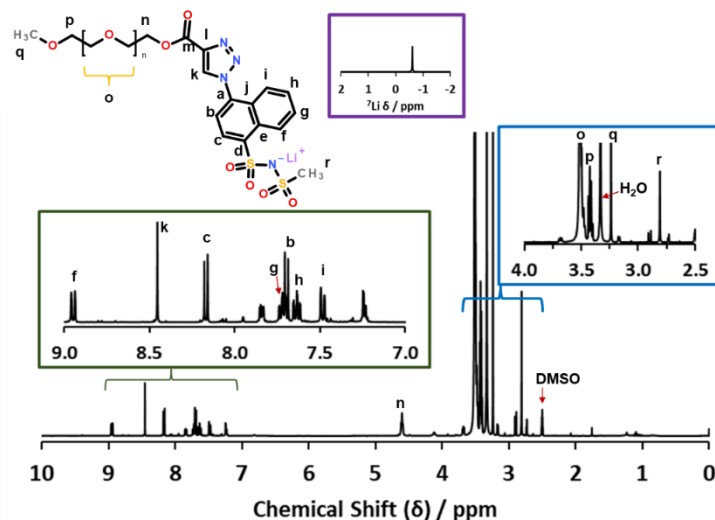
¹³C NMR Spectroscopy



¹³C NMR (DMSO-d₆, 298 K) chemical shift (δ / ppm): 58.04 (CH₃^a), 60.22 (CH₂^d), 65.15 (CH₂^{c'}), 67.78, 69.59, 71.28 (CH₂^c), 72.34 (CH₂^b), 74.65 (C^f≡CH), 79.15 (C≡C^gH), 152.22 (OC^e(O)C≡CH). INSET (blue): ¹³C NMR spectrum (50-80 ppm).

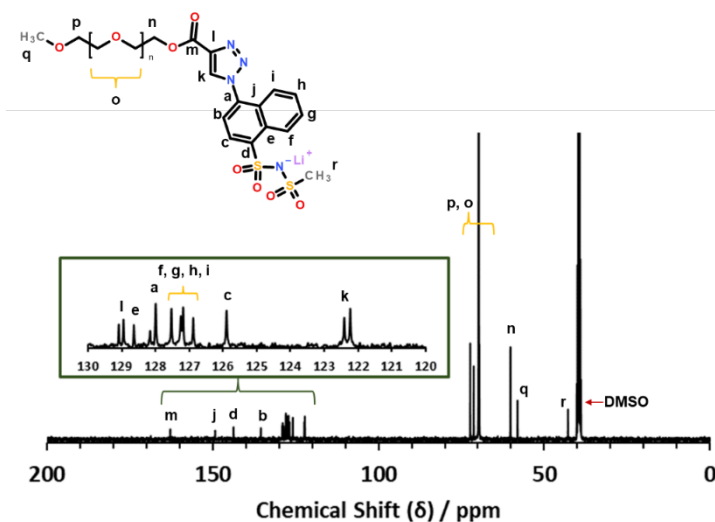
*m*PEO₂₀-NSI(Li)

¹H NMR Spectroscopy



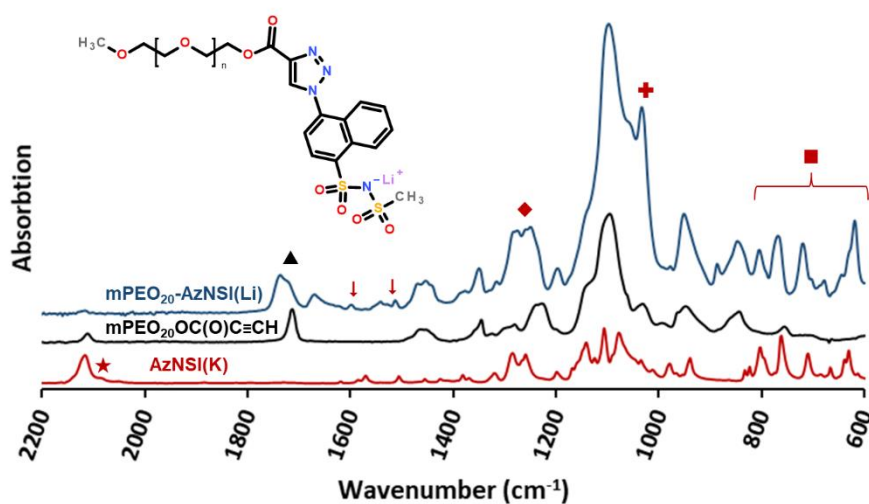
¹H NMR (DMSO-d₆, 298 K) chemical shift (δ / ppm): 2.81 (s, 3H, CH₃^r), 3.24 (s, 3H, CH₃^q), 3.43-3.50 (br, CH₂^{p, o}), 4.60 (br, 2H, CH₂ⁿ), 7.48 (d, J = 8.02 Hz, 1H, H_{Ar}ⁱ), 7.64 (ddd, J = 1.28, 6.77, 7.17 Hz, 1H, H_{Ar}^h), 7.70 (d, J = 7.78 Hz, 1H, H_{Ar}^b), 7.72 (ddd, J = 1.00, 6.77, 7.45 Hz, 1H, H_{Ar}^g), 8.17 (d, J = 7.94 Hz, 1H, H_{Ar}^c), 8.45 (s, 1H, C=CH^kN), 8.95 (d, J = 8.46 Hz, 1H, H_{Ar}^f). INSET (blue): ¹H NMR spectrum (2.5-4.0 ppm). INSET (green): ¹H NMR spectrum (7.0-9.0 ppm). INSET (purple): ⁷Li NMR (DMSO-d₆, 298 K) chemical shift (δ / ppm): -0.61.

¹³C NMR Spectroscopy



¹³C NMR (DMSO-d₆, 298 K) chemical shift (δ / ppm): 42.8 (CH₃^r), 58.0 (CH₃^q), 60.2 (CH₂ⁿ), 69.6, 69.8, 71.3 (CH₂^o), 72.3 (CH₂^p), 122.22, 122.41 (C=C^kHN), 125.89 (C_{Ar}^c), 126.88, 127.18, 127.25, 127.52 (C_{Ar}^{f, g, h, i}), 127.99, 128.15 (C_{Ar}^a), 128.64 (C_{Ar}^e), 128.94, 129.08 (C_{Ar}^j), 135.50 (C_{Ar}^b), 143.77 (C_{Ar}^d), 149.32 (C_{Ar}^j), 162.87 (C_{Ar}^m). INSET (green): ¹³C NMR spectrum (120-130 ppm).

5.6.2. FTIR Spectroscopy



FTIR Spectroscopy frequencies of characteristic peak absorbances (wavenumbers, $\tilde{\nu}$ / cm⁻¹) of mPEO₂₀-AzNSI(Li) (blue —) and mPEO₂₀-OC(O)C≡CH (black —, 50 % relative absorbance intensity) and the precursor AzNSI(K) (red —, 20 % rel. abs. int.). The spectra are normalised in the 4000-600 cm⁻¹ range and displaced by an arbitrary value. **mPEO₂₀AzNSILi** (blue line —): 2870 (not shown, —CH₂—, ether) 1741 (▲, C=O stretching, conjugated ester); 1284, 1250 (◆, —SO₂— asymmetric stretching); 1095 (C—O, ether); 1036 (+, —SO₂— symmetric stretching); 806, 769, 723, 617, 561, 528, 507 (■, Aryl C_{Ar}-H, naphthalene). **AzNSI(K)**: 2117 cm⁻¹ (★, R-N=N=N stretching).

5.7. Synthesis of the Zwitterionic polymer mPEO₂₀- $\text{Az}^+\text{NSI}(\text{LiTFSI})$

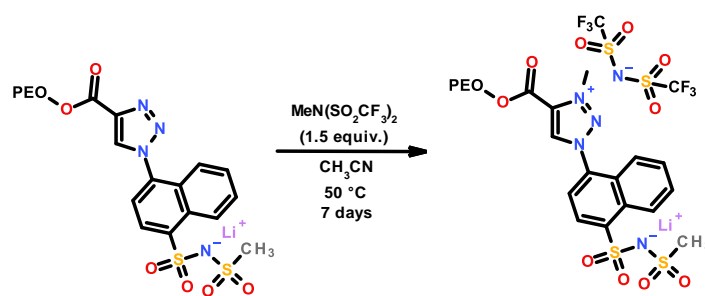
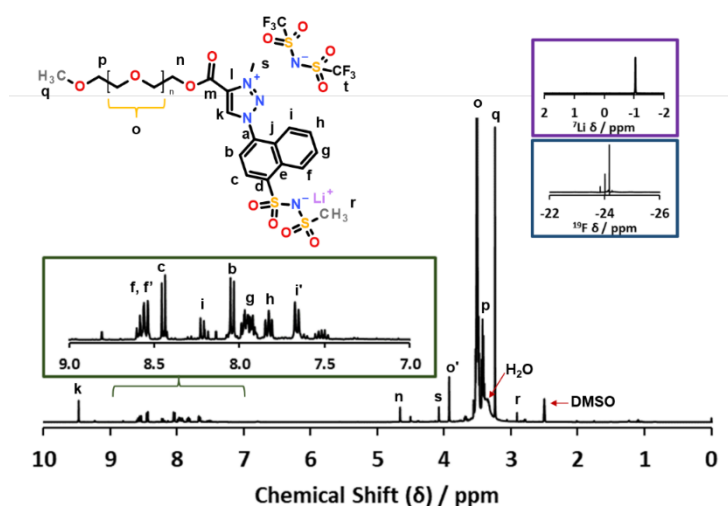


Figure III-12: Quaternisation of mPEO₂₀-AzNSI(Li) to yield the zwitterionic end-capped polymer mPEO₂₀-Az⁺NSI(LiTFSI).

The mPEO₂₀-AzNSI(Li) ($M_n = 1303$ g/mol) was quaternized by reaction with N-methyl[bis(trifluoromethylsulfonyl)]imide in acetonitrile. The method was adapted from the literature.^[19] A dry flask was charged with the polymer (0.177 g, 1.36×10^{-4} mol) as a clear red solution in anhydrous CH₃CN (0.54 mL). The concentration of triazole groups was 0.25 M. The flask was degassed by three freeze-pump-thaw cycles using liquid nitrogen to snap-cool the solution, then placed under argon atmosphere. To this was added MeN(SO₂CF₃)₂ (60 mg, 2.03×10^{-4} mol., 1.5 equiv.), dropwise at room temperature. The flask was sealed and the solution was heated with stirring (50 °C, 7 days). The clear orange solution was evaporated under reduced pressure (80 °C, < 10 mbar, 6 h; 50 °C, < 10 mbar, 48 h) until constant mass to obtain the product mPEO₂₀-Az⁺NSI(LiTFSI) ($M_n = 1598$ g/mol) as a low viscous melt at room temperature (0.216 g, 1.35×10^{-4} mol, quantitative yield). For FTIR and NMR spectroscopy, and representative examples of spectra, please see section 6.8.

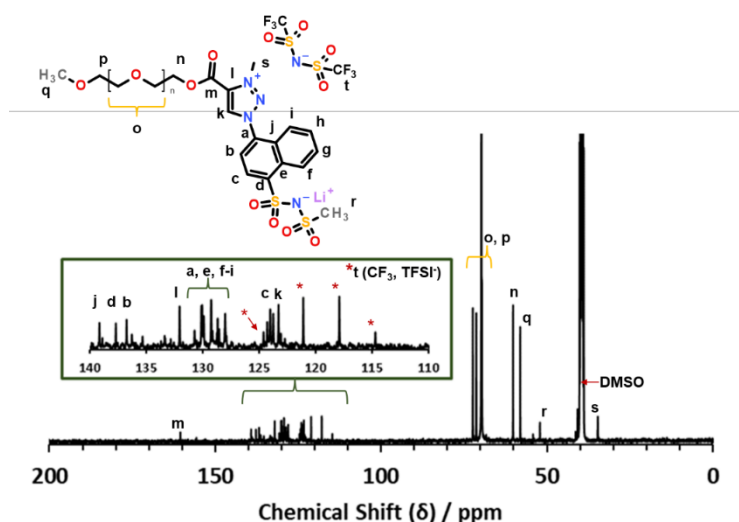
5.8. Chemical Characterisation of the Zwitterionic polymer mPEO₂₀- $\text{Az}^+\text{NSI}(\text{LiTFSI})$

5.8.1. NMR Spectroscopy



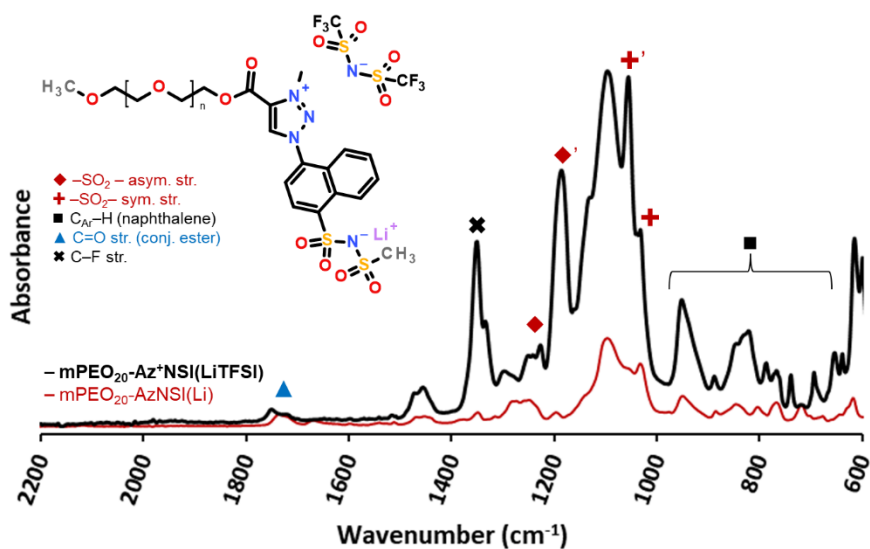
¹H NMR (DMSO-d₆, 298 K) chemical shift (δ / ppm): 2.91 (s, CH₃^r); 2.68 (t, CH₂^k); 3.24 (s, 3H, CH₃^q); 3.33 (residual H₂O); 3.42, 3.50, 3.65 (br, CH₂^{o, p}); 3.93 (s, CH₂^o); 4.08 (s, CH₃^s); 4.66 (s, CH₂ⁿ); 7.67 (br, H_{Ar}^{i'}); 7.82 (br, H_{Ar}^h); 7.97 (br, H_{Ar}^g); 8.05 (d, H_{Ar}^b); 8.21 (d, H_{Ar}ⁱ); 8.43 (H_{Ar}^c); 8.54 – 8.60 (br, H_{Ar}^{f, f'}); 9.47 (H_{Ar}^k). INSET (green): ¹H NMR aromatic protons (H_{Ar}^{b, c, f-i}) 7.0-9.0 ppm. INSET (blue): ¹⁹F NMR

(DMSO-d₆, 298 K, δ / ppm): -76.73, -77.75, -78.70 (CF₃^t). INSET (purple): ⁷Li NMR (DMSO-d₆, 298 K, δ / ppm): -1.03.



¹³C NMR (DMSO-d₆, 298 K) chemical shift (δ / ppm): 34.64 (CH₃^s); 52.10 (CH₃^r); 58.0 (CH₃^q), 60.21 (CH₂ⁿ), 69.6, 69.8, 71.3 (CH₂^o), 72.3 (CH₂^p); 114.68, 117.89, 121.10, 124.62 (N⁻-CF₃^t, TFSI); 123.29 (C=C^kHN), 124.03 (C_{Ar}^c); 128.02, 128.69, 129.26, 129.93, 130.06, 130.76 (C_{Ar}^{a, e, f-i}), 132.07 (C_{Ar}^l), 136.79 (C_{Ar}^b), 137.73 (C_{Ar}^d), 139.19 (C_{Ar}^j), 160.02 (C_{Ar}^m). INSET (green): ¹³C NMR spectrum (110-140 ppm).

5.8.2. FTIR Spectroscopy



FTIR Spectroscopy frequencies of characteristic peak absorbances (wavenumbers, $\tilde{\nu}$ / cm⁻¹) of mPEO₂₀◆⁺NSI(LiTFSI) (black –) with respect to mPEO₂₀-AzNSI(Li) (red –, 30 % intensity). The spectra are normalised to the difference in magnitude of the maximum and minimum absorbance in the range 4000 – 600 cm⁻¹. **mPEO₂₀◆NSILi**: 2872 (–CH₂–, ether, not displayed) 1750 (▲, C=O stretching, conjugated ester); 1440 (S=O stretch); 1350 (✱, C–F stretching); 1227 (◆, –SO₂– asymmetric stretching); 1186 (◆', –SO₂–, TFSI); 1096, 951, 821 (CH₂–O, ether); 1056 (+' , –SO₂–, TFSI); 1032 (+, –SO₂– symmetric stretching); 787, 767, 739, 693, 615, 569 (■, Aryl C_{Ar}-H, naphthalene).

5.9. Synthesis of the "Double-Salt" 4-sulfonylaminonaphthalene-1-sulfonyl(methylsulfonyl)imide-end-capped poly(ethylene oxide) monomethyl ether, mPEO₅₅-SANSI(Li₂)

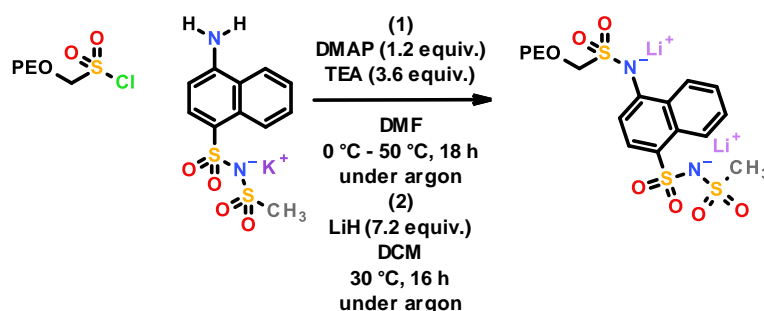


Figure III-13: Synthesis of the mPEO₅₅-SANSI(Li₂) "Double Salt" by reaction of mPEO₅₅-SO₂Cl with amino-functional ANSI(K)

A solution of 4-aminonaphthalene-1-sulfonyl(methylsulfonyl)imide (ANSIK, 339 g/mol, 192 mg, 0.57 mmol, 1.2 equiv.; for synthesis, see section 6.3), DMAP (71 mg, 0.581 mmol, 1.2 equiv.) and TEA (176 mg, 1.743 mmol, 3.6 equiv.) in anhydrous DMF was degassed by three freeze-pump-thaw cycles, using liquid nitrogen to snap-cool the solution, then placed under argon atmosphere. The concentration of the ANSI(K) precursor in this solution was 1 M in DMF. To the stirring solution at 0 °C was added mPEO₅₅-SO₂Cl (2495 g/mol, 1.21 g, 0.48 mmol; for synthesis, see section 5.6), dropwise as a 0.1 M solution in anhydrous DMF. The reaction mixture was allowed to warm to room temperature under argon flow (30 min). The flask was sealed and reaction proceeded under gentle heating (30 °C, 12 h; then 50 °C, 18 h).

The reaction was exposed to air and quenched with (10 % w/w) aqueous K₂CO₃ (2.0 molar equiv.). The reaction solution was diluted to 20 % v/v in (1:2) THF/DCM solvent mixture, to obtain a homogeneous mixture. The reaction mixture was extracted in small batches with aqueous HCl (0.1 M, 20 mL total) water (100 mL total) and brine (100 mL total), using 20 % (v/v) equivalent of the aqueous phase each time. The aqueous phases were each back-extracted with 20 % (v/v) equivalent of DCM. The combined DCM phases were dried over K₂CO₃, evaporated, and then taken up in THF. The product thus obtained as the potassium salt was dissolved in methanol and precipitated from cold diethyl ether (3 x 150 mL). The polymer was dried under reduced pressure (40 °C, < 10 mbar) to obtain an orange solid at room temperature (1.04 g, M_n 2835 g/mol, 0.37 mmol, 76 % yield).

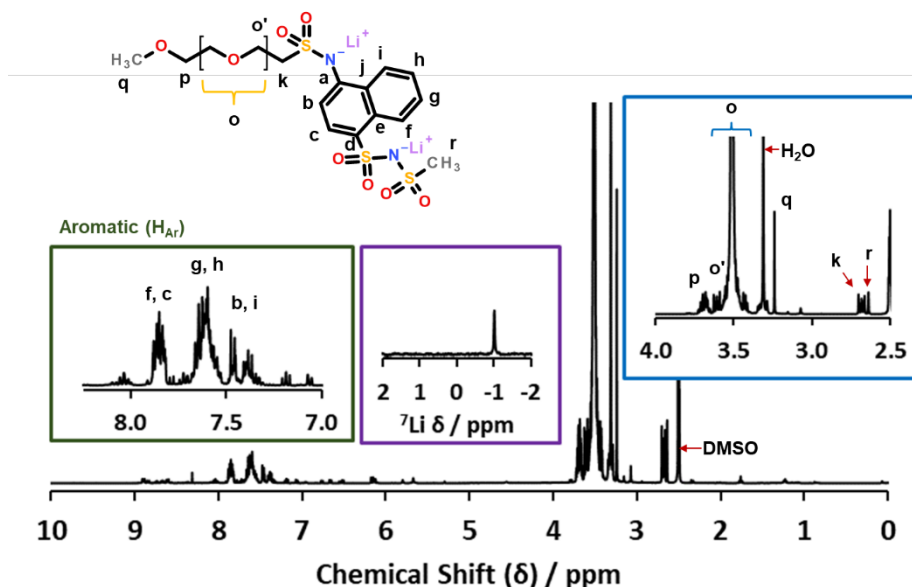
This polymer, mPEO₅₅-SO₂NH-NaphSI(K) in DCM (5 mL) was degassed by three freeze-pump-thaw cycles, using liquid nitrogen to snap-cool the solution, then placed under argon atmosphere. To the stirring solution at room temperature was added LiH (21 mg, 2.65 mmol, 7.2 equiv.) under a blanket of argon. The mixture was stirred (40 °C, 16 h), then exposed to air and quenched by methanol. The solution was diluted with DCM (40 mL), washed with deionised water (3 x 10 mL) and brine (10 mL). The aqueous phases were back-extracted with DCM. The combined organics were dried over K₂CO₃, filtered and evaporated. The poly(ethylene oxide) monomethyl ether end-capped with 4-sulfonylaminonaphthalene-1-sulfonyl(methylsulfonyl)imide lithium salt, mPEO₅₅-SO₂N(Li)-NaphSI(Li), abbreviated to mPEO₅₅-SANSI(Li₂) was isolated by freeze-drying from its solution in deionised water (M_n 2771 g/mol, 0.970 g, 0.35 mmol, 72 % yield with respect to

mPEO₅₅-SO₂Cl). For FTIR and NMR spectroscopy, and representative examples of spectra, please see section 5.10.

5.10. Chemical Characterisation of the mPEO₅₅-SANSLi₂ "Double Salt"

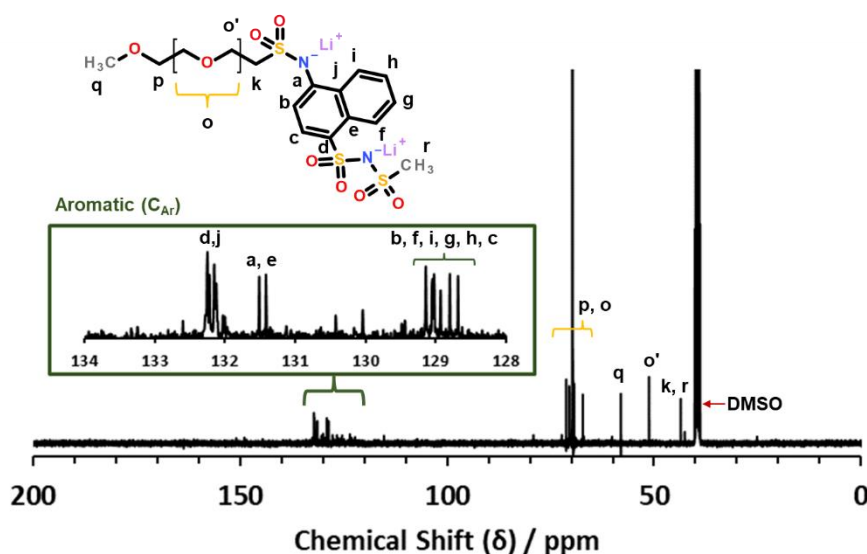
5.10.1. NMR Spectroscopy

¹H and ⁷Li NMR Spectroscopy



¹H NMR (DMSO-d₆, 298 K) chemical shift (δ / ppm): 2.64 (s, CH₃^r); 2.68 (t, CH₂^k); 3.24 (s, 3H, CH₃^q); 3.33 (residual H₂O); 3.43, 3.50, 3.61 (br, CH₂^{o, o'}); 3.67 (br, CH₂^p); 7.37 (br, H_{Ar}ⁱ); 7.47 (d, H_{Ar}^b); 7.51-7.66 (br, H_{Ar}^{g, h}); 7.85 (H_{Ar}^{f, c}). INSET (green): ¹H NMR aromatic protons (H_{Ar}^{b, c, f-i}) 7.00-8.25 ppm. INSET (blue): ¹H NMR, 2.5-4.0 ppm. INSET (purple): ⁷Li NMR (DMSO-d₆, 298 K) chemical shift (δ): -1.01 ppm.

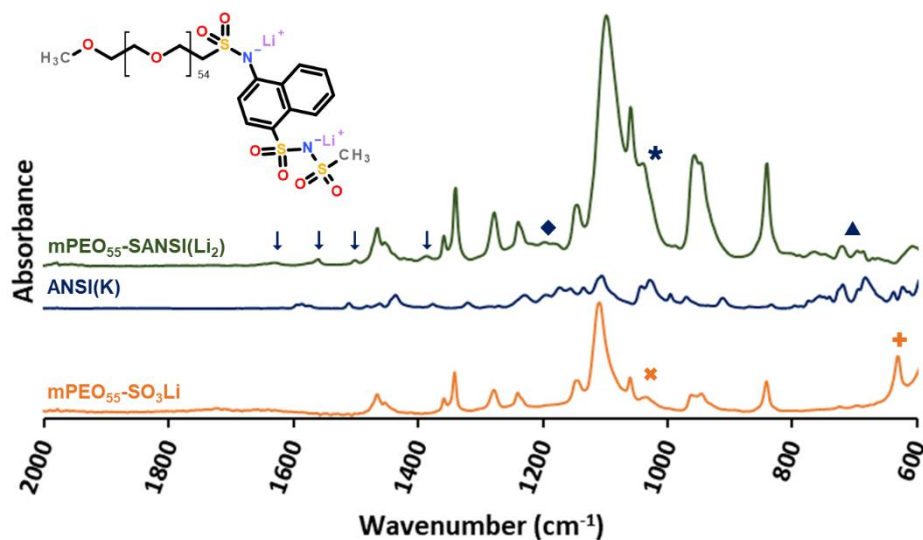
¹³C NMR Spectroscopy



¹³C NMR (DMSO-d₆, 298 K) chemical shift (δ / ppm): 42.60 (CH₃^r), 43.56 (CH₃^k), 51.21 (OCH₂^{o'}CH₂SO₂), 58.03 (CH₂^q), 69.38, 69.75, 70.53 (CH₂^{o, o'}), 71.26 (CH₂^p), 128.68 (C_{Ar}^c), 128.80 (C_{Ar}^h), 128.93 (C_{Ar}^g),

129.02, 129.03 ($C_{Ar}^{f,i}$), 129.14 (C_{Ar}^b), 131.42, 131.51 ($C_{Ar}^{a,e}$); 132.15, 132.25 ($C_{Ar}^{d,j}$). INSET (green): ^{13}C NMR spectrum (128-134 ppm).

5.10.2. FTIR Spectroscopy



FTIR Spectroscopy frequencies of characteristic peak absorbances (wavenumbers, $\tilde{\nu}$ / cm^{-1}) of $mPEO_{55}$ -SANSI(Li₂) (green line –, top). Shown for reference are [i] the precursor **SANSI(K)** (blue –, middle, 20 % relative intensity; see section 5.4.2) and [ii] the synthon **$mPEO_{55}$ -SO₃Li** (orange –, bottom, 50 % relative intensity; see 4.7.2). The spectra are individually normalised and displaced vertically by an arbitrary value. **$mPEO_{55}$ SANSI(Li₂)**: 2884 (–CH₂–, ether, not displayed) 1630, 1561, 1502, 1387 (↓); 1198 (◆, –SO₂– asymmetric stretching); 1032 (*, –SO₂– symmetric stretching); 766, 721, 697, 672 (▲, Aryl C_{Ar}-H, naphthalene).

6. Conclusions on the Synthesis and Chemical Characterisation of MonoEnd-Capped Single-Ion Polymer Electrolytes

The synthesis of monoend-capped single-ion polymer electrolytes (MEC-SPIEs) was conducted using standard techniques. The synthesis strategy (Chapter I, Section 6) relies on the modification of the hydroxyl terminal of commercial poly(ethylene oxide) monomethyl ethers having different degrees of polymerisation (mPEO_n-OH, EO_n = 8, 10, 20, 55, and 160). Bromination of the mPEO_n-OH (Chapter III, Section 4.1) enables the *N*-aryl terminated MEC-SPIEs mPEO_n-N(Li)Naph (4.2) and mPEO_n-N(Li)Pyr (4.3) *via* nucleophilic substitution reactions. The same mPEO_n-Br precursors were used to synthesize mPEO_n-SO₃Li (4.5), in a procedure adapted from the literature.^[10] Reaction with the Vilsmeier reagent^[18] yields thionyl chlorides susceptible to nucleophilic attack to yield *N*-aryl sulfonamide (mPEO_n-SO₂N(Li)Naph, 4.6) and the "double salt" (mPEO₅₅-SANSI(Li)₂, 5.9) end-capped PEO. The synthesis of the "double salt" end-group is a multi-step protocol developed in this work and inspired by a modified Sandmeyer aromatic substitution.^[16-18] The zwitterionic polymer was synthesized using the azide-functional intermediate of this synthetic route.

Isolation and purification of the monoend-capped SPIEs was problematic. Their surfactant-like behaviour at low polymer DP_n decrease the efficacy of standard chromatographic and liquid-liquid extraction techniques, which must be repeated until satisfactory results are obtained. In particular, the removal of triphenyl phosphine oxide (Ph₃P=O) by-product of reduction reactions is complicated by the low solubility of the products in non-polar solvents. Precipitation of Ph₃P=O is achieved by complexation with MgCl₂.^[9] However, ¹H and ¹³C NMR reveal residual Ph₃P=O in mPEO_n-Br (Section 4.4), and in mPEO_n-SO₃Li (4.7). A protocol using ZnCl₂^[20] to the same effect in polar solvents might be a good alternative strategy, noting the good solubility of the present MEC-SPIEs in alcohols.

NMR spectroscopy of the MEC-SPIEs revealed reproducible results of end-group fidelity and the chemical shift of characteristic nuclei. The low concentration of end-groups in the MEC-SPIEs having the longest chains (EO_n= 160) results in low fidelity of these end-groups in the measured spectra. MEC-SPIEs having EO_n= 160 were excluded from characterisation of ion transport properties because the ionic conductivity of these MEC-SPIEs is expected to be low because of low end-group concentration. The values of polymer M_n calculated by integration of MEC-SPIE end-group protons do not agree consistently with the expected M_n determined for the mPEO_n-OH precursors. This might be caused by non-ideal solution behaviours of the samples. Further discussion and example spectra are provided in the Annex (page 233). The designation of aromatic protons in Chapter III was made using predicted values calculated using the CambridgeSoft software package, *ChemDraw Ultra 11.0* (2008). Where possible, the peak assignments were compared to reported values for protocols derived from the literature (*e.g.* mPEO_n-SO₃Li and mPEO_n-OC(O)PhSO₃Li). Additional clarity might be provided by more advance NMR techniques. For example: i) Distortionless Enhancement by Polarisation Transfer (DEPT) NMR could be used to determine the multiplicity of ¹³C nuclei. ii) Peak suppression, using a 90° pulse at a specific frequency prior to measurement of the spectrum, can be used to deduce the coupling of selected protons.

The M_n and calculated dispersity in mass ($\mathcal{D} = M_w/M_n$) of the presented polymers could be characterised by size exclusion chromatography (SEC). Calibration standards of PEO having very low DP_n ($EO_n \approx 8$) would be required. Calibration of SEC measurements to DP_n to small integer values of a polymer's persistent length casts doubt of the assumed correlation of DP_n with hydrodynamic volume. The possible effects of ionic end-groups on the solution properties of the products would need to be acknowledged. However, SEC is an indispensable tool for the determination of \mathcal{D} . This measurement is required for correlation of the polymer physicochemical properties with electrolyte performance. Importantly, conclusions on thermal characterisation will benefit from confirmation that these polymer samples are indeed single populations in M_w with comparable dispersity in mass.

The dispersity in mass and the purity of the samples must be rigorously defined for the wider conclusions, based on the electrochemical and ion transport properties of these electrolytes, to be generally accepted.

7. Bibliography of Chapter III

- [1] Fischer, K. Neues Verfahren zur maßanalytischen Bestimmung des Wassergehaltes von Flüssigkeiten und festen Körpern. *Angewandte Chemie* **1935**, *48* (26), 394-396. DOI: [10.1002/ange.19350482605](https://doi.org/10.1002/ange.19350482605)
- [2] Fulcher, G. S. Analysis of recent measurements of the viscosity of glasses. *Journal of the American Ceramic Society* **1925**, *8* (6), 339-355. DOI: [10.1111/j.1151-2916.1925.tb16731.x](https://doi.org/10.1111/j.1151-2916.1925.tb16731.x)
- [3] Cyrot, M. A Possible Origin for the Vogel-Fulcher Law. *Physics Letters A* **1981**, *83* (6), 275-278. DOI: [10.1016/0375-9601\(81\)90982-8](https://doi.org/10.1016/0375-9601(81)90982-8)
- [4] Tammann, G.; Hesse, W. Die Abhängigkeit Der Viscosität von Der Temperatur Bie Unterkühlten Flüssigkeiten. *Zeitschrift für anorganische und allgemeine Chemie* **1926**, *156* (1), 245-257. DOI: [10.1002/zaac.19261560121](https://doi.org/10.1002/zaac.19261560121)
- [5] Diederichsen, K. M.; Buss, H. G.; McCloskey, B. D. The Compensation Effect in the Vogel-Tammann-Fulcher (VTF) Equation for Polymer-Based Electrolytes. *Macromolecules* **2017**, *50* (10), 3831-3840. DOI: [10.1021/acs.macromol.7b00423](https://doi.org/10.1021/acs.macromol.7b00423)
- [6] Xue, Z.; He, D.; Xie, X. Poly(Ethylene Oxide)-Based Electrolytes for Lithium-Ion Batteries. *Journal of Materials Chemistry A* **2015**, *3* (38), 19218-19253. DOI: [10.1039/C5TA03471J](https://doi.org/10.1039/C5TA03471J)
- [7] Appel, R. Tertiary Phosphane/Tetrachloromethane, a Versatile Reagent for Chlorination, Dehydration, and P-N Linkage. *Angewandte Chemie International Edition* **1975**, *14* (12), 801-811. DOI: [10.1002/anie.197508011](https://doi.org/10.1002/anie.197508011)
- [8] Baughman, T. W.; Sworen, J. C.; Wagener, K. B. The Facile Preparation of Alkenyl Metathesis Synthons. *Tetrahedron* **2004**, *60* (48), 10943-10948. DOI: [10.1016/j.tet.2004.09.021](https://doi.org/10.1016/j.tet.2004.09.021)
- [9] Lukin, K.; Kishore, V.; Gordon, T. Development of a Scalable Synthesis of Oxadiazole Based S1P₁ Receptor Agonists. *Organic Process Research & Development* **2013**, *17* (4), 666-671. DOI: [10.1021/op300345v](https://doi.org/10.1021/op300345v)
- [10] Ito, K.; Nishina, N.; Ohno, H. High Lithium Ionic Conductivity of Poly(Ethylene Oxide)s Having Sulfonate Groups on Their Chain Ends. *Journal of Materials Chemistry* **1997**, *7* (8), 1357-1362. DOI: [10.1039/A700583K](https://doi.org/10.1039/A700583K)
- [11] Johansson, G. Studies on Aqueous Dextran-Poly(Ethylene Glycol) Two-Phase Systems Containing Charged Poly(Ethylene Glycol) I. Partition of Albumins. *Biochimica et Biophysica Acta (BBA) - General Subjects* **1970**, *222* (2), 381-389. https://ac.els-cdn.com/0304416570901273/1-s2.0-0304416570901273-main.pdf?_tid=75cff412-26f7-4588-b783-bc92ba8f2dbd&acdnat=1538316684_1f1254ef885523c7250ef704741d6dc8
- [12] Bückmann, A. F.; Morr, M.; Johansson, G. Functionalization of Poly(Ethylene Glycol) and Monomethoxy-Poly(Ethylene Glycol). *Die Makromolekulare Chemie* **1981**, *182* (5), 1379-1384. DOI: [10.1002/macp.1981.021820509](https://doi.org/10.1002/macp.1981.021820509)
- [13] Tominaga, Y. High Ionic Conductivity of PEO/Sulfonamide Salt Hybrids. *Solid State Ionics* **1999**, *124* (3-4), 323-329. DOI: [10.1016/S0167-2738\(99\)00224-6](https://doi.org/10.1016/S0167-2738(99)00224-6)
- [14] Bosshard, H. H.; Mory, R.; Schmid, M.; Zollinger, H. Eine Methode Zur Katalysierten Herstellung von Carbonsäure- Und Sulfosäure-Chloriden Mit Thionylchlorid. *Helvetica Chimica Acta* **1959**, *42* (5), 1653-1658. DOI: [10.1002/hlca.19590420526](https://doi.org/10.1002/hlca.19590420526)
- [15] Ito, K.; Tominaga, Y.; Ohno, H. Polyether/Salt Hybrid (IV). Effect of Benzenesulfonate Group(s) and PEO Molecular Weight on the Bulk Ionic Conductivity. *Electrochimica Acta* **1997**, *42* (10), 1561-1570. DOI: [10.1016/S0013-4686\(96\)00317-9](https://doi.org/10.1016/S0013-4686(96)00317-9)
- [16] Dai, Z.-C.; Chen, Y.-F.; Zhang, M.; Li, S.-K.; Yang, T.-T.; Shen, L.; Wang, J.-X.; Qian, S.-S.; Zhu, H.-L.; Ye, Y.-H. Synthesis and Antifungal Activity of 1,2,3-Triazole Phenylhydrazone Derivatives. *Organic and Biomolecular Chemistry* **2015**, *13* (2), 477-486. DOI: [10.1039/C4OB01758G](https://doi.org/10.1039/C4OB01758G)
- [17] Clarke, H. T.; Read, R. R. O-Tolunitrile and p-Tolunitrile. *Organic Syntheses* **1925**, *4*, 69. DOI: [10.1002/0471264180.os004.25](https://doi.org/10.1002/0471264180.os004.25)

- [18] Clayden, J.; Greeves, N.; Warren, S. G. *Organic Chemistry*, 2nd ed.; Oxford University Press: Oxford ; New York, 2012.
- [19] Obadia, M. M.; Mudraboyina, B. P.; Allaoua, I.; Haddane, A.; Montarnal, D.; Serghei, A.; Drockenmuller, E. Accelerated Solvent- and Catalyst-Free Synthesis of 1,2,3-Triazolium-Based Poly(Ionic Liquid)s. *Macromolecular Rapid Communications* **2014**, 35 (8), 794–800. DOI: [10.1002/marc.201400075](https://doi.org/10.1002/marc.201400075)
- [20] Batesky, D. C.; Goldfogel, M. J.; Weix, D. J. Removal of Triphenylphosphine Oxide by Precipitation with Zinc Chloride in Polar Solvents. *The Journal of Organic Chemistry* **2017**, 82 (19), 9931–9936. DOI: [10.1021/acs.joc.7b00459](https://doi.org/10.1021/acs.joc.7b00459).
- [21] Truong, V. X.; Ablett, M. P.; Gilbert, H. T. J.; Bowen, J.; Richardson, S. M.; Hoyland, J. A.; Dove, A. P. In Situ-Forming Robust Chitosan-Poly(Ethylene Glycol) Hydrogels Prepared by Copper-Free Azide–Alkyne Click Reaction for Tissue Engineering. *Biomaterials Science* **2014**, 2 (2), 167–175. DOI: [10.1039/C3BM60159E](https://doi.org/10.1039/C3BM60159E).
- [22] Shao, C.; Wang, X.; Xu, J.; Zhao, J.; Zhang, Q.; Hu, Y. Carboxylic Acid-Promoted Copper(I)-Catalyzed Azide–Alkyne Cycloaddition. *The Journal of Organic Chemistry* **2010**, 75 (20), 7002–7005. DOI: [10.1021/jo101495k](https://doi.org/10.1021/jo101495k).

General Conclusion

The **MonoEnd-Capped "Single-Ion" Polymer Electrolytes (MEC-SIPes)** presented in this thesis feature functional, ionic end-groups. Their design is based on a "Low N-High χ " conceptual approach, targeting microphase-separation of the bulk electrolyte morphology through specific end-group interactions. The polymer end-group is elaborated as a design concept for high performance polymer electrolytes. A library of MEC-SIPes was synthesized through modification of the hydroxyl end-group of poly(ethylene oxide) monomethyl ether (mPEO_n-OH). The precursors were selected to have short chain lengths, affording high concentrations of end-groups. The design of the end-groups targets specific interactions through combination of ionic functions with the **Polycyclic Aromatic Hydrocarbons (PAHs)**, naphthalene, and pyrene.

The electrochemical performance of MEC-SIPes is presented in terms of ionic conductivity, electrochemical stability, and **Lithium Transference Number (LTN)**. The MEC-SIPes have ionic conductivity equivalent to the best-in-class "Single-Ion" polymer electrolytes. The best of the MEC-SIPes compare well to model **Salt-In-Polymer (SiP)** electrolytes based on the high-performance salt LiTFSI dissolved in bis-methoxy terminated PEO. The majority of the MEC-SIPes are stable in the potential range of 0-3.6 V vs. Li/Li⁺, qualifying their use in emerging applications such as Li-S cells. The claim of "Single-Ion" transport is validated by high LTNs ($t_{Li}^+ = 0.7-1.0$).

Thermal characterisation of the MEC-SIPes by DSC reveals multiple transitions on heating. This is evidence of the destruction of multiple types of intermolecular bonding. Variation of the thermal history supports the hypothesis of a microphase-separated bulk morphology. It is proposed that phase separation is the result of the Low N-High χ design, with respect to **i)** specific interactions of the end-group and **ii)** the persistent length of the PEO chain defined by a 7/2 helix.

The characterisation of ionic transport is presented first in terms of a simple VTF model. This approach falls short for these MEC-SIPes, which are observed to have different dependences on the thermal activation of ionic conductivity at high and at low temperature. The appearance of low frequency resistive features at high temperature and at low temperature in certain MEC-SIPes is rationalised in a conceptual model for ion transport through the electrolytes. The conduction of ions is proposed to occur along the "boundaries" of PEO "grains". This is provocative because grain boundaries have been traditionally viewed as phenomena that limit ionic conductivity on the meso/microscopic scale. This concept demands further investigation through structural characterisation of bulk EC-SIPes. The hypothesis should be tested through cross-correlation of structural, thermal, optical, and electrochemical analyses. If proven, the concept of ionically conductive grain boundaries would have profound implications on the design of the next generation of polymer electrolytes. Notably, the pursuit of a totally amorphous ionically conductive phase could be surpassed by the pursuit of a percolating network of grain boundaries. The potential for such a system to be defined by the morphology of soft matter and optimised *in situ* is a remarkable in light of how it is based on a simple design.

The design of MEC-SIPes is modular and open to variation. Inventive polymer and end-group combinations should be tested and benchmarked against the existing repertoire. Let "Single-Ion" polymer electrolyte designs based on effective point-group chemistry take a major role in the concerted effort towards high performance electrochemical cells, in response to the ever-increasing demand for safer and more efficient electrochemical energy storage solutions.

Dissemination of Results

Les résultats obtenus au cours de cette thèse ont été présentés (rapports écrits et présentations orales) lors de différentes manifestations et événements scientifiques au cours

*de l'année 2016 :

- 1) à la Journée des Doctorants DGA/CEA (DGA-Paris, 27 janvier 2016)
- 2) à la Journée des Doctorants CEA-Grenoble/Liten-DEHT (3 mars 2016)
- 3) au Comité Suivi Individuel (CSI) N°1 pour l'inscription en 2^{ème} année à l'EDCSV (26 septembre 2016)

* de l'année 2017 :

- 1) à la Journée des Doctorants CEA-Grenoble/Liten-DEHT (7 mars 2017)
- 2) à la Journée des Doctorants DGA/CEA (CEA-Saclay : 27 avril 2017)
- 3) à l'Ecole Doctorale Chimie et Sciences du Vivant (EDCSV) à la Journée Annuelle des Doctorants (15 juin 2017)
- 4) "End-Capped Solid Polymer Electrolytes Designed For Lithium-ion Transport" au congrès de l'**European Polymer Federation** (EPF2017: présentation orale, 5 juillet 2017, Lyon, France)
- 5) au Comité Suivi Individuel (CSI) N°2 pour l'inscription en 3^{ème} année à l'EDCSV (3 octobre 2017)
- 6) dans le cadre d'un séminaire technique au CEA-Grenoble/DEHT/STB/LM (15 décembre 2017)

* de l'année 2018:

- 1) à la Journée des Doctorants CEA-Grenoble/Liten-DEHT (20 mars 2018)
- 2) à la Journée des Doctorants DGA/CEA (CEA-Saclay ; 4 avril 2018)
- 3) "End-Capped Solid Polymer Electrolytes Designed For Lithium-ion Transport" à la 17^{ème} **Conférence Internationale IUPAC "Polymers and Organic Chemistry"** (POC2018: 5 juin 2018, Palavas Les Flots, France).

Publication :

"Macromolécules de type sulfonamide utile à titre d'électrolyte polymère à conduction d'ion unique" (English: "Sulfonamide macromolecules as polymer electrolytes for ion transport")

Demande de brevet d'invention Français n° 17/56291 déposée à l'INPI le 4 Juillet 2017. Brevet WO 2019/008061 (10 Janvier 2019)

List of Figures

- Figure I-1:** (Left) A Ragone plot showing that Lithium Ion Batteries (LIBs) and Lithium Metal Batteries (LMBs) provide exceptional specific energy and energy density. (Right) The high capacity and low potential of lithium metal make this anode material attractive to the development of energy storage technology despite the hazards of its reactivity. *The figures are reproduced from literature.*^[3] 11
- Figure I-2:** (Left to Right) A schematic representation of Li-Ion, Li-O₂ (organic), Li-O₂ (aqueous), and Li-S battery chemistries. *The figure is reproduced from literature.*^[10] 13
- Figure I-3:** An illustration of the motion of oppositely charged ions in a PEO matrix by ether-coordinated Li⁺ (left) and by ion pairs and triplet clusters (right). Top: intrachain motion of ions. Bottom: interchain motion of ions. *The figure is reproduced from the literature.*^[18] 14
- Figure I-4:** The ionic conductivity of LiTFSI in PEO as a function of polymer M_w and at different temperatures. *Left to Right:* (a) HO-PEO-OH, (b) H₃C-PEO-OH, and (c) H₃C-PEO-CH₃. *The figure is reproduced from the literature.*^[22] 16
- Figure I-5:** The fluorinated sulfonate lithium salt (**LiTf**), and the sulfonylimide salts lithium salts (**LiFSI**, **LiTFSI**, and **LiBETI**) 18
- Figure I-6:** The conductivity of **LiTTP** and **LiTF** in PEO at ambient temperature as a function of salt concentration (mol/g). *The figure is reproduced from the literature.*^[41] 19
- Figure I-7:** Illustration of the "Janus-like" POSS-phenyl₇(BF₃Li)₃ salt and its aggregation behaviours in a PEO matrix. *The figure is reproduced from the literature.*^[42] 19
- Figure I-8:** The best-performing "FAST"-salt, featuring both bulky *tert*-butylether and electron-withdrawing substituents. *The figure is reproduced from the literature.*^[43] 19
- Figure I-9:** (Left) An illustration of PEO/LiAsF₆ blended with α-cyclodextrin (α-CD) having a hexagonally packed morphology of PEO chains inside ordered α-CD tubes. (Right) Illustration of PEO inside the α-CD tube, in (a) an *all-trans* and (b) *trans-trans-gauche* (ttg) conformation. *The figures are reproduced from the literature.*^[46] 20
- Figure I-10:** An illustration of the preparation of the blended electrolyte of Halloysite Nanotubes (HNTs), LiTFSI, and PEO. The components are mixed in acetonitrile and cast to form a flexible film. Top: images of the materials. Bottom: the structural formula of the components and the proposed orientation-specific ion-dipole interactions. *The figures are reproduced from the literature.*^[48] .. 21
- Figure I-11:** A theoretical phase diagram of A-*b*-B diBlock CoPolymer (**diBCP**) morphologies as represented by the Flory-Huggins interaction parameter (χ_N) as a function of BCP composition (f). Indicated are regions for lamellar (L), gyroid (G), cylinder (C), spherical (S), close-packed pherical (S_{cp}), orthorhombic network (O⁷⁰), alternating gyroid (G^A), and disordered morphologies. *The figure is reproduced from the literature.*^[53] 22
- Figure I-12:** A theoretical phase diagram of A-*b*-B-*b*-C tri-block copolymer (triBCP) morphologies having specific simulated parameters ($\chi_{AB}N = \chi_{BC}N = 35$ and $\chi_{AC}N = 15$). *The figure is reproduced from the literature.*^[52,54] 22
- Figure I-13:** The End-capped BCP, PS-*b*-PEO-SO₃H. *The figures (A and B) are adapted from the literature.*^[55] 23

Figure I-14: Two representations of the interfacial zone proposed to limit ionic conduction in the PEO domains of PS-*b*-PEO BCPs. The PEO domain is semi-crystalline and the PS domain is amorphous. Left: close-packing of PEO close the PS-*b*-PEO interface is frustrated by the amorphous state of the PS domain.^[61] Right: the ubiquitous salt LiTFSI is mobile only in the centre of the ionically conductive PEO phase.^[63] *The figures are reproduced from the literature.*^[61,63] .. 24

Figure I-15: (Left) SAXS images and illustrations of morphological ordering of poly(styrenesulfonate-*b*-methylbutylene) BCP films (180-220 μm thickness) made by (a) solvent casting, and aligned by (b) pressing, (c) electric field and (d) mechanical shear. (Right) Proton conductivity of the films (S/cm) at 25°C. *The figure is reproduced from the literature.*^[65] 27

Figure I-16: Chemical structure and TEM micrograph of the PS-*b*-PMAA-*b*-PMMA copolymer. *The figure is reproduced from the literature.*^[68] 28

Figure I-17: Chemical structure and illustration of the lamellar arrangement of PS-*b*-PMMA having an orientation specific, H-bonding block junction. Introduction of the junction decreases line-edge roughness by 30 %. *The figure is reproduced from the literature.*^[69] 28

Figure I-18: (A) The point-group defects positioned mid-chain in H₃C-PEO₅₀-●-PEO₅₀-CH₃: (L-R) 1,4-disubstituted-1,2,3-triazole; *ortho*, *meta*, and *para*-substituted phenyl rings. (B) The angle of chain tilt ($\phi = 180^\circ - \xi$) represented from the cross-section of the polymer chain (TR= triazole). (C) An illustration of how thermal annealing permits the defects through the boundary of the crystalline grain. The chain tilt angles are represented at the point-group (green dots). (D) A model illustrating the point-generated chain tilt. *The figure is adapted from the literature.*^[71] 29

Figure I-19: (a) The ionic conductivity at 50°C and (b) T_g of H₃C-PEO_n-SO₃Li MEC-SIPEs as a function of i) PEO M_w (*10⁻² g/mol) and ii) lithium concentration (mol%). *The figure is reproduced from the literature.*^[110] 36

Figure I-20: The chemical structure of poly(electrolyte)s (A) P(STFSiLi)^[131]; (B), the tri-BCP P(STFSiLi)-*b*-PEO₈₀₀-*b*-P(STFSiLi)^[132]; (C), the statistical copolymer P(STFSiLi-co-MPEGA)^[133]; and (D), the tri-BCP P(MTFSiLi)-*b*-PEO₈₀₀-*b*-P(MTFSiLi)^[134]. 39

Figure I-21: Poly(electrolyte)s based on LiTFSI. *The figures are reproduced from the literature.*^[136] 39

Figure I-22: Asymmetric phase segregation behaviour of POSS-based giant surfactants yields a variety of long-range morphologies. The phase diagrams are built from experimental data. The data points represent real samples. The PS volume fraction (V_{PS}^f) is displayed in the range $V_{PS}^f = 0.6-1.0$ (top) and $0.4-1.0$ (bottom). The diagrams have been scaled to aid comparison. **A**, top: DPOSS-PS having 1-4 PS tails. The chemical structure of the three-tailed DPOSS-3PS_n is shown as an example. **B**, bottom: DPOSS-PS_n having 1-4 DPOSS heads. The three-headed 3DPOSS-SP_n is shown as an example. *The figure is adapted from the literature.*^[147,151] 43

Figure I-23: End-capped Poly(olefin)s. *The figures are reproduced from the literature.*^[153,154] 44

Figure I-24: Supramolecular assembly of triptycene end-capped PDMS (18-24 * 10³ g/mol, X_n ≈ 240-320) via locking interactions of the propeller-shaped end-group. **(A)** A schematic illustration of the end-capped PDMS and its structural formula. The geometry of substitution (1,4 or 1,8) determines the long-range assembly and resultant properties of the "2D+1D" morphology. **(B)** Frequency dependence of shear strain (left) and 7-orders of alignment visible by SAXS measurement (right).

(C) The inter-locking structure of triptycene end-groups at the "2D+1D" interface. *The figure is adapted from the literature.*^[156] 45

Figure I-25: An illustration of the synthesis strategy for MEC-SIPEs based on mPEO_n-OH. The names of the polymers given are the ones used in the text. The details of the syntheses are described in the Experimental Chapter (*vide infra*: Chapter III). 50

Figure I-26: The reaction scheme of the synthesis of the ANSI(Li) end-group of mPEO₅₅-SANSI(Li₂). The intermediate compound AzNSI(Li) is used in the synthesis of the mPEO₂₀-◆NSI(Li) featuring a triazole linker. 51

Figure I-27: The reaction scheme illustrating the mPEO₂₀-◆NSI(Li) having a triazole linker and its zwitterionic derivative mPEO₂₀-◆⁺NSI(LiTFSI) having a triazolium, and two counterions (Li⁺ and TFSI⁻). 51

Figure II-1: The conductivity ($\sigma / \text{S.cm}^{-1}$) as a function of Temperature ($T / 10^3.\text{K}^{-1}$) for mPEO₆₀m/LiTFSI (EO/Li= 60) SiP blend (x), mPEO₅₅-SO₃Li (+), mPEO₅₅-OC(O)PhSO₃Li (◇). The VTF fit of each set are represented (red lines,-). The measurements were conducted on cooling (100 → 40°C). 72

Figure II-2: The conductivity ($\sigma / \text{S.cm}^{-1}$) as a function of Temperature ($T / 10^3.\text{K}^{-1}$) for mPEO₆₀m/LiTFSI (EO/Li= 60) SiP blend (x), mPEO₅₅-N(Li)Pyr (□), mPEO₅₅-N(Li)Naph (○), and mPEO₅₅-SO₂N(Li)Naph (△). The VTF fit of each set are represented (red lines,-). The measurements were conducted on cooling (100 → 40°C). 72

Figure II-3: The conductivity ($\sigma / \text{S.cm}^{-1}$) as a function of Temperature ($10^3.\text{K}^{-1}$) for mPEO₅₅-SANSI(Li₂) (filled circles, ●), mPEO₆₀m/LiTFSI (EO/Li= 60) SiP blend (x), mPEO₅₅-N(Li)Pyr (□) and mPEO₅₅-SO₂N(Li)Naph (△). The VTF fit of each set are represented (red lines,-). The measurements were conducted on cooling (100 → 40°C). 73

Figure II-4: The conductivity ($\sigma / \text{S.cm}^{-1}$) as a function of Temperature ($T / 10^3.\text{K}^{-1}$) for the SiP mPEO₆₀m/LiTFSI blend having different EO/Li ratios. The experimental data of the blends EO/Li= 60 (□), EO/Li= 20 (○) and EO/Li= 10 (△) were recorded on cooling from 100°C. The data are fitted to the VTF model (red lines, -). 76

Figure II-5: The conductivity ($\sigma / \text{S.cm}^{-1}$) as a function of Temperature ($T / 10^3.\text{K}^{-1}$) for the MEC-SIPE mPEO_nSO₃Li having different EO/Li ratios. The EO/Li ratio is fixed according to the polymer DP_n (EO_n). The experimental data of EO/Li= 55 (□), EO/Li= 20 (○) and EO/Li= 10 (△) and EO/Li=8 (△) were recorded on cooling from 100°C. The data are fitted to the VTF model (red lines, -). 76

Figure II-6: The conductivity ($\sigma / \text{S.cm}^{-1}$) of mPEO₆₀m/LiTFSI as a function of the mass fraction (ϕ_m) of salt (LiTFSI). The corresponding ratio of EO/Li is also displayed. The lines (···) are drawn as a guide for the eye only. The experimental data correspond to those displayed in **Figure II-4**. 76

Figure II-7: The conductivity ($\sigma / \text{S.cm}^{-1}$) of mPEO_n-SO₃Li as a function of the mass fraction (ϕ_m) of salt (the polymer end-group). The corresponding ratio of EO/Li is also displayed. Here the ratio EO/Li for the MEC-SIPE is determined by the polymer DP_n (EO_n). The lines (···) are drawn as a guide for the eye only. The experimental data correspond to those displayed in **Figure II-5**. 76

Figure II-8: The conductivity ($\sigma / \text{S.cm}^{-1}$) as a function of Temperature ($T / 10^3.\text{K}^{-1}$) for mPEO_nOC(O)PhSO₃Li having different EO/Li ratios. The EO/Li ratio is fixed according to the polymer DP_n (EO_n). The experimental data of EO/Li= 55 (□), EO/Li= 20 (○) and EO/Li= 10 (△) and

EO/Li=8 (Δ) were recorded on cooling from 100°C. The data are fitted to the VTF model (red lines, -). 78

Figure II-9: The conductivity ($\sigma / \text{S.cm}^{-1}$) as a function of Temperature ($T / 10^3.\text{K}^{-1}$) for **mPEO_nSO₂N(Li)Naph** having different EO/Li ratios. The EO/Li ratio is fixed according to the polymer DP_n (EO_n). The experimental data of EO/Li= 55 (\square), EO/Li= 20 (\circ) and EO/Li= 10 (Δ) and EO/Li=8 (Δ) were recorded on cooling from 100°C. The data are fitted to the VTF model (red lines, -). 78

Figure II-10: σ (S.cm^{-1}) of **mPEO_n-OC(O)PhSO₃Li** as a function of the mass fraction (ϕ_m) of the polymer end-group. The corresponding ratio of EO/Li is also displayed. The lines (---) are drawn as a guide for the eye only. The experimental data correspond to those displayed in **Figure II-8**. .. 78

Figure II-11: σ (S.cm^{-1}) of **mPEO_n-SO₂N(Li)Naph** as a function of the mass fraction (ϕ_m) of the polymer end-group. The corresponding ratio of EO/Li is also displayed. The lines (---) are drawn as a guide for the eye only. The experimental data correspond to those displayed in **Figure II-9**. .. 78

Figure II-12: The conductivity ($\sigma / \text{S.cm}^{-1}$) as a function of Temperature ($T / 10^3.\text{K}^{-1}$) for **mPEO_nN(Li)Naph** having different EO/Li ratios. The EO/Li ratio is fixed according to the polymer DP_n (EO_n). The experimental data of EO/Li= 55 (\square), EO/Li= 20 (\circ) and EO/Li= 10 (Δ) and EO/Li=8 (Δ) were recorded on cooling from 100 °C. The data are fitted to the VTF model (red lines, -). 80

Figure II-13: The conductivity ($\sigma / \text{S.cm}^{-1}$) as a function of Temperature ($T / 10^3.\text{K}^{-1}$) for **mPEO_nN(Li)Pyr** having different EO/Li ratios. The EO/Li ratio is fixed according to the polymer DP_n (EO_n). The experimental data of EO/Li= 55 (\square), EO/Li= 20 (\circ) and EO/Li= 10 (Δ) and EO/Li=8 (Δ) were recorded on cooling from 100°C. The data are fitted to the VTF model (red lines, -). 80

Figure II-14: σ (S.cm^{-1}) of **mPEO_nN(Li)Naph** as a function of the mass fraction (ϕ_m) of the polymer end-group. The corresponding ratio of EO/Li is also displayed. The lines (---) are drawn as a guide for the eye only. The experimental data correspond to those displayed in **Figure II-12**. 80

Figure II-15: σ (S.cm^{-1}) of **mPEO_nN(Li)Pyr** as a function of the mass fraction (ϕ_m) of the polymer end-group. The corresponding ratio of EO/Li is also displayed. The lines (---) are drawn as a guide for the eye only. The experimental data correspond to those displayed in **Figure II-13**. 80

Figure II-16: The conductivities ($\sigma / \text{S.cm}^{-1}$) of mPEO₂₀-SO₂N(Li)Naph (\circ), mPEO₅₅-SANSI(Li₂) (\bullet), mPEO₂₀- \blacklozenge NSI(Li) (\diamond), mPEO₂₀- \blacklozenge^+ NSI(LiTFSI) (Δ) and the SiP electrolyte mPEO_{60m}/LiTFSI (EO/Li= 20) (\times) as functions of reciprocal temperature ($T / 10^3.\text{K}^{-1}$). The data are fitted to the VTF model (red lines, -). 81

Figure II-17: CV of mPEO_{60m}/LiTFSI (EO/Li= 20) 85

Figure II-18: CV of mPEO₂₀-SO₃Li 85

Figure II-19: CV of mPEO₂₀-OC(O)PhSO₃Li 86

Figure II-20: CV of mPEO₂₀-SO₂N(Li)Naph 86

Figure II-21: CV of mPEO₂₀-N(Li)Naph 86

Figure II-22: CV of mPEO₂₀-N(Li)Pyr 86

Figure II-23: CV of mPEO₂₀- \blacklozenge NSI(Li) 87

Figure II-24: CV of mPEO₂₀- \blacklozenge^+ NSI(LiTFSI) 87

Figure II-25: CV of mPEO ₅₅ -SANSI(Li ₂)	87
Figure II-26: (top) ρ vs Q of GCPL and (bottom) Nyquist impedance of mPEO ₂₀ -OC(O)PhSO ₃ Li....	89
Figure II-27: (top) ρ vs Q of GCPL and (bottom) Nyquist impedance of mPEO ₂₀ -N(Li)Naph.....	89
Figure II-28: (top) ρ vs Q of GCPL and (bottom) Nyquist impedance of mPEO ₂₀ -N(Li)Pyr	89
Figure II-29: (top) ρ vs Q of GCPL and (bottom) Nyquist impedance of mPEO ₂₀ -SO ₃ Li.....	91
Figure II-30: (top) ρ vs Q of GCPL and (bottom) Nyquist impedance of mPEO ₂₀ -SO ₂ N(Li)Naph....	91
Figure II-31: (A) The resistivity ($\rho / 10^{-3} \cdot \Omega \cdot m$) as a function of charge (Q) during galvanostatic cycling of mPEO ₂₀ - \blacklozenge^+ NSI(LiTFSI). The first five cycles are shown. The arrows (\rightarrow) indicate the evolution of ρ upon cycling ρ vs Q of GCPL. (B) Nyquist plots of GEIS spectra measured before (\circ) and after (\diamond) GCPL. (C) the chemical structure of mPEO ₂₀ - \blacklozenge^+ NSI(LiTFSI).	92
Figure II-32: Analysis of mPEO ₆₀ m/LiTFSI (EO/Li= 20) (A) Nyquist plots of GEIS spectra showing evolution of the cell resistivity during equilibration at 40 °C before GCPL. (B) Nyquist plots of GEIS spectra measured before (\circ) and after (\diamond) GCPL. (C) DSC traces of the polymer electrolyte. Arrows (\rightarrow) indicated the direction of heating and cooling at a rate of 5°C.min ⁻¹ . (D) The resistivity ($\rho / 10^{-3} \cdot \Omega \cdot m$) as a function of charge (Q) during galvanostatic cycling of mPEO ₆₀ m/LiTFSI (EO/Li= 20). The first five cycles are shown. The arrow (\rightarrow) indicates the evolution of ρ upon cycling.....	93
Figure II-33: (top) ρ vs Q of GCPL and (bottom) examples of GEIS of mPEO ₂₀ - \blacklozenge^+ NSI(Li)	94
Figure II-34: (top) ρ vs Q of GCPL and (bottom) examples of mPEO ₅₅ -SANSI(Li ₂).....	94
Figure II-35: Nyquist plots of EIS spectra (1.0 MHz \rightarrow 0.5 Hz) measured of polymer electrolytes in Li Li coin cells before (\circ) and after (\diamond) chronoamperometry (CA). These spectra were used to correct for the change in cell potential resulting from the CA method. EIS was conducted at 40°C (A-E, G-H) and at 60 °C (F). The MEC-SIPEs having EO _n = 20 and different functional end-groups are shown: -SO ₃ Li (A), -OC(O)PhSO ₃ Li (B), -N(Li)Naph (C), -N(Li)Pyr (D), -SO ₂ N(Li)Naph (E), - \blacklozenge^+ NSI(LiTFSI) (G). The long-chain "double salt" EC-SIPE mPEO ₅₅ -SANSI(Li ₂) (F) is shown. The SiP electrolyte mPEO ₆₀ m/LiTFSI (H) is shown for comparison. The experimental data are fitted to an equivalent circuit model (black lines, -). Arrows (\leftarrow) indicate the direction of increasing frequency.	99
Figure II-36: DSC thermograms of mPEO ₆₀ m (A) and mPEO ₆₀ m/LiTFSI having different EO/Li ratios: (B) EO/Li= 60, (C) EO/Li= 20, and (D) EO/Li= 10.....	104
Figure II-37: DSC thermograms of mPEO ₅₅ -OH (A) and MEC-SIPEs based on mPEO ₅₅ - having different end-groups: (B) -SO ₃ Li, (C) -SO ₂ N(Li)Naph, and (D) -SANSI(Li ₂).....	104
Figure II-38: DSC thermograms on heating (left) and cooling (right) of mPEO _n -OH having different PEO chain lengths. The number of repeating units (EO _n = 8, 10, 20, 55, and 160) are labelled for each trace. The arrows indicated the directions of heating (\rightarrow) and cooling (\leftarrow). The traces are individually normalised according to the sample mass (W.g ⁻¹). The heating/cooling rate is 5°C.min ⁻¹ . The second heating and cooling DSC scans for each sample are displayed.	106
Figure II-39: DSC thermograms on heating (left) and cooling (right) of mPEO _n -SO ₃ Li having different PEO chain lengths. The direction of heating (\rightarrow) and cooling (\leftarrow) are indicated. The traces	

are individually normalised according to the sample mass (W.g^{-1}). The heating/cooling rate is 5°C.min^{-1} . The second heating and cooling DSC scans are displayed for each sample. 108

Figure II-40: DSC thermograms on heating (**left**) and cooling (**right**) of MEC-SIPEs having different functional end-groups: $-\text{OC(O)PhSO}_3\text{Li}$ (**A**), $-\text{SO}_2\text{N(Li)Naph}$ (**B**), $-\text{N(Li)Naph}$ (**C**), and $-\text{N(Li)Pyr}$ (**D**). The traces are labelled with the number of EO repeating units of the EC-SIPE ($\text{EO}_n = 8, 10, 20, 55,$ and 160). The arrows indicate the direction of heating (\rightarrow) and cooling (\leftarrow). The traces are individually normalised according to the sample mass (W.g^{-1}). The heating/cooling rate is 5°C.min^{-1} . The second heating and cooling DSC scans for each sample are displayed. 109

Figure II-41: $-\Delta H_{\text{endo}}$ vs. $\phi_{\text{m(EGrp)}}$ of MEC-SIPEs i) $\text{mPEO}_n\text{-OH}$ (\circ) and $\text{mPEO}_{60}\text{m/LiTFSI}$ of different EO/Li ratios (\bullet). $\phi_{\text{m(a)}}$: for $\text{mPEO}_n\text{-OH}$, $a = \text{OH}$; for the SiP, $a = \text{LiTFSI}$ 112

Figure II-42: $-\Delta H_{\text{endo}}$ vs. $\phi_{\text{m(EGrp)}}$ of MEC-SIPEs ii) $\text{mPEO}_n\text{-OH}$ (\circ), $\text{mPEO}_n\text{-SO}_3\text{Li}$ (\oplus), and $\text{mPEO}_n\text{OC(O)PhSO}_3\text{Li}$ (\blacklozenge). 112

Figure II-43: $-\Delta H_{\text{endo}}$ vs. $\phi_{\text{m(EGrp)}}$ of EC-SIPEs iii) $\text{mPEO}_n\text{-OH}$ (\circ), $\text{mPEO}_n\text{-SO}_2\text{N(Li)Naph}$ (\blacklozenge), $\text{mPEO}_n\text{-N(Li)Naph}$ (\bullet), and $\text{mPEO}_n\text{-N(Li)Pyr}$ (\blacksquare) 112

Figure II-44: $-\Delta H_{\text{endo}}$ vs. $\phi_{\text{m(EGrp)}}$ of EC-SIPEs iv) $\text{mPEO}_n\text{-OH}$ (\circ), $\text{mPEO}_n\text{-SO}_2\text{N(Li)Naph}$ (\blacklozenge), $\text{mPEO}_{55}\text{-SANSI(Li}_2\text{)}$ (\times), $\text{mPEO}_{20}\text{-}\blacklozenge\text{NSI(Li)}$ (\blacklozenge), and $\text{mPEO}_{20}\text{-}\blacklozenge^+\text{NSI(LiTFSI)}$ (\blacklozenge) 112

Figure II-45: The conductivity ($\sigma / \text{S.cm}^{-1}$) of $\text{mPEO}_n\text{SO}_3\text{Li}$ as a function of Temperature ($T / 10^3.\text{K}^{-1}$). The data is reproduced from **Figure II-5**. 113

Figure II-46: The conductivity ($\sigma / \text{S.cm}^{-1}$) of $\text{mPEO}_n\text{OC(O)PhSO}_3\text{Li}$ as a function of Temperature ($T / 10^3.\text{K}^{-1}$). The data is reproduced from **Figure II-8**. 113

Figure II-47: The ΔH_{endo} of selected EC-SIPEs as a function of M_n (g.mol^{-1}) are compared with $\text{mPEO}_n\text{-OH}$ precursors (\blacktriangle), and values for $\text{HO-PEO}_n\text{-OH}$ (\circ) reported in the literature.^[16] (Left, **A**): MEC-SIPEs having $-\text{SO}_3\text{Li}$ (\oplus), $-\text{OC(O)PhSO}_3\text{Li}$ (\blacklozenge) end-groups. (Right, **B**): $-\text{SO}_2\text{N(Li)Naph}$ (\blacklozenge), $-\text{N(Li)Pyr}$ (\blacksquare), $-\text{N(Li)Naph}$ (\bullet), $-\text{SANSI(Li}_2\text{)}$ (\diamond), $-\blacklozenge\text{NSI(Li)}$ (\blacklozenge) and $-\blacklozenge^+\text{NSI(LiTFSI)}$ (\blacklozenge) end-groups. The lines are drawn as a guide for the eye only. 115

Figure II-48: The DSC thermograms of $\text{mPEO}_{20}\text{-OH}$ measured *on heating* after cooling DSC scans of decreasing cooling rate (see **Table II-9** for details). The rates of cooling of the precedent DSC scans are indicated. The traces are normalised according to the sample mass and displaced vertically by an arbitrary value. The labelled peaks (a, b, c) refer to values listed in **Table II-9**. 117

Figure II-49: The DSC thermograms of $\text{mPEO}_{20}\text{N(Li)Pyr}$ measured *on heating* after DSC cooling scans of decreasing cooling rate (see **Table II-10** for details). The rates of cooling of the precedent DSC scans are indicated. The traces are normalised according to the sample mass and displaced vertically by an arbitrary value. The labelled peaks (a, b) refer to values in **Table II-10**. 117

Figure II-50: The T_m ($^\circ\text{C}$) reported as values of peak enthalpy change of melting (ΔH_m) as a function of the DP_n of $\text{HO-PEO}_n\text{-OH}$. The data are taken from the literature.^[16,17,19] The lines are logarithmic fits of the data. The equation used: $\text{EO}_n = 9\text{-}46$, $T_m = 29.6 \cdot \ln(M_n) - 168.5$; $T_m = 29.6 \cdot \ln(\text{EO}_n) - 56.5$ [$R^2 = 0.97$]. 119

Figure II-51: An illustration of a hypothetical model of the MEC-SIPE $\text{mPEO}_{20}\text{-N(Li)Pyr}$. The poly(ethylene oxide) methyl ether chain is composed of two parts: i) "Native" EO_n units that

crystallise and melt as expected of those in extended chain conformation, and ii) EO_n^* units that are perturbed by the physicochemical character of the proximal functional End-Group. 120

Figure II-52: The σ ($S.cm^{-1}$) of $mPEO_{60}m/LiTFSI$ ($EO/Li= 10$) (\circ) and $mPEO_{10}m/LiTFSI$ ($EO/Li= 10$) (\triangle) as a function of T (K^{-1}). The red lines are VTF fits of the data. 125

Figure II-53: $W(T)$ plots of the SiP electrolyte $mPEO_{60}m/LiTFSI$ having different $EO/Li= 60$ (\square), 20 (\circ), and 10 (\triangle); and $mPEO_{10}m/LiTFSI$ (marked*) having $EO/Li= 10$ (\diamond). Dotted lines (\cdots) are linear fits of the data. The data series are plotted as a function of $T(K)$ and displaced vertically by an arbitrary value. 125

Figure II-54: (Left) The ionic conductivity [$\log(S.cm^{-1})$] and (Right) $W(T)= T\cdot\{\delta\ln(\sigma)/\delta(T)\}$ of MEC-SIPES having different functional end-groups: $-SO_3Li$ (**A**), $-OC(O)PhSO_3Li$ (**B**), $-SO_2N(Li)Naph$ (**C**), $-N(Li)Naph$ (**D**), $-N(Li)Pyr$ (**E**), $-\blacklozenge NSI(Li)$ and $-\blacklozenge^+ NSI(LiTFSI)$ (**F**), and $-SANSI(Li_2)$ (**G**). The MEC-SIPES having different EO_n are presented: $EO_n= 8$ (\diamond), 10 (\triangle), 20 (\circ), and 55 (\square). The same symbols are used both for the σ and $W(T)$ plots. The MEC-SIPE is indicated within the chart area of each plot. The red lines ($-$) are VTF fits of the experimental ionic conductivity data (symbols). The dotted lines (\cdots) are linear fits of the $W(T)$ function (symbols). The $W(T)$ data series are plotted as a function of temperature and displaced vertically by an arbitrary value. 126

Figure II-55: The slope $-B$ of $W(T)$ is presented as a function of $\phi_{m(salt)}$ of MEC-SIPES (listed below the plots, **A-C**). The slope of $W(T)$ at high T (α , red, filled symbols) and at low T (β , blue, open symbols) are shown. The linear fits of $W(T)$ used to obtain the slope $-B$ are shown in **Figure II-54 (A-G)**. In the case of MEC-SIPES, $\phi_{m(salt)}$ is the mass fraction of the ionic end-group; for the SiP electrolytes, $\phi_{m(salt)}$ is the mass fraction of LiTFSI. For the EC-SIPES, the polymers having $EO_n= 55$, 20, 10 and 8 are shown and some EO_n values are labelled for reference. 128

Figure II-56: The $W(T)$ transition temperature $T[W(\alpha)=W(\beta)]$ (blue, filled symbols; \bullet , \blacksquare , \blacktriangle) on cooling (EIS) and the T_p (red, open symbols, \circ , \square , \triangle) of ΔH_{endo} transitions on heating (DSC) of MEC-SIPES having different end-groups: $-SO_3Li$ (**A**; \bullet , \circ), $-OC(O)PhSO_3Li$ (**B**; \blacksquare , \square), $-N(Li)Naph$ (**C**; \bullet , \circ), $-N(Li)Pyr$ (**D**; \blacksquare , \square), $-SO_2N(Li)Naph$ (**E**; \blacktriangle , \triangle). The polymers $mPEO_{55}-SANSI(Li_2)$ (\diamond), $mPEO_{20}-\blacklozenge NSI(Li)$ (\blacklozenge), and $mPEO_{20}-\blacklozenge^+ NSI(LiTFSI)$ (\blacklozenge) are shown (**F**). The red diamonds (\blacklozenge) indicate the T_p of the first ΔH_{endo} transition on heating of each MEC-SIPE (DSC). Dotted lines (\cdots) are drawn to link data sets of MEC-SIPES of the same DP_n (labelled: $EO_n= 55$, 20, 10, and 8). ... 130

Figure II-57: Nyquist plots of EIS data measured on cooling of $mPEO_n-N(Li)Pyr$ 132

Figure II-58: Nyquist plots of EIS data measured on heating of $mPEO_8-N(Li)Pyr$ 132

Figure II-59: An example Nyquist plot illustrating the high frequency Q_2/R_2 and the lower frequency Q_3/R_3 features observed on heating from $-10^\circ C$. The arrow (\leftarrow) indicates the direction of increasing frequency. 133

Figure II-60: The resistivity (ρ) and the corresponding capacitance (Q , open symbols) at a function of temperature on heating of $mPEO_8-N(Li)Pyr$ from $-10^\circ C$ to $+20^\circ C$. The higher frequency feature Q_2/R_2 (circles; \circ , \bullet) and the lower frequency feature Q_3/R_3 (squares; \square , \blacksquare) are displayed. ... 133

Figure II-61: A double logarithmic plot of real part of the impedance (Z') as a function of frequency (ν). 134

- Figure II-62:** The derivative $\delta(Z')/\delta(\nu)$ of real part of the impedance (Z') as a function of logarithmic frequency (ν)..... 134
- Figure II-63:** A Nyquist plot of the EIS spectrum of mPEO₈N(Li)Pyr. The experimental data (○) was collected at 0°C, on cooling from 100°C. The bulk electrolyte resistivity ($\rho= 441 \Omega.m$) and capacitance ($Q= 0.308 \cdot 10^{-9} F.s^{(a-1)}$; $a= 0.979$). The fit of the equivalent circuit (**Eqn. 17**) is displayed (red line, -)..... 135
- Figure II-64:** A double logarithmic plot of Z' (●) and Z'' (○) as functions of frequency ($f= \nu/2\pi$) of mPEO₈N(Li)Pyr at 0°C on cooling from 100 °C. The corresponding moduli M' (red line, -) and M'' (dotted line, ...) are shown. 135
- Figure II-65:** A double logarithmic plot of the frequency dependence of σ of mPEO_nN(Li)Pyr. MEC-SIPEs having short chains ($EO_n= 8, 10, \text{ and } 20$; ●) are overlapping and the longest chain $EO_n= 55$ (○) is shifted in coordinates. The arrow (→) indicates the direction of increasing temperature. The reference line (-) has a slope of 1. 136
- Figure II-66:** Conductivity vs. Frequency of MEC-SIPEs having $EO_n= 8$ and different functional end-groups: -N(Li)Pyr (□), -N(Li)Naph (△), -SO₂N(Li)Naph (◇), -SO₃Li (○) and -OC(O)PhSO₃Li (●). The arrow (→) indicates the direction of increasing temperature. The reference line (-) has a slope of 1. 136
- Figure II-67:** The EIS spectrum of mPEO₈-N(Li)Pyr measured at 80°C..... 138
- Figure II-68:** The EIS spectrum of mPEO₈-N(Li)Pyr measured at 0°C..... 138
- Figure II-69:** Nyquist plots of the EIS spectra of mPEO₈-N(Li)Pyr measured at 80°C (red, ○) and 0°C (blue, ○) on cooling from 100°C. The experimental data are the same as those shown above (**Fig. II-67** and **Fig. II-68**). Red lines (-) represent the equivalent circuit model (**Eqn. II-18**). Arrows (←) indicate the direction of increasing frequency. 139
- Figure II-70:** The EIS spectrum of mPEO₈-N(Li)Pyr measured at 18°C on cooling from 100°C. The features Q_2 and Q_3 are both visible. The characteristic frequencies f_{Q_3} (□), f_x (○), f_{ρ_2} (●), and f_{Q_2} (◇) are shown. The symbols correspond to those of **Figure 85**. 140
- Figure II-71:** The characteristic frequencies of features observed in EIS spectra of mPEO₈-N(Li)Pyr on cooling from 100°C. The double logarithmic plot of σ vs. f is calculated from the resistance of Z' . The features (right to left) Q_2 (◇), ρ_2 (●), ρ_x (○), Q_3 (□), and ρ_3 (■) are shown. Each feature is labelled with the temperature range over which it is observed, within the instrumental limits. The line (-) is a reference of $y=x$ 140
- Figure II-72:** The bulk ionic conductivity (σ) of mPEO₈-N(Li)Pyr (blue line, -) as a function of $T (10^3.K^{-1})$. The features of the EIS spectra at their characteristic frequencies (f) are plotted relative to σ and $T (^\circ C)$. These are (left to right) ρ_3 (■), Q_3 (□), ρ_x (○), ρ_2 (●), and Q_2 (◇). The temperature at which four features are observed (18°C) is indicated (⋯)..... 141
- Figure II-73:** The reduced activation energy $W(T)$ of mPEO₈-N(Li)Pyr (◇) as a function of temperature. The dashed lines (---) are linear fits of the high (α) and low (β) temperature trends. The intercept of these lines (13°C) is indicated (⋯)..... 141

Figure II-74: The bulk ionic conductivity (σ) of mPEO_n-N(Li)Pyr (blue line, -) as a function of T (10³.K⁻¹). The MEC-SIPE having EO_n= 8 (A), 10 (B), 20 (C), and 55 (D) are shown. The features of the EIS spectra (e.g. Fig II-67 and Fig. II-68) at their characteristic frequencies (f) are plotted and displaced vertically according to the bulk ionic conductivity (σ). These are labelled in A: ρ_3 (■), Q₃ (□), ρ_x (○), and Q₂ (◇). The temperatures (°C) at which certain features enter or exit the frequency window are indicated and labelled (grey dotted lines, ...). 143

Figure II-75: An illustration of a hypothetical model of the MEC-SIPE mPEO₂₀-N(Li)Pyr. The mPEO chain is composed of two parts: i) "Native" EO_n units, and ii) EO_n* units that are perturbed by the proximal functional End-Group. 144

Figure II-76: A Nyquist representation of the EIS spectrum (○) measured of mPEO₅₅-N(Li)Pyr at 60 °C on cooling from 100°C. The data is fitted with an equivalent circuit (Eqn. II-18; red line, -). The diffusion spur (green dotted line, ...) and a hypothetical R₃/Q₃ feature (blue dashed line, - - -) are indicated. The position of Q₃ is obscured by the diffusion spur. 145

Figure II-77 (A-F): The bulk ionic conductivity (σ) as a function of T (10³.K⁻¹) of MEC-SIPEs having EO_n=8 and different functional end-groups: -N(Li)Pyr (A), -SO₃Li (B), -N(Li)Naph (C), -OC(O)PhSO₃Li (D), and -SO₂N(Li)Naph (E). The SiP blend mPEO₁₀m/LiTFSI (EO/Li= 10) is shown for reference (F). The features of the EIS spectra (see Fig. II-67 and Fig. II-68) at their characteristic frequencies (f) are plotted and displaced vertically according to the bulk ionic conductivity (σ). These are Q₃ (□), ρ_x (○), and Q₂ (◇). The temperatures (°C) at which certain features enter or exit the frequency window are indicated and labelled (grey dotted lines, ...). 148

Figure II-78 (A-F): Conductivity (σ) as a function of T (10³.K⁻¹) is shown for MEC-SIPEs having EO_n= 55 and different functional end-groups: -SO₃Li (A), -SO₂N(Li)Naph (B), -N(Li)Naph (C), -N(Li)Pyr (D), and -SANSI(Li₂) (E). A SiP electrolyte mPEO₆₀m/LiTFSI (EO/Li= 60) is shown for reference (F) relative to the 4th cycle (◇) of mPEO₅₅-SANSI(Li₂). An insufficient amount of data was obtained for mPEO₅₅-OC(O)PhSO₃Li to enable comparison here. The impedance measurements were conducted every 2 °C in the temperature range i) 60 → 100°C, ii) 100 → 40°C, and iii) 40 → 100°C, then repeating ramps ii) and iii). The displayed data were collecting during successive cooling (100 → 40°C) cycles: 1st (○), 2nd (□), 3rd (△), and 4th (◇) for all polymers except B (three ramps only). The VTF fits (blue lines, -) were calculated from the 90 → 40°C range. The VTF fitting parameters are tabulated in each plot. 150

Figure II-79: Selected Nyquist plots of EIS spectra measured of mPEO₅₅-SANSI(Li₂) at 80 °C during four successive cycles (labelled 1-4) on cooling from 100°C. The panels are (A) overlapping data represented by red lines; and (B) the experimental data (red circles, ○) are plotted in the complex plane and displaced along the real (Z') axis by an arbitrary value. The dotted lines (...) are a guide for the eye only. 152

Figure II-80: Nyquist plot of EIS spectrum of mPEO₅₅-SANSI(Li₂) measured at 80°C on cooling during cycle 4 (circles, ●) fitted by the equivalent circuit (Eqn. II-18; black line, -). The features at high frequency (ρ_2 /Q₂) and low frequency (ρ_3 /Q₃) are labelled. The shape of ρ_3 /Q₃ is illustrated (dashed line, - - -). 152

Figure II-81: The resistivity (ρ , filled symbols) and the corresponding capacitance (Q, open symbols) of two features in EIS spectra of mPEO₅₅-SANSI at 80°C on cooling from 100°C. Cycle

numbers refer to the spectra illustrated in Figure 86. The higher frequency feature ρ_2/Q_2 (circles; \circ , \bullet) and the lower frequency feature ρ_3/Q_3 (squares; \square , \blacksquare) are displayed. Lines are drawn as a guide for the eye only. 152

Figure II-82: The capacitance ($F.s^{(a-1)}$) of the ρ/Q features of mPEO₅₅-SANSI(Li₂) as functions of T ($10^3.K^{-1}$). The data are calculated by fitted to a single equivalent circuit (**Eqn. 17**). The overlapping values of four successive cooling ramps are shown for ρ_2/Q_2 (open green circles, \circ) and ρ_3/Q_3 (open black squares, \square). 153

Figure II-83: The high frequency ρ_2/Q_2 feature. 153

Figure II-84: The low frequency ρ_3/Q_3 feature. 153

Figure II-85: $W(T)$ of the ρ_2/Q_2 feature of mPEO₅₅-SANSI(Li₂) calculated from the 4th cooling ramp of EIS measurements with thermal cycling. Linear fits of the high T (α) and low T (β) regimes are shown (dotted lines, \cdots). The intercept transition temperature is labelled, $T[W(\alpha)=W(\beta)]=59^\circ C$ 155

Figure II-86: $W(T)$ of the ρ_3/Q_3 feature of mPEO₅₅-SANSI(Li₂) calculated from the 4th cooling ramp of EIS measurements with thermal cycling..... 155

Figure II-87: Representative EIS spectrum of mPEO₅₅-SANSI(Li₂) measured at 60°C on cooling from 100 °C (4th cycle). The Q_2 and Q_3 features are labelled..... 155

Figure II-88: The σ of the ρ_2/Q_2 couple of mPEO₅₅-SANSI(Li₂) as a function of T ($10^3.K^{-1}$). The characteristic frequencies of ρ_2 (\blacksquare), Q_3 (\square), ρ_x (\circ), and Q_2 (\diamond) are plotted on the x-axis and displaced vertically according to σ of the ρ_2/Q_2 couple..... 155

Figure II-89: A graphical abstract illustrating the tentative model of how MEC-SIPEs afford efficient conduction of ions in the bulk state. The MEC-SIPEs (examples shown in panel **A**) are segregated in the bulk state (**B**) due to the low N-high χ macromolecular design based on functional ionic end-groups. Low frequency resistive features (**C**) are evidence of imperfection in ion transport. The ionic conductivity increases with cycling (**D**) under mild conditions of temperature and electromagnetic force. This might be the result of improved the percolation of ionically conductive pathways (**E**) composed of functional ionic end-groups localised at the boundary of PEO grains (**F**). In the panels **B** and **C**, the grain boundaries are represented by blue lines (sometimes incomplete). Panel **E** is an attempt to illustrate a percolating pathway (red dashed line, - - -) as a continuum of grain boundaries. In panel **B** the percolation of grain boundaries is incomplete, so a good path is hard to find. 159

Figure III-1: Synthesis of bromo-end-capped poly(ethylene oxide) monomethyl ether via the Appel reaction with carbon tetrabromide and triphenylphosphine in dichloromethane (DCM)..... 175

Figure III-2: Synthesis of aminonaphthalene-end-capped poly(ethylene oxide) monomethyl ether via reaction of the bromo-end-capped derivative with 1-aminonaphthalene..... 176

Figure III-3: Synthesis of aminopyrene-end-capped poly(ethylene oxide) monomethyl ether via reaction of the bromo-end-capped derivative with 1-aminopyrene under reflux..... 177

Figure III-4: Synthesis of sulfonate-end-capped poly(ethylene oxide) monomethyl ether via reaction of the bromo-end-capped derivative with sodium sulphite under reflux..... 182

Figure III-5: Synthesis of N-(naphthyl)sulfonamide-end-capped poly(ethylene oxide) monomethyl ether.	184
Figure III-6: Synthesis of benzene-sulfonate end-capped mPEO-OC(O)PhSO ₃ Li	188
Figure III-7: Synthesis of 4-azidonaphthalene-1-sulfonic acid sodium salt (AzNSO ₃ Na) via nucleophilic aromatic substitution.....	191
Figure III-8: Synthesis of 4-azidonaphthalene-1-sulfonyl(methylsulfonyl)imide	192
Figure III-9: Synthesis of 4-aminonaphthalene-1-sulfonyl(methylsulfonyl)imide potassium salt [ANSI(K)]	193
Figure III-10: Synthesis of alkyl-functional mPEO ₂₀ C(O)C≡CH ($M_{n(NMR)} = 971$ g/mol) via acid-catalysed esterification under Dean-Stark conditions.	201
Figure III-11: Synthesis of 4-(1,2,3-triazo)-naphthalene-1-sulfonyl(methylsulfonyl)imide lithium salt end-capped poly(ethylene oxide) methyl ether via CuAAC.....	201
Figure III-12: Quaternisation of mPEO ₂₀ -AzNSI(Li) to yield the zwitterionic end-capped polymer mPEO ₂₀ -Az ⁺ NSI(LiTFSI).	206
Figure III-13: Synthesis of the mPEO ₅₅ -SANSI(Li ₂) "Double Salt" by reaction of mPEO ₅₅ SO ₂ Cl with amino-functional ANSI(K)	208

List of Tables

Table I-1: Lithium ion conductivities of selected poly(ether)-based End-Capped Single-Ion Polymer Electrolytes (EC-SIPes) from the literature. References are indicated in the right-hand column (ref.). Mono- (X-●) and bis- (●-X-●) end-capped configurations are indicated. The conductivity is of the neat EC-SIPE. The polymers are organised by end-group (1-9), and by examples (A, B, C, ...) in DP _n and in temperature. The M _w is of the polymer chain only.....	37
Table II-1: The Degree of Polymerisation (DP _n / EO _n), Number Average Molecular Mass (M _n / g.mol ⁻¹), the mass fraction of the end-group (φ _{m(EGrp)}) and the mass fraction of lithium (φ _{m(Li)}) of the presented MEC-SIPes having different functional End-Group Identities.	75
Table II-2: Table of summarised ionic conductivity (σ / S.cm ⁻¹) and corresponding lithium transference number (LTN) of selected MEC-SIPes (for transference of Lithium, see Section 2.3). The LTN was calculated using the Bruce-Vincent method. The σ _{AC} was measured using blocking (gold) electrodes. These data are illustrated above (Section 2.1.3). The two LTNs are the chronoamperometric (t ^{+_{Li}}) and corrected (t ^{+_{Li}*}) values. The data of the SiP electrolyte mPEO ₆₀ m/LiTFSI (EO/Li= 20) are listed for comparison.....	83
Table II-3: Table of the water concentration [H ₂ O] of MEC-SIPes having different end-groups and EO _n = 20 (except 8 , EO _n = 55). The [H ₂ O] is listed as (i) number of moles of water per mole of ionic end-groups (mol/mol), and (ii) parts per million (ppm; μg/g). The σ _{AC} (S.cm ⁻¹) and lithium transference number (LTN, see Section 2.3) is listed for reference. The two LTNs are the chronoamperometric (t ^{+_{Li}}) and corrected (t ^{+_{Li}*}) values. The data of the SiP electrolyte mPEO ₆₀ m/LiTFSI (EO/Li= 20) are listed for comparison.....	84
Table II-4: The Degree of Polymerisation (DP _n / EO _n), Number Average Molar Mass (M _n / g.mol ⁻¹), the mass fraction of the end-group (φ _{m(EGrp)}) and the mass fraction of lithium (φ _{m(Li)}) of the presented MEC-SIPes having different End-Group Identities. The SiP electrolyte mPEO ₆₀ m/LiTFSI (EO/Li =20) is listed for reference.	96
Table II-5: Table of summarised ionic conductivity (σ / S.cm ⁻¹) and corresponding lithium transference number (LTN) of selected MEC-SIPes. The LTN was calculated from chronoamperometry using the Bruce-Vincent method. The σ _{AC} was measured by EIS using either (blocking) gold electrodes (Au Au) or lithium metal (Li Li) electrodes at 40°C (except 8 ; 60 °C). The σ _{AC} [Li Li] is that measured immediately i) before and i) after chronoamperometry (CA). The two LTNs listed are the chronoamperometric (t ^{+_{Li}}) and corrected (t ^{+_{Li}*}) values. The data of the SiP electrolyte mPEO ₆₀ m/LiTFSI (EO/Li= 20) are listed for comparison. ^[12]	97
Table II-6: The mass fraction of salt (φ _{m(salt)}), the endothermic enthalpy change (ΔH _{endo}) and peak temperature (T _p) of the enthalpy change on heating at 5°C.min ⁻¹ from -40 °C. The mPEO ₆₀ m/LiTFSI having different concentrations of salt are compared. The salt concentration is listed in terms of the ratio of ethylene oxide repeating units to lithium ions (EO/Li).....	105
Table II-7: The T _p and ΔH _{endo} of phase transitions observed on heating at 5°C.min ⁻¹ . The MEC-SIPes having EO _n = 55 are compared to the precursor, mPEO ₅₅ -OH.....	105

Table II-8: The peak temperature ($T_p / ^\circ\text{C}$) of thermal transitions observed by DSC of $m\text{PEO}_n\text{-OH}$ having different PEO chain lengths ($\text{DP}_n / \text{EO}_n = 8, 10, 20, 55, \text{ and } 160$). The T_p is defined as the temperature of the maximum recorded change in enthalpy ($\Delta H / \text{J}\cdot\text{g}^{-1}$). The T_p values are listed intuitively, increasing from left to right. Overlapping peaks are grouped by parentheses [T_p]. The data correspond to the DSC thermograms of heating (Fig. 36) and cooling (Fig. 37) shown above (traces A-D).....	107
Table II-9: The peak temperature ($T_p / ^\circ\text{C}$) and endothermic enthalpy change ($-\Delta H_{\text{endo}}$) of thermal transitions observed when heating mPEO₂₀-OH at $5^\circ\text{C}\cdot\text{min}^{-1}$ after cooling ramps of decreasing rates (5.00, 2.50, 1.00, 0.50, 0.25, and $0.10^\circ\text{C}\cdot\text{min}^{-1}$). The $-\Delta H_{\text{endo}}$ marked (*) cannot be calculated due to the poorly defined baseline.	117
Table II-10: The peak temperature ($T_p / ^\circ\text{C}$) and endothermic enthalpy change ($-\Delta H_{\text{endo}}$) of thermal transitions observed when heating mPEO₂₀-N(Li)Pyr at $5^\circ\text{C}\cdot\text{min}^{-1}$ after DSC cooling scans of decreasing rates (5.00, 2.50, 1.00, 0.50, 0.25, and $0.10^\circ\text{C}\cdot\text{min}^{-1}$).	117
Table II-11: Example values obtained from Eqn. II-14.	119
Table II-12: VTF fitting parameters determined by least squares method for the ionic conductivity data of SiP blends of $m\text{PEO}_{60}\text{m}/\text{LiTFSI}$ and $m\text{PEO}_{10}\text{m}/\text{LiTFSI}$. The symbols correspond to those used in Figures 52 and 53	125
Table II-13: The Degree of Polymerisation ($\text{DP}_n / \text{EO}_n$), Number Average Molar Mass ($M_n / \text{g}\cdot\text{mol}^{-1}$), the mass fraction of the functional end-group ($\phi_{m(\text{EGrp})}$) and the mass fraction of lithium ($\phi_{m(\text{Li})}$) of the presented MEC-SiPEs having different End-Group Identities.....	146
Table II-14: Fitting parameters of the ρ_2/Q_2 and ρ_3/Q_3 features calculated by fitting of the σ of $m\text{PEO}_{55}\text{-SANSI}(\text{Li}_2)$ on cooling from 100°C to 40°C . The fits were made over the $90^\circ\text{C} \rightarrow 40^\circ\text{C}$ range. Both features were fitted to the VTF equation. The ρ_3/Q_3 feature is additionally fitted to the Arrhenius equation. The numbers (#) in the sequence of the cooling ramps are listed. In the Arrhenius equation E_a is the activation energy ($\text{J}\cdot\text{mol}^{-1}$) and R is the ideal gas constant ($8.314 \text{ J}\cdot\text{K}^{-1}\cdot\text{mol}^{-1}$).	154
Table III-1: Commercial poly(ethylene oxide) monomethyl ether used in the synthesis of SiPEs, quoting the $M_n(\text{NMR})$ and $\text{DP}_n(\text{EO}_n)$ determined in this work.....	174
Table III-2: The masses and moles of $m\text{PEO}_n\text{-OH}$, CBr_4 and PPh_3 used in the synthesis of polymers of different $\text{DP}_n(\text{EO}_n)$	175
Table III-3: The synthesis of $m\text{PEO}_n\text{-Br}$ from $m\text{PEO}_n\text{-OH}$ via the Appel reaction. The commercial mass average molar masses ($M_{w(\text{comm})}$) of $m\text{PEO}_n\text{-OHs}$ were used to calculate the masses of reagents required. The number-average molar mass ($M_{n(\text{nmr})}$), as determined in this work using NMR spectroscopy, is quoted and the yield is calculated using these values. For ease of reading, the polymers are referred to by their commercially designated M_w and calculated number-average degree of polymerisation (DP_n, EO_n), as determined by NMR spectroscopy.....	176
Table III-4: Masses and moles of $m\text{PEO}_n\text{-Br}$, 1-aminonaphthalene, and triethylamine used in the synthesis of aminonaphthalene-end-capped poly(ethylene oxide) monomethyl ether, $m\text{PEO}_n\text{-N(Li)Naph}$, of different PEO $\text{DP}_n(\text{EO}_n)$	177

Table III-5: Masses and yields of aminonaphthalene-end-capped poly(ethylene oxide) monomethyl ether of different PEO DP _n (EO _n). Molar quantities and yields are calculated according to the M _{n(NMR)}	177
Table III-6: Masses and moles of mPEO _n -Br, 1-aminopyrene and triethylamine used in the synthesis of aminopyrene-end-capped poly(ethylene oxide) monomethyl ether, mPEO _n -N(Li)Pyr, of different PEO DP _n (EO _n).	178
Table III-7: Masses and yields of aminopyrene-end-capped poly(ethylene oxide) monomethyl ether of different PEO DP _n (EO _n). Molar quantities and yields are calculated according to the M _{n(NMR)}	178
Table III-8: Masses and moles of bromo-end-capped poly(ethylene oxide) monomethyl ether, mPEO _n -Br, and sodium sulfite used in the synthesis of mPEO _n -SO ₃ Li of different DP _n (EO _n). The M _w of the mPEO _n -Br is calculated arithmetically from the commercial M _w of the corresponding mPEO _n -OH precursor (see synthesis of mPEO _n -Br for reference).	183
Table III-9: Yields of lithium sulfonate-end-capped poly(ethylene oxide) monomethyl ether obtained by reaction of mPEO-Br with sodium sulphite. Molar quantities and yields are calculated according to the M _{n(NMR)}	183
Table III-10: The masses and moles of mPEO-SO ₃ H, SOCl ₂ (126.04 g/mol, d= 1.64 g/cm ³ at 25°C) and DMF (73.10 g/mol, d= 0.95 g/cm ³ at 25°C) used in the synthesis of mPEO-SO ₂ Cl of different DP _n (EO _n).	184
Table III-11: Masses and moles of mPEO-SO ₂ Cl and 1-aminonaphthalene (143.19 g/mol) used in the synthesis of N-(naphthyl)sulphonamide-end-capped poly(ethylene oxide) monomethyl ether. The M _w of the polymers was calculated according to the commercial designation.	185
Table III-12: The moles and yield of N-(naphthyl)sulphonamide-end-capped poly(ethylene oxide) monomethyl ether from the corresponding sulfonyl chloride. The number-average molar mass (M _{n(nmr)}) and DP _n (EO _n) were determined by NMR spectroscopy. The yield is calculated using these values.	185
Table III-13: The masses and moles of mPEO and SBACA used in the synthesis of polymers of different DP _n (EO _n).	189
Table III-14: The synthesis of mPEO _n -OC(O)Ph-SO ₃ Li via ring-opening of SBACA by reaction with mPEO-OH. The commercial mass average molar masses (M _{w(comm)}) of mPEO _n -OHs were used to calculate the masses of reagents required. The number-average molar mass (M _n), calculated in this work using NMR spectroscopy, is quoted. The yield is calculated using M _{n(NMR)} . For ease of reading, the polymers are referred to by their DP _n , as calculated from M _{n(NMR)}	189

List of Abbreviations

ATR	Attenuated Total Reflectance (FTIR-ATR)
BCP	(di-, tri-) Block Copolymer
CP-MAS	Cross-Polarisation Magic-Angle Spinning (NMR)
CuAAC	Copper-Catalysed Azide-Alkyne [3+2] Cycloaddition
CV	Cyclic Voltammetry
DP _n	Number Average Degree of Polymerisation
DSC	Differential Scanning Calorimetry
EIS	Electrochemical Impedance Spectroscopy
FTIR	Fourier-Transform Infrared Spectroscopy
GCPL	Galvanostatic Cycling with Potential Limitation
GEIS	Galvanostatic Electrochemical Impedance Spectroscopy
H	Enthalpy (J.g ⁻¹)
HMBC	Heteronuclear Multiple Bond Correlation (NMR)
HPLC	High Performance Liquid Chromatography
HSQC	Heteronuclear Single Quantum Coherence (NMR)
IoT	Internet of Things
J	Joule
LAM	Lamellar
LiB	Lithium-ion Battery
LMB	Lithium Metal Battery
LTN	Lithium Transference Number (t_{Li}^+)
MEC-SIPE	MonoEndCapped-"Single Ion" Polymer Electrolyte
M _n	Number Average Molar Mass (g/mol)
MS	Mass Spectroscopy
M _w	Mass Average Molar Mass (g/mol)
NMR	Nuclear Magnetic Resonance Spectroscopy
ODT	Order-Disorder Transition
PAH	Polycyclic Aromatic Hydrocarbon
PEIS	Potentiostatic Electrochemical Impedance Spectroscopy
R	Ideal Gas Constant = 8.314 J·mol ⁻¹ ·K ⁻¹
s	second
S	Siemens (Ω ⁻¹)
SAXS	Small-Angle X-ray Scattering
SiP	<i>Salt-in-Polymer</i> (electrolyte)
SIPE	"Single-Ion" Polymer Electrolyte
SPE	Solid Polymer Electrolyte
T _c	Crystallisation Temperature
T _g	Glass Transition Temperature
TGA	Thermogravimetric Analysis
TLC	Thin Layer (silica gel) Chromatography
T _m	Melting Temperature
TOF	Time of Flight (HPLC-MS-TOF)
T _o	Onset Temperature

T_p	Peak Temperature
VTF	Vogel-Tamman-Fulcher relation
$W(T)$	Reduced Activation Energy, $([\delta\sigma/\delta T]*T)$
WAXS	Wide-Angle X-ray Scattering
X_n	Degree of Polymerisation (number of repeating "X" units)

Greek Alphabet

ν	Frequency (Hz)
ρ	Resistivity ($\Omega.m$)
σ	Conductivity ($S.cm^{-1}$)
ϕ_m	Mass Fraction
χ	Flory-Huggins Interaction Parameter
Ω	Resistance (Ohm)
ω	Angular frequency ($\nu*2\pi$)

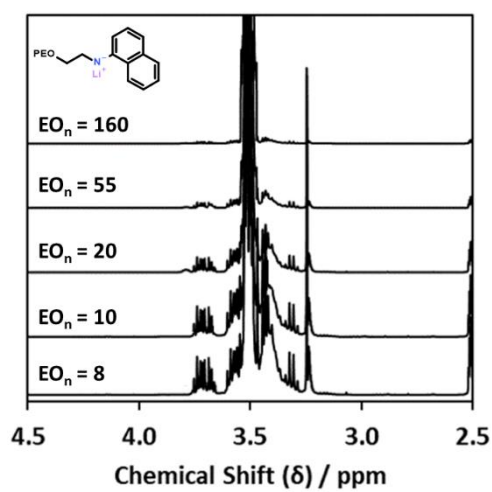
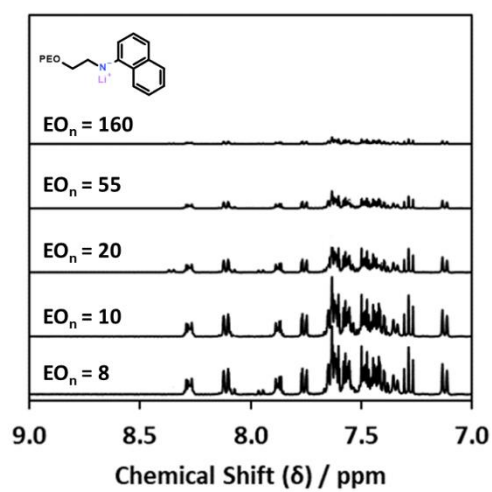
Annex: ^1H NMR Spectra of MEC-SIPES

The MEC-SIPES having different polymer chain lengths were analysed by NMR spectroscopy. Proton NMR is a quantitative technique and permits the calculation of M_n by comparison of the integrals of the assigned peaks. This value of M_n is accepted only under the assumption that the integrals are quantitative, which requires that i) the analyte is completely dissolved in the solvent and ii) the sample is a dilute, ideal solution. The presented MEC-SIPES have poly(ethylene oxide) chains and ionic end-groups. They have a surfactant-like polymer architecture, so complete dissociation of the polymers into ideal, 'dilute' solutions is not expected. Further, a sample of high concentration (30 g/L) is required to observe the end-groups of the MEC-SIPES having the longest chains ($\text{EO}_n > 20$). Quantitative analysis of end-group integrals also requires that the protons of the end-groups and of the polymer chain have the same spin-lattice relaxation time (T_1). This is unlikely for the chemically different parts of the MEC-SIPES (*i.e.* aromatic end-group protons vs. ether unit protons).

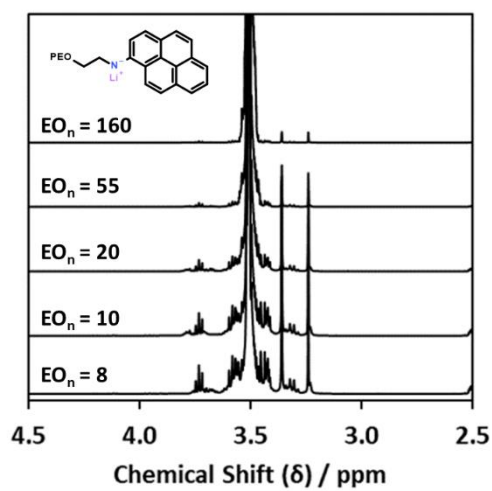
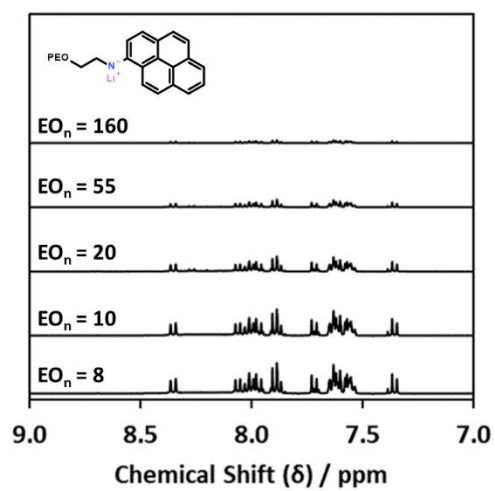
The general trend is that the integral of the end-groups decreases with the polymer chain length at constant sample concentration. However, the integrals of the end-group protons of the MEC-SIPES do not agree with the M_n determined by ^1H NMR analysis of their $m\text{PEO}_n\text{-OH}$ precursors. Quantitative analysis of the protons at the alpha position to the end group (CH_2^{d}) is prohibited by overlap of these peaks with those of the ether unit protons ($\text{CH}_2^{\text{b-c}}$). The ^{13}C , ^7Li , and ^{19}F NMR spectra are not quantitative.

The ^1H NMR spectra of the MEC-SIPES are shown below to illustrate that the peak chemical shifts of the MEC-SIPES are similar, and that the spectra presented in the *Experimental* (Chapter III) are representative. The spectra are individually normalised to the maximum height of the ether proton peak ($\delta \approx 3.4\text{-}3.6$ ppm). The primary chain (δ : 2.5-4.5 ppm) and aromatic (δ : 7.0-9.0 ppm) regions are shown separately. The chemical shift ranges are chosen to illustrate the characteristic parts of the spectra. Each spectrum is labelled with the polymer DP_n ($\text{EO}_n = 8, 10, 20, 55, \text{ and } 160$).

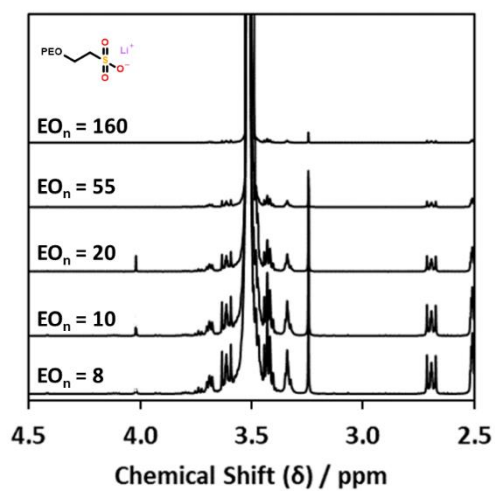
mPEO_n-N(Li)Naph



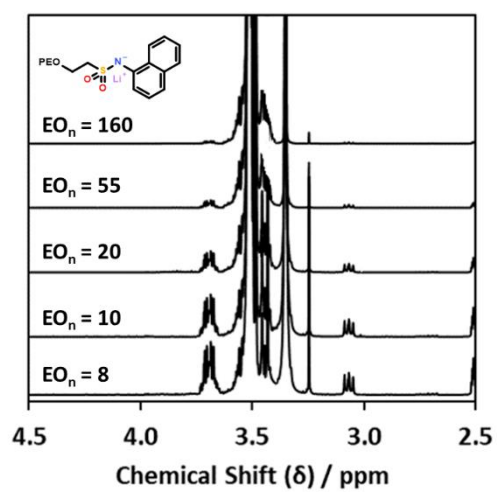
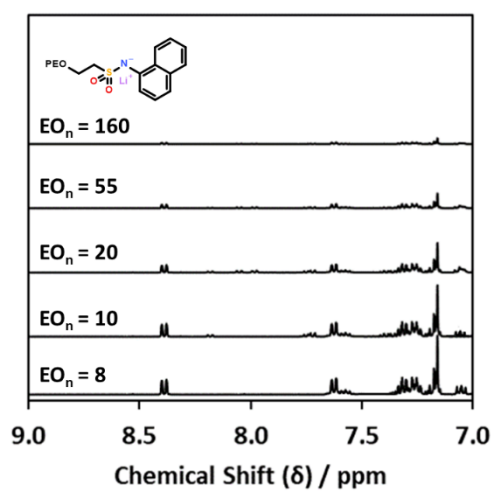
mPEO_n-N(Li)Pyr



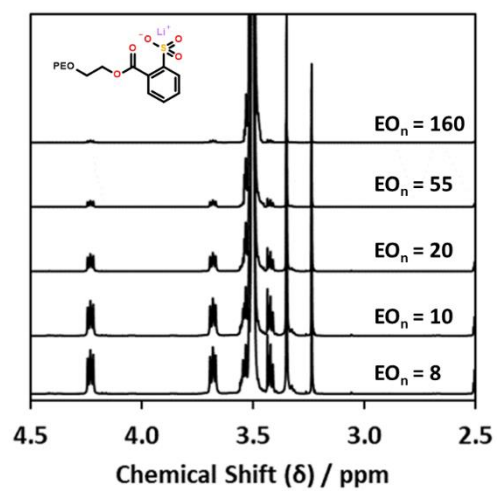
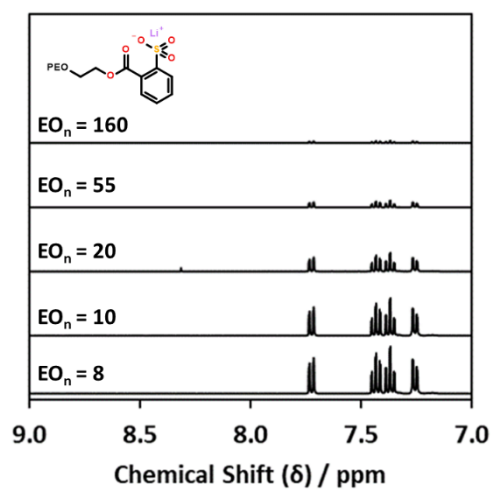
mPEO_n-SO₃Li



mPEO_n-SO₂N(Li)Naph



mPEO_n-PhSO₃Li



Résumé de Thèse en Français

Une batterie est composée de deux électrodes séparées par un électrolyte. La décharge de la batterie est déterminée par sa tension (c'est-à-dire la différence entre les potentiels chimiques des électrodes). Le flux de courant à travers le circuit externe est équilibré par le flux d'ions à travers l'électrolyte. Si une excellente conductivité ionique est nécessaire, l'électrolyte doit également **i)** être compatible avec l'électrochimie des électrodes, **ii)** former des interfaces stables pour l'échange d'ions et **iii)** fonctionner en toute sécurité dans une plage de températures donnée. Les polymères sont des matériaux viscoélastiques non-inflammables bien adaptés à des cellules sûres à haute densité d'énergie. La conception spécifique d'électrolyte polymère ici présentée offre une conductivité ionique élevée à température ambiante sur une plage de potentiels applicable pour des batteries. Un modèle conceptuel pour le transport des ions lithium dans ces électrolytes polymères est proposé.

Mots-Clés: Chimie macromoléculaire, Polymère, Electrolyte, Transport Ionique

General Abstract in English

A battery comprises two electrodes separated by an electrolyte. The spontaneous discharge of the battery is determined by its voltage (*i.e.* the difference between the chemical potentials of the electrodes). The flow of current through the external circuit is balanced by the flow of ions through the electrolyte. Not only is excellent ionic conductivity needed, but the electrolyte must also **i)** be compatible with the (electro)chemistry of the electrodes, **ii)** form a stable interface for the exchange of ions, and **iii)** function safely and as intended over a practical temperature range. Polymers are non-flammable, viscoelastic materials well-suited for the construction of safe, high energy density cells. The specific polymer electrolyte design developed here affords high ionic conductivity at ambient temperatures over an applicable range of cell potentials. A conceptual model for the transport of lithium ions in these polymer electrolytes is proposed.

Key words: Macromolecular Chemistry, Polymer, Electrolyte, Ionic Transport